**Phone : +90 (312) 201 10 00**
**Fax : +90 (312) 287 91 88**
**Adress : MTA 06530 - Ankara - TURKEY**
**www.mta.gov.tr**

166

BULLETIN OF THE MINERAL RESEARCH AND EXPLORATION

2021

# BULLETIN OF THE MINERAL RESEARCH AND EXPLORATION

Foreign Edition | 2021 | 166 | ISSN : 0026-4563 E-ISSN : 2651-3048

## CONTENTS

# BULLETIN OF THE MINERAL RESEARCH AND EXPLORATION

Foreign Edition | 2021 | 166 | ISSN : 0026-4563 E-ISSN : 2651-3048

# CONTENTS

**LOCATION OF MANAGEMENT**
MTA Genel Müdürlüğü
BDT Dairesi Başkanlığı
Çukurambar Mahallesi Dumlupınar Bulvarı No: 33/A 06530 Çankaya/ANKARA
e-mail: bilimsel_dairesi@mta.gov.tr

The translation of Ergüler et al. was made by Gülsüm TURGUT. The translations of Güney et al. and Meriç et al. were made by Alper BOZKURT. The translation of Darbaş et al. was made by Ekrem ÖZCAN. The translation of Deniz et al. was made by Catherien YİĞİT.

Bull. Min. Res. Exp. is indexed and abstracted in TR Dizin, Emerging Source Citation Index (ESCI), Scopus, The ICI Journals Master List (Copernicus), Directory of Open Access Journals (DOAJ), Open Academic Journals Index (OAJI), Georef, MIAR, EBSCO and Zoological Record.

The Bulletin of the Mineral Research and Exploration is published in three issues in a year. Each bulletin is printed in Turkish and English languages as two separate issues. The English and Turkish issues of the "Bulletin of the Mineral Research and Exploration" can be obtained from "BDT Department" free of charge, either directly or ordered by adding postage fee from the correspondence address. Typesetting and printing operations are carried out and followed by the Publication Service of the Scientific Documentation and Publicity Department. Typesetting and Print Review: Yaşar Özkan, Tuğba Uğur Aydın e-mail: bdt@mta.gov.tr

The section of "notes to the authors", format, copyright and other information can be obtained from www.mta.gov.tr as PDF files.
Printed Date:
Printing House: Kuban Matbaacılık - İvedik Organize Sanayi Matbaacılar Sitesi 1514. Sokak No: 20 • Phone: 0312 395 2070 • Fax: 0312 395 3723 • www.kubanmatbaa.com
Periodical
ISSN: 0026-4563
E-ISSN: 2651-3048

Bulletin of the Mineral Research and Exploration

http://bulletin.mta.gov.tr

# Investigation of the effect of fly ash released from Kütahya thermal power plants by using remote sensing methods

Güzide KALYONCU ERGÜLER[a*], Fatma Melis BAYINDIR[b] and Ayşe DAĞLIYAR[b]

[a]*General Directorate of Mineral Research and Exploration, Department of Environmental Research, Çankaya, Ankara,Turkey*
[b]*General Directorate of Mineral Research and Exploration, Department of Geological Research, Çankaya, Ankara, Turkey*

*Research Article*

Keywords:
Ash Vegetation Interaction, Landsat 8, Seyitömer, Tunçbilek, Fly Ash.

*Received Date: 23.05.2020*
*Accepted Date: 22.05.2021*

**ABSTRACT**

In order to determine the long-term effect of thermal power plants, the satellite images of Seyitömer and Tunçbilek Thermal Power Plants and their vicinities were analyzed by using the software of ERDAS IMAGINE v9.1 and PCI Geomatica 2017. The normalized difference vegetation index (NDVI) was determined by using red and near-infrared bands of Landsat satellite images, and areas containing vegetation were revealed in the images. In order to obtain the temporal change in the vegetation areas, the relevant image change detection analysis was applied and the one-year and thirty-year temporal change of vegetation cover is for r = 4 km, r = 12 km, r = 50 km. In the remote sensing mapping studies, it was determined that as the diameter of the assessment area increases, the dominant wind loses its effect, and geomorphological conditions are more prominent.

## 1. Introduction

Our country is foreign-dependent because of energy needs and has to provide 95% of this need from neighboring countries. On the other hand, with high-speed train technology and increasing industrialization, it also provides some of this need with domestic resources. Fossil fuels such as lignite, especially in the western Anatolia found in the Neogene basins, have been used for many years. Despite climate change caused by greenhouse gases caused by the use of fossil fuels such as lignite and coal, and air pollution that directly affects human health, its use in global electricity generation continues both in our country and internationally. In their analyzes and evaluations based on the information obtained from different sources, Health and Environment Alliance (HEAL, 2018) stated that 65% of global electricity was generated from fossil fuels in 2016 and in Turkey, as of November 2018, lignite was used in 16 of 27 thermal power plants in operation and 52% of 19.9 GW coal-based installed power.

Consider the factors that may cause a decrease in vegetation; cases such as the effect of population, mining activities, climate, etc. come to mind first. While an increase is expected in the cultivated area as the population increases, there is a decrease in cultivation areas due to the reduction of population in the provinces such as Kütahya, which gives large numbers of immigrants. Due to the production methodology in mining activities, especially in open-pit mining, a reduction in vegetation areas is likely due to the removal of the cover soil. However, it is possible to see partial increases in vegetation areas with re-rehabilitation works in areas where production is completed. The impact of climate change can be

Citation Info: Kalyoncu Ergüler, G., Bayındır, M. F., Dağlıyar, A. 2021. Investigation of the effect of fly ash released from Kütahya thermal power plants by using remote sensing methods. Bulletin of the Mineral Research and Exploration 166, 1-18. https://doi.org/10.19111/bulletinofmre.946782

**Corresponding author: Güzide KALYONCU ERGÜLER, guzidek.erguler@mta.gov.tr*

evaluated by observing with longer-term studies. It has been emphasized in previous studies that thermal power plants cause environmental problems on a local scale, such as a decrease in vegetation areas in their vicinity, as well as their impact on human health and climate change. The main pollutants formed as a result of the burning of fossil fuels such as lignite used in these power plants can be listed as; carbon dioxide ($CO_2$), carbon monoxide (CO), nitrogen oxides ($NO_x$), volatile organic compounds (UOC), sulfur dioxide ($SO_2$), methane ($CH_4$) and such gases and particulate matters. Fossil fuels such as coal and lignite burned in thermal power plants cause ash and heavy metals such as cadmium, mercury, lead, arsenic, etc., contained in the ash (Kır, 2008) spread easily and quickly to the environment. In addition, sulfur, nitrogen, and carbon oxides released from the chimneys combine with water vapor in the air to form acid rain, and as a result, they mix with the groundwater and cause the stomata that control transpiration and gas exchange in the plant, not to work effectively. This condition of plant stomata can dry out the plant (Mol, 1986; Haktanır and Karaca, 1996; Ölgen and Gür, 2012). As a result of the effect of $SO_2$, $NO_x$ and particulate matter released from the power plant chimneys, the fruit yield of many field crops, fruit trees, and olives in large areas may decrease significantly (Goncaloğlu et al., 2000). In the study by Haktanır et al. (2010), the effects of emissions of Muğla - Yatağan thermal power plant on the heavy metal content based on the dominant wind direction of agricultural and forest soils surrounding the plant were investigated. Karaca et al. (2009) stated in their study on the vicinity of Çayırhan thermal power plant that the total Cd values of the soils taken from the dominant wind direction are quite high compared to the soils taken from the opposite of the dominant wind direction and above the limit values of the soil pollution control regulation.

When examined as chemical composition, it is observed that fly ash consists of compounds including $SiO_2$, $Fe_2O_3$, and MgO. Fly ash surface areas are quite high and vary between 1 - 16 $m^2/cm^{-3}$ according to grain size (Adriano et al., 1980; Schure, 1985). The amount of carbon that can be found in it varies according to the type of coal and the burning process. In addition, fly ash has been used as a raw material in various applications for over 80 years (Heidrich et al., 2013). According to the 2017 data of the Turkish Statistical Institute (TURKSTAT), a total of 19.5 million tons of waste, 87.8% of which is ash and slag, was generated in the thermal power plants. TURKSTAT (2017) stated that only 16.7% of these produced wastes were sent to waste recovery facilities and mines for filling material usage.

Subjects such as researching the effects of waste generated by thermal power plants on the environment and doing sustainable projects against possible environmental problems (Davraz and Kılınçarslan, 2020) have been studied by scientists using different methods in recent years. In this sense, in the study carried out by Akkartal et al. (2005) and Şekertekin et al. (2015), it was stated that remote sensing technology is also an effective method in terms of observing critical environmental changes. For this purpose, vegetation indices are used to determine the distribution of green vegetation on the earth and monitor the change in vegetation density. Many factors such as migration, population decrease, easy supply in developing city life, fly ash emission from thermal power plants are effective on the reduction in vegetation areas obtained in remote sensing. In order to determine the factor on the main plant decline, it is crucial to examine the wind direction, which is one of the meteorological data, to determine whether the reduction directions in the vegetation areas are related to the wind.

Ability to read satellite images by computer without the need for digitization and to be integrated with Geographic Information Systems (GIS), allowing them to be updated regularly and to monitor the changes that occur, and to display situations that the human eye cannot see with its multi-band sensors, make remote sensing methods even more important (Duran, 2007). Generally, plants absorb rays with a wavelength of 0.4 – 0.7 μm, called the visible ray region. Infrared rays, on the other hand, absorb very little and reflect a large part of it (Teillet et al., 1997). Singh et al. (1997) revealed that from 1975 to 1991, fly ash and other impacts from coal mining caused significant loss of forest cover and agricultural lands. Feng et al. (2013) analyzed the change in Wucai Wan open-pit coal mine between 2006 and 2011 based on vegetation index and Landsat TM satellite remote sensing data.

As summarized above, in international studies, many studies covering the effect of thermal power plants on plant decline and the investigation of

the measures taken have been carried out until today. Also, in our country, many studies on the environmental effects of thermal power plants have been carried out in the form of soil, water and plant studies. Makineci and Sevgi (2005) investigated the effects of fly ash from the Seyitömer thermal power plant on the annual ring growth of larch trees. Akçın and Şekertekin (2016) generated pollution maps for the Western Black Sea Region with variogram models and kriging approximation in their study on the temporal investigating coal-based pollution using Landsat 8 images and geostatistical analyses for sustainable basin management. In order to investigate the air quality of Zonguldak province, Zeydan and Yıldırım (2013) examined the emission factors used in the calculation of the Çatalağzı thermal power plant emissions. The analysis of the environmental effects of Kangal and Çan thermal power plants based on their material properties was carried out by Şengül (2002) and Ilgar (2008), respectively. However, as can be clearly seen from these previous studies, it is understood that remote sensing analysis maps, which are thought to be important in terms of providing more accurate results and being less costly, are not used to investigate the effect of fly ash released from thermal power plants on the spatial change of plant reduction. Therefore, within the scope of this study, considering these limitations and the presence of 264 endemic plant species belonging to 40 plant families and many monumental trees in and around Kütahya (Tatlı et al., 1999), the release of two different fly ashes from Tunçbilek and Seyitömer thermal power plants was investigated in the remote sensing maps of the spatial variation of the plants originating from the thermal power plant. The increase or decrease in the vegetation areas with the dominant wind direction studies, the annual change with the remote sensing maps and the change in the thirty-year time period in order to compare with the situation before the thermal power plants were opened were examined.

## 2. Background and Geology of Study Areas

Tunçbilek and Seyitömer thermal power plants and their surroundings, located within the provincial borders of Kütahya, which provide a significant part of our country's energy needs, have been determined as the study area (Figure 1). The province of Kütahya is well-known as one of the most generous provinces in terms of many different mining activities, mainly lignite and boron, silver, magnesite, etc. Seyitömer thermal power plant is located approximately 20 km northwest of Kütahya city centre. This thermal power plant consists of four units, which were put into operation in 1973, 1974, 1977 and 1989, respectively, and has a total power of 600 MW. Tunçbilek thermal power plant is located approximately 51 km northwest of Kütahya city center, and it is nearly 36.4 km away from the Seyitömer thermal power plant. Tunçbilek thermal power plant, with an installed power of approximately 365 MW, uses about 7000 tons of lignite extracted from the Tunçbilek basin in the region (Oruç, 1999; Çiçek and Koparal, 2004).

Seyitömer lignite basin consists of Neogene aged lacustrine deposits (Sarıyıldız, 1987; Türkmenoğlu and Yavuz Işık, 2008; Özburan et al., 2012). Based on the paleontological studies, these sediments were dated as Late Miocene - Early Pliocene (Özcan, 1986). Serpentinites belong to the Mesozoic ophiolite assemblage from the basement rocks of the Seyitömer lignite basin. Basement sediments starting with conglomerate continue with base clays varying in blue-green hue. The main lignite seam, which is one of the most important sources of the Seyitömer thermal power plant, is located on the units consisting of these base sediments. On the ceiling of the main lignite seam, there is a series of clay-containing rocks such as marl. Above these units forming the ceiling series, there is an upper lignite seam with claystone, mudstone and marl interlayers. As mentioned in previous studies, the Seyitömer lignite field does not show a complicated case in terms of its geological structure since it is not under the influence of large-scale tectonic movements, and the layers generally have a low slope to the south in most of the basin. The thickness of the main lignite seam is about 16 meters, and the thickness of the upper lignite seam is about 10 meters (Sarıyıldız, 1987). The Kocayatak formation overlies the Seyitömer formation unconformably (Sarıyıldız, 1987). The Kocayatak formation generally consists of conglomerate and sandstones occurring in various components. The conglomerates are greenish grayish, less hardened and very loose. The layers of the conglomerates are thick and partly irregular, and the grains are medium and poorly sorted.

Metamorphics and ophiolitic melange constitute the basement rocks of the geological units outcropping in the Tunçbilek region. The Neogene units of the

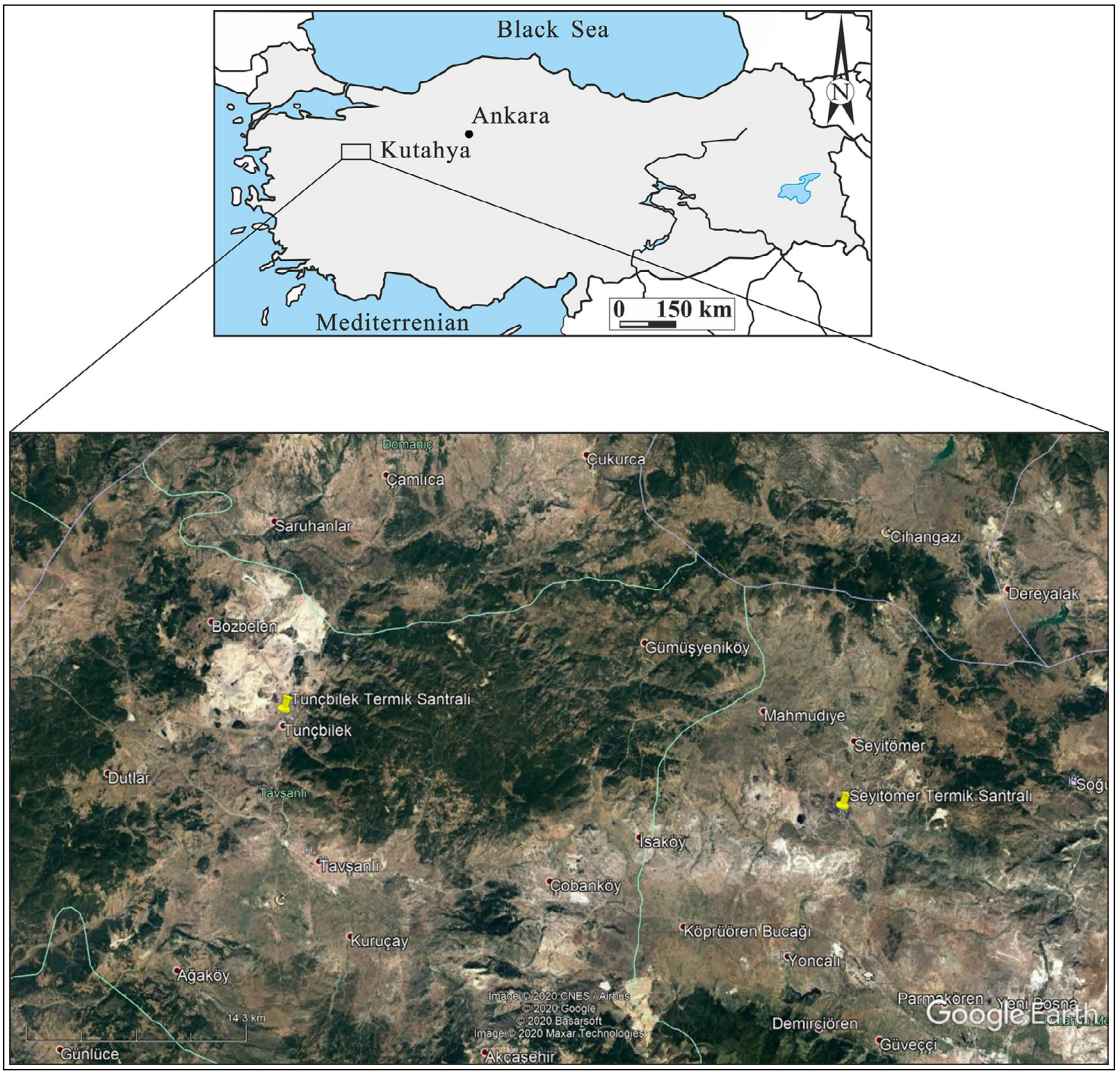


Figure 1- Location map of the study area (close-up satellite image prepared using Google Earth in 2020).

Tunçbilek basin begin with the Beke formation formed by the stream regime. The Beke formation, reaching up to 1000 m in thickness in some sections, is observed in the form of conglomerate, sandstone, mudstone and fine coal seams that thin out upwards (Çelik, 2000). It is determined that the conglomerates of this formation are generally older ophiolitic rocks. This unit is overlain by the Tunçbilek formation, which includes the economically important lignite layers in the Tunçbilek basin. As mentioned by previous researchers (Baş, 1983), the thickness of these lignite layer levels varies between 7 - 15 m. In addition, thin claystone layers are occasionally found in the lignite levels. Younger units occur an alternation of claystone and marl, which can reach up to 300 m, are located on the Tunçbilek formation, and the geological sequence in the region is complemented by clayey limestone. Lavas, tuffs, and limestones belonging to the Domanic Series are found on the top of the lignite and fine clastic sediments (Nebert, 1960).

## 3. Characteristics of Fly Ash Released from Thermal Power Plants

Fly ash released from Tunçbilek and Seyitömer thermal power plants was used in this study, and the ash samples are taken, typical images of the thermal power plant and its surroundings are given in Figure 2. The fly ashes taken from the Seyitömer thermal power plant generally have a composition with a high concentration of an amorphous substance, KCaFeMgAl - silicate. Fly ash grains contain silica, feldspar and Fe-oxide minerals, and the Ca and Fe content of the gray parts are low, while the Ca and


Figure 2- a) General view of the thermal power plant, b) taking the fly ash sample from the thermal chimney, and c) a general view of the area affected by fly ash.

Fe content of the white-coloured non-porous parts of the same grain are higher. Also, unburned carbon, Ca and S are present, and small amounts of pentlandite, apatite, melilite and Ti-Oxide have been observed. The detected mullites contain small amounts of Mg, K, Fe. The fly ash released by the Tunçbilek thermal power plant was commonly found to be an amorphous and MgAl - silicate composition. There is relatively more Fe, Ca and lesser amounts of Na, K and Ti. Mullite and albeit a little micron-sized ankerite, Ni-Sulfur containing traces of Co and Fe, FeAl - Oxide (spinel / hersinite), rutile and ilmenite were determined in the fly ash. The major element analyzes on fly ash samples taken from Tunçbilek and Seyitömer thermal power plants and analyses for determining their physical properties were carried out in MTA laboratories. The values and physical properties of the major elements obtained from the analyzes made in the XRF spectrometer are presented in Table 1. The physical properties of fly ash are the most important parameters that carry out transport, and the effect it gives to the environment varies in proportion to the amount of heavy metal it contains.

## 4. Meteorological Data and Vegetation

Although Kütahya is located in the Aegean Region, its climate is quite different from the coastal Aegean, depending on the distance from the sea and the altitude. The climate of Kütahya and its surroundings are transitional with the Aegean, Central Anatolia and Marmara climates. Based on climate and temperature conditions, it covers the characteristics of the surrounding regions, its temperature characteristics are more like Central Anatolia and its precipitation characteristics resemble the Marmara Region. The monthly variation of the average meteorological data of Kütahya province between 1929 - 2019 was obtained from the Turkish State Meteorological Service (TSMS) and presented in Table 2.

Considering the records given in Table 2, it is understood that Kütahya has a hot and dry climate in summers and a cold and rainy climate in winters. The annual average temperature in the region was 10.7º and the highest measured temperature was 39.5º. It was determined that the lowest temperature measured in Kütahya between the relevant dates was -28.1º. The

Table 1- Major element values and physical properties of fly ash emitted from Tunçbilek and Seyitömer thermal power plants.

| Major element | | | | | | | | | | | |
|---|---|---|---|---|---|---|---|---|---|---|---|
| Central | A.Za. (%) | $Al_2O_3$ (%) | $SiO_2$ (%) | $Fe_2O_3$ (%) | $Cr_2O_3$ (%) | CaO (%) | $K_2O_3$ (%) | MgO (%) | $Na_2O$ (%) | $SO_3$ (%) | $SiO_2$ (%) |
| Seyitömer | 2.21 | 24.01 | 37.18 | 6.27 | 0.02 | 3.06 | 2.1 | 3.22 | 0.60 | 0.32 | 21.01 |
| Tunçbilek | 1.49 | 11.87 | 41.57 | 9.21 | 0.01 | 1.39 | 0.98 | 3.72 | 0.32 | 0.56 | 28.88 |

| Physical properties | | | | |
|---|---|---|---|---|
| Central | Grain size (µm) | Specific surface area ($m^2/g$) | Density ($mg/m^3$) | pH |
| Seyitömer | 0.5-17.0 | 0.36 | 2.14 | 8.3 |
| Tunçbilek | 1.0-22.0 | 0.38 | 2.25 | 8.1 |

Table 2- Monthly variation of the average meteorological data for Kütahya 1929 - 2019 (TSMS, 2020).

| Meteorological data | January | February | March | April | May | June | July | August | Septemper | October | November | Decemper | Annual |
|---|---|---|---|---|---|---|---|---|---|---|---|---|---|
| T (°C) | 0.3 | 1.7 | 4.9 | 9.9 | 14.5 | 18.2 | 20.7 | 20.7 | 16.6 | 11.8 | 6.8 | 2.3 | 10.7 |
| $T_{avg-max}$ (°C) | 4.6 | 6.6 | 10.8 | 16.2 | 21.1 | 25.0 | 28.0 | 28.3 | 24.5 | 19.0 | 12.7 | 6.5 | 16.9 |
| $T_{avg-min}$ (°C) | -3.3 | -2.4 | -0.1 | 3.8 | 7.8 | 10.8 | 13.0 | 13.0 | 9.1 | 5.5 | 1.9 | -1.1 | 4.8 |
| S (hour) | 2.3 | 3.4 | 4.6 | 6.1 | 7.5 | 9.3 | 10.3 | 9.6 | 7.6 | 5.2 | 3.6 | 2.1 | 71.6 |
| $P_{day}$ | 14.6 | 13.1 | 13.0 | 11.6 | 12.2 | 8.1 | 3.9 | 3.3 | 4.7 | 8.3 | 10.0 | 14.2 | 117.0 |
| $P_{top}$ | 72.2 | 59.2 | 57.1 | 50.4 | 55.9 | 38.9 | 19.7 | 17.7 | 23.3 | 41.1 | 49.2 | 78.1 | 562.8 |
| $T_{max}$ (°C) | 17.1 | 24.2 | 27.0 | 30.2 | 33.8 | 36.2 | 39.5 | 38.8 | 36.1 | 31.6 | 25.4 | 21.7 | 39.5 |
| $T_{min}$ (°C) | -26.3 | -27.4 | -16.6 | -7.8 | -2.8 | 0.5 | 2.6 | -0.2 | -3.9 | -6.9 | -11.0 | -28.1 | -28.1 |

T: average temperature. $T_{avg-max}$: average highest temperature. $T_{avg-min}$: average lowest temperature. S: average sunshine duration. $P_{day}$: average number of rainy days. $P_{top}$: average monthly total precipitation. $T_{max}$: highest temperature. $T_{min}$: lowest temperature.

wettest and driest months in the region are December and August, respectively and the annual average precipitation was recorded as 565 mm. It has been determined that 38.8% of these precipitations occur in winter, 29.4% in spring, 12.5% in summer and 19.3% in autumn. In winter, precipitation is generally in the form of snow due to the low temperature and high altitude while it is observed as rain in other seasons. The annual average number of snowy days is 19 days and the average snow thickness is around 12 cm.

As indicated in previous studies, wind speed and direction are the most important input parameters that are effective in the transport of fly ash released from thermal power plants. Considering the importance of these parameters in terms of fly ash transport, the records from the 17155 coded meteorology stations between 2010 and 2016 were evaluated. Based on these records, it was determined that the dominant wind direction was effective in all directions, especially N, NW, and NE. Although the dominant wind direction is similar in spring, summer and autumn periods. It has been determined that the E and SE winds are more dominant in the winter months (Figure 3). For Kütahya, the average wind speed was determined as

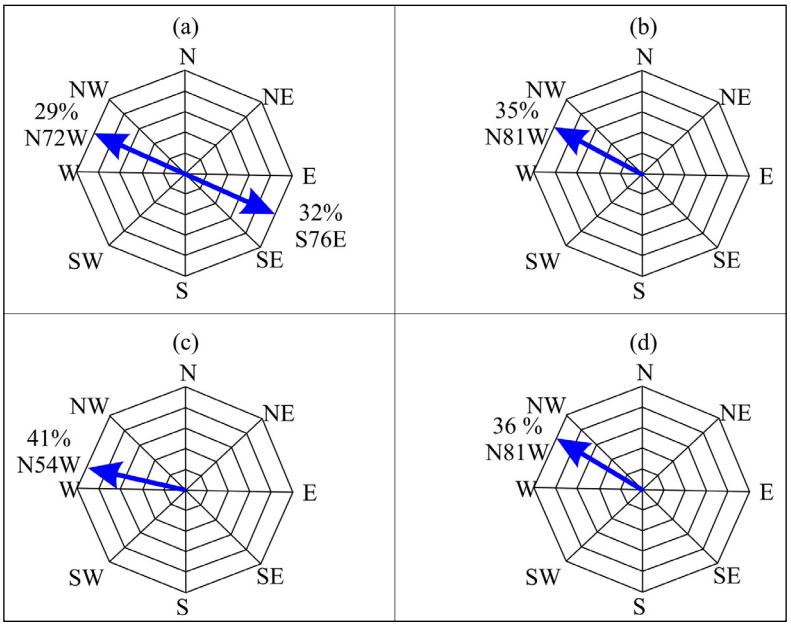


Figure 3- Kütahya province dominant wind direction diagrams; a) winter, b) spring, c) summer, and d) autumn (modified from Karpuz, 2015).

1.7 m/s when all seasons were evaluated with 5% frequency of 0 - 2 km/h calm breezy winds in annual and seasonal wind roses. 11% frequent north and northeast winds in the summer. It was determined that the highest measured wind speed was 27.6 m/s and it belongs to the northwestern wind. Since the winds at low speeds observed in Kütahya will not contribute much to the horizontal transport of emissions from air pollution sources. They will be more effective in the region where pollution occurs at these speeds. Air pressure around Kütahya varies between 873 and 928.4 millibars with an average value of 904.7 millibars. Karpuz (2015) examined the climate of Kütahya province between 1971 and 2014 in his study.

Kütahya has an area of 1.279.000.000 hectares. and 611.592.000 hectares of this area are forests. According to Tatlı and Tel (1999), 52.97% of the province comprises forest areas while the proportion of forests in the plateaus is around 2 - 3%. 296.644.000 hectares of forest areas can be defined as productive forests with an economic value of 48%. Nearly half of the trees are larch. The rest is 14% oak, 6% juniper, 5% red pine, 2% beech and rarely cedar, alder, chestnut, poplar, fir as listed according to the degree of density. On the other hand, steppe plants such as poppy, sagebrush, sorrel, shepherd's purse, snapdragon are also commonly observed (Tatlı et al., 1999). As altitude increases, temperature and relative humidity decrease, and precipitation, evaporation, daily temperature differences and radiation intensity from wind and sun increase in general. In addition, with the increase in height the vegetation and soil formation period is shortened. The effect of topography on plant life depends on the exposure as well as altitude. It has been mentioned in previous studies (Aydınözü, 2008) that tectonic movements as well as the river network play an important role in the change of morphology in the region.

## 5. Remote Sensing Studies

Landsat is a series of earth observation satellites that was launched with the name of Earth Resources Technology Satellite by the United States on 23 July 1972 Landsat 1 sent to space by NASA in 1972 can make land mapping by 3 multispectral bands in the near - infrared region. The dimensions of the images taken from these satellites are 170 x 183 km. Landsat 8 is the latest launched (in 2013) Landsat satellite and carries Operational Land Imager (OLI) and the Thermal InfraRed Sensor (TIRS) devices. The data obtained from uninterrupted space-sourced earth images in over fifty years are very commonly used in application areas such as mining, geology, forestry, city - region planning, oceanography, land applications and field change determinations. Used images were provided from the web page of the United States Geological Survey (USGS).

In this study, Seyitömer and Tunçbilek thermal power plants and their surroundings are examined by using remote sensing data and techniques. Landsat MSS image dated 1987 and Landsat 8 OLI/TIRS image dated 2017 were used. Information on satellite images is given in Table 3. Satellite images were analyzed by using the Global Mapper 12 ERDAS IMAGINE v9.1 and PCI Geomatica 2017 software and mapped to 1/250.000 scale with the ArcMap v9.2 software by performing geometric and atmospheric corrections.

Table 3- Satellite information of Landsat MSS and 8 OLI/TIRS used in the study area.

| Image Name | Granul ID - Path/Row | Date |
|---|---|---|
| Landsat MSS | LM05_L1TP_179032 | 30.06.1987 |
| | LM05_L1TP_179033 | 30.06.1987 |
| | LC08_L1TP_179032 | 02.07.2017 |
| Landsat 8 OLI/TIRS | LC08_L1TP_179033 | 02.07.2017 |
| | LC08_L1TP_179032 | 05.07.2018 |
| | LC08_L1TP_179033 | 05.07.2018 |

## 6. Research Findings

The remote sensing methods have a great importance in determining the information to be used in the correct determination, usage and protection of natural resources, ensuring balanced and sustainability, multi-faceted use and approaches that can adapt to environmental changes in the long term. With today's conditions, the right decisions can be made in a short time with less costs.

The Landsat 8 OLI / TIRS images were mapped by using pseudo-color composites in order to observe the vegetation areas in the study area. Red hues in pseudo-color composite images show the flora. The 2018 dated Landsat 8 OLI / TIRS image used in the study indicates a cloud and its shadow. To analyze the correct vegetation, the water, cloud and cloud

shadows in the images were masked and were not included in the analysis. By using the red and near-infrared bands of the Landsat satellite images, the normalized plant diversity index was calculated and the areas containing vegetation were revealed in the images. The plant areas are shown with a red colour in Figures 4a and b by using pseudo-color composite (KYM: 543) on the Landsat 8 OLI / TIRS images. Normalized plant difference index maps obtained for Landsat 8 OLI / TIRS images are given in Figures 4c and d. NDVI parameters are shown in Table 4. Among the parameters required for the temporal variation technique; i) two satellite images with different dates covering the same area, ii) the same resolution value, and iii) having the same projection information are provided in this study in order to obtain the temporal change in the vegetation areas of the study area. Change detection analysis was applied by using the

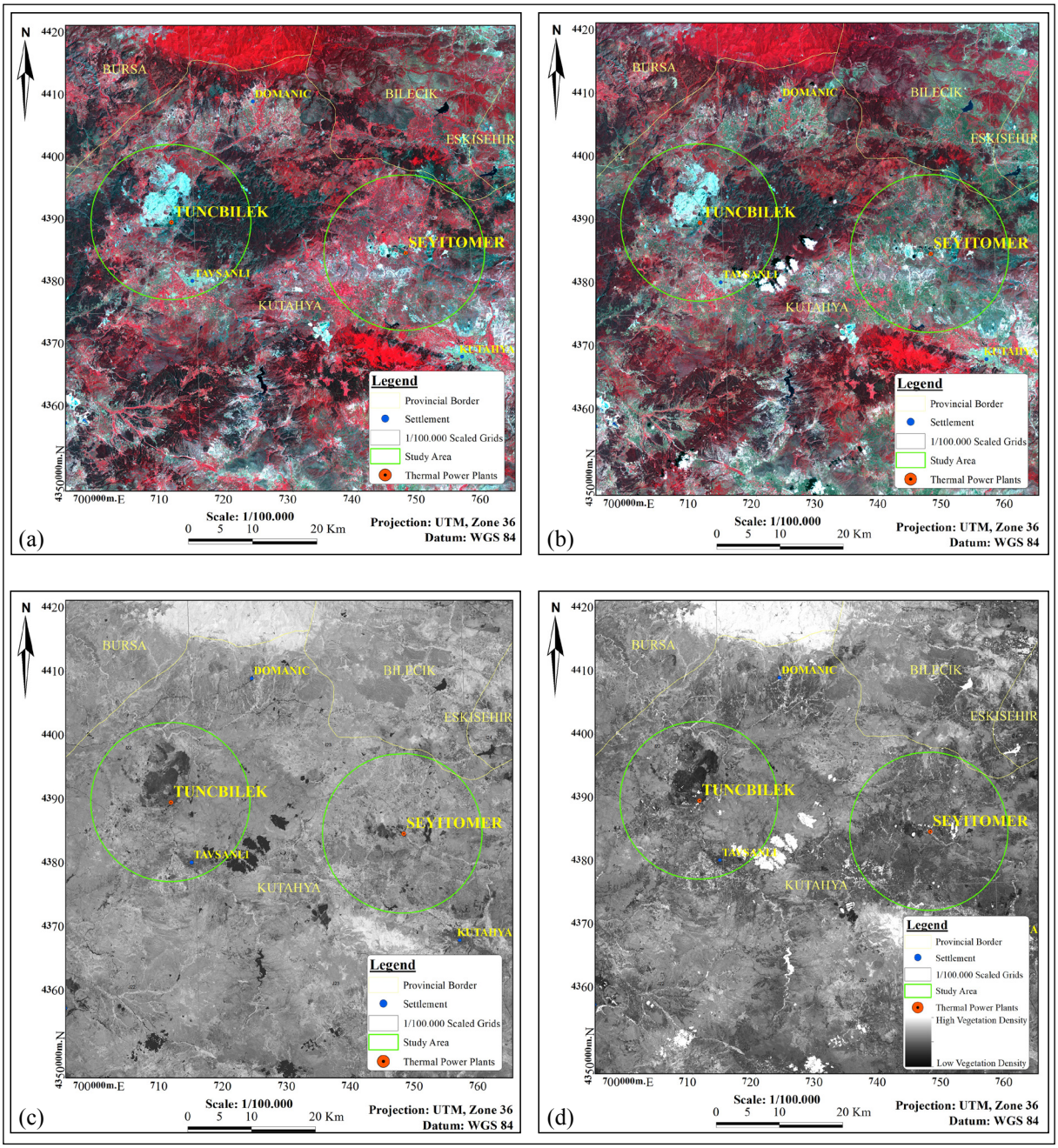


Figure 4- 1/100.000 scale false color composite (KYM: 543) of Landsat 8 OLI / TIRS images; a) 2017, b) 2018 and normalized plant diversity index maps, c) 2017 (threshold value = 0.51) and, d) 2018 (threshold = 0.47).

relevant images and the 1-year temporal change of the vegetation was obtained. Very light (white and near-white) and dark (black) tones emphasize the changes of vegetation over time. Lighter tones indicate an increase in the plant while darker tones indicate a decrease in the plant.

Table 4- NDVI parameter findings belongs to the examination area.

| Parameters | NDVI 2017 | NDVI 2018 |
|---|---|---|
| Arithmetic Mean | 0.251449 | 0.2264444 |
| Standard Deviation | 0.163527 | 0.151905 |
| 0.5 sigma | 0.3332125 | 0.3023969 |
| 1 sigma | 0.414976 | 0.3783494 |
| 1.5 sigma | 0.4967395 | 0.4543019 |
| 2 sigma | 0.578503 | 0.5302544 |
| 2.25 sigma | 0.6193848 | 0.5682307 |
| 2.5 sigma | 0.6602665 | 0.6062069 |
| 3 sigma | 0.74203 | 0.6821594 |
| Mask | Vnir Mask | Vnir Mask |
| Threshold Value | 0.51 | 0.47 |

NDVI is a standard and effective method that is one of the important classification methods widely used in determining land cover and land use changes (Lyon et al., 1998; Rouse et al., 1974). The NDVI positive values indicate active vegetation while values are close to zero or negative represent other types of material. Accuracy analyses were carried out including both conditions considering the field of study with and without vegetation. 40 points were determined on the Google Earth program. 20 of which were vegetated and 20 of which were not vegetated (Figure 6). The 2017 and 2018 NDVI images were classified into two groups: i) the vegetated area above and below the threshold value and ii) the non-vegetated area below the threshold value. The characteristics of the NDVI images and the characteristics of the points taken from Google Earth were combined in the same table and their differences were taken. According to this, the accuracy of the 2017 NDVI image is 67.5% while the accuracy of the 2018 NDVI image is 62.5%. Since it is taken into consideration that the dates of the Google Earth image and NDVI images are different. The accuracy percentages for the same possible dates are going to be higher and therefore the comparison is going to be quite meaningful.

As Erener (2011) stated in her study when traditional data collection methods and remote sensing studies are compared, changes in plant areas can be determined with a clearer and lower cost in environmental conditions. Mondal et al. (2016) stated the change according to the dominant wind direction in their study to interpret the effect of a thermal power

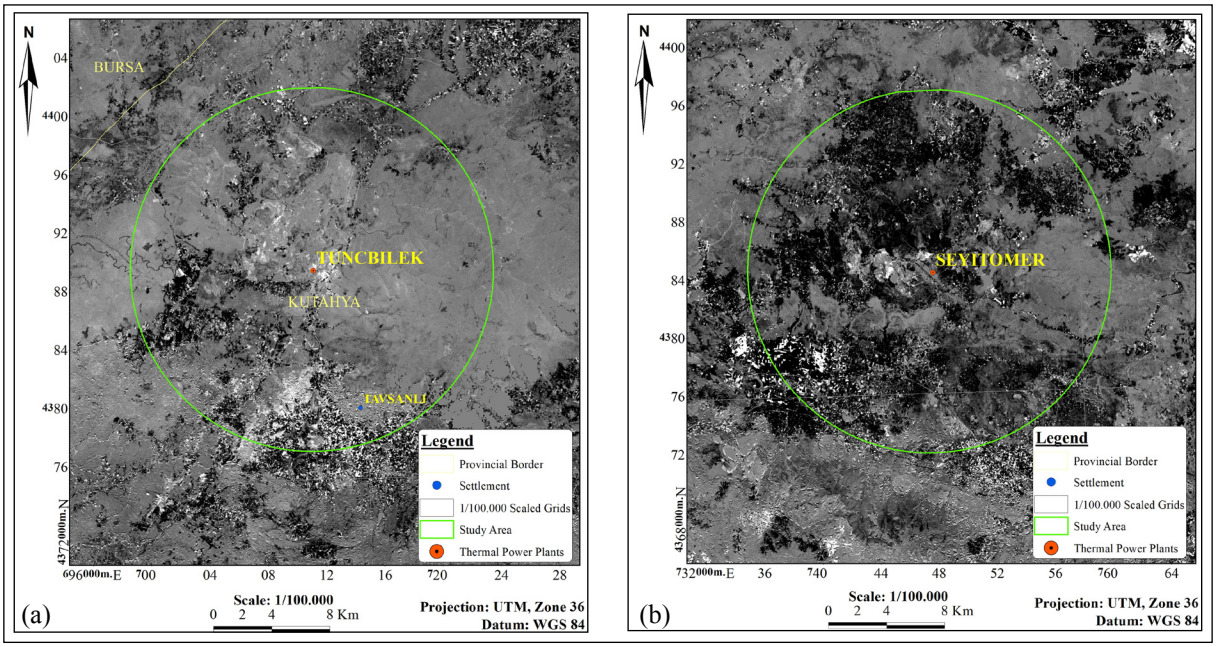


Figure 5- 1/50.000 scaled temporal change map of ; a) Tunçbilek and, b) Seyitömer thermal power plant and its surrounding vegetation obtained from Landsat images dated 2017 and 2018.

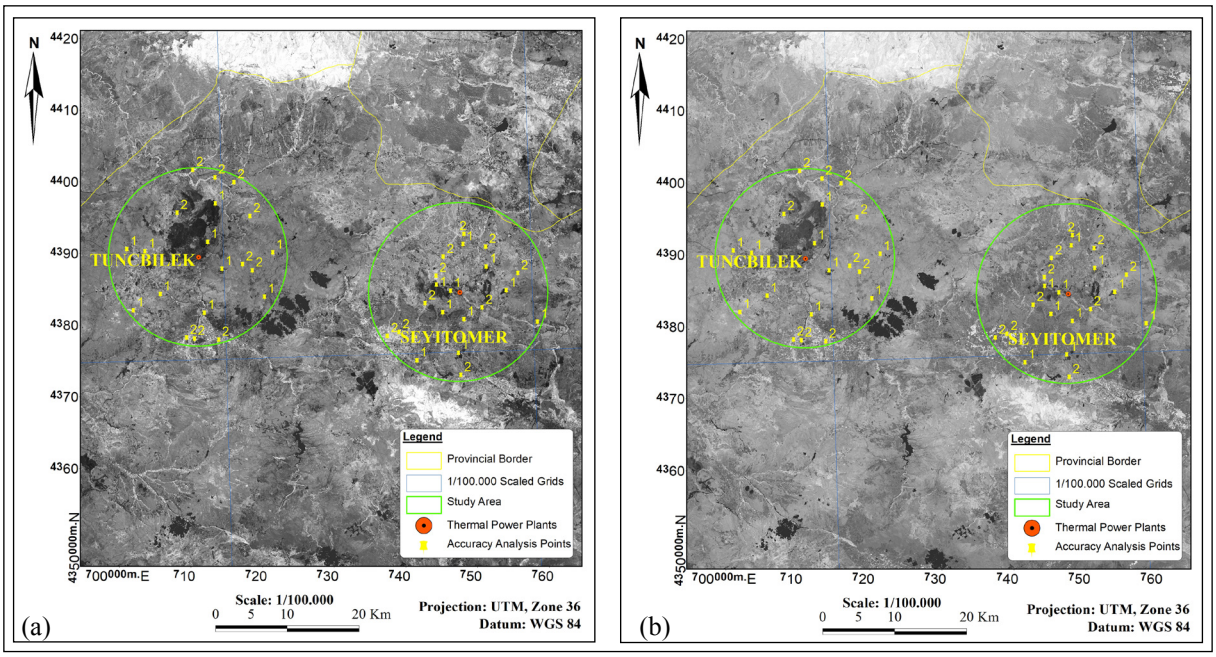


Figure 6- Accuracy analysis points shown on the 1/100.000 scaled normalized plant diversity index maps of Landsat 8 OLI / TIRS images of ; a) 2017 and b) 2018.

plant in Kolaghat on the vegetation and soil in the surrounding areas. For the one-year change finding within the scope of this study; the decrease in the vegetation areas on the map obtained as a result of the temporal variation technique applied to the images dated 02.07.2017 and 05.07.2018 were calculated by means of remote sensing techniques considering the spatial resolutions of the satellite images (Figure 5). The direction of change in plant areas was determined with the help of the ArcGIS program - Polar Plots application and shown with the direction diagram in Figure 7. The decrease in the vegetation areas in Tunçbilek and its surroundings is N - S oriented and is shown in Figure 7a with green. The increase in the plant areas observed in this vicinity was determined to be predominantly N30° E - S30° W oriented, and N - S and N45° E - S45° W oriented in the second degree. According to this, while a decrease of approximately 65.8 km$^2$ was observed in the plant areas in Tunçbilek and its surroundings (Figure 7a; black areas), 8.9 km$^2$ increase was determined (Figure 7a; white areas). The increase in the vegetation areas in Seyitömer and its surroundings is N30° W - S30° E oriented and shown in Figure 7b with red while a decrease of approximately 250 km$^2$ was observed in the plant areas around the same thermal power plant (Figure 7b; black areas). It was determined that there was an increase of 5.8 km$^2$ (Figure 7b; white areas). The decrease in the vegetation areas in Seyitömer and its surroundings is N - S directional and is shown in Figure 7b with green.

In this study, a period of thirty years has been examined by using remote sensing data and techniques covering the area which includes Seyitömer and Tunçbilek thermal power plants and their surroundings. For this long process time period, the 1987 Landsat MSS image and the 2017 Landsat 8 OLI/TIRS image were used. The satellite images were analyzed using ERDAS IMAGINE v9.1 and PCI Geomatica 2017 software and mapped at 1/250.000 scale with ArcMap v9.2 software. In the study, the temporal vegetation change analysis map obtained by

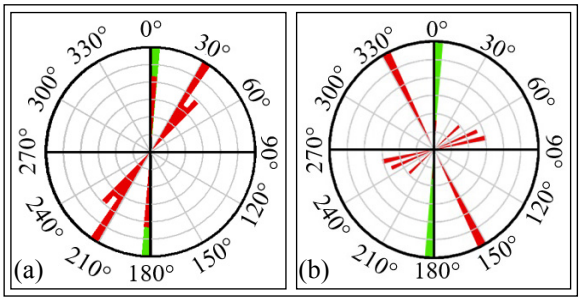


Figure 7- Rose diagrams showing the increase and decrease in the plant areas in and around the thermal power plant; a) Tunçbilek power plant and, b) Seyitömer power plant.

using Landsat satellite data dated 1987 and 2017 is given in Figure 8.

The decrease in the vegetation areas on the map obtained as a result of the temporal variation technique applied to the images dated 30.06.1987 and 02.07.2017 used within the scope of the project was calculated as 1137 km$^2$ in a radius of approximately 50 km with the help of remote sensing techniques applied considering the spatial resolutions of the satellite images. Among the necessary parameters for the temporal variation technique: i) two satellite images with different dates covering the same area, ii) the same resolution value and, iii) having the same projection information were taken into consideration in the analysis studies. In order to obtain the temporal change in the vegetation areas of the study area, change detection analysis was applied using the relevant images and the 30-year temporal change belonging to the vegetation was obtained. Very light (white and near-white) and dark (black) tones emphasize the change of vegetation over time. While lighter tones indicate an increase in the plant, darker tones indicate a decrease in the plant. This area is shown with dark colored areas in Figure 8. The direction of change in the plant areas was determined with the help of the ArcGIS program

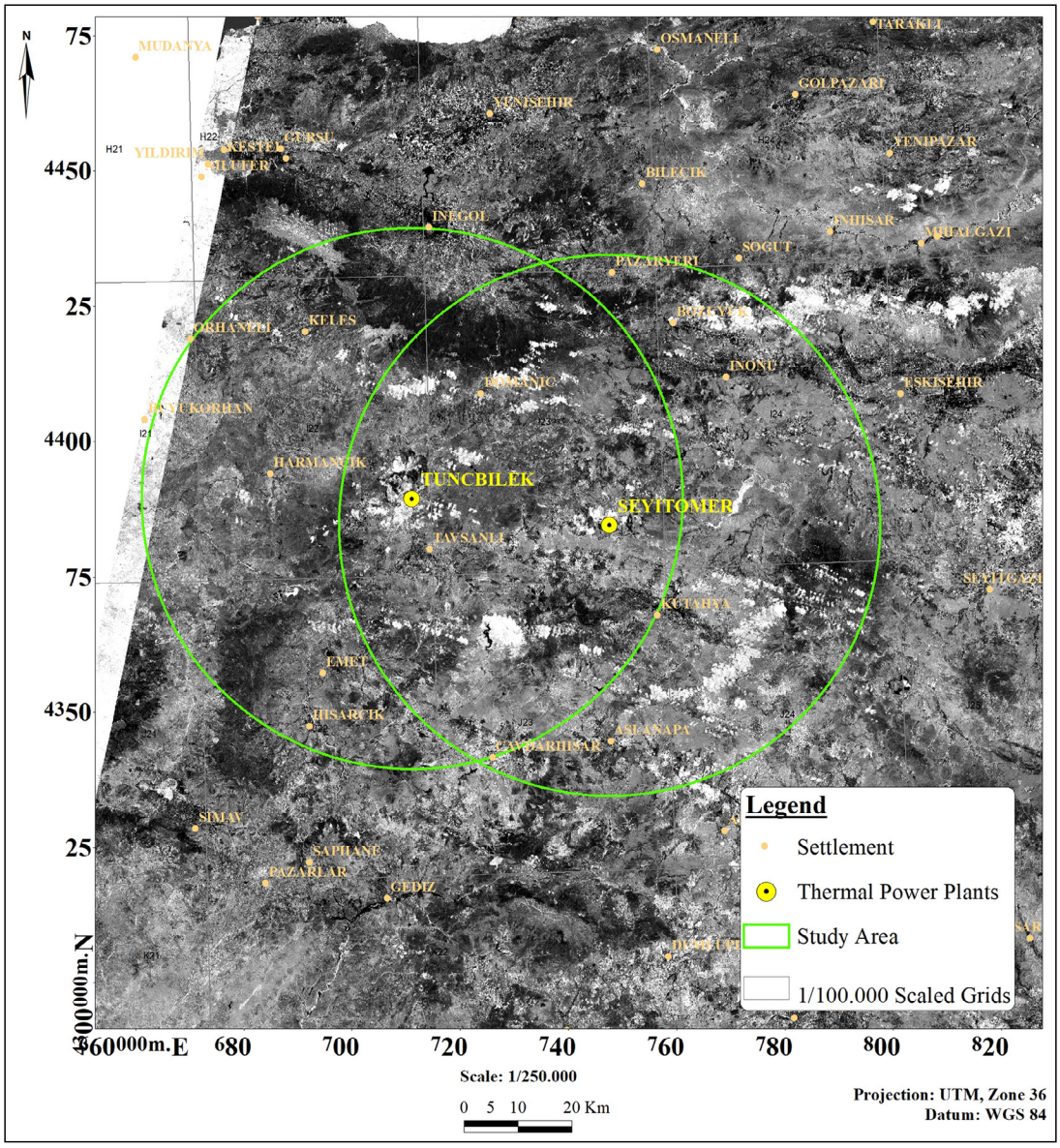


Figure 8- Temporal variation map of vegetation obtained from Landsat images dated in 1987 and 2017.

- Polar Plots application. and the directional diagrams of Seyitömer and Tunçbilek thermal power plants are shown in Figure 9 and Figure 10, respectively.

There could be many reasons for reductions in plant areas obtained in remote sensing; migration, population decrease, lack of soil cultivation that requires more labor due to easy supply in the developing city life, fly ash emissions from thermal power plants. etc.

In order to determine the main factor, it was necessary to examine the wind direction. which is one of the meteorological data in order to determine whether the reduction directions in the plant areas are related to the wind. With this method, it provides the most obvious view of the long-term effect. It has been determined that there has been a decrease of 1137 $km^2$ in a radius of approximately 50 km in a 30-year period in the plant areas around Seyitömer thermal power plants. The direction of change in plant areas was determined with the Polar Plots application and shown with a directional diagram. The decrease in the plant areas in and around the thermal power plants is in the N - S direction and it has been determined that it has similar characteristics with the dominant wind direction in the region.

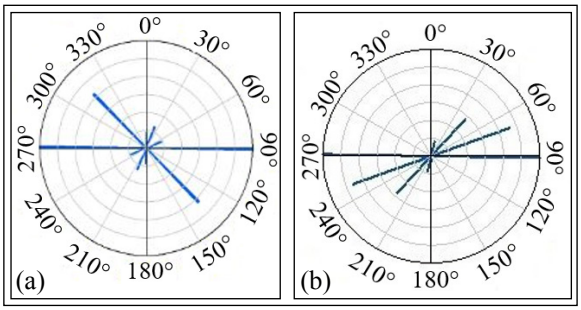


Figure 9- a) Direction diagram showing the total change in plant areas around Seyitömer and, b) Tunçbilek thermal power plants (r=50 km, thirty years change).

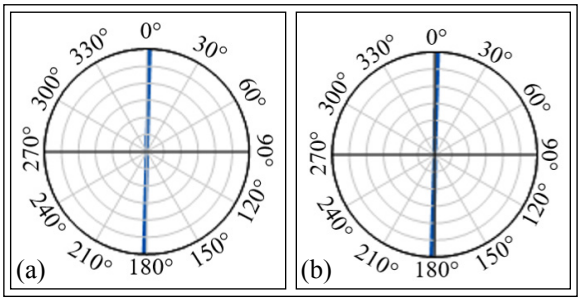


Figure 10- a) Direction diagram of Seyitömer (azimuth N number in the area; 370) and, b) Tunçbilek (azimuth N number in the area; 290) showing the total change in the plant areas around the thermal power plants (r=4 km. 2017 - 2018 years between and shown in the bearing method).

## 7. Discussion

Keser (2002) stated that Kütahya's basin geomorphology and slope (orographic) lines extending perpendicular to the dominant wind direction constitute the main topographical negativities. Similarly, dynamic origin inversion formations are controlled by the geomorphological structure, high local pressure values and humidity in winter months when the amount of emissions increases. accumulation of industrial emissions on the city and the low number of days with strong winds are considered as the main climatic negativities that increase the effects of air pollution in the city (Keser, 2002). Karpuz (2015) examined the climate of Kütahya province between 1971 and 2014 in his study. The study includes the meteorological data covering the year 2019 also shows that the dominant wind direction is compatible with Karpuz (2015).

The effect and orientation of unwanted particles for geomorphological data which contains important information in terms of environmental management with remote sensing maps has been examined within the scope of this study. Within the scope of the study, a three-dimensional (3D) digital elevation model (DEM) was created with the help of Landsat satellite images of Tunçbilek and Seyitömer thermal power plants using a 3' x 3' resolution digital elevation model produced by using SRTM (Shuttle Radar Topography Mission) data supported by local altitude information. In the specified digital elevation model, SRTM data digitized from 1/25.000 scale topographic maps and supplemented with elevations produced by interpolation technique were used. The digital elevation model of Tunçbilek and Seyitömer thermal power plants and their surroundings is given in Figure 11. The digital elevation data used within the scope of the study were converted to the UTM - WGS84 projection system and a 3D model of the field was obtained in the ArcGIS / ArcScene program together with the Landsat satellite images.

There are 22 settlements around Seyitömer and Tunçbilek thermal power plants and around 10.000 people live in these settlements. It is thought that

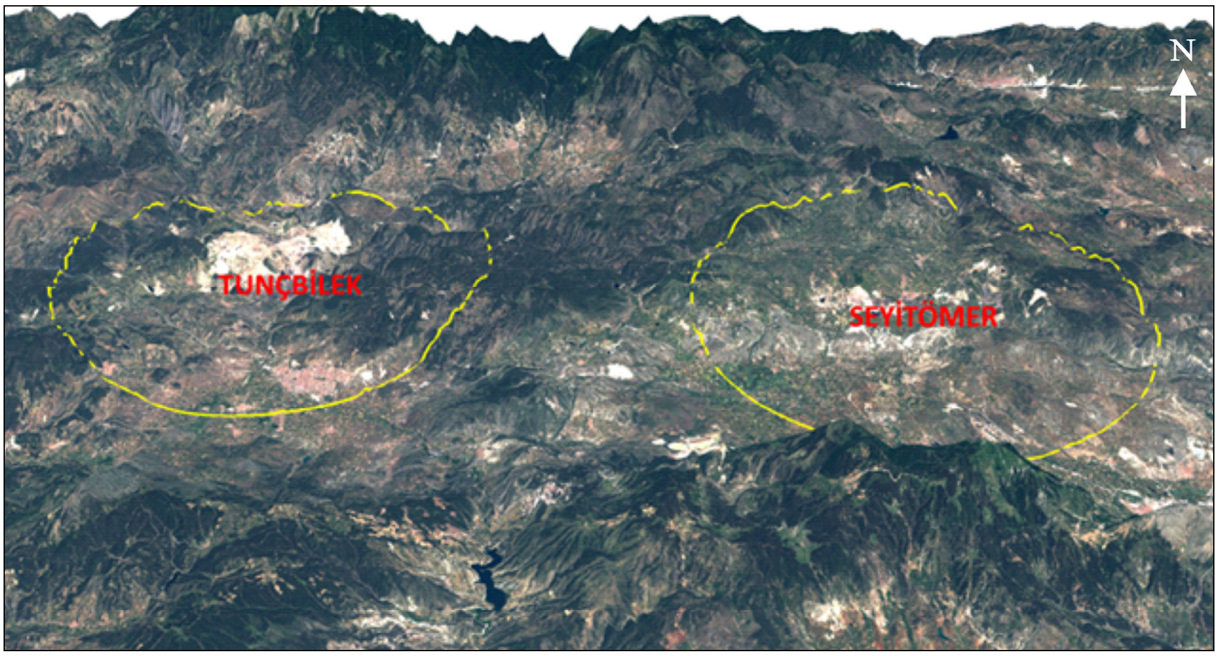


Figure 11- Physical factors seen in the digital elevation model of Tunçbilek and Seyitömer thermal power plants and their surroundings.

this population will be affected by the possible environmental problems of the thermal power plants in the region. Air pollution emissions of Seyitömer thermal power plant; particulate matter 650 - 1330 kg/hr. $SO_2$ 8000-18000 kg/hr, NOx 1600-3600 kg/hr, CO 80-180 kg/hr, volatile organic compounds 10 - 24 kg/hr, $CH_4$ average 4-9 kg/hr. It has been determined that the amount of $SO_2$ given to the air is very high (Çiçek et al., 2001). The $SO_2$ emission of the Tunçbilek thermal power plant is 3.30 g $SO_2$/106 cal and the upper limit value was determined by the Enviromental Protection Agency (EPA,1991) as 2.20 g $SO_2$/106 cal. Çiçek and Koparal (2004) stated that both thermal power plants were among the two hundred largest $SO_2$ pollutants in Europe in 2004. The pollutant emissions of the 11$^{th}$ - ranked Seyitömer thermal power plant are 149 kt $SO_2$, 20 kt NOx. 4 Mt $CO_2$ and 0.1 kt PM per year. Tunçbilek thermal power plant is in the 56th place with pollutant emissions measured as 43 kt $SO_2$, 8 kt NOx, 2 Mt $CO_2$ and 10.1 kt PM per year (Barret, 2004). In addition, $SO_2$ pollution reaches even higher values in Kütahya city center due to the use of coal for heating purposes, especially in winter. When looking at the values of four years between 1998 and 2001 (Makineci and Sevgi , 2005). It is emphasized that the $SO_2$ value can rise up to 450 µg/m$^3$. The annual average values vary between 148 and 201 µg/m$^3$ and these values are well above the limit values for plant growth. As a result of the literature research, it has been determined that the environmental effects of the lignite - based thermal power plants are the most effective in the first 4 - 5 km of the power plant and the effects of the power plants are minimized between 20 - 25 km (Haktanır and Karaca, 1996; Mol. 1986; Akbay et al., 2011; Güleç et al., 1999). Güleç et al. (1999) in their study on the suspended particulate matter and $SO_2$ content in the air with the ISCT computer model in order to determine the environmental impact of Seyitömer thermal power plant ash stated that no regional pollution occurred and was limited to Bozcahöyük and Kınık villages.

Bajpai et al. (2010) found that wind direction plays an important role in distributing heavy metals. On the other hand, Shahzad Baig and Yousaf (2017) stated that the fly ash released from thermal power plants could be transported between 40 - 50 km even at low wind speeds. Feng et al. (2013) stated that the average distance affected by fine coal ash is about 3.2 km. Bajpai et al. (2010) found that the wind direction plays an important role in the distribution of heavy metals. Considering the results obtained in these studies, what kind of effect will occur on a wider scale has been examined within the scope of this research. In Figures 12 and 13, the temporal changes in the vegetation, which were made by taking thermal power plants in the center, were examined at a radius of 12 km and 50 km. respectively and it was determined that

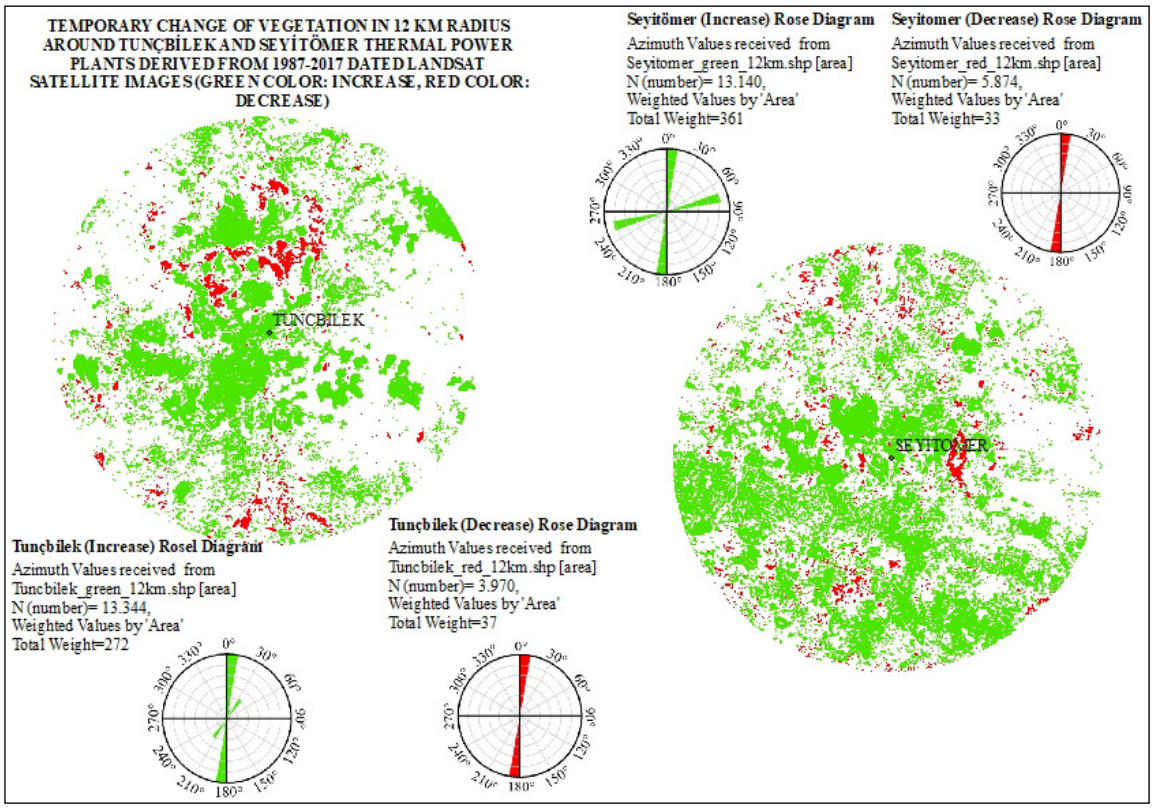


Figure 12- Temporal variation of the vegetation of the long - term Tunçbilek and Seyitömer thermal power plants and their surroundings (12 km radius).

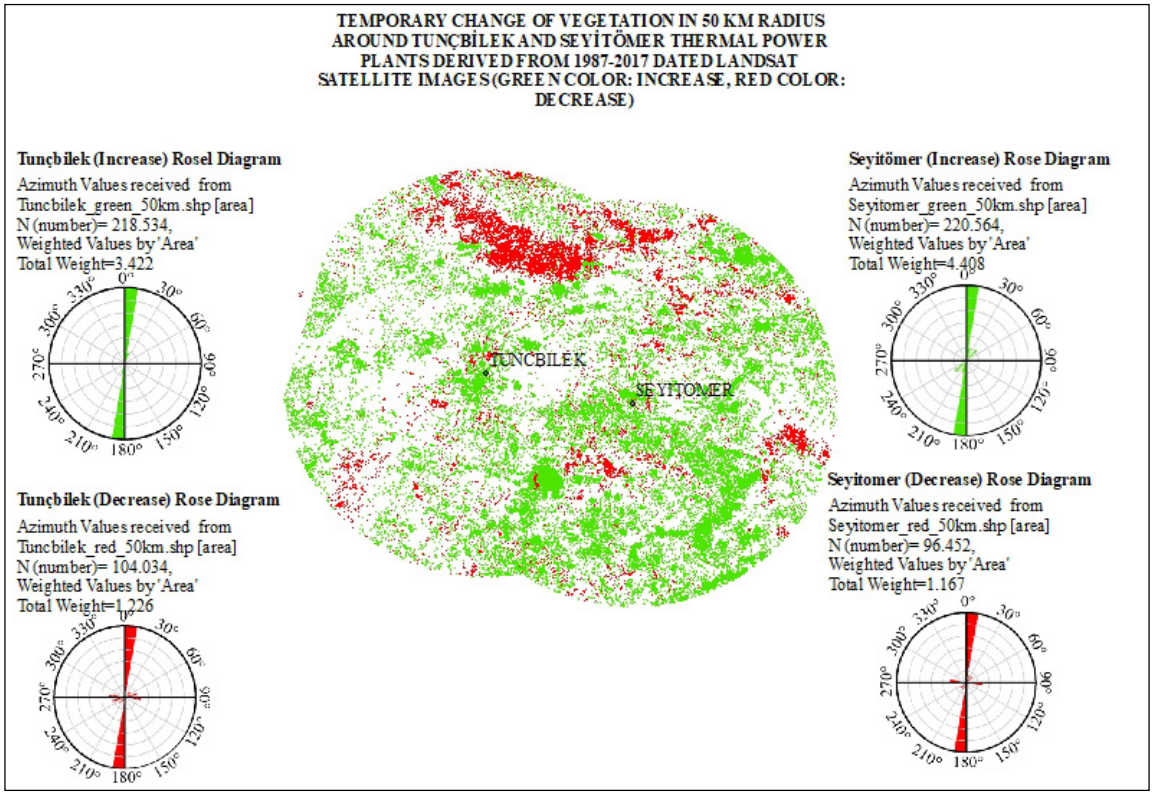


Figure 13- Temporal variation of the vegetation of the long - term Tunçbilek and Seyitömer thermal power plants and their surroundings (50 km radius).

the effect depending on the dominant wind direction disappeared. The numerical findings of these analyzes are presented in Table 5 and it has been determined that the effect of fly ash on plant areas decreases with the increase in diameter. It is observed that the effect of fly ash decreases as the diameter increases while the ratio decreases in plant areas because of urbanization.

A directional chart is a circular graph used to display directional data. In this study, while creating the direction diagram, the area polygons of the increase and decrease changes were calculated within themselves. The area was chosen as the source of the direction of the azimuth values and the source of the weight. In the findings given in Figure 13 as a result of investigating whether the two power plants have an environmental effect that causes a decrease in plant areas in case of coexistence (Haktanır and Karaca, 1996; Mol, 1986; Akbay et al., 2011; Güleç et al., 1999; Feng et al., 2013). Similarly, there was no evidence of a change in the dominant wind direction. It has been determined that there is an effect in the basin due to geomorphological conditions.

## 8. Results

Remarkable results have been found by detailed evaluation of the numerical data obtained as a result of meteorological data and remote sensing studies for the purpose of determining environmental impacts that may occur in the immediate vicinity of Seyitömer and Tunçbilek thermal power plants due to fly ashes. By transferring change in plant areas to the direction diagram, the similarities of the direction of the dominant wind and direction diagram were identified.

Within the scope of this study, it was observed that annual change is approximately 65.8 $km^2$ decrease in the plant areas in and around Tunçbilek while there is 8.9 $km^2$ increase due to rehabilitation studies. The change in the plant areas in and around Seyitömer is in the N-S direction while a decrease of 250 $km^2$ was observed. It was determined that there was an increase of 5.8 $km^2$ with planting studies.

The decrease in the vegetation areas on the map obtained as a result of the temporal variation method applied to the images dated 30.06.1987 and 02.07.2017 used within the scope of the study was calculated as 1137 $km^2$ in a radius of approximately 50 km around the Seyitömer thermal power plant with the help of remote sensing techniques applied considering the spatial resolutions of the satellite images. While a decrease of approximately 65.8 $km^2$ was observed in the plant areas in and around Tunçbilek, it was determined that there was an increase of 8.9 $km^2$ mainly due to rehabilitation studies. The change in the plant areas in and around Seyitömer is in the N - S direction while a decrease of 250 $km^2$ was observed. It was determined that there was an increase of 5.8 $km^2$ with planting studies.

It has been observed that the decrease in the plant areas in and around the thermal power plants has similar characteristics with the dominant wind direction in the region. It has been determined that as the remote sensing mapping diameter increases, the relationship with the change of plant areas and the dominant wind direction loses its significance and that the ashes of both power plants do not carry each other due to geomorphological conditions. In

Table 5- Numerical findings of both power plants.

| Change Time | Reactor | Change in Vegetation ($km^2$) | Radius (r=12 km) | Rate of Change (r=12 km) | Radius (r=50 km) | Rate of Change (r=50 km) |
|---|---|---|---|---|---|---|
| 30 years (1987-2017) | Tunçbilek | Increase | 136 | +7.55* | 1711 | +2.79* |
| | | Decrease | 18 | | 613 | |
| | Seyitömer | Increase | 181 | +10.64* | 2204 | +3.77* |
| | | Decrease | 17 | | 584 | |
| One Year (2017-2018) | | Change in Vegetation ($km^2$) | Radius (r=4 km) | Rate of Change (r=4 km) | | |
| | Tunçbilek | Increase | 0.8 | -6.4* | | |
| | | Decrease | 5.12 | | | |
| | Seyitömer | Increase | 0.53 | -446.03* | | |
| | | Decrease | 236.4 | | | |

*The *(-) sign indicates the decrease multiple and the (+) sign indicates the increase multiple.*

other words, as the study area increases, the effect of geomorphological conditions comes to the fore. It has been determined that the dominant wind impact area the radius for both power plants is 4 km and this situation remains within the radius range specified for lignite thermal power plants in the literature. It is thought that it would be beneficial to examine the effects of thermal power plants on human health on the scale of Kütahya with the central thermal power plant in a circle with a radius of four km.

**Acknowledgments**

This study was supported by the General Directorate of MTA within the scope of the 2020-38-14-01-3 project named as Investigation of the characteristics of fly ashes and their effects on the environment: its usability in the making of synthetic zeolite.

**References**

Adriano, D. C., Page, A. L., Elseewi, A. A., Chang, A. C., Straughan, I. 1980. Utilization and disposal of fly ash and other coal residues in terrestrial ecosytems: a rewiew. Journal Environmental Quality 9, 333-334.

Akbay, C., Dikici, H., Arı, H., Bilgiç, A. 2011. Afşin-Elbistan termik santralinin neden olduğu çevre kirliliğinin ekonomik analizi. TUBİTAK TAGOV, 109R027.

Akçın, H., Şekertekin, A. 2016. Sürdürülebilir havza yönetimi için kömüre dayalı kirliliğin Landsat 8 görüntüleri ve jeoistatistiksel analizlerle zamansal incelenmesi. 6. Uzaktan Algılama - Coğrafi Bilgi Sistemleri Sempozyumu (Uzal-CBS 2016), Adana.

Akkartal, A., Türüdül, O., Sunar Erbek, F. 2005. Çok zamanlı uydu görüntüleri ile bitki örtüsü değişim analizi. 10. Türkiye Harita Bilimsel ve Teknik Kurultayı, TMMOB Harita ve Kadastro Mühendisleri Odası, Ankara.

Aydınözü, D. 2008. Maki formasyonunun Türkiye'deki yayılış alanları üzerine bir inceleme. Kastamonu Eğitim Dergisi 17(1), 203-212.

Bajpai, R., Upreti, D. K., Nayaka, S., Kumari, B. 2010. Biodiversity. bioaccumulation and physiological changes in lichens growing in the vicinity of coal-based thermal power plant of Raebareli district, North India. Journal of Hazardous Materials 174(1–3), 429-436.

Barrett, M. 2004. Atmospheric Emissions from Large Point Sources in Europe. Swedish NGO Secreteriat on Acid Rain Air Pollution and Climate Series 17.

Baş, H. 1983. Tertiary geology of the Domaniç -Tavşanlı - Kütahya - Gediz region. Geological Engineering 27, 11-18.

Çelik, Y. 2000. Domaniç (Kütahya) Neojen havzasının stratigrafisi ve depolanma ortamları, Batı Anadolu. 53. Türkiye Jeoloji Kurultayı Bildiri Özetleri, Ankara, 177-178.

Çiçek, A., Koparal, A. S. 2004. Accumulation of sulfur and heavy metals in soil and tree leaves sampled from the surroundings of Tunçbilek thermal power plant. Chemosphere 57, 1031-1036.

Çiçek, A., Koparal, S. A., Catak, S., Uğur, S. 2001. The levels of some heavy metals and nutritional elements in the samples from soils and tree-leaves growing in the vicinity of Seyitömer thermal power plant in Kütahya (Turkey). In Topcu, S.,Yardi, M. F. and Incecik, S. (Eds): Proceedings of the Second International Symposium on Air Quality Management at Urban, Regional and Global Scales, Istanbul Technical University 25-28, 157-162.

Davraz, M., Kılınçarslan, Ş. 2020. Usability of PC - ash as lightweight aggregate in foam concrete. Bulletin of the Mineral Research and Exploration 161, 49-56.

Duran, C. 2007. Uzaktan algılama teknikleri ve bitki örtüsü analizi. Doğu Akdeniz Ormancılık Araştırma Müdürlüğü (DOA) Dergisi 13, 45-67.

Environmental Protection Agency, U. S. 1991. Indoor air facts no: 4 (revised) sick building syndrome. Research and Development MD-56.

Erener, A. 2011. Remote sensing of vegetation health for reclaimed areas of Seyitömer open cast coal mine. International Journal of Coal Geology 86(1), 20-26.

Feng, Y., Guli, J., AnMing, B., JianXiong, Z., ChangChun, L., JinPing Damage, L. 2013. Assessment of the vegetable types based on remote sensing in the open coalmine of arid desert area. China Environmental Science 33(4), 707-713.

Goncaloğlu, B. İ., Ertürk, F., Erdal. A. 2000. Termik santrallerle nükleer santrallerin çevresel etki değerlendirmesi açısından karşılaştırılması. Ekoloji Çevre Dergisi 34(9), 9-14.

Google Earth Pro. 2020. http://www.earth.google.com.

Güleç, N., Erler, A., Tuncel, G., Çancı, B., Hamzaoğlu, A., Arcasoy, A. 1999. Seyitömer termik santrali

küllerinin çevreye etkisinin incelenmesi. TÜBİTAK, Rapor No: YDABÇAG-523, Ankara.

Haktanır, K., Karaca, A. 1996. Afşin Elbistan termik santralı emisyonlarının çevre topraklarının fiziksel, kimyasal ve biyolojik özellikleri üzerine etkileri. TÜBİTAK, Rapor No: KTÇAG 125, Ankara.

Haktanır, K., Sözüdoğru, O. S., Karaca, A., Arcak, S., Çimen, F., Topçuoğlu, B., Türkmen, C., Yıldız, H. 2010. Muğla-Yatağan termik santrali emisyonlarının etkisinde kalan tarım ve orman topraklarının kirlilik veri tabanının oluşturulması ve emisyonların vejetasyona etkilerinin araştırılması. Ankara Üniversitesi Çevrebilimleri Dergisi 2(1), 13 - 30.

HEAL. 2018. https://www.env-health.org/wp-content/uploads/2018/12/HEAL-Lignite-Briefing-TR-web.pdf.

Heidrich, C., Feuerborn, H. J., Weir, A. 2013. Coal combustion products: a global perspective. World of Coal Ash Conference, 22-25, Kentucky.

Ilgar, R. 2008. Çan termik santral projesi. Marmara Coğrafya Dergisi 17, 154-171.

Karaca, A., Türkmen, C., Arcak, S., Haktanır, K., Topçuoğlu, B., Yıldız, H. 2009. Çayırhan termik santralı emisyonlarının yöre topraklarının bazı ağır metal ve kükürt kapsamlarına etkilerinin belirlenmesi. Ankara Üniversitesi Çevrebilimleri Dergisi 1(1).

Karpuz, İ. 2015. Kütahya'nın iklimsel özellikleri. Akademik Sosyal Araştırmalar Dergisi 3(17), 416-428.

Keser, N. 2002. Kütahya'da hava kirliliğine etki eden topoğrafik ve klimatik faktörler. Marmara Coğrafya Dergisi 5.

Kır, T. 2008. Afşin - Elbistan termik santralinde çalışan kazan işletmecilerinin genotoksik risklerinin saptanması. Kahramanmaraş. Yüksek Lisans Tezi, Sütçü İmam Üniversitesi, Fen Bilimleri Enstitüsü, Kahramanmaraş (unpublished).

Lyon, J. G., Yuan, D., Lunetta, R.S., Elvidge, C. D.1998. A change detection experiment using vegetation indices. Photogrammetric Engineering and Remote Sensing 64(2), 143-150.

Makineci, E., Sevgi, O. 2005. Seyitömer termik santralinin kuruma alanlarındaki karaçam (Pinus nigra Arnold.) yıllık halkalarına etkisinin araştırılması. Süleyman Demirel Üniversitesi Ziraat Fakültesi Dergisi 2, 11-22.

MGM. 2020. https://www.mgm.gov.tr/veridegerlendirme/il-ve-ilceler-istatistik.aspx?m=kutahya.

Mol, T. 1986. Yatağan termik santrali ve ormanlardaki zararları. İstanbul Üniversitesi Orman Fakültesi Dergisi 36 (2), 1-20.

Mondal, I., Maity, S., Das, B., Bandyopadhyay, J., Mondal, A. K. 2016. Modeling of environmental impact assessment of Kolaghat thermal power plant area, West Bengal, using remote sensing and GIS techniques. Modeling Earth Systems and Environment 2(139).

Nebert, K. 1960. Vergleichende stratigraphie und tektonik der lignitführenden neogengebiete westlich und nördlich von Tavşanlı. Bulletin of the Mineral Research and Exploration 54, 7-35.

Oruç, N. 1999. Seyitömer termik santralinin çevreye etkisi. In: Tatli, A.. Ölçer, H.. Bingöl, N., Akan, A. (Eds): 1st International Symposium on Protection of Natural Environment and Ehrami Karaçam, 23 - 25 Eylül 1999, Kütahya, 604 - 610.

Ölgen, M. K., Gür, F. 2012. Yatağan termik santrali çevresinden toplanan likenlerde (Xanthoria parietina) saptanan ağır metal kirliliğinin coğrafi dağılışı. Türk Coğrafya Dergisi 57, 43-54.

Özburan, M., Gürer, Ö. F. 2012. Late Cenozoic polyphase deformation and basin development Kütahya region, Western Turkey. International Geology Review 54(12), 1401-1418.

Özcan, N. 1986. Seyitömer (Kütahya) linyitlerinin palinolojik özellikleri. Yüksek Lisans Tezi, Dokuz Eylül Üniversitesi, Fen Bilimleri Enstitüsü, İzmir (unpublished).

Rouse, J. W., Haas, R. H., Deering, D. W., Schell, J. A., Harlan, J. C. 1974. Monitoring the vernal advancement and retrogradation (green wave effect) of natural vegetation. NASA/GSFC type III Report, NASA, Greenbelt, Maryland, 371.

Sarıyıldız, M. 1987. Seyitömer (Kütahya) KB'sindeki Kömürlü Neojen Kayaların Jeolojisi. Yüksek Lisans Tezi, Dokuz Eylül Üniversitesi, İzmir, Türkiye.

Schure, M. 1985. Surface area and porosity of fly ash. Environmental Science Technology 19(1), 82-86.

Shahzad Baig, K., Yousaf, M. 2017. Coal fired power plants: emission problems and controlling techniques. Journal of Earth Science and Climatic Change 8, 404.

Singh, N. P., Mukherjee, T. K., Shrivastava. B. B. P. 1997. Monitoring the impact of coal mining and thermal power industry on land use pattern in and around Singrauli Coalfield using remote sensing data and

GIS. Journal Indian. Society of Remote Sensing 25, 61.

Şekertekin, A. İ., Kutoğlu, Ş. H., Marangoz, A. M. 2015. Uzaktan algılama teknolojisi ve uydu görüntüleri yardımıyla önemli çevresel (su ve kara yüzeyi) etkilerin gözlemlenmesi. Karaelmas Fen ve Mühendislik Dergisi 5(2), 105-112.

Şengül, Ü. 2002. Kangal termik santralinde uçucu kül atımının çevresel etkileri. Ekoloji ve Çevre Dergisi 11(44), 21-24.

Tatlı, A., Tel, A. Z. 1999. Kütahya ve çevresinin bitki örtüsüne genel bir bakış. Dumlupınar Üniversitesi Fen Bilimleri Dergisi 1.

Tatlı, A., Memiş, R., Akan, H., Temel, M. 1999. Kütahya'da yayılış gösteren endemik bitkilerin tehlike sınıfları açısından değerlendirilmesi. 1st International Symposium on Protection of Natural Environment and Ehrami Karaçam Bildiriler Kitabı 280- 294.

Teillet, P. M., Staenz, K., Williams, D. J. 1997. Effects of spectral. spatial. and radiometric characteristics on remote sensing vegetation indices of forested regions. Remote Sensing of Environment 61(1), 139-149.

TSMS. 2020. Turkish State Meteorological Service.

TURKSTAT. 2017. http://www.tuik.gov.tr/PreHaber Bultenleri.do?id=24873.

Türkmenoğlu, A. G., Yavuz Işık, N. 2008. Mineralogy. chemistry and potential utilization of clays from coal deposits in the Kütahya province, Western Turkey. Applied Clay Science 42, 63-73.

Zeydan, Ö., Yıldırım, Y. 2013. Çatalağzı enerji havzasındaki termik santrallerden kaynaklanan emisyonların belirlenmesi. V. Hava Kirliliği ve Kontrolü Sempozyumu, 18 - 20 Eylül 2013, Eskişehir, 322-330.

Bulletin of the Mineral Research and Exploration

http://bulletin.mta.gov.tr

# Ilk_inv: a Matlab based algorithm for rapid computation of pseudo-3D density contrast distribution by using Bouguer gravity data

İlkin ÖZSÖZ[a]*

[a]*General Directorate of Mineral Research and Exploration, Ankara, Turkey*

*Research Article*

Keywords:
Singular Value Decomposition, Pseudo-3D Density Map, Gravity Modelling.

*Received Date: 05.06.2020*
*Accepted Date: 23.06.2021*

**ABSTRACT**

The new generation Matlab-based algorithm provides a rapid estimation of density contrast distribution. The 3D assumption, which is based on the 1D equation, is used. Therefore, the output is called pseudo-3D instead of 3D. The algorithm uses singular value decomposition and the median filter to produce pseudo-3D results. The success of the method is tested by theoretical and field studies. For synthetic studies, single-source models produce reasonable outputs, compared to the true density contrast value. However, the multiple source model shows slight deviations which are ±0.3 g/cm$^3$, with respect to the true density contrast value. The acceptable results are observed for the Bouguer anomaly of the eastern Mediterranean region. The resolution matrix indicates that the inversion process is biased due to the generalised inverse. The algorithm provides a quite different qualitative interpretation perspective to the interpreter.

## 1. Introduction

In geophysics, gravity modeling is can be considered a commonly used method. Tectonic studies (Tontini et al., 2008; Tadjou et al., 2009), resource exploration (Paterson and Reeves, 1985; Allen et al., 2001; Nagihara and Hall, 2001) and engineering solutions (Hinze, 1990; Roberts et al., 1990; Peacock, 1992) can be solved via gravity modelling. Subsurface mass variations generate gravity anomalies. The origin of gravity modeling can be traced back to Newton's Law (Cai et al., 2018). The primary objective of gravity modeling is to detect geometrical and physical parameters of the causative bodies (Grandis and Dahrin, 2014).

Inversion techniques provide the desired parameters by matching the observed data to the theoretical response (Grandis and Dahrin, 2014). Hence, inversion is a prominent part of the quantitative interpretation of the observed gravity data (Bear et al., 1995; Hinze et al., 2013).

In conventional inversion method, the underground is divited into regtangular prism of unknown density unknown density (Grandis and Dahrin, 2014). Moreover, these prisms should be uniform. Since rectangular blocks are in the same shape and size, estimating densities is a linear inverse problem (Parker, 1977; Grandis and Dahrin, 2014). In other words, there is a linear dependence between data and model parameters (Grandis, 2009; Menke, 2018). This linear relationship can be evaluated as an ill-posed problem.

Errors in the theoretical model and insufficient knowledge about the nature of the potential field cause difficulties during the inversion (Fedi and Rapolla,

Citation Info: Özsöz, İ. 2021. Ilk_inv: a Matlab based algorithm for rapid computation of pseudo-3D density contrast distribution by using Bouguer gravity data. Bulletin of the Mineral Research and Exploration 166, 19-31. https://doi.org/10.19111/bulletinofmre.959011

**Corresponding author: İlkin ÖZSÖZ, ilkin.ozsoz@mta.gov.tr*

1999). However, the major difficulty for this method is inherent nonuniqueness (Fedi and Rapolla, 1999). Namely, there might be many other models that fit the data (Blakely, 1996; Grandis, 2009). It should be noted that there may be infinite subsurface density distribution models that can generate the observed gravity field (Li and Oldenburg, 1998). Therefore, this technique requires a well-constructed density contrast as an initial model (Li and Oldenburg, 1998). Furthermore, there are many papers that deal with inherent nonuniqueness. Smith (1959, 1960), Parker (1974, 1975) and Hammer et al. (1991) showed that upper and lower bounds of source and density can be uniquely derived by constraining density via analytical equations of known models. There are other papers (Roy, 1962; Parker, 1972; Pedersen, 1977; Pilkington and Crossley, 1986; Xia and Sprowl, 1992; Fedi, 1997) that use nonlinear inversion techniques to estimate the depth and density contrast.

The depth and density contrast of given gravity anomaly can be calculated in either wavenumber domain (Parker, 1972, 1974, 1975; Oldenburg, 1974; Enmark, 1981; Mareschal, 1985; Granser, 1987; Huestis, 1988; Reamer and Ferguson, 1989; Guspi, 1992; Xia and Sprowl, 1992) or spatial domain (Cordell and Henderson, 1968; Al-Chalabi, 1972; Pedersen, 1977, 1979; Tarantola and Valette, 1982; Menichetti and Guillen, 1983). The wavenumber domain methods show effective results deriving the depth between the sedimentary basin and basement rock (Bear et al., 1995). However, determining density distribution cannot be effectively provided with wavenumber domain methods (Bear et al., 1995). On the other hand, the effectiveness of the spatial domain methods is proven in terms of determining subsurface density contrast (Bear et al., 1995).

In this paper, the linear inversion technique in the spatial domain is used with Levenberg-Marquart (Levenberg, 1944) damping factor. The damping parameter prevents the solution from unnecessary outcomes which produce noisy data (Grandis and Dahrin, 2014). Moreover, this parameter provides independence between the initial density contrast model and objective function where geological information is missing (Grandis and Dahrin, 2014).

In general, geophysical problems suffer from ill-posed inverse problems. Stabilization of the inverse problem can be done with singular value decomposition (SVD) (Press et al., 2007). The SVD method can decompose matrix G into different series of eigen images (Zhao and Chen, 2011). SVD was used for signal and noise separation (Vrabie et al., 2004; Clifford, 2005). Ulrych et al. (1988) and Freire and Ulrych (1988) showed that SVD can be used for separating upgoing and downgoing waves in the vertical seismic profiling (VSP) method.

The inversion method, described in this paper, computes the initial density contrast model from a given gravity field. Then, it applies a linear inversion technique using SVD to estimate the final density contrast model.

## 2. Methods

The fundamental theory of linear density inversion algorithm is based on Bott (1960) and Cordell and Henderson (1968). Nevertheless, it should be noted that the algorithm has undergone slight adjustments. The workflow of the algorithm is displayed in Figure 1.

$$\Delta\rho = \frac{g_j}{2\pi G t_j} \tag{1}$$

where $g_j$ is the gravity field of the infinite slab whose thickness is $t_j$ and density contrast is $\Delta\rho$ and G is the universal gravitational constant.

Basically the algorithm can be divided into three fundamental steps:

The first step of the method is computing the initial density contrast map from a given thickness value using Equation (1). Furthermore, an optional background density contrast value might be selected. This parameter allows the interpreter to mask the contribution of the density values above the slab.

The second step involves SVD inversion fit and moving median filtering. The output of the inversion provides slight changes in the initial density contrast map. Furthermore, the median filter removes sharp variations from the output. The final density contrast map is obtained.

The last phase of the estimation is assessing the quality of inversion by resolution and covariance matrices.

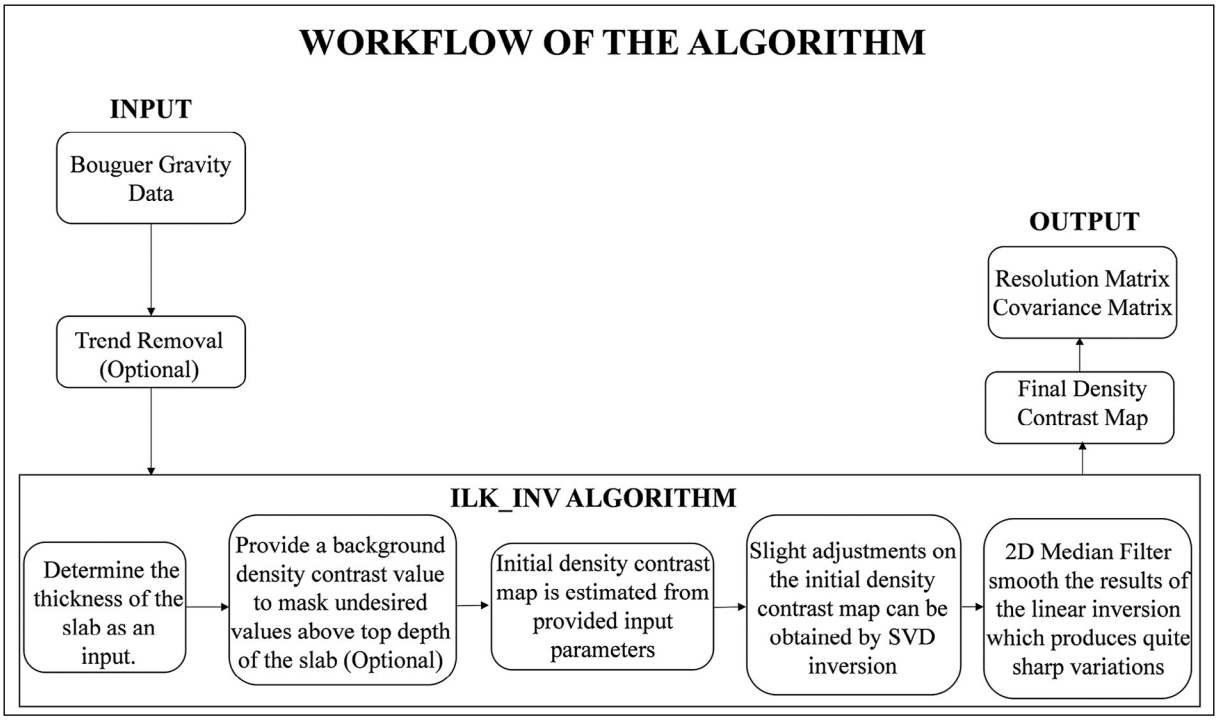


Figure 1- Workflow of the ilk_inv algorithm.

2.1. Singular Value Decomposition (SVD)

Observations, d, can be calculated by a simple forward modeling equation which can be constructed by using Kernel matrix, G, and geometrical or physical parameters of the source, m. This equation can be written as:

$$d = G * m \quad (2)$$

The initial model is calculated from the given thickness and calculated constant density contrast from 1D Bouguer Slab formula and observed gravity. Equation 1 can be used for calculating the gravity anomaly over a constant thickness and variable density. The difference between theoretical values, calculated from Equation 2, and observed values can be written as $\Delta g_B$. Hence (2) can be modified as:

$$\Delta g_B = G\Delta\rho \quad (3)$$

where $\Delta\rho$, difference between initial and estimated density distribution. For n number of observations and m number of parameters, the length of $\Delta g_B$ and $\Delta\rho$ is (n * 1) (n * m) and (m * 1), respectively.

According to Lawson and Hanson (1974), matrix G can be decomposed into data space, model space and singular values via SVD. Furthermore, the SVD can be used for solving ill-conditioned and/or rank deficient inverse problems (Strang, 1988; Golub and Van Loan, 1996; Lanczos, 1997). The matrix G can be factored into;

$$G = USV^T \quad (4)$$

where U is an (n * n) orthogonal matrix whose vectors are spanning the data space, V is an (m * m) orthogonal matrix whose vectors are spanning the model space and S is (m * n) diagonal matrix of the singular values (Aster et al., 2018). It should be noted that some singular values might be zero. If nonzero singular values are called $S_q$, S can be partitioned as;

$$S=\begin{bmatrix} S_q & 0 \\ 0 & 0 \end{bmatrix} \quad (5)$$

where $S_q$ is (q * q) matrix that has positive singular values. Hence, matrix G can be modified as;

$$G=\begin{bmatrix} U_q & U_0 \end{bmatrix} \begin{bmatrix} S_q & 0 \\ 0 & 0 \end{bmatrix} \begin{bmatrix} V_q & V_0 \end{bmatrix}^T \quad (6)$$

$$G = U_q S_q V_q^T \quad (7)$$

where the size of $U_q$ and $V_q$ are (n * q) and (m * q). According to Aster et al. (2018), $U_0$ and $V_0$ contribute

nothing to matrix G. Furthermore, if $V_0$ is multiplied by any model, observations are not affected. The result will appear in the model null space. On the other hand, if $d_{obs}=d+\alpha U_0$, $d_{obs}$, $d_{obs}$ cannot be exactly fit by any model. In other words, there is a data component in the data null space. Table 1 shows the effect of data null space and model null space on the uniqueness and data fit (Menke, 1984).

In this paper, case number 4 is used. Since the exact fit cannot be provided, the damping factor should be used to avoid overfitting (Grandis and Dahrin, 2014). The over-fitting problem results from the residual model solutions. Damping parameter can be determined by a trial-error approach or eigenvalues of $GG^T$. Density distribution can be estimated from the following equation:

$$S_{qq} = \frac{(\lambda^2 + S_q^2)}{\lambda} \tag{8}$$

$$\Delta\rho_e = V_q S_{qq}^{-1} U_q^T \Delta g_B \tag{9}$$

where λ is the damping parameter and $\Delta\rho_e$ is the estimated density contrast.

## 2.2. Resolution and Covariance Matrix

The generated model can be tested in terms of how the model represents the true situation (Aster et al., 2018). It is known that the least square estimator is unbiased. However, the generalised inverse solution cannot be considered as an unbiased estimator (Aster et al., 2018). The bias can be measured by a model resolution matrix (Aster et al., 2018). The calculation of covariance and model resolution matrices is shown in the following equations;

$$C = G^{\$} cov(\Delta g_B)(G^{\$})^T \tag{10}$$

$$R = V_q V_q^T \tag{11}$$

where C is a covariance matrix and R is the resolution matrix. Basically, the resolution matrix can associate the biased true solution with the estimated parameters. It is prominent that the resolution matrix cannot be related to the data and data errors (Vasco, 1989). It is the function of the geometry of the survey or properties of G (Vasco, 1989; Aster et al., 2018). If matrix G is not rank deficient and zero, the resolution matrix will be an identity matrix (Vasco, 1989). In this paper, zero values of $U_q$, $V_q$ and $S_q$ are not taken into account. Therefore, the resolution matrix is not an identical matrix. However, it is worth noting that this is an unbiased solution. Moreover, the covariance matrix provides a map of Gaussian errors (Vasco, 1989).

## 2.3. Median Filter

Linear filtering can be used for suppressing the noise in the signal. The simple linear filter uses the mean value of the selected dataset along a sliding window (Arias - Castro and Donoho, 2009). However, this type of filter has a major drawback at the edges of the structures (Church et al., 2008).

Furthermore, smooth low-pass filtering is useful for eliminating sharp points and noise. Nevertheless, this type of filter may produce blurring on a geophysical image in some cases.

Hence, Tukey (1974) introduced an alternative concept of linear filtering. As it is known that median is the centre value of the given series. In certain situations, median filtering has two major advantages. Firstly, it can preserve information on structures with a sharp edge (Justusson, 1981). Secondly, outliers and spikes can be reasonably suppressed with a median filter (Justusson, 1981, Arias-Castro and Donoho, 2009).

Table 1- Generalised inverse solution for different cases where $G^{\$}$ indicates the generalised inverse.

| Case Number | Case | Uniqueness | Data Fit | Solution |
|---|---|---|---|---|
| **1** | $U = U_q$<br>$V = V_q$ | UNIQUE | EXACT FIT | $G^{\$} = (U_q S_q V_q^T)^{-1}$ |
| **2** | $U = U_q$<br>$V_q$ *is not square* | NON-UNIQUE | EXACT FIT | $G^{\$} = G^T(GG^T)^{-1}$<br>Minimum Norm Solution |
| **3** | $V = V_q$<br>$U_q$ *is not square* | UNIQUE | NOT EXACT FIT | $G^{\$} = (G^T G)^{-1} G^T$<br>Least-Squares Solution |
| **4** | $U_q$ *is not square*<br>$V_q$ *is not square* | NON-UNIQUE | NOT EXACT FIT | Use generalised inverse.<br>$G^{\$} = V_q S_q^{-1} U_q^T$ |

If the length of the median filter is even, the average of the multiple centre values can be used. On the other hand, it is recommended to use the median filter whose length is odd (Church et al., 2008). The median filter can be performed by taking the median of the windowed series. Then, the median value is used to replace the studied point. Figure 2 illustrates a schematic application of N-length and N * N sized median filter.

The effect of the median filter is tested on the random dataset. Different lengths of 1D median filters are applied to the dataset. Figure 3 demonstrates the results of the median filter, whose length is 3, 5 and 7, on the random data.

As it is shown in Figure 3, median filtering suppresses outliers and extreme points. It reveals the true extremum points of the noisy data. Spiky points are removed but smoother extreme points are preserved. In this paper, the median filter is required for masking the outliers and spiky points. The major drawback of the algorithm on the gridded data is outliers and spiky points. These extreme points are filtered out by using 2D median filtering.

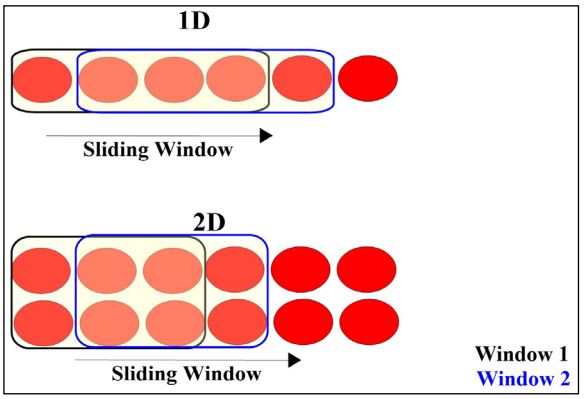


Figure 2- Application of 1D (N=3) and 2D (N=3*3) median filtering.

## 3. Synthetic Studies

In order to analyse the effectiveness of the proposed method, three different synthetic models and field data are used. Synthetic models include a single prism with positive density contrast, multiple prisms with positive density contrast and a 3D cylinder model with negative density contrast. The produced synthetic studies are not contaminated by Gaussian error. Field data set is obtained from the International Gravimetric Bureau.

### 3.1. Single Prism with Positive Density Contrast

The gravity anomaly of a single prism is calculated within 100 * 100 $km^2$ area. The top and bottom depths of the prism are 3 and 5 km, respectively. Prism has a +1 $g/cm^3$ density contrast with respect to the

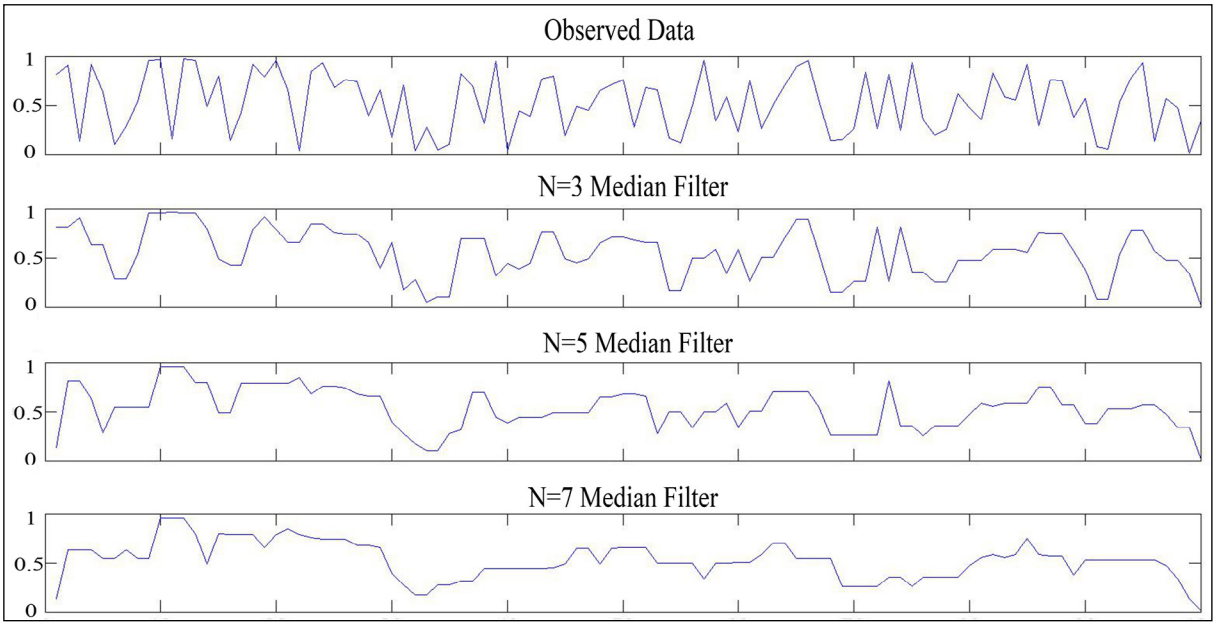


Figure 3- Effect of the median filter and its length on the fluctuating random dataset.

background density. Matlab-based program (ilk_inv) is used for producing density contrast of the prism.

The gravity field of prism and gridding interval along x and y axes assumed background density contrast (optional) and thickness are used as an input parameter. The description of the model is demonstrated in Figure 4.

Regarding the input parameters, 1 km grid spacing in both x and y directions is used for 100 * 100 $km^2$ area. A slab thickness value is required for the calculation. In this case, thickness is chosen as 3 km, which increases the accuracy of the output.

The Matlab-based algorithm (ilk_inv) can produce two major outputs which are the initial density contrast and final density contrast. The output of the ilk_inv for the gravity anomaly of a single prism with positive density contrast is shown in Figure 5.

### 3.2. Multiple Prisms with Positive Density Contrast

In this synthetic example, two different prisms which have different top and bottom depths are used within 100 * 100 $km^2$ area. The top and bottom depths of prism 1 are 2 km and 6 km respectively. Prism 1 has a +0.3 $g/cm^3$ density concerning the background density. Additionally, the top and bottom depths of Prism 2 are 7 km and 11 km correspondingly. Prism 2 has a +0.8 $g/cm^3$ density contrast for the background density. The geometrical and physical parameters of the model are shown in Figure 6.

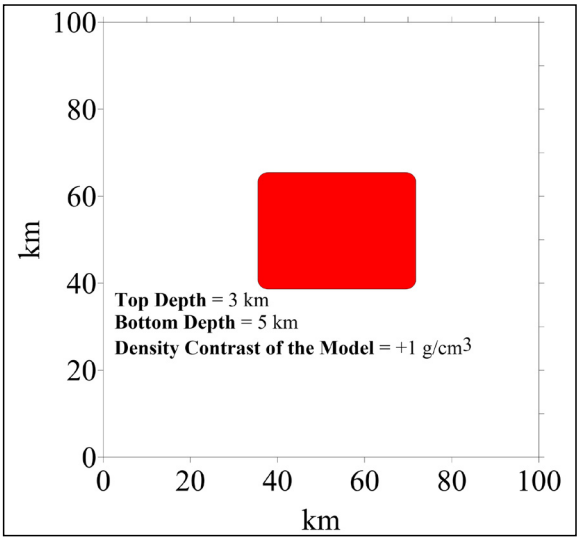


Figure 4- Physical and geometrical parameters of the single prism synthetic model.

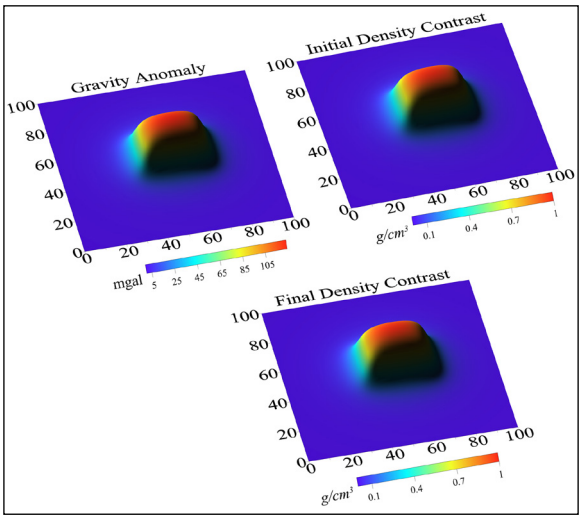


Figure 5- Products of ilk_inv for a single prism with positive density contrast.

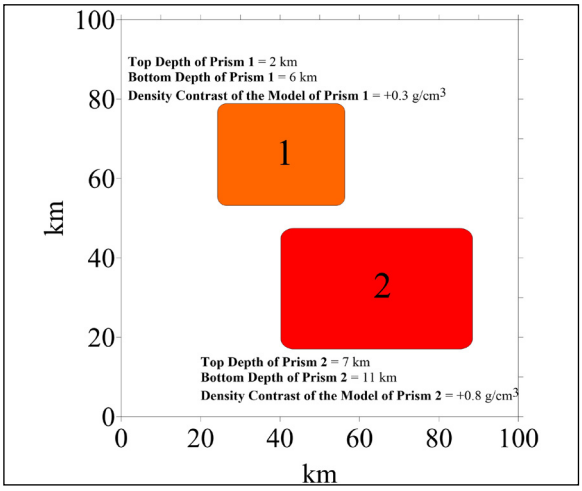


Figure 6- Physical and geometrical parameters of the multiple prism synthetic model.

The slab thickness is chosen 7 km (top depth of the deeper prism) since the deeper source controls the density distribution for this synthetic model. The outputs for the selected input parameters are shown in Figure 7.

### 3.3. 3D Cylinder Model with Negative Density Contrast

A synthetic cylinder model which is surrounded by sedimentary rocks is used within 100 * 100 $km^2$ area. The top and bottom depths of the cylinder model are 10 and 12 km. The density contrast of the cylinder is -0.3 $g/cm^3$. The parameters of this synthetic model are indicated in Figure 8.

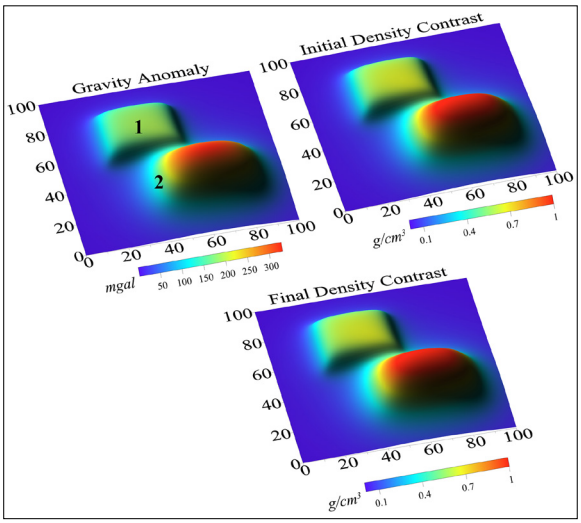


Figure 7- Outputs of ilk_inv for multiple prisms with positive density contrast.

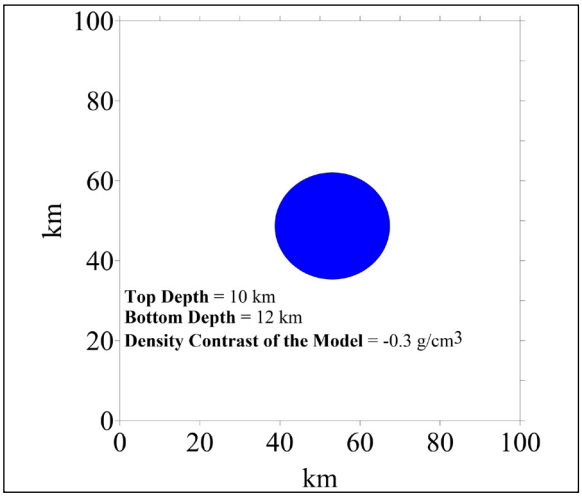


Figure 8- Physical and geometrical parameters of the cylinder synthetic model.

The slab thickness is chosen 10 km since it corresponds to the top depth of the cylinder model. The output of ilk_inv for the cylinder model covered by sedimentary rocks is demonstrated in Figure 9.

## 4. Field Study

### 4.1. Tectonic Setting of the Study Area

Eastern Mediterranean tectonics resulted from tectonic movements of African, Eurasian and Arabian plates. The W - SW movement of the Anatolian Block can be associated with extension in Western Anatolia, compression in Eastern Anatolia and

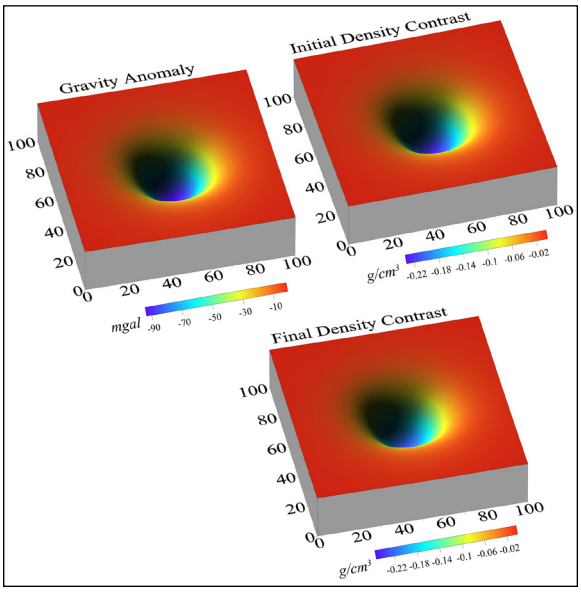


Figure 9- Products of the synthetic cylinder model with negative density contrast.

faulting throughout the North and East Anatolian fault zones, and movement of the African Plate relative to the Eurasian Plate formed Hellenic Subduction Zone (McKenzie, 1972; Le Pichon and Angelier, 1979; McClusky et al., 2000; Mart and Ryan, 2003; Pamukçu, 2016; Kahveci et al., 2019). A major subduction along the Hellenic Arc stems from the roll-back mechanism under the Aegean Sea (Le Pichon and Angelier, 1979; Le Pichon, 1983; Sorel et al., 1988; Mercier et al., 1989; Kahveci et al., 2019).

The Hellenic Arc comprises three trenches, Helen, Pliny and Strabo. These trenches formed 3500 - 4000 m depth in the Mediterranean Sea. Fairly variable bathymetric values are observed in the southern part of the Hellenic Arc (Gönenç and Akgün, 2012). Furthermore, the southern part of Crete is characterised by active seismicity at 20 - 40 km depth (Delibasis et al., 1999; Meier et al., 2004). Additionally, studies of Papazachos et al. (2000) and Gönenç et al. (2006) showed that Wadati - Benioff Zone reaches 150 - 200 km depth owing to the northward movement of the Hellenic Arc.

### 4.2. Geophysical Findings

The eastern Mediterranean region is studied. The field gravity data is obtained from the International Gravimetric Bureau (BGI). The gravity data is part of the World Gravity Map (WGM 2012) (Bonvalot et al., 2012).

Briefly, WGM 2012 data is derived from the EGM2008 geopotential model and ETOPO1 model (Bonvalot et al., 2012). WGM 2012 handles regional and global variations in the gravity field of the Earth. WGM 2012 provides free-air, Bouguer and isostatic anomalies. In this study, the Bouguer anomaly is required. The Bouguer anomaly of the study was given in Figure 10.

If the slab thickness is chosen too shallow regarding the resolution of data, the output will be an exaggerated density contrast map. Since the resolution of WGM 2012 is not as high as land gravity data, the slab thickness is tried to be chosen from the long-wavelength component of the data. The outputs were demonstrated in Figure 11.

In order to examine the success of the inversion process and the effect of the Gaussian errors on the solution, resolution and covariance matrices should be analysed. Figure 12 illustrates the covariance and resolution matrices for the field data.

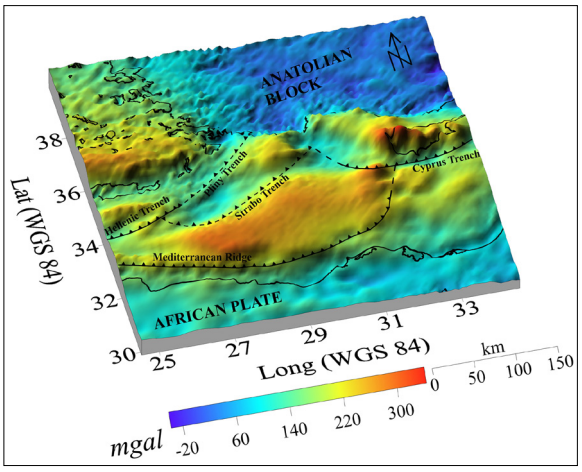


Figure 10- Bouguer anomaly of the East Mediterranean region with the major tectonic elements (Lat: latitude, Long: longitude; Dilek, 2006; Öner et al., 2010).

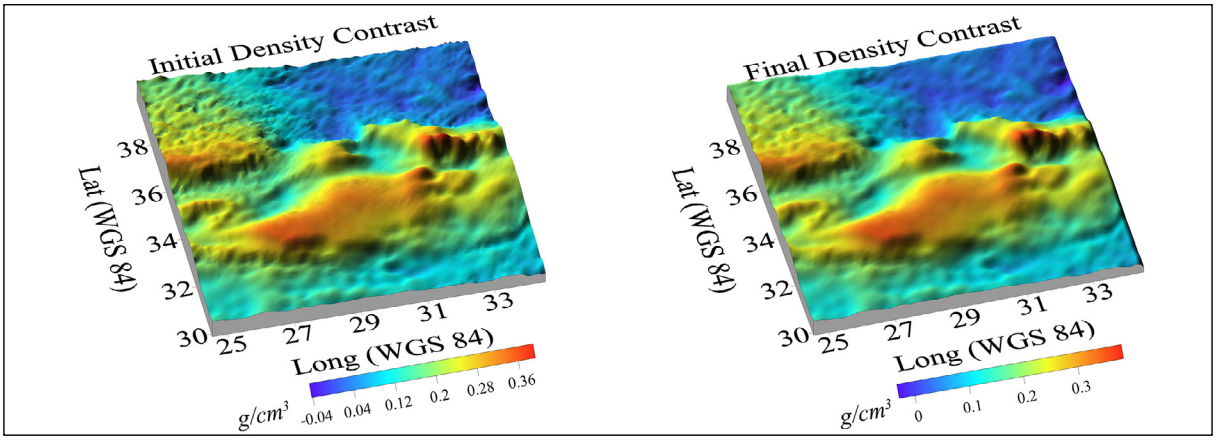


Figure 11- Estimated density contrast maps map for the eastern Mediterranean region (Lat: latitude, Long: longitude).

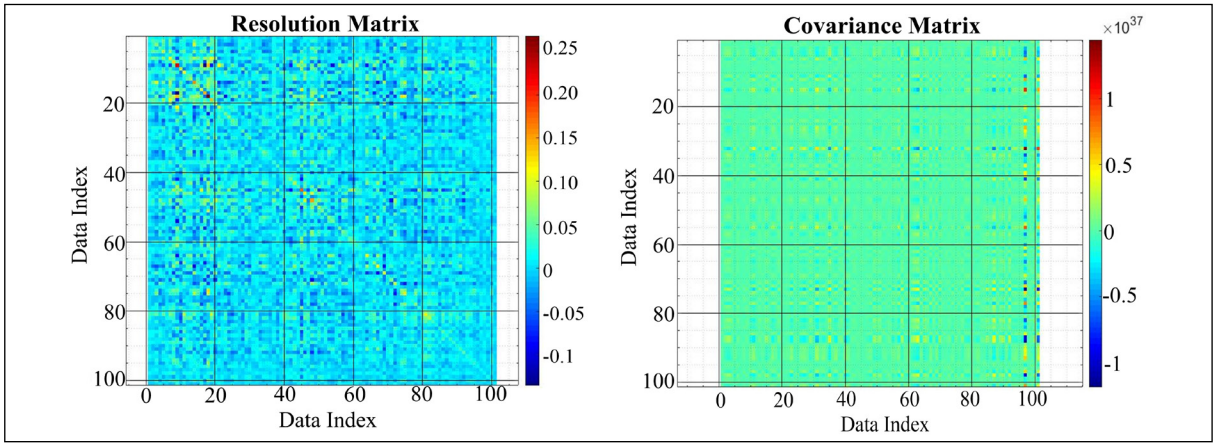


Figure 12- Resolution and covariance matrices.

Furthermore, the validity of this approach can be illustrated by calculating RMS error between estimated gravity data and observed data. Figure 13 indicates how computed gravity data from pseudo-3D density contrast match the observed gravity data. As it can be seen from Figure 13, the calculated RMS error is 8.63 mgal.

Since gravity data and density values are linearly correlated, interrelationship between the gravity inversion results and the satellite gravity data is considerably high. It can be said that the gravity inversion results are a smoothed representation of the observed gravity data. Strabo Trench, Hellenic Trench, Pliny Trench, Cyprus Trench and Mediterranean Ridge are adequately represented in the inversion results as well as the gravity data.

Geologically, the subducting plate is characterised by higher density contrast in the gravity inversion results. To exemplify, the southern part of the Strabo Trench which is a subducting plate is represented by higher density contrast and gravity anomaly.

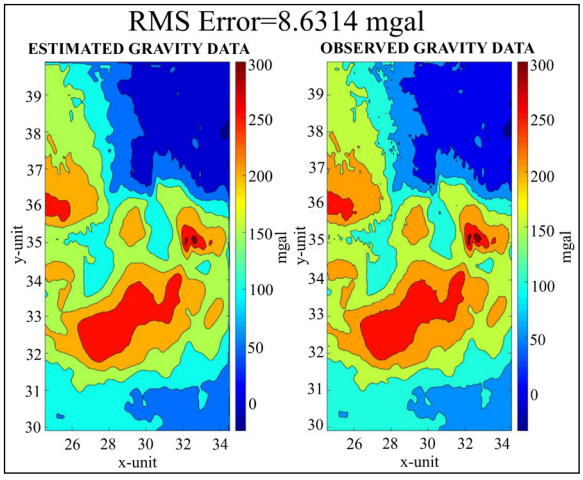


Figure 13- Comparison of estimated and observed gravity anomaly.

## 5. Discussion

The density contrast map is computed by the ilk_inv algorithm. The algorithm uses 1D Bouguer Slab Formula to produce a constant initial density value and SVD for modelling the gravity field and estimating the density contrast. Then it applies a 2D median filter to the estimated values in order to remove sharp variations. It is worth noting that the algorithm cannot produce 3D estimations. It only imitates 3D estimations.

The input parameters are the slab thickness, grid spacing and background density contrast (optional). The slab thickness value must be a positive number. Grid spacing parameter along x and y direction has a major impact on the computation time. It is recommended to use optimum grid spacing since extremely small grid spacing does not improve results. The optional background density contrast can be chosen with a specific value or 0 g/cm$^3$. If it is chosen as 0 g/cm$^3$, the result shows the raw computed density contrast map with respect to 0 g/cm$^3$. On the other hand, if a background density contrast is used, the background density effect on the geological structures can be filtered. It is recommended to use background density contrast value in case that lithological information of the study area is well-known.

Various synthetic models and a field model is used for testing the success of the ilk_inv algorithm. The first synthetic study, a single prism with positive density contrast, produced fairly reliable results. The initial density contrast and final density contrast value are almost the same since the data are not contaminated by noise. The final density contrast map found the density contrast of prism 1 g/cm$^3$, corresponding to the true density contrast value. For obtaining the best result, slab thickness should be similar to the top depth of the basement rock.

The second synthetic study, multiple prisms with positive density contrast, produced slightly acceptable results. Similar to the first synthetic study, initial and final density contrasts cannot be distinguished. Prism 2 is located deeper than Prism 1. Furthermore, the density contrast of Prism 1 is dominant. Therefore, the depth of the Prism 2, 7 km, ought to be used as slab thickness. Prism 2 can be considered as a basement rock. It can be said that if there are two dominant sources in the study area, the produced results might contain moderate uncertainty.

The final synthetic study evaluates the reliability of the algorithm in terms of modelling structures with negative density contrast. The final density contrast of the cylinder model is roughly -0.23 g/cm$^3$ and it deviates from the true density contrast, -0.3 g/cm$^3$. It might be said that the algorithm tends to produce slightly deviated results from the true density contrast while computing a model with a negative density contrast.

The other prominent observation is the difference between initial and final density contrast maps. It is clear that the final density contrast map converges true density contrast value with slight uncertainty.

Apart from the synthetic study, the field data is used for the evaluation of the algorithm. Eastern Mediterranean gravity data is used as a field data example. There is a considerable positive anomaly, 300 mgal, at the south-western part of the Cyprus region. It can be said that a positive density contrast anomaly will be observed around the same region because of a positive correlation between estimated density contrast and the observed gravity anomaly.

The slab thickness for the field study is chosen as 20 km. Since the gravity data have limited resolution and are dominated by considerably long wavelengths, crustal scale inversion over the large study area would be more suitable. If density contrast maps, initial and final density contrast, at 20 km are compared, it can be said that the final density contrast map is substantially smoother than the initial density contrast map. Namely, if the thickness is chosen significantly deep, variations in the long wavelength component are dominant rather than short wavelength components in the computed density contrast map.

The validity of the approach is tested by comparison of estimated and observed gravity anomalies. If Figure 13 is analysed, the estimated gravity data produces smoother results than observed gravity data as the estimated gravity anomaly is computed from median filtered pseudo-3D density contrast values. It can be said that the anomalies related to the small wavelength components cannot be modelled in an estimated gravity anomaly map. However, longer wavelength components are modelled successfully.

The amount of bias and distribution of errors can be evaluated via resolution and covariance matrices. Since it is a biased solution, the resolution of the solution is quite low. The bias in the solution is related to the generalised inverse operator. Nonetheless, this operator is required for solving the inverse problem. For the unbiased solution, the identity matrix is required as a resolution matrix. In this case, the output of the algorithm is the biased pseudo-3D distribution of density contrast. Consequently, since the algorithm is biased and the solution is not actually 3D, the resolution of the solution produces significantly low values. Additionally, the covariance matrix presents quite high values in some parts of the solution. It is clear that the Gaussian errors increase certain data indexes.

The regional tectonic structures in the field study, Hellenic Trench, Pliny Trench, Strabo Trench, Mediterranean Ridge and Cyprus Trench, are clearly represented on the Bouguer Gravity Anomaly (Figure 10a).

Initial and final density contrast maps have a linear relationship with the observed gravity anomaly. However, these maps can indicate density contrast between sediment accumulation zones and basement rocks, which is roughly 0.2 - 0.4 g/cm$^3$.

The output is considerably dependent on the input data rather than the damped inversion process. If input data is dominated by the longer wavelengths, the result will be smooth. On the other hand, if data have relatively short wavelengths, the produced output will be relatively sharp.

The algorithm is directly associated with the residual gravity anomaly and indirectly related with the actual density variations. Therefore, it cannot produce entirely reliable density variations for the complex tectonics even if you have noise-free data. It is designed for obtaining regional density contrast for the large study area. The regional density contrast, obtained from the algorithm, can be used as initial density contrast values or constraining parameters. Also, if the output is used as a constraining parameter, it is highly possible to reduce the effect of non-uniqueness.

## 6. Results

Rapid pseudo-3D computation of density contrast map can be done by the ilk_inv algorithm. Theoretical studies showed that if there is a single dominant source in the survey area, estimations are reliable. However, the estimation of density contrast slightly diverges from the true density contrast if there are multiple dominant sources.

The computed density contrast map from the field study reflects the same spectral characteristics of the observed gravity data and crustal thickness. The density contrast map indicated that density variation

between sediment accumulation zones and basement rocks is approximately 0.2 - 0.4 g/cm$^3$.

The algorithm presents a fast computation of density contrast automated initial estimation. It computes the initial estimation from the given Bouguer Anomaly. However, the final and initial estimation outputs are quite similar in some cases. Furthermore, it requires few parameters to compute density contrast distribution. Nevertheless, the major limitation is that the algorithm assumes the output is 3D by using a calculated initial density from the 1D equation. The outputs contain all limitations of the 1D formula. Since the algorithm uses generalised inverse the outputs are biased. Therefore, the resolution matrix produces poor results. The other limitation is the inversion process is linear which means estimated density contrast map and observed data has a linear relation. Even though the outputs are reasonable, the limitations of the method should be taken into account for the interpretation step.

**Acknowledgements**

I would like to offer my special thanks to Dr. Chris GREEN for his insightful contributions to the theory of the algorithm. Moreover, I am grateful to anonymous reviewers for their comments.

**References**

Al Chalabi, M. A. 1972. Interpretation of gravity anomalies by non-linear optimisation. Geophysical Prospecting 20(1), 1-16.

Allen, T. I., Cooper, S. A., Cull, J. P. 2001. High definition gravity surveys and density modelling for kimberlite exploration. Exploration Geophysics 32(2), 89-94.

Arias Castro, E., Donoho, D. L. 2009. Does median filtering truly preserve edges better than linear filtering?. The Annals of Statistics 37(3), 1172-1206.

Aster, R. C., Borchers, B., Thurber, C. H. 2018. Parameter Estimation and Inverse Problems. Elsevier.

Bear, G. W., Al-Shukri, H. J., Rudman, A. J. 1995. Linear inversion of gravity data for 3-D density distributions. Geophysics 60(5), 1354-1364.

Blakely, R. J. 1996. Potential Theory in Gravity and Magnetic Applications. Cambridge University Press.

Bonvalot, S., Balmino, G., Briais, A., Kuhn, M., Peyrefitte, A., Vales, N., Biancale, R., Gabalda, G., Reinquin, F. 2012. World Gravity Map: a set of global complete spherical Bouguer and isostatic anomaly maps and grids. International European Geosciences Union General Assembly Conference Abstracts 14, 11091.

Bott, M. H. P. 1960. The use of rapid digital computing methods for direct gravity interpretation of sedimentary basins. Geophysical Journal International 3(1), 63-67.

Cai, Y. F., Li, C., Saridakis, E. N., Xue, L. Q. 2018. f(T) gravity after GW170817 and GRB170817A. Physical Review 97(10), 103513.

Church, J. C., Chen, Y., Rice, S. V. 2008. A spatial median filter for noise removal in digital images. Institute of Electrical and Electronics Engineers Southeast Conference, 618-623.

Clifford, G. D. 2005. Singular value decomposition and independent component analysis for blind source separation. Biomedical, Signal Image Process 44, 489-499.

Cordell, L., Henderson, R. G. 1968. Iterative three-dimensional solution of gravity anomaly data using a digital computer. Geophysics 33(4), 596-601.

Delibasis, N., Ziazia, M., Voulgaris, N., Papadopoulos, T., Stavrakakis, G., Papanastassiou, D., Drakatos, G. 1999. Microseismic activity and seismotectonics of Heraklion area (central Crete Island, Greece). Tectonophysics 308(1-2), 237-248.

Dilek, Y. 2006. Collision tectonics of the Mediterranean region: causes and consequences. Geological Society of America Special Papers 409, 1.

Enmark, T. 1981. A versatile interactive computer program for computation and automatic optimization of gravity models. Geoexploration 19(1), 47-66.

Fedi, M. 1997. Estimation of density, magnetization, and depth to source: a nonlinear and noniterative 3-D potential-field method. Geophysics 62(3), 814-830.

Fedi, M., Rapolla, A. 1999. 3-D inversion of gravity and magnetic data with depth resolution. Geophysics 64(2), 452-460.

Freire, S. L., Ulrych, T. J. 1988. Application of singular value decomposition to vertical seismic profiling. Geophysics 53(6), 778-785.

Golub, G. H., Van Loan, C. F. 1996. Matrix Computations. Johns Hopkins University Press, Baltimore, London.

Gönenç, T., Akgün, M., Ergün, M. 2006. Girit yayının sismolojik ve bouguer gravite anomalisi verilerine göre yorumlanması. Geosound 48(1), 51-68.

Gönenç, T., Akgün, M. 2012. Structure of the Hellenic subduction zone from gravity gradient functions and seismology. Pure and Applied Geophysics 169(7), 1231-1255.

Grandis, H. 2009. Introduction to Geophysical Inversion Modeling. Indonesia Geophysical Expert Association (HAGI).

Grandis, H., Dahrin, D. 2014. Constrained two-dimensional inversion of gravity data. Journal of Mathematical and Fundamental Sciences 46(1), 1-13.

Granser, H. 1987. Nonlinear inversion of gravity data using the Schmidt-Lichtenstein approach. Geophysics 52(1), 88-93.

Guspi, F. 1992. Three-dimensional Fourier gravity inversion with arbitrary density contrast. Geophysics 57(1), 131-135.

Hammer, P. T. C., Hildebrand, J. A., Parker, R. L. 1991. Gravity inversion using semi-norm minimization: density modeling of Jasper Seamount. Geophysics 56(1), 68-79.

Hinze, W. J. 1990. Geotechnical an Environmental Geophysics. SEG, I, 75-126.

Hinze, W. J., Von Frese, R. R., Saad, A. H. 2013. Gravity and Magnetic Exploration: Principles, Practices, and Applications. Cambridge University Press.

Huestis, S. P. 1988. Uniform norm minimization for two-signed solutions. Geophysics 53(5), 721-722.

Justusson, B. I. 1981. Median Filtering: Statistical Properties. In Two-Dimensional Digital Signal Processing II. Springer, Heidelberg, Berlin, 161-196.

Kahveci, M., Çırmık, A., Doğru, F., Pamukçu, O., Gönenç, T. 2019. Subdividing the tectonic elements of Aegean and Eastern Mediterranean with gravity and GPS data. Acta Geophysica 67(2), 491-500.

Lanczos, C. 1997. Linear Differential Operators. Society for Industrial and Applied Mathematics, 564.

Lawson, C. L., Hanson, R. J. 1974. Solving Least Squares Problems. Society for Industrial and Applied Mathematics, U.S., 350.

Le Pichon, X. 1983. Land-locked oceanic basins and continental collision: the eastern Mediterranean as a case example. Hsu, K. (Ed.) Mountain Building, Academic Press, London, 201-211.

Le Pichon, X., Angelier, J. 1979. The Hellenic arc and trench system: a key to the neotectonic evolution of the eastern Mediterranean area. Tectonophysics 60(1-2), 1-42.

Levenberg, K. 1944. A method for the solution of certain nonlinear problems. Quarterly Applied Mathematics 2, 164-168.

Li, Y., Oldenburg, D. W. 1998. 3-D inversion of gravity data. Geophysics 63(1), 109-119.

Mareschal, J. C. 1985. Inversion of potential field data in Fourier transform domain. Geophysics 50(4), 685-691.

Mart, Y., Ryan, W. 2003. The tectonics of Cyprus Arc: a model of complex continental collision. European Geophysical Society - American Geophysical Union - European Union of Geosciences Joint Assembly, 2282.

McClusky, S., Balassanian, S., Barka, A., Demir, C., Ergintav, S., Georgiev, I., Gürkan, O., Hamburger, M., Hurst, K., Kahle, H., Kastens, K. 2000. Global positioning system constraints on plate kinematics and dynamics in the eastern Mediterranean and Caucasus. Journal of Geophysical Research: Solid Earth 105(B3), 5695-5719.

McKenzie, D. 1972. Active tectonics of the Mediterranean region. Geophysical Journal International 30(2), 109-185.

Meier, T., Rische, M., Endrun, B., Vafidis, A., Harjes, H. P. 2004. Seismicity of the Hellenic subduction zone in the area of western and central Crete observed by temporary local seismic networks. Tectonophysics 383(3-4), 149-169.

Menichetti, V., Guillen, A. 1983. Simultaneous interactive magnetic and gravity inversion. Geophysical Prospecting 31(6), 929-944.

Menke, W. 1984. Geophysical Data Analysis. Discrete Inverse Theory. Academic Press, New York, 312.

Menke, W. 2018. Geophysical Data Analysis: Discrete Inverse Theory. Academic Press, New York.

Mercier, J. L., Sorel, D., Vergely, P., Simeakis, K. 1989. Extensional tectonic regimes in the Aegean basins during the Cenozoic. Basin Research 2(1), 49-71.

Nagihara, S., Hall, S. A. 2001. Three-dimensional gravity inversion using simulated annealing: constraints on the diapiric roots of allochthonous salt structures. Geophysics 66(5), 1438-1449.

Oldenburg, D. W. 1974. The inversion and interpretation of gravity anomalies. Geophysics 39(4), 526-536.

Öner, Z., Dilek, Y., Kadıoğlu, Y. K. 2010. Geology and geochemistry of the synextensional salihli granitoid in the Menderes core complex, western Anatolia, Turkey. International Geology Review 52(2-3), 336-368.

Pamukçu, O. 2016. Geodynamic assessment of eastern Mediterranean region: a joint gravity and seismic b value approach. Arabian Journal of Geosciences 9(5), 360.

Papazachos, B. C., Karakostas, V. G., Papazachos, C. B., Scordilis, E. M. 2000. The geometry of the Wadati–Benioff zone and lithospheric kinematics in the Hellenic arc. Tectonophysics 319(4), 275-300.

Parker, R. L. 1972. The rapid calculation of potential anomalies. Royal Astronomical Society Geophysical Journal, 31.

Parker, R. L. 1974. Best bounds on density and depth from gravity data. Geophysics 39(5), 644-649.

Parker, R. L. 1975. The theory of ideal bodies for gravity interpretation. Geophysical Journal International 42(2), 315-334.

Parker, R. L. 1977. Understanding inverse theory. Annual Review of Earth and Planetary Sciences 5(1), 35-64.

Paterson, N. R., Reeves, C. V. 1985. Applications of gravity and magnetic surveys: The state-of-the-art in 1985. Geophysics 50(12), 2558-2594.

Peacock, R. J. 1992. Cavity detection? an engineering application for gravity. Exploration Geophysics 23(4), 567-570.

Pedersen, L. B. 1977. Interpretation of potential field data a generalized inverse approach. Geophysical Prospecting 25(2), 199-230.

Pedersen, L. B. 1979. Constrained inversion of potential field data. Geophysical Prospecting 27(4), 726-748.

Pilkington, M., Crossley, D. J. 1986. Determination of crustal interface topography from potential fields. Geophysics 51(6), 1277-1284.

Press, W. H., Teukolsky, S. A., Vetterling, W. T., Flannery, B. P. 2007. Numerical Recipes 3rd Edition: The Art of Scientific Computing. Cambridge University Press.

Reamer, S. K., Ferguson, J. F. 1989. Regularized two-dimensional Fourier gravity inversion method with application to the Silent Canyon caldera, Nevada. Geophysics 54(4), 486-496.

Roberts, R. L., Hinze, W. J., Leap, D. I., Ward, S. H. 1990. Application of the gravity method to the investigation of a landfill in glaciated midcontinent, USA. Geotechnical and Environmental Geophysics 2, 253-260.

Roy, A. 1962. Ambiguity in geophysical interpretation. Geophysics 27(1), 90-99.

Smith, R. A. 1959. Some depth formulae for local magnetic and gravity anomalies. Geophysical Prospecting 7(1), 55-63.

Smith, R. A. 1960. Some formulae for interpreting local gravity anomalies. Geophysical Prospecting 8(4), 607-613.

Sorel, D., Mercier, J. L., Keraudren, B., Cushing, M. 1988. Le rôle de la traction de la lithosphère subductée dans l'évolution géodynamique plio-pléistocène de l'arc égéen: mouvements verticaux alternés et variations du régime tectonique. Comptes rendus de l'Académie des sciences. Série 2, Mécanique, Physique, Chimie, Sciences de l'univers, Sciences de la Terre 307(19), 1981-1986.

Strang, G. 1988. Linear Algebra and Its Applications. Hartcourt Brace Jovanovich College Publishers.

Tadjou, J. M., Nouayou, R., Kamguia, J., Kande, H. L., Manguelle Dicoum, E. 2009. Gravity analysis of the boundary between the Congo Craton and the Pan-African belt of Cameroon. Austrian Journal of Earth Sciences 102(1).

Tarantola, A., Valette, B. 1982. Generalized nonlinear inverse problems solved using the least squares criterion. Reviews of Geophysics 20(2), 219-232.

Tontini, F. C., Cocchi, L., Carmisciano, C. 2008. Potential-field inversion for a layer with uneven thickness: the Tyrrhenian Sea density model. Physics of the Earth and Planetary Interiors 166(1-2), 105-111.

Tukey, J. W. 1974. Nonlinear (nonsuperposable) methods for smoothing data. Proceedings of Congress Record EASCOM, 673-681.

Ulrych, T. J., Freire, S., Siston, P. 1988. Eigen image processing of seismic sections. International Society of Exploration Geophysicists Technical Program Expanded Abstracts, 1261-1265.

Vasco, D. W. 1989. Resolution and variance operators of gravity and gravity gradiometry. Geophysics 54(7), 889-899.

Vrabie, V. D., Mars, J. I., Lacoume, J. L. 2004. Modified singular value decomposition by means of independent component analysis. Signal Processing 84(3), 645-652.

Xia, J., Sprowl, D. R. 1992. Inversion of potential-field data by iterative forward modelling in the wavenumber domain. Geophysics 57(1), 126-130.

Zhao, B. B., Chen, Y. Q. 2011. Singular value decomposition (SVD) for extraction of gravity anomaly associated with gold mineralization in Tongshi gold field, Western Shandong Uplifted Block, Eastern China. Nonlinear Processes in Geophysics 18(1), 103.

Bulletin of the Mineral Research and Exploration

http://bulletin.mta.gov.tr

# New age findings with microfossils of the Van Formation (Van, Eastern Anatolia)

Ayşegül GÜNEY[a*], Elvan DEMİRCİ[b], Kemal KORKMAZ[c] and Sefer ÖRÇEN[d]

[a]*Aksaray University, Faculty of Engineering, Department of Geological Engineering, Aksaray, Turkey*
[b]*Hacettepe University, Graduate School of Science and Engineering, Department of Geological Engineering, Beytepe, Ankara, Turkey*
[c]*Yenidoğan Street, Toki Sites, C2-3, 27, 12, 48, Talas, Kayseri, Turkey*
[d]*Sokullu Mehmet Paşa Avenue, 93/12, Çankaya, Ankara, Turkey*

*Research Article*

Keywords:
Calcareous Nanoplankton, Planktonic Foraminifera, Serravallian, Tortonian, Van Formation.

**ABSTRACT**

Van Formation, which is mainly represented by conglomerate, sandstone, marl and limestone, covers a large area around the Van province. The age of the unit was assigned in different localities of the region as late Oligocene - middle Miocene, early Miocene, Burdigalian - Langhian (early - middle Miocene) by previous studies. In order to determine the age of the upper levels of the formation in the east and southeast of Lake Van, a total of 98 samples collected from three measured stratigraphic sections. These samples have been examined in terms of calcareous nannoplankton and planktonic foraminiferal content. 33 species of 12 calcareous nannoplankton genera and 18 species of 9 planktonic foraminiferal genera representing the Serravalian - Tortonian interval have been identified. Calcareous nannoplankton and planktonic foraminiferal biozones of the unit could not be defined in the study area because of some samples do not contain calcareous nannoplankton and planktonic foraminifera, some samples are scarce in fossils and not all of the zonal markers have been identified. Considering the stratigraphic distribution of the calcareous nannoplankton and planktonic foraminiferal species that the formation contains, age of the Van Formation in the study area is re-evaluated as Serravallian - Tortonian (middle - late Miocene). This shows that marine features continued in the Tortonian (late Miocene) in the study area.

*Received Date: 12.07.2020*
*Accepted Date: 15.03.2021*

## 1. Introduction

The study area, located in the Eastern Anatolia Region, is located in the E - SE of Lake Van, within the Van L50 - $b_2$ sheet (Figure 1). In the study area, Maxon (1936) first investigated the petroleum possibilities of Lake Van and its surroundings and named the unit consisting of the alternation of conglomerate, sandstone, claystone and siltstone overlying the crystallized limestone as Van Formation. In the succeeding years, Arni (1939) made a geological map of the region at 1/100.000 scale and stated that the metamorphites in the region were Paleozoic, the ophiolites were Late Cretaceous-Paleocene and the limestones were Eocene aged. Ternek (1953), Şener (1992) and Yeşilova (2004) studied the geological features of the regions in the southeast of Van province, the south of Van province and the north of Lake Van, respectively. Ortynski and Tromp (1944) in Van province, Kıraner (1959) in the east of Lake Van, Demirtaşlı and Pisoni (1965) around Adilcevaz and Ahlat areas, Gelati (1975) around Lake Van - Erciş area made researches on the stratigraphic characteristics. Aksoy (1988) surveyed the stratigraphy and tectonics of the area around the Lake Van. Acarlar et al. (1991) stated that clastic deposits of the Oligocene - middle Miocene Van Formation were initially formed as

Citation Info: Yıldız, A., Demirci, E., Korkmaz, K., Örçen, S. 2021. New age findings with microfossils of the Van Formation (Van, Eastern Anatolia). Bulletin of the Mineral Research and Exploration 166, 33-52. https://doi.org/10.19111/bulletinofmre.897859

**Corresponding author: Ayşegül GÜNEY, ayildiz10@hotmail.com*

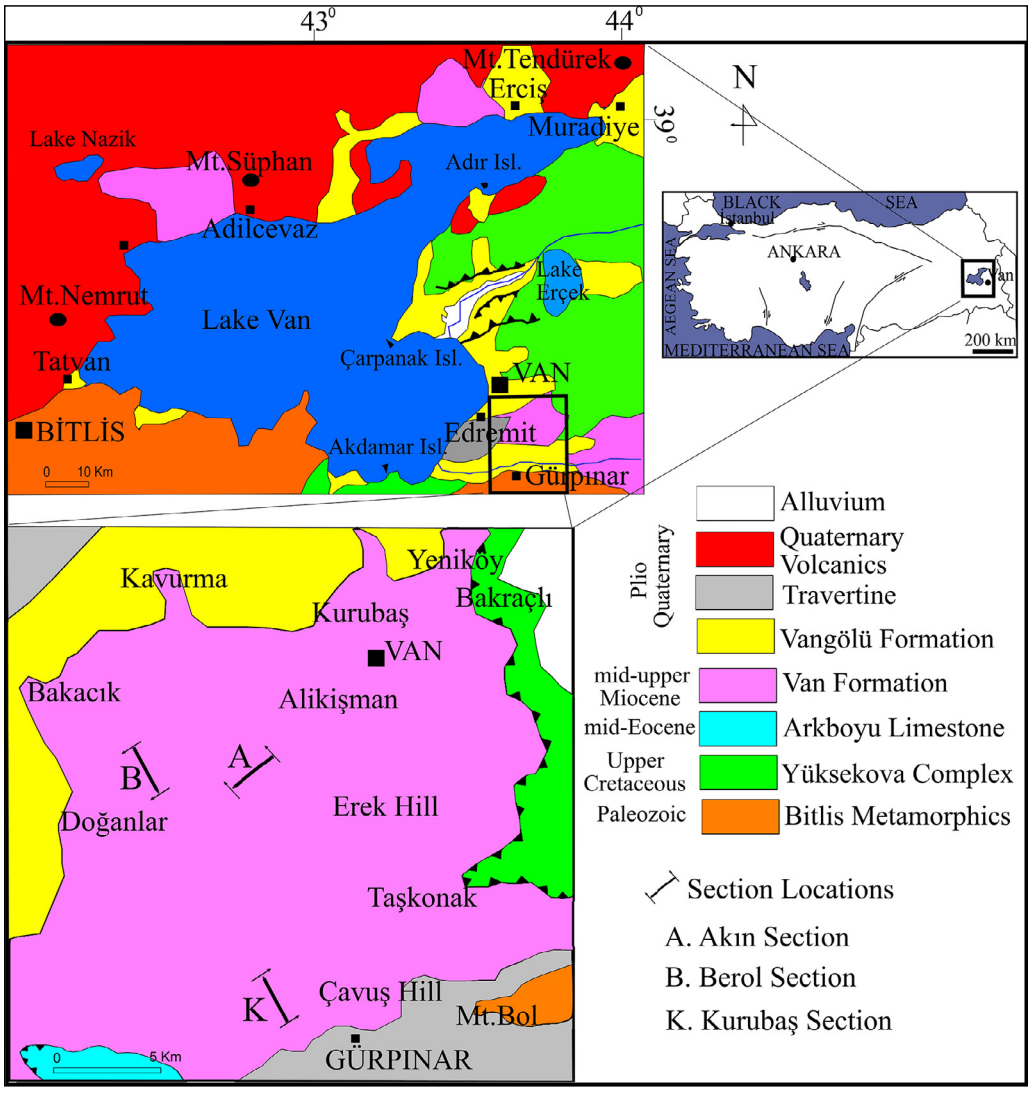


Figure 1- Location and geological maps of the study area, and the section locations (modified from Acarlar et al., 1991; Aksoy, 1988; Şener, 1992; Üner, 2003; Demirci, 2016).

autochthonous-para-autochthonous cover units, then the allochthonous units thrusted over each other and the Van Formation during various phases within the Late Cretaceous-middle Miocene interval. Moreover, structural geological studies were carried out in the area between Lake Van and Iranian border by Ketin (1977), around Van - Gürpınar - Başkale - Çatak areas by Balkaş (1980), around Van province by Şaroğlu and Yılmaz (1984) and Yılmaz (1990), in the Özalp-Iranian border by Şenel et al. (1984), throughout the Eastern Anatolia Region by Dewey et al. (1986), Yılmaz et al. (1987), Adıyaman et al. (1998), Trifonov et al. (1998), Koçyiğit and Beyhan (1998), Gürsoy et al. (2009), Okuldaş et al. (2013). Researches on volcanism in the region were conducted by Degens and Kurtman (1978), Savcı (1980), Elmas (1994), Sümengen (2008), Oyan (2018). Kempe et al. (1978) analyzed the hydrochemistry of water tributaries and mainstream rivers of Lake Van. Valeton (1978) made morphological and petrological investigations of terraces located in the vicinity of Lake Van. Wong and Degens (1978) and Degens and Kurtman (1978) prepared the bathymetric map of Lake Van. Wong and Finckh (1978) analyzed the water level changes of Lake Van for the 18,000 years and determined the resultant coastal terraces. Acarlar and Türkecan (1986) worked on the travertines formed along the eastern and the western border faults of Başkale Basin, and Barka and Şaroğlu (1995) on the Edremit Travertine. Sağlam (2003) made a detailed micropaleontological

study on the Van Formation cropping out in the east of Lake Van based on the five measured stratigraphic sections, and revealed the biostratigraphy of the formation according to the micropaleontological examination of the washing samples and the thin sections. As a result, Sağlam (2003) assigned a Burdigalian-Langhian (early-middle Miocene) age to the Van Formation; and based on the petrographic descriptions made on the limestone and calcarenite samples taken from the formation, it was revealed that the formation was a transgressive sequence and represented a deep marine environment considering the sedimentary structures obtained from the turbiditic sediments of the upper slope of the basin. Demirci (2016) examined the microfacies characteristics of the Van Formation outcropping around Van and revealed that the formation consists of rocks indicating environments from carbonate shelf to basin and that the sedimentary rocks of the Van Formation were formed in the submarine fan environment developed on the slope of a carbonate platform during the closure of the Neotethys.

The sediments of Van Formation, which covers a wide area around Van and are generally represented by conglomerate, sandstone, marl and limestone, play an important role in revealing the geological evolution and neotectonic characteristics of the region. It has been stated that the Van Formation was deposited in the late Oligocene-middle Miocene, early Miocene or Burdigalian-Langhian (early - middle Miocene) periods, considering the rock composition, macro and microfossil assemblages (Acarlar et al., 1991; Şener, 1992; Sağlam, 2003). In this study carried out on the Van Formation in the study area, the calcareous nannoplankton and planktonic foraminiferal content of the Van Formation were examined and the age of the formation in the study area was redefined.

## 2. Material and Method

A total of 98 samples of three measured stratigraphic sections taken from Van Formation constitute the materials of this study.

In the examination of calcareous nannoplankton, the clean inner surfaces of the samples were scraped in powder form with a pin, and a drop of distilled water was added to the fine powder. The prepared suspension was dried in a thermostatted oven, and a small amount of liquid Canada Balsam was dropped on the coverslip and adhered on the dried slide. During this bonding process, air bubbles were eliminated with a metal rod. Later, the dried preparate was cleaned with a chemical cleaner (Xylol) and made ready for examination. 98 preparates prepared in this way were examined with and x1600 magnification and immersion oil under the Leica DM 2500P polarization microscope in the laboratory of the Department of Geological Engineering at Aksaray University, Faculty of Engineering, they were identified paleontologically and photographed by a Leica DFC 295 camera (Figures 6 - 8). Descriptions and stratigraphic distributions of the calcareous nannoplankton genera and species in slides were made by based on Martini (1971), Okada and Bukry (1980), Perch-Nielsen (1985), Young (1998), Bown (1999), Galovic and Young (2012), Grandstein et al. (2012) and Nannotax 1 - 26 sources (Table 4a). Wei (1988) method was

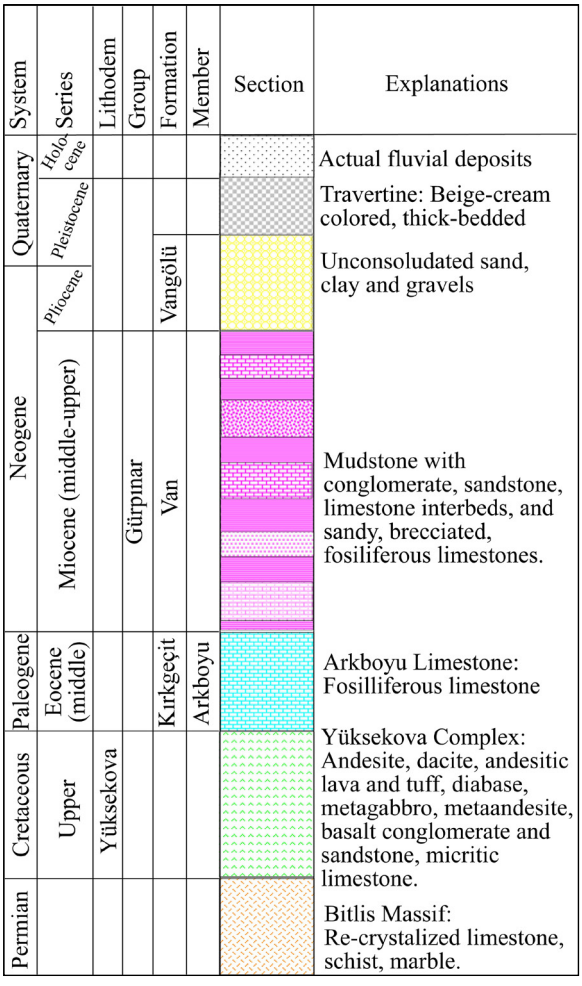


Figure 2- Generalized stratigraphic section of the study area (not to scale; modified from Şener, 1992 and Demirci, 2016).

taken as a basis while determining the abundance distribution of calcareous nannoplankton species. According to this method, the following descriptions were used: abundant for species with 1-10 individuals in a microscope field, common for species with 1 individual in 2 - 10 microscope field, few for species with 1 individual in 11 - 100 microscope field, rare for species with 1 individual in 101 - 1000 microscope area.

In order to determine the planktonic foraminifera, examinations were made on the thin sections for carbonate rock samples and by washing processes for the samples taken from marl, mudstone and claystone. In washing the samples, each 100-gram sample was decomposed with hot water containing 10% Perhydrol ($H_2O_2$) in a beaker. Decomposed samples were washed by passing through 60, 125 and 250 µm sieves with pressurized water. The residue on the sieves were separately dried in the oven, and the planktonic foraminifera were sorted under binocular microscope. Planktonic foraminiferal genera and species obtained in this way were examined and photographed under the Leica DCM 295 binocular microscope and Leica DFC 295 camera, respectively at the laboratory of Aksaray University, Faculty of Engineering, Department of Geological Engineering (Figures 9 - 10). Descriptions and stratigraphic distributions of planktonic foraminiferal genera and species in the slides were made by using the sources as Bolli (1957), Bolli and Bermudez (1965), Martini (1971), Bolli and Premoli Silva (1973), Okada and Bukry (1980), Bolli and Saunders (1985), Jenkins (1985), Young (1998), Grandstein et al. (2012), Rybar et al. (2015) (Table 4b). In calculation of the abundance of planktonic foraminifera by considering the same species in a 100-gram sample, following scale was used: abundant for 60 - 100, common for 30 - 60, few for 10 - 30, rare for 1 - 10 specimens.

Three stratigraphic sections taken from the Van Formation, geological map of the area involving the section locations, generalized stratigraphic section (not to scale) of the study area, and the tables showing the abundance and distribution of calcareous nannoplankton and planktonic foraminifera

Table 1- Abundance and distributions of the nannoplankton and planktonic foraminiferal species in the Akın measured stratigraphic section.

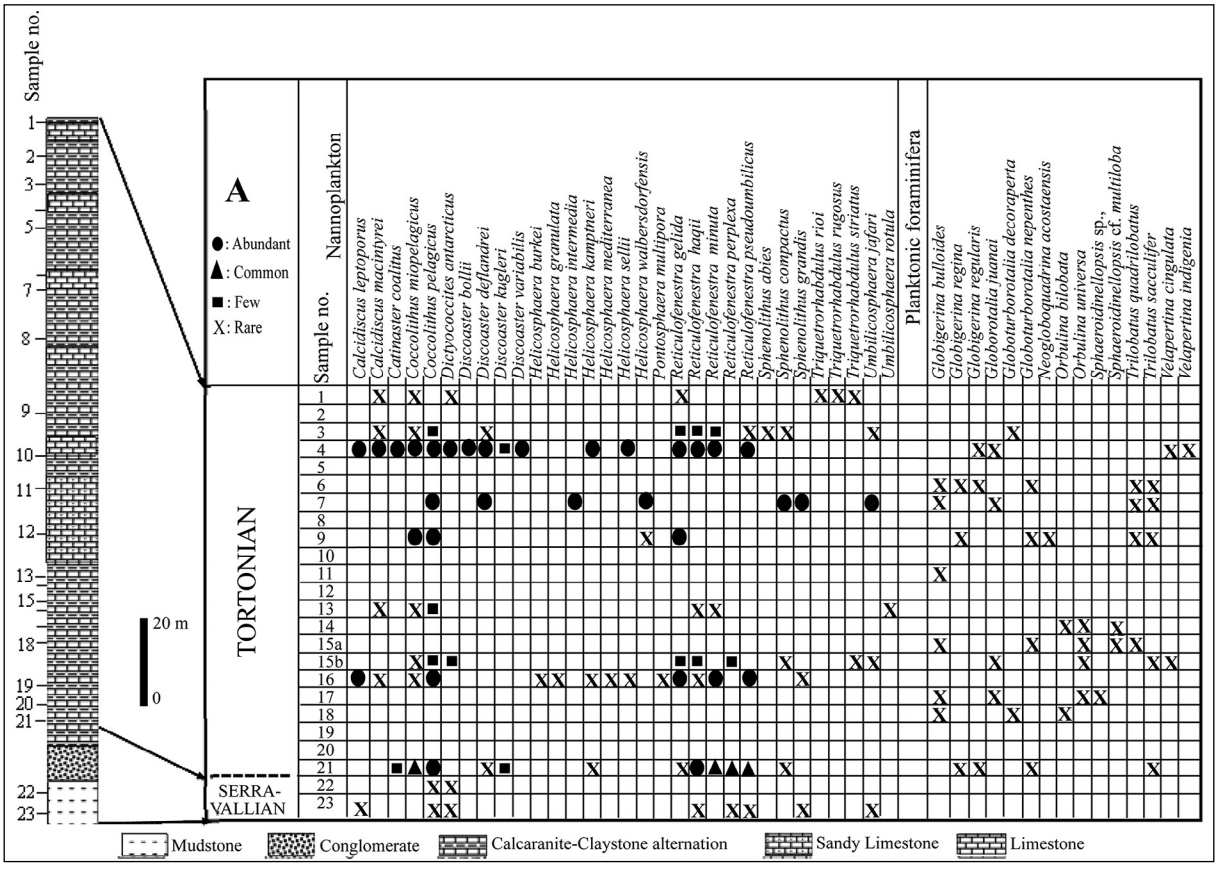

obtained from these sections were drawn in the computer. Calcareous nannoplankton and planktonic foraminiferal assemblages of the Van Formation illustrated as plates (Figures 1, 2; Tables 1 - 3). The age of the Van Formation in the study area was interpreted by using these tables.

### 3. Regional Geological Setting and Stratigraphy

Convergence between the Arabian - African plates and the Anatolian Plate and the resultant compressional regime played a prominent role in the geological evolution of Turkey. The most important effects of this N - S trending compressional regime are the strike-slip faults with NW and NE striking and the reverse faults with WNW - ESE striking in the Eastern Anatolia Region. Numerous active fault systems such as East Anatolia Fault Zone, Doğubeyazıt Fault Zone, Balıklıgöl Fault Zone, Ağrı Fault, Çaldıran Fault, Tutak Fault, Erciş Fault, Bulanık Fault have been formed due to the compressional regime within the scope of the young tectonics of the Eastern Anatolia Region

Table 2- Abundance and distributions of the nannoplankton and planktonic foraminiferal species in the Berol measured stratigraphic section.

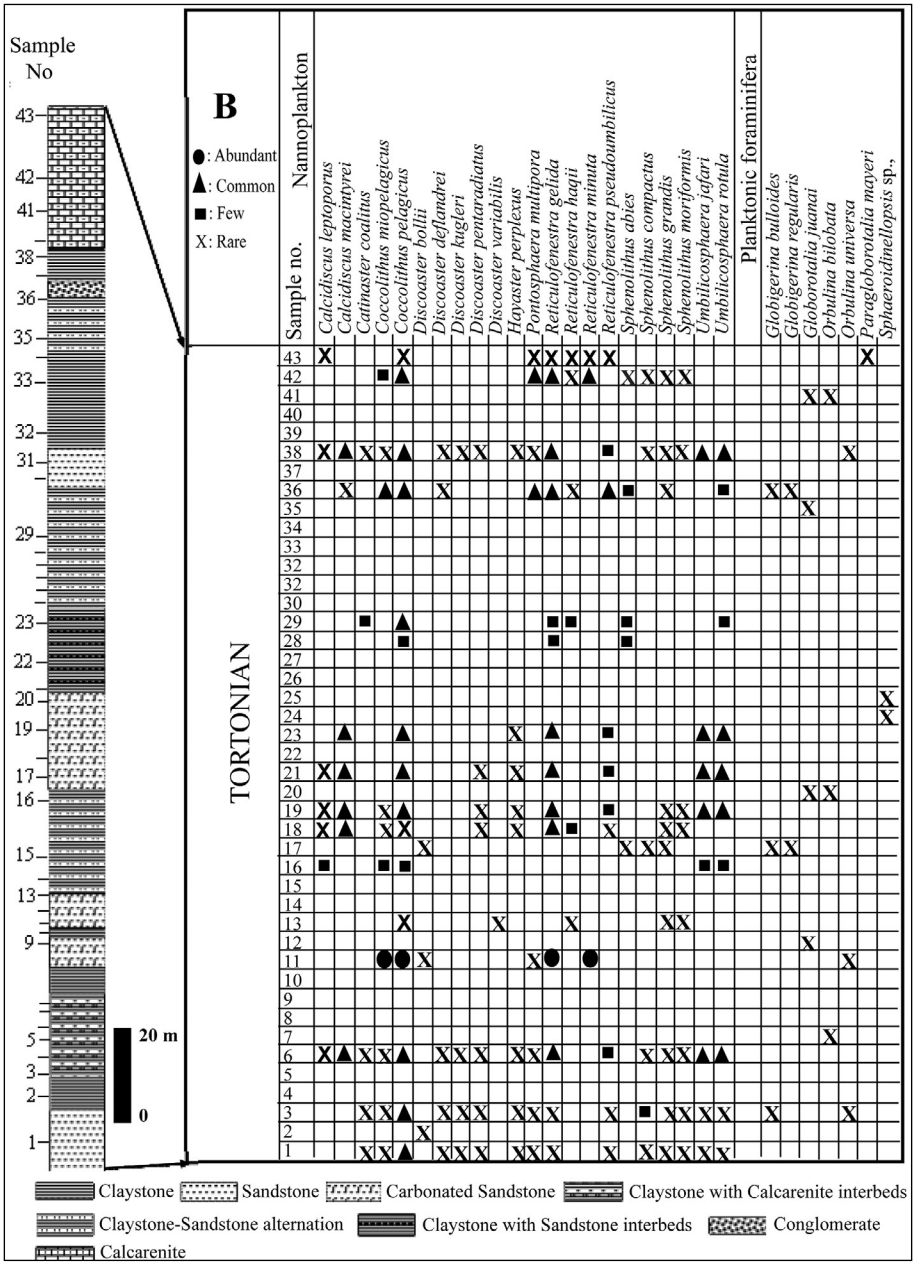

(Şaroğlu and Yılmaz, 1984). It was determined that the Erciş Fault, located in the north of Van, consists of several parallel blocks, and traces of the Erciş Fault were determined generally within Plio-Quaternary deposits (Şaroğlu and Yılmaz, 1984). However, considering the predominant rocks, the basin could be generalized as comprising metamorphic rocks of the Bitlis Massif to the south, young volcanoclastic rocks in the west and north; and volcanic rocks and ophiolite of the Yüksekova Complex and young-actual fluvial and lacustrine clastics and carbonates to the east (Özkaymak, 2003).

The stratigraphic sequence in the study area begins with the Permian metamorphics of the Bitlis Massif at the base. The sequence continues upwards with the Upper Cretaceous Yüksekova Complex, the Akkuyu Member of the middle Eocene Kırkgeçit Formation consisting of fossiliferous limestone, the middle - late Miocene Van Formation, Plio-Quaternary Vangölü Formation. The Van Formation, the subject of this study, is described in detail below (Figure 2).

### 3.1. Van Formation

Description: The formation was first described by Acarlar et al. (1991). The name of the formation was derived from the Van province where it outcrops.

Type locality and type section: There is no type locality presenting a complete type section of the formation. Different levels of the formation are observed in different places. The late Oligocene aged base of the unit is well observed in Koçköy, while the early Miocene part is in the north of Tekmal and east of Alabayır village. The base of the formation consisting of ophiolite-derived conglomerates outcrop in the northern slope of the Çilehane Mountain. The lower-middle levels formed of the alternation of sandstone-shale-breccia limestone are best observed between the are Alabayır, Beyüzümü, Aşıt villages and Tekmal. The olistostromal conglomerate level is best seen in the Kırma Hill. Its middle parts bearing olistoliths are best observed around Şahgeldi and Esenpınar villages. Its upper part, which is composed of calcarenite - sandy limestone - carbonated sandstone alternation, is well exposed in the south of Ovapınar village. Kurubaş strait is the best place where the uppermost parts of the formation consisting of claystone - siltstone - sandstone alternation is observed (Acarlar et al., 1991; Demirci, 2016).

Lithological features: The Van Formation consists of clastics (conglomerate, sandstone etc.), carbonate and clayey (claystone, mudstone etc.) rocks. At the basal levels of the formation, white colored tuffites and yellowish - light grey colored, thin- to mid-bedded clayey limestones containing tuff clasts are seen between the basaltic lava flows, sandstones and calcarenites as interbeds. The Van Formation begins with different rock types in the localities where its base is best observed such as: northern slope of Çilehane Mountain, north of Koçköy (around Erciş), northwest of Tekmal and east of Alabayır village. The formation unconformably overlies the Dirbi Mélange with its ophiolite-derived conglomerates at the northern of Çilehane Mountain. In Kocaköy, there are Miogypsina- and coral-bearing pebbly limestones at the base of the unit. Van Formation unconformably overlies the Karataş Formation in this area. In the northwest of Tekmal, the formation begins with coral-bearing conglomerate and brecciated limestones at the bottom. To the east of Alabayır village, brecciated limestone, calcarenite and clayey limestone are observed at the base of the formation. These various lithologies at the base of the formation are generally overlain by sandstone, shale alternation which consists of various. This alternation includes variable thickness of brecciated limestone, calcarenite and fine conglomerate levels. In the upper parts of the sequence, olistostromal conglomerate and blocky levels are also added to the alternation of sandstone, shale. An alternation of calcarenite, sandy limestone, carbonated sandstone is dominant in the upper levels of the unit. The dominant lithology of the unit is sandstone, shale alternation. Sandstones, thin to mid-bedded, occasionally thick-bedded, contains ophiolitic components and plant traces, and are usually carbonate-cemented. Some sandstone levels contain abundant mica minerals, and in places they are coarse grained and pebbly. These parts are in the form of intercalations within the sandstone-shale alternation. Sandstones sometimes contain macrofossil shells and there are greyish brown, thin-bedded, sandy carbonate levels between them. Sandstones and shales are greenish brown and brown colored. Conglomerates, mostly polygenic, contain ophiolite gravels (derived from Yüksekova Complex and Erekdağı Ophiolite) and fragments of recrystallized limestone, schist, volcanite and limestones. They are in the form of intercalations within the sandstone, shale alternation

and have thicknesses generally varying between 1 - 2 m to 20 m. The conglomerates contain a sandy matrix and are carbonate cemented. Brecciated limestones, observed as interbeds within the shales, are carbonate cemented, grey colored, thick-bedded or massive, and bears pelecypod shells. Their thicknesses range between 1 - 2 m to 30 - 40 m. Calcarenites are more common in the upper parts of the Van Formation. All the lithologies that the Van Formation comprises show lateral and vertical transition. In addition, Adilcevaz Limestone seen in the north and west of Lake Van represents the lateral change of the calcarenite - sandy limestone alternation in the upper parts of the formation (Acarlar et al., 1991).

Contact relations: the Van Formation unconformably overlies all the older units, and covered by terrestrial units with an unconformity (Acarlar et al., 1991).

Distribution and thickness: The formation, widely distributed in the northwest, east and southeast of Lake Van, is observed at the Ovapınar village in the Van K51 - $a_2$ sheet; at Sürüyolu and Otlakbaşı villages in the K51 - $a_3$ sheet; Bağdaşan, Aşağı Kalecik and Değirmenözü villages K51 - $a_4$ sheet; at Kevenli and Bakraçlı villages and in the Kurubaş Strait in the L50 - $b_2$ sheet; at Pirgarip village and on the northern slope of the Çilehane Mountain in the K50 - $b_3$ sheet; at Esenpınar and Şahgeldi villages in the K50 - $b_4$ sheet; at Yeniköy in the K50 - $c_1$ sheet; at Aşıt and Kolsatan villages and around Koçköy in the K50 - $c_2$ sheet; around Alabayır village and Kırma Hill in the K50 - $c_3$ sheet; at İrenini Mountain in the K50-$d_2$ (Acarlar et al., 1991).

According to Acarlar et al. (1991), thickness of the formation is about 1200 m Sağlam (2003) determined its thickness as 256 m. The thickness of the formation was determined as 66 - 277 m in the study area located in the east and southeast of Lake Van.

Correlation: According to Acarlar et al. (1991) and Demirci (2016), the Van Formation can be correlated with the early Miocene aged Adicevaz Limestone sequence, with transgressive shelf characteristics, located around Adilcevaz and Ahlat areas in Demirtaşlı and Pisoni (1965) and Yeşilova (2004)'s studies. It has been stated that the formation could also be correlated with the Mendikdere Formation of Şenel et al. (1984) which contains the Oligocene - Miocene coarse detritals located in the area between Özalp - Başkale (Iranian border), and with the early Miocene Alibonca Formation described by Şener (1992).

Depositional environment: According to Acarlar et al. (1991), the Van Formation started to develop due to the transgression in the Oligocene. The conglomerates deposited in the shallow marine environment in this phase formed the base of the unit. Transgressive development continued with coral- and miogypsinid-bearing limestones, and in the last phase of transgression, the development of the submarine fan began with the tilting in the basin. The rock units forming the basement were added to the submarine fan environment probably developed in the east as olistoliths. The fan deposits contain thick sandstones and conglomerates representing channel facies and debris flows and calciturbidites carried from canyons incised in Adilcevaz Limestone. The depositional environment of the formation was interpreted by Sağlam (2003) and Demirci (2016) as the transgressional products that show transition between shallow-deep carbonate shelf and submarine fans due to sea level changes and tectonism during the closure of the southern branch of Neotethys.

Fossil content and age: The age of the formation was stated as late Oligocene-middle Miocene by Acarlar et al. (1991), as early Miocene by Şener (1992), as late Oligocene? - Langhian by Sağlam (2003).

Acarlar et al. (1991) assigned a late Oligocene age for the lower boundary of the formation in the locality of Koçköy (around Erciş) to the north of Lake Van. This age was determined based on the corals species as *Astrocoenia bodellei, A.nana, Cereiphyllia* cf. *tenuis, Diploria* cf. *dumblei, Heliastraea canalis, Hydnophora affinis, Hydronophyllia oligocenica, Pavona* cf. *hypocrateriformis, Phyllocoena lucasiana* from the pebbly limestones at lower levels of the formation. The researchers identified benthic foraminifera such as *Miogypsina irregularis, M.*cf. *intermedia, Miogypsinoides* cf. *dehaarti, Lepidocyclina (Nephrolepidina)* cf. *taurnoueri* in calcarenite, sandy limestones, clayey limestones, carbonated sandstone from the base of the formation in the northwest of Tekmal and the east of Alabayır village, and middle and upper levels of some localities; and planktonic foraminifera such as *Catapsydrax dissimilis, Globigerinoides sicanus,*

*Globorotalia obesa, Globoquadrina* cf. *dehiscens, G.*cf. *altispira, Trilobatus* cf. *trilobus* in the shales of the Van Formation. According to these determinations, they assigned an early Miocene (Burdigalian) age to the lower and middle levels of the formation. The same researchers, determined the coral species such as *Aphrastraea autignacensis, Aquitanastraea* cf. *pruvosti, Chydnophora solidior, Cladocora* cf. *manipulata, Favites neglecta, F.neglecta* var. *minor, F.mimbastensis, F.neugeboreni* var. *burdigalensis, Heiastrea nerthensis, H.taurinensis, H.saucatsensis, Hydnopora solidor, Lithophyllia michelotti, Meandrina africana, Paleoplesiastreaea desmoulinsi, Platycoenia tarbellensis, Porites collegniana, P.conoidea, Tarbellastrae abditaxis, T.conoidea, T.eggenburgiensis, T.*cf. *ellisiana, T.mimbastenis, T.reussiana, Thegioastrea crassicostata, T.diversiformis, T.*cf. *rosacea*, and aged the middle - upper levels of the formation as early-middle Miocene (Burdigalian - Langhian - Helvetian). Considering all these data, Acarlar et al. (1991) accepted the age of the Van Formation as late Oligocene - middle Miocene.

Sağlam (2003), in the study conducted in the east of Lake Van, could not be obtained any paleontological findings since the lower part of the Van Formation is represented by alluvial fan sediments. The author considered that due to the early Burdigalian age obtained from the carbonates overlying this unit, he thought that the lower boundary of the formation might be of late Oligocene? - Aquitanian age.

Sağlam (2003) identified the benthic foraminifera such as *Amphistegina lessonii, Lepidocyclina* sp., *Miyogypsina irregularis, Operculina complanata*, and a macrofossil assemblage containing *Ostrea* sp., *Pecten* sp., (pelecypod), *Clypeaster* sp. (echinoid), tabulate corals in the benthic foraminiferal-algal-echinoid packstone-grainstone facies which overlie the alluvial fan located at the bottom of the Van Formation. Benthic foraminiferal species as *Amphistegina lessonii, Bulumina* sp., *Cibicides* sp., *Gavelinella* sp., *Guttulina* sp., *Lenticulina* sp., *Lepidocyclina* sp., *Miogypsina irregularis, M.intermedia, Nodosaria* sp., *Operqulina complanata, Peneroplis* sp., *Textularia* sp.; planktonic foraminiferal species as *Catapsydrax dissimilis, Globigerinoides bisphericus, G.ruber, G.subquadratus, Globoquadrina altispira altispira, G.dehiscens, Globorotalia continuosa, G. scitula, Globigerina praebulloides, Orbulina sturalis, Paragloborotalia mayeri, Praeorbulina sicana, Trilobatus immaturus, T.sacculifer, T.trilobus*; gastropod, coral and pelecypod fossils were from the algal-benthic-planktonic foraminiferal packstone (calcarenite) levels in upper levels of the Van Formation which overlie the aforementioned levels. Based on the fossil assemblages, *Miogypsina irregularis* (lower Burdigalian) and *Miogypsina intermedia* (upper Burdigalian) benthic foraminiferal biozones, and *Trilobatus trilobus* (? lower - upper Burdigalian) and *Orbulina sturalis* (Langhian) planktonic foraminiferal biozones were determined from the bottom towards the top of the formation respectively. According to the Sağlam (2003), age of the upper boundary of the Van Formation to the east of Lake Van was assigned as Langhian (middle Miocene).

The age of upper levels of the formation within the study area have been determined as Serravallian-Tortonian (middle-late Miocene) based on the calcareous nannoplankton and planktonic foraminiferal assemblages determined in the study area located in the east and southeast of Lake Van (Figures 3 - 10, Tables 1 - 4).

## 4. Measured Stratigraphic Sections and Microfossils Findings in the Study Area

### 4.1. Akın (A) Measured Stratigraphic Section

The section, approximately 160 m-thick, was taken from the Akın village on the Van - Gürpınar highway (start coordinate: ($A^1$) 38S 0357773 / UTM 4252495, end coordinate: ($A^2$) 38S 0358479 / UTM 4253010, bedding: N35W/15ºNE, elevations for start and end coordinates are 1916 m and 2064 m, respectively). In the measured section, the base of the Van Formation cannot be clearly observed since it is covered by


Figure 3- Akın measured stratigraphic section (view from Bekir Hill; modified from Demirci, 2016).


Figure 4- Berol measured stratigraphic section (view from Doğanlar village, modified from Demirci, 2016).


Figure 5- Kurubaş measured stratigraphic section (modified from Demirci, 2016).

Table 3- Abundance and distributions of the nannoplankton and planktonic foraminiferal species in the Kurubaş measured stratigraphic section.

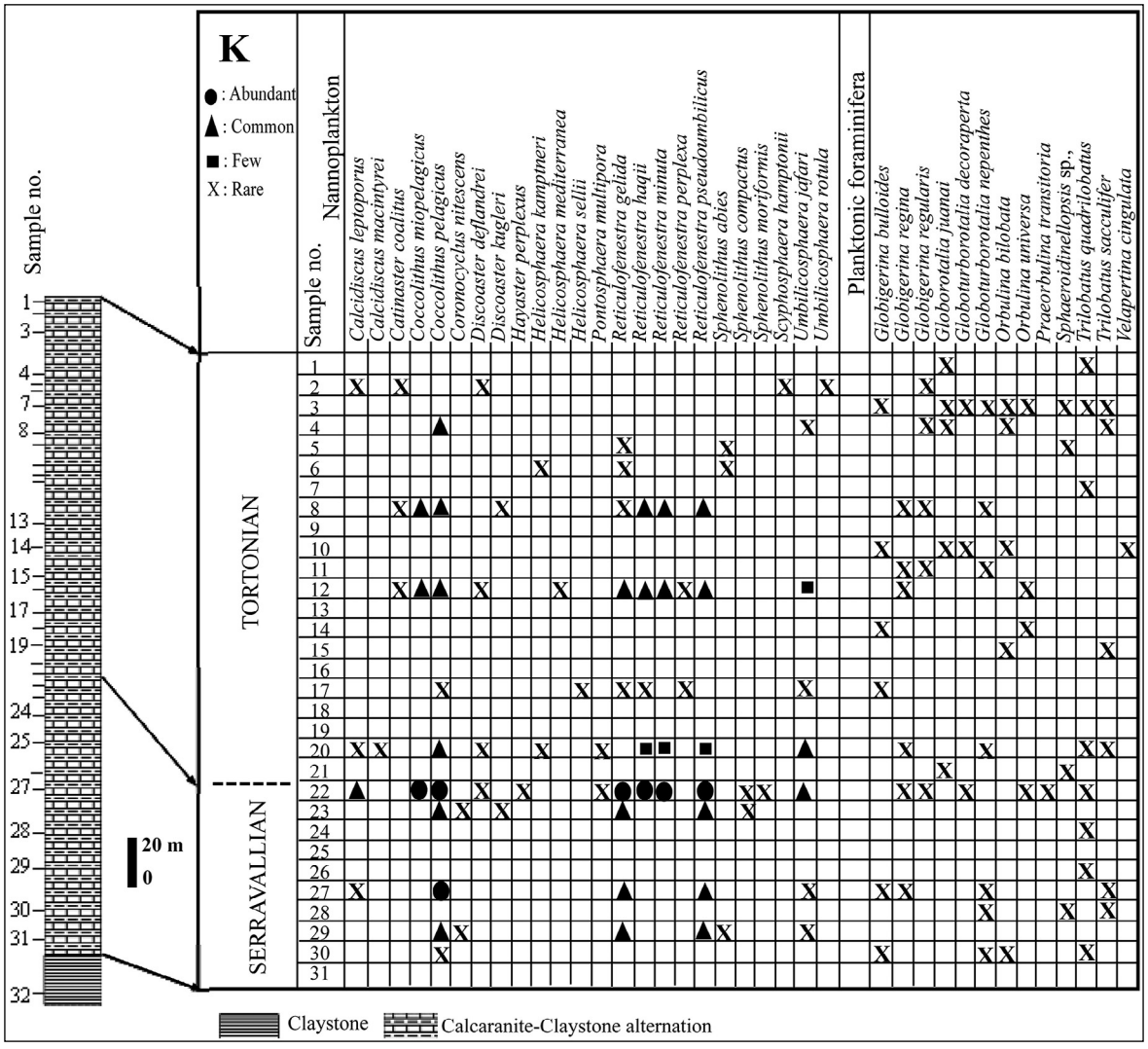

young sediments. The section starts with 10 m-thick, red colored, unconsolidated mudstone. It is overlain by 8 m-thick conglomerate which comprising ophiolite-derived clasts ranging between the size of 0.5 mm - 26 cm. An alternation of pinkish calcarenites and greenish claystone with 41 m thickness rests on these conglomerates. Towards the upper levels of the section, 20 m-thick, grey colored (brown in altered surfaces), pelecypod-bearing, occasionally granully, sandy limestones sequence with ophiolite-derived conglomerate interbeds is observed. Towards the top of the section, a 46 m-thick alternation of limestone,

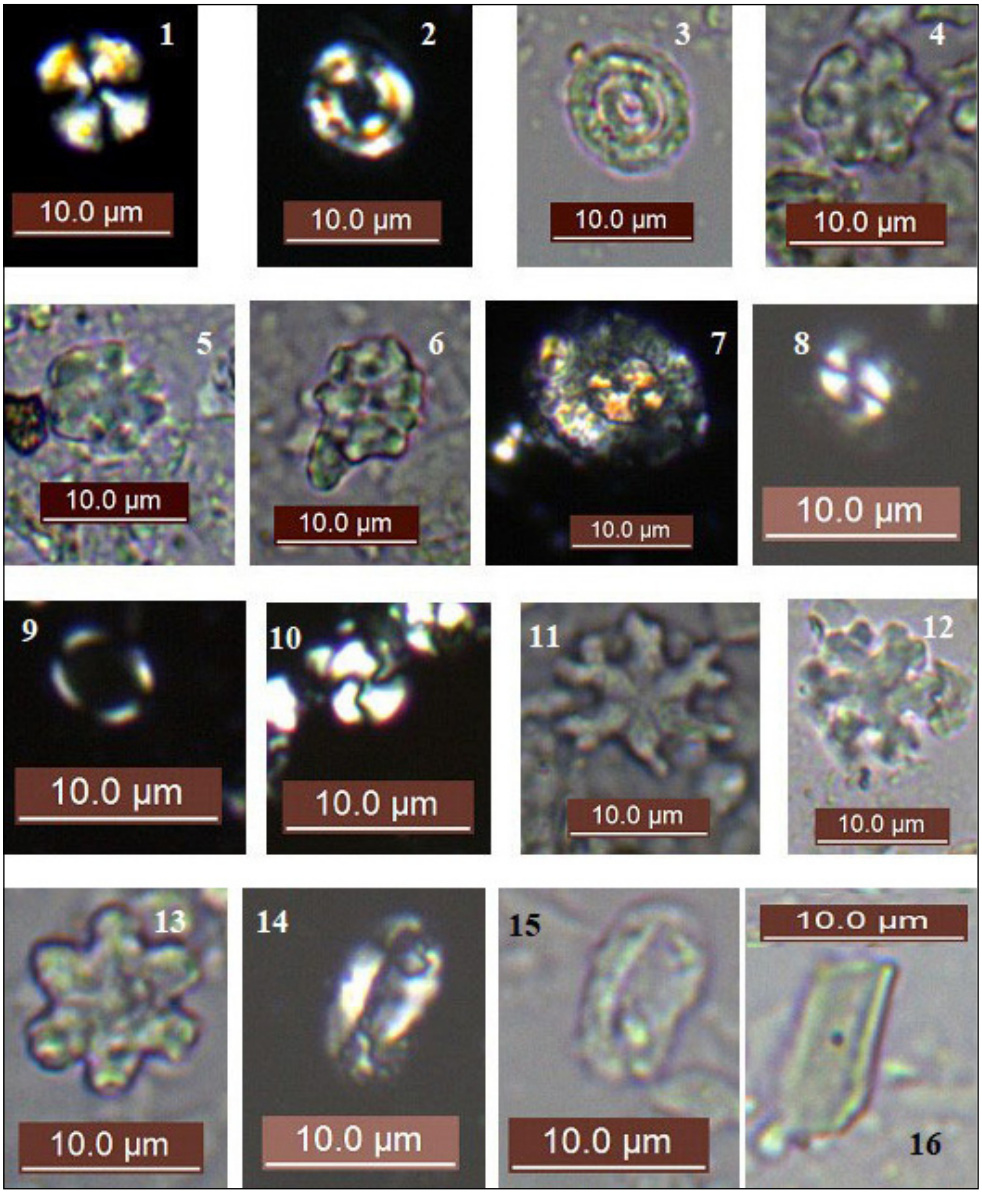


Figure 6- Photomicrographs of calcareous nannoplankton identified in the samples collected from the study area (P: under polarized light, N: under normal light; 1 (P) - *Calcidiscus leptoporus* (Murray and Blackman), sample no: A - 16; 2 (P), 3 (N) - *Calcidiscus macintyrei* (Bukry and Bramlette), sample no: K - 20; 4 - 6 (N) - *Catinaster coalitus* Martini and Bramlette, sample no: K - 2, A - 4, A - 21; 7 (P) - *Coccolithus miopelagicus* Bukry, sample no: B - 19; 8 (P) - *Coccolithus pelagicus* (Wallich), sample no: A - 16; 9 (P) - *Coronocyclus nitescens* (Kamptner), sample no: K - 23; 10 (P) - *Dictyococcites antarcticus* Haq, sample no: A - 1; 11 (N) - *Discoaster bollii* Martini and Bramlette, sample no: A - 4; 12 (N) - *Discoaster deflandrei* Bramlette and Riedel, sample no: A - 4; 13 (N) - *Discoaster kugleri* Martini and Bramlette, sample no: A - 4; 14(P), 15 (N) - *Helicosphaera burkei* Black, sample no: A - 16; 16 (N) - *Scyphosphaera hamptonii* da Gama and Varol, sample no: K - 2).

calcarenite and claystone is seen. This part of the sequence consists of the beige colored limestones with micro-, macrofossils, *Ostrea* sp., bioturbation structures, and grey colored calcarenites and claystones. This alternation is covered by a 35 m-thick limestones-calcarenite-claystone alternation at the uppermost part of the sequence (Figure 3, Table 1).

Calcareous nannoplankton species *Calcidiscus leptoporus, Coccolithus pelagicus, Dictyococcites antarcticus, Reticulofenestra haqii, R. perplexa, R. pseudoumbilicus, Sphenolithus grandis* and *Umbilicosphaera jafari* were identified approximately in the first 10 m of the section from the base where samples numbered 23 - 22 were taken. Considering the stratigraphic distribution of the determined calcareous nannoplankton genera and species, this part of the section has been aged as Serravallian.

In the part between 10 m - 160 m of the section from where samples numbered 21 - 1 were taken, calcareous nannoplankton species occurring in Tortonian such as

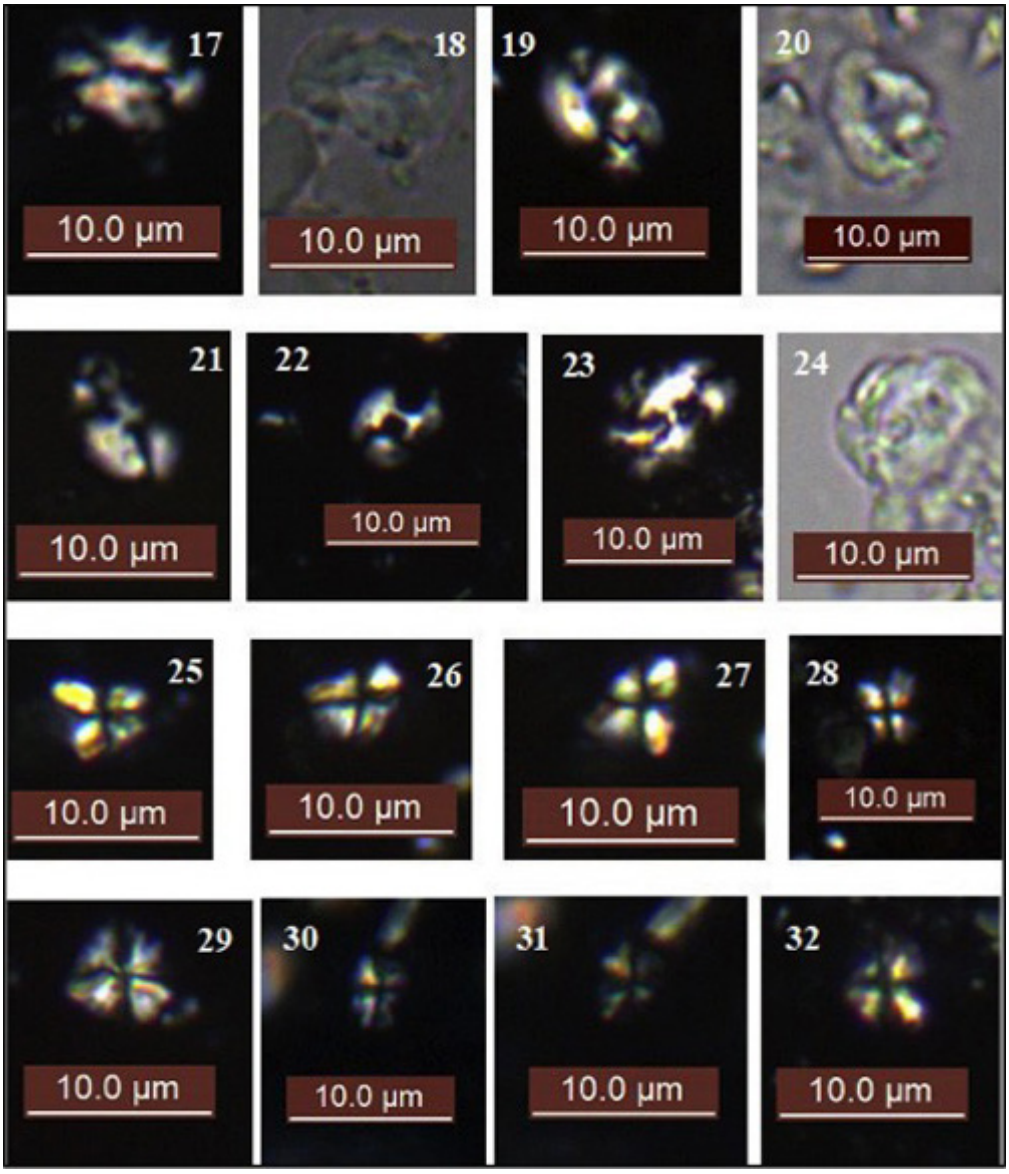


Figure 7- Photomicrographs of calcareous nannoplankton identified in the samples collected from the study area (P: under polarized light, N: under normal light; 17 (P), 18 (N) - Helicosphaera *kamptneri* Hay and Mohler, sample no: A - 4; 19 (P), 20 (N) - *Helicosphaera mediterranea* Muller, sample no: A - 16; 21 - 23 (P), 24 (N) - *Helicosphaera sellii* Bukry and Bramlette, sample no: A - 4, K - 7; 25 - 32 (P) - *Sphenolithus abies* Deflandre, sample no: B - 23, K – 29).

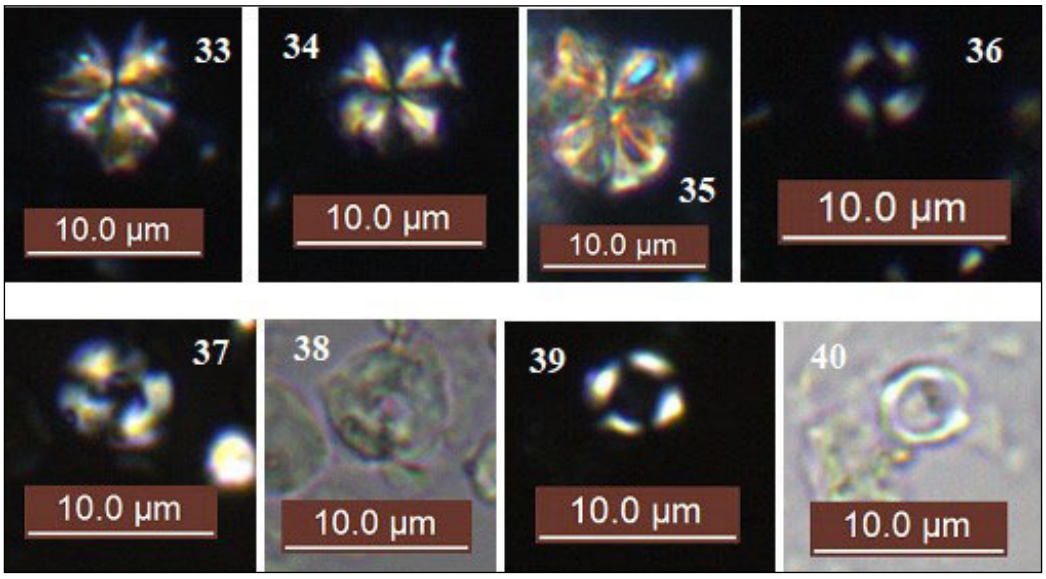


Figure 8- Photomicrographs of calcareous nannoplankton identified in the samples collected from the study area (P: under polarized light, N: under normal light; 33 - 35 (P) - *Sphenolithus grandis* Haq and Berggren, sample no: B - 1, A - 7; 36 - 37 (P), 38 (N) - *Umbilicosphaera jafari* Muller, sample no: B - 38, A - 3; 39 (P), 40 (N) - *Umbilicosphaera rotula* (Kamptner), sample no: B - 23).

*Catinaster coalitus*, *Discoaster bollii, Helicosphaera sellii* and *Triquetrorhabdulus striatus* were identified, accordingly, this part has been aged as Tortonian. In this part of the section, calcareous nannoplankton species ranging in the Tortonian such as *Calcidiscus leptoporus, C.macintyrei, Coccolithus miopelagicus, C.pelagicus, Dictyococcites antarcticus, Discoaster deflandrei, D.kugleri, D.variabilis, Helicosphaera burkei, H.granulata, H.intermedia, H.kamptneri, H.mediterranea, H.walbersdorfensis, Pontosphaera multipora, Reticulofenestra gelida, R.haqii, R.minuta, R.perplexa, R.pseudoumbilicus, Sphenolithus abies, S.compactus, S.grandis, Triquetrorhabdulus rioi, T.rugosus, Umbilicosphaera jafari* and *U. rotula* were determined.

The planktonic foraminifera first appearing in the Tortonian such as *Neogloboquadrina acostaensis* and *Globorotalia juanai,* and the species, common in the Tortonian, such as *Globigerina bulloides, G. regina, G. regularis, Globoturborotalia decoraperta, G. nepenthes, Trilobatus quadrilobatus, T. sacculifer, Orbulina bilobata, O.universa, Sphaeroidinellopsis* sp., *Sphaeroidinellopsis* cf. *multiloba, Velapertina cingulata, V.indigenia* were also identified from the same levels of the section and this part of the section is also dated as Tortonian according to planktonic foraminifers. (Figures 6 - 10, Tables 1, 4a,b).

4.2. Berol (B) Measured Stratigraphic Section

The section, 160 m-thick, was taken from the north of Doğanlar village (start coordinate: ($B^1$) 38S 0355499 / UTM 4252566, end coordinate: ($B^2$) 38S 0356158 / UTM 4252951, bedding: N70E/10ºNW, elevations for start and end coordinates are 1822 m and 1991 m, respectively). The section starts with 15 m-thick, beige colored sandstone with ophiolitic origin. The section towards the top is as follows, respectively: 4 m-thick, greenish grey claystone; 18 m-thick greenish dark grey claystone with calcarenite interbeds; 5 m-thick green claystone; 6 m-thick yellowish carbonated sandstone; 2 m-thick greenish-black claystone; 8 m-thick beige colored carbonated sandstone with 1 - 1.5 m bedding thickness; 22 m-thick alternation of greenish claystone and grey sandstone; 21 m-thick yellowish grey colored carbonated sandstone bearing ophiolitic and siliciclastic fragments; 19 m-thick, green colored claystone intercalated with ophiolitic-siliciclastic sandstone; 22 m-thick alternation of green claystone and brown siliciclastic sandstone; 14 m-thick, yellowish colored, siliciclastic sandstone with ophiolitic materials; 16 m-thick greenish claystone; 11 m-thick alternation of green claystone and greenish grey siliciclastic sandstone; 3 m-thick, reddish colored, ophiolitic conglomerate with a bedding thickness of 1 - 5 cm; 9 m-thick greenish

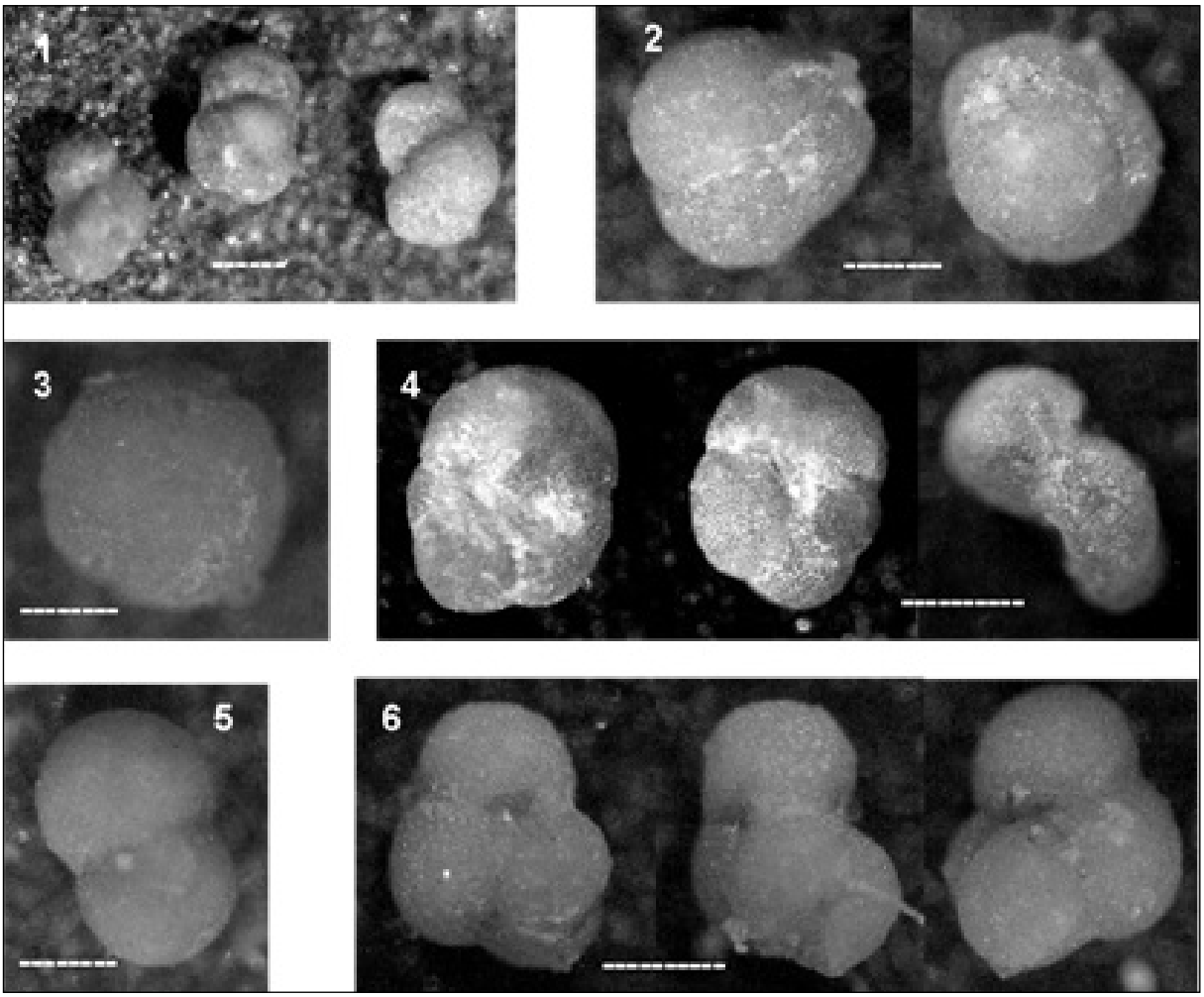


Figure 9- Photomicrographs of plantonic foraminifera identified in the samples collected from the study area (scale 200 µm; 1 - *Globoturborotalia nepenthes* Todd, sample no: A 21; 2 - *Globigerina regina* Crescenti, sample no: K 27; 3- *Orbulina universa* d'Orbigny, sample no: K 12; 4 -*Globigerina regularis* d'Orbigny, sample no: A 21; 5 - *Orbulina bilobata* (d'Orbigny), sample no: K 4; 6 - *Trilobatus quadrilobatus* (d'Orbigny), sample no: K 22).

grey claystone; 18 m-thick, grey colored (brown in altered surfaces) calcarenites containing abundant benthic foraminifera and macrofossils (gastropod, lamellibranch, echinoid, coral etc.) and with 0.5 mm to 4 cm sized gravels in places; and in the uppermost levels of the section, 15 m-thick, grey colored (yellowish in altered surfaces), foraminifera- and macrofossil-bearing biocalcarenites (Figure 4, Table 2).

The calcareous nannoplankton species such as *Catinaster coalitus, Discoaster bollii* and *D. Pentaradiatus* which first appeared in the Tortonian were identified from the levels where samples numbered 1 - 43 were taken along the whole section. In addition, the calcareous nannoplankton species such as *Calcidiscus leptoporus, C.macintyrei, Coccolithus miopelagicus, C.pelagicus, Discoaster deflandrei, D.kugleri, D.variabilis, Hayaster perplexus, Pontosphaera multipora, Reticulofenestra gelida, R.haqii, R.minuta, R.pseudoumbilicus, Sphenolithus abies, S.compactus, S.grandis, S.moriformis, Umbilicosphaera jafari* and *U.rotula*, ranging in the Tortonian, were identified from the samples collected throughout the whole section.

Towards the upper levels of the section where the samples numbered 1-43 were taken, planktonic foraminiferal species *Globorotalia juanai* occurring only in the Tortonian, and the species *Globigerina bulloides, G.regularis, Orbulina bilobata, O.universa, Paragloborotalia mayeri, Sphaeroidinellopsis* sp.

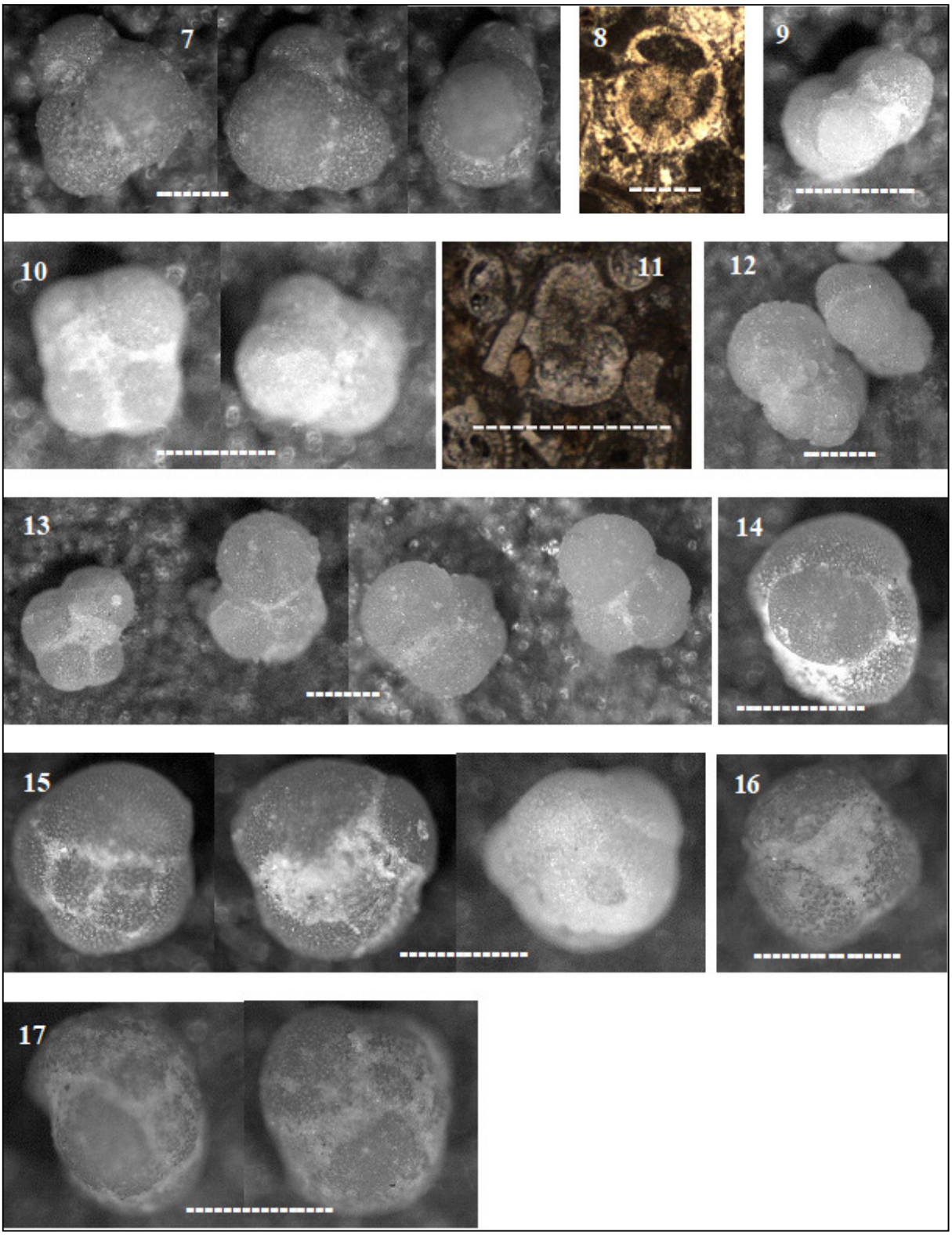


Figure 10- Photomicrographs of plantonic foraminifera identified in the samples collected from the study area (scale 200 µm; 7 - *Trilobatus sacculifer* (Brady), sample no: K 2; 8 - *Sphaeroidinellopsis* sp., sample no: B 25; 9 - 10 - *Neogloboquadrina acostaensis* Blow, sample no: A 9; 11 - *Sphaeroidinellopsis* cf. *multiloba* (Le Roy), sample no: A 15; 12 - 13- *Globorotalia juanai* Bermudez and Bolli, sample no: A 7; 14 - 15 - *Velapertina cingulata* Popescu, sample no: A 21; 16 - 17- *Velapertina indigenia* (Luczkowska), sample no: A 4).

Table 4- Stratigraphic distributions of; a) calcareous nannoplankton and b) planktonic foraminifera species identified from the measured stratigraphic sections taken from the study area.

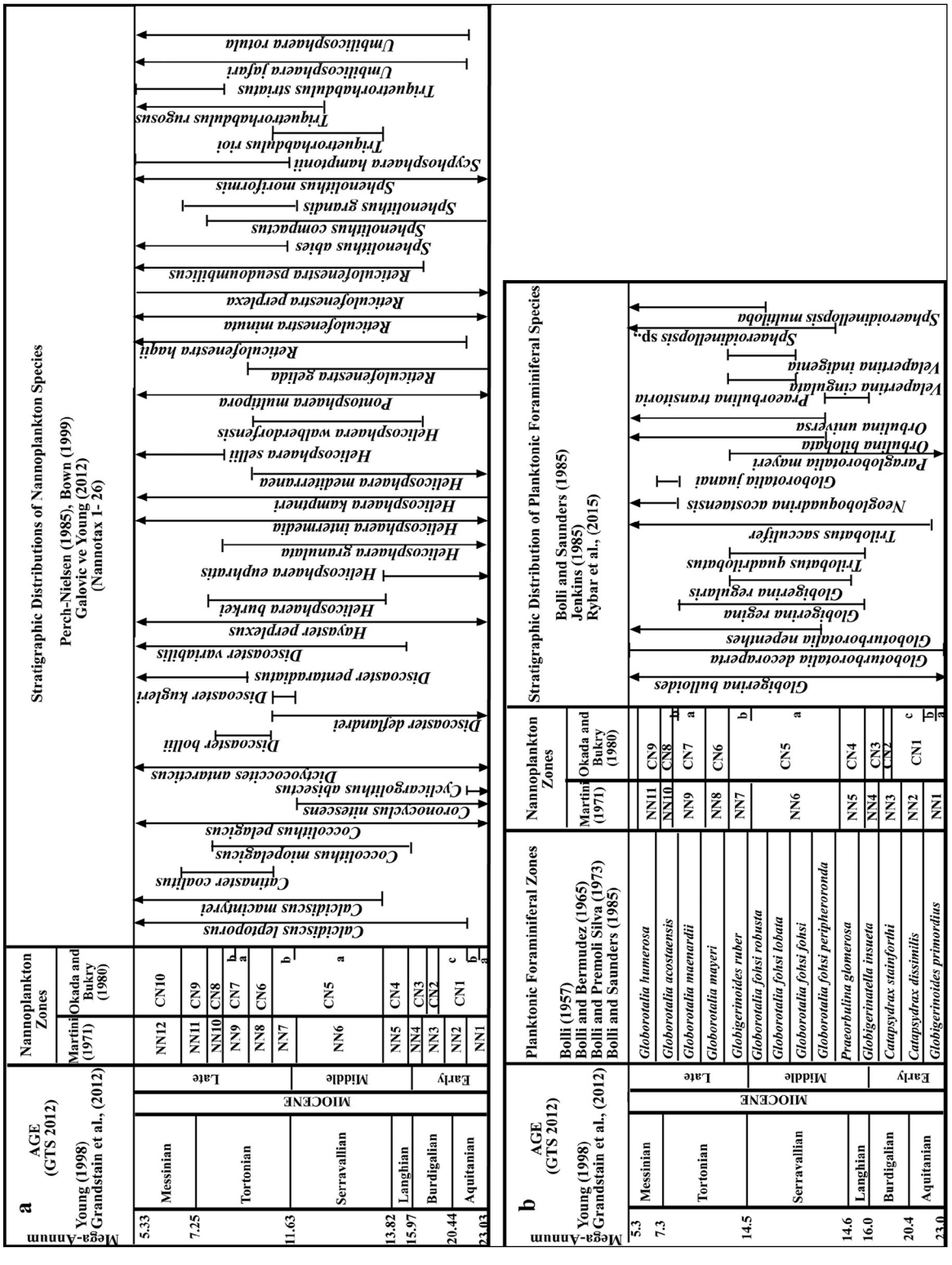

ranging in the Tortonian were identified. Accordingly, these parts of the section have been aged as Tortonian (Figures 6 - 10, Tables 2, 4a, b).

3.3. Kurubaş (K) Measured Stratigraphic Section

The section, with a total thickness of 277 m, was taken from the 4 km northwest of Gürpınar on the Van -Gürpınar highway (start coordinate: ($K^1$) 38S 0360208 / UTM 427283, end coordinate: ($K^2$) 38S 0360072 / UTM 4247580, bedding: N60E/40ºSE, elevations for start and end coordinates are 1985 m and 2012 m, respectively). The section starts at the bottom with 20 m-thick grey claystone; and continues with 257 m-thick, yellowish, beige, brown colored calcarenite and grey claystone (Figure 5, Table 3).

The planktonic foraminiferal species *Globigerina bulloides, Globoturborotalia nepenthes* representing a Serravallian age and the species ranging in the Serravallian such as *Globigerina regina, G.regularis, Globoturborotalia decoraperta, Orbulina bilobata, O.universa, Praeorbulina transitoria, Sphaeroidinellopsis* sp., *Trilobus quadrilobatus,* and *T.sacculifer* were identified in the part of 130 m-thickness from the base of the section where samples numbered 31 - 22 were taken; hence, a Serravallian age has been assigned to the this part of the section. The calcareous nannoplankton species, ranging in the Serravallian, such as *Calcidiscus leptoporus, Coccolithus miopelagicus, C.pelagicus, Coronocyclus nitescens, Discoaster deflandrei, D.kugleri, Hayaster perplexus, Pontosphaera multipora, Reticulofenestra gelida, R.haqii, R.minuta, R.pseudoumbilicus, Sphenolithus compactus, S.moriformis* and *Umbilicosphaera jafari* were determined from the same levels of the section. Based on these findings, this part of the section as well has been aged as Serravallian.

Planktonic foraminifera *Globorotalia juanai* indicating a Tortonian age, and the species, common in the Tortonian, such as *Globigerina bulloides, G.regina, G.regularis, Globoturborotalia decoraperta, G.nepenthes, Orbulina bilobata, O.universa, Sphaeroidinellopsis* sp., *Trilobatus quadrilobatus, T.sacculifer, Velapertina cingulata* were identified in the upper levels of the section where the samples numbered 21 - 1 were taken. Thus, this part of the section has been aged as Tortonian.

The calcareous nannoplankton species appearing in the Tortonian such as *Catinaster coalitus, Helicosphaera sellii* and the species, common in the Tortonian, such as *Calcidiscus leptoporus, C.macintyrei, Coccolithus miopelagicus, C.pelagicus, Discoaster deflandrei, D.kugleri, Helicosphaera kamptneri, H.mediterranea, Pontosphaera multipora, Reticulofenestra gelida, R.haqii, R.minuta, R.perplexa, R.pseudoumbilicus, Scyphosphaera hamptonii, Sphenolithus abies, Umbilicosphaera jafari, U.rotula* were determined in the same levels. Therefore, the age of these levels of the section has been appointed as Tortonian (Figures 6 - 10, Tables 3, 4a,b).

## 5. Results

The Van Formation which has a wide distribution around Van province and is represented mainly by conglomerate, sandstone, marl, limestone, has been stated in the previous studies from different localities considering the rock composition, macro and microfossil assemblages as being deposited in the late Oligocene-middle Miocene, early Miocene or Burdigalian-Langhian (early-middle Miocene) periods (Acarlar et al., 1991; Şener, 1992; Sağlam, 2003).

In this study carried out on the Van Formation in the east and southeast of Van (L50 - $b_2$ sheet), three measured stratigraphic sections have been taken. A total of 98 samples including 24 samples from Akın (A) section, 43 samples from Berol (B) section and 31 samples from Kurubaş (K) section have been examined in terms of calcareous nannoplankton and planktonic foraminiferal content. Consequently, 33 species of the 12 calcareous nannoplankton genera and 18 species of 9 planktonic foraminiferal genera representing the Serravallian - Tortonian (middle - late Miocene) interval have been identified. In this study, the calcareous nannoplankton content was studied for the first time in the deposits of the Van Formation in the study area. Calcareous nannoplankton and planktonic foraminiferal biozones of the formation could not be determined in the study area since some samples from the Van Formation neither contains calcareous nannoplankton nor planktonic foraminifera, some samples are scarce in fossils and not all of the index fossils have been identified. The age of the Van Formation within the study area has been considered as Serravallian-Tortonian (middle - late Miocene) based on the calcerous nannoplanton and planktonic foraminiferal content the formation has.

The base of the Van Formation in the study area cannot be observed since it is covered by young sediments in the Akın measured section, and in Kurubaş-Doğanlar region, lying with a thrust contact over the Upper Cretaceous and Eocene units (Figures 1 - 10, Tables 1 - 4a,b).

In the light of the findings obtained from this study, this can be inferred that the Van Formation which covers a large area around Van deposited transgressively during the closure of the Neotethys in an environment showing a transition between shallow to deep carbonate shelf and even submarine fan.

The study area is located within the Van Gölü Basin. The evolution of the Van Gölü Basin is related to geological events from the continental collision that initiated as a result of the subduction of the Arabian Plate beneath the Eurasian Plate and causing the closure of the southern branch of Neotethys. The continental collision started about 10 - 14 million years ago is still continuing today (Şengör and Kidd, 1979; Şaroğlu and Güner, 1981; Dewey et al., 1986; Şaroğlu and Yılmaz, 1986). The Eastern Taurides extending in an area from Hatay to Iran and bordering the Southeastern Anatolia Region to the north, have been shaped as a folded mountain belt that has been uplifting from the beginning of this continental collision. Van Gölü Basin is located just north of the basin named as Bitlis - Zagros Suture Zone in the literature. According to Koçyiğit et al. (2001), the Bitlis Ocean (southern branch of Neotethys) did not close until the middle-late Miocene (Serravallian), later on with its closure, amalgamation of the Arabian Plate to the Eurasian Plate occurred, and the continental collision took place (Özkaymak, 2003). According to the age findings based on the marine organisms (calcareous nannoplanktons and planktonic foraminifera) in this study, it can be concluded that the marine conditions in the study area maintained in Tortonian (late Miocene) as well. Within the scope of these findings, it can be interpreted that the closure phase of the southern branch of Neotethys in the east and southeast of Van province lasted until the Tortonian.

**Acknowledgements**

This study was supported by the Scientific Research Projects Department of Yüzüncü Yıl University within the scope of the Master Thesis Project no 2015 - FBE - YL033.

**References**

Acarlar, M., Türkecan, A. 1986. Başkale (Van) batı ve kuzeybatısının jeolojisi, Maden Tetkik ve Arama Genel Müdürlüğü, Rapor No: 7913, 87, Ankara (unpublished).

Acarlar, M., Bilgin, A. Z., Elibol, E., Erkan, T., Gedik, İ., Güner, E., Hakyemez, Y., Şen, A. M., Uğuz, M. F., Umut, M. 1991. Van Gölü doğusu ve kuzeyinin jeolojisi. Maden Tetkik ve Arama Genel Müdürlüğü, Rapor No: 9469, 94, Ankara (unpublished).

Adıyaman, Ö., Chorowicz, J., Köse, O. 1998. Relationships between volcanic patterns and neotectonics in Eastern Anatolia from analysis of satellite images and digital elevation models. Journal of Volcanolgy and Geothermal Research 85, 17- 32.

Aksoy, E. 1988. Van ili doğu - kuzeydoğu yöresinin stratigrafisi ve tektoniği. Doktora Tezi, Fırat Üniversitesi, Fen Bilimleri Enstitüsü, Jeoloji Mühendisliği Anabilim Dalı, 171.

Arni, P. 1939. Van vilayetinin jeolojisi hakkında rapor. Maden Tetkik ve Arama Genel Müdürlüğü, Rapor No: 883, Ankara (unpublished).

Balkaş, Ö. 1980. Başkale - Gürpınar - Çatak - Van alanının jeolojisi ve petrol olanakları. Türkiye Petrolleri Anonim Ortaklığı, Arşiv No: 1455, Ankara.

Barka, A., Şaroğlu, F. 1995. Van Gölü su yükselmesinin tektonik ile ilişkisi. Van Gölü'nün Su Seviyesinin Yükselmesi Nedenleri, Etkileri ve Çözüm Yolları Sempozyumu, 20 - 22 Haziran 1995, Van, 74-90.

Bolli, H. M. 1957. Planktonik foraminifera from the Oligocene - Miocene Cipero and Lengua formations of Trinidad. B.W.I. Bulletin of U. S. National Museum 215, 97-123.

Bolli, H. M., Bermudez, P. J. 1965. Zonation based on planktonik foraminifera of middle Miocene to Pliocene warm water sediments. Baletin Informativo, Asociation Venezolana de Geologia. Mineria Petroleo 8, 119-49.

Bolli, H. M., Premoli Silva, I. 1973. Oligocene to recent planktonik foraminifera and stratigraphy of the Leg 15 sites in the Caribbean Sea. Initial Report of Deep Sea Drilling Project No: 15, 475-97.

Bolli, H. M., Saunders, J. B. 1985. Oligocene to Holocene low latitude planktonic foraminifera. Bolli, H. M., Saunders, J. B., Perch-Nielsen, K. (Ed.). Plankton Stratigraphy 155-262.

Bown, R. 1999. Calcereous Nannofosil Biyostratigraphy. Department of Geologial Science University, Collage London, 312.

Degens, E. T., Kurtman, F. 1978. The geology of lake Van. The Mineral Research and Exploration Publications 169, 64-80, 6-11, Ankara.

Demirci, E. 2016. Akın ve Taşkonak Köyleri dolayında yüzeyleyen Serravaliyen - Tortoniyen (alt - orta Miyosen) yaşlı Van Formasyonu çökellerinin mikrofasiyes ve mikropaleontoloji özellikleri. Yüksek Lisans Tezi, Yüzüncü Yıl Üniversitesi, Fen Bilimleri Enstitüsü, Jeoloji Mühendisliği Anabilim Dalı, 138.

Demirtaşlı, E., Pisoni, C. 1965. Ahlat - Adilcevaz Bölgesi'nin jeolojisi (Van Gölü kuzeyi). Maden Tetkik ve Arama Dergisi 64, 22-23.

Dewey, J. F., Hempton, M. R., Kidd, W. S. F., Şaroğlu, F., Şengör, A. M. C. 1986. Shortening of continental lithosphere: the neotectonics of Eastern Anatolia – a young collision zone. Geological Society of London. Special Publication, 19, 3-36.

Elmas, A. 1994. Güneydoğu Anadolu'da geç Lütesiyen - geç Oligosen aktif kıta kenarı volkanizmasına bir örnek: Gövelek volkanitleri (Van - Erçek). Yerbilimleri Dergisi 3, 43-54.

Galovic, I., Young, J. R. 2012. Revised taxonomy and stratigraphy of Middle Miocene calcareous nannofossils of the Paratethys. Micropaleontology 58 (4), 305-334.

Gelati, R. 1975. Miocene marine sequence from the Lake Van Area, Eastern Turkey. Rivista Italiana di Paleontologia Stratigrafia 81 (4), 477-490.

Grandstein, F. M., Ogg, J. G., Schmitz, M. D., Ogg, G. M. 2012. The Geologic Time Scale 2012, Elsevier, 1, 144.

Gürsoy, H., Tatar, O., Piper, J. D. A., Heimann, A., Koçbulut, F., Mesci, B. L. 2009. Palaeomagnetic study of Tertiary volcanic domains in Southern Turkey and Neogene anticlockwise rotation of the Arabian Plate. Tectonophysics 465, 114-127.

Jenkins, D. G. 1985. Southern mid-latitude Paleocene to Holocene planktonik foraminifera. Bolli, H. M., Saunders, J. B., Perch-Nielsen, K. (Ed.). Plankton Stratigraphy 263-282.

Kempe, St., Khoo, F., Gürleyik., Y. 1978. Hydrography of lake Van and its drainage area. The geology of lake Van. Mineral Research and Exploration Publications 30-44.

Ketin, İ. 1977. Van Gölü ile İran sınırı arasındaki bölgede yapılan jeoloji gözlemlerinin sonuçları hakkında kısa bir açıklama. Türkiye Jeoloji Kurumu Bülteni 20, 79-85.

Kıraner, F. 1959. Van Gölü doğu bölgesinin jeolojik etüdü, Nafta Vek. Demiryolları İnşaat Dairesi.

Koçyiğit A., Beyhan A. 1998. A new intracontinental transcurrent structure: the central Anatolian Fault Zone, Turkey. Tectonophysics 284, 317-336.

Koçyiğit, A., Yılmaz, A., Adamia, S., Kuloshvili, S. 2001. Neotectonics of east Anotolian Plateau (Turkey) and lesser caucasus: implication for transition from thrusting to strike-slip faulting. Geodinamica Acta 14, 177-195.

Martini, E. 1971. Standard Tertiary and Quaternary calcareous nannoplankton zonation. Proceedings of the 2nd Planktonic Conference 1071, Roma, 739-785.

Maxon, J. H. 1936. Geology and petroleum possibilities of the Hermis dome. Derleme No: 225, 25.

Nannotax 1. 2019. http://www.mikrotax.org/Nannotax3/index.php?dir=Coccolithophores/Coccolitales/Calcidiscaceae/Calcidiscus/C.%20leptoporus%20group/Calcidiscus%20leptoporus.11 September 2019.

Nannotax 2. 2019. http://www.mikrotax.org/Nannotax3/index.php?dir=Coccolithophores/Coccolithales/Calcidiscaceae/Calcidiscua/C.%20leptoporus%20group/Calcidiscus%20macintyrei. 11 September 2019.

Nannotax 3. 2019. http://www.mikrotax.org/Nannotax3/index.php?taxon=Catinaster%20coalitus&module=Coccolithophores. 11 September 2019.

Nannotax 4. 2019. http://www.mikrotax.org/Nannotax3/index.php?dir=Coccolithophores/Coccolithales/Coccolithaceae/Coccolithus/C.%20pelagicus%20group/Coccolithus%20miopelagicus. 11 September 2019.

Nannotax 5. 2019. http://www.mikrotax.org/Nannotax3/index.php?dir=Coccolithophores/Coccolithales/Coccolithaceae/Coronocyc lus/Coronocyclus%20nitescens. 11 September 2019.

Nannotax 6. 2019. http://www.mikrotax.org/Nannotax3/index.php?dir=Coccolithophores/Discoasterales/Discoasteraceae/Discoas ter/D.%20variabilis%20group/Discoaster%20bollii. 12 September 2019.

Nannotax 7. 2019. http://www.mikrotax.org/Nannotax3/index.php?taxon=Discoaster%20deflandrei&module= Coccolithophores. 12 September 2019.

Nannotax 8. 2019. http://www.mikrotax.org/Nannotax3/index.php?taxon=Discoaster%20kugleri&module=Coccolithophores. 12 September 2019.

Nannotax 9. 2019. http://www.mikrotax.org/Nannotax3/index.php?taxon=Discoaster%20pentaradiatus&module= Coccolithophor es. 12 September 2019.

Nannotax 10. 2019. http://www.mikrotax.org/Nannotax3/index.php?dir=Coccolithophores/Discoasterales/Discoasteraceae/ Discoas ter/D.%20variabilis%20group/Discoaster%20variabilis. 12 September 2019.

Nannotax 11. 2019. http://www.mikrotax.org/Nannotax3/index.php?dir=Coccolithophores/Zygodiscales/Helicosphaeraceae/ Helicos phaera/H.%20carteri%20group/Helicosphaera%20granulata. 12 September 2019.

Nannotax 12. 2019. http://www.mikrotax.org/Nannotax3/index.php?taxon=Helicosphaera%20intermedia&module= Coccolithopho res. 14 September 2019.

Nannotax 13. 2019. http://www.mikrotax.org/Nannotax3/index.php?taxon=Helicosphaera%20mediterranea&module= Coccolithoph ohores. 14 September 2019.

Nannotax 14. 2019. http://www.mikrotax.org/Nannotax3/index.php?taxon=Helicosphaera%20sellii&module= Coccolithophores. 14 September 2019.

Nannotax 15. 2019. http://www.mikrotax.org/Nannotax3/index.php?taxon=Helicosphaera%20walbersdorfensis&module= Coccolit hophores. 14 September 2019.

Nannotax 16. 2019. http://www.mikrotax.org/Nannotax3/index.php?taxon=Reticulofenestra%20perplexa&module= Coccolithop hores. 14 September 2019.

Nannotax 17. 2019. http://www.mikrotax.org/Nannotax3/index.php?dir=Coccolithophores/Isochrysidales/Noelaerhabdaceae/Reticulofenestra/R.%20pseudoumbilicus%20group/Reticulofenestra%20pseudoumbilicus. 14 September 2019.

Nannotax 18. 2019. http://www.mikrotax.org/Nannotax3/index.php?taxon=Sphenolithus%20abies&module= Coccolithophores. 14 September 2019.

Nannotax 19. 2019. http://www.mikrotax.org/Nannotax3/index.php?taxon=Sphenolithus%20grandis&module=Coccolithophores. 14 September 2019.

Nannotax 20. 2019. http://www.mikrotax.org/Nannotax3/index.php?dir=Coccolithophores/Discoasterales/Sphenolithaceae /Spheno lithus/S.%20moriformis%20group/Sphenolithus%20moriformis. 17 September 2019.

Nannotax 21. 2019. http://www.mikrotax.org/Nannotax3/index.php?dir=Coccolithophores/Nannolith%20families%20 inc%20sed/ Ceratolithaceae/Orthorhabdus/Orthorhabdus%20rioi. 17 September 2019.

Nannotax 22. 2019. http://www.mikrotax.org/Nannotax3/index.php?dir=Coccolithophores/Nannolith%20families%20inc %20 sed/Ceratolithaceae/Orthorhabdus/Orthorhabdus%20rugosus. 17 September 2019.

Nannotax 23. 2019. http://www.mikrotax.org/Nannotax3/index.php?taxon=Orthorhabdus%20striatus&module= Coccolithophores. 17 September 2019.

Nannotax 24. 2019. http://www.mikrotax.org/Nannotax3/index.php?taxon=Umbilicosphaera%20jafari&module= Coccolithopho res. 17 September 2019.

Nannotax 25. 2019. http://www.mikrotax.org/Nannotax3/index.php?dir=Coccolithophores/Coccolithales/Calcidiscaceae/ Umbili cosphaera/Umbilicosphaera%20rotula. 17 September 2019.

Nannotax 26. 2020. http://www.mikrotax.orgNannotax3 index.phpdir=Coccolithophores Zygodiscales PontosphaeraceaeScyphosphaera Scyphosphaera%20hamptoni. 24 Aralık 2020.

Okada, H., Bukry, D. 1980. Supplementary modification and introduction of code numbers to the low-latitude coccolith biostratigraphic zonation. Marine Micropaleontology 5, 321-325.

Okuldaş, C. 2013. Alaköy Fayı'nın jeomorfolojik özellikleri ve tektonik etkinliği (Van Gölü Havzası - Doğu Anadolu). Yerbilimleri 34 (3), 161-176.

Ortynski, I., Tromp, S. W. 1944. Geological report on atrip to the Van area, Maden Tetkik ve Arama Genel Müdürlüğü, Rapor No: 1519, Ankara (unpublished).

Oyan, V. 2018. Van Gölü'nün doğusundaki Otlakbaşı bazaltik volkanizmasının petrolojik ve jeokimyasal evrimi. Bulletin of the Mineral Research and Exploration 157, 1-23.

Özkaymak, Ç. 2003. Van şehri yakın çevresinin aktif tektonik özellikleri. Yüksek Lisans Tezi, Yüzüncü Yıl Üniversitesi, Fen Bilimleri Enstitüsü, Jeoloji Mühendisliği Anabilim Dalı, 95, Van.

Perch-Nielsen, K. 1985. Cenozoic Calcareous Nannofossils. Bolli, H. M., Saunders, J. B., Perch-Nielsen, K. (Ed.). Plankton Stratigraphy, Cambridge University Press, 427-554.

Rybar, S., Halasova, E., Hudackova, N., Kovaç, M., Kovacova, M., Sarinova, K., Sujan, M. 2015. Biostratigraphy, sedimentology and paleoenvironments of the northern Danube Basin: Ratkovce 1 well case study. Geologica Carpathica 66 (1), 51-67.

Sağlam, A. 2003. Van Gölü doğusu ve güneydoğusunda yüzeyleyen Van Formasyonu'nun stratigrafisi, paleontolojisi ve çökelme ortamları. Yüksek Lisans Tezi, Yüzüncü Yıl Üniversitesi, Fen Bilimleri Enstitüsü, Jeoloji Mühendisliği Anabilim Dalı, Van (unpublished).

Savcı, G. 1980. Doğu Anadolu Volkanizma'sının neotektonik önemi. Yeryuvarı ve İnsan 5, 3-4.

Sümengen, M. 2008. Başkale - L52 paftası: Türkiye 1/100.000 ölçekli jeoloji haritaları serisi. Maden Tetkik ve Arama Genel Müdürlüğü Yayınları, Ankara.

Şaroğlu, F., Güner, Y. 1981. Doğu Anadolu'nun jeomorfolojik gelişimine etki eden öğeler: tektonik volkanizma ilişkileri. Türkiye Jeoloji Kurumu Bülteni 24, 39-50.

Şaroğlu, F., Yılmaz, Y. 1984. Doğu Anadolu'nun neotektoniği ve ilgili magmatizması. Ketin Sempozyumu, İstanbul, 149-162.

Şaroğlu, F., Yılmaz, Y. 1986. Doğu Anadolu'da neotektonik dönemdeki jeolojik evrim ve havza modelleri. Maden Tetkik ve Arama Genel Müdürlüğü, Jeoloji Etütleri Dairesi, Ankara.

Şenel, M., Acarlar, M., Çakmakoğlu, A., Dağer, Z., Erkanol, D., Örçen, S., Taşkıran, M. A., Ulu, Ü., Ünal, M. F., Yıldırım, H. 1984. Özalp (Van) - İran sınırı arasındaki alanın jeolojisi. Maden Tetkik ve Arama Genel Müdürlüğü Rapor No: 7623, Ankara (unpublished).

Şener, S. 1992. Van ili yakın güneyinin jeolojisi ve denizel miyosen istifinin fasiyes özellikleri. Yüksek Lisans Tezi, Ankara Üniversitesi, Fen Bilimleri Enstitüsü, Ankara (unpublished).

Şengör, A. M. C., Kidd, W. S. F. 1979. Post-collisional tectonics of the Turkish Iranian Plateau and a comparison with Tibet. Tectonophysics 55, 361-376.

Ternek, Z. 1953. Van Gölü güneydoğu bölgesinin jeolojisi. Türkiye Jeoloji Kurultayı Bülteni 4 (2), 1-27.

Trifonov, V. G., Vostrikov, G. A., Trifonov, R. V., Karakhanian, A. S., Soboleva., O. V. 1998. Recent geodynamic characteristic in the Arabian - Eurasian and Indian Eurasian collision region by active fault data. Tectonophysics 308, 119-131.

Valeton, I. 1978. A morphological and petrological study the terraces around lake Van. Bulletin of the Mineral Reseach and Exploration 169, 64-80.

Yeşilova, Ç. 2004. Van Gölü kuzeyinde yüzeyleyen Adilcevaz Kireçtaşı'nın (Van Gölü kuzeyi) mikrofasiyes özellikleri. Yüksek Lisans Tezi, Yüzüncü Yıl Üniversitesi, Fen Bilimleri Enstitüsü, Jeoloji Mühendisliği Anabilim Dalı, 77.

Yılmaz, Y. 1990. Comparison of young volcanic associations of Western and Eastern Anatolia formed under a compressional regime: a review. Journal of Volcanology and Geothermal Research 44, 69-87.

Yılmaz, Y., F. Şaroğlu, Güner, Y. 1987. Initiation of the neomagmatism in East Anatolia. Tectonophysics 134, 177-199.

Young, J. R. 1998. Neogene. Bown, P. R. (Ed.). Calcareous Nannofossil Biostratigraphy, Cambridge 225-265.

Wei., W. 1988. A new technique for preparing quantitative nannofossil slides. Journal of Paleontology 62, 472-473.

Wong, H. K., Degens, E. T. 1978. The bathymetry of lake Van, Eastern Turkey: Degens, E. T., Kurtman, F. (Ed.). The Geology Lake Van, General Directorate of Mineral Reseach and Exploration Press 6-10.

Wong, H. K., Finckh, P. 1978. Shallow structures in lake Van, in the geology of lake Van. Degens, E. T., Kurtman, F. (Ed.). The Mineral Research and Exploration Institute of Turkey, Report No: 169.

Bulletin of the Mineral Research and Exploration

http://bulletin.mta.gov.tr

# Usability value of the Yenicekale formation exposure around the Pazarcık (Kahramanmaraş) as a cement raw material

Güldemin DARBAŞ[a*], Fatma BAYRAK[a] and Ali GÜREL[b]

[a]*Kahramanmaraş Sütçü İmam University, Faculty of Engineering and Architecture, Department of Geology, Kahramanmaraş, Turkey*
[b]*Niğde Ömer Halisdemir University, Faculty of Engineering, Department of Geology, Niğde, Turkey*

*Research Article*

Keywords:
XRD, Geochemical Analyzes, Yenicekale Formation, Pazarcık, Kahramanmaraş.

**ABSTRACT**

The study area is located around Pazarcık - Narlı, Kahramanmaraş province. The aim of the study is to investigate the value of units belonging to the Yenicekale Formation Kışla Marl Member as cement raw material. As a result of XRD studies, it was determined that Yenicekale formation Kışla Marn Member which is exposed to large areas in the region is composed of illite, quartz, dolomite, calcite and chlorite minerals by rock analyzed. By geochemical analysis, $SiO_2$, $Al_2O_3$, $Fe_2O_3$, CaO, MgO, $K_2O$, $Na_2O$, $SO_3$ contents of the units were determined and these values were compared with the limit values used in cement raw materials. When the results were evaluated, it was determined that the total alkali elements ($Na_2O$ + $K_2O$) were within the limit values, but others were below or above these limit values. In addition, with geochemical analyses, it was calculated Silicate and Aluminium Modules. The most suitable values for Silicate Modules in Turkish Cement Factories are 2.2 - 2.6. In this study, Silicate Modulus values are in the range of 1.94 - 5.22. Standard values for Aluminum are between 1.5 and 2.5. The values of Aluminum Modules determined in this study are in the range of 0.43 - 1.38. For Hydrolic Module, the standard values are in the range of 1.8 - 2.2. The values determined in this study are in the range of 0.4 - 5.

*Received Date: 28.07.2020*
*Accepted Date: 05.01.2021*

## 1. Introduction

The study area is located in the Söğütlü-Şahintepe, around the Pazarcık, Kahramanmaraş province (Figure 1). The survey area is in the southeastern part of the Kahramanmaraş basin, on a scale of 1/25.000 the sheet of M38. Until now, numerous studies were presented in order to reveal the geological features of the region. (Arpat and Şaroğlu, 1972, 1975; Gözübol and Gürpınar, 1980; Önalan, 1986; Yılmaz et al., 1988; Dizer, 1991; İmamoğlu, 1993; Baydar and Yergök, 1996; Derman, 1999; Gül, 2000; 2004 ; Robertson and Ünlügenç, 2001; Gül et al., 2005; Darbaş and Gül, 2006; Varol et al., 2012; Kop et al., 2014)

The aim of the study is to reveal the availability of the claystone - siltstone - marl units that exposure around the Pazarcık - Narlı for the cement industry. Clays, hydrous aluminum silicates, are abundant in the sedimentary, igneous, and metamorphic units. Due to the wide range of using the field of the clay minerals, it should be investigated in which type of application it will take place. In terms of clay studies in Turkey, the number of studies has increased in recent years (Orhun, 1965; Seyhan, 1967; Özkan, 1977; Gündoğdu and Yılmaz, 1983; Erdoğan, 1994; Çelik and Karakaya, 1997; Abdioğlu, 2002; Yalçın, 2004; Özpınar et al., 2006; Çelik Karakaya, 2006; Bor, 2008).

Citation Info: Darbaş, G., Bayrak, F., Gürel, A. 2021. Usability value of the Yenicekale formation exposure around the Pazarcık (Kahramanmaraş) as a cement raw material. Bulletin of the Mineral Research and Exploration 166, 53-69. https://doi.org/10.19111/bulletinofmre.856536

**Corresponding author: Güldemin DARBAŞ, guldemin@ksu.edu.tr*

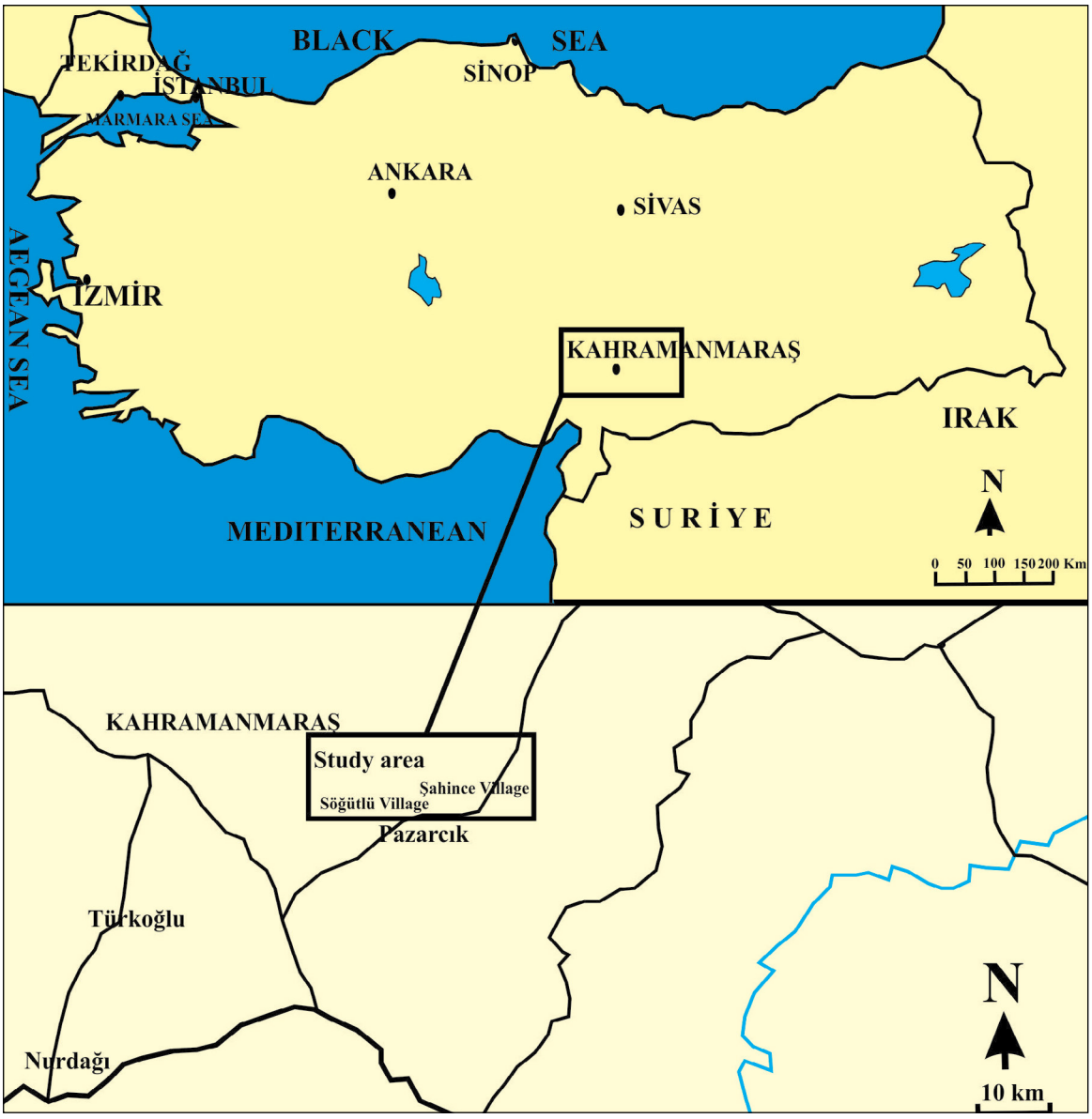


Figure 1- Location of the study area.

According to the study purpose, firstly, sections were taken within the well-exposed outcrops of the Yenicekale formation, and samples were collected. The rock analysis of the collected samples was run by using the XRD method, moreover, detailed clay analysis was done on the clay-rich samples. While the major oxide contents such as $SiO_2$, $Al_2O_3$, $Fe_2O_3$, CaO, MgO, $K_2O$, $Na_2O$, $SO_3$ were measured by using the geochemical analysis, our findings were compared with the standard values.

## 2. Method

### 2.1. X-Ray Diffraction (XRD) Analysis

28 samples were collected from the 3 different sections (Section 1, 2 and 4) and those samples were prepared for the XRD analysis. The jaw crusher and rod mills were used for mineralogical (XRD) analysis. Initially, the grain size of the samples was reduced to smaller than 1 centimeter by using the jaw crusher. After that, the broken samples were pulverized in a ball mill at a certain period and time. Totally the powdered 28 samples were individually extracted by XRD - WR (3 - 70º) and XRD - CF (2 - 20º) were

performed by separating the clay fraction by physical and chemical methods in the two samples.

The XRD - WR and XRD - CF were done at the faculty of engineering of the geology department laboratory of Ankara University.

The XRD patterns were obtained with an Inel Equinox 1000 diffractometer operating at tube voltage and current 30 kV and 20 mA, respectively using monochromatic CoKα1 radiation (λ= 1.788970 Å). Diffraction patterns were recorded between $0^o$ - $116.455^o$ with a scanning rate of 0.03.

For the XRD - CF analysis, the two samples from the different levels taken from the clay beds were used. After the pulverization, the washing, decantation, pickling, centrifugation, and sedimentation (holding for 3 hours and 40 minutes) and plaquing processes were performed one by one. The plaquing process was run to obtain a more clear 001 plane reflections of the clays. According to Çelik Karakaya (2006), if platy clay minerals are parallel to the plane surface of the diffractometer, the intensities of the basal reflection increase. After this stage, those 2 samples performed 3 separate processes. At first, these samples were dried in the air for the real image, and then waited at ethylene glycol steam (hold in a desiccator around 16 hours about 60 $^oC$) and the heating treatments were applied (in the oven about 550 $^oC$ for 2 hours) at the end.

### 2.2. Geochemical Analysis

The 28 samples were taken from three different sections, and the analyses were performed in the Aksaray University Scientific Technological Application and Research Center of Geochemical Analysis Laboratory. The soil samples were powdered in a ball mill carbide mortar to pass through a 20-micron size. The 5.000 gr of the pulverized sample was mixed with the 1.000 gr of Micropulver Wachs C homogeneously. After that, the obtained pellets from a heterogeneous mixture by using a die attachment under the 13 kg/N conditions by pressing. The pressed pellets obtained were analyzed by Pananalytical Axios Max model wavelength diffraction XRF. For instance, the values of the loss of ignition were determined by keeping the ash oven at 950 $^oC$ for 12 hours.

### 2.3. Used Modules in Cement Industry

Hydraulic module: $HM = CaO / SiO_2+Al_2O_3+Fe_2O_3$

If the HM < 1.7; the strength of cement is usually insufficient.

If the HM > 2.4; the strength of volumetric cement is absent.

Silicate module: $SM = SiO_2 / Al_2O_3 / Fe_2O_3$

If the SM > 4; the heating could be harder.

Aluminum module: $AM = Al_2O / Fe_2O_3$

If the AM < 1.3; it causes problems at the pulverisation stage.

## 3. Regional Geology

Although numerous studies were presented about the geological features of the region, this study is based on Sümengen (2014). According to Sümengen (2014), the general characteristics of regional geology are presented in the following paragraphs (Figure 2).

The Neogene units in the studied area accounted for autochthon sequence and overlie the basement unconformably (Figure 2 and 3). The bottom of the Neogene sequence of the study area occurs the Maastrihctyen Besni formation, composed of Keklikpınarı conglomerate, Sıraca marl and Elmalı limestone members. The Besni formation is underlie conformably by marl - limestone - sandstone units of the Maastrihtiyen - Early Eocene Germav formation. The Early Eocene Gercüş formation units such as sandstone, siltstone, and limestone are disconformably overlied the Germav formation. The Middle - Late Eocene sedimentary sequence in the study area is represented by the limestone units of the Midyat formation and Hoya formation, respectively. The Gaziantep formation conformably overlies this sequence. The Gaziantep formation consists of late Eocene -Early Oligocene chert and clay - rich limestone. The Miocene units of the sequence are represented by cherty and fossiliferous limestone rocks of the Late Oligocene - Early Miocene Fırat formation.

In the study area, the Early Miocene Zeytin Formation (sandstone - mudstone), Lice formation (limestone), and Beşenli formation (sandstone - marl - conglomerate) are exposed conformably.

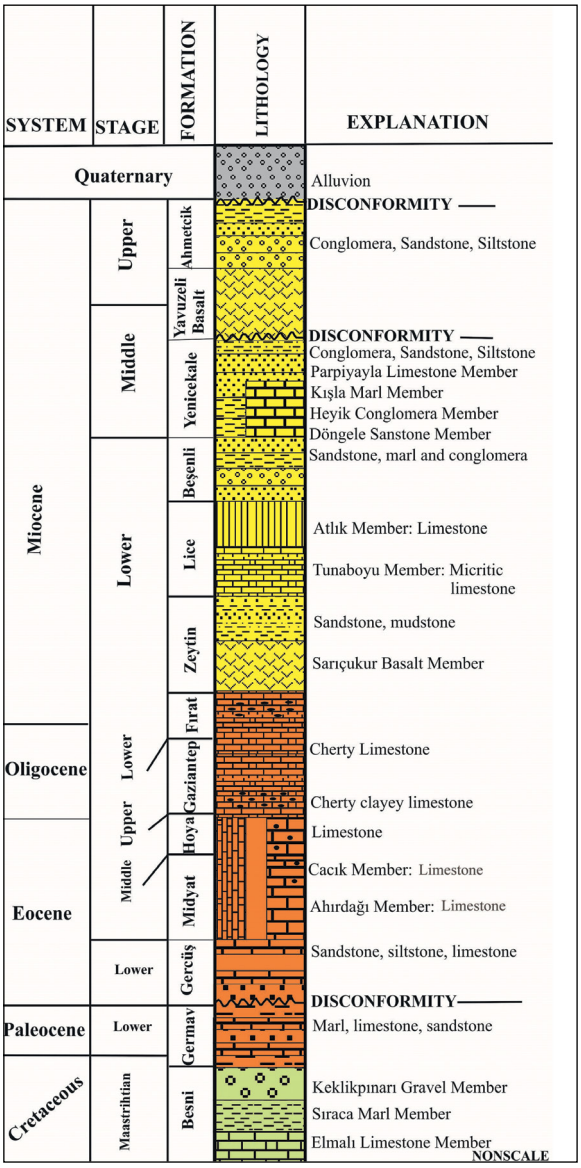


Figure 2- General stratigraphy section of study area (Sümengen, 2014).

The Middle Miocene units in the survey area are represented by Yenicekale formation which is the main unit of this study. The Yenicekale formation consists of conglomerate, sandstone, and siltstone. This unit is divided into 4 different members by Baydar and Yergök (1996) as Parpiyayla Limestone Member, Kışla Marl Member, Heyik Conglomerate Member, and Döngele Sandstone Member.

The main material of this study is Kışla Marl Member of Yenicekale formation that mainly includes claystone and marl units and these units will be summarized below. The Yenicekale formation in the Middle - Late Miocene is overlained disconformably by Yavuzeli basalts. Moreover, the Late Miocene Ahmetçik formation that consists of conglomerate, sandstone, and siltstone, is unconformably overlaid by the Yavuzeli basalts.

The Pliocene period is represented by the Gölbaşı formation in the study area. The Gölbaşı formation mainly contains conglomerate, sandstone, marl, and tuff units. The Quaternary alluvial units are found on the top.

## 4. Stratigraphy of the Study Area

The clay units that accounted for this study belonged to the Yenicekale formation Kışla Marl Member that exposed around the Pazarcık, Şahintepe. The general features of these units were given in the following chapter (Figure 4).

### 4.1. Yenicekale formation, Kışla Marl Member

Definition: firstly, it is described by Baydar and Yergök (1996).

Stratotype: Kışla district which is the south of Zeytin (Süleymanlı).

Thickness: 300 - 350 m (Baydar and Yergök, 1996).

Base - top - lateral Relations: according to Baydar and Yergök (1996), the Yenicekale Kışla Marl Member show gradual transition with lower level of the Miocene Zeytin formation and it was reported that the Sazak Member of the Saraycık formation, overlies the Yenicekale Kışla Marl Member, is gradually transitive.

Lithology: The member consists of greyish-whitish marl units. There are claystone layers in some places.

Depositional environment and dating: Baydar and Yergök (1996) reported that the age of Kışla Marl Member is the Middle - Miocene.

## 5. Measured Stratigraphic Sections

### 5.1. Section 1

Section 1 was measured at the entrance of the Şahintepe village. The altitude of the section is 847 m. The starting and ending points in the coordinates

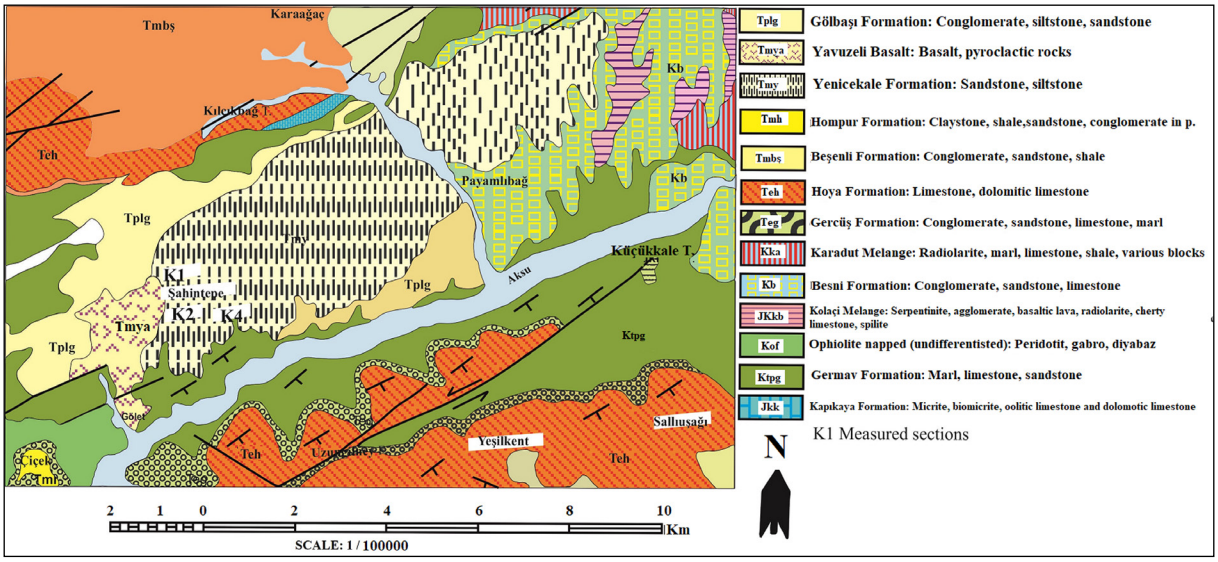


Figure 3- General geology map of study area (Sümengen, 2014).


Figure 4- General view of marl units belonging to Yenicekale formation Kışla Marl Member in the study area.

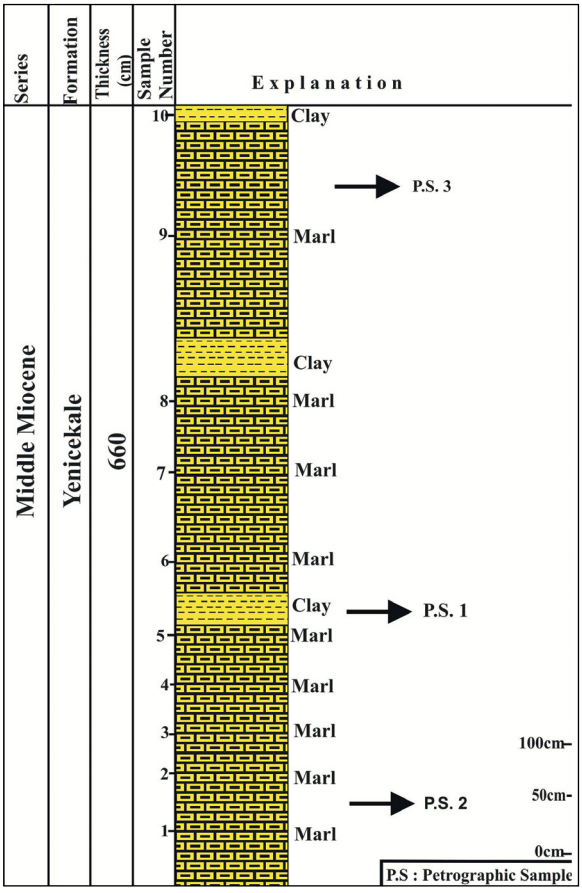


Figure 5- Time-stratigrafic section for section 1.

of the section are 37S 0351431, 4156872, and 37S 0351386, 4156932, respectively. The bottom of the sequence starts with marl units. It rarely occurs in clay laminates (Figure 5) and the thickness of the sequence is 660 cm. The XRD and geochemical analysis were done on 10 samples and 3 samples were collected for the petrographic analyses from section 1.

Section 1 continues with a sequence dominated by plant remains and clay nodules within the marl units exposed at the upper levels. At the higher level of the section, there is a layer where yellowish and brownish claystone units are intercalated.

## 5.2. Section 2

The starting and ending point in the coordinates of the section are 37S 035202, 4156089, and 37S 0352085, 4156061, respectively. The thickness of the sequence is 753 m. The section is composed of light-colored marl units and also contains claystone layers (Figure 6). For section 2, 8 samples were collected for

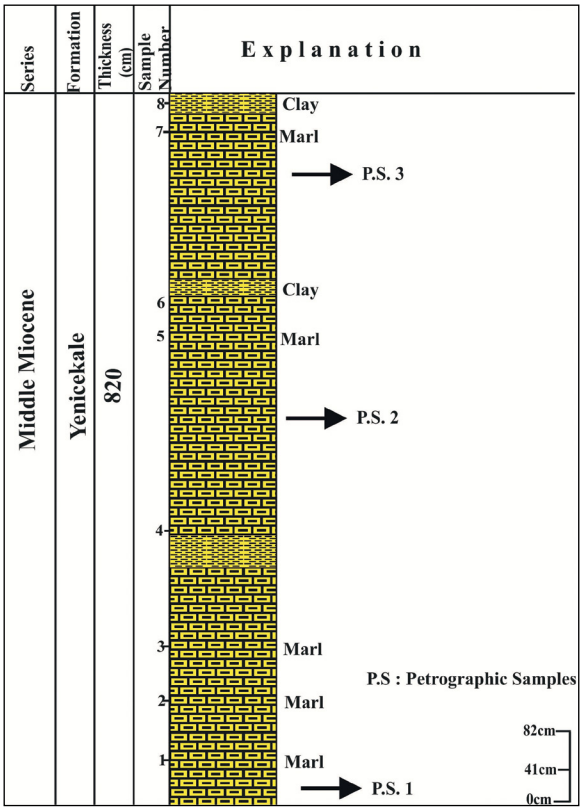


Figure 6- Time-stratigrafic section for section 2.

the XRD and geochemical analysis, while 3 samples were selected for the petrographic analysis.

The sandstone units, the thickness changes 5 - 20 cm, are found at the higher level of section 2. Those sandstone units are overlaid by greenish colored and 10 cm thick clay layers. The intercalation of sandstone and claystone continues through approximately 2 m. Generally, the sandstone units are thinner than the claystone units.

5.3. Section 4

The thickness of section 4 is 827 m (Figure 7). The coordinates of the section are 37S 0354136, 415666, and 37S 0354154, 4157803, respectively. The sequence completely consists of light whitish-beige marl layers. The marl units can be seen at the higher level of the section. 10 samples were used for the XRD and geochemical analysis and 2 samples for the petrographic analysis.

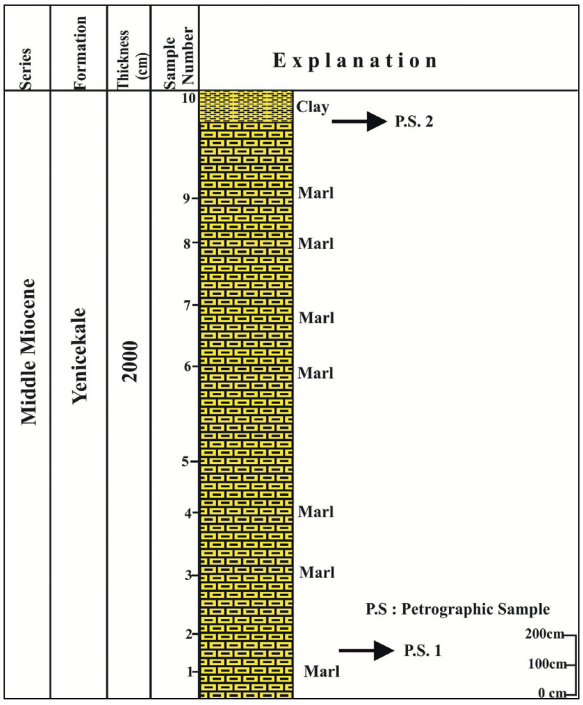


Figure 7- Time-stratigraphic section for section 4.

## 6. Petrographic Investigation

6.1. Section 1

In total 3 samples were collected from section 1. The locations of the samples on section 1 were given in Figure 5. The detailed petrographic features of those samples for this section are presented below.

Section 1, petrographic sample 1: it can be defined as mudstone according to Dunham (1962) and as intramicrite according to Folk (1965). The desiccation cracks are limited in this sample (Figure 8).

The section 1, petrographic sample 2: likewise, this sample is named mudstone according to Dunham (1962), and intramicrite by the Folk classification system (1965). The parts of rock can be examined as extraclast and lithoclast. Also, sample 2 includes quartz minerals. The secondary rock disintegration occurred and those fragments were recemented. All these pores were filled by the desiccation cracks. The shells that formed at the edges of the desiccation cracks by the microorganisms and the dissolved materials with fragmental structures such as the quartz minerals were recemented. The increased pores were filled by dog-tooth cement during the exhumation (Figure 9).

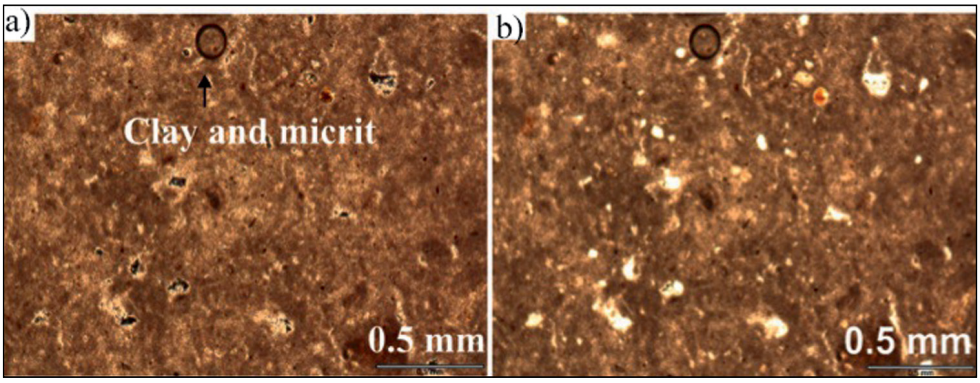


Figure 8- Section 1, petrographic sample 1: intramicrite (Folk, 1965), mudstone (Dunham, 1962); a) double nicol view, b) one nicol view.

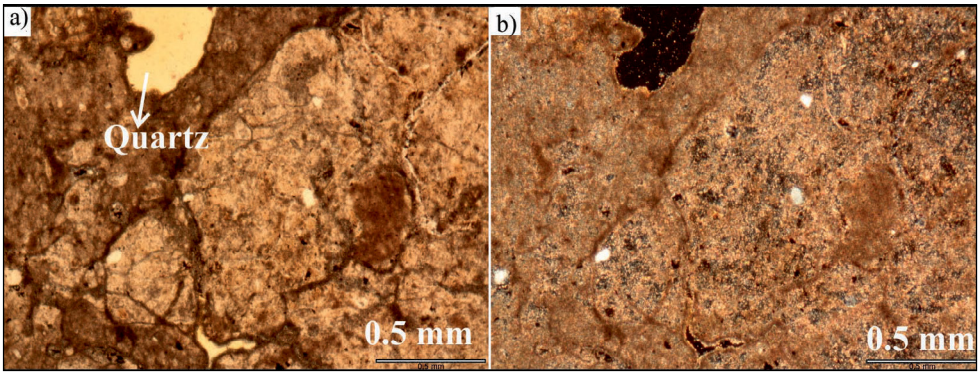


Figure 9- Section 1, petrographic sample 2: intramicrite (Folk, 1965), mudstone (Dunham, 1962); a) double nicol view, b) one nicol view.

Section 1, petrographic sample 3: The sample is named as mudstone based on the Dunham (1962), and intramicrite by Folk classification system (1965). Due to the differences in the grain sizes within the same sample, the gradation can be interpreted as poor. The pores between the grains were filled with transparent calcite crystals. In addition, the sample contains quartz and feldspar fragments (Figure 10).

6.2. Section 2

3 samples were collected from section 2 for the purpose of petrography**.** The locations of the samples within section 2 were illustrated in Figure 6.

Section 2, petrographic sample 1: Under the Dunham classification (Dunham, 1962) system, the

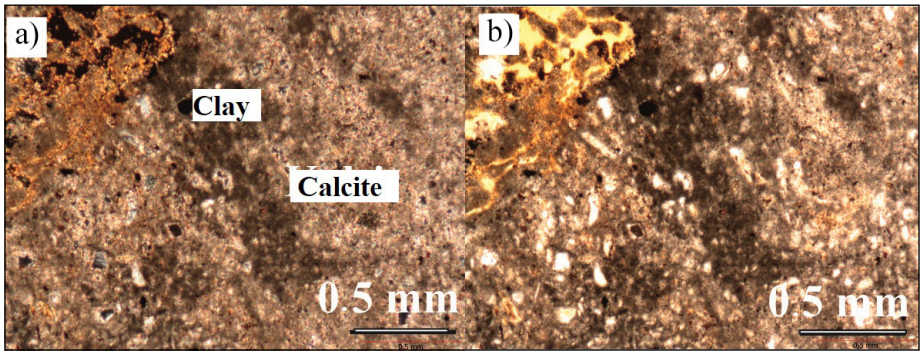


Figure 10- Section 1, petrographic sample 3: intramicrite (Folk, 1965), mudstone (Dunham, 1962); a) double nicol view, b) one nicol view.

sample is called wackestone, and extra litho micrite based on the Folk classification (1965) system. Some levels of the sample contain fossils. Because of this, the sample points out the shallow marine environment. Also, the sample includes abundant quartz - feldspar - lots of rock fragments. For this reason, it is indicated that the depositional area was affected by terrestrial transportation. Additionally, the sample contains plant branches (Figure 11).

Section 2, petrographic sample 2: The sample was named as mudstone according to the Dunham classification (Dunham, 1962) system and bio-micrite based on the Folk classification system (Folk, 1965). The sample contains planktonic foraminifera valves with a Globigerinid structure (Figure 12).

Section 2, petrographic sample 3: According to the Dunham (1962) classification system, the sample was called as grainstone and biosparite based on the Folk (1965) classification system (Figure 13).

6.3. Section 4

2 samples were collected for the petrographic investigation from this section. It can be seen in Figure 7 for the location of the samples of section 4.

Section 4, petrographic sample 1: According to Dunham (1962), the sample is called a mudstone and litho-micrite based on the Folk (1965) classification (Figure 14). The sample rarely includes the plant branches (Figure 14).

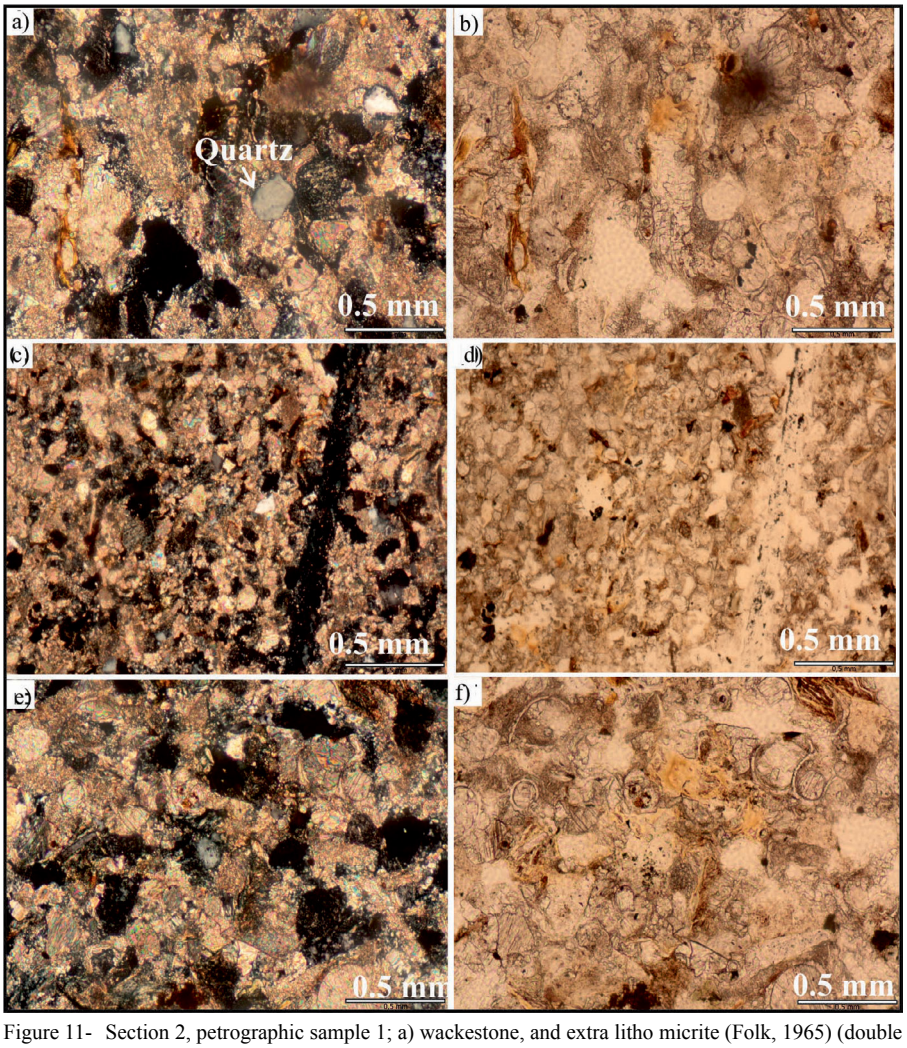


Figure 11- Section 2, petrographic sample 1; a) wackestone, and extra litho micrite (Folk, 1965) (double nikol), b) wackestone (Dunham, 1962), extra litho micrite (Folk, 1965) (one nikol), c) plant branches in section (double nikol view), d) plant branches in section (one nikol view), e) fossils in layers (double nikol view) , f) fossils in layers (one nikol view).

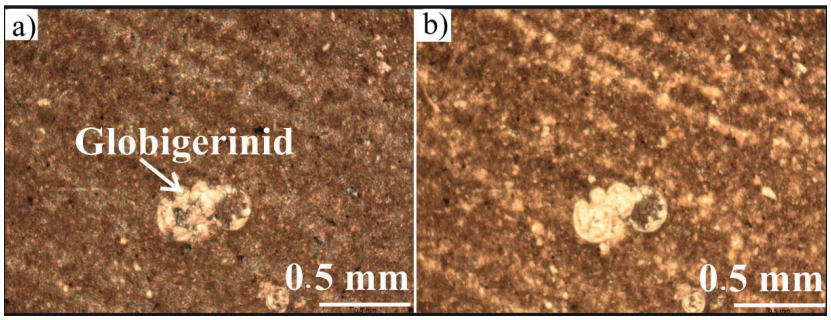


Figure 12- Section 2, petrographic sample 2: Mudstone (Dunham,1962), biomicrite (Folk,1965); a) double nicol view, b) one nicol view.

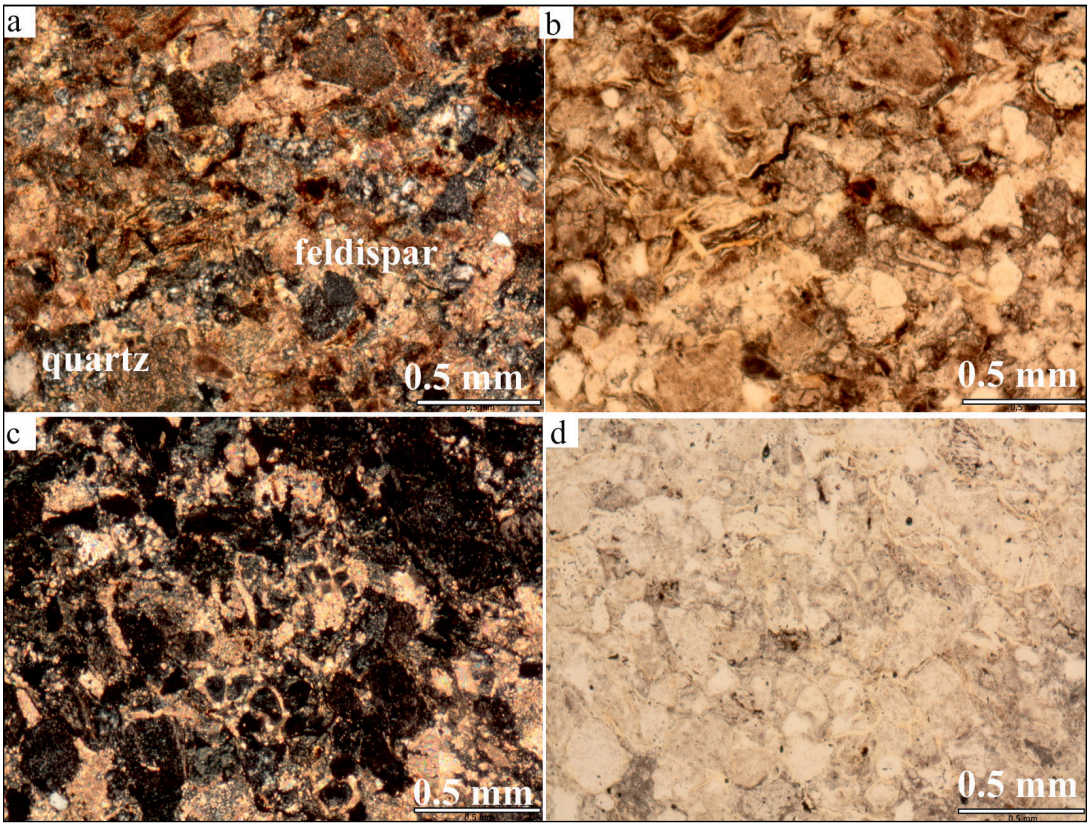


Figure 13- Section 2, petrographic sample 3: Grainstone (Dunham, 1962), biosparite (Folk, 1965); a) double nicol view, b) one nicol view, c) double nicol view of fossils – rich parts, d) c) one nicol view of fossils - rich parts.

Section 4, petrographic sample 2: likewise, the sample was named as mudstone by the Dunham (1962) classification system, and litho-micrite according to the Folk (1965) (Figure 15) classification system. The sample occasionally contains aventurine coarse quartz crystals.

## 7. Clay Mineralogy of the Study Area

In order to investigate the value of marl - claystone units exposed in the study area as cement raw material, 3 sections were taken, and all the rock properties of 28 samples belonging to these sections, which were determined by the XRD, are given in detail below.

### 7.1. XRD Whole Rock Analysis (XRD - WR)

The clay samples pulverised after the crushing and grinding processes. After this step, the quartering method is applied for the pulverized samples, and then the XRD - WR scans were taken without any processing (Figure 16).

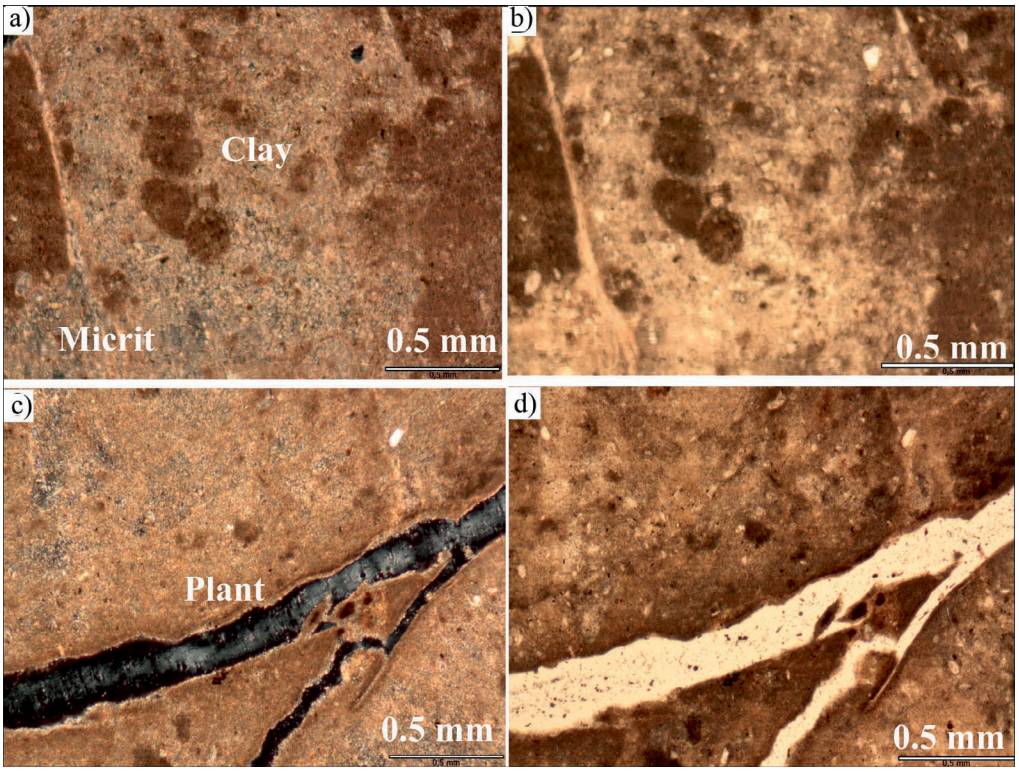


Figure 14- Section 4, petrographic sample 1: Mudstone (Dunham,1962), litho-micrite (Folk,1965); a) double nicol view, b) one nicol view, c) double nicol view of the section with plant branches in the section, d) one nicol view of the section with plant branches in the section.

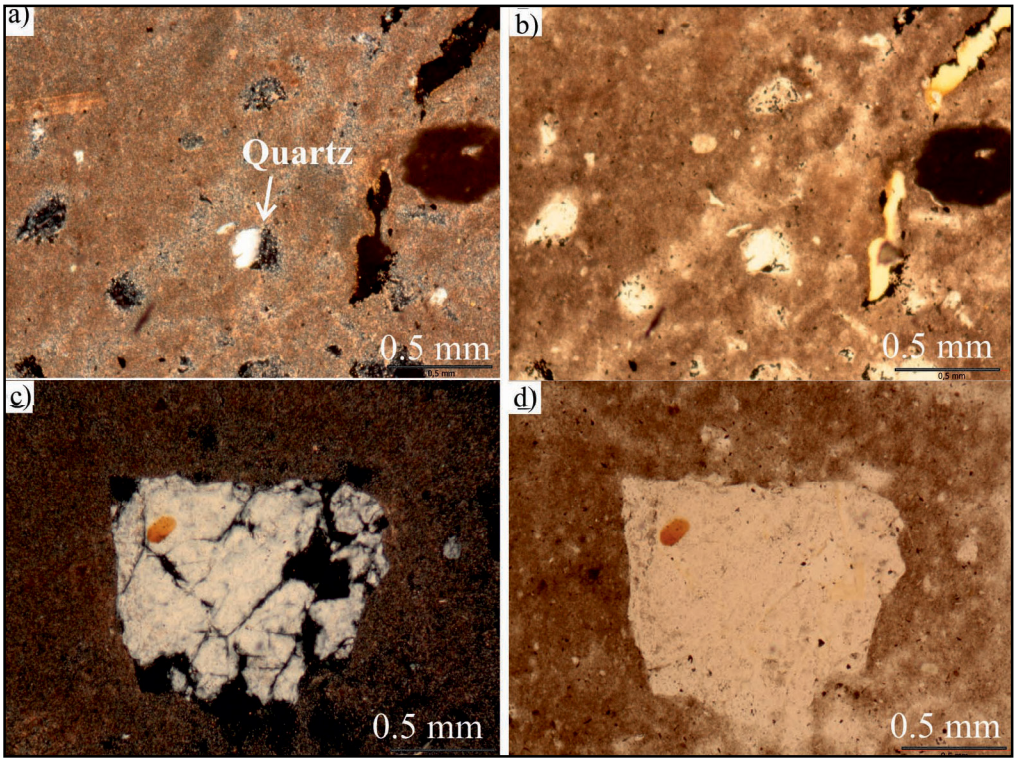


Figure 15- Section 4, petrographic sample 2: Mudstone (Dunham, 1962), litho-micrite (Folk, 1965); a) double nicol view, b) one nicol view, c) double nicol view of the section with calcite crystal in the section, d) one nicol view of the section with calcite crystal in the section.

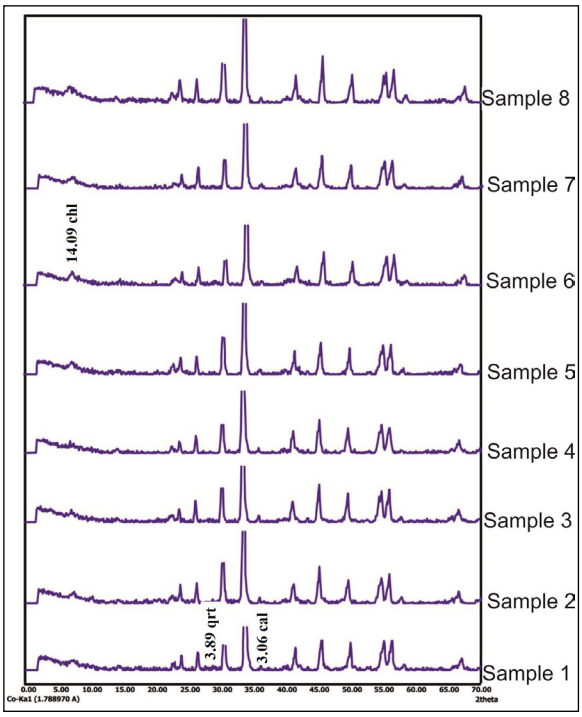


Figure 16- XRD - WR and XRD - CF diffractomes of section 1 (chl: chlorite; ill: illite; cal: calcite; qtz: quartz).

The clay units that constitute the subject of the study and exposed around the Pazarcık - Şahintepe Yenicekale formation, and generally, calcite, quartz, dolomite, chlorite were determined by the samples, collected from clay beds belongs to Kışla Marl member. Moreover, the type and amount of these minerals show variety.

*7.1.1. Section 1*

10 samples collected from section 1, consist of 8 claystone and 2 marl units (Figure 16). For this analysis, 2θ: 3° to 70° were used and the XRD diffractions were obtained (Table 1). Those diffractions are pointed out the dolomite, illite, quartz, and opaque minerals, respectively.

*7.1.2. Section 2*

All of the 8 samples taken from this section consist of calcite minerals (Figure 17). To obtain the suitable diffraction for the determination of the minerals, 2θ, from 3° to 70°, were applied (Table 2).

Table 1- Minerals belonging to section 1 for which XRD - WR and XRD - CF analyzes were made.

| SAMPLE NUMBER | XRD - WR | XRD - CF |
|---|---|---|
| SECTION 1 - SAMPLE 1 | Dolomite, Illite, Quartz | |
| SECTION 1 - SAMPLE 2 | Dolomite, Illite, Quartz | |
| SECTION 1 - SAMPLE 3 | Dolomite, Illite, Quartz | |
| SECTION 1 - SAMPLE 4 | Dolomite, Illite, Quartz | |
| SECTION 1 - SAMPLE 5 | Dolomite, Illite, Quartz | Illite |
| SECTION 1 - SAMPLE 6 | Dolomite, Illite, Quartz | |
| SECTION 1 - SAMPLE 7 | Calcite, Dolomite, Illite, Quartz | |
| SECTION 1 - SAMPLE 8 | Calcite, Dolomite, Illite, Quartz | Illite |
| SECTION 1 - SAMPLE 9 | Calcite, Dolomite, Illite, Quartz | |
| SECTION 1 - SAMPLE 10 | Calcite, Dolomite, Illite, Quartz | |

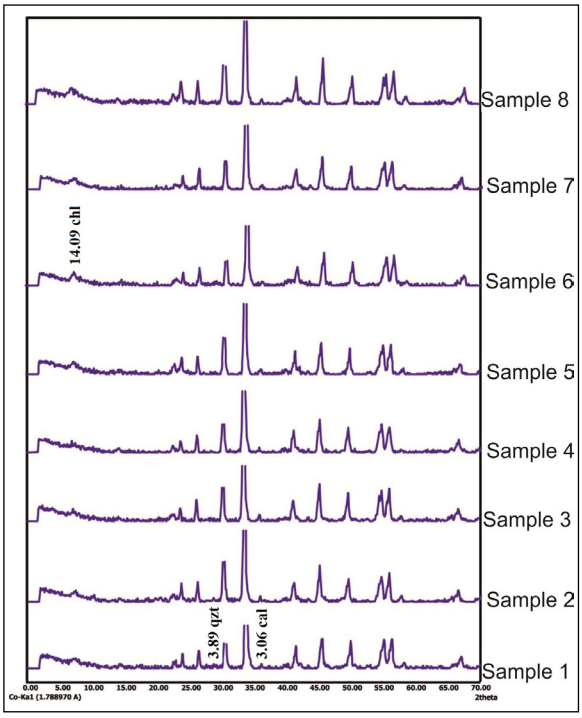


Figure 17- XRD - WR diffractoms of section 2 (chl: chlorite; cal: calcite; qtz: quartz).

Table 2- Minerals belonging to section 2 for which XRD - WR and XRD - CF analyzes were made.

| SAMPLE NUMBER | XRD - WR | XRD - CF |
|---|---|---|
| SECTION 2 - SAMPLE 1 | Quartz, Calcite | |
| SECTION 2 - SAMPLE 2 | Quartz, Calcite | |
| SECTION 2 - SAMPLE 3 | Quartz, Calcite | |
| SECTION 2 - SAMPLE 4 | Quartz, Calcite | |
| SECTION 2 - SAMPLE 5 | Quartz, Calcite | |
| SECTION 2 - SAMPLE 6 | Quartz, Calcite, Chlorite | |
| SECTION 2 - SAMPLE 7 | Quartz, Calcite | |
| SECTION 2 - SAMPLE 8 | Quartz, Calcite | |

*7.1.3. Section 4*

All of the 10 samples taken from this section consist of the dolomite units. The samples were scanned by using 2θ, from 3° to 70° (Table 3).

7.2. XRD Clay Fraction Analysis (XRD - CF)

The clay fraction analysis was applied to sample 5 and sample 8 in section 1 from 28 samples taken from 3 different sections. These samples were scanned under normal conditions, ethylene glycol, and plus by heating up to 550 °C. As a result of the XRD diffraction, the most dominant primary mineral in these samples is illite (Figures 16, 17, and 18; Tables 1, 2 and 3).

Table 3- Minerals belonging to section 4 for which XRD - WR was made.

| SAMPLE NUMBER | XRD - WR |
|---|---|
| SECTION 4 - SAMPLE 1 | Dolomite, Calcite |
| SECTION 4 - SAMPLE 2 | Dolomite |
| SECTION 4 - SAMPLE 3 | Dolomite |
| SECTION 4 - SAMPLE 4 | Dolomite |
| SECTION 4 - SAMPLE 5 | Dolomite |
| SECTION 4 - SAMPLE 6 | Dolomite |
| SECTION 4 - SAMPLE 7 | Dolomite |
| SECTION 4 - SAMPLE 8 | Dolomite |
| SECTION 4 - SAMPLE 9 | |
| SECTION 4 - SAMPLE 10 | |

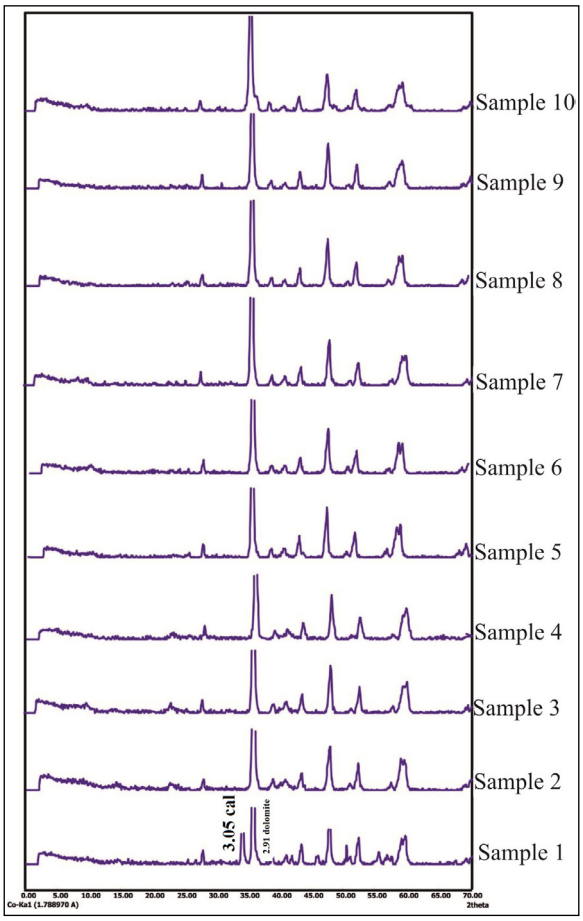


Figure 18- XRD - WR diffractoms of section 4 ( cal: calcite).

## 8. Geochemistry

$SiO_2$, CaO, MgO, $Al_2O_3$, $Fe_2O_3$, $TiO_2$, $Na_2O$, $K_2O$, MnO, $P_2O_5$, and values of LOI at a total of 28 samples were determined for the geochemical analysis (Table 4).

The CaO oxide concentrations of 10 samples collected from section 1, changes between 5.17% and 24.26%. The CaO contents of the samples stem from the presence of calcite or dolomite. Besides, the XRD results of sample 8, sample 9, and sample 10 confirm the presence of calcite and dolomite (Table 1). Likewise, in section 2, 8 samples show the CaO values in a range of 26.99% and 41.74%. Moreover, all samples in section 2 contain the calcite minerals and this case was approved by the XRD results (Table 2) . On the other hand, the CaO values in the total 10 samples of section 4 are between 18.66% and 37.19%. The calcite mineral only was observed in sample 1 of section 4. These analyses were approved by the XRD results (Table 3).

Table 4- Chemical analysis results of clay samples in sections 1 - 2 and 4 (SM: Silicate modulus, AM: Aluminum modulus, HM: Hydraulic modulus).

| Section Name | Element / Sample Number | $SiO_2$% | $TiO_2$% | $Al_2O_3$% | $Fe_2O_3$% | MnO% | MgO% | CaO% | $Na_2O$% | $K_2O$% | $P_2O_5$% | LOI | TOTAL% | SM | AM | HM |
|---|---|---|---|---|---|---|---|---|---|---|---|---|---|---|---|---|
| Section I | SectionI-Sample 1 | 27.86 | 0.48 | 4.709 | 4.302 | 0.06 | 12.92 | 18.16 | 0.028 | 0.419 | 0.034 | 32.35 | 101.31 | 3.09 | 1.09 | 0.49 |
| | SectionI-Sample 2 | 19.59 | 0.407 | 3.475 | 3.911 | 0.067 | 14.39 | 23.04 | 0.045 | 0.343 | 0.034 | 35.45 | 100.75 | 2.65 | 0.88 | 0.85 |
| | SectionI-Sample 3 | 18.17 | 0.404 | 3.147 | 3.592 | 0.062 | 14.68 | 23.97 | 0.058 | 0.237 | 0.03 | 37.38 | 101.72 | 2.69 | 0.87 | 0.96 |
| | SectionI-Sample 4 | 32.07 | 0.555 | 5.566 | 5.209 | 0.078 | 12.79 | 14.42 | 0.01 | 0.465 | 0.032 | 30.09 | 101.28 | 2.97 | 1.06 | 0.33 |
| | SectionI-Sample 5 | 36.67 | 0.539 | 5.772 | 5.19 | 0.059 | 12.58 | 11.65 | 0.002 | 0.423 | 0.032 | 27.15 | 100.07 | 3.34 | 1.11 | 0.24 |
| | SectionI-Sample 6 | 26.45 | 0.438 | 4.273 | 4.178 | 0.058 | 13.69 | 18.66 | 0.034 | 0.391 | 0.034 | 33.33 | 101.55 | 3.13 | 1.02 | 0.53 |
| | SectionI-Sample 7 | 24.36 | 0.358 | 3.653 | 4.883 | 0.069 | 14.47 | 19.93 | 0.012 | 0.209 | 0.04 | 34.55 | 102.53 | 2.85 | 0.74 | 0.6 |
| | SectionI-Sample 8 | 47.13 | 0.539 | 7.319 | 6.45 | 0.09 | 11.22 | 5.17 | 0.084 | 0.489 | 0.065 | 21.67 | 100.22 | 3.42 | 1.11 | 0.08 |
| | SectionI-Sample 9 | 25.78 | 0.352 | 3.987 | 4.746 | 0.083 | 9.86 | 24.26 | 0.018 | 0.426 | 0.07 | 30.39 | 99.98 | 2.95 | 0.84 | 0.7 |
| | SectionI-Sample 10 | 31.08 | 0.315 | 4.018 | 5.691 | 0.083 | 13.19 | 17.01 | 0.035 | 0.385 | 0.045 | 30.43 | 102.3 | 3.2 | 0.7 | 0.41 |
| Section 2 | Section 2-Sample 1 | 24.61 | 0.413 | 4.307 | 3.605 | 0.066 | 2.12 | 29.5 | 0.025 | 0.769 | 0.095 | 36.73 | 102.24 | 3.11 | 1.19 | 0.9 |
| | Section 2-Sample 2 | 19.53 | 0.316 | 3.863 | 3.543 | 0.103 | 2.76 | 41.74 | 0.222 | 0.455 | 0.097 | 28.23 | 100.87 | 2.63 | 1.09 | 1.54 |
| | Section 2-Sample 3 | 24.3 | 0.359 | 4.653 | 3.353 | 0.092 | 2.89 | 34.24 | 0.013 | 0.69 | 0.092 | 31.2 | 101.88 | 3.03 | 1.38 | 1.05 |
| | Section 2-Sample 4 | 23.79 | 0.419 | 4.503 | 3.879 | 0.09 | 2.64 | 34.6 | 0.038 | 0.802 | 0.012 | 30.87 | 101.63 | 2.83 | 1.16 | 1.07 |
| | Section 2-Sample 5 | 33.31 | 0.445 | 5.637 | 4.01 | 0.088 | 2.59 | 26.99 | 0.038 | 0.859 | 0.095 | 27.09 | 101.15 | 3.45 | 1.4 | 0.62 |
| | Section 2-Sample 6 | 25.48 | 0.468 | 5.953 | 4.641 | 0.087 | 2.83 | 30.79 | 0.052 | 0.692 | 0.12 | 30.61 | 101.72 | 2.4 | 1.28 | 0.85 |
| | Section 2-Sample 7 | 27.72 | 0.434 | 4.777 | 3.822 | 0.092 | 2.47 | 27.93 | 0.053 | 0.883 | 0.11 | 32.24 | 100.54 | 3.22 | 1.24 | 0.76 |
| | Section 2-Sample 8 | 28.31 | 0.417 | 5.056 | 3.66 | 0.06 | 1.83 | 31.3 | 0.007 | 0.573 | 0.826 | 29.48 | 101.5 | 3.24 | 1.38 | 0.84 |
| Section 4 | Section 4-Sample 1 | 5.68 | 0.06 | 0.884 | 0.861 | 0.062 | 15.45 | 37.19 | nd | 0.058 | 0.085 | 40.08 | 100.39 | 3.24 | 1.02 | 0.5 |
| | Section 4-Sample 2 | 18.6 | 0.198 | 2.16 | 2.93 | 0.061 | 20.72 | 20.4 | 0.067 | 0.26 | 0.09 | 36.18 | 101.66 | 3.65 | 0.73 | 0.85 |
| | Section 4-Sample 3 | 21.68 | 0.261 | 2.831 | 3.386 | 0.069 | 19.18 | 18.66 | 0.064 | 0.405 | 0.085 | 33.94 | 100.56 | 3.48 | 0.83 | 0.66 |
| | Section 4-Sample 4 | 19.01 | 0.218 | 2.345 | 2.655 | 0.064 | 21.13 | 20.2 | 0.103 | 0.343 | 0.117 | 34.35 | 100.53 | 3.8 | 0.88 | 0.84 |
| | Section 4-Sample 5 | 7.8 | 0.095 | 1.068 | 1.303 | 0.048 | 19.51 | 29.77 | 0.047 | 0.132 | 0.044 | 40.05 | 99.85 | 3.29 | 0.81 | 2.92 |
| | Section 4-Sample 6 | 10.07 | 0.102 | 1.162 | 1.453 | 0.046 | 20.07 | 27.63 | nd | 0.141 | 0.057 | 40.93 | 101.65 | 3.85 | 0.79 | 2.17 |
| | Section 4-Sample 7 | 8.93 | 0.079 | 0.824 | 0.886 | 0.035 | 20.78 | 28.64 | 0.005 | 0.08 | 0.073 | 40.57 | 100.9 | 5.22 | 0.93 | 2.7 |
| | Section 4-Sample 8 | 6.77 | 0.101 | 1.112 | 1.362 | 0.048 | 19.61 | 30.32 | 0.042 | 0.139 | 0.037 | 40.36 | 99.9 | 2.74 | 0.81 | 3.27 |
| | Section 4-Sample 9 | 7.4 | 0.124 | 1.43 | 2.072 | 0.092 | 17.52 | 31.79 | 0.014 | 0.202 | 0.06 | 40.22 | 100.93 | 2.11 | 0.69 | 2.91 |
| | Section 4-Sample 10 | 7.52 | 0.12 | 1.165 | 2.708 | 0.111 | 17.22 | 36.35 | 0.031 | 0.181 | 0.07 | 33.81 | 99.28 | 1.94 | 0.43 | 3.19 |

The MgO values on the clay samples in section 1, are in the range of 9.86% and 14.68%, and these values confirm the presence of dolomite minerals in the rocks of all samples. When section 2 is checked, due to the MgO content, it has not contained the dolomite between 1.83% and 2.89% of all samples values. Similar to section 1, the MgO values of section 4 are in the range of 15.45% and 21.13%. Thus, all samples of section 4 contain dolomite minerals abundantly. Also, the existence of the dolomite minerals in the system was verified by the XRD results (Tables 1 and 3).

The range of $Al_2O_3$ contents in the section 1 samples is between 3.14% and 7.31%. In this range, the clay minerals were evaluated as illite. While the illite minerals were found within all samples of section 1, and the presence of the illite minerals was confirmed by the XRD results (Table 1). Besides, sample 5 and sample 8 of section 1 were done with a clay fraction analysis. The $Al_2O_3$ value of sample 5 is 5.77%, while sample 8 contains up to 7.31%, and those two samples include a high amount of the illite minerals as a result of XRD clay fraction analysis (Table 1). The $Al_2O_3$ values are in the range of 3.86% and 5.9% in section 2 and are between 0.83% - 2.83% for section 4. However, the illite minerals could not be found in both two sections.

As a result of the performed analysis, the $SiO_2$ concentration in section 1 is in the range of 18.18% - 47.13%. These values obtained by the XRD and geochemical analysis approve that the $SiO_2$ concentration is based on the quartz phases in the rock (Table 1). Also, the $SiO_2$ content is between 19.53% - 33.31% on section 2, and this section contains the quartz minerals. Section 4 does not include the quartz minerals due to the amount of $SiO_2$ concentrations (5.68% - 21.68%).

When LOI values in section 1 were checked, these are in between 21.67% and 37.38%, thus, in sample 8, sample 9 and sample 10 contain dolomite and calcite minerals abundantly. Calcite was found in all samples in the value range of 28.23% and 36.73% in section 2. The highest LOI was measured in section 4 (33.81% - 40.39%), and most probably those samples of section 4 contain a higher amount of dolomite and also sample 1 includes calcite minerals.

The $Fe_2O_3$ values are between 4.17% - 5.69%, 3.35% - 4.64%, and 0.86% - 3.38% for section 1, section 2, and section 4, respectively. The $Fe_2O_3$ content of the rocks, obtained by the geochemical and XRD analyses, may depend on the presence of the minor or accessory ankerite minerals (Table 3). For this reason, finding the ankerite minerals in section 2 and section 4 is possible.

When the silica module, aluminum module, and hydraulic module values are checked as a result of the geochemical analyses, SM is over 2.7, making the clinker burning process more difficult (Duda, 1988). The values of the silica modules are between 2.65 - 3.42% for section 1, 2.40 - 3.45% for section 2, and 1.94 - 5.22% for section 4 (Table 4). In section 2, there are 2 samples (sample 2 and sample 3) with a silica module less than 2.7 that only 20 percent of the samples does not cause any problem for the burning process when those samples are compared to the whole section, while other 80% of the samples has a difficulty for the burning process. Likewise, two samples (sample 2 and sample 6) of section 2, and sample 9 and sample 10 point out the same situation. It might be said that the clay samples in the whole study area require more heat to increase burnability capacity. The acceptable value range of the AM for the cement industry is between 1.5 - 2.5 (Duda, 1988). When sections 1 and 4 are examined, samples cause problems during the pulverization process because all samples are under the accepted values. On the other hand, only sample 5 of section 2 has a higher value than the acceptable range of the aluminum module so it does not pose a problem in the pulverization process. The standard values range of the hydraulic module is between 1.8 - 2.2 based on the Duda (1988). The cement with lower than 1.7 showed mostly insufficient strength, thus, it can be said that the concrete in which this cement is used show brittle properties. However, when this value is 2.4 for HM, the volume of the produced cement changes and swells, thus it causes damage to the concrete. In this case, when section 1 and section 2 are checked, all samples are under the standard value ranges that's why the cements, produced by concrete, might show brittle behavior. Also, samples 1, 5, 6, 7, 8, 9, and 10 of section 4, may create havoc for the concrete because of higher hydraulic values than 2.4.

## 9. Results

This study was carried out on the marl - sandstone - claystone units of the Yenicekale formation Kışla member where exposed between Söğütlü and Şahintepe villages of Pazarcık district in Kahramanmaraş. The purpose of the study is to reveal whether the marl and clay units can be used as cement raw material. For this purpose, 3 stratigraphic sections were measured throughout the 3 different profiles where the formation is well observed, and 28 samples were collected for the purpose of geochemical analyses as well as 8 samples for petrographic analyses.

The XRD (X-ray diffraction) and geochemical studies were carried to test the usage of samples as cement raw material (Table 4). As a result of the XRD analysis, the calcite, dolomite, quartz, and chlorite in

section 1; the quartz, calcite, and chlorite in section 1; the dolomite and calcite minerals were determined (Tables 1, 2 and 3).

Especially samples with high clay content were analyzed by XRD - WR (XRD - Whole Rock) without any other processing (Figure 16). In the samples separated by clay fraction, the illite is the dominant mineral in the XRD - diffractom extracted under the normal conditions (Figure 16, Tables 1, 2 and 3). Also, the same situation was observed in the samples treated with ethylene glycol at 550 $^{o}$C condition (Figure 16). According to $d_{001}$ values in the detailed clay fraction XRD analyses, the mineral was determined as illite in sample 5 and sample 8 of section 1.

Based on the Akıncı (1968) studies, the illite minerals were formed as a result of alteration processes. The author also mentioned that the illite beds may occur at the limestone form in marine layers, whose origin is sedimentary. Akıncı (1968) stated that the clayey limestone and dolomites which are exposed in large areas and observed in all rock samples, mainly contain illite minerals in terms of the clay content, while montmorillonite type cannot be seen much in such environments. Therefore, under the light of Akıncı (1968) studies, the depositional environment of the Yenicekale formation Kışla Marl Member which is exposed in the study area is of shallow marine origin and the study of Akıncı (1968) explain why Kışla Marl Member contain only illite type clay mineral or why does not contain any other type of clay minerals.

In geochemical analyses that carried out the samples collected from the Yenicekale formation, $SiO_2$ quartz, CaO calcite, $K_2O$ illite, $Fe_2O_3$ ankerite, MgO dolomite, $Al_2O_3$ clayey minerals, and high loss of ignition values are depending on the carbonate-rich minerals (Bor, 2008).

When the obtained results of the geochemical analyses with the product which using as a cement raw material were compared with the limit values, the MgO values (Bor, 2008) were determined in between 9,86 - 14,68% at section 1, 1,83 - 2,89% at section 2, and 15.45 - 21.13% at section 4 respectively. When the limit values of the MgO for the cement raw material, the values of section 1 and section 4 were being over the limit values (max = 5%), while section 2 stayed under the limit values.

The limit values of $Al_2O_3$ (Bor, 2008) which will be used as a cement raw material, are in the range of 3.14 - 7.31% at section 1, 3.86 - 5.9% at section 2, and 0.82 - 2.83% at section 4 (min: 4%). Obviously, the values of section 2 and section 4 were below the required limit values, while the content of section 1 is in the range of limits.

The $SiO_2$ values (Bor, 2008) are expected to be around 31% for the cement industry, and the $SiO_2$ contents are between 18.17 - 47.13% in section 1, 19.53 - 33.31% in section 2, and 5.68 - 21.68% in section 4. In this case, the $SiO_2$ contents of section 4 were determined to be under the limit values.

The number of alkalis ($K_2O$ and $Na_2O$) to be used in the cement industry is limited (approximately 2%) and it was observed that these values are so low in all samples.

The silicate and alimuna modules were calculated by using the $SiO_2$, $Fe_2O_3$, and $Al_2O_3$ values of the geochemical analyses. The required silica module values are between 2.2 - 2.6 % (Duda, 1988) in the Turkish cement industry, even though these values are 1.9 - 3.2 % based on the standards. The obtained silica module values after the geochemical analysis for the study area are in the range of 2.65 - 3.42% in section 1, 2.40 - 3.45% in section 2, and 1.94 - 3.85% in section 4. According to the results mentioned above, only a few samples fit with the standard limit values.

On the other hand, the standard values which belong to the alumina module are in 1.5 - 2.5 (Duda, 1988). In this study, the alumina modules were determined between 0.7 - 1.11% in section 1, 1.09 - 1.38% in section 2, and 0.43 - 1.02% in section 4, respectively. In this case, it is understood that all the results of the alumina module of the samples were below the standard values.

In summary, both the aluminum module values and the silicate module values determined as a result of the geochemical analysis are out of the standard values for the clay to be used in the cement industry, and as such, these units which belonging to the Yenicekale formation Kışla Marl Member are not suitable for use in the cement industry. However, it is feasible to produce a portland cement for trial purposes by adding some corrective additives (such as bauxite and iron ore) to the cement.

**Acknowledgements**

This study was supported by KSU Scientific Research Projects Management Department within the scope of the project numbered 2015/3 - 2YLS.

**References**

Abdioğlu, E. 2002. Kavaklar (Ünye - Fatsa, Ordu) yöresindeki kil oluşuklarının mineralojik, jeokimyasal ve kökensel incelemesi. Yüksek Lisans Tezi, KTÜ, Fen Bilimleri Enstitüsü, Trabzon.

Akıncı, Ö. 1968. Bilecik bölgesi kaolin yatakları ve civarının jeolojisi, kaolinlerin seramik özellikleri. Bulletin of Mineral Research and Exploration 18**,** 67-83.

Arpat, E., Şaroğlu, F. 1972. Doğu Anadolu Fayı ile ilgili bazı gözlem ve düşünceler. Bulletin of Mineral Research and Exploration 78, 44-50

Arpat, E., Şaroğlu, F. 1975. Türkiye'deki bazı önemli genç tektonik olaylar. Türkiye Jeoloji Kurumu Bülteni 18(1), 91-101

Baydar, O., Yergök, A. F. 1996. Güneydoğu Anadolu - Kenar Kıvrım Kuşağı - Amanos Dağları kuzeyi ve Doğu Torosların Jeolojisi. Maden Tetkik ve Arama Genel Müdürlüğü, Rapor No: 3344, 90, Ankara (unpublished).

Bor, E. 2008. İğdecik yöresi (Isparta) Eosen yaşlı kil yataklarının endüstriyel hammadde olarak kullanılabilirliğinin araştırılması. Yüksek Lisans Tezi, Süleyman Demirel Üniversitesi, Fen Bilimleri Enstitüsü, 60, Isparta.

Çelik, M., Karakaya, N. 1997. Ordu ve Giresun civarında gözlenen hidrotermal kil oluşumlarının incelenmesi. VIII. Ulusal Kil Sempozyumu, Kütahya.

Çelik Karakaya, M. 2006. Kil Minerallerinin Özellikleri ve Tanımlama Yöntemleri. Bizim Büro Basımevi, 640, Ankara.

Darbaş, G., Gül, M. 2006. Alacık formasyonuna (Kahramanmaraş havzası) ait kömürlü seviyelerin paleontolojisi. KSÜ Fen ve Mühendislik Dergisi 9(2), 71–81.

Derman, A. S. 1999. Proximal submarine fan conglomerate and valley fill pattern. 12. Türkiye Petrol Kongresi Bildirileri, Ankara, 207-218.

Dizer, A. 1991. Kuzey Kahramanmaraş'ta Langiyen ve Serravaliyen katlarının biyostratigrafisi. Jeoloji Sempozyumu 301, 71-81.

Duda, W. H. 1988. Cemen - Data - Book, Bauverlag Gmb, Wiesbaden und Berlin, 3.

Dunham, E. J. 1962. Classification of carbonate rocks according to depositional texture. Ham, W. E. (Ed.). Classification of carbonate rocks. American Association. Petroleum, Geologists Bulletin 1, 108-121.

Erdoğan, S. 1994. İnşaat tuğlası üretiminde kullanılan hammaddelerin etkilerinin incelenmesi, Lisans Tezi*,* İTÜ Metalürji Fakültesi, İstanbul.

Folk, R. L. 1965. Some aspects of recrystallization in ancient limestones. Pray L. C. and Murray R. C. (Eds.) Olomitization and limestone diagenesis. Society for Sedimentary Geology 13, 14-48.

Gözübol, A. M., Gürpınar, O. 1980. Kahramanmaraş kuzeyinin jeolojisi ve tektonik evrimi, 5. Türkiye Petrol Kongresi Bildirileri, Ankara, 21-29.

Gül, M. A. 2000. Kahramanmaraş yöresinin jeolojisi. Hacettepe Üniversitesi, Fen Bilimleri Enstitüsü, Doktora Tezi, 304, Ankara.

Gül, M. 2004. Evolution of turbidite system in the Kahramanmaraş basin, Çukurova Üniversitesi, Fen Bilimleri Enstitüsü, Doktora Tezi, 354, Adana (unpublished).

Gül, M., Darbaş, G., Gürbüz, K. 2005. Alacık Formasyonunun (En Geç Orta Eosen - Erken Miyosen) Kahramanmaraş havzası içindeki tektonik - stratigrafik konumu. İstanbul Üniversitesi, Mühendislik Fakültesi, Yerbilimleri Dergisi 18(2), 183-197.

Gündoğdu, M. N., Yılmaz, O. 1983. Kil mineralojisi yöntemleri, I. Ulusal Kil Sempozyumu, Çukurova Üniversitesi, Adana, Bildiriler Kitabı, 319-330.

İmamoğlu, M. Ş. 1993. Gölbaşı (Adıyaman) - Pazarcık - Narlı (Kahramanmaraş) arasındaki sahada Doğu Anadolu Fayı'nın neotektonik incelemesi. Doktora Tezi, Ankara Üniversitesi, Fen Bilimleri Enstitüsü, Ankara (unpublished).

Kop, A., Ezer, M., Bodur, M. N., Darbaş, G., İnan, S., Ergintav, S, Seyis, C., Yalçın, C. 2014. Geochemical monitoring along the Türkoğlu - Kahramanmaraş - Gölbaşı - Adıyaman segments of the East Anatolian Fault System (EAFS). The Arabian Journal for Science and Engineering 39(7), 5521-5536.

Norvich, B. E., Martin, R. T. 1983. Solvation methods for expandable layers. Clays and clay minerals 31, 235-238.

Orhun, O. 1965. Yurdumuzda bulunan önemli kaolin ve killerin diferansiyel termik analizleri. Türkiye Mühendis ve Mimarlar Odalar Birliği Kimya Mühendisleri Odası Yayını.

Önalan, M. 1986. Kahramanmaraş Tersiyer istifinin sedimanter özellikleri ve çökelme ortamları. İstanbul Üniversitesi Mühendislik Fakültesi, Yerbilimleri Dergisi C5, 39-78.

Özkan, T. O. 1977. Türkiye'deki ticari bentonit killerinin özellikleri ve kullanım alanlarının tespiti, TÜBİTAK Marmara Araştırma Enstitüsü, İstanbul.

Özpınar, Y., Hançer, M. ve Semiz, B. 2006. Belevi (Çal) kil yatakları, Çal Sempozyumu, Pamukkale Üniversitesi, 1 - 3 Eylül 2006, Denizli.

Robertson, A. H. F., Ünlügenç, U. C. 2001. Role of the Misis - Andırın lineament in closure and suturing of the southern Neotethys ocean in the Eastern Mediterranean region. Fourth International Turkish Geology Symposium, Adana, 89.

Seyhan, L. 1967. Seramik hammaddeler. Maden Tetkik ve Arama Genel Müdürlüğü, Enerji ve Hammaddeler Arama ve Araştırmaları Dairesi, Rapor No: 292, Ankara (unpublished).

Sümengen, M. 2014. 1/100.000 ölçekli Türkiye Jeoloji Haritaları, Gaziantep - M38 paftası, Maden Tetkik ve Arama Genel Müdürlüğü, Jeoloji Etütleri Dairesi, Ankara.

Varol, L., Kop, A., Darbaş, G**.** 2012. Koçlar - Sarıgüzel (Kahramanmaraş Kuzeyi) arasında kalan bölgenin Jeolojik özellikleri, Doğu Toroslar, KSU Mühendislik Bilimleri Dergisi 15(1), 43-56.

Yalçın, H. 2004. Kil mineralojisi ve jeolojisi ders notları. Cumhuriyet Üniversitesi Jeoloji Mühendisliği Bölümü, Sivas.

Yılmaz, Y., Gürpınar, O., Yiğitbaş, E. 1988. Amanos Dağları ve Maraş dolaylarında Miyosen havzalarının tektonik evrimi. Türkiye Petrolleri Anonim Ortaklığı Bülteni C1(1), 52-72.

Bulletin of the Mineral Research and Exploration

http://bulletin.mta.gov.tr

# Investigation of the coefficient of consolidation of fine-grained soils using combined apparatus

Ramin ASADI[a], Kamil KAYABALI[a] and Mehmet Can BALCI[b*]

[a]*Ankara University, Faculty of Engineering, Department of Geological Engineering, Ankara, Turkey*
[b]*Batman University, Engineering and Architecture Faculty, Department of Civil Engineering, Batman, Turkey*

*Research Article*

Keywords:
Coefficient of Consolidation, Coefficient of Permeability, Oedometer Test, Combined Apparatus.

**ABSTRACT**

The scope of this investigation is to compare the coefficient of consolidation ($c_v$) values defined by the Taylor's Square Root of Time Fitting Method, which is obtained from the conventional oedometer tests, with the $c_v$ values calculated by Terzaghi's One Dimensional (1D) Consolidation Theory, which is obtained from the permeability-consolidation tests performed with a combined apparatus specifically designed for this study. In addition, an empirical relation is developed to determine $c_v$ using the coefficient of permeability (k) and index properties of the soils. The $c_v$ values obtained from the permeability-consolidation tests using the combined apparatus were found to be larger than the $c_v$ values defined by the Taylor's method, which is one of the oedometer tests. The findings showed that the difference was more prominent in the soil samples with a high plasticity. It was also found that the $c_v$ calculated by the Taylor's method exhibited a distribution in a wide range with the increased load depending on the degree of plasticity of the soil. The $c_v$ obtained from the combined apparatus it decreased with low load values and increased with higher load levels. The $c_v$ obtained by the proposed empirical relationship showed good agreement with the $c_v$ defined by permeability-consolidation relationships.

*Received Date: 06.08.2020*
*Accepted Date: 04.12.2020*

## 1. Introduction

Identification of the characteristics of the soil on which structures are built and estimation of soil behaviour for different load cases are quite important to reveal potential soil problems so that engineering structures can be designed in a sound and economical manner. Settlement is one of the significant issues that may be encountered in essential projects. The acceptable amount of settlement is defined depending on the building's important factor and the type of soil. If the settlement components exceed the permissible limits throughout the design life planned for the structure, some undesirable inconveniences such as fractures, cracks, and splits occur in the superstructure. When this effect reaches an advanced level, the structure is partially damaged or becomes completely unusable.

Consolidation settlement constitutes a large part of the settlement that occurs when soils with a low coefficient of permeability (k) are subjected to load. Consolidation settlement ($s_c$) is a time-dependent process that can take considerable time with some soil types. In determining the building's design life, it is of great importance to estimate how long it will take for the $s_c$ in the soil to take place under loading conditions. Holtz and Kovacs (1981) reported that the coefficient of consolidation ($c_v$) is the only parameter that controls the consolidation settlement in terms

Citation Info: Asadi, R, Kayabalı, K., Balcı, M.C. 2021. Investigation of the coefficient of consolidation of fine-grained soils using combined apparatus. Bulletin of the Mineral Research and Exploration 166, 71-83. https://doi.org/10.19111/bulletinofmre.835936

**Corresponding author: Mehmet Can BALCI, mcanbalci@gmail.com*

of rate (speed). This parameter is crucial in soil improvement and the use of the preloading technique. The $c_v$ is a term derived from Terzaghi's (1925) 1D Consolidation Theory. Based on Terzaghi's (1925) 1D Consolidation Theory, there is a relationship between soil permeability (k), coefficient of consolidation ($c_v$), and coefficient of volume compressibility ($m_v$) as follows:

$$c_v = k / (m_v \gamma_w) \quad (1)$$

where $\gamma_w$ unit weight of water (kN/m$^3$).

Numerous methods have been developed for calculating $c_v$ from conventional oedometer tests. These methods generally involve different mathematical approaches and curve-fitting methods. The advanced curve fitting methods for computing $c_v$ are summarized in Table 1.

Casagrande and Fadum (1940), and Taylor (1948) developed empirical methods to approximately adapt observational laboratory test data to Terzaghi's 1D consolidation theory. Feng and Lee (2001) reported that both methods are known to be the most useful methods in routine laboratory tests. However, the $c_v$ defined by Casagrande's logarithm of time fitting method is affected by the primary compression and secondary compression of the axial strain (ε) - time (t) curve. Since 90% of the degree of consolidation is used instead of 100% in Taylor's Square Root of Time Fitting Method, the $c_v$ is affected less from the secondary compression but more from the first compression (Sridharan and Prakash, 1995; Cortellazzo 2002). Sridharan et al. (1995) assert that the $c_v$ should be higher when affected by the primary compression and lower when affected by the secondary compression.

Table 1- Advanced curve fitting methods for computing $c_v$.

| References | Method |
|---|---|
| Casagrande and Fadum (1940) | log $t_{50}$ |
| Taylor (1948) | $\sqrt{t_{90}}$ |
| Su (1958) | Maximum slope |
| Sivaram and Swamee (1977) | Computational |
| Sridharan et al. (1987) | Rectangular hyperbola |
| Sridharan and Prakash (1993) | δt-t/δt |
| Robinson and Allam (1996) | Early stage log-t |
| Mesri et al. (1999) | Inflection point |
| Feng and Lee (2001) | $\sqrt{t_{60}}$ |
| Al-Zoubi (2010) | SRS |

However, the presence of a large number of methods in the literature is an indication that these methods are not applicable under all circumstances. Furthermore, since the $c_v$ values obtained by different methods are very different, it is difficult to make a reasonable decision regarding the $c_v$ merely based on the soil behavior under laboratory test conditions. According to Sridharan and Nagaraj (2004), none of the curve fitting methods applied under different circumstances and using different materials provides an exactly correct result or an approximate result. Al-Zoubi (2004) notes that large-scale variations between $c_v$ defined by curve fitting methods may arise from reasons such as variation of the $c_v$ during a specific load level, the procedure for determining the final sc, loading time including secondary compression, and additional assumptions used in these methods. Lovisa and Sivakugan (2013) compared $c_v$ values, which are determined using curve-fitting methods. Despite many controversial points mentioned above regarding the curve fitting methods, Taylor's Square Root of Time Fitting Method is widely used to determine $c_v$ in current geotechnical engineering applications. Taylor (1948) devised a method based on the square root of the time spent during the consolidation test to calculate $c_v$. In this method, a curve that depicts the relationship between two dial gauge readings made during the consolidation test and the square root of the applied load's interaction time on the sample, is drawn. The early flat part of this curve is extended until it intersects the vertical axis. Again, a second line is drawn from the start point, which has 1.15 times the value of the obtained intersection point. The projection of the intersection point of the second line and the curve obtained from the consolidation experiments on the horizontal axis shows the time it takes for 90% of the primary consolidation (U=%90) to occur. $c_v$ is calculated using the equation given below, taking the time factor as 0.848, for U = 90%.

$$c_v: T_v\, d^2/t_{90} \quad (2)$$

Where $T_v$ time factor, d drainage path, and $t_{90}$ time when U is 90%. Various researchers conducted different studies due to the problems encountered in $c_v$ calculations by curve fitting methods. Some researchers have tried to calculate $c_v$ using the soil's

index properties, independently from the oedometer tests shown in Table 2.

Carrier (1985) developed an equation for the definition of $c_v$ considering the liquidity index, plasticity index, and activity of soils. Narasimha et al. (1995) suggested another empirical equation for the calculation of $c_v$ for normally consolidated clay, taking into account the void ratio in the liquid limit condition and the existing overburden pressure in the field. Solanki and Desai (2008) examined the consolidation parameters of alluvium clays in India's southern Gujarat region, suggesting a relationship between liquid limit and plasticity and $c_v$. Sridharan and Nagaraj (2004) indicated that the relationship between shrinkage index and $c_v$ was more consistent than the liquid limit or the plasticity index. Al-Ameri et al. (2011) investigated silty clay from 280 different points and defined a new relationship between liquid limit and $c_v$. Some studies focus on using different methods for the determination of $c_v$. Olek and Pilecka (2019) used large-scale Rowe cell, Chow et al. (2020), and Vinod and Sridharan (2015) evaluated the measurement of pore water pressure for determination of $c_v$. Nguyen et al. (2019) predicted $c_v$ values of soft soil using an artificial intelligence approach. In addition to the studies listed above, Olson (1986) suggested that the only rational Method of defining $c_v$ was with Terzaghi's method, taking into account the large variations between the $c_v$ obtained from curve fitting methods.

The present study aims to determine the $c_v$ according to Taylor's square root of time fitting method by performing conventional oedometer tests on identical soil samples prepared from remolded soils with different plasticity characteristics, and determine $c_v$ based on the relationship defined by Terzaghi's equation by carrying out permeability-consolidation tests on the same samples using the combined apparatus specially developed for this study to compare the results of both methods and to question the degree of reliability of $c_v$ obtained from the conventional oedometer tests. Besides, an empirical relationship is provided for the $c_v$ based on the soils' permeability and index properties.

Table 2- Some empirical relationships for calculations of $c_v$.

| | |
|---|---|
| Carrier (1985) | $c_v = \frac{9.04(10^{-7})(1.192 + ACT^{-1})^{6.993}(4.135LI + 1)^{4.29}}{PI(2.03LI + 1.192 + ACT^{-1})^{7.993}}$ |
| Narasimha et al. (1995) | $c_v = \left(\frac{1+e_{LL}(1.23-0.276\,log\sigma_v')}{e_{LL}}\right)\left(\frac{1}{\sigma_v'^{(0.353)}}\right)(10^{-3})\; e_{LL} = \left(\frac{LL(\%)}{100}\right)G_s$ |
| Sridharan and Nagaraj (2004) | $c_v = \frac{3}{100(SI)^{3.54}}$ |
| Solanki and Desai (2008) | $c_v = 10^8(LL^{-6.7591}),\; c_v = 7.7525(PI^{-3.1021})$ |
| Al-Ameri et al. (2011) | $c_v = 4258(LL^{-1.75})$ |

ACT: Activity, eLL: Void Ratio at The Liquid Limit, $G_s$: Spesific Gravity, LI: Liquidity Index, LL: Liquid Limit, PI: Plasticity Index, SI: Shrinkage Index, $\sigma_v'$: Vertical Effective Stress

## 2. Material

### 2.1. Combined Apparatus

Permeability-consolidation tests were performed on combined cells specifically designed for this study. These cells allow for the flow of water through them during the loading of the samples. Combined cells consist of a base, ahead, and a rigid plexiglass body. The cylindrical rigid plexiglass body has an inner diameter of 50 mm, an outer diameter of 70 mm and a height of 125 mm. A water outlet point was provided for discharging the water accumulating on the base. At the centre of the head lies the inlet of the loading piston. Particular attention was paid to minimizing the friction at the junction between the loading piston and the head. After combining the cell, an O-ring was added to prevent the escape of water through this point. The details of the combined apparatus are given in Figure 1.

### 2.2. Soil Samples

Tests were carried out on 12 remoulded soil samples. Since the study was a parametric one and plenty of soil samples were needed, the remoulded soil mixtures were prepared in the laboratory environment to meet soil samples' needs. The index properties of the soils used in the study are given in Table 3.

## 3. Methodology

### 3.1. Sample Preparation

Each of the soil samples was sifted using a sieve no. 40. The samples were then thoroughly mixed in water content between the values of LL and PL (in a water content closer to LL) until they were homogenized. Subsequently, they were filled into rings of 50 mm

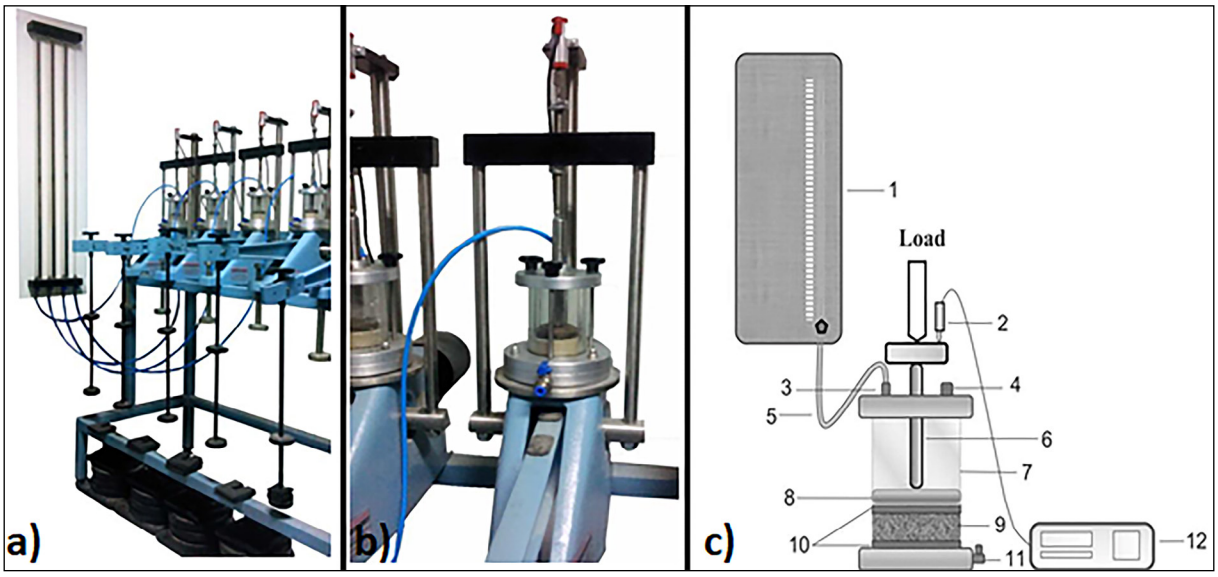


Figure 1- Details of the combined apparatus; a) overview, b) close-up view on the oedometer test set-up, c) schematic cross-section (not to scale): 1) water indicator panel, 2) deformation dial gauge, 3) water inlet valve, 4) air bleed valve, 5) transparent pipe, 6) loading piston, 7) plexiglas cell, 8) loading cap, 9) soil sample, 10) porous stone, 11) water outlet valve, 12) data logger.

Table 3- Index properties of the soil tested.

| Sample Number | SL | PL | LL | PI | USCS | $G_s$ |
|---|---|---|---|---|---|---|
| 1 | 17.2 | 19.6 | 38.0 | 18.4 | CL | 2.69 |
| 2 | 13.6 | 29.8 | 48.2 | 18.4 | ML | 2.73 |
| 3 | 14.8 | 28.0 | 53.2 | 25.2 | CH | 2.80 |
| 4 | 26.1 | 33.0 | 69.0 | 36.0 | CH | 2.78 |
| 5 | 13.8 | 22.0 | 59.7 | 37.7 | CH | 2.96 |
| 6 | 14.8 | 35.6 | 74.1 | 38.5 | MH | 2.60 |
| 7 | 18.9 | 27.5 | 67.0 | 39.5 | CH | 2.84 |
| 8 | 15.1 | 21.0 | 64.6 | 43.6 | CH | 2.65 |
| 9 | 11.4 | 20.0 | 64.4 | 44.4 | CH | 2.65 |
| 10 | 22.7 | 37.0 | 82.0 | 45.0 | CH | 2.77 |
| 11 | 20.9 | 37.0 | 87.0 | 50.0 | CH | 2.71 |
| 12 | 19.7 | 37.0 | 92.0 | 55.0 | CH | 2.70 |

SL: Shrinkage Limit, PL: Plastic Limit, LL: Liquid Limit, PI: Plasticity Index, USCS: Unified Soil Classification System, $G_s$: Specific Gravity

in diameter and 20 mm in height. The rings were placed in the cells specifically designed for the sample preparation centrifuge device.

The soil samples used in the study were consolidated and prepared in the laboratory according to the soil sample preparation procedures used in Balci et al. (2018). Each soil was subjected to 6 different pre-consolidation stresses for 6 hours in a soil sample preparation centrifuge, resulting in a total of 72 different artificial soil samples. By preparing two samples for each type of soil sample, tests were carried out on a total of 144 soil samples. During the sample preparation, the effect of RPM values applied in incremental values in the soil sample preparation centrifuge on the compaction of the samples is shown in Figure 2 and Table 4. It was observed that the void ratio of the samples decreases with the RPM values increases used for sample preparation. It is determined that the increase in RPM values also causes an increase in the degree of compression.

### 3.2. Permeability-Consolidation Test

The coefficient of permeability (k) values was obtained in permeability-consolidation tests by applying the falling head permeability test principles. The permeability-consolidation test from the conventional oedometer test is that the permeability

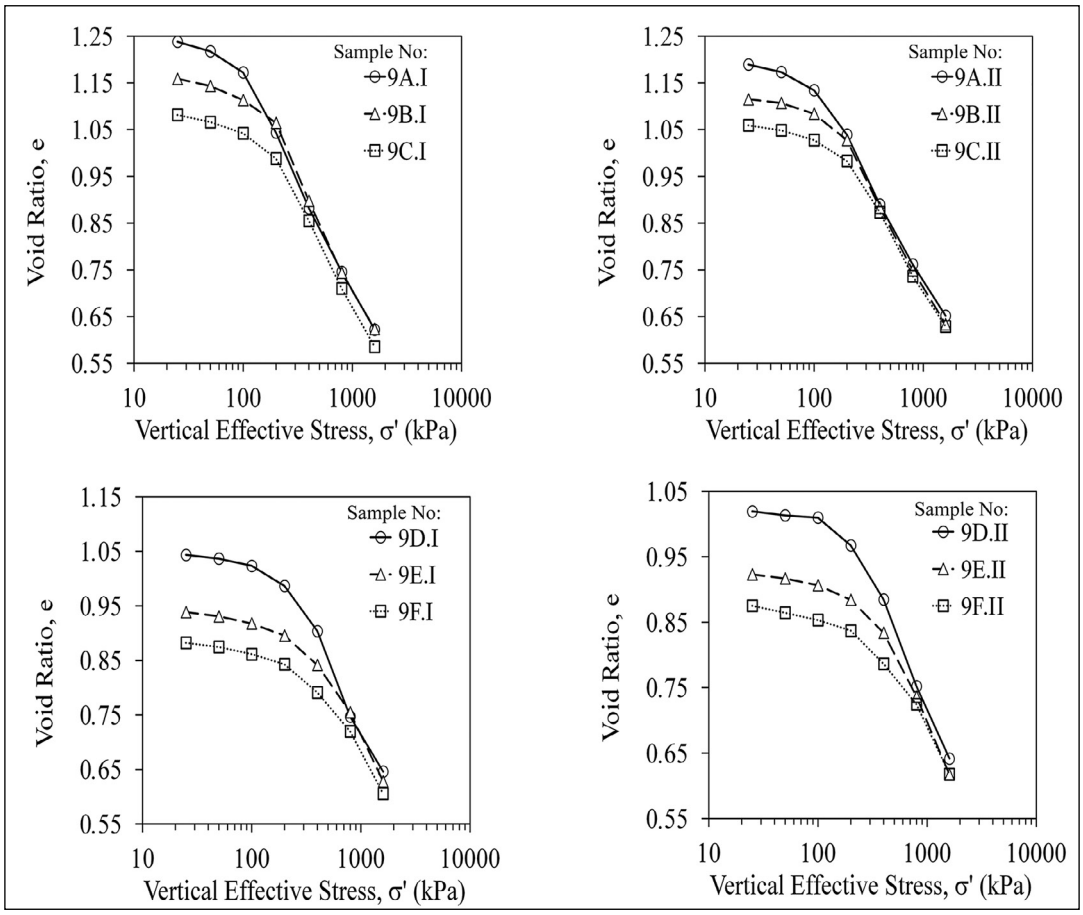


Figure 2- e-σ' curves obtained from conventional oedometer tests.

Table 4- e-σ' values obtained from conventional 1D oedometer tests.

| | | σ' (kPa) | | | | | | |
|---|---|---|---|---|---|---|---|---|
| | | 25 | 50 | 100 | 200 | 400 | 800 | 1600 |
| Sample Number | RPM | | | | e | | | |
| 9A.I | 500 | 1.24 | 1.22 | 1.17 | 1.04 | 0.88 | 0.75 | 0.62 |
| 9B.I | 600 | 1.16 | 1.14 | 1.11 | 1.06 | 0.90 | 0.74 | 0.62 |
| 9C.I | 700 | 1.08 | 1.07 | 1.04 | 0.99 | 0.86 | 0.71 | 0.59 |
| 9D.I | 800 | 1.04 | 1.04 | 1.02 | 0.99 | 0.90 | 0.75 | 0.65 |
| 9E.I | 900 | 0.94 | 0.93 | 0.92 | 0.90 | 0.84 | 0.75 | 0.63 |
| 9F.I | 1000 | 0.88 | 0.87 | 0.86 | 0.84 | 0.79 | 0.72 | 0.61 |
| 9A.II | 500 | 1.19 | 1.17 | 1.13 | 1.04 | 0.89 | 0.76 | 0.65 |
| 9B.II | 600 | 1.12 | 1.11 | 1.08 | 1.03 | 0.88 | 0.75 | 0.63 |
| 9C.II | 700 | 1.06 | 1.05 | 1.03 | 0.98 | 0.87 | 0.74 | 0.63 |
| 9D.II | 800 | 1.02 | 1.01 | 1.01 | 0.97 | 0.88 | 0.75 | 0.64 |
| 9E.II | 900 | 0.92 | 0.92 | 0.91 | 0.88 | 0.83 | 0.74 | 0.62 |
| 9F.II | 1000 | 0.88 | 0.86 | 0.85 | 0.84 | 0.79 | 0.72 | 0.62 |

RPM: revolutions per minute. σ': effective stress. e: void ratio.

and consolidation tests are carried out together and in the same cells. Permeability-consolidation tests were carried out in two phases, namely, the consolidation phase and permeability phase.

In the consolidation phase, after placing the combined apparatus in the loading unit, it was filled with water up to 1 cm above its upper level so that the tested soil sample was utterly saturated, was

kept there for one day to check the swelling effect. After the sample was subjected to the swelling effect, it could not swell by increasing the load on it in a controlled manner. The loading process was carried out in the conventional oedometer unit. The applied load was transferred to the soil sample by means of the loading piston, and the amount of deformation that developed was transferred to the data logger using the deformation gauge on the piston and was recorded. According to ASTM D2435 / D2435M-11 (2020) standard test methods for 1D consolidation properties of soils using incremental loading, the loading process was carried out as in conventional oedometer tests.

In the permeability phase, the loading arm was initially fixed with supporting screws to prevent the continuation of loading. Then, the empty section of the combined apparatus was filled with water and was connected to the water indicator panel using a hose. The water-filled hose was connected to the water inlet valve located on the top of the cell to provide water flow. The other end of the hose was connected to the water indicator panel so that the reduction in the hydraulic level of the water could be shown during the permeability test. Before starting the test, air bubbles were removed from the hose and the cell using the air valve on the top of the cell. The permeability process was carried out for one day. Attention was paid to ensure that the hydraulic gradient was within the range of 20 to 30 in this process. In the subsequent loading phases, the loading arm was removed from its fixed state, and the same procedures were repeated. At the beginning and end of each permeability test, the hose's water level was recorded, noting the time, and the coefficient of permeability was calculated. After completing the test, the soil sample was removed from the cell, and saturated/dry unit weights were recorded.

The results obtained from the permeability-consolidation test include the amounts of settlement under different loads, the drop in water level during the permeability process, and the time-dependent deformations obtained under different loads. The $c_v$ values obtained from the conventional oedometer tests conducted using the Taylor's square root of time fitting Method were compared with the $c_v$ values obtained from the permeability-consolidation tests conducted with the Terzaghi's equation by using the combined apparatus.

## 4. Experimental Findings

The comparison of the ε-σ' graphs and consolidation parameters, obtained from permeability-consolidation tests on the combined apparatus and conventional 1D oedometer tests are given in Figure 3, and Table 5. A high level of consistency is observed between the combined apparatus for different load levels and the results obtained from the experiments performed on conventional oedometers. It is noted that the $c_v$ values are not drastically affected by the differences in the design of the combined apparatus and or by changes in the loading steps. Therefore, it can be suggested that curve fitting methods for the calculation of $c_v$, such as the Taylor method, can also be used for the time-strain curves obtained from different loading stages of permeability-consolidation experiments.

The change in k and $c_v$ values obtained using the combined apparatus and those obtained from the conventional 1D tests using Taylor's square root of time fitting method ($t_{90}$) method for each load level is shown in Figure 4 and 5. At low load levels, the difference between the results is more remarkable. It is apparent that the differences between results may be attributed to plasticity, and for samples with high plasticity, this difference is smaller.

Comparing the $c_v$ values obtained from the combined apparatus using the permeability-consolidation relationship and the $c_v$ values obtained from the conventional 1D oedometer tests using Taylor's square root of time fitting method ($t_{90}$) on a 1:1 graph is given in Figure 6. It is obvious that the $c_v$ values obtained from the combined set-up at high load values are greater than the $c_v$ values determined via the Taylor $t_{90}$ method. It is from this point of view that the following empirical equation was developed between the e, SL, LL and k values of the soil samples with a coefficient of regression ($R^2$) of 0.66. Details of the regression analysis are given in Table 6.

$$k\ (m/s)=\exp\ (0.113\ SL-0.084\ LL+3.792\ e-23.154) \quad (3)$$

The comparison between the k values defined from the combined apparatus in soil samples and the k values defined from the newly developed empirical equation on a 1:1 graph is shown in Figure 7. When the distribution is evaluated, it is possible to say that the results are compatible with each other.

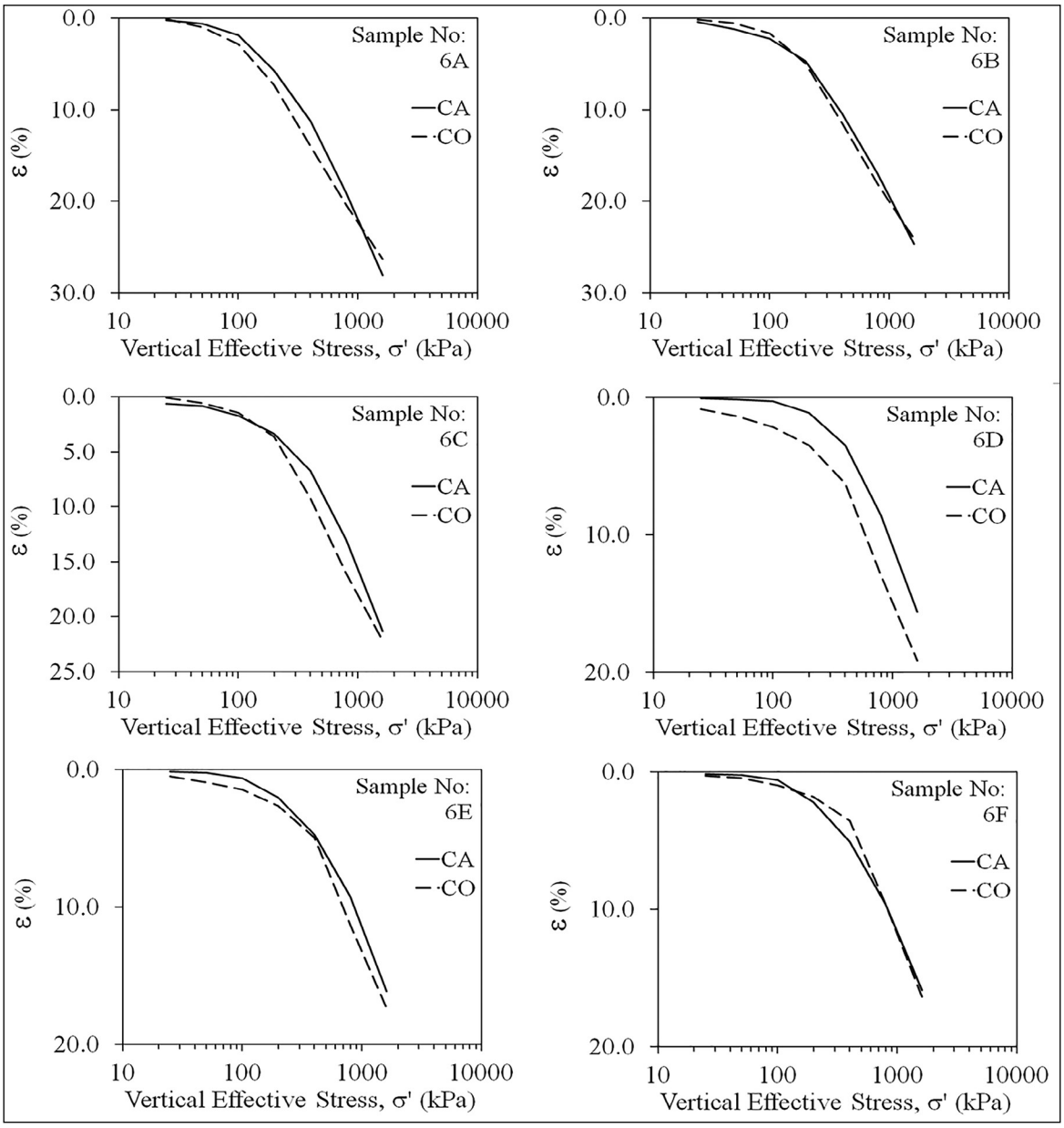


Figure 3- Comparison of the ε-σ' curves obtained from the conventional apparatus and the combined apparatus (CA: combined apparatus, CO: conventional 1D oedometer).

The $c_v$ values calculated from k values obtained from the combined apparatus and the $c_v$ values obtained from k values calculated from the newly developed empirical equation are compared in Figure 8. It is seen that the $c_v$ values obtained from both methods are close to each other. Figure 9 shows that the $c_v$ values calculated from the empirical relationship by using k values and the $c_v$ defined from Taylor's $t_{90}$ Method were compared graphically. High differences were observed between the values determined by both methods. The relationships between $c_v$ values calculated from the empirical equation Equation 3 developed with the combined apparatus and different parameters, including the soils' index properties, were investigated. As a result of the regression analysis, the following empirical equation Equation 4 was proposed between $c_v$ and mv-LL with a coefficient of regression ($R^2$) of 0.96. Details of the regression analysis are given in Table 7.

$$c_v\ (m^2/s) = (1.5)(10^{-10}) / (LL^{1.053})(m_v^{1.247}) \quad (4)$$

Table 5- Consolidation parameters obtained from conventional 1D oedometer (CO) and combined apparatus (CA) tests.

| Sample Number | RPM | CO | | | CA | | |
|---|---|---|---|---|---|---|---|
| | | $C_r$ | $C_c$ | $\sigma'_p$ (kPa) | $C_r$ | $C_c$ | $\sigma'_p$ (kPa) |
| 6A.I | 500 | 0.072 | 0.45 | 130 | 0.055 | 0.40 | 120 |
| 6B.I | 600 | 0.021 | 0.37 | 180 | 0.035 | 0.41 | 250 |
| 6C.I | 700 | 0.039 | 0.32 | 200 | 0.030 | 0.35 | 270 |
| 6D.I | 800 | 0.036 | 0.46 | 330 | 0.021 | 0.34 | 350 |
| 6E.I | 900 | 0.030 | 0.51 | 390 | 0.020 | 0.29 | 420 |
| 6F.I | 1000 | 0.013 | 0.44 | 400 | 0.013 | 0.29 | 400 |
| 6A.II | 500 | 0.062 | 0.50 | 140 | 0.044 | 0.45 | 140 |
| 6B.II | 600 | 0.030 | 0.48 | 180 | 0.052 | 0.34 | 200 |
| 6C.II | 700 | 0.037 | 0.49 | 200 | 0.035 | 0.36 | 290 |
| 6D.II | 800 | 0.037 | 0.44 | 380 | 0.029 | 0.34 | 350 |
| 6E.II | 900 | 0.030 | 0.49 | 400 | 0.028 | 0.43 | 440 |
| 6F.II | 1000 | 0.015 | 0.48 | 420 | 0.010 | 0.45 | 400 |
| 9A.I | 500 | 0.066 | 0.47 | 100 | 0.029 | 0.41 | 160 |
| 9B.I | 600 | 0.050 | 0.35 | 180 | 0.019 | 0.37 | 240 |
| 9C.I | 700 | 0.050 | 0.31 | 190 | 0.009 | 0.35 | 340 |
| 9D.I | 800 | 0.023 | 0.20 | 240 | 0.009 | 0.37 | 355 |
| 9E.I | 900 | 0.025 | 0.12 | 400 | 0.002 | 0.24 | 480 |
| 9F.I | 1000 | 0.024 | 0.12 | 450 | 0.006 | 0.23 | 300 |
| 9A.II | 500 | 0.053 | 0.39 | 100 | 0.030 | 0.39 | 140 |
| 9B.II | 600 | 0.027 | 0.41 | 180 | 0.031 | 0.38 | 200 |
| 9C.II | 700 | 0.034 | 0.40 | 190 | 0.002 | 0.34 | 260 |
| 9D.II | 800 | 0.020 | 0.40 | 220 | 0.012 | 0.34 | 320 |
| 9E.II | 900 | 0.021 | 0.35 | 450 | 0.009 | 0.28 | 340 |
| 9F.II | 1000 | 0.035 | 0.28 | 500 | 0.012 | 0.28 | 300 |

RPM: Revolution per minute, Cr: Recompression Index, $C_c$: Compression Index, $\sigma'_p$: Preconsolidation Index.

The comparison between $c_v$ values calculated from Equation 3 and $c_v$ values calculated Equation 4 is shown in Figure 10. It appears that there is a strong correlation between the $c_v$ values obtained from the two approaches. The comparison of the $c_v$ values, calculated from Equation 4 and defined by Taylor's $t_{90}$ method is given in Figure 11. It was observed that there was not a good correlation between the results. This is thought to be related to the fact that while the samples prepared in the laboratory have high plasticity, those in the field represent a narrower interval in terms of plasticity.

## 5. Discussion

It was also found that the $c_v$ values obtained from the permeability-consolidation tests using the combined apparatus were greater than the $c_v$ values obtained from the conventional 1D oedometer tests using Taylor's $t_{90}$ method. Furthermore, it can be said that the difference between the $c_v$ values determined through the two testing methods, particularly on the soil samples with a high degree of plasticity, is more significant. It was found that more stable results were obtained from the samples with high plasticity than those with low plasticity when applying Taylor's $t_{90}$ method. It is recommended to evaluate the results of both experimental methods with other curve fitting methods (log $t_{50}$, maximum slope, computational, rectangular hyperbola, $\delta t$-t/$\delta t$, early-stage log-t, inflection point, $\sqrt{t}$60, SRS).

One of the primary reasons for the variation between the consolidation coefficients that are obtained based on the permeability-consolidation relationship when using the combined apparatus, and

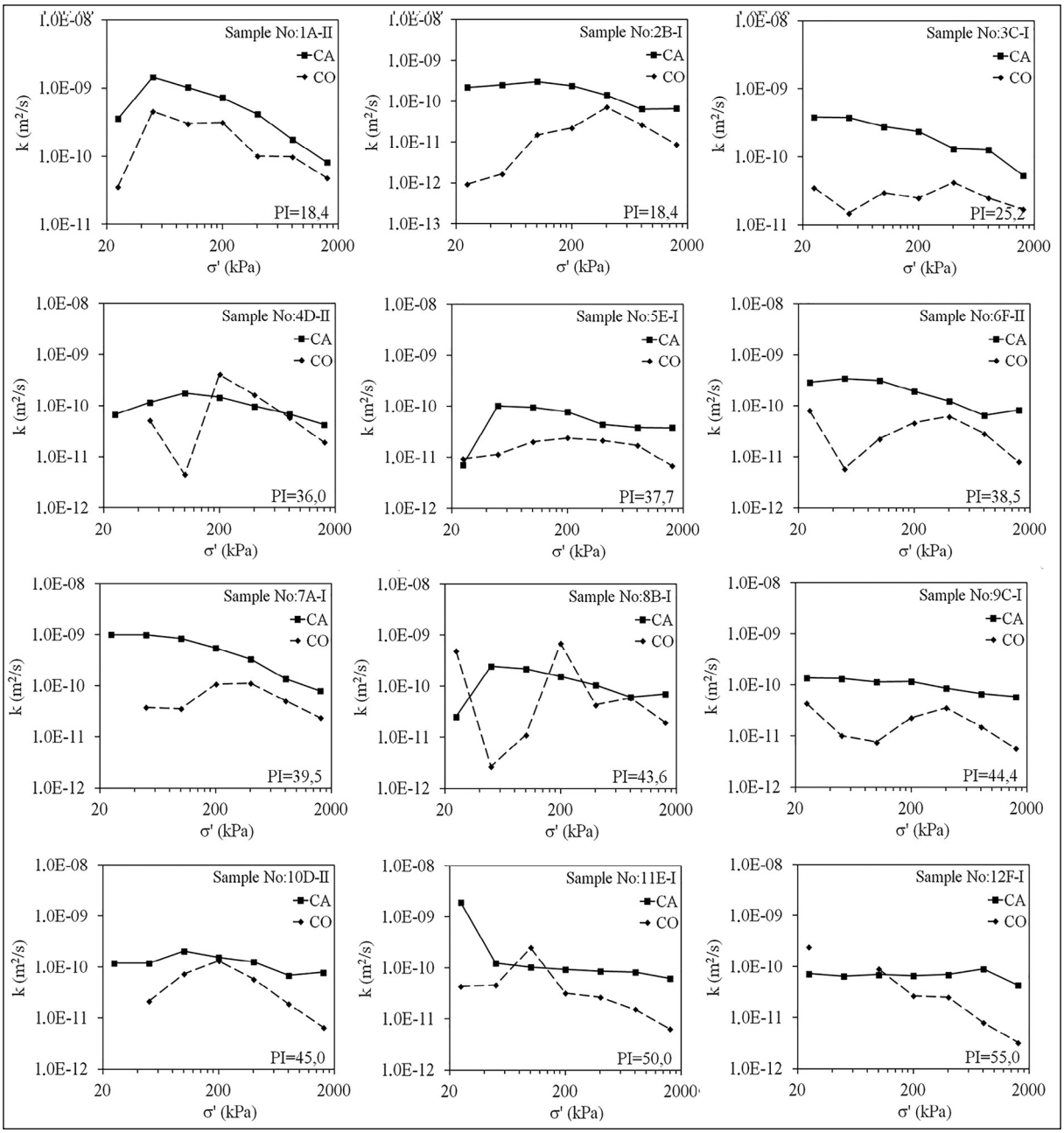


Figure 4- Changes in the k values with increases in load levels (CA: combined apparatus, CO: conventional 1D oedometer).

the $c_v$ obtained from the conventional 1D oedometer tests when using curve fitting methods such as Taylor's $t_{90}$, must be that Taylor's $t_{90}$ method takes into account only the compression of the sample and the contraction of length, but not the variations in the void ratio of the soil. In this regard, the $c_v$ values calculated using Taylor's $t_{90}$ method at high load levels where secondary compression is observed were lower than the actual $c_v$ values, resulting in a more significant difference between the $c_v$ values obtained from the combined apparatus.

The differences between the $c_v$ values obtained from the permeability-consolidation relation and those obtained from the Taylor $t_{90}$ method at high loads are attributable to the secondary compression. Based on this study results, a comparison of the $c_v$ values obtained from the oedometer tests at high load levels with those obtained from the permeability-consolidation relation and an assessment of the influence of the secondary compression on $c_v$ is suggested.

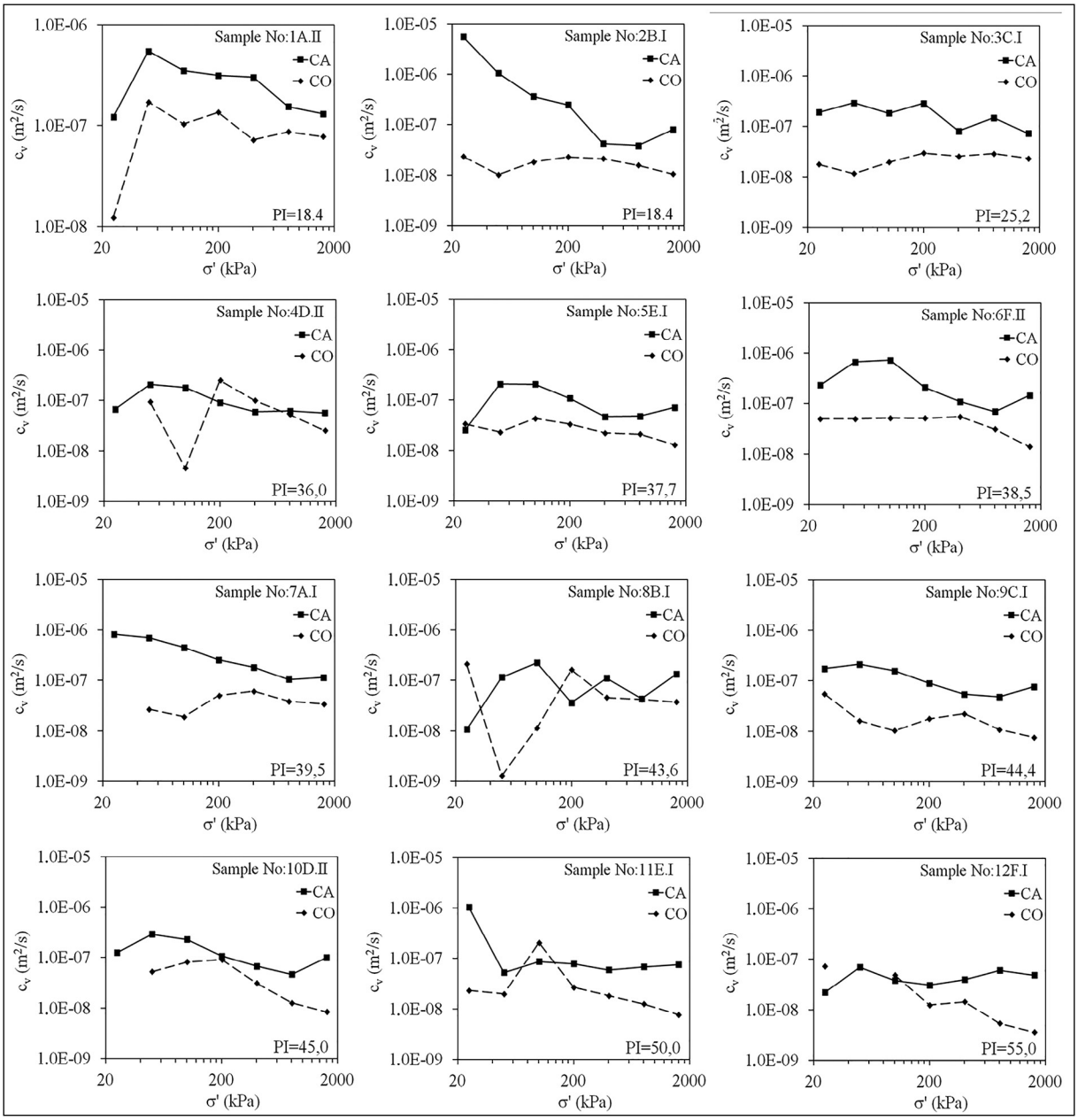


Figure 5- Changes in the $c_v$ values with increases in load levels (CA: combined apparatus, CO: conventional 1D oedometer).

## 6. Results

The results obtained in this study for the evaluated soil samples can be listed as follows:

Considering the relationship between the two testing methods, it was found that the values obtained from the combined apparatus designed specifically for this study were comparable with the $c_v$ values obtained from the conventional 1D oedometer tests. The possibility of determining $c_v$ through the permeability-consolidation relation and curve fitting method, and the compatibility with the results obtained from conventional methods, further increases the advantages offered by this set-up and its application.

By using regression analysis, the relationship between k values and the index properties of the soils, the following correlation between k and SL-LL-e was proposed with $R^2$=0.66:

$$k\ (m/s)=\exp(0.113\ SL-0.084\ LL+3.792\ e-23.154) \quad (3)$$

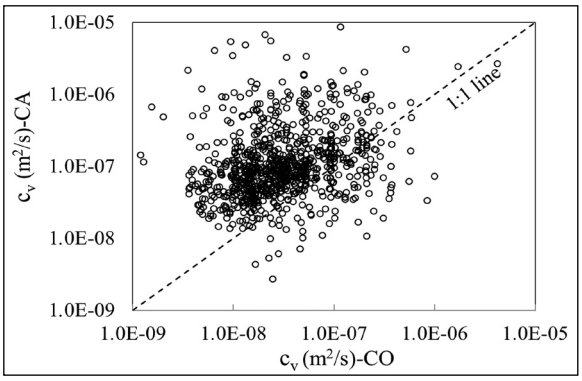


Figure 6- Comparison of $c_v$ values obtained from the combined apparatus and conventional 1D oedometer (CO: conventional oedometer, CA: combined apparatus).

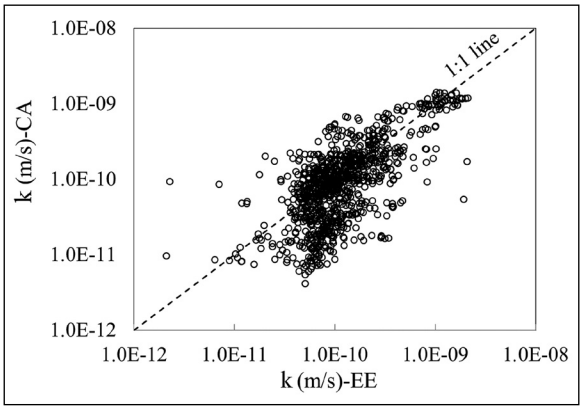


Figure 7- Comparison of the k values obtained from the empirical equation and the combined apparatus (EE: empirical equation, CA: combined apparatus).

Table 6- Regression analysis details of equation (3).

| | |
|---|---|
| Equation | k (m/s) = exp (0.113 SL – 0.084 LL + 3.792 e – 23.154) |
| Model Definition | Y = exp(ax+bx2+cx3+d) |
| Number of Observations | 991 |
| Solver Type | Nonlinear |
| Nonlinear Iteration Limit | 250 |
| Number of Nonlinear Iterations Performed | 10 |
| Residual Tolerance | 1E-10 |
| Sum of Residuals | 2.30E+06 |
| Average Residual | 2.32E+03 |
| Residual Sum of Squares (Absolute) | 2.95E-03 |
| Residual Sum of Squares (Relative) | 2.95E-03 |
| Standard Error of the Estimate | 1.73E+03 |
| Coefficient of Multiple Determination ($R^2$) | 0.658620984 |
| Durbin-Watson statistic | 1.040230 |
| Confidence Interval | 99% |
| F Ratio | 634.738 |

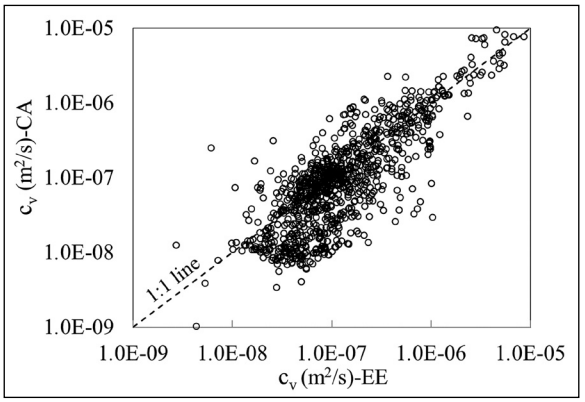


Figure 8- Comparison of the calculated $c_v$ values obtained from the empirical equation and the combined apparatus (EE: empirical equation, CA: combined apparatus).

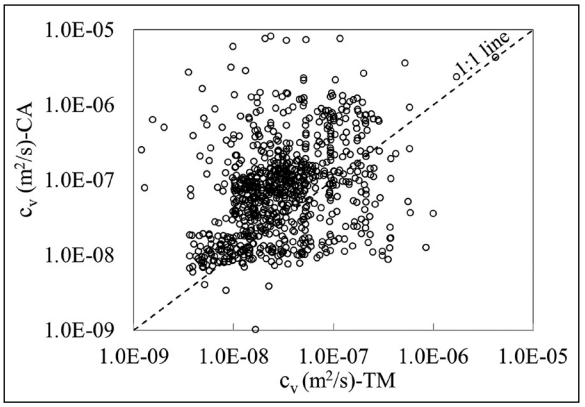


Figure 9- Comparison of the calculated $c_v$ values obtained from the Taylor's $t_{90}$ method and the combined apparatus (TM: Taylor's $t_{90}$ method, CA: combined apparatus).

It is possible to calculate $c_v$ using k (obtained from the proposed empirical equation) and $m_v$ (defined experimentally) together in Terzaghi's permeability-consolidation relationship. The relationship between $c_v$ (calculated from the permeability-consolidation relationship) and different parameters (e and $m_v$) were evaluated. As a result of the regression analysis, the following empirical relationship between $c_v$ and $m_v$-LL was proposed with $R^2$=0.96:

Table 7- Regression analysis details of Equation (4).

| | |
|---|---|
| Equation | $c_v$ ($m^2/s$) = (1.5) ($10^{-10}$) / ($LL^{1.053}$) ($m_v^{1.247}$) |
| Model Definition | $Y = ax1^bx2^c$ |
| Number of Observations | 976 |
| Solver Type | Nonlinear |
| Nonlinear Iteration Limit | 250 |
| Number of Nonlinear Iterations Performed | 250 |
| Residual Tolerance | 1E-10 |
| Sum of Residuals | 1.76E+10 |
| Average Residual | 1.80E+07 |
| Residual Sum of Squares (Absolute) | 3.36E+04 |
| Residual Sum of Squares (Relative) | 3.36E+04 |
| Standard Error of the Estimate | 5.88E+07 |
| Coefficient of Multiple Determination ($R^2$) | 0.956013 |
| Durbin-Watson statistic | 0.968071 |
| Confidence Interval | 99% |
| F Ratio | 10.5736 |

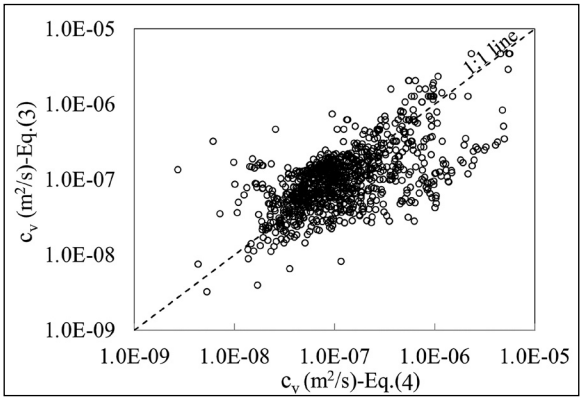


Figure 10- The comparison between $c_v$ values calculated from Equation 3 and 4.

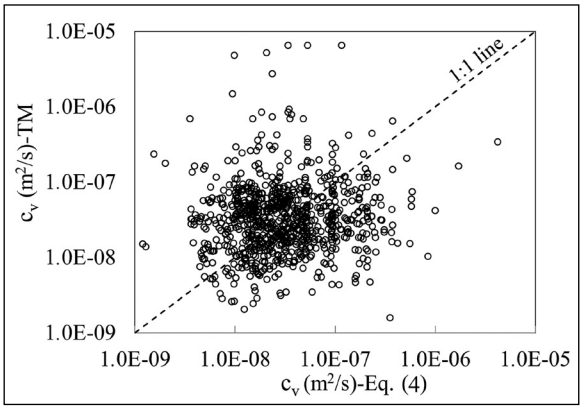


Figure 11- The comparison of the $c_v$ values, calculated from Equation 4 and defined by the Taylor's $t_{90}$ method (Eq. (4): equation 4, TM: Taylor's $t_{90}$ method).

$$c_v\ (m^2/s) = (1.5)(10^{-10}) / (LL^{1.053})(m_v^{1.247}) \quad (4)$$

While a decrease was observed in the $c_v$ values determined using Taylor's $t_{90}$ method, one of the conventional 1D consolidation tests on the soil samples with high plasticity when the load was increased, no stable behaviour was observed in the $c_v$ values on the samples with low plasticity. However, the $c_v$ values obtained from the permeability-consolidation tests using the combined apparatus generally decreased as the load was increased from the initial load levels and then increased as the load was increased to the higher load levels.

It is apparent that the $c_v$ values obtained based on the permeability-consolidation relationship when using the combined apparatus on the soil samples with low plasticity exhibited less scattering than the $c_v$ values obtained when using Taylor's $t_{90}$ method.

## References

Al-Ameri, A. F., Al-Tae, A. Y. 2011. Estimation of relationship between coefficient of consolidation and liquid limit of middle and south Iraqi soils. Journal of Engineering 17(3), 430-440.

Al-Zoubi, M. S. 2004. Coefficient of Consolidation (v c) from The Linear Segment of the t p− δ Curve. Proceedings of the International Engineering Conference at Mutah University, 26-29.

Al-Zoubi, M. S. 2010. Consolidation analysis using the settlement rate-settlement (SRS) method. Applied Clay Science 50, 34-40.

Balcı, M. C., Kayabalı, K., Asadi, R. 2018. Miniature centrifuge modeling for conventional consolidation test. Geotechnical Testing Journal 41(3), 590-600.

Carrier, W. D. 1985. Consolidation parameters derived from index tests. Geotechnique 35(2), 211-213.

Casagrande, A., Fadum, R. E. 1940. Notes on Soil Testing for Engineering Purposes, Harvard University Graduate School of Engineering Publications.

Chow, J. K., Wang, Y. H., Lui, H. L., Huang, E. 2020. Determination of consolidation parameters based on the excess pore water pressure measurement using a newly developed U-oedometer. Acta Geotechnica 15, 2665-2680.

Cortellazzo, G. 2002. Comparison between laboratory and in situ values of the coefficient of primary consolidation cv. Canadian Geotechnical Journal 39(1), 103-110.

Feng, T. W., Lee, Y. J. 2001. Coefficient of consolidation from the linear segment of the t 1/2 curve. Canadian Geotechnical Journal 38(4), 901-909.

Holtz, R. D., Kovacs, W. D., Sheahan, T. C. 1981. An Introduction to Geotechnical Engineering. Prentice Hall, 733.

Lovisa, J., Sivakugan, N. 2013. An in-depth comparison of cv values determined using common curve-fitting techniques. Geotechnical Testing Journal 36(1), 30-39.

Mesri, G., Feng, T. W., Shahien, M. 1999. Coefficient of consolidation by inflection point method. Journal of Geotechnical and Geoenvironmental Engineering 125(8), 717-718.

Narasimha, R. P., Pandian, N. S., Nagaraj, T. S. 1995. Analysis and estimation of the coefficient of consolidation. Geotechnical Testing Journal 18(2), 252-258.

Nguyen, M. D., Pham, B. T., Tuyen, T. T., Yen, H., Phan, H., Prakash, I., Dou, J. 2019. Development of an artificial intelligence approach for prediction of consolidation coefficient of soft soil: a sensitivity analysis. The Open Construction and Building Technology Journal 13(1).

Olek, B. S., Pilecka, E. 2019. Large-scale Rowe cell experimental study on coefficient of consolidation of coal mine tailings. E3S Web of Conferences 2019.

Olson, R. E. 1986. State of the art: consolidation testing. Consolidation of Soils: Testing and Evaluation. ASTM International.

Robinson, R., Allam, M. 1996. Determination of coefficient of consolidation from the early stage of log t plot. Geotechnical Testing Journal 19(3), 316-320.

Sivaram, B., Swamee, P. 1977. A computational method for consolidation-coefficient. Soils and Foundations 17(2), 48-52.

Solanki, C. H., Desai, M. D. 2008. Role of Atterberg limits on time rate settlement of alluvial deposits. Journal of Engineering and Technology, Sardar Patel University 21, 12-15.

Sridharan A., Prakash, K. 1993. δ-t/δ Method for the determination of coefficient of consolidation. Geotechnical Testing Journal 16(1), 131-134.

Sridharan, A., Prakash, K. 1995. Critical Appraisal of Laboratory Determination of Cv. Compression and Consolidation of Clayey Soils, 561-572.

Sridharan, A., Nagaraj, H. B. 2004. Coefficient of consolidation and its correlation with index properties of remolded soils. Geotechnical Testing Journal 27(5), 469-474.

Sridharan, A., Murthy, N. S., Prakash, K. 1987. Rectangular hyperbola method of consolidation analysis. Geotechnique 37(3), 355-368.

Sridharan, A., Prakash, K., Asha, S. R. 1995. Consolidation behavior of soils. Geotechnical Testing Journal 18(1), 58-68.

Su, H. L. 1958. Procedure for rapid consolidation test. Journal of the Soil Mechanics and Foundations Division 84(3), 1729-1.

Taylor, D. W. 1948. Fundamentals of Soil Mechanics. John Wıley and Sons Inc., 711.

Terzaghi, K. A. R .L. 1925. Principles of soil mechanics, Engineering News - Record 95, 19-32.

Vinod, J. S., Sridharan, A. 2015. Laboratory determination of coefficient of consolidation from pore water pressure measurement, Géotechnique Letters 5(4), 294-298.

Bulletin of the Mineral Research and Exploration

http://bulletin.mta.gov.tr

# Active tectonics of Gülpınar-Tuzla area (Biga Peninsula, NW Turkey): the source of 6 February-24 March 2017 earthquake cluster

Ali KOÇYİĞİT[a] and Şule GÜRBOĞA[b*]

[a]*Middle East Technical University, Department of Geological Engineering, Active Tectonics and Earthquake Research Laboratory, Ankara, Turkey*

[b]*General Directorate of Mineral Research and Exploration, Department of Geological Research, Ankara, Turkey*

*Research Article*

Keywords:
Active Tectonics, Recent Seismicity, Southern Major Strand, NAFS, Biga Peninsula.

**ABSTRACT**

The variation in the motion sense of Anatolian platelet in Aegean Sea resulted in a strike-slip tectonic regime and related neotectonic domain, the central to northern Aegean neotectonic province, which also includes both western Marmara Sea and Biga Peninsula. Our study focuses mostly on the Gülpınar-Tuzla earthquake area located at the southwestern tip of Biga Peninsula, which is controlled by the southern major strand of the North Anatolian Fault System (NAFS). The strand consists of two sections, the onshore Biga and offshore Babakale-Skyros sections. Both sections are seismically very active. The Gülpınar-Tuzla earthquake area is composed of the Paleozoic metamorphic rocks, the Oligo-Miocene granitoid pluton, Lower-Middle Miocene calc-alkalic volcanic rocks and the Upper Miocene-Pliocene sedimentary sequence. All of these rocks, which formed and deformed (folded to tilted) in palaeotectonic period, are overlain with an angular unconformity by the Quaternary neotectonic basin fill, that is nearly flat-lying except for the faulted basin margins. Both the onshore and offshore sections of the southern strand are linked to each other in terms of the structures characterizing the Babakale pull-apart basin and the Gülpınar-Tuzla earthquake area. The latter is shaped by the NE-trending Gülpınar (GFZ) and Yenice-Gönen Fault Zone (YGFZ), the ENE-trending Edremit fault zone (EFZ), the WNW-trending Tuzla Fault Zone (TFZ) and three strike-slip basins (Ayvacık, Behramkale and Tuzla basins) developed along them. Some segments of both the TFZ and GFZ were reactivated by the occurrences of seven moderate-to small-sized independent earthquakes and related aftershocks over 2760. Five of the independent earthquakes have an origin of oblique-slip normal faulting, while the rest two seismic events are strike-slip faulting in origin. Focal mechanism solution diagrams of these two groups of earthquakes reveal that the Gülpınar-Tuzla area is under the control of a strike-slip neotectonic regime, which commenced in Early Quaternary time owing to the major inversion in extensional palaeotectonic regime. This is also supported by the palaeostress analysis of slip-plane data measured on fault slickensides. The uniform slip rates on both the YGFZ and EFZ are 10.8 mm/yr and 7.3 mm/yr, respectively.

*Received Date: 06.08.2020*
*Accepted Date: 19.08.2021*

## 1. Introduction

There is a close relationship between the plate tectonic configuration of Turkey and the current neotectonic regimes operating across it. From the palate tectonic point of view, Turkey and its near vicinity are shaped by several plates such as the African, Arabian, Eurasian and Anatolian plates, and their boundary fault systems of dissimilar character

Citation Info: Koçyiğit, A., Gürboğa, Ş. 2021. Active tectonics of Gülpinar - Tuzla area (Biga peninsula, NW Turkey): the source of 6th February - 24th March 2017 earthquake cluster. Bulletin of the Mineral Research and Exploration 166, 85-112. https://doi.org/10.19111/bulletinofmre.984922

**Corresponding author: Şule GÜRBOĞA, sule.gurboga@gmail.com*

(Figure 1a). Major plate boundaries are the South Aegean-western Cyprian convergent plate boundary or subduction zone, the sinistral Dead Sea, East Anatolian and the dextral North Anatolian Fault systems. NAFS is in the nature of intra-continental transform fault. It accommodates the westward relative motion of the southerly located Anatolian Platelet. In the Aegean Sea, the Anatolian platelet and its westward motion are blocked and forced to move in south-southwest direction by a barrier, the mainland Greece (Şengör, 1980). This process results in a principal compressive stress. It operates in approximately E-W direction across the northern to central Aegean Sea and northwestern Anatolia. Thus, the bifurcation of the NAFS into two major fault strands around Sea of Marmara, their bending at ~30° towards south in just west of the imaginary Bandırma-Tekirdağ line (Figure 1b), and blocking and forcing of the Anatolian platelet to move southwestwards altogether change the architecture of the westernmost section of the NAFS, and leads to the emergence of a new neotectonic regime and province, namely the central to northern Aegean neotectonic province. It is characterized by the strike-slip neotectonic regime. The eastern boundary of this neotectonic province is the Balıkesir-İzmir fault zone (BİFZ) (Koçyiğit, 2020) (Figure 1a). This mega shear zone was previously named as the İzmir-Balıkesir Transfer Zone by Sözbilir et al. (2013). This neotectonic province includes western Marmara Sea, Biga Peninsula, and central to northern Aegean seas (Figure 1b). In this neotectonic domain both major strands of the NAFS are seismically very active. It is indicated by a series of destructive big earthquakes occurred in them (Ambraseys, 1988; Kiratzi et al., 1991; Papazachos et al., 1991; Taymaz et al., 1991; Ambraseys and Jackson, 1998; Papazachos et al., 1998; Papazachos, 2003; Tan et al., 2008; Aksoy et al,. 2010; Karakaisis et al., 2010; Kürçer et al., 2015) (Table 1). The eastern half of the southern strand trends in approximately E-W direction and follows the southern coastal area of Marmara Sea up to Lakes Ulubat-Manyas and Edincik areas, where it bends south at different angles (30°-60°) and then forms the structurally very complicated Biga section of the southern strand. In general, the Biga section trends in SW direction and consists of, from NW to SE, the Çan-Biga, Sarıköy-Inova, Bayramiç-Ezine, Yenice-Gönen, Balıkesir-İzmir, Ilıca-Darıca, Havran-Danişment, and the Edremit fault zones (Figure 1b). These fault zones first combine with the E-W trending Edremit fault zone and then are linked with the offshore Babakale-Skyros fault zone in terms of the intervening oblique-slip normal faults and related strike-slip basins such as the Balıkesir, Edremit Gulf, Ayvacık, Tuzla, Babakale (Bababurnu) and Skyros basins (Figure 1b) (Eryılmaz and Yücesoy, 1999; Koukouvelas and Aydın, 2002). Both the Babakale-Edremit gulf basins and their margin boundary faults were previously studied and reported (Güney et al., 2001; Beccaletto and Steiner, 2005; Yaltırak et al., 2013; Sözbilir et al., 2016). The remaining Çan-Biga, Sarıköy-Inova, Bayramiç-Ezine, Yenice-Gönen, Havran-Danişment, Ilıca-Darıca and the Balıkesir-İzmir fault zones were also studied in detail and mapped on 1/25.000 scale by authors of the present paper. However, except for their key sections (inserts in the Figure 1b), their descriptions are outside the present paper owing to avoid of increasing the volume of present manuscript.

Basic problems in the central to northern Aegen neotectonic province are: 1) type and onset age of the neotectonic regime, 2) total displacement and slip rates on fault zones, and 3) confusion of neotectoctonic strike-slip basins with the grabens of palaeotectonic origin. These points are still under debate, i.e., there is no a common agreement among researchers on these points (Herece, 1990; Karacık and Yılmaz, 1998; Yılmaz et al., 2000; Güney et al., 2001; Yılmaz and Karacık, 2001; Beccaletto and Steiner, 2005; Kürçer et al., 2008; Emre and Doğan, 2010). The present paper introduces some key structures comprising the southwesternmost tip of the Biga Peninsula. This area was also previously studied and interpreted as graben and horst originated from N-S extension (Yılmaz and Karacık, 2001). Whereas our recent studies based on detailed field geological mapping indicated that this area is under the control of a strike-slip neotectonic regime governed by a major principal compressive stress operating in approximately WNW direction. The Behramkale-Babakale, Gülpınar and Tuzla areas, which comprise the southwest onshore tip of Biga Peninsula, have a very significant linkage role between offshore (the Babakale-Skyros fault zone) and onshore (Yenice-Gönen fault zone) sections of the southern strand of the NAFS (Figure 1b). Consequently, the present paper has two basic goals: 1) to evaluate the major inversion in earlier extensional palaeotectonic regime, and commencement age of the strike-slip neotectonic regime, and 2) to describe both the active tectonics and related very recent seismic activity (the

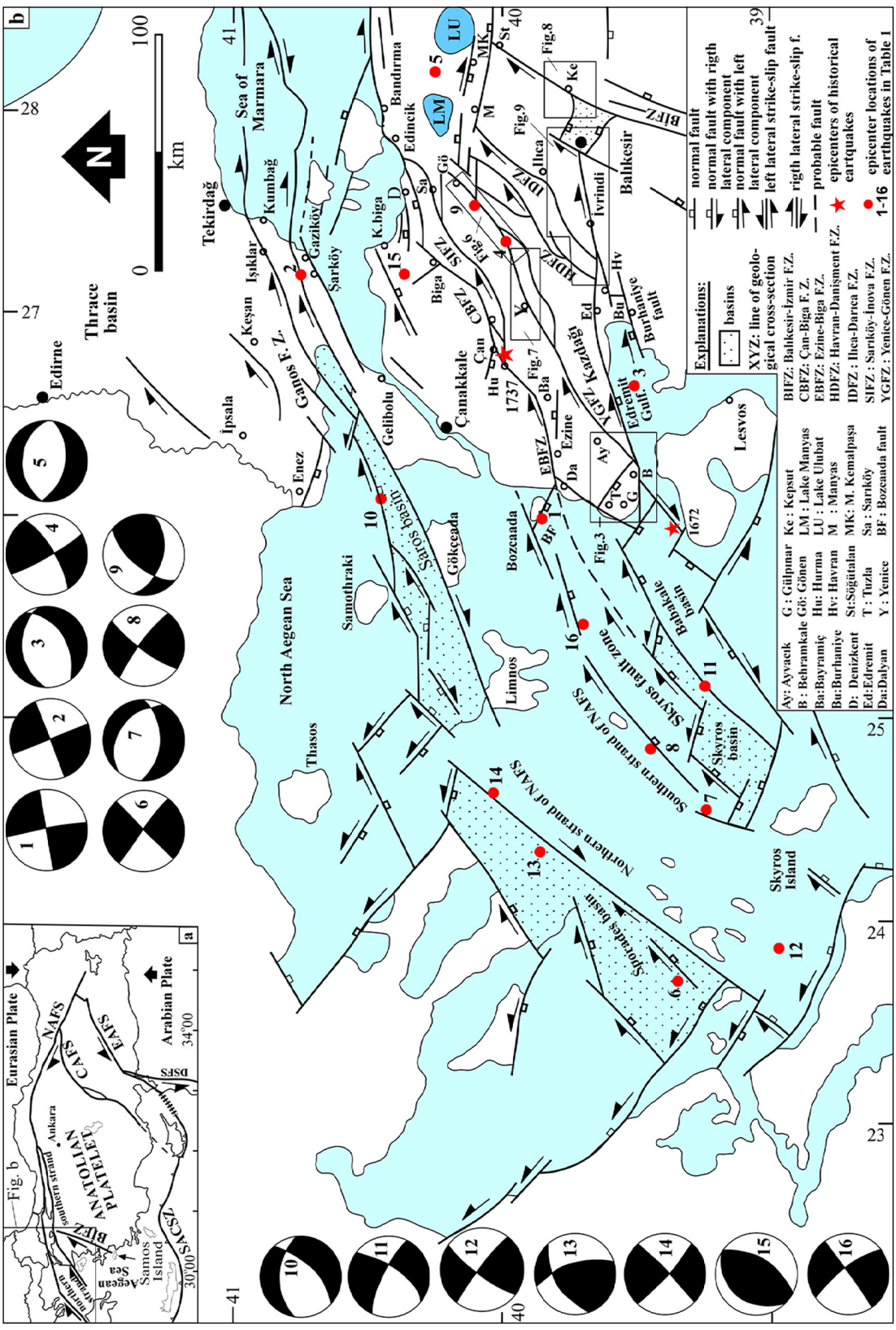


Figure 1- a) Simplified map showing major fault systems in Turkey and adjacent areas. BİFZ: Balıkesir-İzmir fault zone, CAFS: Central Anatolian Fault System, DSFS: Dead Sea Fault System, EAFS: East Anatolian Fault System, NAFS: North Anatolian Fault System, and SACSZ: South Aegean-Cyprus subduction zone, b) simplified seismotectonic map showing both the northern and southern major strands of the North Anatolian Fault Systems, epicenters of destructive earthquakes occurred in them and the location of the study area. EFZ: Edremit fault zone; GFZ: Gülpınar fault zone, and TFZ: Tuzla fault zone (offshore sections of faults and basins were modified from Koukouvelas and Aydın, 2002).

Table 1- Significant destructive earthquakes occurred within both the northern and southern major strands of the North Anatolian Fault System.

| No | Date | Origin time | Epicentral coordinate | | Depth (km) | Magnitude | Nodal plane 1 | | | Nodel plane 2 | | | References |
|---|---|---|---|---|---|---|---|---|---|---|---|---|---|
| | | | Northing | Easting | | | strike | dip | rake | strike | dip | rake | |
| 1 | 1672.02.14 | -- | 39.8 | 26.0 | 5-15 | Mw=7.0 | 260 | 90 | 177 | -- | -- | -- | Papazachos, 2003; Karakaisis et al., 2010 |
| 2 | 1912.08.09 | 01:29 | 40.7 | 27.2 | 16 | Ms=7.4 | 68 | 55 | -145 | -- | -- | -- | Aksoy et al., 2010; Ambraseys and Jackson 1998; Kalafat et al., 2011 |
| 3 | 1944.10.06 | 02:34 | 39.48 | 26.56 | 40 | Ms=6.8 | -- | -- | -- | -- | -- | -- | Ambraseys, 1988; Kalafat et al., 2011; Papazachos et al., 1991 |
| 4 | 1953.03.18 | 19:06:13 | 40.0 | 27.30 | 5-15 | Ms=7.4 | 150 | 84 | 14 | 59 | 76 | 174 | Tan et al., 2008 |
| 5 | 1964.10.06 | 14:31:23 | 40.3 | 28.2 | 5-15 | Ms=6.9 | 273 | 46 | -95 | 101 | 44 | -87 | Papazachos et al., 1991 |
| 6 | 1965.03.09 | 17:57:54 | 39.3 | 23.8 | 5-15 | Ms=6.1 | 40 | 90 | -6 | 310 | 86 | -180 | Papazachos et al., 1991 |
| 7 | 1967.03.04 | 17:58:09 | 39.2 | 24.6 | 8 | Ms=6.6 | 98 | 54 | -107 | 302 | 42 | -70 | Kiratzi et al., 1991 |
| 8 | 1968.02.19 | 22:45:42 | 39.4 | 24.9 | 9 | Ms=7.1 | 217 | 86 | 175 | 310 | 82 | 4 | Kiratzi et al., 1991 |
| 9 | 1969.03.03 | 00:59:10 | 40.1 | 27.5 | 6 | Ms=6.0 | 221 | 64 | 41 | 112 | 54 | 149 | Tan et al., 2008 |
| 10 | 1975.03.27 | 05:15:08 | 40.4 | 26.1 | 15 | Ms=6.6 | 41 | 60 | -128 | 279 | 46 | -42 | Papazachos et al.,1991 |
| 11 | 1981.12.19 | 14:10:51 | 39.2 | 25.2 | 8 | Ms=7.2 | 37 | 67 | -166 | 303 | 77 | -22 | Tan et al., 2008 |
| 12 | 1981.12.27 | 17:39:13 | 38.9 | 24.9 | 8 | Ms=6.5 | 212 | 85 | -174 | 123 | 84 | -66 | Taymaz et al., 1991 |
| 13 | 1982.01.18 | 19:27:25 | 39.8 | 24.4 | 9 | Ms=7.0 | 235 | 50 | 153 | 343 | 70 | 43 | Tan et al., 2008 |
| 14 | 1983.08.06 | 15:43:52 | 40.0 | 24.7 | 8 | Ms=6.8 | 48 | 83 | 178 | 136 | 88 | 07 | Papazachos, 2003; Karakaisis et al., 2010 |
| 15 | 1983.07.05 | 12:01:27 | 40.3 | 27.2 | 10 | Ms=6.1 | 248 | 70 | -155 | 149 | 66 | -22 | Harvard GCMT catalogue |
| 16 | 2013.01.08 | 14:16:07 | 39.64 | 25.48 | 8 | Mw=5.7 | 54 | 89 | -166 | -- | -- | -- | Kürçer et al., 2015 |

6 February-24 March 2017 Gülpınar-Tuzla eartquakes cluster) occurred at the tip of Biga Peninsula under the light of our field data and the international literature including mostly submarine geophysical studies and related seismic data (Eryılmaz and Yücesoy, 1999; Güney et al., 2001; Koukouvelas and Aydın, 2002; Beccaletto and Steiner, 2005; Kurtuluş et al., 2009; Yaltırak et al., 2013; Sözbilir et al., 2016). Thus, we aim to contribute to the solution of abovementioned basic problems. In addition, in the present paper the term "earthquake cluster" was used in the meaning of that a series of small- and moderate-sized earthquakes occurred in a relatively short time slice and confined to a definite area. They have magnitudes close to each other.

## 2. Stratigraphic Outline of Study Area

The rocks exposed in the study area can be subdivided into four categories based on their lithology, age, and contact relationships. These are, from oldest to youngest, the low-grade Karadağ metamorphic rocks, the Kestanbol granitoid pluton, the Ayvacık-Balabanlı volcanic rocks, the fluvial to shallow marine sedimentary sequence (Gülpınar Group), and the Quarternary basin fill or neotectonic fill (Figure 2). Both the Cambrian-Upper Permian Karadağ metamorphic rocks and the Upper Oligocene-Lower Miocene Kestanbol granitoid pluton are older basement rocks. The latter intrudes the metamorphic rocks but displays a gradational transition into the

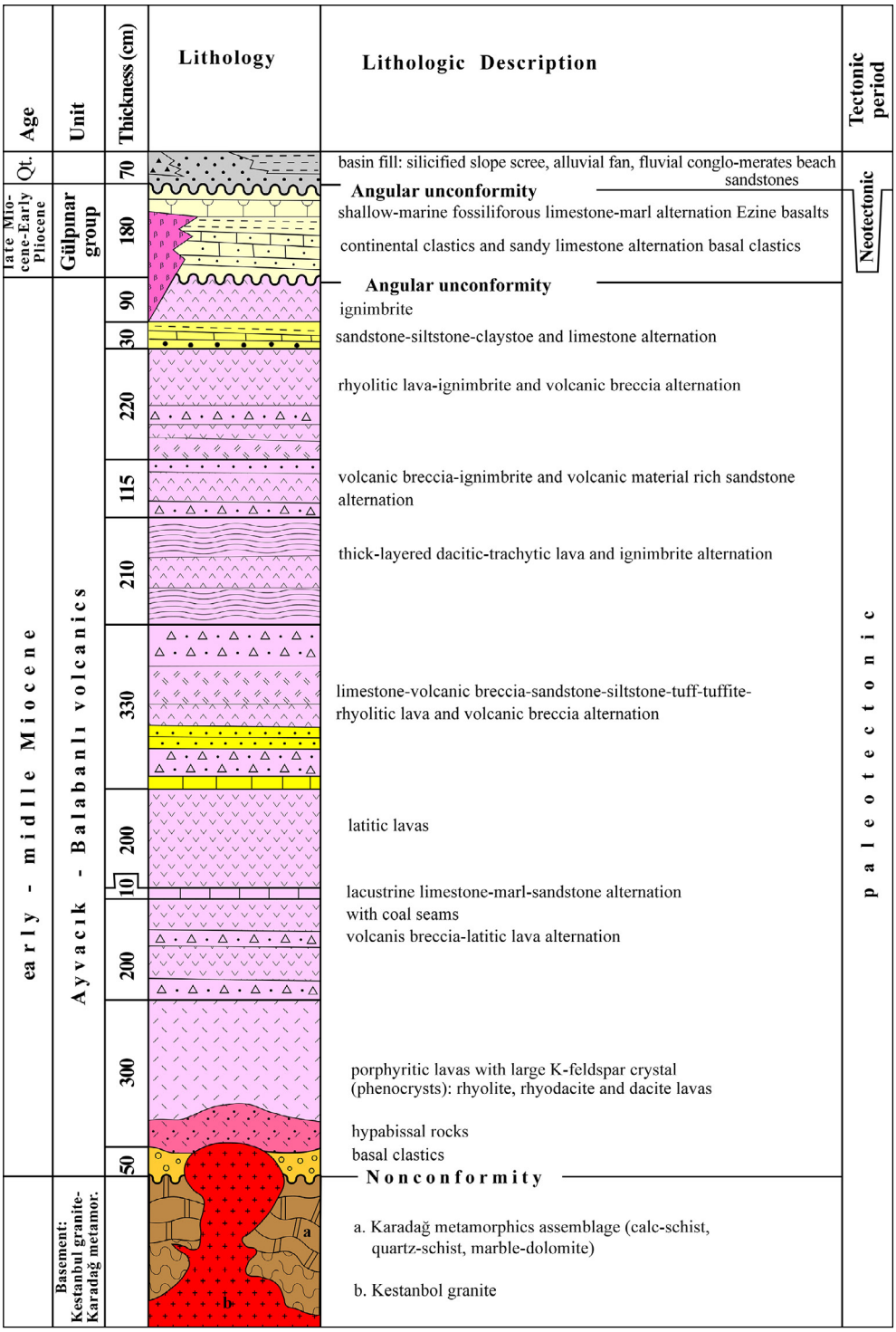


Figure 2- Combined stratigraphic column of the study area.

finegrained hypabyssal rocks with a composition same as those of the pluton (Şahin et al., 2010). At the top, these intrusive rocks are overlain conformably by the volcanic rocks. The Kestanbol pluton is also drilled at a shallow depth inside the Tuzla Dome, which is the key structure for the Tuzla geothermal field controlled by the active faults (Şamilgil, 1983; Gevrek et al., 1985).

Based on the prominent product in the sequence, volcanic rocks are subdivided into two categories (Karacık and Yılmaz, 1998). These are the lava-

dominated Ayvacık volcanic rocks and the ignimbrite-dominated Balabanlı volcanic rocks. They are cropped out on the northern footwall and southern hanging wall blocks of the Çamköy master fault segment respectively (Figure 3a). The Ayvacık volcanic rocks comprise relatively lower section of the volcanic sequence. They consist of gray and black rhyolite, rhyodacite and dacite lavas. They rest directly on the underlying hypabyssal rocks at the bottom and then are followed upward by the alternation of latitic lava, volcanic breccia, lacustrine limestone, marl and sandstone. The Balabanlı volcanic rocks are composed mostly of pyroclastites, among which ignimbrites are prominent. Ignimbrites are represented by three sections. These are, from bottom to top, base-surge deposits, welded ignimbrite and non-welded tuff. Ignimbrite packages range from several meters up to 80 m in thickness. Common lavas comprising the Balabanlı volcanic rocks are latitic and andesitic lavas. The K/Ar ages obtained from various levels of the Ayvacık-Balabanlı volcanic sequence range from 21.5 Ma to 15.9 ± 0.4 Ma, i.e., they are early Middle Miocene in age (Borsi et al., 1972; Ercan et al., 1995). The third unit in the study area is the Gülpınar Group. It is exposed widely along the coastal area between Akliman Bay in the southwest and the Babadere settlement in the northeast (Figure 3a). In addition, it also occurs in diverse sized and discontinuous outcrops around Kızılkeçili, Yukarıköy and Tabaklar villages. The Gülpınar Group rocks rest on all of abovementioned rocks with a regional angular unconformity. They begin with fluvial clastic rocks on the erosional surface of older rocks and then continue upward with the sandstone, siltstone, sandy limestone, and shale-marl alternation. This alternation is succeeded by medium to thick-bedded and fossiliferous shallow marine limestone at the top (Figure 2). The limestone and marls are full of micro- and macro-fossils such as Ostracod, Ostrea, Brachiopod and Gastrapod. Basal clastics of this sedimentary sequence are unsorted and polygenetic in composition. They contain pebbles derived from metamorphic rocks, granitoid pluton and the volcanic rocks. Pebbles are set in a volcanic material rich sandy matrix and range from sand size to 30 cm in diameter. In the east and outside the study area (in the Ezine-Bayramiç basin) the fluvial conglomerates alternate with the alkali olivine basaltic lavas (the Ezine Basalt). Same basalts crop out and cut across the Balabanlı volcanic rocks around the Kuşkaya promontory along the northern coastal area of the Edremit Gulf (Figure 3a). The K/Ar method applied on samples of the Ezine basalt yielded a radiometric age of 11.0 ± 0.4 Ma-8.4 ± 0.3 Ma (Ercan et al., 1995), i.e., alkali olivine basalts are late Miocene in age and the product of a younger magmatic activity. Consequently the Gülpınar Group is also late Miocene-early Pliocene in age. The last and youngest sedimentary sequence in the study area is the modern basin fill. It exposes widely in the Ayvacık, Behramkale, and Tuzla strike-slip basins (Figure 3a). It consists of coarse grained marginal and fine grained axial plain facies. These are the slope scree, fault terraces, alluvial fan, flood plains, beaches and delta deposits. In general, they are unsorted, weakly lithified to loose and polygenetic in composition. Modern basin fill is non-deformed (flat-lying), and overlies all of the pre-Quaternary rocks with a regional angular unconformity which reveals that the major inversion in extensional palaeotectonic regime occurred at the beginning of Quaternary. The deposition of modern basin fill is still lasting under the control of an active strike-slip faulting.

## 3. Tectonic Settings

### 3.1. Faults and Faulting Mechanism

In the identification of faults, both the seismological and the geological criteria (morphotectonic and fault plane related criteria) were used. These are the steep scarps, sudden break in slope and back-tilting of fault-bounded blocks, triangular facets, deflected to offset drainage systems, the incised stream valleys carved deeply into their beds, fault parallel aligned cold to hot water springs, sag ponds, pressure ridges, fault parallel aligned to degraded alluvial fans and deltas, contractional to extensional double bending and stepovers, braided pattern of faults peculiar to strike-slip faulting, tectonic juxtaposition of older rocks with the Quaternary alluvial sediments, faulted uplifted dissected and fault suspended terrace deposits, liner to actively growing basins, curvilinear fault traces, long, deep and narrow depressions (fault corridors), hanging valleys, active earth flows, sudden change in strike and dip amounts of rocks, strips of intensely crushed to pulverized rocks, ruins of ancient settlements, well-preserved slickenside, the earthquakes and their focal plane solution diagrams and the epicenters distribution pattern. These are common and widespread criteria for the recognition and identification of faults. These criteria will not be repeated once more for each of the

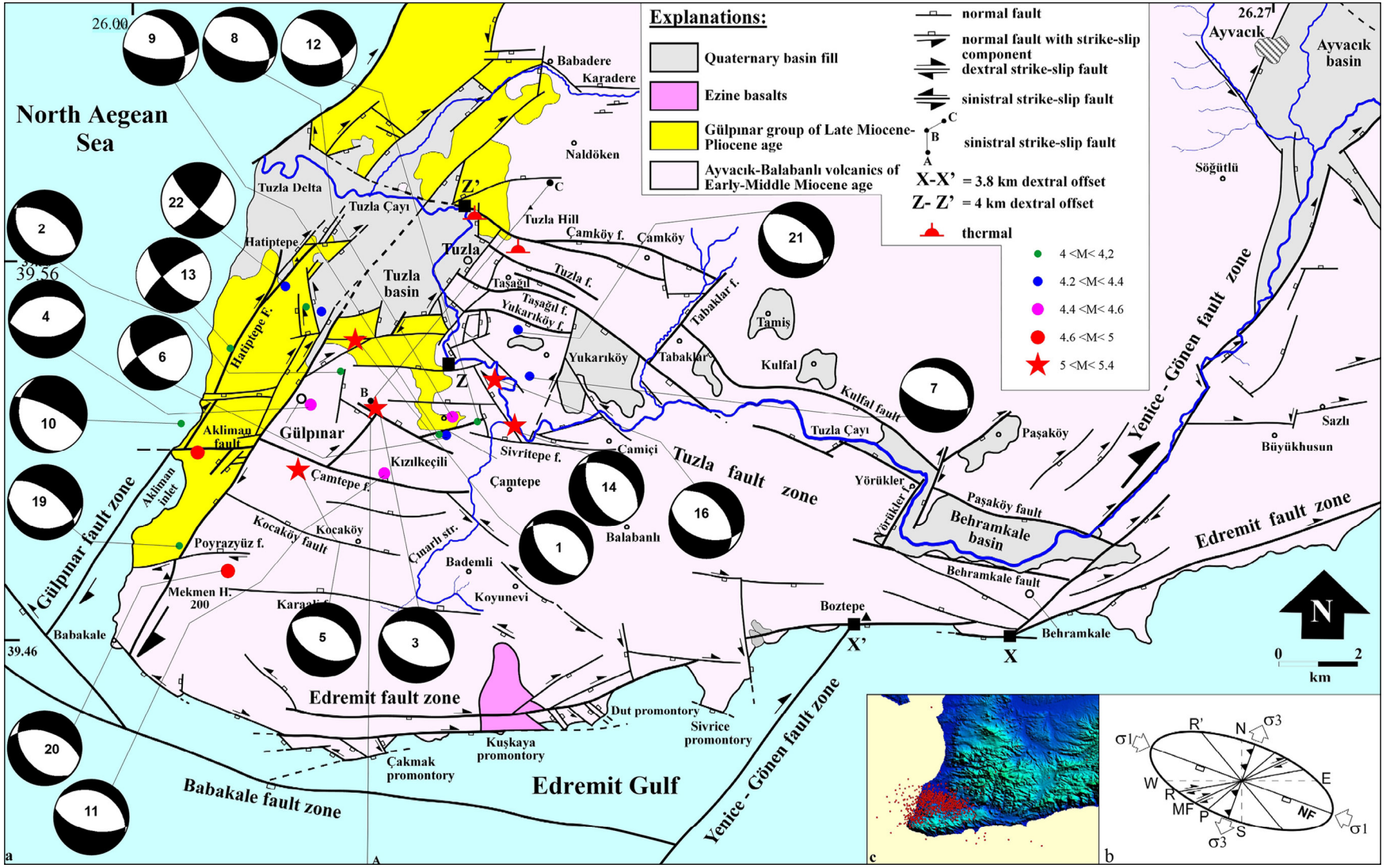


Figure 3- Seismotectonic map of the Gülpınar-Tuzla (Ayvacık-Çanakkale) earthquake area and near environment (the seismologic data from AFAD, 2017 and GFZ, 2017; the offshore faults were drawn by using Güney et al., 2001, Yaltırak et al., 2013 and the bathymetric maps of general command of the map; the onshore geological map is original and it was carried out directly in the field).



Bull. Min. Res. Exp. (2021) 166: 85-112

faults below. However, the origin, faulting mechanism and earthquake-induced faults are described and analyzed below.

Both the normal and strike-slip faults were reactivated and caused the occurrence of a moderate- and small-sized earthquakes cluster in the Gülpınar-Tuzla area (Figure 3b). Focal mechanism solution diagrams of the earthquakes of $4.0 \leq Mw \leq 5.3$ indicated that the major principal compressive stress ($\sigma1$) is operating in approximately WNW direction. However at a regional scale, i.e., in the central to northern Aegean Sea and Biga Peninsula, this direction is changing spatially from WNW to WSW, and it may be accepted that the average operation direction of $\sigma1$ is E-W. This stress system is responsible for the development of the strike-slip faulting pattern characterizing the study area (Figure 4).

In addition, angular relationships among components of strike-slip faulting pattern may change in time as a natural response to both internal and external rotations (Figure 3c). Based on the operation direction of the $\sigma1$, the WNW-trending fault segments are oblique-slip normal faults, while the NW-, NE- to ENE-trending fault segments are sinistral strike-slip and dextral strike-slip faults respectively (Figures 3a, c and 4). It is also known that normal components of fault segments increase as their strikes approach to the orientation of $\sigma1$. The strike-slip faulting pattern comprising the structural configuration of the study area is represented by the NE-trending Gülpınar, the NE-trending Yenice-Gönen, the E-W-trending Edremit and the WNW-trending Tuzla fault zones (Figure 3a). Earlier three fault zones are strike-slip, while the latter is normal fault in character. However the prominent fault segments comprising the Edremit fault zone have a considerable amount of normal components. Indeed, the most of fault segments comprising the EFZ were originally normal faults inherited from the Miocene-Pliocene extensional palaeotectonic period. They have taken a significant role in the evolution of Edremit palaeotectonic graben. This is evidenced by the well-preserved slickenside with two sets of slip lines of dissimilar origin overprinted on each other on the pre-Quaternary sedimentary sequence and volcanic rocks. The EFZ was reactivated to be a secondary dextral strike-slip fault (R-shear in Figure 4) with a

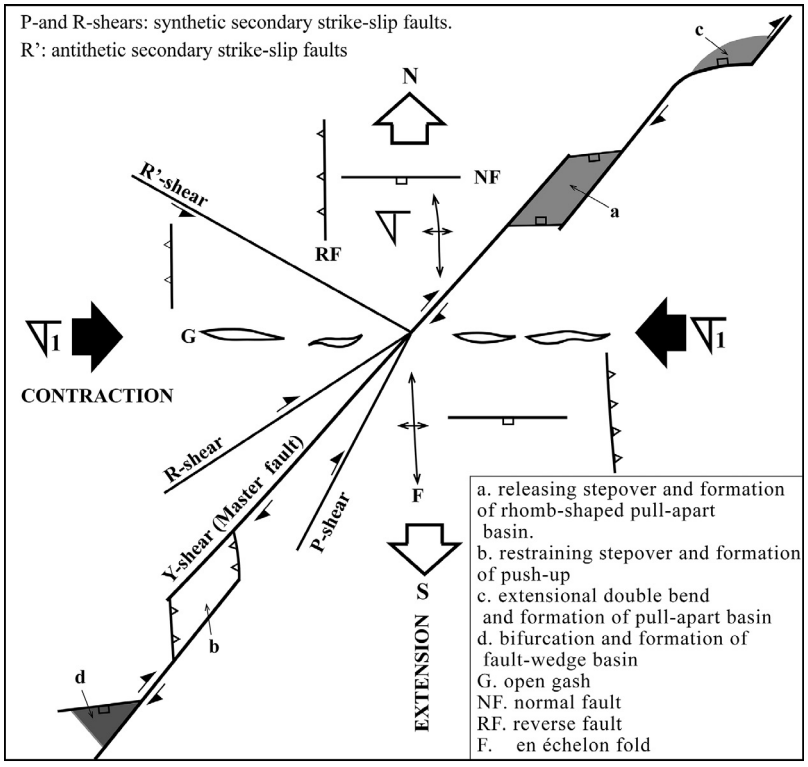


Figure 4- Faulting mechanism in the central to northern Aegean strike-slip neotectonic domain including the study area.

considerable amount of normal component during the Quaternary strike-slip neotectonic period. In general, faulting mechanisms are classified into three categories based on the orientations of three stress axes (least σ3, intermediate σ2 and greatest principal axes σ1). These are the thrust-reverse, strike-slip and normal faulting mechanisms in which σ3, σ2 and σ1 are vertical to subvertical in position respectively. Only mechanism is the strike-slip faulting by which both contractional and extensional features may develop simultaneously, i.e., folds, thrust to reverse faults, strike-slip faults and normal faults may develop under the control of strike-slip faulting mechanism (Figure 4). Therefore, this mechanism is also accepted as a model to explain the opening and closure histories of basins. In addition, in this mechanism both the amount and duration of motion on each fault/fault zone are not constant and continuous, i.e., they decrease, increase or stop from time to time. For this reason, different faults or fault zones originated or reactivated from the same strike-slip faulting mechanism may cut and offset to each other in time as in the case of the Gülpınar-Tuzla earthquake area (Figure 3a). These fault zones and the origins of the abovementioned earthquakes are described below.

### 3.2. Tuzla Fault Zone (TFZ)

This structure was previously defined and named as a single fault, the Tuzla Fault, by Karacık and Yılmaz (1998). Indeed it is a zone of deformation consisting of numerous structural fault segments (Figure 3a). It is about 2.8-11 km wide, 19 km long and WNW (N65°W)-trending normal fault zone with considerable amount of sinistral strike-slip component. It is represented by the open fractures (NR) parallel to the σ1 in Figure 3c). The TFZ is confined into a westward widening wedge-shaped area bounded by the YGFZ in the east, the EFZ in the south and the GFZ in the west (Figure 3a). It consists of 0.4-11 km long, E-W- to WNW-trending, both southerly and northerly dipping (up to 60°) normal fault segments (Figures 3a and 5). The Ayvacık-Balabanlı volcanics are crossed, sheared and brecciated by these fault segments (Figure 6). They display a graben like depression truncated and downthrown by the GFZ in the west (Figure 7). In addition, both the NE-trending dextral and NW-trending sinistral strike-slip fault segments also occur within the TFZ. Some of them are the Tabaklar, Yörükler and the Sivritepe dextral strike-slip faults. The first two segments cut and offset the northernmost normal fault in the dextral direction and divide it into three segments, namely the Çamköy, Kulfal and Paşaköy faults (Figure 3a). The Tuzla River (Çay) is the major drainage system in the Gülpınar-Tuzla earthquake area. In general, it flows in WNW direction and follows the traces of both the normal and strike-slip fault segments. For this reason its flow direction varies frequently and displays an uneven bed in shape throughout the TFZ. However it changes the flow direction toward NNE and gains a relatively straight bed when it enters into the NNE-trending GFZ (Figures 3a and 7).

The northerly-located but southerly-dipping fault segments comprising the TFZ are more active than others. It was proved once more by the epicenters distribution pattern of the 2017 Gülpınar-Tuzla earthquake cluster (Figure 3b). These are, from NW to SE, the 11 km long Çamköy, 3.3 km long Tuzla, 7.7 km long Taşağıl, 3 km long Yukarıköy, 7.8 km long Kulfal and the 5.5 km long Paşaköy faults (Figure 3a). Based on their lengths, magnitudes of peak earthquakes to be sourced from these faults are the Mw = 6.2, 5.6, 6.1, 5.6, 6.1 and 5.8 respectively (Wells and Coppersmith, 1994). It seems that the independent earthquakes No. 1, 3, 5, 14 and 16 might have been originated from

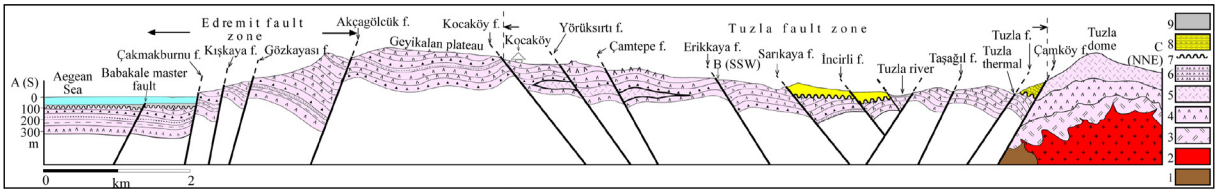


Figure 5- Geological cross-section along the line A-B-C in Figure 3. It illustrates fault-controlled Tuzla geothermal area, internal structure of the Tuzla dome and both the Tuzla and Edremit fault zones. 1. Karadağ metamorphic rocks, 2. Kestanbol granitoid pluton, 3. Hyp-abyssal intrusive rocks, 4. porphyritic lavas, 5. ignimbrites, 6. various lavas and pyroclastic alternation with sedimentary intercalations, 7. angular unconformity, 8. terrestrial and shallow sea water sedimentary sequence (Gülpınar Group), and 9. modern basin fill.

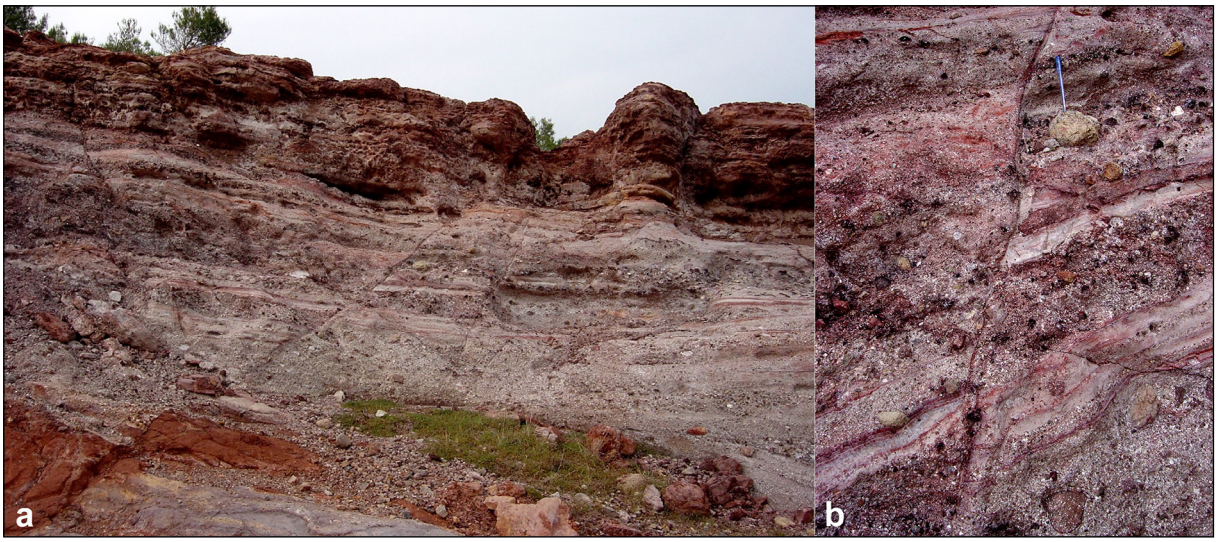


Figure 6- a) and b) field photographs illustrating normal faults developed in Lower-Middle Miocene tuff-volcanic breccia alternation cut and deformed (crushed, brecciated and sheared) by the Tuzla fault zone.

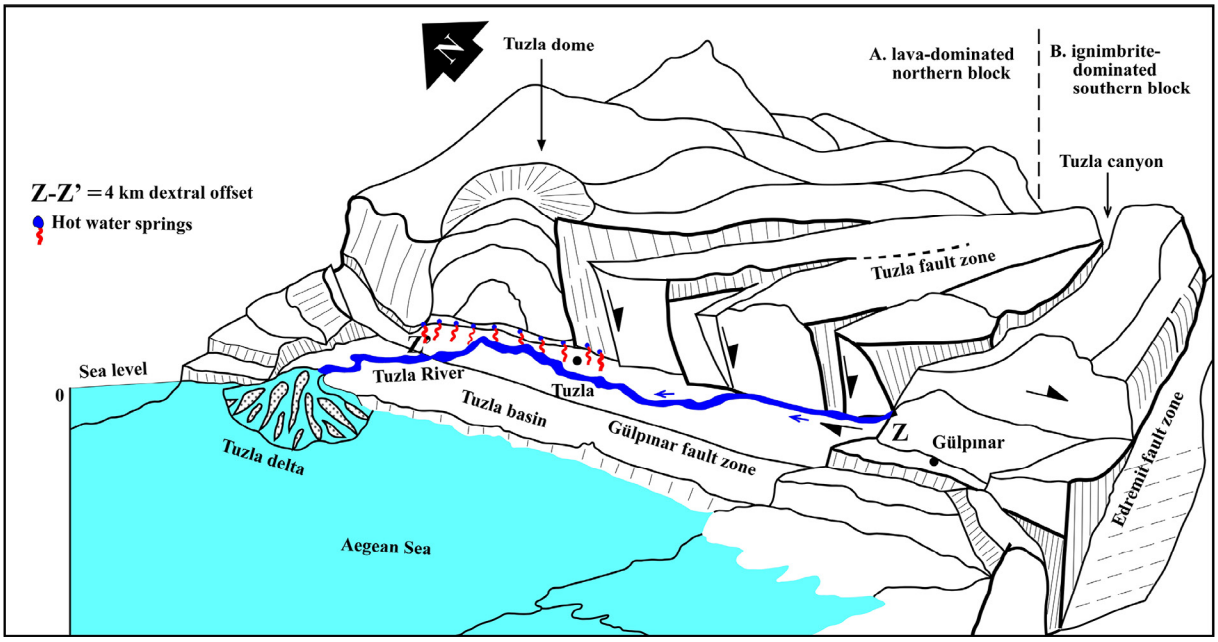


Figure 7- Sketched block diagram depicting the graben-like structure of the Tuzla fault zone truncated and offset in right-lateral direction (Y-Y' = 4 km) by the Gülpınar fault zone.

the first four fault segments based on the earthquakes parameters such as the dip amount to dip direction, focus depth, epicenter site and the patterns of the focal mechanism diagrams (Figure 3a). The latter parameter also indicates that the extension direction in the study area is NNE (Figure 3a). This is also evidenced by the palaeostress analysis of slipplane data measured on slickensides of the fault segments (Figures 8a, b and c). Several reverse faults, which dip steeply to NNE, were also observed on the southern slope of the Tuzla dome. But they could not be mapped due to the small scale of the map. Indeed these faults might have been originated from vertical motion related to the forceful injection and emplacement of the Kestanbol granitoid pluton. The Upper Miocene-Pliocene Gülpınar group overlies with an angular unconformity the Oligo-Miocene Kestanbol pluton. Its basal clastics contain pebbles of pluton. This observation reveals that the

emplacement and uplift of the pluton were completed and began to be eroded before late Miocene. Consequently, outcrop scale reverse faults might have formed in palaeotectonic period not during the Quaternary neotectonic period.

### 3.3. Gülpınar Fault Zone (GFZ)

This structure was previously defined and introduced to the literature as a single fault, the Gülpınar fault (Karacık and Yılmaz, 1998). Indeed it is an approximately 1.7-5.5 km wide, 37 km long and N 20°-35° E-trending dextral strike-slip fault zone with a considerable amount of thrust component, by which its southeastern block was uplifted up to 0.4 km with respect to the western block. The Gülpınar fault zone is located in the area between Dalyan Town in the northeast and 1.5 km west of Babakale in the southwest along the coastal area of Aegean Sea (Figure 1b). The 19 km long southwestern section of fault zone is included in the study area (Figure 3a). However its 18 km long northeastern section lies outside. The external section was previously mapped and named as a single fault (the Kestanbol Fault) and then interpreted to be an oblique-slip normal fault (Emre and Doğan, 2010). The Gülpınar fault zone consists of numerous closely to medium spaced (0.1-2 km) and diversesized (0.2-9.5 km) fault segments of dissimilar trends such as NE, NW and E-W. The prominent and longer segments are NE in trend (Figure 3a). In and outside the study area, the Paleozoic metamorphic rocks, the Upper Cretaceous ultrabasic rocks, the Oligo-Miocine Kestanbol pluton, the Lower-Middle Miocene felsic volcanic rocks (Ayvalık-Balabanlı volcanics), the Upper Miocene-Middle Pliocene sedimentary sequence (Gülpınar group) and the Quaternary modern basin fill are cut, displaced in both vertical (0.4 km) and lateral (4 km) directions and juxtaposed tectonically with to each other in places by fault segments. The Tuzla River is offset (up to 4 km) in the dextral direction by several fault segments when it enters into the Tuzla strike-slip basin developed along the Gülpınar fault zone (Z-Z' = 4 km in Figures 3a and 7). In the same way, the Gülpınar fault zone is also cut and displaced up to 2 km in both sinistral and dextral directions by the NNW- and NW-trending faults. One of these offset structures is exposed well around Kösedere village outside and 0.5 km north of the study area, i.e., there is a strong interaction among the fault segments of dissimilar origin and trends comprising the strike-slip fault pattern. This is evidenced strongly by thermal waters, which use their intersection areas, such as the Kestanbol and Tuzla thermals, and come out of the ground (Figure 3a).

The 4.4 km long and NE-trending Hatiptepe fault segment of the Gülpınar fault zone reactivated on Monday 24 March 2017 and caused to the occurrence of a small sized (Mw = 4.2), shallow-focus (h = 9.7 km) and independent earthquake of pure strike-slip origin (No.22 in Figure 3a). Based on the length of the longest (9.5 km) segment, the magnitude of the peak earthquake to be sourced from the Gülpınar fault zone is Mw = 6.2 (Wells and Coppersmith, 1994). This seismic data reveals that the Gülpınar fault zone is a dextral strike-slip fault not oblique-slip normal fault as has been reported in previous works (Karacık and Yılmaz, 1998; Emre and Doğan, 2010). This fault zone is represented by the secondary synthetic strikeslip fault (P-shear in Figure 3c).

### 3.4. Yenice-Gönen Fault Zone (YGFZ)

This is the most significant and active dextral stike-slip fault zone (Şaroğlu et al., 1987; Barka and Kadinsky-Cade, 1988; Herece, 1990; Kürçer et al., 2008). It includes the master fault (Y-shear or MS in Figure 3c) of the southern strand of the NAFS. In general, the YGFZ trends NE and has a total length of 335 km. It consists of two sections, the onshore and the offshore sections respectively. The 165 km long onshore section is located in the area between Gönen County in the northeast and Behramkale in the southwest (Figures 1b and 3a). It was previously studied and documented well (Herece, 1990; Kürçer et al., 2008; Koçyiğit, 2011; Yaltırak et al., 2013). The 6-20 km wide and N55°-60°E-trending onshore section consists of numerous parallel and subparallel, closely to widely spaced (0.4-8 km) and diverse-sized (0.5-40 km) structural fault segments. A limited number of N-S-, E-W- and NW-trending fault segments in the nature of reverse, normal and sinistral stike-slip faults, respectively, also occur in this zone. The onshore section of the YGFZ runs in southwest direction across the Gönen River, Koca Çay valley, Yenice County, Zeybekçayırı and the northern foot of the Kazdağ mega pressure ridge in the east (Figures 9 and 10). Approximately 3 km east of Ayvacık County, it enters into the study area, bends south at about 30° and then runs for about 16 km in SW direction up to Behramkale Town (Historical Asos City) along the

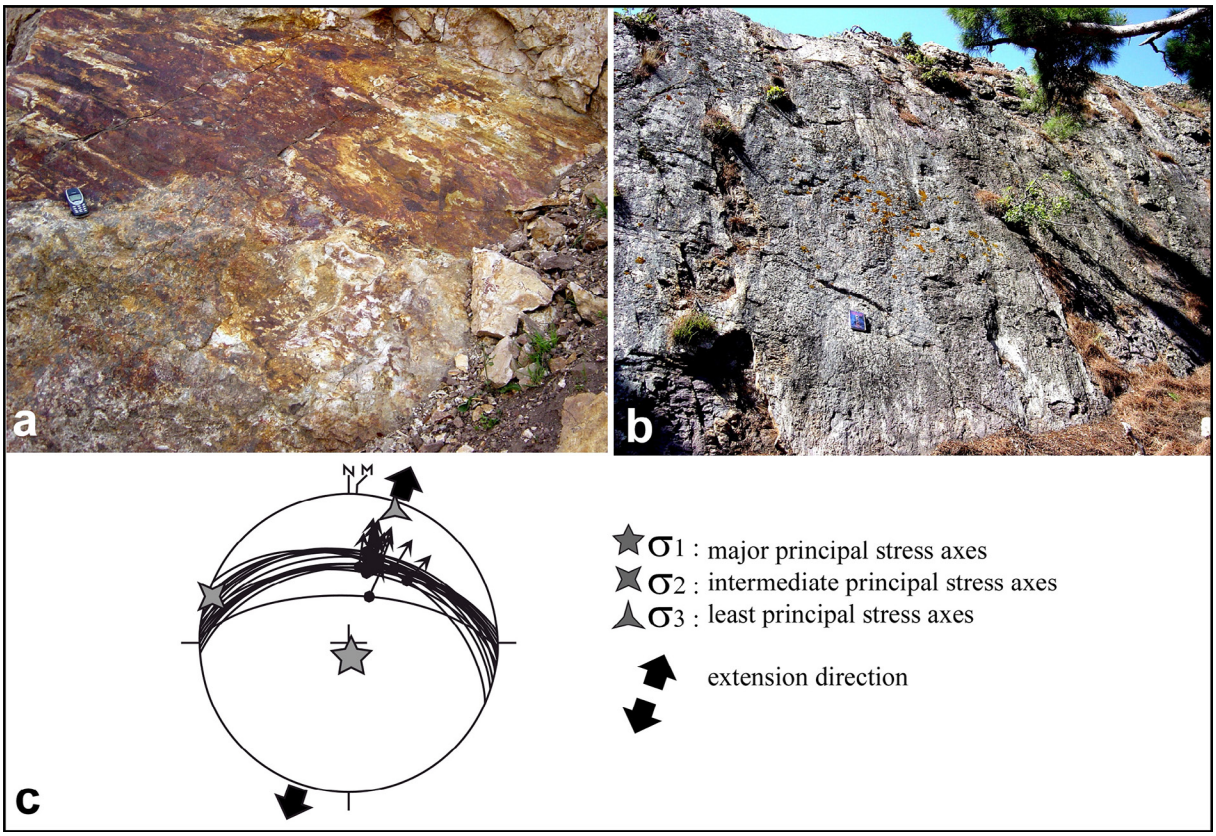


Figure 8- a) and b) field photographs of normal fault slickensides, and c) the stereographic plot of slip-plane data on the Schmidt lower hemisphere net.

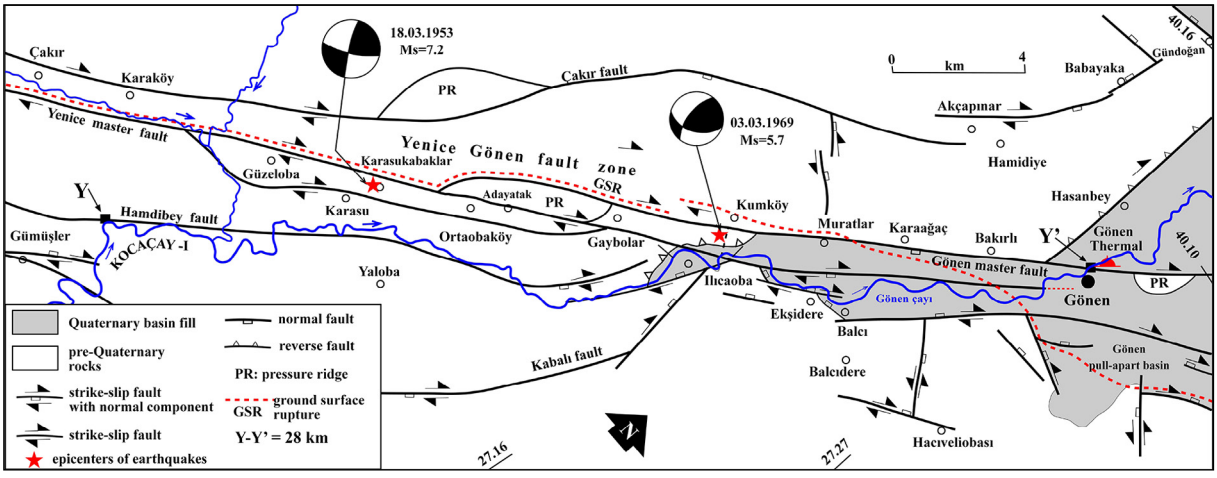


Figure 9- Seismotectonic map of the Gönen section of the Yenice-Gönen Fault zone (YGFZ).

Tuzla Çayı Canyon. At this locality, it is cut and offset in the right lateral direction by the Edremit fault zone along the northern margin of Edremit Gulf (X-X'= 3.8 km in Figure 3a). At the point X' near Boztepe, it enters into sea water and then continues in the same direction to be the offshore section (southern margin boundary faults of both the Babakale and Skyros basins) along the sea bottom of Edremit Gulf. Along the whole length of the onshore section, various rocks of dissimilar age and facies are cut and divided into numerous lenticular bodies by the bifurcation, rejoining and rebifurcation of fault segments comprising the fault zone. Thus a braided strike-slip fault pattern, which is peculiar to the strike-slip faulting, develops (Figures 9 and 10).

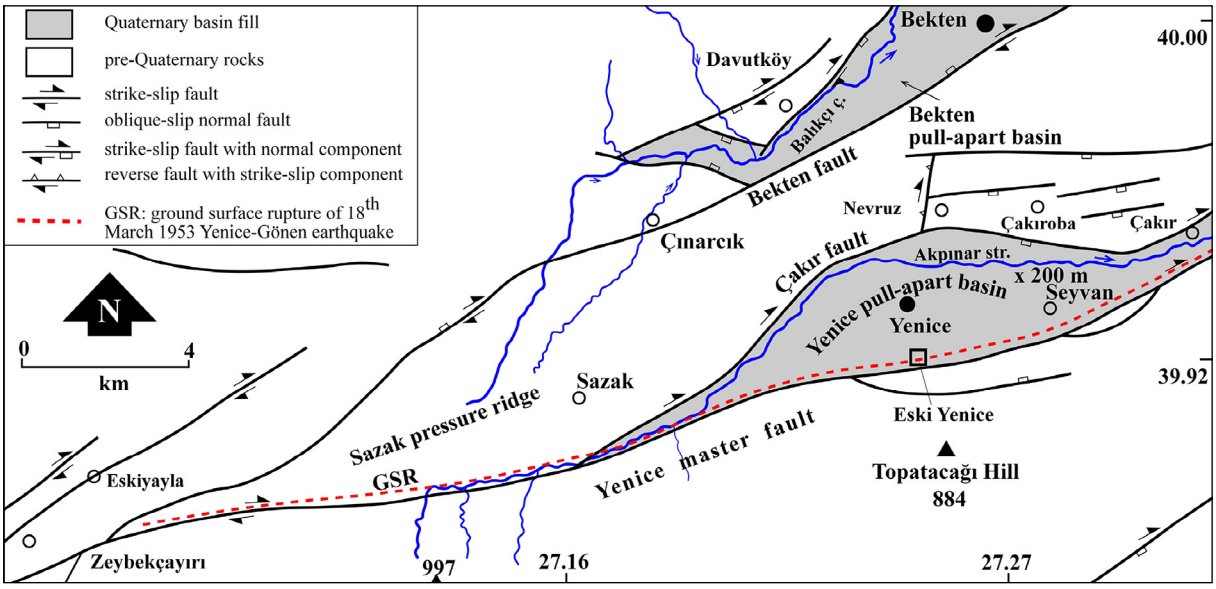


Figure 10- Fault map illustrating the Yenice-Bekten pull-apart basins and ground surface rupture of the 8 March 1953 Yenice-Gönen earthquake.

In this pattern long axes of lenticular bodies are nearly parallel to the general trend of the fault zone. In addition, numerous pressure ridges and pull-apart basins have developed due to the uplift and subsidence of these fault bounded lenticular bodies. The most outstanding of them are, from northeast to southwest, the Gönen, Yenice, Bekten and Ayvacık basins and the intervening Kazdağ mega pressure ridge. Some major drainage systems, such as Gönen Çayı, Koca Çay and the Tuzla Çay, are fault-controlled and offset. For instance, the Koca Çay-Gönen Çay drainage system is offset up to 28 km in the right lateral direction by the onshore section of the YGFZ (Y-Y' in Figure 9). This value implies a uniform slip rate of 10.9 mm/yr (Koçyiğit, 2011). Whereas it has been previously reported that the total right-lateral displacement accumulated along the Yenice section of the fault zone is only 2.8 km (Herece, 1990). Based on the length of the longest (40 km) fault segment comprising the onshore section, the magnitude of the peak earthquake to be sourced from it is Mw = 7.0 (Wells and Coppersmith, 1994). Its truthfulness was proved by the reactivation of the Yenice-Gönen section and occurrence of the 18 March 1953 Yenice earthquake of Ms = 7.4 (Tan et al., 2008). This destructive earthquake has also led to the development of an approximately 40 km long surface rupture with a maximum 1.3 m vertical and 4.2 m right-lateral displacements in the area between Kalfaköy (Gönen) in the northeast and south-southwest of Eskiyayla settlement (Yenice) in the southwest (Figures 9 and 10) (Herece, 1990; Kürçer et al., 2008). This destructive earthquake attracted attentions of several researchers, who have carried out detailed but local field geological mapping and palaeoseismological studies (Pınar and Lahn, 1952; Ketin and Roesly, 1953; Herece, 1985, 1990; Kürçer, 2006, 2008). Based on the palaeoseismological data, a recurrence interval of 660 ± 160 years was suggested for the large destructive earthquakes to be sourced from the Yenice-Gönen master fault (Kürçer et al., 2008, 2019). These authors have also reported that the Yenice-Gönen master fault has been active since Miocene and the slip rate along it is about 6.3 mm/yr. If this is true, the total right lateral displacement accumulated along the Yenice-Gönen fault since Miocene must be at least 32 km. Whereas they have reported that it was only 2.8 km, i.e., there is a contradiction between the reported slip rate (6.3 mm/yr) and the total right-lateral displacement (2.8 km). Consequently, the total right-lateral displacement on the Yenice-Gönen fault zone is much more than 2.8 km. It was determined to be 28 km (Y-Y' = 28 km in Figure 9) in the present study.

The 175 km long offshore section runs across the Aegean Sea floor between Boztepe along the northern margin of Edremit Gulf in the northeast and the Skyros Island in the southern North Aegean Sea in the southwest (Figures 1b and 3a). It is about 60 wide, 180 km long and N50°-60°E trending zone of deformation. The offshore section consists

of NE-trending dextral strike-slip faults and the intervening NW-trending oblique-slip normal faults. Three large pull-apart basins developed within the offshore southern strand. These are the Bozcaada, Babakale and the Skyros basins (Figure 1b). The deep, long and narrow depressions bounded by steep fault scarps, closely spaced and straight bathymetric contours, positive and negative flower structures, active underwater earthflows and intensely deformed Quaternary sediments are common morphotectonic criteria for the existence of active faults (Eryılmaz and Yücesoy, 1999; Güney et al., 2001; Koukouvelas and Aydın, 2002; Kurtuluş et al., 2009; Yaltırak et al., 2013; Gürer et al., 2016). On the other hand, this area is also seismically very active as indicated by both the historical and recent destructive earthquakes, such as the 14 February 1672 Babakale-Lesvos Island and the 4 March 1967, 19 February 1968, 19 December 1981 and the 27 December 1981 Skyros Island earthquakes, occurred within it (No. 7, 8, 11 and 12 on Table 1 and Figure 1b) (Papazachos et al., 1984, 1991; Ambraseys and Finkel, 1995). Both the onshore and the offshore sections of the major southern strand are linked to each other by the Bozcaada, Babakale and Edremit Gulf strike-slip basins and related NNW-trending oblique-slip normal faults. In this frame, the NE-trending southern and the northern margin boundary faults of both the Skyros and Babakale basins are the offshore extents of both the YGFZ and the Bayramiç-Ezine fault zone respectively. Consequently the southern strand of the NAFS continues across the Biga Peninsula and the North Aegean Sea floor up to Skyros Island in the farther southwest (Figure 1b).

### 3.5. Balıkesir-İzmir Fault Zone (BİFZ)

This is an about 5-25 km wide, 250 km long and NE-trending dextral strike-slip fault zone located in the area between Lake Ulubat in the northeast and Samos Island in the southwest (Figures 1a and 1b) (Uzel and Sözbilir, 2008; Koçyiğit, 2012, 2020). Indeed, the BİFZ is an originally palaeotectonic structure inherited from the late Cretaceous. It reactivated to be a megashear zone in the nature of dextral strike-slip fault zone in the Quaternary neotectonic period. It forms a transitional zone between the easterly located southwest Anatolian extensional and westerly located central to northern Aegean compressional provinces (Koçyiğit, 2012). These two neotectonic regimes interact with each other along this transitional zone. The BİFZ is seismically very active. This was proved once more by the occurrence of several earthquake clusters such as the 10 December 2019 Balıkesir, 22 January 2020 Akhisar and 18 February 2020 Kırkağaç earthquakes (EMSC, 2019, 2020). The seismic activity migrated along the BİFZ in a southwestward direction up to Saruhanlı County, and it is still lasting. One of the type localities, where faulting-induced morphotectonic features are exposed well, of the BİFZ is the Kepsut County. It is located along the eastern margin of the Balıkesir pull-apart basin. In this area, the Susurluk River is displaced up to 23 km in the dextral direction by the BİFZ (P-P'= 23 km in Figure 11). This value implies a uniform slip rate of 8.9 mm/yr along this fault zone.

### 3.6. Edremit Fault Zone (EFZ)

This is an approximately 2-12 km wide, 160 km long and ENE-trending dextral strike-slip fault zone with a considerable amount of normal component. It is located between Balıkesir in the east and Babakale in the west (Figures 3a and 12). Its western half and various characteristics including kinematics and seismicity were previously studied and reported (Kurtuluş et al., 2009; Koçyiğit, 2011; Altınok et al., 2012; Gürer et al., 2016; Sözbilir et al., 2016). The EFZ determines the southern outline of Biga Peninsula. It contains four strike-slip basins. These are, from E to W, the Balıkesir, Gökçeyazı, İvrindi and Edremit Gulf basins (Figures 3a, 11 and 12). In terms of these basins, the EFZ is linked to the easterly located Balıkesir-İzmir (BIFZ) and northerly located Ilıca-Darıca dextral strike-slip fault zones (Figures 11 and 12). The Edremit Gulf basin and the Kazdağ mega pressure ridge, which rises up to 1700 m above sea level along its northern margin, have been interpreted to be a graben and horst in some of previous works (Yılmaz et al., 2000, Güney et al., 2001). As is to be explained in the sentences below, this interpretation is not true. The EFZ consists of numerous parallel to subparallel, closely to medium-spaced (0.2-4 km) and diverse-sized (1-40 km) structural fault segments. They are ENE, N-S, NW and NE in trend, but the ENE-trending segments are more prominent and longer than others (Figures 3a and 12).

Some of these fault segments are inherited from the Pre-Quaternary palaeotectonic period. They cut across various rocks (e.g., Paleozoic Kazdağ metamorphic rocks, Permo-Triassic Karakaya Complex, Upper

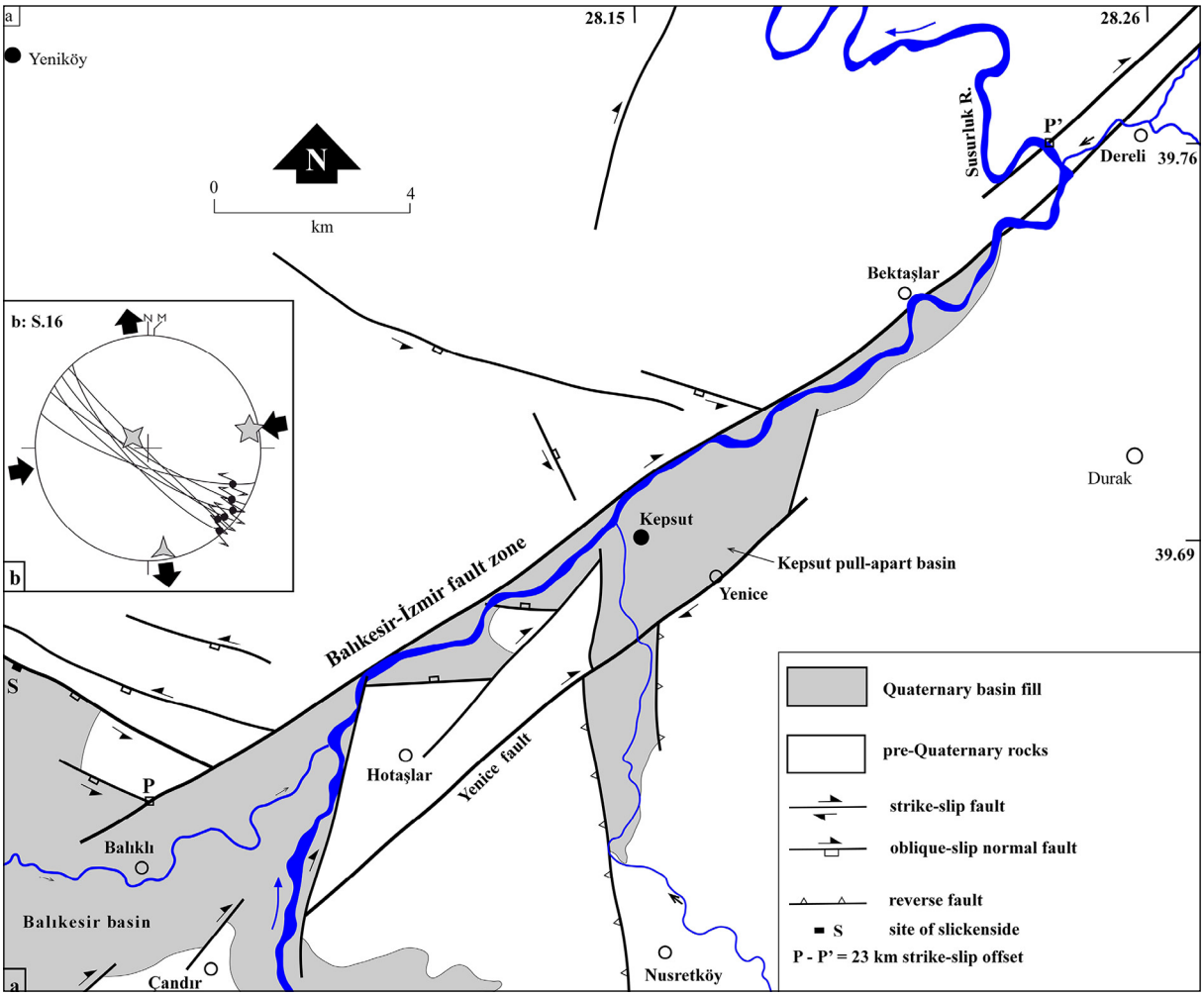


Figure 11- Neotectonic map of the Kepsut section of the Balıkesir-İzmir Fault Zone (BİFZ). It illustrates the easternmost tip of the Edremit fault zone (Balıkesir pull-apart basin) and the offset drainage system (Susurluk River) along the BİFZ.

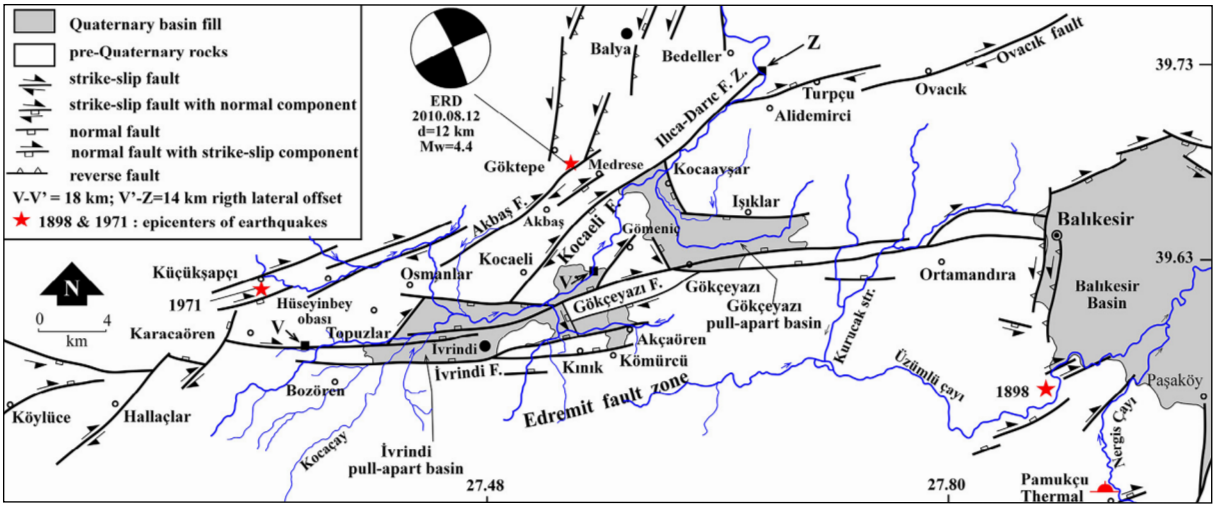


Figure 12- Seismotectonic map of the eastern half of the Edremit fault zone (EFZ).

Cretaceous-Paleocene ophiolitic mélange to ultramafic rocks, Oligocene volcanic rocks, Oligo-Miocene granodiorite, Lower-Middle Miocene volcanic rocks and the Upper Miocene-Pliocene sedimentary sequence), and tectonically juxtapose them with each other and also with the Quaternary neotectonic basin fill. The thickness of the modern basin fill of Edremit Gulf basin ranges from 200 m to 700 m (Emre and Doğan, 2010), and it rests with an angular unconformity on the Pliocene erosional surface of the underlying older deformed rocks. Thus, the total throw amount accumulated on the EFZ can be estimated as 2-2.5 km by the comparison of the 1700 m high onshore erosional surface of Pliocene age with the 300-800 m deep offshore erosional surface of the same age. In addition, some structural and geographical features are displaced in right-lateral directions. Around İvrindi in the farther east of Edremit Gulf, the Koca Çay-I drainage system is controlled and offset up to 18 km in the right lateral direction by the fault segments (V-V'=18 km in Figure 12). In the same way, based on the data obtained from the drilling studies carried out in the offshore section of the Edremit Gulf basin, it has been reported that the Lower Miocene rocks had been displaced more than 20 km in right-lateral direction (Saka, 1979; Yazman, 1996). Based on these lateral displacements, the uniform slip rates along the EFZ are 7.0-7.7 mm/yr, respectively. In addition, the multichannel seismic reflection studies carried out around Bababurnu promontory in the offshore section of the Edremit Gulf basin, some well-developed positive and negative flower structures have also been identified (Eryılmaz and Yücesoy, 1999; Güney et al., 2001; Kurtuluş et al., 2009). Consequently the great right-lateral offset, positive to negative flower structures and the WNW operation of the major principal compressive stress ($\sigma 1$) altogether reveal obviously that this area has been experiencing a strike-slip tectonic regime since the beginning of Quaternary, i.e., the Edremit fault zone is represented by the synthetic strike-slip fault (R-shear in Figure 3c). In this frame, the Quaternary configuration of the Edremit Gulf is not a graben, in contrast, it is an actively growing and westward widening fault-wedge-type of strike-slip pull-apart basin. It results from the bifurcation of the EFZ into two fault zones around Hallaçlar settlement in the east of Havran County (Figures 1b and 12). These fault zones determine and control both the southern and northern margins of the basin and display basinward-facing stepped landscape bounded by the one master and a number of second order fault segments with a considerable amount of normal component. Both the mappable and outcrop scale mimics of these fault zones are well-exposed within the intensely sheared Miocene sedimentary sequence exposing along the southern fault-bounded margins of the Edremit Gulf pull-apart basin (Figure 13).

The longest (30-40 km) and most significant fault segments comprising the EFZ are the Gökçeyazı, Burhaniye and Altınoluk faults (Figures 1b and 12). Based on their lengths, magnitudes of the peak earthquakes to be sourced from these faults are Mw = 6.7 and 7.0 respectively (Wells and Coppersmith, 1994). The Altınoluk fault reactivated and led to the occurrence of the 6 October 1944 Altınoluk-Ayvacık earthquake of Ms = 6.8 and 35- 40 km long surface rupture between Akçay Town in the east and Ahmetçe village in the west along the coastal area (Ambraseys and Jackson, 1998; Emre and Doğan, 2010; Altınok et al., 2012; Yaltırak, 2003; Yaltırak et al., 2013).

### 4.6. February- 24 March 2017 Earthquake Cluster

4.1. Recent Seismicity

A moderate-sized (Mw = 5.3) and shallow-focus (h = 8.8 km) earthquake struck on Monday 6 February 2017 at 03: 51: 40 (local time) at the locality 2 km NNE of Gülpınar Town (AFAD, 2017). This seismic event is here named as the Gülpınar (Ayvacık-Çanakkale) earthquake due to its proximity to the epicenter (No.1 in Figure 3a). It was felt strongly over a very wide region including the cities of Çanakkale, Balıkesir and İzmir. However the severe damage was confined to Yukarıköy settlement. The Gülpınar main shock was followed by 33 aftershocks with Mw ranging from 1.4 to 4.0 in a time slice of four hours (AFAD, 2017). Approximately 7 hours later than the first event, a second independent moderate-sized (Mw = 5.3) and shallow-focus (h = 9.8 km) earthquake struck on the same day at 10:58:40 (local time) in the 1.7 km west of Kızılkeçili village (No.2 in Figure 3a). This new event is termed to be the Kızılkeçili earthquake. These two events were also followed by the occurrences of three moderate-sized, shallow-focus and independent earthquakes in the intervals of one day, three days and two days respectively in the same region. These are, in turn, the Mw = 5.2 Kocaköy, Mw = 5.0 Çamtepe and Mw = 5.3 Yukarıköy earthquakes (No. 5, 14 and


Figure 13- Field photograph of the Lower Miocene sedimentary sequence cut and deformed by the Burhaniye sub-fault zone at location~3 km SSW of Burhaniye along road cut (view to west).

16 in Figure 3a). The number of aftershocks with the Mw between 4.0 and 4.6 is 16 (Table 2). The most of seismic events described here was caused by normal faulting. On Friday 24 March 2017 at 15:19:06 (local time), a small-sized (Mw = 4.2), shallow-focus (h = 9.6 km) and independent earthquake occurred around the Hatiptepe and approximately 4 km west of Tuzla village along the coastal area (No. 22 in Figure 3a). Origin of this new event (the Hatiptepe earthquake) is strike-slip faulting, i.e., it is different than previous seismic events. These six independent earthquakes were succeeded by totally 2768 aftershocks with moment magnitudes ranging from 1.0 to 4.6 until the date of 24 March 2017. Based on data given by AFAD (2017), the total number of heavily and slightly-damaged structures are 290 and 216 respectively. In addition, one Mosque and one Thermal facility were also damaged until the date of 24 March 2017.

## 5. Discussion: Inversion in Palaeotectonic Regime and Onset of Neotectonic Regime

### 5.1. Palaeotectonic History

Starting from late Paleocene onward, the convergence between Menderes-Tauride platform to the south and the Sakarya continent to the north continued and gave rise to the occurrence of some significant events. These are: a) internal imbrication of platform sequences, b) tectonic transportation of allochthon rock assemblages (particularly ophiolitic nappes, e.g., Lycian nappes) towards farther south-southeast and their emplacement first onto the marine Eocene sequence and lastly onto the Lower-Middle Miocene marine clastics, c) the overthickening of the lithosphere up to 50-55 km (Şengör et al., 1984), d) the Barrovian type of regional metamorphism (MMM: the main Menderes Massif metamorphism) (Brunn et al., 1971; Şengör and Yılmaz, 1981; Koçyiğit, 1983; Özgül, 1984; Okay, 1986; Bozkurt, 1996, 2004; Bozkurt and Park, 1999; Sözbilir, 2005), e) a very rapid regional uplift and deposition of 2 km thick boulder block conglomerate in molassic facies (Koçyiğit, 1984), and f) exhumation of both the Kazdağ and Menderes Massifs. This long lived contractional deformation period was also accompanied by a wide-spread collisional to post-collisional magmatic activity and related felsic intrusions such as batholith, stock and dome (Ercan et al., 1985; Harris et al., 1986; Seyitoğlu and Scott, 1991; Bozkurt and Park, 1997; Genç, 1998; Karacık and Yılmaz, 1998; Wilson and Bianchini, 1999; Emre and Sözbilir, 2005; Erkül et al., 2005*a, b*; Glondy and Hetzel, 2007). They added

Table 2- Various seismic parameters of significant earthquakes happened in the Gülpınar-Tuzla (Çanakkale) area in the time slice of 6 February-24 March-2017.

| No | Date | Origin time | Epicentral coordinate | | Depth (km) | Magnitude | Nodal plane 1 | | | Nodel plane 2 | | | References |
|---|---|---|---|---|---|---|---|---|---|---|---|---|---|
| | | | Latitude | Longitude | | | strike | dip | rake | strike | dip | rake | |
| 1 | 06.02.2017 | 03:51:40 | 39.5423 | 26.1318 | 8.9 | Mw 5.3 | 142.00 | 54.00 | -76.00 | 298.00 | 38.00 | -109.00 | ERD(AFAD) |
| 2 | 06.02.2017 | 04:17:29 | 39.5356 | 26.1278 | 9.0 | Mw 4.0 | 132.00 | 35.00 | -81.00 | 301.00 | 56.00 | -96.00 | AFAD |
| 3 | 06.02.2017 | 10:58:02 | 39.5275 | 26.1373 | 9.8 | Mw 5.3 | 113.00 | 50.00 | -93.00 | 298.00 | 40.00 | -86.00 | AFAD |
| 4 | 06.02.2017 | 11:45:01 | 39.5283 | 26.1196 | 11 | Mw 4.4 | 263.00 | 40.00 | -92.00 | 86.00 | 50.00 | -88.00 | AFAD |
| 5 | 07.02.2017 | 02:24:03 | 39.514 | 26.1161 | 11.9 | Mw 5.2 | 115.00 | 49.00 | -93.00 | 300.00 | 41.00 | -86.00 | AFAD |
| 6 | 07.02.2017 | 05:15:51 | 39.5216 | 26.1568 | 8.9 | Mw 4.3 | 140.00 | 53.00 | -17.00 | 241.00 | 76.00 | -142.00 | AFAD |
| 7 | 07.02.2017 | 05:17:08 | 39.5345 | 26.1796 | 4.9 | Mw 4.2 | 108.00 | 64.00 | -98.00 | 305.00 | 27.00 | -75.00 | AFAD |
| 8 | 07.02.2017 | 21:00:54 | 39.5256 | 26.1585 | 6.9 | Mw 4.4 | 107.00 | 57.00 | -109.00 | 319.00 | 38.00 | -64.00 | AFAD |
| 9 | 07.02.2017 | 21:35:00 | 39.5218 | 26.1548 | 7 | Mw 4.1 | 91.00 | 66.00 | -127.00 | 333.00 | 43.00 | -36.00 | AFAD |
| 10 | 07.02.2017 | 22:53:30 | 39.5241 | 26.084 | 11 | Mw 4.1 | 162.00 | 23.00 | -47.00 | 296.00 | 74.00 | -106.00 | AFAD |
| 11 | 08.02.2017 | 01:38:03 | 39.5133 | 26.1398 | 10.4 | Mw 4.5 | 104.00 | 59.00 | -98.00 | 299.00 | 32.00 | -77.00 | AFAD |
| 12 | 08.02.2017 | 02:16:14 | 39.5245 | 26.1653 | 6.2 | Mw 4.1 | 83.00 | 53.00 | -136.00 | 322.00 | 56.00 | -47.00 | AFAD |
| 13 | 09.02.2017 | 10:13:10 | 39.5405 | 26.0975 | 9.8 | Mw 4.0 | 136.00 | 68.00 | -15.00 | 232.00 | 76.00 | -157.00 | AFAD |
| 14 | 10.02.2017 | 08:55:25 | 39.5236 | 26.1755 | 7.8 | Mw 5.0 | 154.00 | 52.00 | -71.00 | 304.00 | 42.00 | -113.00 | AFAD |
| 15 | 12.02.2017 | 12:14:50 | 39.5496 | 26.1183 | 5.4 | Mw 4.0 | - | - | - | - | - | - | AFAD |
| 16 | 12.02.2017 | 13:48:16 | 39.5336 | 26.17 | 7 | Mw 5.3 | 107.00 | 49.00 | -115.00 | 322.00 | 47.00 | -64.00 | AFAD |
| 17 | 16.02.2017 | 00:19:00 | 39.5 | 26.1 | 11 | Mw 4.6 | 116.00 | 43.00 | -85 | 291.00 | 47.00 | -93.00 | GFZ |
| 18 | 23.02.2017 | 01:55:14 | 39.5486 | 26.1225 | 9.5 | Mw 4.3 | - | - | - | - | - | - | AFAD |
| 19 | 27.02.2017 | 22:52:23 | 39.4975 | 26.0835 | 10.5 | Mw 4.0 | 96.00 | 29.00 | -117.00 | 307.00 | 64.00 | -76.00 | AFAD |
| 20 | 28.02.2017 | 23:27:34 | 39.492 | 26.0968 | 10.7 | Mw 4.7 | 138.00 | 41.00 | -65.00 | 286.00 | 53.00 | -110.00 | AFAD |
| 21 | 20.03.2017 | 07:00:18 | 39.5446 | 26.1765 | 4.6 | Mw 4.3 | 114.00 | 39.00 | -105.00 | 313.00 | 53.00 | -78.00 | AFAD |
| 22 | 24.03.2017 | 15:19:06 | 39.5541 | 26.1126 | 9.6 | Mw 4.2 | 41.00 | 75.00 | 167.00 | 135.00 | 77.00 | 15.00 | AFAD |

a considerable amount of thermal anomaly to the overthickening lithosphere, and so, triggered both the orogenic collapse (Dewey, 1988) and the emergence of tensional forces (Dewey, 1988; Pinet and Colletta, 1990). Consequently, the contractional period was replaced by the tensional tectonic period during latest Oligocene-early Miocene (Seyitoğlu and Scott, 1991; Koçyiğit et al., 1999; Koçyiğit, 2005). This extensional tectonic regime began to affect the whole of the west and southwestern Anatolia at a regional scale throughout the Miocene-early Pliocene time, except for the intervening shortterm compressional episodes. Thus, the west-southwestern Anatolia has been divided into numerous grabens and horsts of dissimilar trend, size and age by the normal faulting. One of them was the WNW-trending older Edremit graben of palaeotectonic origin (Figure 14a).

From the tectonic point of view, there were two domains at the earlier site of both the study area and older Edremit graben during the late Oligocene. These are the western Ezine and the eastern Kazdağ areas. They were being separated by an intervening, NNE-trending and west-northwesterly dipping thrust-reverse fault zone (a mylonitic zone) (Siyako et al., 1989; Okay et al., 1990; Yılmaz and Karacık, 2001; Beccaletto and Steiner, 2005). The Kazdağ area is composed of relatively high-grade metamorphic rocks, such as amphibolite schist, gneiss and metabasites overlain tectonically by the Permo-Triassic Karakaya Complex (1a and 2 in Figure 14a) (Okay et al., 1990; Yılmaz and Karacık, 2001). The Ezine area is made up of low-grade metamorphic rocks (Karadağ metamorphic rocks) of various schist, recrystallized limestone and dolomite overlain tectonically by the combination of a thick ultrabasic to basic oceanic crust slab and mélange (Düzgören ophiolite and the Çetmi Mélange) (1b and 3 in Figure 14a) (Okay et al., 1990). These two tectonic domains were under the influence of the erosional processes occupied partly by lakes in places during the late Oligocene (Figure 14a). Starting from latest Oligocene onwards, both areas became the site of a widespread calc-alkalic volcanic activity under the control of the N-S directed extensional stress regime, in which the major principal stress axis ($\sigma 1$) is more or less vertical to subvertical in position. This is evidenced by the N-S trending line of volcanic centers, the Upper Oligocene-Lower Miocene petrified wood (forest) in Lesvos Island (Katsikatsos et al., 1982), the WNW-trending older Edremit graben and its northern margin boundary normal fault (detachment fault) (Figure 14a). This time slice is also the commencement of the early exhumation phase of the Kazdağ Massif and the intrusion of granodioritic pluton (Evciler and Kestanbol plutons) into both tectonic domains (4 in Figure 14a) (Beccaletto and Steiner, 2005; Şahin et al., 2010). The volcanic activity continued up to the end of the middle Miocene and accompanied to the sedimentation in a deep lake across the older Edremit graben. So, a thick volcano-sedimentary sequence formed. This continental sedimentary sequence began with a package of relatively fine grained sandstone-siltstone at the bottom and then continued upward with the alternation of thin-bedded to laminated siltstone, mudstone, bituminous shale, limestone, turbiditic sandstone, tuff-tuffite, volcanic breccia, ignimbrite and various felsic lavas (Ayvacık and Balabanlı Volcanics) (5 and 6 in Figure 14a). Later on, this volcanic activity and the graben formation were interrupted by an intervening short and relatively local compressional stress regime at the end of middle Miocene time. This is evidenced by both the folds (open and box to isoclinal folds) developed in the volcano-sedimentary sequence, and the variation in the geochemical composition of volcanic rocks, e.g., transition from calc-alkalic nature to the subalkalic and alkalic character of the volcanic rocks (Yılmaz and Karacık, 2001). The sedimentation was lasted in a fluvio-lacustrine depositional setting along its western margin opened to the Aegean Sea waters. A subalkalic and alkali olivine basaltic volcanic activity (Ezine olivine basalt) has also accompanied to the sedimentation during late Miocene-Pliocene time. Thus, another continental sedimentary sequence with the shallow-marine intercalations (Gülpınar group) developed (Figure 2). But, the major inversion in the study area occurred in the extensional stress regime, as well as those all over Anatolian platelet, at the beginning of Quaternary (Hempton, 1987; Koçyiğit and Beyhan, 1998; Koçyiğit et al., 2000, 2001; Koçyiğit and Özacar, 2003; Çolak et al., 2012; Koçyiğit, 2013; Koçyiğit and Canoğlu, 2017).

### 5.2. Neotectonic History

The geologically complicated deformation pattern of Turkey has been formed by the entire demise of the southern Tethyan seaway, the Bitlis Ocean, between Indian Ocean and Mediterranean Sea, and by the continent-continent collision of northerly moving

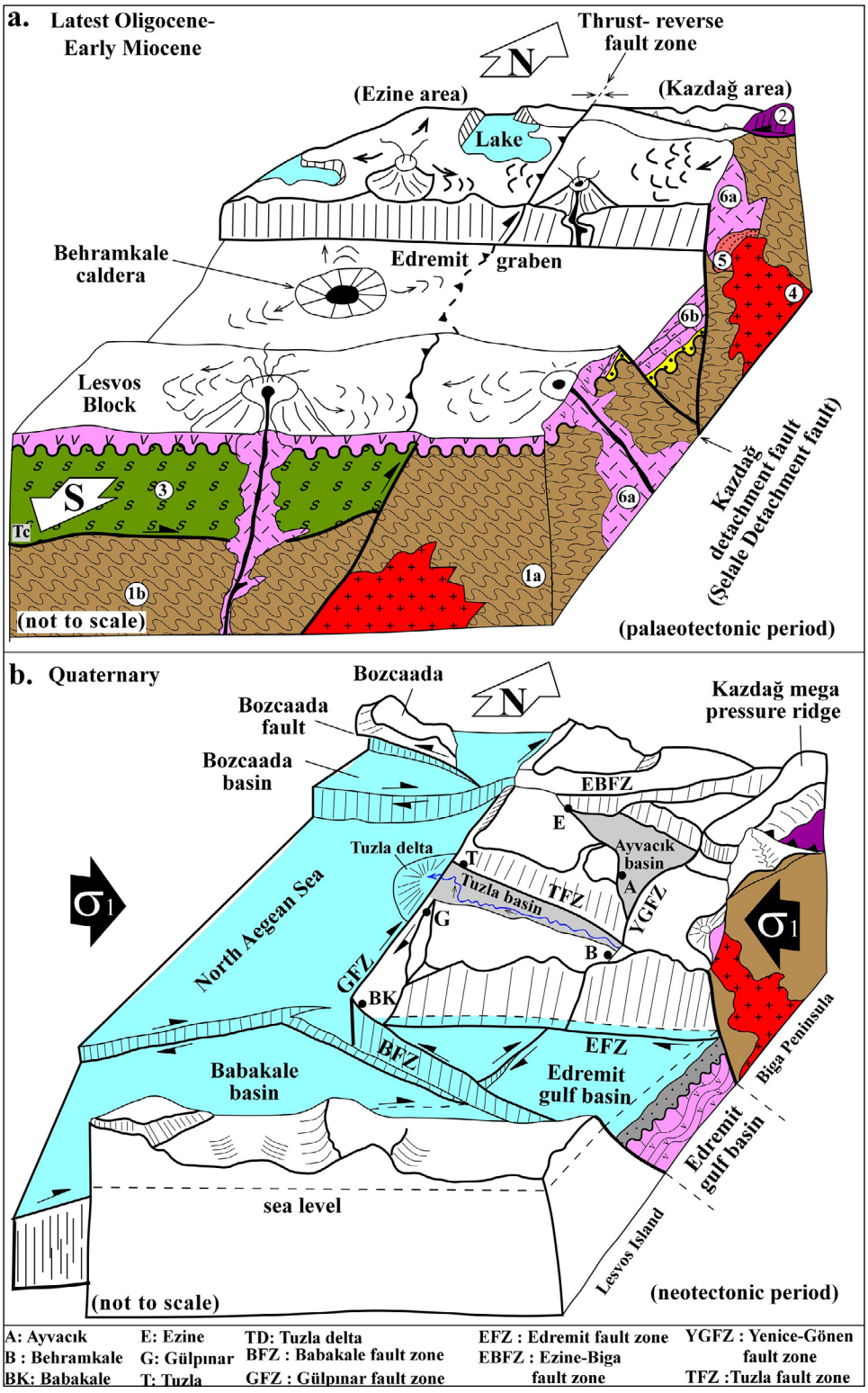


Figure 14- a) Tensional tectonic regime and graben-horst formation by the N-S directed ex-tension (white diverging arrows) (Miocene-Pliocene). 1. Karadağ and Kazdağ metamorphic rocks of Paleozoic-Triassic age, 2. Karakaya Complex of Permo-Triassic age, 3. Ophiolitic rocks of late Cretaceous age, 4-5. Granodiorite pluton and related hypabissal rocks, 6a. Calc-alkaline volcanic rocks, 6b. volcano-sedimentary sequence of terrestrial origin (older graben fill), TC. Tectonic contact, b) strike-slip neotectonic regime and development of present day configuration of the southwest tip of Biga Peninsula by the major compressive stress ope-rating in approximately WNW direction (black converging arrows) (Quaternary).

Arabian plate with the Eurasian plate in the Late Serravalian (Şengör and Yılmaz, 1981; Dewey et al., 1986). These authors accept this time slice as the onset age of the neotectonic regime in Turkey. After final collision and formation of the Bitlis suture zone, the N-S-directed intracontinental convergence between the Arabian and Eurasian plates continued over a time period of ~9 Ma. This time slice is here termed as the transitional period between the contractional palaeotectonic and the strike-slip neotectonic regimes. During this transitional period, a series of deformations such as the thickening of crust, regional tectonic uplift, formation of folds with E-W-trending axis, thrust to reverse faults, resetting of new drainage system, disappearance of marine conditions, development of short- to long-term stratigraphic gaps and prominent calc-alkaline volcanic activity occurred (Şengör and Kidd, 1979; Innocenti et al., 1980; Dewey et al., 1986; Şaroğlu and Yılmaz, 1986; Yılmaz et al., 1987; Ercan et al., 1990; Koçyiğit and Beyhan, 1998; Koçyiğit et al., 2001; Koçyiğit, 2013). The contractional deformation and development of fold-thrust belts continued until the latest Pliocene, and then this transitional period was replaced by the emergence of a new tectonic regime (prominent strike-slip faulting-related tectonic regime) (Koçyiğit et al., 2001; Aksoy et al., 2007; Çolak et al., 2012; Koçyiğit, 2013; Koçyiğit and Canoğlu, 2017). It is evidenced by the occurrence of a series of inversions such as the deformation style of faulting, types of geological structures, the nature of sedimentation and basin formation, geochemical characteristics of the volcanic activity (e.g., from calc-alkali nature to prominent alkali composition) and the nature of seismic activity. Hence the initiation age of strike-slip-dominated neotectonic regime is latest Pliocene (Koçyiğit et al., 2001). This is also proved by a regional angular unconformity separating the intensely deformed Pre-Quaternary paleotectonic rock units from the nearly flatlying Quaternary units (Koçyiğit et al., 2001).

Starting from latest Pliocene-early Quaternary onwards, the southern frontal part of the Eurasian plate was fragmented and divided into several mega and numerous micro blocks resulting in the Anatolian platelet and its margin-boundary faults, such as the dextral NAFS and the sinistral EAFS, along which the Anatolian platelet started to escape in WSW direction onto the oceanic lithosphere of the African Plate (Hempton, 1987; Koçyigit and Beyhan, 1998). In Aegean Sea, the westward motion of the Anatolian platelet was blocked and forced to move in south-southwestward by a barrier, the mainland of northern Greece. Thus, this variation in the motion direction of plate, resulted in a regional principal compressive stress ($\sigma 1$) operating in approximately E-W direction (Şengör, 1980), and led to the emergence of a new neotectonic regime and province, the central to northern Aegean neotectonic province. One of the well-developed structures of this strike-slip neotectonic province is the NE-trending Balıkesir-İzmir dextral strike-slip fault zone (BİFZ) (Koçyiğit, 2020) (Figures 1a and 11). It was an originally palaeotectonic structure. In the present it forms a transitional zone between the easterly located extensional and westerly located strike-slip faulting-dominated neotectonic domains. Our study area is included in the central to northern Aegean neotectonic province. The structures and related seismic activity in the study area are the records of this new strike-slip neotectonic regime. It is being dominated by the well-developed strike-slip faulting pattern (Figures 4 and 3b), not an extensional stress regime reported by some of previous researchers (Yılmaz and Karacık, 2001; Beccaletto and Steiner, 2005; Emre and Doğan, 2010). This is the major difference between our idea and those of most of previous workers. The strike-slip faulting pattern is composed of NW- and NE-trending strike-slip faults, E–W to WNW-trending oblique-slip normal faults and an approximately NNE-trending thrust to reverse faults (Figures 3a, b and 4). This is evidenced by both the focal mechanism solution diagrams of earthquakes sourced from these faults and the palaeostress analysis of slip plane data measured on fault slickensides (Figures 3a and 8). Consequently, at a regional scale the Biga Peninsula, and at the local scale the study area gained their present day configuration under the control of the strike-slip neotectonic regime during Quaternary. This regime is still lasting under the control of the same tectonic regime and related faulting pattern (Figures 4 and 14b). It was proved once more by the occurrence of the Gülpınar-Tuzla earthquake cluster of strike-slip tectonic origin. In a short time period of 2017.02.06-2017.03.24, at least seven moderate-to small-sized independent earthquakes occurred in the Gülpınar-Tuzla (Ayvacık-Çanakkale) area. These are, in turn, the Gülpınar, Kızılkeçili, Kocaköy, Çamtepe, Yukarıköy, Derecikbağ and Hatiptepe earthquakes respectively (No.1, 3, 5, 14, 16, 13 and 22 on Table

2). The first five seismic events are the normal faulting-induced earthquakes, while the latter two are related to strike-slip faulting in origin. Based on the earthquakes parameters such as the dip amount to dip direction, focus depth, epicenter site and the patterns of the focal mechanism solution diagrams, the first five earthquakes seem to have been originated from the southerly dipping Çamköy, Tuzla, Taşağıl and Yukarıköy normal faults respectively. The latter two earthquakes were sourced from the Hatiptepe strike-slip fault, i.e., both the Tuzla normal fault zone and the Gülpınar strike-slip fault zone were reactivated by the occurrence of the Gülppınar-Tuzla earthquake cluster. The patterns of focal mechanism solution diagrams reveal a stress system, in which the major principal stress ($\sigma_1$) is operating in approximately WNW direction, while the intermediate stress ($\sigma_2$) operates vertically and the least principal stress ($\sigma_3$) horizontally in NNE direction respectively. This stress system indicates that the Gülpınar-Tuzla earthquake area, which is included in the central to northern Aegean Sea neotectonic province, has been experiencing a strike-slip neotectonic regime since at least early Quaternary.

In general, the geodetic slip rate throughout the NAFS ranges from 20 mm/yr to 30 mm/yr (Barka and Reilinger, 1997; McClusky et al., 2000; Reilinger et al., 2006; Dolan and Meade, 2017). However, the NAFS is divided into two major strands, namely the northern and southern strands, respectively, in the Marmara region. Accordingly the slip rate on it is also partitioned by these two strands. In most of geodetic studies, the Marmara region is taken into account as a single block or a geodetic velocity field bounded by the northern strand in the north and by the southern strand in the south (Meade et al., 2002; Aktuğ et al., 2009). They also accepted that these boundary strands consist of single fault zones such as the northerly located Kuzey Marmara-Ganos Fault Zone and the southerly located Yenice-Gönen Fault Zone, i.e., other fault zones comprising the southern strand were ignored. According to the geodetic data, the slip rate on the northern strand is faster than those on the southern strand. It ranges from 24 mm/yr to 10 mm on the northern strand, and from 12 mm/yr to 4 mm/yr on the southern strand (Meade et al., 2002; Flerit et al., 2003; Aktuğ et al., 2009; Gasperini et al., 2011; Kurt et al., 2013).

In contrast to the geodetic studies, the southern strand of the NAFS consists of multiple fault zones of dissimilar character ranging from strike-slip fault to oblique-slip normal fault (Koçyiğit, 2000, 2006, 2011, 2012). These are, from north to south, the Çan-Biga, Sarıköy-İnova, Yenice-Gönen and the Edremit fault zones on the land (Figures 1 and 3b). In the same way, the slip rate on the southern strand is also partitioned among these fault zones. Based on the morphotectonic markers (mostly offset drainage systems) the average geologic slip rates on the Çan-Biga, Sarıköy-İnova, Yenice-Gönen, and Edremit fault zones are 7.7 mm/yr, 4.6 mm/yr, 10.8 mm/yr and 7.3 mm/yr respectively. The total slip rate on the southern strand is approximately 30 mm/yr. The geologic slip rate seems to contradict with the geodetic slip rate. This can be explained in two ways: 1) the drainage systems have not been displaced by the fault zones, i.e., they followed the fault zone of weakness after they have entered into them; 2) they have been offset by the related fault zones. In our study, the second possibility was preferred. Because, the Aegean Sea and southwest Anatolia altogether move at a rate of 30-40 mm/yr on the asthenosphere in SSW direction (Barka and Reilinger, 1997). This relatively faster motion leads to internal deformation, i.e., accumulation of high elastic strain in the overlying Anatolian platelet. This high elastic strain can't be accommodated by slow slip rate along fault zones. Therefore the total slip rate on the southern strand must be faster than the abovementioned geodetic slip rates on the southern strand of the NAFS. For this reason, the central to northern Aegean Sea and its eastern coastal areas bounded by the BİFZ must be evaluated under a separate neotectonic domain.

## 6. Results

The central to northern Aegean Sea and its coastal areas are a new neotectonic domain characterized by prominent strike-slip faulting. For this reason, fault-bounded depressions in it are pull-apart basins of dissimilar shape and origin. Its eastern approximate boundary is the Balıkesir-İzmir Fault Zone (BİFZ) located between Lake Ulubat in the NNE and Samos Island in the SSW. This Quaternary neotectonic domain is governed by the WNW-directed operation of principal compressive stress ($\sigma_1$). The Biga Peninsula and our study area are also included in this domain shaped mostly by the southern strand of the NAFS. The total slip rate on this strand is about 30 mm/yr. But

it is partitioned by four major and numerous second- and third-order fault zones to single faults. Therefore, return period of peak earthquakes with Mw 6.5 or greater than it to be sourced from major fault zones, such as the Çan-Biga, Sarıköy-İnova, Yenice-Gönen and Edremit fault zones, will be at least 400 hundred years or longer than it. However, the return periods of small earthquakes are shorter than 400 hundreds years. This was proved once more by the occurrence of the Gülpınar-Tuzla earthquake cluster.

The most active and well-known structure of the southern strand is the YGFZ. It consists of onshore Biga and the offshore Behramkale-Skyros sections. The master fault (Y-shear) of the southern strand is included in the YGFZ. The age of the YGFZ is early Quaternary (approximately 2.6 ma yr. BP), and the total right lateral strike-slip displacement accumulated on it is about 28 ± 2 km. This value implies an average uniform slip rate of 10.8 mm/yr. The Yenice-Gönen section of the master fault reactivated and caused the occurrence of the 18 March 1953 Yenice destructive earthquake and the 40 km long surface rupture. The average coseismic dextral strike-slip displacement was 4.2 m during this big earthquake (Ms = 7.4). The recurrence interval of the big earthquakes to be sourced from the southern major strand of the NAFS seems as at least 400 years based on the uniform slip rate (10.8 mm/yr) and the coseismic dextral displacement.

## References


AFAD. 2017. Disaster and Emergency Management Presidency, Earthquake Catalog.

Aksoy, M. E., Meghraouil, M., Vallée, Çakır, Z. 2010. Rupture characteristics of the A. D. 1912 Mürefte (Ganos) earthquake segment of the North Anatolian fault (western Turkey). Geology 38(11), 991-994.

Aksoy, E., İnceöz, M., Kocyiğit, A. 2007. Lake Hazar basin: a negative fl ower structure on the East Anatolian fault system (EAFS), SE Turkiye. Turkish Journal of Earth Sciences 16, 319-338.

Aktuğ, B., Nocquet, J. M., Cingöz, Z., Parsons, B., Erkan, Y., England, P., Lenk, O., Gürdal, M. A., Kılıçoğlu, A., Akdeniz, H., Tekgül, A. 2009. Deformation of Western Turkey from a combination of permanent and campaign GPS data: Limits to blocklike behavior. Journal of Geophysical Research 114, B10404.

Altınok, Y., Alpar, B., Yaltırak, C., Pınar, A., Özer, N. 2012. The earthquakes and related tsunamis of October 6, 1944 and March 7, 1867; NE Aegean Sea. Natural Hazards 60, 3-25.

Ambraseys, N. N. 1988. Engineering seismology. Journal of Earthquake Engineering and Structure Dynamics 17, 1-105.

Ambraseys, N. N., Finkel, C. 1995. The Seismicity of Turkey and Adjacent Areas: A Historical Review. 1500-1800. Eren Yayıncılık, İstanbul, 240.

Ambraseys, N., Jackson, J. 1998. Faulting associated with historical and recent earthquakes in the Eastern Mediterranean. Geophysical Journal International 133, 390-406.

Barka, A. A., Kadinsky Cade, K. 1988. Strike-slip fault geometry in Turkey and its influence on earthquake activity. Tectonics 7, 66-684.

Barka, A., Reilinger, R. 1997. Active tectonics of the eastern Mediterranean region: deduced from GPS, neotectonic, and seismicity data. Annali Di Geofisica 40(3), 587-610.

Beccaletto, L., Steiner, C. 2005. Evidence of two-stage extensional tectonics from the northern edge of the Edremit graben, NW Turkey. Geodinamica Acta 18, 283-297.

Borsi, J., Ferrara, G., Innocenti, F., Mazzuoli, R. 1972. Geochronology and petrology of recent volcanics in the Eastern Aegean Sea (West Anatolia and Lesvos Island). Bulletin of Volcanology 36, 473-496.

Bozkurt, E. 1996. Metamorphism of Paleozoic schists in the Southern Menderes Massif: field, petrographic, textural and microstructural evidence. Turkish Journal of Earth Sciences 5, 105-121.

Bozkurt, E. 2004. Granitoid rocks of the southern Menderes Massif (southwestern Turkey): field evidence for Tertiary magmatism in an extensional shear zone. International Journal of Earth Sciences (Geologische Rundschau) 93, 52-71.

Bozkurt, E., Park, R. G. 1997. Evolution of a mid-Tertiary extensial shear zone in the southern Menderes Massif, Western Turkey. Bulletin De La Societe Géologique De France 168, 3-14.

Bozkurt, E., Park, R. G. 1999. The structure of the Paleozoic schists in the Southern Menderes Massif, Western Turkey: a new approach to the origin of the main Menderes metamorphism and its relation to the Lycian Nappes. Geodinamica Acta 12, 25-42.

Brunn, J. H., Graciansky, P. C., Gutnie, M., Juteau, T. H., Fevere, R., Marcous, J., Monod, O., Poisson, A. 1971. Structures majeurs et correlations stratigraphiques dans Taurides occidentals: Bulletin Geological Society of France 12, 516-556.

Çolak, S., Aksoy, E., Koçyiğit, A., İnceöz, M. 2012. Palu-Uluova strike-slip basin on the East Anatolian Fault System, Turkey: transition from paleotectonic period to neotectonic period. Turkish Journal of Earth Sciences 21(4), 547-570.

Dewey, J. F., Hempton, M. R., Kidd, W. S. F., Şaroğlu, F., Şengör, A. M C. 1986. Shortening of continental lithosphere: the neotectonics of Eastern Anatolia - a young collision zone. Coward, M.P., Ries, A.C. (Ed.). Collisional Tectonics. Geological Society, London, Special Publications 19, 3-36.

Dewey, J. F. 1988. Extensional collapse of orogens. Tectonics 7, 1123-1139.

Dolan, J. F., Meade, B. J., 2017. A comparison of geodetic and geologic rates prior to large strike-slip earthquakes: a diversity of earthquake-cycle behaviors? Geochemistry, Geophysics, Geosystems 18.

Emre, T., Sözbilir, H. 2005. Küçük Menderes Grabeni doğu ucundaki andezitlerin (Başova-Kiraz/İzmir) jeolojisi, petrografisi ve jeokimyası. Bulletin of the Mineral Research and Exploration 131, 1-19.

Emre, Ö., Doğan, A. 2010. 1/250000 ölçekli Türkiye aktif fay haritaları serisi, Ayvalık (NJ 35-2) paftası (Seri No: 4). Maden Tetkik ve Arama Genel Müdürlüğü (MTA), Ankara.

EMSC. 2020. European-Mediterranean Seismological Centre.

Ercan, T., Satır, M., Kreuzer, H., Türkecan, A., Günay, E., Çevikbaş, A., Ateş, M., Can, B. 1985. Batı Anadolu Senozoyik volkanitlerine ait yeni kimyasal, izotopik ve radyometrik verilerin yorumu. Geological Society of Turkey Bulletin 28, 121-136 (In Turkish with English abstract).

Ercan, T., Fujitani, T., Madsuda, J. I., Notsu, K., Tokel, S., Ui, T. 1990. Doğu ve Güneydoğu Anadolu Neojen-Kuvaterner volkaniklerine ilişkin yeni jeokimyasal, radiometrik ve izotopik verilerin yorumu. Bulletin of the Mineral Research and Exploration 110, 143-164.

Ercan, T., Satır, M., Dora, A., Sarıkoğlu, E., Yıldırım, T., Adis, C., Walter, H. J., Özbayrak, İ. H. 1995. Biga Yarımadası, Gökçeada, Bozcaada ve Tavşan Adaları'ndaki Tersiyer yaşlı volkanitlerin petrolojisi ve bölgesel yayılımı. Bulletin of the Mineral Research and Exploration 117, 55-86.

Erkül, F., Helvacı, C., Sözbilir, H. 2005*a*. Stratigraphy and geochronology of the Early Miocene volcanic units in the Bigadiç borate basin, western Turkey. Turkish Journal of Earth Sciences 14, 227-253.

Erkül, F., Helvacı, C., Sözbilir, H. 2005*b*. Evidence for two episodes of volcanism in the Bigadic¸ borate basin and tectonic implications for western Turkey. Geological Journal 40, 545-570.

Eryılmaz, M., Yücesoy Eryılmaz, F. 1999. Ege Denizi'nin tektonik yapısı. 52. Türkiye Jeoloji Kurultayı Bildiriler Kitabı, 10-12 Mayıs. Ankara, 358-365.

Flerit, F., Armijo, R., King, G. C. P., Meyer, B., Barka, A. 2003. Slip partitioning in the Sea of Marmara pull-apart determined from GPS velocity vectors. Geophysical Journal International 154**,** 1-7.

Gasperini, L., A. Polonia, Çağatay, N., Bortoluzzi, G., Ferrante, V. 2011. Geological slip rates along the North Anatolian Fault in the Marmara region. Tectonics 30, TC1010.

GCMT. 2017. Global Centroid Moment Tensor Catalog. Harvard University, USA.

GCMT. 2020. Global Centroid Moment Tensor Catalog. Harvard University, USA.

Genç, Ş. C. 1998. Evolution of the Bayramiçi magmatic complex. Journal of Volcanology and Geothermal Research 85, 233-249.

Gevrek, A. İ., Şener M, Ercan, T. 1985. Çanakkale-Tuzla jeotermal alanının hidrotermal alterasyon etüdü ve volkanik kayaçların petrolojisi. Bulletin of the Mineral Research and Exploration 103-104, 82-103.

GFZ. 2017. German Research Centre for Geosciences.

Glodny, J., Hetzel, R. 2007. Precise U–Pb ages of syn-extensional Miocene intrusions in the central Menderes Massif, western Turkey. Geological Magazine 144, 235–246.

Güney, A., Yılmaz, Y., Demirbağ, E., Ecevitoğlu, B., Arzuman, S., Kuşçu, İ. 2001. Reflection seismic study across the continental shelf of Baba Burnu promontory of Biga Peninsula, Northwest Turkey. Marine Geology 176, 75-85.

Gürer, Ö. F., Sangu, E., Özburan, M., Gürbüz, A., Gürer, A., Sinir, H. 2016. Plio-Quaternary kinematic development and paleostress pattern of the Edremit Basin, western Turkey. Tectonophysics 679, 199-210.

Harris, N. B. W., Pearce, J. A., Tindle, A. G. 1986. Geochemical Characteristic of Collision-Zone Magmatism. Coward, M. P., Reis, A. C. (Ed.). In Collision Tectonics. Geological Society of London, Special Publication 19, 67-81.

Harvard. 2017. GCMT catalogue.

Hempton, M. R. 1987. Constraints on Arabian plate motion and extensional history of Red Sea. Tectonics 6, 687-705.

Herece, E. 1985. The fault trace of 1953 Yenice Gönen Earthquake and Some Examples of Recent Tectonic Events in the Biga Peninsula of Northwest Turkey. MSc Thesis, Pennsylvania State University, 143, US (unpublished).

Herece, E. 1990. 1953 Yenice-Gönen deprem kırığı ve Kuzey Anadolu fay sisteminin Biga Yarımadası'ndaki uzantıları. Bulletin of the Mineral Research and Exploration 111, 47-59.

Innocenti, F., Pısa, R., Mazzuoli, C., Pasquare, G., Serri, G., Villari, L. 1980. Geology of the volcanic area north of Lake Van (Turkey). Geologische Rundschau 69, 292-322.

Kalafat, D., Güneş, Y., Kekovalı, K., Kara, M., Deniz, P., Yılmazer, M. 2011. Türkiye için 1900 yılından bu yana revize edilmiş ve genişletilmiş deprem kataloğu (M≥4.0). Boğaziçi University Publications 1049, 640.

Karacık, Z., Yılmaz, Y. 1998. Geology of ignimbrites and the associated volcano-plutonic complex of the Ezine area, Northwestern Anatolia. Journal of Volcanology and Geothermal Research 85, 251-264.

Karakaisis, G. F., Papazachos, C. B., Scordilis, E. M. 2010. Seismic sources and main seismic faults in the Aegean and surrounding area. Bulletin of the Geological Society of Greece 43(4), 2026-2042.

Katsikatsos, G., Mataragas, D., Migiros, G., Triandafillou, E. 1982. Geological study of Lesbos Island. IGME, Special Report No: 92.

Ketin, I., Roesly, F. 1953. Makroseismische untersuchungen über das nord-westanatolische Beben vom 18 Marz 1953. Eclogae Geologicae Helvetiae 46(2), 187-208.

Kiratzi, A. A., Wagner, G. S., Langston, C. A. 1991. Source parameters of some large earthquakes in Northern Aegean determined by body waveform inversion. Pure and Applied Geophysics 135, 515-527.

Koçyiğit, A. 1983. Hoyran gölü (Isparta Büklümü) dolayının tektoniği. Geological Society of Turkey Bulletin 26, 1-10 (In Turkish with English abstract).

Koçyiğit, A. 1984. Güneybatı Türkiye ve yakın dolayında levha içi yeni tektonik gelişim. Geological Society of Turkey Bulletin 27, 1-16 (In Turkish with English abstract).

Koçyiğit, A. 2000. Güneybatı Türkiye'nin depremselliği. Symposium on the Seismicity of Western Turkey (Badsem) 2000 Abstracts and Proceedings 30, 2000, 30-38 (In Turkish with English abstract).

Koçyiğit, A. 2005. Denizli Graben-Horst System and the eastern limit of the West Anatolian continental extension: basin fill, structure, deformational mode, throw amount and episodic evolutionary history, SW Turkey. Geodinamica Acta 18, 167-208.

Koçyiğit, A. 2006. Çan kömür havzasının jeolojik yapısı, yapısal analizi ve fayların kazılara etkisi. ODTÜ, Mühendislik Fakültesi, Jeoloji Mühendisliği Bölümü, Aktif Tektonik ve Deprem Araştırma Laboratuvarı, Proje No. 2006-03-05-2-00-13, 20 (unpublished).

Koçyiğit, A. 2011. Gönen (Balıkesir) ruhsat sahalarının aktif tektonik yönden değerlendirilmesi. ODTÜ, Jeoloji Mühendisliği Bölümü, Aktif Tektonik ve Deprem Araştırmaları Laboratuvarı, Proje No: 11-03-09-1-0018, 43 (unpublished).

Koçyiğit, A. 2012. Saruhanlı (Manisa) ruhsat sahaları jeotermal potansiyelinin Aktif tektonik yönden değerlendirilmesi. Middle East Technical University, Enginering Faculty, Department of Geological Engineering, Active Tectonic and Earthquake Research Laboratory, Report, 31 (unpublished).

Koçyiğit, A. 2013. New field and seismic data about the intraplate strike-slip deformation in Van region, East Anatolian plateau, E. Turkey. Journal of Asian Earth Sciences 62, 586-605.

Koçyiğit, A. 2020. İzmir ili Seferihisar ilçesi 2107 nolu jeotermal işletme ruhsatı ile 1586 nolu arama ruhsatlarının bulunduğu sahanın jeolojik çalışması ve toplanan verilerin değerlendirilmesiyle igili teknik rapor. Middle East Technical University, Department of Geological Engineering, Active Tectonics and Earthquake Research Labaratory, 81, Ankara.

Koçyiğit, A., Beyhan, A. 1998. A new intracontinental transcurrent structure: the Central Anatolian Fault Zone, Turkey. Tectonophysics 284, 317-336.

Koçyiğit, A., Özacar, A. 2003. Extensional neotectonic Regime through the NE edge of the outer Isparta angle, SW Turkey: new field and seismic data. Turkish Journal of Earth Sciences 12, 67-90.

Koçyiğit, A., Canoğlu, M. C. 2017. Neotectonics and seismicity of Erzurum pull-apart basin, East Turkey. Russian Geology and Geophysics 58, 99-122.

Koçyiğit, A., Yusufoğlu, H., Bozkurt, E. 1999. Evidence from the Gediz graben for episodic two-stage extension in Western Turkey. Journal of the Geological Society of London 156, 605-616.

Koçyiğit A. Ünay, E., Saraç, G. 2000. Episodic graben formation and extensional neotectonic regime in west Central Anatolia and the Isparta Angle: a key study in the Akşehir-Afyon graben, Turkey. Geological Society of London, Special Publications 173, 405-421.

Koçyiğit, A., Yılmaz, A., Adamia, S., Kuloshvili, S. 2001. Neotectonic of East Anatolian Plateau (Turkey) and Lesser Caucasus: implication for transition from thrusting to strike-slip faulting. Geodinamica Acta 14, 177-195.

Koukouvelas, I. K., Aydın, A. 2002. Fault structure and related basins of the North Aegean Sea. Tectonics 21(5), 1046.

Kurt, H., Sorlien, C. C., Seeber, L., Steckler, M. S., Shillington, D. J., Çifçi, G., Cormier, M. H., Dessa, X., Atgin, O., Dondurur, D., Demirbağ, E., Okay, S., İmren, C., Gürçay, S., Carton, H. 2013. Steady late quaternary slip rate on the Çinarcik section of the North Anatolian fault near Istanbul, Turkey. Geophysical Research Letter 40, 4555-4559.

Kurtuluş, C., Doğan, B., Sertçelik, F., Canbay, M., Küçük, H. M. 2009. Determination of the tectonic evolution of the Edremit Gulf based on seismic reflection studies. Marine Geophysical Research 30, 121-134.

Kürçer, A. 2006. Neotectonic features of the vicinity of Yenice - Gönen and paleoseismology of March 18, 1953 (Mw: 7.2) Yenice - Gönen Earthquake Fault (NW Turkey). MSc Thesis, Çanakkale Onsekiz Mart University.

Kürçer, A., Chatzipetros, A., Tutkun, S. Z., Pavlides, S., Ateş, Ö., Valkaniotis, S. 2008. The Yenice-Gönen active fault (NW Turkey): active tectonics and palaeoseismology. Tectonophysics 453, 263-275.

Kürçer, A., Yalçın, H., Gülen, L., Kalafat, D. 2015. 8 January 2013 Mw = 5.7 North Aegean Sea earthquake and its seismotectonic significance. Geodinamica Acta 27, 175-188.

Kürçer, A., Özalp, S., Özdemir, E., Uygun Güldoğan, Ç., Duman, T. Y., 2019. Active tectonic and paleoseismologic characteristics of the Yenice-Gönen Fault, NW Turkey, in light of the 18 March 1953 Yenice-Gönen Earthquake (Ms=7.2). Bulletin of the Mineral Research and Exploration 159, 29-62.

McClusky, S., Balassanian, S., Barka, A., Demir, C., Ergintav, S., Georgiev, I., Gürkan, O., Hamburger, M., Hurst, K., Kahle, G. H., Kastens, K., Kekelidze, G., King, R., Kotzev, V., Lenk, O., Mahmoud, S., Mishin, A., Nadariya, M., Ouzounis, A., Paradissis, D., Peter, Y., Prilepin, M., Reilinger, R., Sanli, I., Seeger, H., Tealeb, A., Toksöz, M. N., Veis, G. 2000. Global positioning system constrains on plate kinematics and dynamics in the Eastern Mediterranean and Caucasus. Journal of Geophysical Research B3(105), 5695-5719.

Meade, B. J., Hager, B. H., McClusky, S., Reilinger, R. E., Ergintav, S., Lenk, O.,Özener, H. 2002. Estimates of seismic potential in the Marmara Sea region from block models of secular deformation constrained by global positioning system measurements. Bulletin of the Seismomlogical Society of America 92, 208-215.

Okay, A. 1986. High-pressure-low-temperature metamorphic rocks of Turkey. Geological Society of America Memoir 164, 333-347.

Okay, A. I., Siyako, M., Bürkan, K. A. 1990. Geology and tectonic evolution of the Biga Peninsula. Turkish Association of Petroleum Geologists Bulletin 2, 83-121.

Özgül, N. 1984. Torosların bazı temel jeoloji özellikleri. Bulletin of the Geological Society of Turkey 19, 65-78 (In Turkish with English abstract).

Papazachos, B. C. 2003. The earthquakes of Greece. Ziti Publications, Thessaloniki, 286.

Papazachos, B. C., Kiratzi, A., Hatzidimitriou, P., Rocca, A. 1984. Seismic faults in the Aegean area. Tectonophysics 106, 71-85.

Papazachos, B. C., Kiratzi, A., Papadimitriou, E. 1991. Regional focal mechanisms for earthquakes in the Aegean area. Pure Applied Geophysics 136, 405-420.

Papazachos, B. C., Papadimitriou, E. E., Kiratzi, A., Papazachos, B. C. 1998. Fault plane solutions in the Aegean Sea and the surrounding area and their tectonic implication. Bollettino Di Geofisica Teorica Ed Applicata 39, 3.

Pınar, N., Lahn, E. 1952. Türkiye depremleri izahlı kataloğu. Bayındırlık ve İskân Bakanlığı, İmar Reisliği Publications 6, 36, Ankara (in Turkish).

Pinet, B., Colletta, B. 1990. Probing into extensional sedimentary basins: comparison of recent data and derivation of tentative models. Tectonophysics 173, 185-197.

Reilinger, R., McClusky, S., Vernant, P., Lawrence, S., Ergintav, S., Çakmak, R., Karam, G. 2006. GPS constraints on continental deformation in the Africa-Arabia-Eurasia continental collision zone and implications for the dynamics of plate interactions. Journal of Geophysical Research 111(B05411).

Saka, K. 1979. Edremit Körfezi ve civarı Neojeni'nin jeolojisi ve hidrokarbon olanakları. Türkiye Petrolleri Anonim Ortaklığı, Rapor No: 1342, 17.

Seyitoğlu, G., Scott, B. C. 1991. Late Cenozoic crustal extension and basin formation in West Turkey. Geological Magazine 128, 155-166.

Siyako, M., Bürkan, K. A., Okay, A. İ. 1989. Tertiary geology and hydrocarbon potential of the Biga and Gelibolu peninsulas. Bulletin of Turkish Petroleum Geologists 1, 183-199.

Sözbilir, H. 2005. Oligo-Miocene extension in the Lycian orogen: Evidence from the Lycian molasse basin, Southwestern Turkey. Geodinamica Acta 18, 255-282.

Sözbilir, H., İnci, U., Erkül, F., Sümer, Ö. 2013. An active intermitten transform zone accommodating N-S extension in Western Anatolia and its relation to the North Anatolian Fault System International Workshop on the North Anatolian and Dead Sea Fault Systems: Recent Progress in Tectonics and Paleoseismology, and Field Training Course in Paleoseismology, Ankara.

Sözbilir, H., Özkaymak, Ç., Uzel, B., Sümer, Ö., Eski, S., Tepe, Ç. 2016. Palaeoseismology of the Havran-Balıkesir Fault Zone: evidence for past earthquakes in the strike-slip-dominated contractional deformation along the southern branches of the North Anatolian fault in northwest Turkey. Geodinamica Acta 28, 254-272.

Şahin, S. Y., Örgün, Y., Güngör, Y., Göker, A. F., Gültekin, A. H., Karacık, Z. 2010. Mineral and whole-rock geochemistry of the Kestanbol Granitoid (Ezine-Çanakkale) and its mafic mikrogranular enclaves in Northwestern Anatolia: evidence of felsic and mafic magma interaction. Turkish Journal of Earth Sciences 19, 101-122.

Şamilgil, E. 1983. Geothermal energy fields of Canakkale and Tuzla drillings. Bulletin of Geology Congress Turkey 4, 147-159.

Şaroğlu, F., Boray, A., Emre, Ö. 1987. Türkiye'nin aktif fayları. General Directorate of Mineral Research and Exploration, Report No: 8643, 394, Ankara (unpublished).

Şaroğlu, F., Yılmaz, Y., 1986. Doğu Anadolu'da neotektonik dönemdeki jeolojik evrim ve havza modelleri. Bulletin of the Mineral Research and Exploration 107, 73-94.

Şengör, A. M. C. 1980. Türkiye'nin neotektoniğinin esasları. Türkiye Jeoloji Kurumu, Conference Series 2, Ankara, 40.

Şengör, A. M. C., Kidd, W. S. F. 1979. Post-collisional tectonics of the Turkish-Iranian plateau and a comparison with Tibet. Tectonophysics 55, 361-376.

Şengör, A. M. C., Yılmaz, Y. 1981. Tethyan evolution of Turkey: a plate tectonic approach. Tectonophysics 75, 181-241.

Şengör, A. M. C., Satır, M., Akkök, R. 1984. Timing of tectonic events in the Menderes Massif, western Turkey: implications for tectonic evolution and evidence for Pan-African basement in Turkey. Tectonics 3, 693-707.

Tan, O. M., Tapırdamaz, C., Yörük, A. 2008. The earthquake catalogues for Turkey. Turkish Journal of Earth Sciences 17, 405-418.

Taymaz, T., Eyidoğan, H., Jackson, J. 1991. Source parameters of large earthquakes in the East Anatolian Fault Zone (Turkey). Geophysical Journal International 106, 537-550.

Uzel, B., Sözbilir, H. 2008. A first record of a strike-slip basin in Western Anatolia and its tectonic implication: The Cumaovası basin. Turkish Journal of Earth Sciences 17, 559-591.

Wells, D. L., Coppersmith, S. R. 1994. New empirical relationships among magnitude rupture length, rupture width, rupture area and surface displacement. Bulletin of the Seismological Society of America 84, 974-1002.

Wilson, M., Bianchini, G. 1999. Tertiary-Quaternary magmatism within the Mediterranean and surrounding regions. Geological Society of London, Special Publications 156, 141-166.

Yaltırak, C. 2003. Edremit Körfezi ve kuzeyinin jeodinamik evrimi. PhD Thesis, İTÜ Eurasia Institute of Earth Sciences, 242.

Yaltırak, C., İşler, E. B., Aksu, A. E., Hiscott, R. H. 2013. Evolution of the Bababurnu Basin and shelf of

the Biga Peninsula: Western extension of the middle strand of the North Anatolian Fault Zone, Northeast Aegean Sea, Turkey. Journal of Asian Earth Sciences 57, 103-119.

Yazman, M. 1996. Batı Anadolu Grabenleri Jeolojisi Gezisi (Field excursion on the geology of western Anatolian grabens). Türkiye Petrolleri Anonim Ortaklığı, Saha Raporu No: 13-20 August, 77.

Yılmaz, Y., Karacık, Z. 2001. Geology of the northern side of the Gulf of Edremit and its tectonic significance for the development of the Aegean grabens. Bozkurt, E. (Ed.). Neotectonics of Turkey. Geodinamica Acta 14, 31-43.

Yılmaz, Y., Şaroğlu, F., Güner, Y. 1987. Initiation of the neomagmatism in East Anatolia. Tectonophysics 134, 177-194.

Yılmaz, Y., Genç, S.C., Gürer, F., Bozcu, M., Yılmaz, K., Karacık, Z., Altunkaynak, S., Elmas, A. 2000. When did the Western Anatolian grabens begin to develop? Geological Society of London, Special Publications 173, 353-384.

Bulletin of the Mineral Research and Exploration

http://bulletin.mta.gov.tr

# Segmentation and classification algorithms applied to sentinel-2A images for geological mapping: case of the Al Glo'a sheet (1/50000), Morocco

Abdessamad EL ATILLAH[a]*, Mouhssine EL ATILLAH[b], Zine El Abidine EL MORJANI[a], Khalid EL FAZAZY[b] and Mustapha SOUHASSOU[a]

[a]*Ibn Zohr University, Polydisciplinary Faculty of Taroudant, Egerne, Taroundant, Morocco*
[b]*Computer Science, Signals, Automation and Cognitivism Laboratory (LISAC), FSDM, USMBA, Fes, Morocco*

*Research Article*

Keywords:
Segmentation Algorithms, Classification Algorithms, Sentinel 2A, Geological Mapping, Anti-Atlas.

**ABSTRACT**

The multispectral image, of Landsat 7 and 8; Aster and Sentinel-2A, has good results in lithological, structural, hydrothermal and mineralogical alteration mapping. Segmentation and image classification are two complementary steps as they are allowed the most important operations in the field of image processing. In this sense, this work aims at evaluating the potential of segmentation and classification algorithms for the generation of surface geological maps, hydrothermal alterations and lineaments. Given the good resolution of the Sentinel 2A (10m), the three images, (11/12; 11/2; 11/8), 12.8.2, main component 1, 2 and 3 (11.12.2), processed by five algorithms (K-means, isodata, watershed, efficient graph-based image segmentation, thresholding) for geological mapping and then mining exploration. The study displayed that 1) Watershed algorithm can be used for topographic and hydraulic studies, it can be very useful in the preparation phase of geological and mining infrastructures; 2) threshold segmentation does not give good results in terms of geological discrimination since it divides each image into two parts; 3) the same thing for the effective thresholding and segmentation of graph-based images; 4) The Isodata and K-means algorithms show good geological discrimination.

*Received Date: 25.08.2020*
*Accepted Date: 19.01.2021*

## 1. Introduction

The new Moroccan Mining Code, Law 33-13, has provided opportunities for exploration and research of a large-area of mineral resources through the introduction of the exploration permit with an area of 2.400 square kilometer maximum and the merger of research license.

The multispectral image (Landsat 7, Landsat 8 and Aster) processing generally have good results in litho-structural mapping. The Sentinel 2A image at 10 m resolution has shown great capacity in mapping areas with mineral potential by assembling lithological, structural and hydrothermal alteration data.

The aim of this work is to evaluate the potential of segmentation and classification algorithms for the generation of surface geological maps, hydrothermal alterations and lineaments. These areas may be the subject of a study on conventional methods of mining research to identify the physicochemical and mining characteristics of the geological formations of the Al Glo'a sheet (1/50000).

Citation Info: El Atillah, A., El Atillah, M., El Morjani, Z.E.A., El Fazazy, K., Souhassou, M. 2021. Segmentation and classification algorithms applied to sentinel-2A images for geological mapping: case of the Al Glo'a sheet (1/50000), Morocco. Bulletin of the Mineral Research and Exploration 166, 113-125. https://doi.org/10.19111/bulletinofmre.864492

**Corresponding author: Abdessamad EL ATILLAH, elatillah@gmail.com*

## 2. Local Geological Setting (Test Area)

The Al Glo'a sheet (1/50000) is a part of the Precambrian inlier of Bou Azzer El Graara of the Central Anti-Atlas in South East Morocco. This inlier (Figure 1) is a pivotal area whose study has greatly contributed to the improvement of our knowledge of the pan-African chain. The Precambrian outcrops along two contiguous massifs, Bou Azzer and El Graara, following a Variscan antiform structure that runs along the major accident of the Anti-Atlas (Choubert, 1947). Precambrian sites in the Bou Azzer-El Graara inlier can be divided into two large sets, one metamorphic, the other non-metamorphic which is discordant on the first (Oukassou, 2013).

The Tonien, Cryogenian, and Lower to Middle Ediacarean terrains (Precambrian II2 and II3) outcrop in the center of the Al Glo'a sheet (Figure 2), and they are covered elsewhere by a volcano-sedimentary cover of the Upper Ediacaran (Ouarzazate Group) then Lower Palaeozoic sedimentary (Soulaimani, et al., 2013).

## 3. Material and Method

Segmentation and classification are two complementary steps: segmentation consists of cutting out the elements constituting an image while classification is the identification to which category or class belongs each element or part of the image. In geology, categories or classes are known a priori in the case of supervised classification.

Image segmentation is one of the most important operations in the image processing field. Its purpose is to gather pixels together according to predefined criteria. The pixels are thus grouped into segments, which constitute a partition of the image. It can be for example to separate the objects from the bottom if the number of classes is equal to two, it is also called binarization (Maarir et al., 2014). The objective of this operation is to classify the image into homogeneous areas called segments. Thus, the segmentation of an image makes it possible to find forms or areas having a meaning for the user or for another image processing operation (Dupas, 2009). The methods used are based on contour detection, threshold, histogram, region-based methods and watershed transformation (Khan, 2014). This technique is based on two important approaches: approach regions and approach contours or border; there are other less important approaches: Mumford Shah, deformable models, level sets, and Markov fields (Vialard, 2018). We have several algorithms that deal with this theme.

A segmentation is parameterized by a homogeneity predicate P: R → {true, false} indicating whether a region is homogeneous according to the criterion tested. In order to predicate to be consistent, it is necessary that each subset of a homogeneous region be homogeneous. A segmentation algorithm is thus

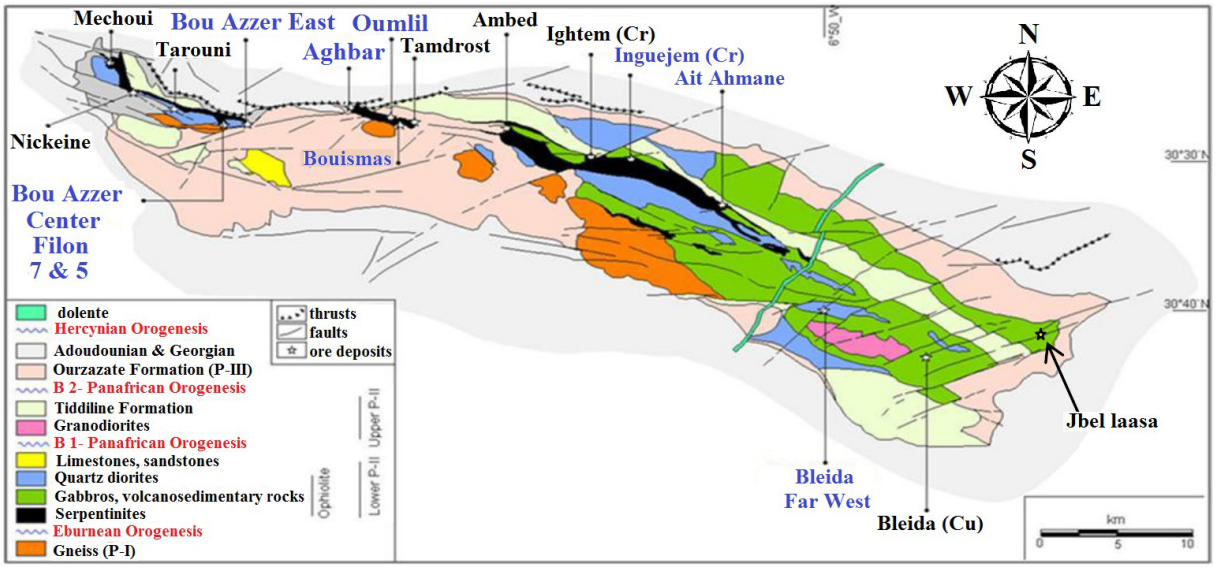


Figure 1- Map diagram of the El Graara - Bou Azzer inlier (modified from Maacha et al., 2014).

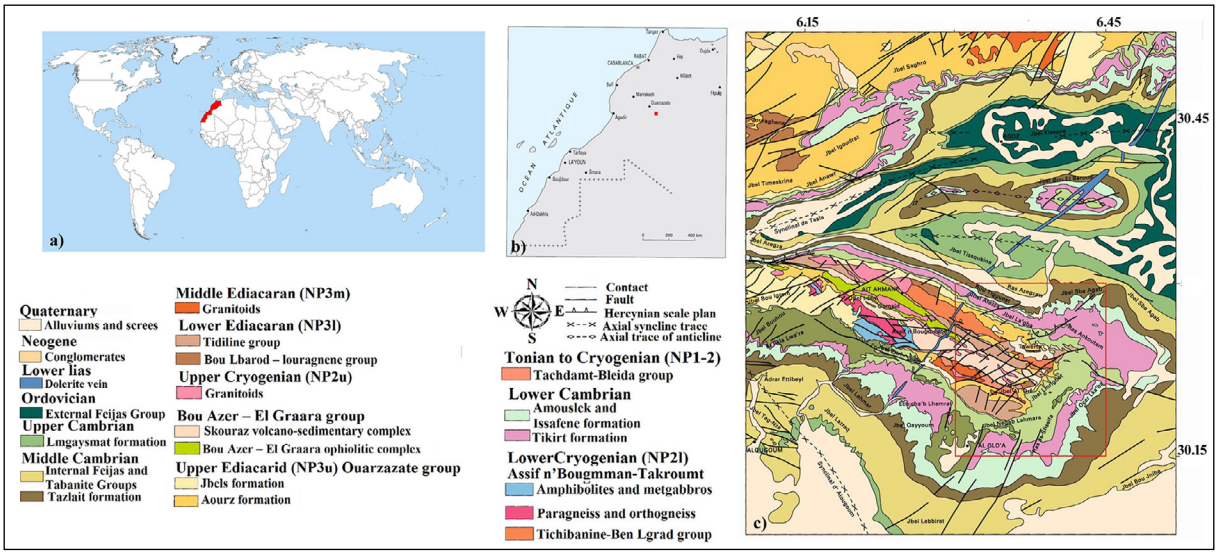


Figure 2- Study area location; a) Morocco's location in the world, b) the location of the sheet of Al Glo'a in Morocco, c) geological map of the study area (Al Glo'a sheet, rectangle in red, 1/500000) (modified from Soulaimani et al., 2013).

parameterized by a predicate P and an image. It returns a partition of the image in homogeneous zones (Pavlidis, Horowitz, and Theodosios, 1976).

Segmentation in homogeneous regions of an image I for a predicate P is a partition R of I such that:

1. $I = \cup_{r \in R} r$

2. $r_i \cap r_j = \varnothing$ for all $r_i, r_j \in R^2$, $i \neq j$.

3. P(r) = true for all $r \in R$ için.

4. P $r_i \cap r_j$ = false for all $r_i, r_j \in R^2$, $i \neq j$, $r_i$ and $r_j$ adjacent.

The first condition ensures that all elements of an image belong to a region and therefore the union of regions represents the entire image. The second condition states that regions do not overlap: there is no intersection between regions. The third condition indicates that each region must be homogeneous according to the criterion defined by the oracle. Finally, the last condition specifies that the fusion of two adjacent regions must not be homogeneous.

Starting from these conditions, numerous segmentation methods exist to solve many different problems. According to (Serra, 2006), there are more than a thousand distinct approaches.

### 3.1. Watershed

The watershed is a powerful tool for analyzing the topography of an image, since it can delimit a set of areas that form a partition of the original image. In this context, the watershed is generally applied to the contour image, where the strong contours can be seen as ridges that separate fairly flat valleys (homogeneous regions). This transformation is usually applied to the image gradient; so the basins correspond to homogeneous zones of the image (Urtasun, 2017). Like most classic segmentation methods this transformation gives over-segmented images which produces deferent instances on the same object. The Watershed algorithm (Vincent and Soille, 1991) is a method derived from mathematical morphology, which directly extracts closed and skeletonized contours from a contour power image (gradient module image). This algorithm is very interesting to reduce the number of false contours; the basin dynamics associated with a local minimum is defined as the difference in altitude between this minimum and the lowest peak point that must be crossed to arrive in a basin with a minimum lower than the first. The dynamics of a contour arc are defined as being the maximum value of the threshold for which this contour arc remains, when all the basins with a dynamics lower than the threshold are deleted (Ducrot, 2005).

The watershed is a supervised segmentation method based on the growth of regions using the segmented gradient image standard whose pixels with the lowest intensity form the initial watersheds. So the efficiency of this algorithm is related to the gradient of the image that is to say the number of minima obtained. If it is close to many of the objects constituting the original image, the result will be a well-segmented image. On the other hand, the result obtained will be segmented. Watershed segmentation is a region-based growth segmentation technique inspired by watersheds for rivers. The algorithm task on the gradient image representing the image. The gradient image associates with each element of the image a numerical value expressing the gradient between the values of the pixels of the image. The seeds are automatically selected as local minimums of the gradient image (i.e. all neighbors of a seed have a greater or equal gradient value). Each seed determines a new pool. The elements of the image are then attributed to the seed so as to fill the basins. The boundaries between two basins are called ridges.

Algorithm:

Calculate the gradient (or Laplacian) of the image.

Pixels with the lowest intensity form the initial watersheds.

For each intensity level i:

For each pixel group of intensity i:

If adjacent to exactly one existing region:

add these pixels in this region.

If adjacent to several regions simultaneously:

mark as the watershed.

If not, start a new region.

### 3.2. Segmentation by Thresholding

Thresholding aims to segment an image into several classes using only the histogram (MacQueen, 1967) (Figure 3).

The principle of Segmentation by thresholding is to extract thresholds from the histogram (image / region) and the classification of a pixel p by comparison of I (p) with the thresholds. There are three types of thresholding methods:

• Global threshold: S (x; y) def = S (I (x; y))

• Local threshold: S (x; y) def = S (I (x; y); P (x; y))

• Dynamic thresholding: S (x; y) def = S (I (x; y); P (x; y); x; y)

Here we should demonstrate that we talk about binarization if the image cantains 2 classes. (such as: pixel: (x; y), gray level: I (x; y), local property: P (x; y), and threshold used to classify the pixel (x; y): S (x; y )) (Vialard, 2018).

### 3.3. Effective Image Segmentation Based on Graphs

Efficient image segmentation based on PEGIS, Python Efficient Graph Based Image Segmentation, graphs made by (Felzenszwalb and Huttenlocher, 2004). This algorithm runs in time almost linearly in the number of edges of the graph and is also fast in practice. An important characteristic of the method is its capacity to retain detail in low variability image zones while ignoring details in zones of high variability. The algorithm deals with the problem of segmenting an image into regions. It defines a predicate to measure the evidence of a border between two regions using a graphic representation of the image. It then develops an efficient segmentation algorithm based on this predicate; and shows that even if this algorithm makes greedy decisions; it produces segmentations satisfying global properties (Felzenszwalb and Huttenlocher, 2004).

### 3.4. The k-Means Algorithm

The k-means algorithm (or k-means in English) is a method of data partitioning and a combinatorial optimization problem. Given points and an integer

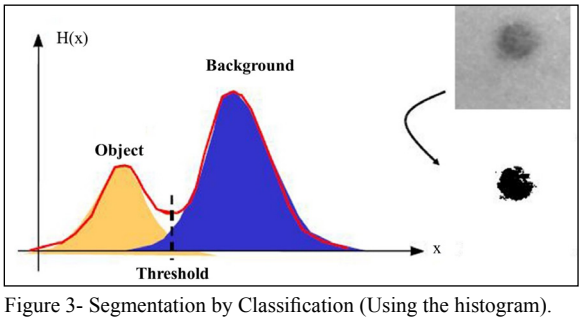

Figure 3- Segmentation by Classification (Using the histogram).

k, the problem is to divide the points into k groups, often called clusters, in order to minimize a certain function. We consider the distance of a point to the average of the points of its cluster; the function to be minimized is the sum of the squares of these distances (simplilearn, 2020), (Fahim, 2006).

K-means is an unsupervised learning algorithm dedicated to non-hierarchical clustering. It is an iterative algorithm that minimizes the sum of the distances between each individual and the centroid. The initial choice of centroids determines the final result.

Admitting a cloud of a set of points, K-Means changes the points of each cluster until the sum cannot decrease. The result is a set of compact and clearly separated clusters, subject to choosing the right value of the number of clusters (Mrmint, 2018).

### 3.5. The Isodata Algorithm

The ISODATA-algorithm is an iterative method that utilizes Euclidean distance as a measure of similarity to group data elements into different classes. To reduce the processing load and increase the throughput, the ISODATA procedure is usually applied to the first principal component derived from the original set of multi-spectral images. The disadvantage of the principal component approach is that it relies entirely on the statistical significance of the spectra, rather than on the uniqueness of the individual spectra (Dhodhi et al., 1999). The Iterative Self-Organizing Data Analysis Technique (ISODATA) (Ball and Hall, 1965) is sometimes used to refine the clusters obtained by a partitioning algorithm. This technique consists in exploding or merging the clusters according to pre-established thresholds. For example, two groups Ci and Cj will be merged if their inter-center distance d (x * i, x * j) is less than a certain threshold α. Likewise, a Ci cluster of inertia greater than a given threshold β will be exploded. In this family of algorithms, the number of expected clusters is not fixed a priori (Cleuziou, 2004).

### 3.6. MSI Images of the Sentinel 2A

Sentinel 2A's MSI instrument captures images of thirteen spectral bands ranging from visible to mid-infrared over a width of 290 km: The four spectral bands (blue (490 nm), green (560 nm), red (670 nm) nm) and near infrared (850 nm) having a resolution of 10 m, three spectral bands (440, 940 and 1370 nm) are provided with a resolution of 60 m while the resolution of the other six bands is 20 m.

Good practices in this area of use of satellite imagery (including Landsat 7, Landsat 8, Aster) for mineral exploration have proved to be useful and effective. And given the good resolution of the Sentinel 2A, we have opted for an analogy between the bands of these satellites and those of the Sentinel 2A in order to find derivative methods with a great capacity of geological discrimination; this work concludes that the RGBs (Red-Green-Blue) of the following Sentinel 2A images (Figure 4): (11/12; 11/2; 11/8), 12.8.2, Main Component 1,2 and 3 (11.12.2) show a good discrimination.

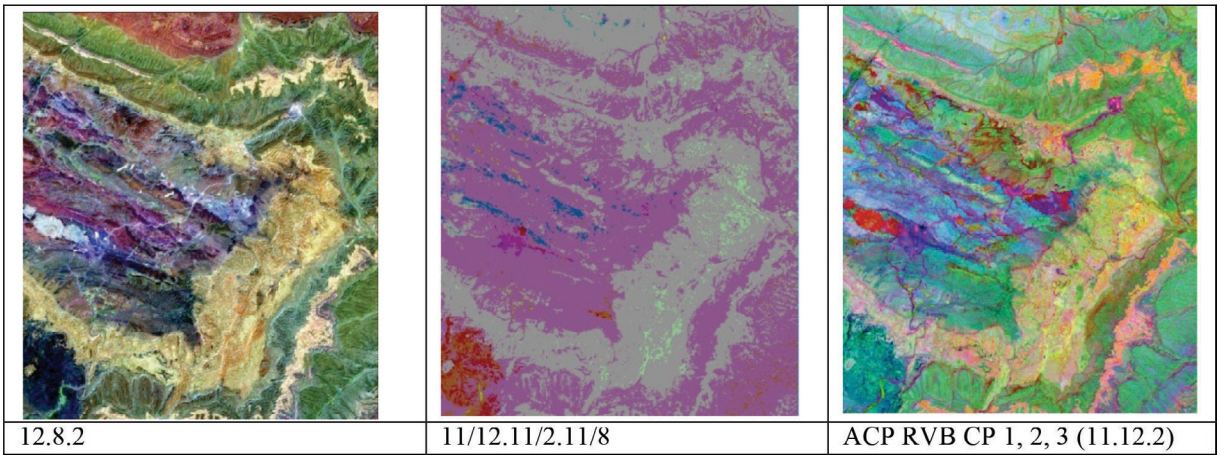

| 12.8.2 | 11/12.11/2.11/8 | ACP RVB CP 1, 2, 3 (11.12.2) |
|---|---|---|

Figure 4- RGB Sentinel 2A images.

These three images will be processed by the aforementioned algorithms in order to perform geological mapping with good discrimination. All these processed images listed in this paper have the same scale (1/50000) and the same coordinates as the GLO'A geological map; They are oriented North.

## 4. Findings and Discussion

### 4.1. Watershed

In our case where the initial image is composed of three bands, the processing of this image goes through several stages; the first step is to convert the RGB values to grayscale; panchromatic image; forming a weighted sum of R; G and B according to the following relation: (0.2989 * R) +( 0.5870 * G) + (0.1140 * B). These are the same weights used by the same function to calculate the Y component coefficients used to calculate the gray scale values which are identical to those used to calculate the luminance after being rounded to 3 decimals; calculation of the luminance using the following formula: (0.299 * R) + (0.587 * G) + (0.114 * B); while the second step aims at detecting the outlines of objects (areas of high values) and local minima (areas of low values). Using markers on the lowest values in the third step will ensure discovery of segmented objects. The combination of the last two stages gives us the final image (team, s.d.). To obtain an efficient segmentation, the disk value (the number of neighbors surrounding a pixel) is chosen correctly; if 3: the algorithm tests the three pixels surrounded by a pixel has a local minimum in the four locations (right, left, up, down), if the density of a pixel is one less than 20, the algorithm will add it to the tested pixel and gives them the same label, et cetera until the end of local minima. The same for the disk value. According to the results obtained for the first image below, the disk value 3 gives a more precise segmentation than the value 5 which means that the image contains several local minima (Figures 5 to 10).

On the other hand, the second image gives a more precise segmentation for the disk value, which means that the image gradient is minimized by the number of local minima relative to the first image.

Disk value 5 shows the weakness of watershed algorithm in the third image which is totally based on the results obtained by the gradient of images. This means that the absence of local minima here forces the algorithm to consider the image as a single object.

The discrimination achieved by this algorithm is not adequate with maps and existing geological documents; but it can be good for topographic image segmentation.

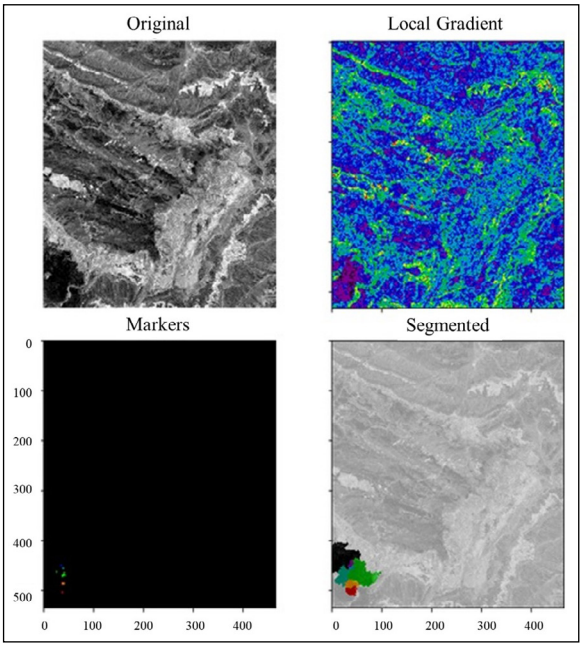


Figure 5- Watershed (RVB 12.8.2) [rank gradient (disk 3) <20].

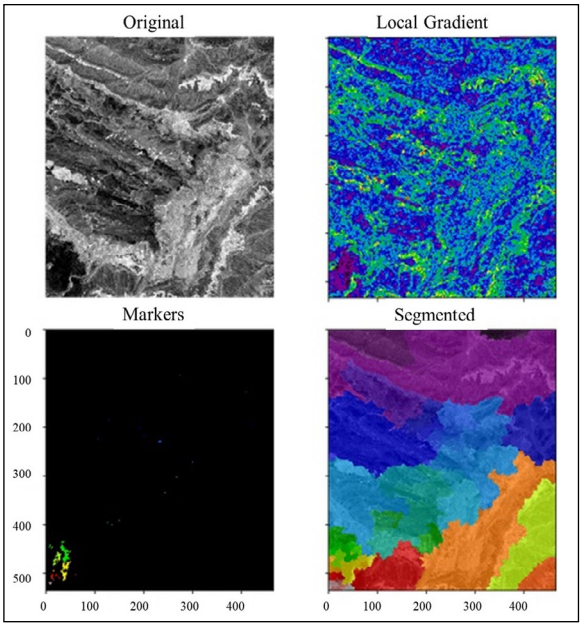


Figure 6- Watershed (RVB 12.8.2) [rank gradient (disk 5) <20].

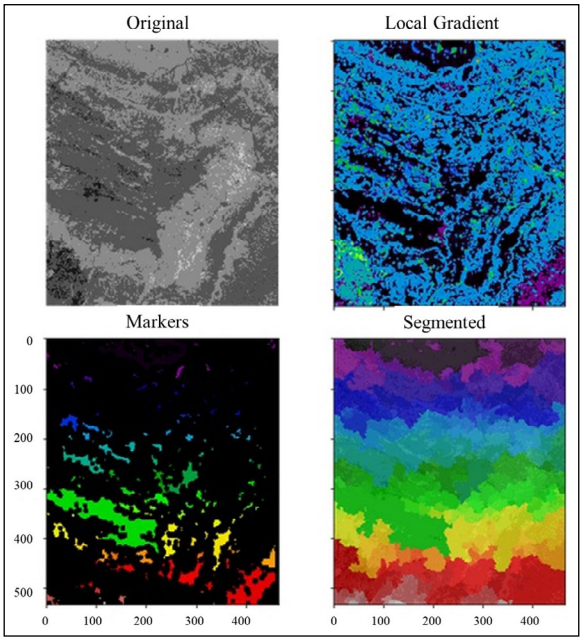


Figure 7- Watershed (RVB 11/12.11/2.11/8) [rank gradient (disk3) <20].

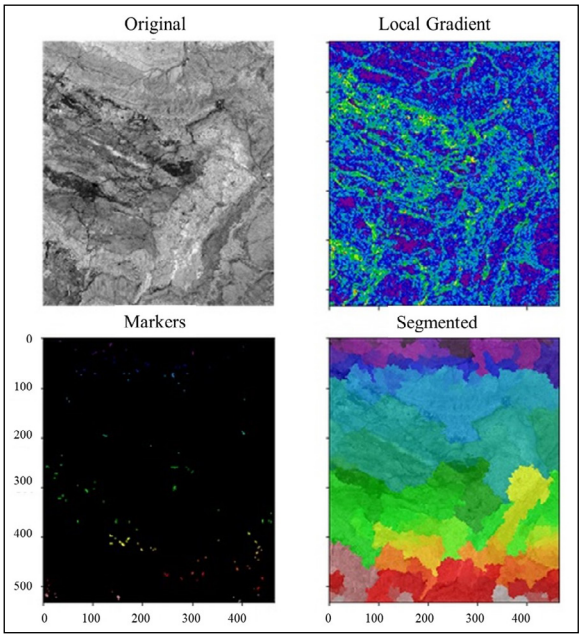


Figure 9- Watershed (RVB CP 1, 2, 3 (11.12.2)) [rank gradient (disk 3)<20].

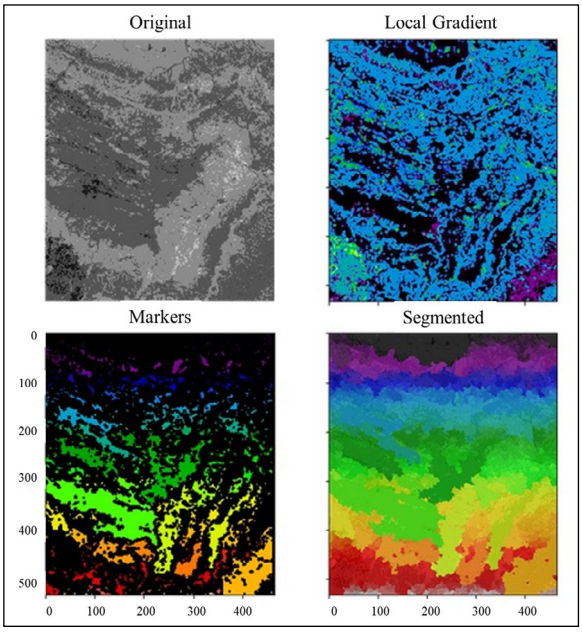


Figure 8- Watershed (RVB 11/12.11/2.11/8) [rank gradient (disk5) <20].

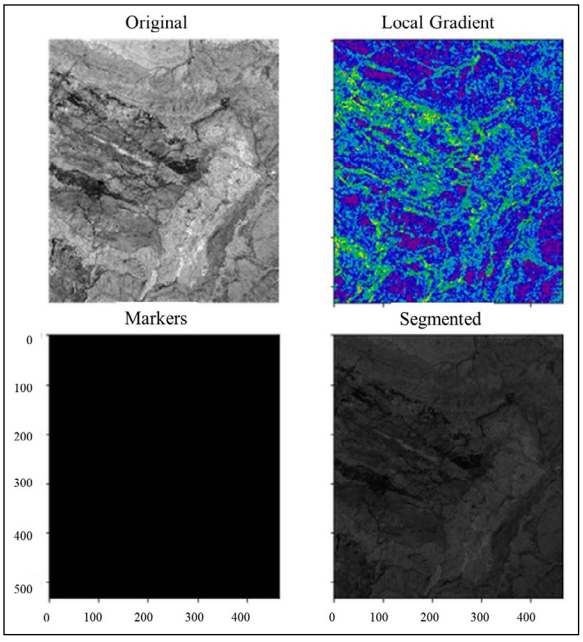


Figure 10- Watershed (RVB CP 1, 2, 3 (11.12.2)) [rank gradient (disk 5) <20].

## 4.2. Efficient Image Segmentation Based on Graphs

This algorithm produces a segmented image based on a graphical representation (Graph (V, E): the vector V contains the pixels and E contains a set of non-directed edges between pairs of pixels) of original image. The algorithm defines a predicate to measure the evidence of a boundary between two regions, this predicate will be the basis for constructing an efficient algorithm as a result. The problem is that the image segmentation is based on its graph and its predicates which sometimes gives undesirable results like our case because the algorithm considers the image as a homogeneous unit (Huttenlocher, 2004), (Figures 11 to 13).

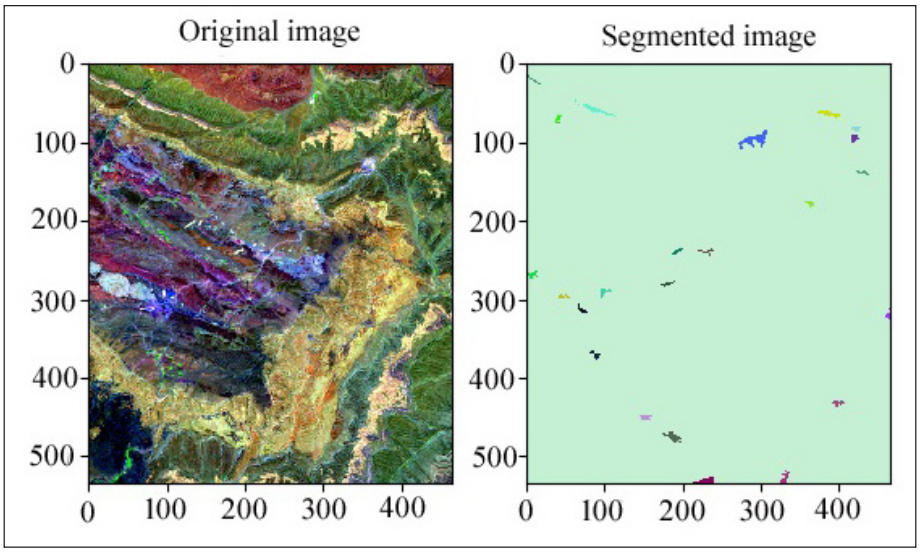


Figure 11- Effective graph-based image segmentation (RGB 12.8.2).

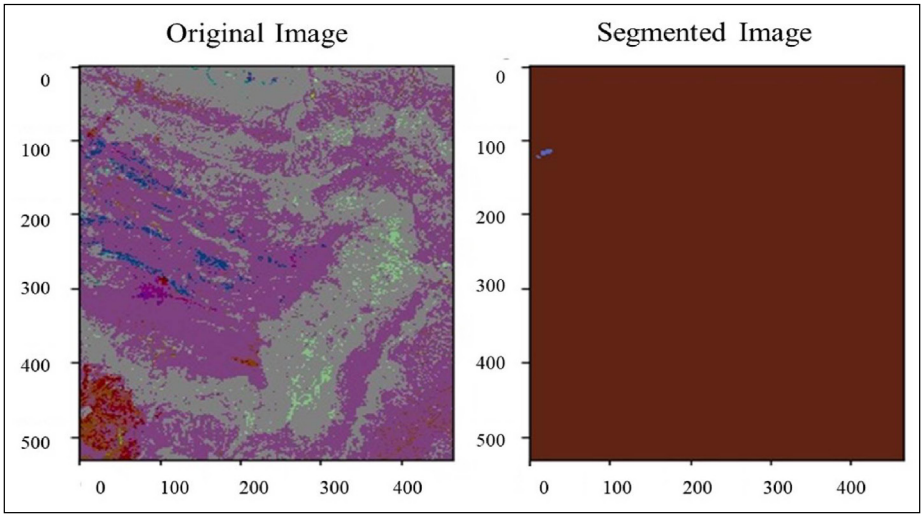


Figure 12- Effective graph-based image segmentation (RGB 11 / 12.11 / 2.11 / 8).

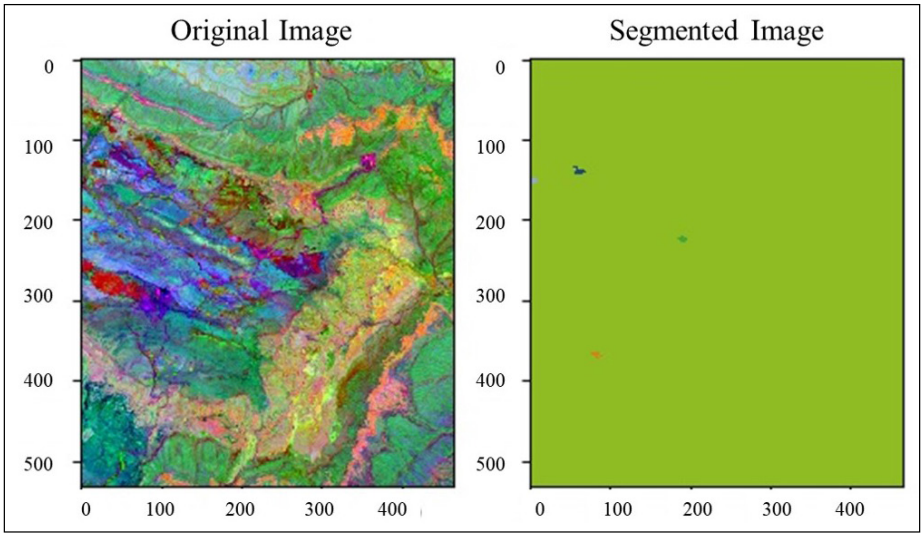


Figure 13- Effective graph-based image segmentation (RGB CP 1, 2, 3 (11.12.2)).

4.3. Segmentation by Thresholding

This algorithm remains the simplest at it transforms the image into grayscale and subdivides the image into two parts according to a threshold calculation via the histogram (number of pixels having the same level of gis) (Figures 14 to 16).

The geological discrimination of the thresholding is not detailed.

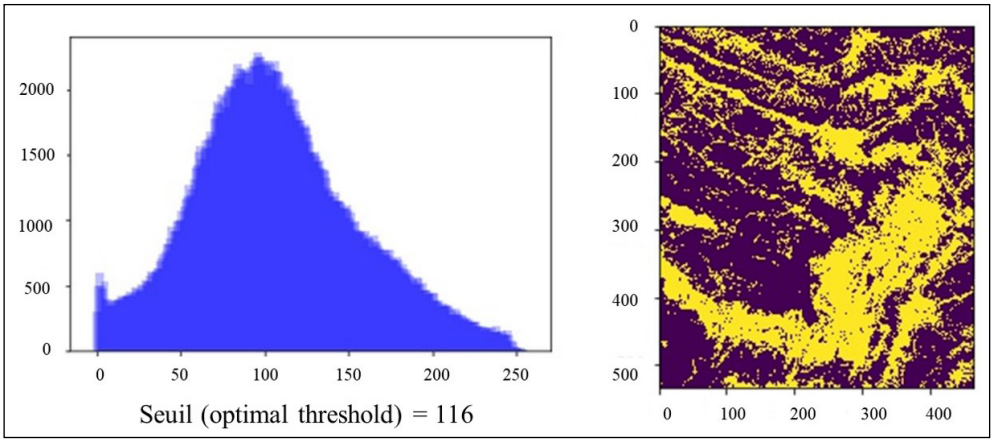


Figure 14- Segmentation by thresholding (RGB 12.8.2).

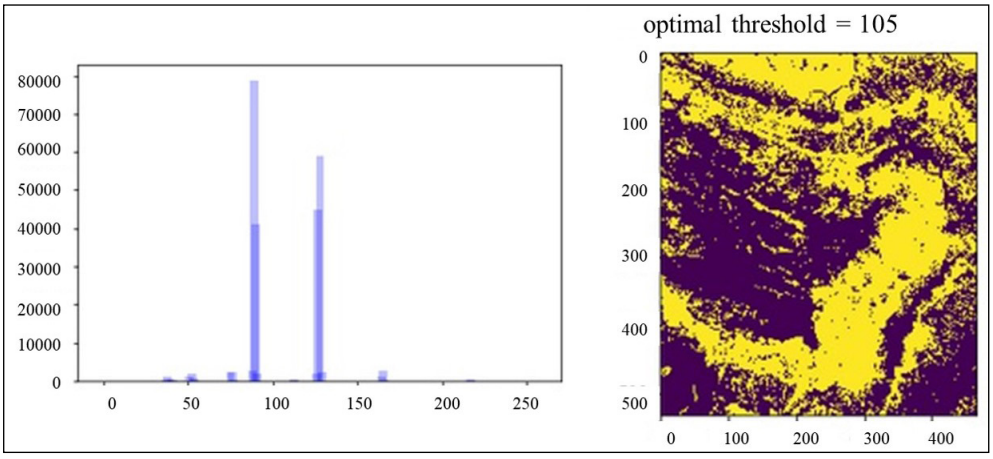


Figure 15- Segmentation by thresholding (RGB 11 / 12.11 / 2.11 / 8).

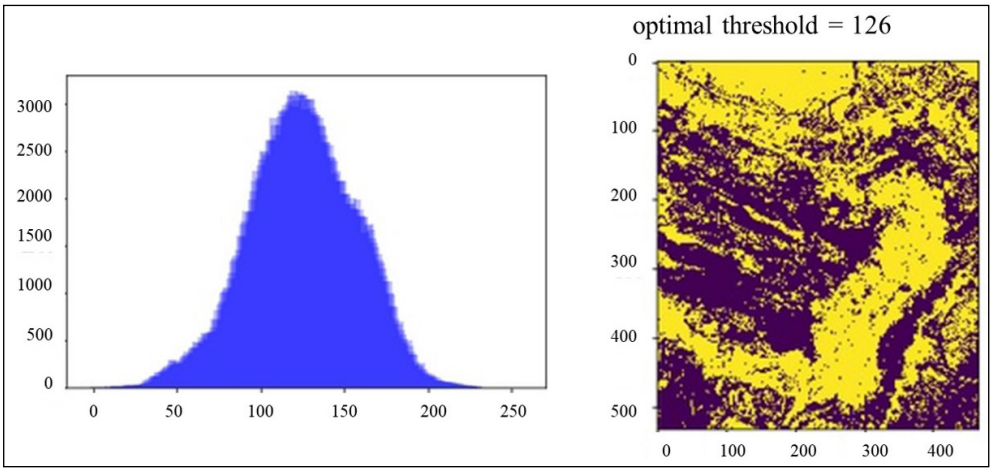


Figure 16- Segmentation by thresholding (RGB CP 1, 2, 3 (11.12.2)).

4.4. The k-Means and Isodata Algorithms

These two k-Means and Isodata algorithms have demonstrated a great capacity for segmentation and geological discrimination. Furthermore, the automatic comparison between the six resulting images below of these two algorithms asserts that each produced unsupervised classification image of the Isodata algorithm is similar to that of K-Means. This comparison takes into consideration a variety of criteria: Layer info, Raster data, map info, info projection, log file, table description, statistics, pyramid layers, XForms (Figures 17 to 22).

We choose in the previous treatment, either by Isodata or K-Means, 18 classes based on the simplified geological map of the Al Glo'a sheet mentioned in Figure 23.

Thanks to Figures 17 to 22 and to the detailed geological map of Al Glo'a (1/50000) we can create geological maps resulting from images processed by Isodata or K-Means. Figure 24 presents a geological map of the unsupervised k-Means RGB 12.8.2 classification with 18 lithological classes, which is characterized by a very good geological discrimination.

K-Means algoritması

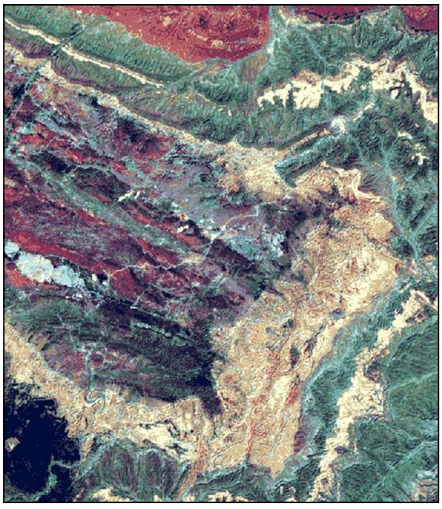

Figure 17- Unsupervised classification by RGB k-Means 12 8 2 (18 classes).

Isodata algoritması

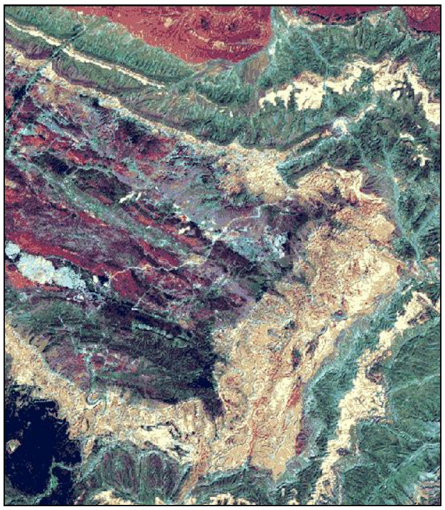

Figure 18- Unsupervised Isodata classification of RGB 12 8 2 (18 classes).

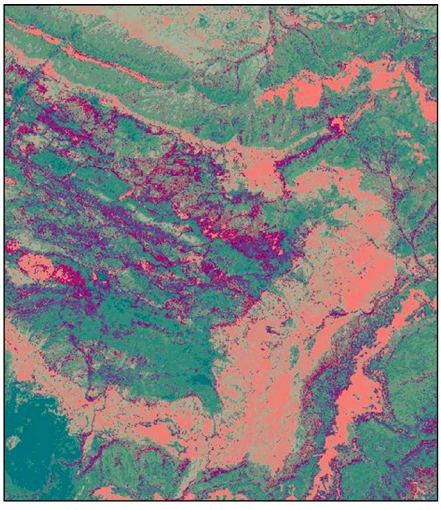

Figure 19- Unsupervised CP RGB 1, 2 and 3 (11 12 2) k-Means Classification (18 classes).

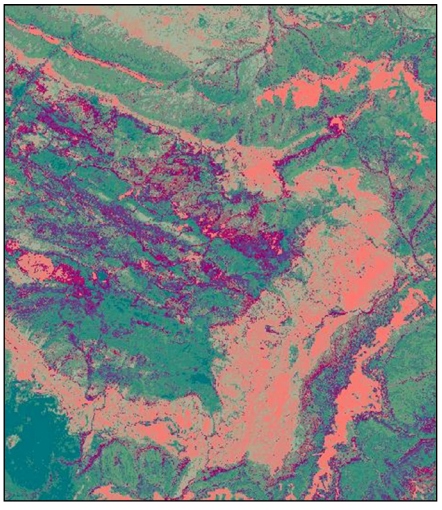

Figure 20- Non-supervised Isodata RGB classification of CP 1, 2 and 3 (11 12 2) (18 classes).

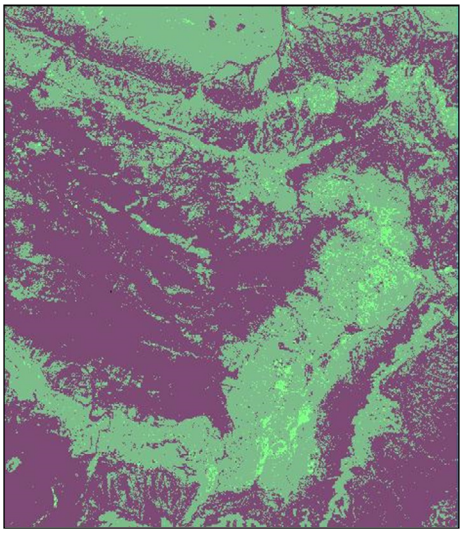

Figure 21- Unsupervised RGB K-Means Classification of Ratios 11/12 11/2 11/8 (18 Classes).

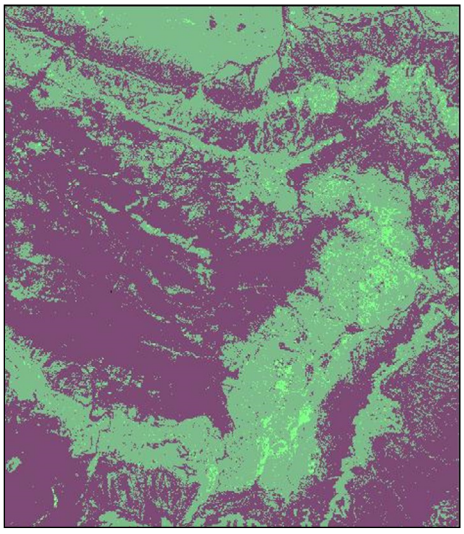

Figure 22-SODATA unsupervised RGB classification of ratios 11/12 11/2 11/8 (18 classes).

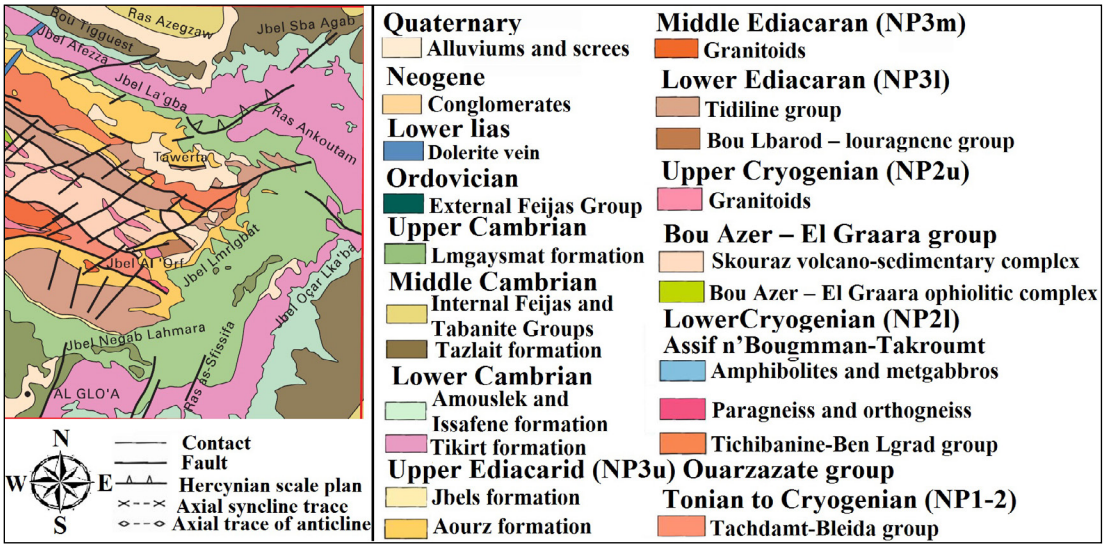


Figure 23- Simplified geological map of the Al Glo'a sheet (1/500000). (edited from Soulaimani, et al., 2013).

## 5. Results

We can see that threshold segmentation does not give good results in terms of geological discrimination since it divides each image into two parts, especially that the geological map is a variety of geological formations. It is recommended to use the thresholding principle but with several thresholds like the ISODATA type algorithm which is based on the concept of optimal thresholding (we measure the (statistical) separation between two regions from a criterion function).

The contribution of the Watershed algorithm for geological mapping is limited but is of interest from the point of view of topographic and hydraulic studies. It can be very useful in the preparation phase of geological and mining infrastructures.

After knowing: 1) the limited role of segmentation algorithms (the watershed), the effective thresholding and segmentation of graph-based images in this area of mineral exploration; 2) the good potential of unsupervised classification algorithms (Isodata and K-Means), it is recommended to extend the study

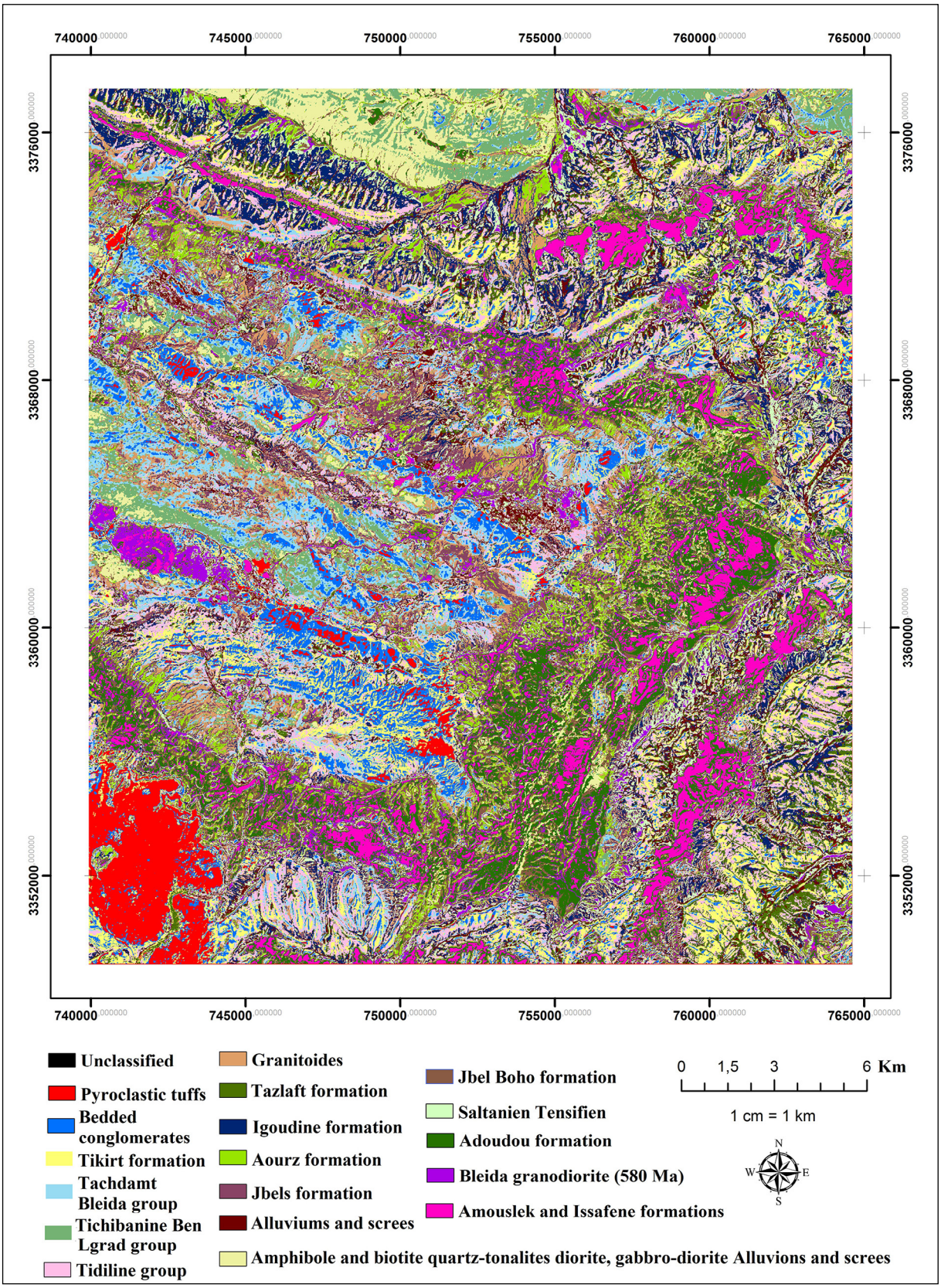


Figure 24- Geological map of the Glo'a for the application of the K-Means to RGB algorithm 12 8 2.

to: 1) supervised classification algorithms (including SVM); 2) deep learning algorithms; and 3) algorithms related to the creation of (structural) lineament maps.

## References


Ball, G., Hall, D. 1965. A novel method of data analysis and pattern classification. Rapport technique, Menlo Park, CA, Stanford Research Insitute.

Choubert, G. 1947. L'accident majeur de l'Anti-Atlas. Comptes Rendus de l'Academie des Sciemces 224, 16, 1172-1173.

Cleuziou, G. 2004. Une méthode de classification non-supervisée pour l'apprentissage de règles et la recherche d'information. Université d'Orléans.

Dhodhi, K. M., Saghri, J. A., Ahmad, I., Ul-Mustafa, R. 1999. D-ISODATA: A Distributed Algorithm for Unsupervised Classification of Remotely Sensed Data on Network of Workstations. Journal of Parallel and Distributed Computing, 59(2), 280-301.

Ducrot, D. 2005. Méthodes d'analyse et d'interprétation d'images de télédétection multi-sources : Extraction de caractéristiques du paysage. Habilitation à diriger des recherches, INP TOULOUSE.

Dupas, A. 2009. Opérations et Algorithmes pour la Segmentation Topologique d'Images 3D.

Fahim, A. S. 2006. An efficient enhanced k-means clustering algorithm. J. Zhejiang Univ- Sci, A 7, 1626–1633. https://doi.org/10.1631/jzus.2006.A1626.

Felzenszwalb, P., Huttenlocher, D. 2004. Efficient graph-based image segmentation. International Journal of Computer Vision 59(2).

Huttenlocher, P. F. 2004. Efficient graph-based image segmentation. International Journal of Computer Vision.

Khan, M. 2014. A survey: image segmentation techniques. Lahore. International Journal of Future Computer and Communication, 3.

Maarir, A., Agnaou, I., Bouikhalene, B. 2014. Evaluation de Quelques Méthodes de Segmentation -Application aux Caractères Tifinagh, https://tal.ircam.ma/conference/docs/TICAM2014/1.pdf.

MacQueen, J. 1967. Some methods of classification and analysis of multivariate observations. Berkeley Symposium on Mathematical Statistics and Probability, 81-297.

Maacha, L., Elghorfi, M., Zouhair, M., Sadiqui, O., Soulaimani, A. 2014. Reconsidérations des systèmes métallogéniques de la Boutonnière de Bou Azzer-El Grâara (Anti-Atlas occidental). Maroc.

Mrmint. 2018, 11, 26. algorithme-k-means. Retrieved from mrmint: https://mrmint.fr/algorithme-k-means.

Oukassou, M. 2013. Mouvements verticaux de la bordure nord du craton ouest africain (anti-atlas central, maroc) apport de la thermochronologie basse temperature. thèse de Doctorat, Faculté des Sciences-Aïn Chock, Casablanca.

Pavlidis, S., Horowitz, L., Theodosios. 1976. Picture segmentation by a tree traversal. Journal of ACM, 23 (2), 366-388.

Serra, J. 2006. A lattice approach to image segmentation. Journal of Mathematical Imaging, 24.

Simplilearn. Apprentissage profond. Retrieved from simplilearn:https://www.simplilearn.com/tutorials/machine-learning-tutorial/k-means-clustering-algorithm. 13 July 2020.

Soulaimani, A., Egal, E., Razin, P., Youbi, N., Admou, H., Blein, O., Anzar, C. 2013. Notice explicative de la carte géologique du maroc au 1/50 000 -feuille al glo'a-. Département de lEnergie et des Mines. éditions du service géologique du Maroc.Team, s.-i. d. (n.d.), from scikit-image: http://scikitimage.org/docs/dev/auto_examples/segmentation/plot_marked_watershed.html?fbclid=IwAR2zYJ0VCkLBvsWUJuku-x9sGdzx7pz0W_O5-ho4O5KgPTVfsYl35flDFIc#sphx-glr-auto-examples-segmentation-plot-marked-watershed-py. 29 November 2018.

Bai, M., Urtasun, R. 2017. Deep watershed transform for instance segmentation. Toronto.

Vialard, A. 2018. Segmentation et Analyse d'images (partie 1). LaBRI, Université Bordeaux 1.

Vincent, L., Soille, P. 1991. Watersheds in digital spaces: an efficient algorithm based on immersion simulations. IEEE Transactions on Pattern Analysis and Machine Intelligence 13(6).

Bulletin of the Mineral Research and Exploration

http://bulletin.mta.gov.tr

# The relationship between seismic quality factor and peak ground acceleration, a case study: M=4.3, 17.01.2015 Eskişehir Earthquake

Muammer TÜN[a]*

[a]*Eskişehir Technical University, Institute of Earth and Space Sciences, Department of Earth Sciences and Earthquake Engineering, Eskişehir, Turkey*

*Research Article*

Keywords:
Quality Seismic Factor, EstuNet Seismic Network, Strong Ground Motion, Peak Ground Acceleration, Eskişehir Graben.

**ABSTRACT**

Seismic wave propagation in subsurface media endures from absorption, which can be evaluated by the seismic quality factor Q (Q-factor). Absorption is frequency-dependent. Lower frequencies are absorbed less, while higher frequencies are absorbed more. Therefore, the Q Factor should be determined in the frequency domain. Q-factor is determined by the slope of the natural logarithm of the output-input signals ratio. Surface waves (Rayleigh and Love waves) are particularly important, as they are the more destructive phases of an earthquake. This study was focused on the Q-factor computation of the surface waves and demonstrated that the determination of the Q-factor is not affected from the dispersive properties of the surface waves. Data were obtained from surface wave signals of earthquake recorded at Eskişehir Technical University Seismic Network - EstuNet. The obtained Q-factor values represent the average values of the rocks that the waves cross between the input and output stations. Finally, the Q-factor map to the Peak Ground Acceleration (PGA) map using the M=4.3, 17.01.2015 Eskişehir earthquake data was compared. These records, show the arrival time of the earthquake from the epicenter to the stations of the seismic waves, and the peak ground acceleration values. In this study, local site effects of EstuNet accelerometric stations have been calculated by using the Standard Spectral Ratio (SSR) method. It is concluded that an inverse relationship exists between the computed Q-factor and measured PGA values. Therefore, the sites where the Q factor is very low should be analyzed in more detail in ground-based earthquake risk assessments.

*Received Date: 30.08.2020*
*Accepted Date: 11.12.2020*

## 1. Introduction

Seismic quality factor (Q-factor) studies date back to the early 1940s (Ricker, 1940). Since then, many researchers have studied the attenuation properties of earth substance (Johnston et al., 1979; Jongmans, 1990; Moya and Irikura, 2003; Raghukanth and Nadh Somala, 2009; Naresh et al., 2019) both in the field and in the laboratory. In-situ Q measurements are of interest in engineering geophysics. Absorption is usually measured by the inverse of the dimensionless Q. Amplitude is affected by energy loss due to anelastic processes or internal friction during wave propagation. This intrinsic attenuation may be distinguished from scattering attenuation. The strength of intrinsic attenuation is given by Q in terms of the fractional energy loss per cycle. Q is sometimes called the quality factor (Shearer, 2009; Stein and Wysession, 2009) and is inversely related to the strength of attenuation; low-Q regions are more attenuating than

Citation Info: Tün, M. 2021. The relationship between seismic quality factor and peak ground acceleration, a case study: M=4.3, 17.01.2015 Eskişehir Earthquake. The Bulletin of the Mineral Research and Exploration 166, 127-144. https://doi.org/10.19111/bulletinofmre.841785

**Corresponding author: Muammer TÜN, mtun@eskisehir.edu.tr*

high-Q regions. Seismic wave/soil (subsurface layers) interactions and responses are caused reflectors, refractors, or diffractors. Spherical divergence or absorption always exist as seismic waves propagate. These effects concurrently affect seismic waves as they travel. In this study, continuous factors that affect seismic waves were considered.

Attention of seismic waves has been measured for many years (Anderson and Archambeau, 1964; Anderson and Hart, 1978; Anderson and Kovach, 1964; Jackson and Anderson, 1970). The resultant distribution of attenuation versus depth (usually expressed by the dimensionless quality factor Q) is an important source of information in the earth's interior (Press, 1964). Accurate estimation of the Q factor is of great importance for the resolution enhancement of seismic data. Estimates of the quality, Q, factor are commonly obtained from vertical seismic data or stacked surface seismic data (Zhang and Ulrych, 2002; Li et al., 2016). This paper describes a method that Q-factor can be measured from the recording of strong ground motion.

The Q-factor provides valuable information on the physical properties of soil. A low Q-factor indicates the presence of an absorptive medium; absorption is frequency-dependent. Moreover, the effect of absorption becomes more prominent at higher frequencies (Gurevich and Pevzner, 2015). Some of the mechanical energy of a seismic wave is transferred to an irreversible dislocation and deformation within the rocks, producing friction and heat. Rock types, formation of fissures, cracks within the rocks, fault zones, liquefaction (migration of fluids in cracks and pores), landslides, and a change in water table level are the major indicators of absorption with low Q values. In the case of elastic behavior, after the passage of seismic waves, vibrating particles assume their original position. Elastic behavior causes minimum earthquake damage. In the case of anelastic, or plastic behavior, after the passage of seismic waves, vibrating particles cannot assume their original equilibrium position. Anelastic behavior causes maximum earthquake damage (Luzi et al., 2019; Mayoral et al., 2019; Miyakoshi et al., 2019).

The frequency dependent attenuation (Q) value which gives Quality factor ($Q_0$) of S-waves of the Punjab basin and this study is important to develop the ground motion model and simulations for seismic hazard studies (Naresh et al., 2019). Quality factor and site amplification are derived from the strong-motion data. The Quality factor represents a part of the total attenuation of Fourier spectral amplitudes reaching the ground surface (Raghukanth and Nadh Somala, 2009). Two strong motion networks, K-NET and KiKnet, recorded the aftershocks of the 2000 Tottori, Japan, earthquake. The results suggest that the study area presents a low Q value and that there is also amplification at borehole sites (Moya and Irikura, 2003).

The earthquake data from years 1900–2019 were downloaded from the KOERI (Kandilli Observatory and Earthquake Research Institute) web portal (http://www.koeri.boun.edu.tr/sismo/zeqdb/). During downloading, all the parameters were selected as accurately as possible with coordinated boundaries to cover Eskişehir Province for earthquakes with magnitudes greater than 3. The downloaded data was in .txt format, so it was first organized in Excel and then reformatted to .xls format so that it could be opened in ArcGIS. There were 161 earthquakes in total with magnitudes of greater than 3 that occurred within the study area within the selected date range. The result of the analysis shows that most of the earthquakes with magnitudes between 3 and 6.4 occurred in the southern part of Tepebaşı District and the northern part of Odunpazarı District. The earthquake occurrence is attributed to faults, because most of the earthquake epicenters are distributed between active faults. The 3499 houses, 10 schools, 15 mosques, and 3 official buildings were demolished, along with 1303 barns and haystacks in that earthquake in Eskişehir city center in the 20 February 1956 (Ms 6.4) Eskişehir earthquake. One person died (Ersoy, 1956). In the 17 August 1999 Kocaeli earthquake (Mw 7.4), which was approximately 250 km from Eskişehir city center, 86 people lost their lives in the city of Eskişehir, and 95 people were injured. Also, 70 houses/workplaces suffered severe damage, one building collapsed during the earthquake, and four buildings collapsed after the earthquake (Özmen, 2000).

The aim of this study is to show that the Q-factor can be measured from the recording of strong ground motion and to examine the relationship between Seismic Quality Factor (Q) and Peak Ground Acceleration (PGA). Q measurements were performed from EstuNet Seismic Network data that it is composed

of 18 strong-motion and 8 weak-motion stations mainly distributed in Quaternary- and Neogene-aged units in the Eskişehir Basin. The spectral ratio technique was used for calculating the absorption Q-factor.

## 2. Theory and Methods

The site response is a function accounting for attenuation that includes the effect of geometrical spreading and the intrinsic and scattering quality factor. Q(f) is the quality factor which includes both anelastic absorption and scattering (Parolai, 2012).

### 2.1. Spectral Ratio Method

The Standard Spectral Ratio technique (SSR) of earthquake recording involves comparing records at nearby sites using one site as the bedrock reference site (Figure 1) (Parolai, 2012). SSR, a reference site technique, involves considering the spectral ratio of the same component of strong ground motions recorded at two nearby stations. The SSR technique was initiated by (Borcherdt, 1970). In Borcherdt (1970)'s study, ground motion generated by nuclear explosions in Nevada were measured at 37 locations near San Francisco Bay, California. These results were compared with those of the San Francisco earthquake of 1906. This technique has previously been used in many geological environments (Borcherdt, 1989; Field et al., 1992; Gök et al., 2014; Mittal et al., 2015; Özer, 2019).

The assumption of this technique is that the two sites have a similar source and path effects. If the separation between the stations' input and output is much less than their hypocentral distances from the source, it is probably a good assumption that the path terms will cancel. The critical assumption in these methods is that the surface- rock-site record (reference) is equivalent to the input motion at the base of the soil layers (Steidl et al., 1996).

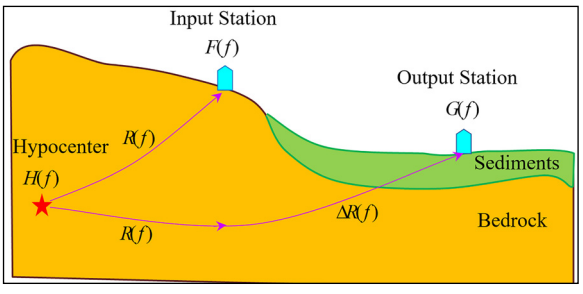


Figure 1- Typical geological structure of sedimentary basin and input-output station spectral-ratio method.

f Frequency

$H(f)$ Earthquake source function

$F(f)$ Input station function

$G(f)$ Output station function—the spectral amplitude of the ground motion observed at a recording site for an event.

$R(f)$ Path function between hypocenter and input station

$DR(f)$ Path function between input and output stations

$$F(f) = H(f)\,R(f \tag{1}$$

$$G(f) = H(f)\,R(f)\,DR(f) \tag{2}$$

$$\Delta R(f) = \frac{G(f)}{F(f)} \tag{3}$$

where H(*f*), R(*f*), ΔR(*f*) represent the spectral contribution of the source, the wavepath and local geology, respectively. At the two observation sites, with amplitude G(*f*) on sediment and amplitude F(*f*) on bedrock, the source function H(*f*) is the same (as the same signal is compared), and the wavepath function R(*f*) is also the same (with good approximation for closely located sites); whereas the local-geology function ΔR(*f*) is different (Borcherdt, 1970; Bath, 1974). Equations 1 and 2 denote input and output station functions, respectively. The path function between input and output stations is given by Equation 3 and holds if the path function between hypocenter and input station is identical to the initial part of the path function between hypocenter and output station functions. In this case, the terms H(*f*) and R(*f*) are eliminated in Equation 3.

### 2.2. Earthquake Wave Phases and Seismic-Q Measurements

The absorption phenomenon affects all earthquake wave phases. To measure the absorption of body waves (P- and S-waves), the analysis window should be carefully placed on the body wave arrivals. There is a problem of frequency dependence for all the component velocities of P- and S-waves, but in fact the

problem lies the more accurate interpretation (Barton, 2007). A quality factor Q-seismic was popularized by Knopoff, 1964 with the briefest possible title: Q. Generally, Q measurement methods can be classified into two main categories. In one category Q is extracted in the time domain (Engelhard, 1996). The other category comprises frequency-domain methods (Quan and Harris, 1997; Sams and Goldberg, 1990; Zhang and Ulrych, 2002). Besides, Q analysis based on amplitude attenuation and compensation functions (Wang, 2004). Estimations of the quality, Q, factor are commonly obtained from vertical seismic data or stacked surface seismic data and many techniques for estimating Q have been proposed (Bano, 1996; Dasgupta and Clark, 1998; De Castro Nunes et al., 2011; Blias, 2012; Yang et al., 2014)

In this study, the absorption measurements of surface waves were only considered (Rayleigh and Love waves); therefore, the analysis windows can cover all the seismic wave phases, including the initial body waves. By their nature, low frequency/high amplitude surface waves occupy the low frequency band of the amplitude spectrum. Conversely, low amplitude/high frequency body waves occupy the high frequency band of the amplitude spectrum. This natural discrimination of surface waves and body waves allows us to measure the absorption of surface waves in the low frequency band of the amplitude spectrum. The time domain analysis window can embrace all phases of a seismic event, therefore there is no need to position the analysis window over only the surface waves.

### 2.3. Computation of Q-factor

Seismic wave attenuation expressed by the quality factor Q is another field where spectral analysis is the natural approach. Attenuation methods are naturally applicable to both body waves and surface waves (Bath, 1974). The quality factor Q is often assumed to be frequency-independent and is regarded as a constant within the seismic frequency band. Several Q models have been proposed to describe attenuation mathematically (Futterman, 1962; Kjartansson, 1979; Wang and Guo, 2004). According to Q model of Futterman (1962), if one only consider the attenuation of the amplitude spectrum of the seismic wave, the attenuation mechanism can be depicted as

$$G(f) = F(f)\, e^{-\frac{\pi t f}{Q}} = F(f)\, e^{-af} \quad (4)$$

t Travel time (s); the travelling time difference between the received waveform and the source wavelet.

$Q$ Q-factor

$a$ Slope (s)

$f$ Frequency (Hz)

$F(f)$ Input station function

$G(f)$ Output station function

Based on the above attenuation mechanism, proposed to obtain Q using the spectral ratios. The spectral-ratio technique has been applied to real data but is unstable and not very reliable (Sams and Goldberg, 1990). The logarithmic spectral ratio (LSR) is frequency domain methods. This method is based on the change of spectral properties of seismic waves as they propagate through anelastic medium (Dasios et al., 2001). The LSR method uses a selected band of the Fourier frequency spectra. This phenomenon was investigated by using real data.

The slope is given as:

$$a = -\frac{\pi t}{Q} \quad (5)$$

From Equation 3, the natural logarithm of output to input functions ratio:

$$ln\,\Delta DR(f) = ln\frac{G(f)}{F(f)} = -\frac{\pi t}{Q} f = -af \quad (6)$$

The Q-factor is then given as:

$$Q = -\frac{\pi t}{a} = -\frac{\pi tf}{\ln\frac{G(f)}{F(f)}} \quad (7)$$

According to the third term of Equation 7, Q-factor can be computed for each value of the frequency *f*. However, real data values scatter around the slope segment (Figure 2), yielding to different Q-factor values. If the real data values fall on the slope segment, the same Q-factor values should be obtained. Therefore, based on the distribution of the real data, a slope segment should first be selected and then the slope value determined. The second term in the Equation 7 may be used for Q-factor computations

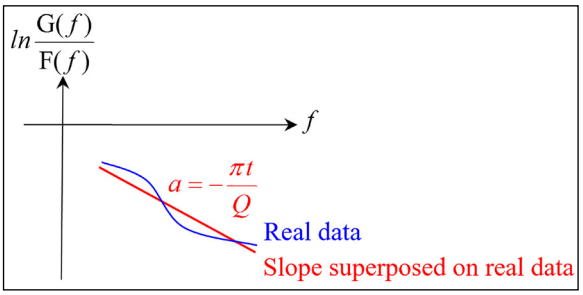


Figure 2- Measurement of slope.

eliminating the undesired effects of data scattering. The travel time *t* is a monotonically increasing variable as the seismic waves travel in space. The slope *a* in the denominator of Equation 7 is the most effective term in the determination of Q-factor. Along the travel path, inclusion and exclusion of low or high Q-value rocks severely influence the value of slope *a*. Therefore, the slope *a* should be carefully determined.

### 2.4. Computation of Surface Waves Q-factor from P-Waves Travel Time

Although it is easy to observe the onset times of P-waves in seismograms, the onset times of surface waves cannot be clearly determined due to the crowdedness caused by body waves prior to surface wave arrivals.

$$Q = -\frac{\pi t_R}{a} = -\frac{\pi x}{a V_R} \tag{8}$$

$$v_R = 0.92 v_S \tag{9}$$

$$\frac{V_S}{V_P} = \sqrt{\frac{0.5-\sigma}{1-\sigma}} \tag{10}$$

$$Q = -\frac{\pi x}{a V_R} = -\frac{\pi x}{a\, 0.92 V_S} = -\frac{\pi x}{a V_P 0.92 \sqrt{\frac{0.5-\sigma}{1-\sigma}}} \tag{11}$$

$$Q \approx -\frac{\pi x}{a V_P 0.92 \sqrt{\frac{0.5-0.26}{1-0.26}}} = -\frac{6x}{a V_P} = -\frac{6 t_P}{a} \tag{12}$$

In Equation 8, $t_R$ denotes the travel time of surface waves, *a* is the slope, *x* is the travel distance, and $V_R$ is velocity of the fastest phase of the surface waves. Equation 9 gives the relation between surface waves and S- waves. Equation 10 represents Poisson's ratio. Equation 11 is obtained from the substitution of Equations 8, 9 and 10.

In dry rocks, Poison's ratio may be taken as $\sigma = 0.26$ (Christensen, 1996). In such a case, the overall multiplier assumes the value of 6. Hence, Equation 12 can be used to obtain surface waves Q-factor from P-wave travel times $t_P$.

### 2.5. Surface Waves Dispersion and Q-factor Computation

Insertion of dispersive velocity function to Equation 4 yields:

$$G(f) = F(f)\, e^{-\frac{\pi t}{Q} f}\, e^{-i\frac{2\pi x}{V(f)} f} \tag{13}$$

In Equation 13, output *G(f)* and input *F(f)* are complex functions where *i* denotes the imaginary term and *V(f)* is the dispersive velocity function. The computation of Q-factor is performed on the real function $exp(-\pi tf/Q)$ only. Therefore, computation of Q-factor is not affected by the imaginary function $exp(-i2\pi xf/V(f))$. When positioning the time analysis window over the seismogram, all wave trains related to surface waves should be included in the computations.

## 3. EstuNet Seismic Network and Geological Structure

The establishment of the EstuNet Seismic Network and operation studies first began in 2005 with the creation of 5 stations, which subsequently increased to 21 with the support of two Anadolu University Research Projects (Figure 3). Thirteen of the stations are strong motion; eight are weak motion.

All stations were free-field and equipped with the CMG-5TD, three-axis strong-motion accelerometer, a 24-bit digitizer, and a flexible data acquisition and storage unit packaged together in a single sealed case. The systems contain two supply boxes with ADSL, GPRS, a satellite modem for communication, and uninterruptible power (Figure 4). Since 2015, EstuNet Seismic Network comprises 13 accelerometers spatially distributed in Eskişehir basin to represent the behaviors of different sediment thickness and different geologic formations of the half-graben structured basin (Figure 5). Stations are also located near active fault segments. The location of the accelerometer stations was chosen according to faults, local soil conditions, and settlement density. The parameters of the stations were given in Table 1.

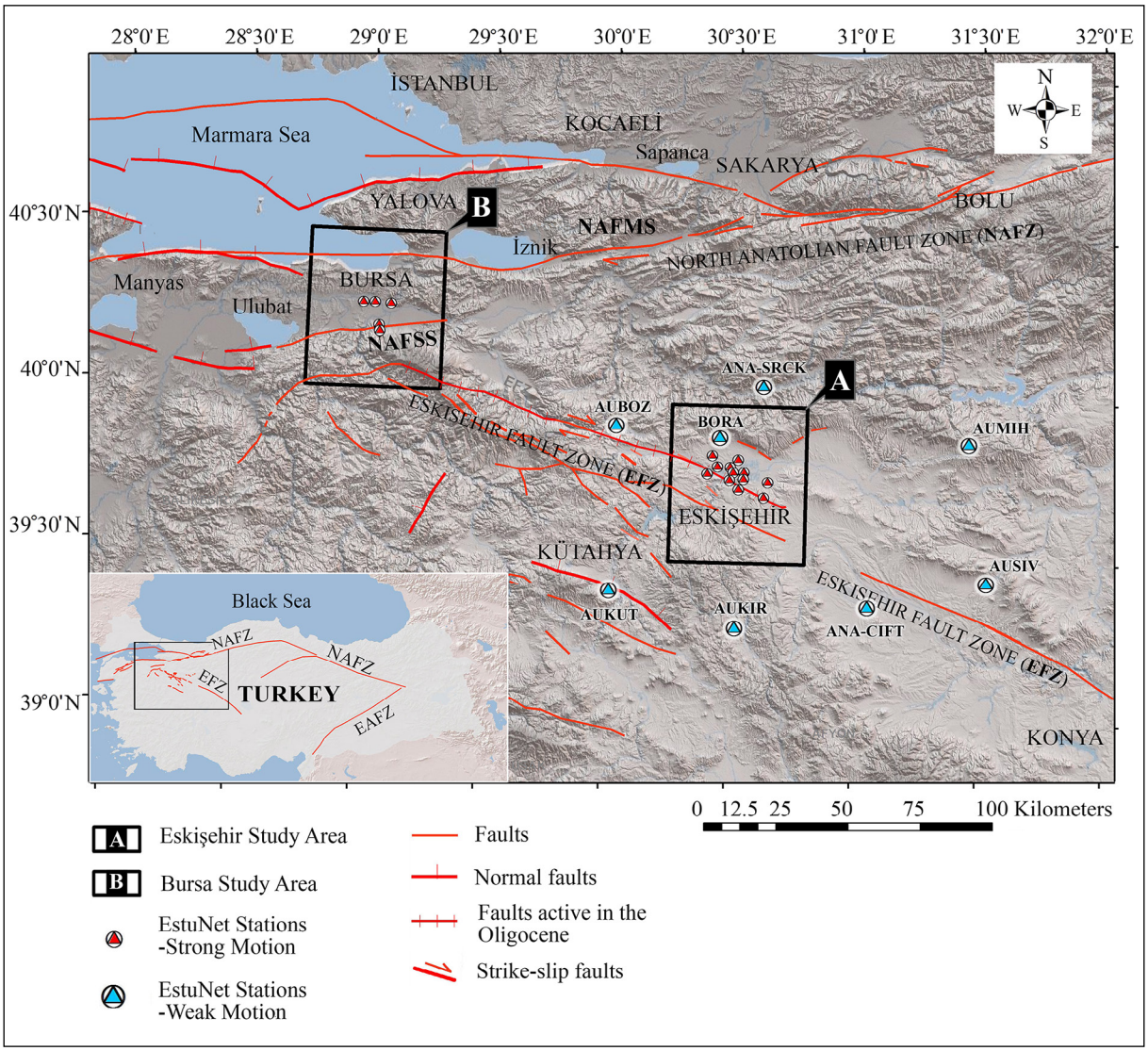


Figure 3- Regional map showing the active faults in Western Anatolia, Turkey (modified from Şaroğlu et al., 1992; Emre et al., 2013) and the location of EstuNet Seismic Network stations. NAFZ-North Anatolian Fault Zone, NAFMS-middle strand of North Anatolian Fault, NAFSS- southern branch of the North Anatolian Fault, EFZ- Eskişehir Fault Zone, EAFZ-East Anatolian Fault Zone, EG-Eskişehir Graben.

## 4. Implementation: M= 4.3 Eskişehir 17.01.2015 Earthquake

The dataset considered in this study includes the strong ground motion data of the 2015 Alınca, Eskişehir earthquake. The Alınca, Eskişehir earthquake of January 17, 2015, magnitude 4.3, was thought to have taken place in the Alınca segment, located northwest of the Eskişehir basin at a depth of 5.5 km (from KOERI). Identified as having a normal fault, the earthquake was recorded by 11 strong motion stations of the EstuNet Seismic Network. Table 2 reports these records, which show the arrival time of the earthquake from the epicenter to the stations, and the peak ground acceleration values. Distance values reported in Table 2 refer to the distance between the accelerometer station and the epicenter of the earthquake. The first row in Table 2 (bold typeface) reports records from the nearest station. The other rows report records from further stations.

In Figure 6, the components for each station are arranged with the vertical component at the top in red and the two horizontal components below. The N-S component is shown in blue and E-W component in green (Figure 6a). Fourier transformations were

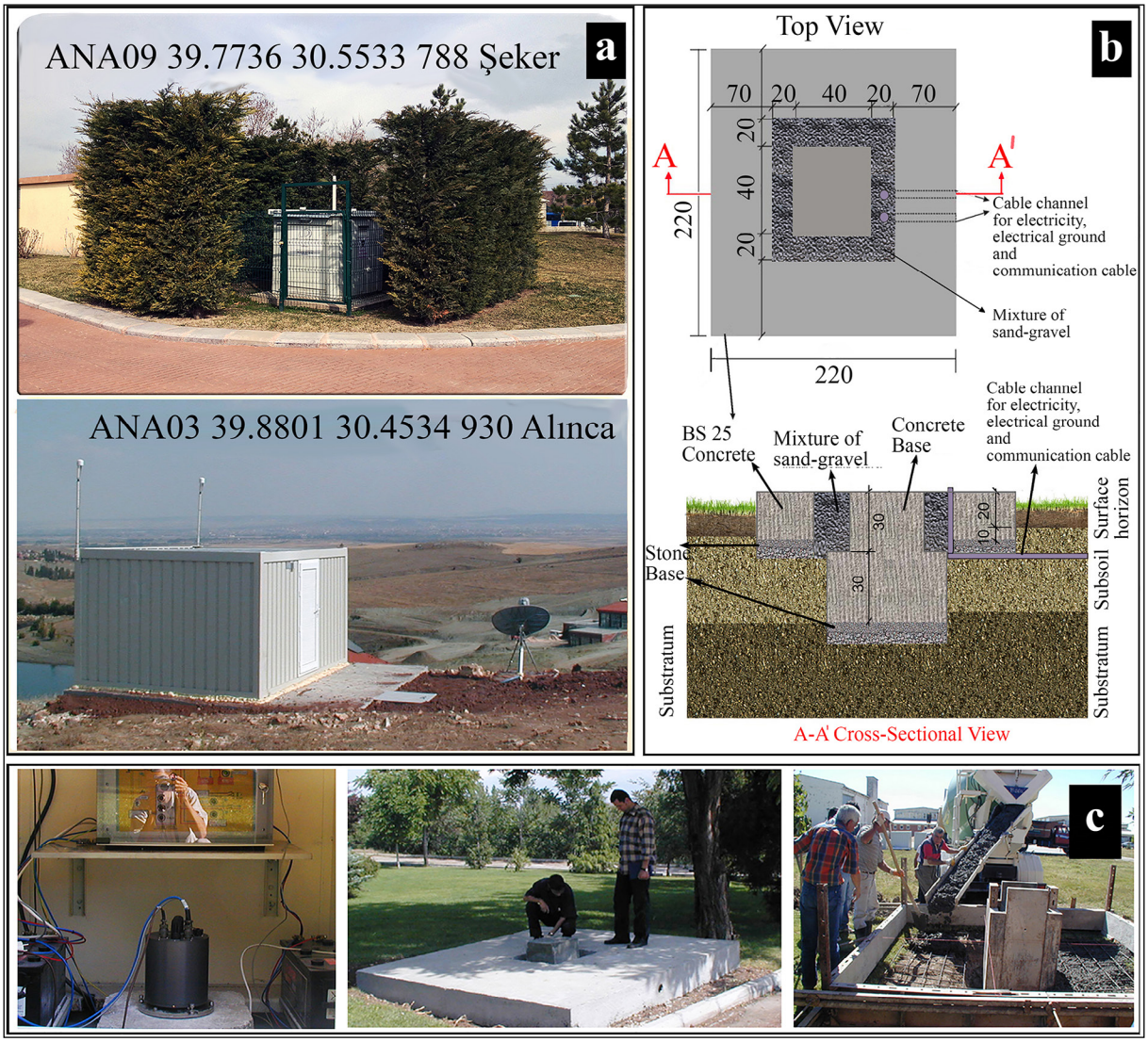


Figure 4- Typical installation of EstuNet strong/weak-motion network; a) recording stations are cabined in the standardized small galvanized hut as shown at ANA09, OSG5 locations, b) infrastructure of strong-motion stations is built according to the schema, c) pictures of the stages of construction, inner view of a container with a typical installation of free-field station, Guralp CMG-5TCDE built-in system mounted on a concrete base (modified from Tün et al., 2020).

calculated for each of the records, taking the frequency upper limit into consideration; amplitude spectrum curves were drawn (Figure 6b). The amplitude spectrum curves provide information on which station to use as the reference (the station in denominator of the ratio). ANA03 station (curves with a light color) is the best candidate to use as the reference, as it is the closest to the focus of the earthquake (data that are rich in terms of frequency content) and it contains no alluvial deposit (data that have no resonance effects). The amplitude spectrum curves of the reference station should be as straight as possible (ie, should contain few peaks) and have a large frequency band in order to detect anomalies such as site fundamental periods in the other stations with which it is compared (the station in the numerator of the ratio). Because data are from the same earthquake, the source functions are the same. Thus, the ratios can serve as indicators of ground differences between the two stations. The analysis windows cover all seismic wave phases, including the initial body waves. Their spectra were then computed (Figure 6).

Subsequently, all the stations were divided by the reference station, ANA03. Because the curve obtained was a noisy one, it had to be smoothed before

Table 1- Stations parameters AnaNet strong motion network.

| No | STATION CODE | Lat. Deg N | Lon. Deg E | Elev. (m) | Location | Instrument Type | Installation Date | Connection Type |
|---|---|---|---|---|---|---|---|---|
| **1** | 2601 ANA01 | 39.8135 | 30.5284 | 787 | İki Eylül Campus | Guralp 5TCDE | 07.12.2005 | Local Network |
| **2** | 2602 ANA02 | 39.7893 | 30.4972 | 815 | Yeşiltepe | Guralp 5TD | 14.03.2005 | Local Network |
| **3** | 2603 ANA03 | 39.8801 | 30.4534 | 930 | Alınca | Guralp 5TD | 09.03.2005 | Satellite |
| **4** | 2604 ANA04 | 39.7732 | 30.5101 | 770 | Kırmızıtoprak | Guralp 5TCDE | 09.12.2005 | 3G/EDGE |
| **5** | 2606 ANA05 | 39.7488 | 30.4956 | 833 | Büyükdere | Guralp 5TD | 10.12.2005 | ADSL |
| **6** | 2610 ANA06 | 39.8245 | 30.4243 | 837 | Yukarısöğütönü. | Guralp 5TD | 14.06.2010 | ADSL |
| **7** | 2611 ANA07 | 39.7900 | 30.4453 | 813 | Batıkent | Guralp 5TCDE | 30.09.2014 | 3G/EDGE |
| **8** | 2612 ANA08 | 39.7669 | 30.4049 | 833 | Karabayır | Guralp 5TD | 15.09.2012 | ADSL |
| **9** | 2613 ANA09 | 39.7736 | 30.5533 | 788 | Şeker | Guralp 5TD | 07.09.2012 | ADSL |
| **10** | 2614 ANA10 | 39.7529 | 30.5521 | 860 | Erenköy | Guralp 5TD | 08.09.2012 | ADSL |
| **11** | 2615 ANA11 | 39.7443 | 30.6503 | 814 | Organized Industry | Guralp 5TD | 14.06.2010 | 3G/EDGE |
| **12** | 2616 ANA12 | 39.6974 | 30.6346 | 916 | Sultandere | Guralp 5TD | 15.06.2010 | ADSL |
| **13** | 2617 ANA13 | 39.7211 | 30.5326 | 936 | Asrı Cemetery | Guralp 5TCDE | 11.09.2012 | 3G/EDGE |

Lat.: latitude, Deg: degree, Long.:longitude, Elev.: elevation.

Table 2- The recording of Eskişehir earthquake, M:4.3-17.01.2015 at accelerometer stations at the AnaNet seismic network.

| Station | Arrival time | Travel time *tP*(s) | Distance (km) | PGA (gal) |
|---|---|---|---|---|
| **ANA03** | **02:42:36:90** | **2.90** | **4.98** | **80.9** |
| ANA01 | 02:42:38:40 | 4.40 | 13.86 | 11.8 |
| ANA02 | 02:42:38:55 | 4.55 | 13.72 | 15.7 |
| ANA05 | 02:42:39:25 | 5.25 | 17.36 | 13.8 |
| ANA06 | 02:42:37:40 | 3.40 | 7.14 | 49.7 |
| ANA07 | 02:42:38:35 | 4.35 | 11.36 | 27.9 |
| ANA08 | 02:42:38:70 | 4.70 | 13.11 | 7.80 |
| ANA09 | 02:42:39:20 | 5.20 | 18.30 | 12.9 |
| ANA10 | 02:42:39:60 | 5.60 | 19.86 | 2.10 |
| ANA11 | 02:42:40:70 | 6.70 | 26.83 | 11.6 |
| ANA12 | 02:42:31:15 | 7.15 | 29.19 | 1.90 |

Earthquake: 2015.01.17, ML:4.3, Depth:5.5 km.
Lat (Deg N): 39.8848, Lon (Deg E): 30.3955, Karacobanpınarı (Alınca)-Tepebaşı-Eskişehir,
Time: 02:42:34:00 (koeri.boun.edu.tr)

continuing with the analysis. The filtering effect of the moving average window lengths applied to the ratio curves of ANA12 and ANA03 stations on moving average window length.

MAWL (1, 10 and 20), E, N and Z components, is shown in Figure 7. This operation was also carried out for the other distant station records. In logarithmic ratio graphs, where the frequency upper limit is 10 Hz, fundamental frequencies of the sites are indicated by the peaks on the curves.

ANA12/ANA03 was shown in Figure 8a. The difficulty in the measurement of the Q-factor results from the need to make the calculations in a frequency environment. The calculation method requires having

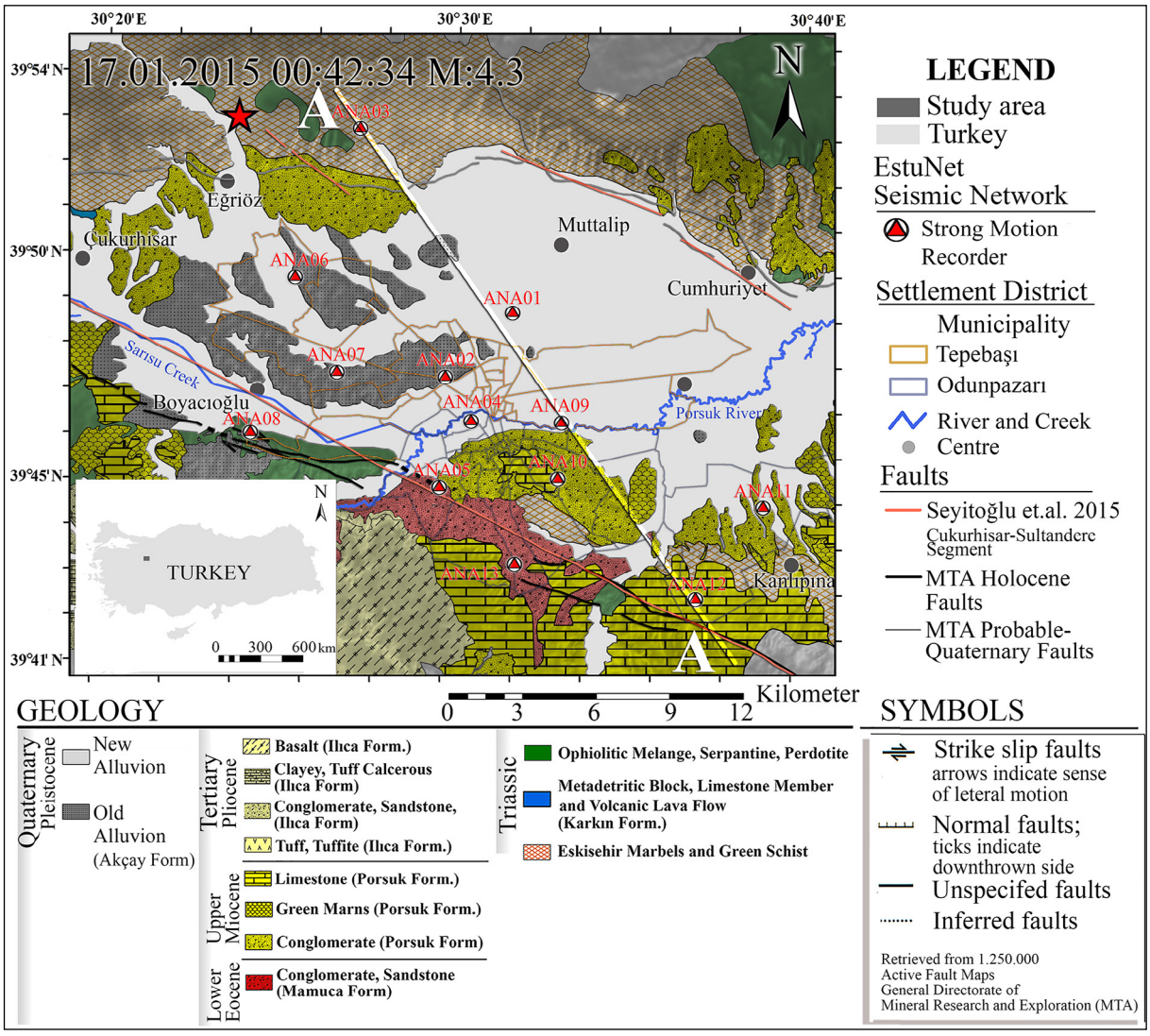


Figure 5- Regional map showing the active faults and geology in Western Anatolia, Turkey (modified from Şaroğlu et al., 1992; Orhan et al., 2007; Emre et al., 2013; Seyitoğlu et al., 2015) and the location of EstuNet seismicnNetwork stations.

the natural logarithm of the amplitude spectrum ratios of earthquake data collected from both close and distant stations. The Q-factor is calculated using the slope of a line segment (Figure 8b) located on the obtained curve. In this study, Q- factor was calculated using Equation 12. In this equation, *t* refers to the travel time for P-waves to travel between close and distant stations, and *a* refers to the slope value obtained in the spectral environment. Figure 9 displays close/distant and ln(close/distant) station data recorded by ANA03 and ANA12 stations for the M4.3 Alınca earthquake. Q values from these data were calculated by solving Equation 12 using the slopes of the line segments placed on ln(close/distant) curves and the differences in travel times between close and distant stations, as shown in Table 2.

## 5. Findings and Discussion

For each accelerometer station, PGA values reported in Table 2 and Q values, calculated by using ANA03 as the reference station, were compared (Figure 9). The figure shows the peak acceleration values calculated for each station on the left vertical axis and the quality factor values calculated on the right vertical axis. The first issue to note in this graph is the inverse relationship between Q values and PGA values, depending on the distance between the source

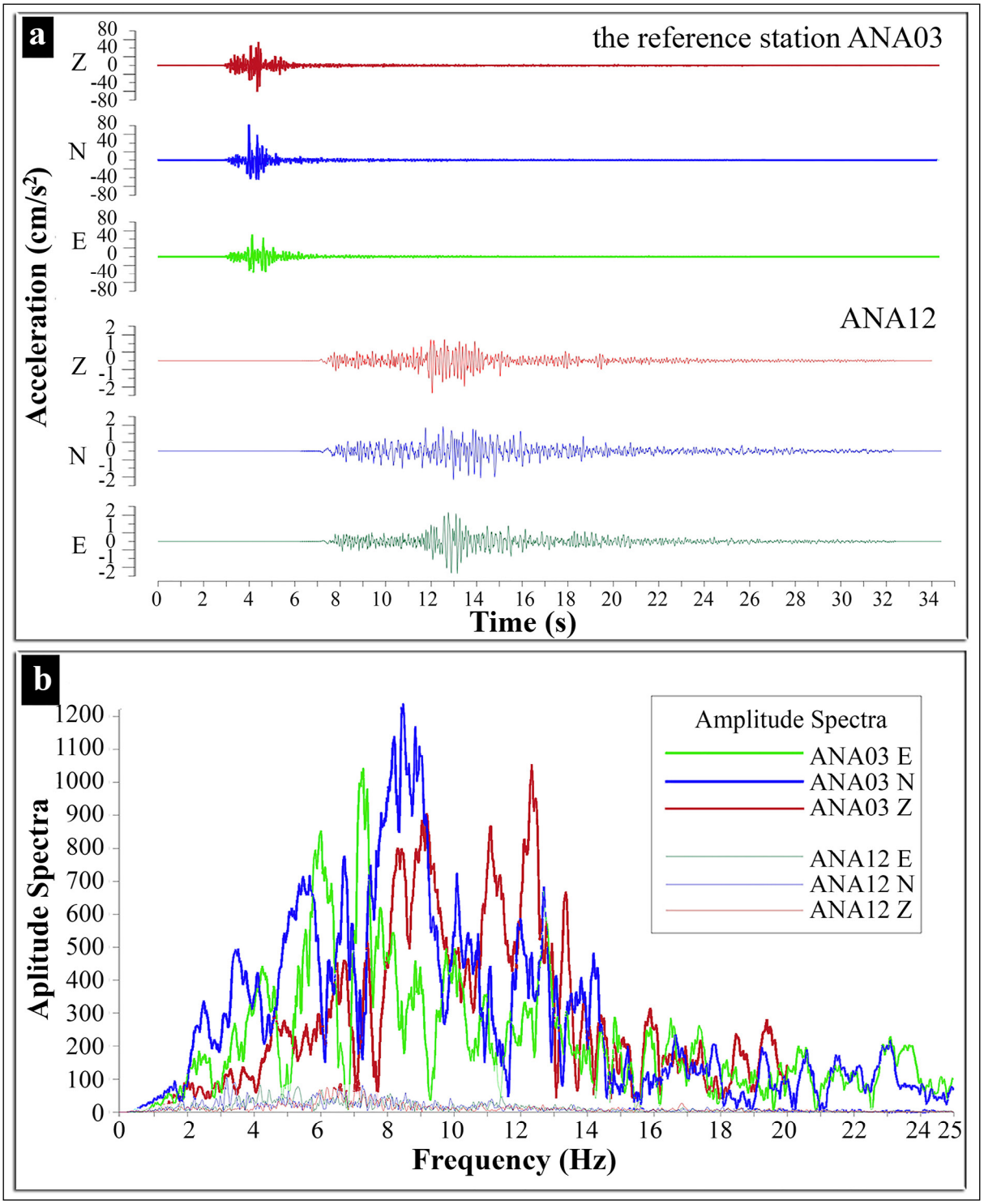


Figure 6- a) The time histories of accelerations recorded at Eskişehir Basin from the ML 4.3, 17 January 2015, Alınca Segment, Eskişehir earthquake, b) computed amplitude spectra curves.

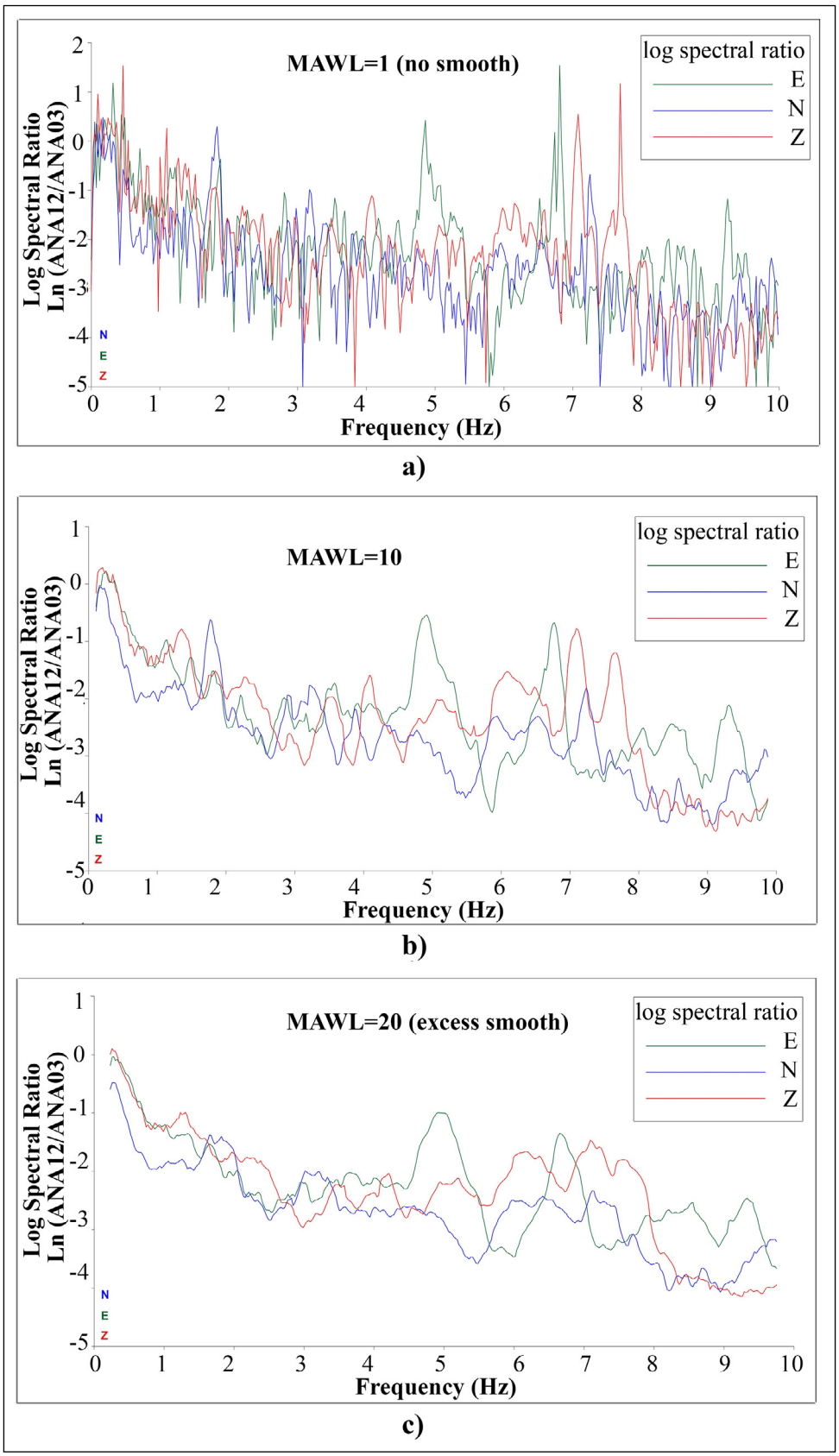


Figure 7- The filter effect results from moving average window length MAWL=1, 10, 20 for Ln(ANA12/ANA03).

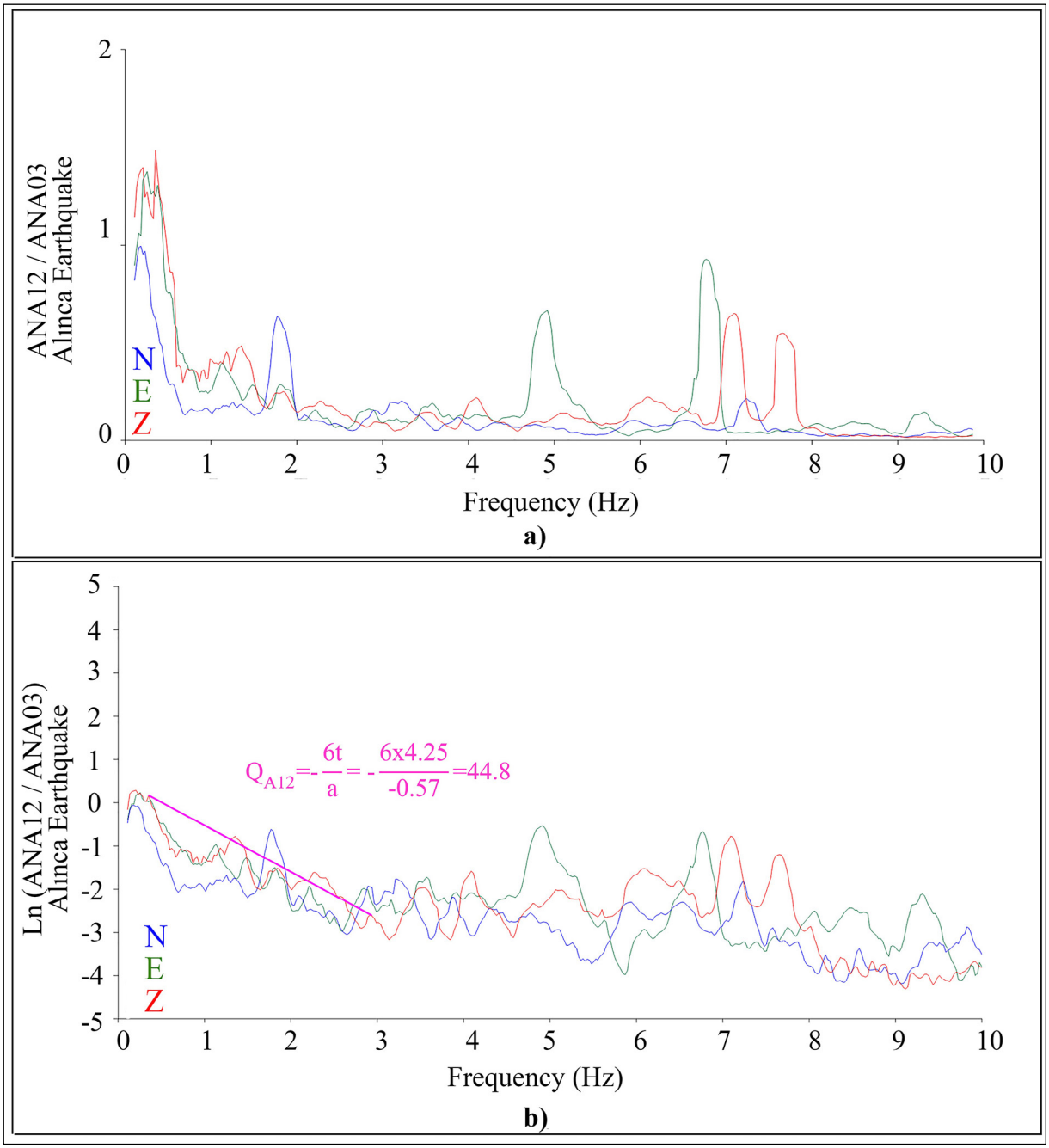


Figure 8- The calculation of quality factor Q in the Alınca Earthquake M= 4,3; a) spectral ratio: ANA12/ANA03; b) ln(ANA12/ANA03) and quality factor were calculated by Equation 12. Blue is N-S, green is E-W, and red is the vertical components. Q was calculated from the slope of the purple curve belonging to ANA03 and ANA12.

and the station. Peak ground acceleration values are known to decrease depending on the attenuation of the earthquake waves and vary by local ground conditions. High PGA values observed may be attributed to proximity to the source of the earthquake or to low quality factors. In addition, the observation that stations with high quality factors had lower peak acceleration values can be attributed to high Q values decreasing surface tremor.

For the Q-factor on the seismic wave route to remain constant, the *t/a* ratio must remain constant. Assuming that this ratio remains constant, an increase in *t* causes a proportional increase in *a*, which is the slope of the Ln|Y(f)/U(f)| curve. Equation 12 shows that *a* varies

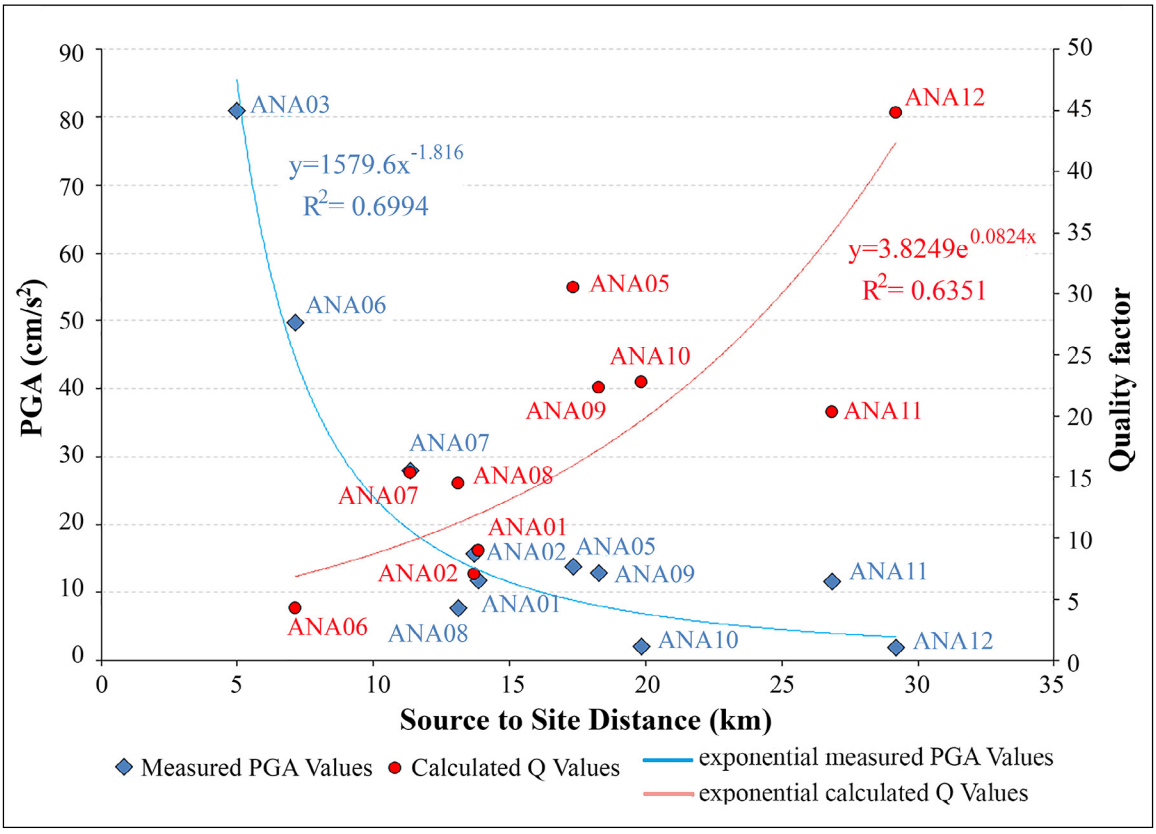


Figure 9- Blue denotes observed PGAs; red is calculated Q-factor for Alınca Earthquake ML:4.3 in the Eskişehir basin.

as the seismic quality of the rocks on the seismic wave route changes. When the seismic quality of the rocks on this route decreases (when average Q decreases), *a* is observed to increase. When the seismic quality of the rocks increases (when average Q increases), *a* is observed to decrease. As the seismic wave proceeds, *t* constantly increases, but *a* is observed to increase or decrease, depending on the seismic quality of the rocks on the route.

As can be seen in Figure 10, for the Q value calculated as 9.0 for the route between ANA03 (close) and ANA01 (distant) stations to remain the same on the route between ANA03 (close) and ANA12 (distant) stations, the slope at ANA12 station would have to be a=-6×t/Q=-6×4.25/9.0=-2.83 s. The actual slope measured at ANA12 station, however, is a=-0.57 s. This decrease in the slope shows that there are rocks with higher seismic quality on the route between ANA03 and ANA12 stations (Q=44.8). If there were rocks with a lower seismic quality on this route, the slope would have been 'a<-2.83 s' (Q<9.0).

The geological and tectonic model through the A-A' cross-section shown in Figure 5 was built using previous studies. To this end, horizontal-to-vertical spectral ratio (HVSR) measurements previously conducted in the region were used and bedrock depth through the A-A' cross-section was estimated. The HVSR method calculates the spectral ratio of the horizontal component to the vertical component (Kanai et al., 1954). These studies show that peaks in the HVSR curves result from a large impedance contrast between the soft sediments and the bedrock. The relationship between the top sediment thickness and the fundamental resonance frequency (fr) values was studied (Tün, 2013). The relationship of fundamental frequency and bedrock depth is a simplified representation without considering the complexities of shallow subsurface structure. A section of the basin was taken along a NW-SE diagonal in order to be able to see the half-graben structure and the compatibility of the graben geometry with the existing faults (Figure 11). As Figure 12b shows, the Q value calculated for ANA12 station, located on limestone, is 44.8. Peak acceleration value which was measured as 80.9 gal at

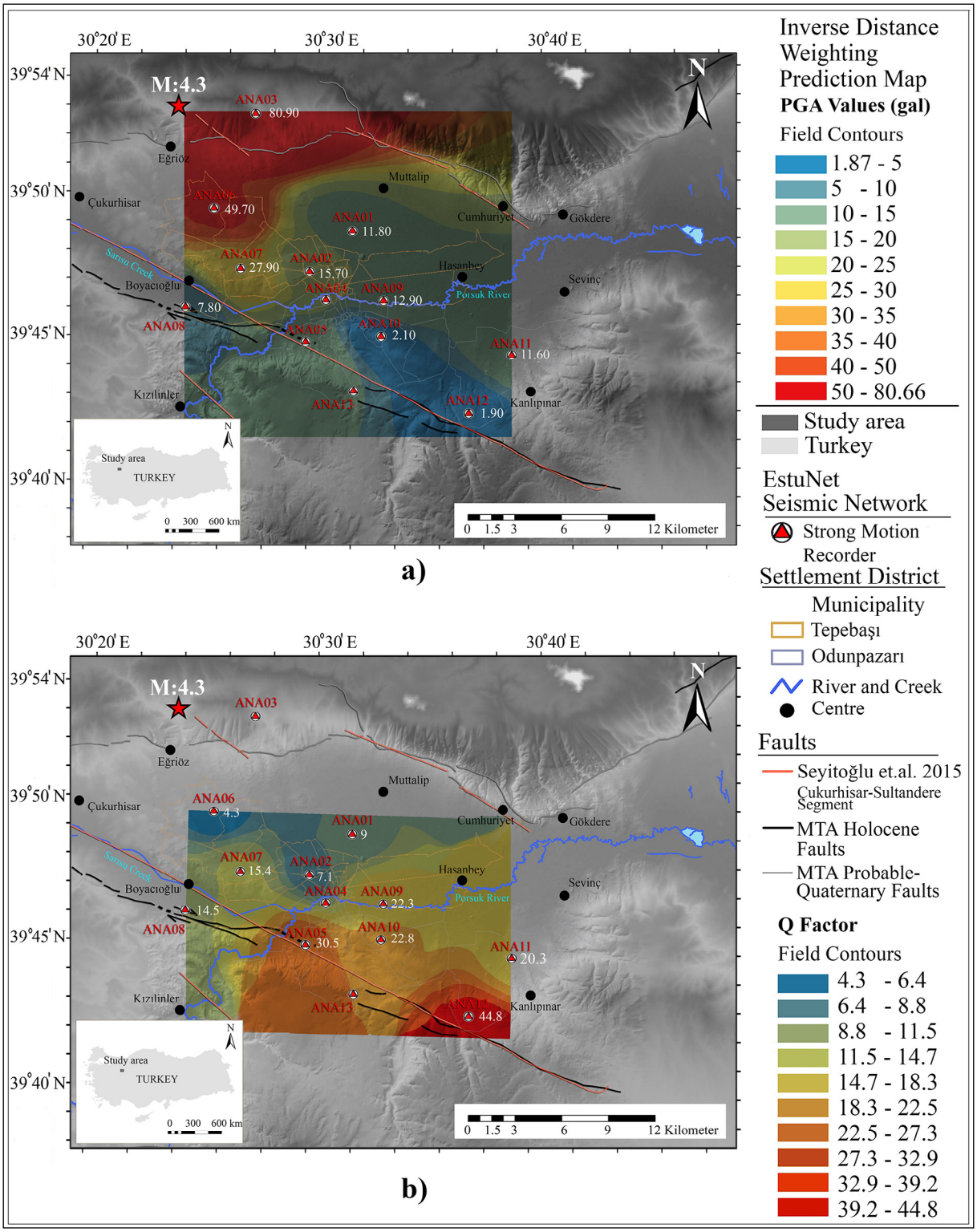


Figure 10- a) Map of PGA values for the ML 4.3, 17 January 2015, Alınca Segment, Eskişehir, earthquake, b) map of Q values for the Alınca, Eskişehir earthquake.

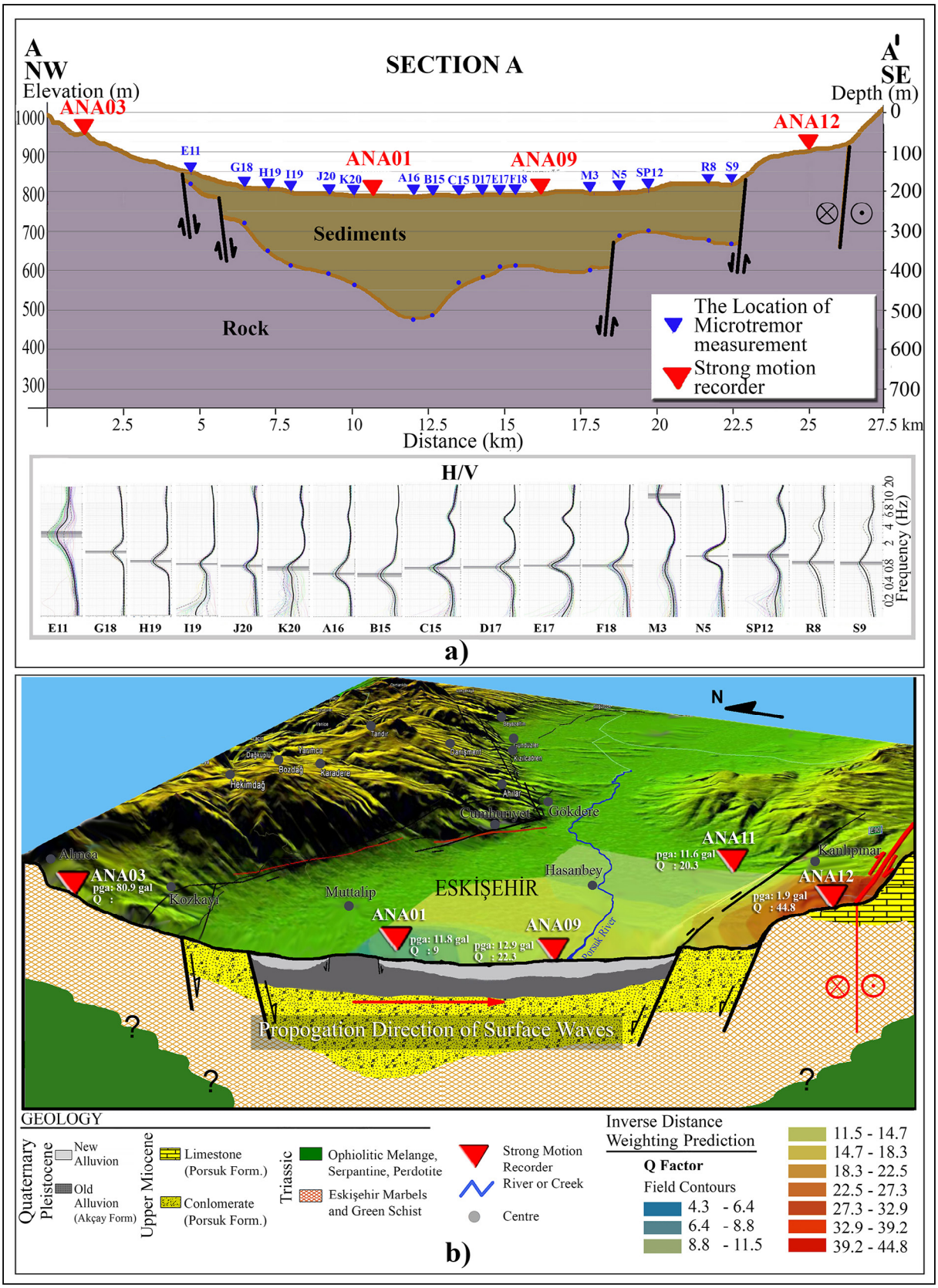


Figure 11- a) The locations of the selected HVSR curves (blue inverted triangles) and strong motion stations are projected on topography and the approximate bedrock depth along the A-A' profile, b) generalized geologic and tectonic model within the study area.

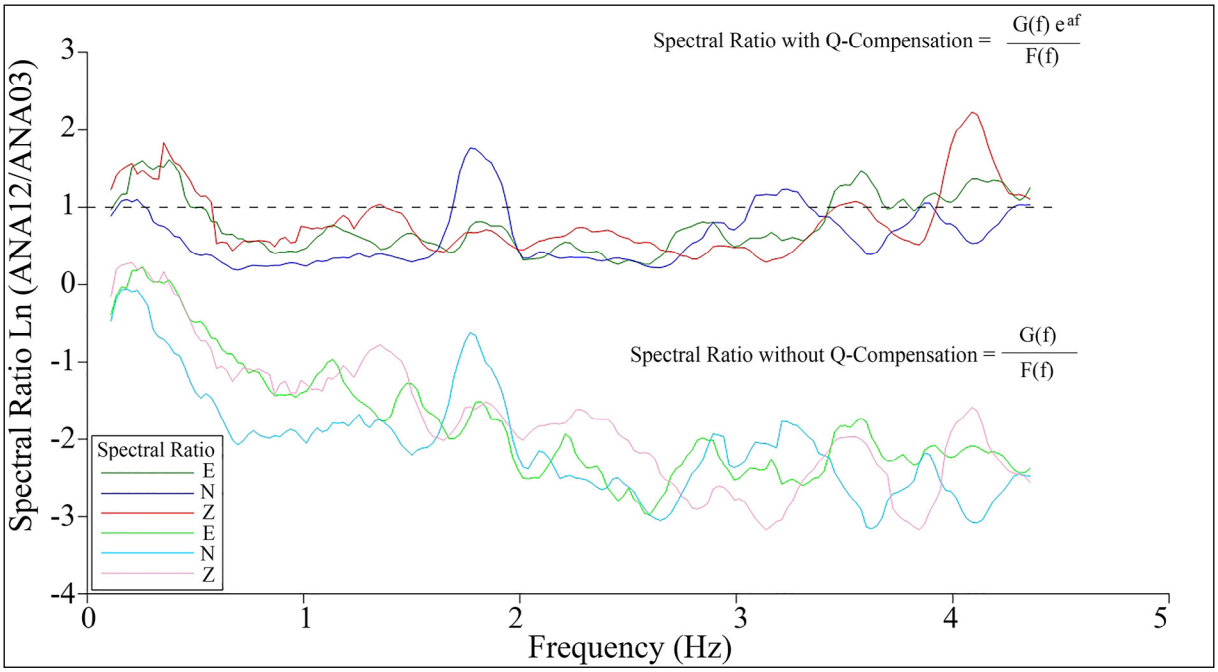


Figure 12- Removal of absorption: Q-compensation.

ANA03, the closest station to the source, decreased to 1.9 gal at ANA12 station, which is located on a bedrock segment with a high seismic quality factor. On the other hand, the peak acceleration value measured at the ANA01 station, which has a seismic quality factor of 9, was 11.6 gal.

5.1. Removal of Absorption: Q-Compensation

A Q-factor compensation process to the ln (output/input) curve was added to remove the absorption effect so that the transfer function of the earthquake waves and soil interaction can be independently analyzed.

The absorption of the seismic waves and their interaction with subsurface layers are both frequency-dependent phenomena. Both events simultaneously influence seismic waves. It was demonstrated in this study that it is possible to discern the absorption process from an interaction with layers (Figure 12).

## 6. Results

The contributions of this study are as follows: (1) the relationship between the computed Q-factor and measured Peak Ground Acceleration values was established; (2) an empirical formula to relate surface waves travel time $t_R$ to P-waves travel time $t_P$ was derived; (3) an analytical expression to prove that Q-factor computation is not affected by surface wave dispersion was derived; (4) the Q compensation step to improve the earthquake waves and soil response curves was proposed.

In this study, the quality factor in sediments was derived from the recordings of strong ground motion for frequencies ranging mainly from 1 to 5 Hz. The measured quality factor ranges between 5 and 45 in the Eskişehir Basin. The comparisons between Q values and PGA values also show good agreement. When Q-factor values are high, PGA values are low and vice-versa. Therefore, the sites where the Q factor is very low should be analyzed in more detail in ground-based earthquake risk assessments.

These basin effects, identified in the cross-section A in Figure 12, should be complemented with findings from further studies on the amplification effects of current sediment deposits, sediment thickness, velocity, and three dimensional geometry of the bedrock depth in the region.

## Acknowledgements

This work was supported by the Anadolu University Research Fund under Project Numbers 1705F255. I

would like to thank Prof. Dr. Berkan ECEVİTOĞLU (Eskişehir Technical University, Eskişehir) for sharing with us his experience related to seismic interpretation.

## References

Anderson, D. L., Archambeau, C. B. 1964. The anelasticity of the earth. Journal of Geophysical Research 69(10), 2071- 2084.

Anderson, D. L., Kovach, R. L. 1964. Attenuation in the mantle and rigidity of the core from multiply reflected core phases. Proceedings of the National Academy of Sciences 51(2), 168-172.

Anderson, D. L., Hart, R. 1978. Q of the Earth. Journal of Geophysical Research: Solid Earth 83(B12), 5869-5882.

Bano, M. 1996. Q-phase compensation of seismic records in the frequency domain. Bulletin of the Seismological Society of America 86(4), 1179-1186.

Bath, M. 1974. Spectral Analysis in Geophysics: Elsevier Science Publication Cooperation, Amsterdam.

Barton, N. 2007. Rock Quality, Seismic Velocity, Attenuation and Anisotropy. CRC Press, 721.

Borcherdt, R. D. 1970. Effects of local geology on ground motion near San Francisco Bay. Bulletin of the Seismological Society of America 60, 29-61.

Borcherdt, R. D. 1989. Results and data from seismologic and geologic studies following earthquakes of December 7, 1988, near Spitak, Armenia SSR (No. 89-163-A). US Geological Survey.

Blias, E. 2012. Accurate interval Q-factor estimation from VSP data. Geophysics 77(3), WA149-WA156.

Christensen, N. I. 1996. Poisson's ratio and crustal seismology. Journal of Geophysical Research Solid Earth 101, 3139-3156.

Dasgupta, R., Clark, R. A., 1998. Estimation of Q from surface seismic reflection data. Geophysics 63(6), 2120-2128.

Dasios, A., Astin, McCann, T. C. 2001. Compressional-wave Q estimation from fullwaveform sonic data. Geophysical Prospecting 49(3), 353-373.

De Castro Nunes, B. I., De Medeiros, W. E., Do Nascimento, A. F., Moreira, J. A. M. 2011. Estimating quality factor from surface seismic data: a comparison of current approaches. Journal of Applied Geophysics 75(2), 161-170.

Emre, Ö., Duman, T., Özalp, S., Elmacı, H., Olgun, Ş., Şaroğlu, F. 2013. Active fault map of Turkey with explanatory text. General Directorate of Mineral Research and Exploration, Special Publication Series 30, Ankara, Turkey.

Engelhard, L. 1996. Determination of seismic-wave attenuation by complex trace analysis. Geophysical Journal International 125(2), 608-622.

Ersoy, İ. 1956. Eskişehir Depremi, ARKİTEKT, 74-75.

Field, E., Jacob, K., Hough, S. 1992. Earthquake site response estimation: a weak-motion case study, Bulletin of the Seismological Society of America 82, 2283-2307.

Futterman, W. I. 1962. Dispersive body waves. Journal of Geophysical Research 67(13), 5279-5291.

Gok, E., Chávez-García, F.J., Polat, O. 2014. Effect of soil conditions on predicted ground motion: Case study from Western Anatolia, Turkey. Physics of the Earth and Planetary Interiors 229, 88-97.

Gurevich, B., Pevzner, R. 2015. How frequency dependency of Q affects spectral ratio estimates. Geophysics 80, A39- A44.

Jackson, D. D., Anderson, D. L. 1970. Physical mechanisms of seismic-wave attenuation. Reviews of Geophysics 8(1), 1-63.

Johnston, D. H., Toksöz, M., Timur, A. 1979. Attenuation of seismic waves in dry and saturated rocks: II. Mechanisms. Geophysics 44, 691-711.

Jongmans, D. 1990. In-situ attenuation measurements in soils, Engineering Geology 29, 99-118.

Kanai, K., Tanaka, T., Osada, K. 1954. Measurement of the microtremor I, Bulletin of the Earthquake Research Institute of Tokyo 32, 199-209.

Kjartansson, E. 1979. Constant Q-wave propagation and attenuation. Journal of Geophysical Research: Solid Earth 84(B9), 4737-4748.

Knopoff, L. 1964. Department of Physics and Institute of Geophysics and Planetary Physics University of California, Los Angeles. Reviews of Geophysics 2(4), 625-660.

Li, J., Wang, S., Yang, D., Dong, C., Tao, Y., Zhou, Y. 2016. An improved Q estimation approach: the weighted centroid frequency shift method. Journal of Geophysics and Engineering 13(3), 399.

Luzi, L., D'Amico, M., Massa, M., Puglia, R. 2019. Site effects observed in the Norcia intermountain basin (Central Italy) exploiting a 20-year monitoring. Bulletin of Earthquake Engineering 17, 97-118.

Mayoral, J., Asimaki, D., Tepalcapa, S., Wood, C., Roman-de la Sancha, A., Hutchinson, T., Franke, K., Montalva, G. 2019. Site effects in Mexico City basin: past and present. Soil Dynamics and Earthquake Engineering 121, 369-382.

Mittal, H., Kumar, A., Kumar, R. 2015. Analysis of ground motion in Delhi from earthquakes recorded by strong motion network, Arabian Journal of Geosciences 8, 2005-2017.

Miyakoshi, H., Tsuno, S., Chimoto, K., Yamanaka, H. 2019. Investigation of site amplification factors for S-and P-waves from spectral inversions in the Tokyo metropolitan area, Japan—for application to earthquake early warnings. Journal of Seismology 23(3), 561-578.

Moya, A., Irikura, K. 2003. Estimation of site effects and Q factor using a reference event. Bulletin of the Seismological Society of America 93, 1730-1745.

Naresh, B., Venkatesh, K., Mishra, L. K. 2019. Q-factor of the Punjab Basin. International Journal of Scientific Research and Review 7(9).

Orhan, A., Seyrek, E., Tosun, H. 2007. A probabilistic approach for earthquake hazard assessment of the Province of Eskişehir, Turkey, Natural Hazards and Earth System Science 7, 607-614.

Özer, Ç. 2019. Erzurum ve çevresinin yerel zemin etkilerinin incelenmesi. Dokuz Eylül Üniversitesi Mühendislik Fakültesi Fen ve Mühendislik Dergisi 21, 247-257.

Özmen, B. 2000. Ağustos 1999 İzmit Körfezi depreminin hasar durumu (rakamsal verilerle). Türkiye Deprem Vakfı 010-53, 132.

Parolai, S. 2012. Investigation of site response in urban areas by using earthquake data and seismic noise, New Manual of Seismological Observatory Practice 2, 1-38.

Press, F. 1964. Seismic wave attenuation in the crust. Journal of Geophysical Research 69(20), 4417-4418.

Quan, Y., Harris, J. M. 1997. Seismic attenuation tomography using the frequency shift method. Geophysics 62(3), 895- 905.

Raghukanth, S., Nadh Somala, S. 2009. Modeling of strong-motion data in northeastern India: Q, stress drop, and site amplification. Bulletin of the Seismological Society of America 99, 705-725.

Ricker, N. 1940. The form and nature of seismic waves and the structure of seismograms, Geophysics 5, 348-366.

Sams, M., Goldberg, D. 1990. The validity of Q estimates from borehole data using spectral ratios. Geophysics 55(1), 97-101.

Seyitoğlu, G., Ecevitoğlu, G. B., Kaypak, B., Güney, Y., Tün, M., Esat, K., Avdan, U., Temel, A., Çabuk, A., Telsiz, S., Aldaş, G. 2015. Determining the main strand of the Eskişehir strike-slip fault zone using subsidiary structures and seismicity: a hypothesis tested by seismic reflection studies. Turkish Journal of Earth Sciences 24, 1-20.

Shearer, P. M. 2009. Introduction to Seismology, 241-300.

Stein, S., Wysession, M. 2009. An Introduction to Seismology, Earthquakes, and Earth Structure. Blackwell Publishing, John Wiley and Sons, 515.

Steidl, J. H., Tumarkin, A. G., Archuleta, R. J. 1996. What is a reference site? Bulletin of the Seismological Society of America 86, 1733-1748.

Şaroğlu, F., Emre, Ö., Kuşcu, İ. 1992. Active fault map of Turkey with explanatory text, Mineral Research and Exploration General Directorate, Ankara, Turkey.

Tün, M. 2013. Interpretation of ground response and shear wave velocity (Vs) structure in microzonation studies: a case study in Eskişehir. PhD Thesis, İstanbul University.

Tün, M., Mutlu, S., Pekkan, E. 2020. EstuNet: A new weak/strong-motion network with Geodatabase for Metropolitan Eskişehir and Bursa, West Anatolia, Turkey. Journal of Earthquake Research 2(2), 193-208.

Wang, Y. 2004. Q analysis on reflection seismic data. Geophysical Research Letters 31(17).

Wang, Y., Guo, J. 2004. Modified Kolsky model for seismic attenuation and dispersion. Journal of Geophysics and Engineering 1(3), 187.

Yang, J., Cao, S., Yuan, D., Zhang, H., Shi, W. 2014. A new method for quality factor Q estimation: spectrum attributes method. 2014 SEG Annual Meeting.

Zhang, C., Ulrych, T. J. 2002. Estimation of quality factors from CMP records. Geophysics 67(5), 1542-1547.

Bulletin of the Mineral Research and Exploration

http://bulletin.mta.gov.tr

# Alien foraminifers of the northern and northeastern coastlines of Cyprus Island

Engin MERİÇ[a], M. Baki YOKEŞ[b], İpek F. BARUT[c], Atike NAZİK[d]*, Mustafa ERYILMAZ[e], Fulya YÜCESOY ERYILMAZ[e], M. Fatih HÜSEYİNOĞLU[f], Mustafa KUMRAL[g] and Erol SARI[c]

[a]*Moda Hüseyin Bey Street, 15/4, Kadıköy, İstanbul, Turkey*
[b]*AMBRD Laboratories, Hanımefendi Street,160/9, Şişli, İstanbul, Turkey*
[c]*İstanbul University, Institute of Marine Sciences and Management, Vefa, İstanbul, Turkey*
[d]*Çukurova University, Faculty of Engineering, Department of Geological Engineering, Balcalı, Adana, Turkey*
[e]*Mersin University, Faculty of Engineering, Department of Geological Engineering, Çiftliköy Campus, Yenişehir, Mersin, Turkey*
[f]*University of Girne, Faculty of Maritime Studies, Girne, Turkish Republic of Northern Cyprus*
[g]*İstanbul Technical University, Faculty of Mines, Department of Geological Engineering, Maslak, İstanbul, Turkey*

*Research Article*

Keywords:
Benthic Foraminifera, Mollusc, Ostracod, ICP-MS Analysis, Geochemistry, Cyprus.

**ABSTRACT**

The study area covers the northern coasts of Cyprus from the Güzelyurt Gulf to the Gazimağusa Gulf. This study was carried out in order to reveal the presence of the alien foraminifera, which are widely distributed in the Eastern Mediterranean particularly *Amphistegina lobifera* in the study area, and the effects of trace elements on faunal assemblages (foraminifera, ostracod and mollusc). The bottom sediment samples were taken from eighteen different points and depths, the faunal assemblages were examined, and the sediment distribution map of the studied area was made by ICP-MS analysis and geochemical evaluations. 30 genera and 48 species of foraminifera have been identified, of which 9 species belonging to 6 genera are the alien foraminifera. These are: *Spiroloculina angulosa, S. antillarum, Hauerina diversa, Coscinospira hemprichii, Peneroplis pertusus, P. planatus, Amphisorus hemprichii, Sorites orbiculus* and *Amphistegina lobifera*. Amphistegina lobifera was observed to be abnormally abundant in most of the samples. This foraminiferal assemblage of Red Sea origin constitutes a poor assemblage compared to the alien assemblages in Turkish Mediterranean coastal areas. It has been determined that the ostracod and mollusc genera and species found in the same samples belong to the typical Mediterranean and Aegean Sea community.

*Received Date: 10.09.2020*
*Accepted Date: 08.12.2020*

## 1. Introduction

Data revealing the presence of large number of alien species and their origins have been unpublished in several studies concerning benthic foraminiferal assemblages in the Mediterranean and Aegean coasts of Turkey (Meriç et al., 2008*a*, 2015*a*, *b*, 2016, 2018 *a*, *b*, Yokeş et al., 2014). In these studies, it was observed that the diversity of alien foraminifera on the Aegean coasts was higher than those obtained in the studies conducted on the Mediterranean coasts. Alien foraminifera such as *Spiroloculina antillarum*, *Coscinospira hemprichii*, *Peneroplis pertusus*, *P. planatus*, *Sorites orbiculus*, *Astacolus insolithus*, *Siphonina tubulosa*, *Amphistegina lessonii*, *A. lobifera*, which were found in the Middle Pleistocene-Holocene sediments of Turkey, are accepted to have reached Eastern Mediterranean via Suez Canal (Meriç et al., 2018*a*). In addition, it was also stated in these studies that the alien foraminifera have increased

Citation Info: Meriç, E., Yokeş, M. B., Barut, İ. F., Nazik, A., Eryılmaz, M., Yücesoy Eryılmaz, F., Hüseyinoğlu, F. M., Kumral, M., Sarı, E. 2021. Alien foraminifers of the northern and northeastern coastlines of Cyprus Island. Bulletin of the Mineral Research and Exploration 166, 145-165. https://doi.org/10.19111/bulletinofmre.838609

**Corresponding author: Atike NAZİK, anazik@cu.edu.tr*

populations in the areas with hot springs. This study was carried out to determine the sediment distribution, faunal content (benthic foraminifers, ostracods and molluscs) and trace elements of the bottom sediments in samples from the northern coasts of Cyprus, located in the Eastern Mediterranean, and also to investigate test coloration in alien foraminifera. In addition, alien foraminifera observed in the Mediterranean and the Aegean coasts of Turkey were compared in terms of assemblages and the coloration characteristics of their tests.

## 2. Material and Methods

In the study area, paleontological samples were collected from 0.10-40.00 m depths from 18 points in northern and northeastern coasts of the island in 2019 summer (Figure 1, Table 1). Microorganism analyses in sediment samples were performed according to Babin (1980) and Bignot (1985). 5 g of dry samples weighed and 10% $H_2O_2$ was added, kept for 24 hours, and subsequently washed in a 0.063 mm sieve with pressurized water, dried in a 50 ºC oven, and were further sieved in 2.00, 1.00, 0.500, 0.250, 0.125 mm sieves. These samples were examined under a binocular microscope and the benthic foraminifera, ostracods and molluscs it contained were separated (Table 2-4).

Seasonal physical parameters of sea water were evaluated in-situ by using CTD (temperature, salinity and depth) device and current meters. Current velocity and directions were measured at three different depths (surface, middle and bottom) for a short time.

In addition, 563 recent sediment samples collected from the sea floor of the Northern Cyprus coasts via Orange-peel and other samplers were analyzed according to their grain size distribution. Sieve and pipette analysis methods were applied to these samples, the results were classified in triangular diagram (Wentworth, 1922; Folk, 1974), and a sediment distribution map of the region at 1: 50,000 scale was prepared according to the grain size.

In the study, the grain size content of 18 samples in which paleontological data were evaluated were determined by using the methods proposed by Galehouse (1971) and McManus (1991) (gravel, sand, silt and clay amounts). Gravel- and sand-size materials were determined by sieve analysis, and silt- and clay-size materials were determined by particle size analyzer (sedigraph method).

The geochemical analyzes of sediments were carried out at İstanbul Technical University by ICP-MS (Inductively Coupled Plasma Mass Spectrometer). Trace elements including Cd, Ce, Cs, Dy, Er, Eu, Ga, Gd, Ho, In, La, Lu, Nd, Pr, Rb, Sm, Tb, Tl, Tm, Y, Yb, Th, U were measured.

## 3. Oceanography and Recent Sediment Distribution of the Marine Space Between Girne and Gazimağusa

Kyrenia (Girne) is located in the north of Beşparmak Mountains which extend from Zafer Cape (Karpass) to Koruçam Cape (Kormacit) in the east. The coasts generally extend in the E-W direction and are quite indented, protruding. The shores of Güzelyurt Bay, from Koruçam Cape to Gemikonağı (Yedidalga Beach), have a rather flat and arc-shaped appearance. The Beşparmak Mountains with steep-slopes, which played an important role in shaping the coast, extend parallel to the shore at approximately 4-6 km far from the coast. There are many riverbeds that cut the steep slopes of these mountains. This steep topography continues with the same slope up to 200 meters deep of the sea. The slope of the land topography increases again in the section from Yeşilyurt to Gemikonağı. In this mountainous region, which constitutes the northern slopes of the Troodos Mountains, rivers flow through deep and relatively long valleys and reach the sea (Figure 1).

Famagusta (Gazimağusa) Bay is the marine space between Zeytin Cape and Poyraz Cape (Ayili Cape) in the east of Cyprus Island. Karpass mountainous region, which does not exceed 400 m in elevation, is located at the north of this area. In the south of the mountainous region, wide flatlands where Boğaz town is also located, with less than 100 m height as the continuation of Nicosia Plain are located. Although there are stream beds in places in this region, there is no river discharging waters into the bay. Due to factors such as the drought, the flatness of the stream beds and evaporation, the waters collected by precipitation cannot reach the sea (Figure 1).

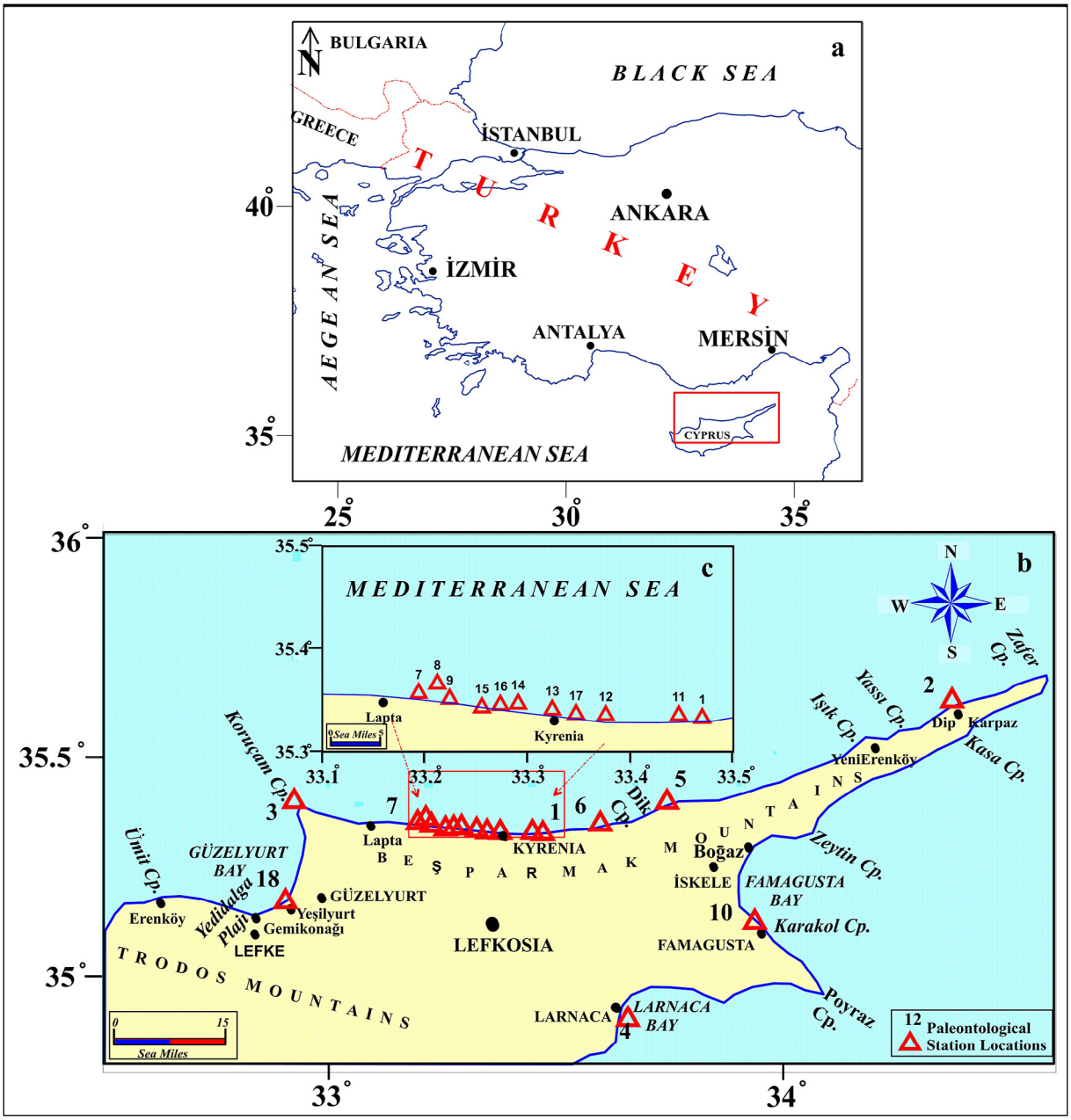


Figure 1- Location map ; a) general view, b) locations of the studied samples and c) locations of paleontological samples in detail. (Cp.: Cape).

### 3.1. Coastal and Sea Bottom Topography

The slope of the bottom topography is less in the Güzelyurt Bay which is located in the northern part of Cyprus Island. In this region, contour lines (isobaths) become denser towards the west. The 200 m depth curve is 5.5 km distant in the west of Koruçam Cape, 13 km in the middle of Güzelyurt Bay, and 3 km distant in the west of Gemikonağı Village. Sea floor inclination, starting to increase as from the north of Gemikonağı, is at the highest value in the region that is the seaward extension of the Troodos Mountains in the west. The sea bottom topography in the Kyrenia (Girne) Region changes in concordance with the land structure on land. Inclination of the sea bottom topography in the section eastward from Koruçam Cape up to a depth of 500 meters, varies between 4.5-9.0%. However, in this area there are regions which has an inclination of more than 10% in places (Figure 2a) (TR-341, 2007; TR-342, 2014; TR-343, 2017; TR-344, 2012; Özhan, 1988; Eryılmaz and Yücesoy Eryılmaz, 2003; Report 1 (1987), Report 2 (1988), Report 3 (1990), Report

Table 1- Depths of the paleontological sampling and coordinates of the stations.

| SAMPLE STATIONS | LATITUDE | LONGITUDE | DEPTH (m) |
|---|---|---|---|
| **1** | 35.33264 | 33.46905 | 1.0 |
| **2** | 35.62875 | 34.37109 | 5.0 |
| **3** | 35.40415 | 32.92118 | 2.0 |
| **4** | 34.9179 | 33.65669 | 40 |
| **5** | 35.40266 | 33.74286 | 0.1 |
| **6** | 35.35401 | 33.59583 | 0.1 |
| **7** | 35.35682 | 33.19328 | 7.0 |
| **8** | 35.36594 | 33.21136 | 25 |
| **9** | 35.35118 | 33.2235 | 0.1 |
| **10** | 35.13519 | 33.93623 | 1.0 |
| **11** | 35.33516 | 33.44621 | 0.1 |
| **12** | 35.33532 | 33.37515 | 0.1 |
| **13** | 35.34071 | 33.32322 | 0.1 |
| **14** | 35.34659 | 33.2899 | 0.1 |
| **15** | 35.3449 | 33.27534 | 0.1 |
| **16** | 35.3454 | 33.27273 | 0.1 |
| **17** | 35.33633 | 33.34624 | 0.1 |
| **18** | 35.18084 | 32.90192 | 0.1 |

4 (1991), Report 5 (1992); http://users.metu.edu.tr/kktctntm/KKTC_tarihi/ adacogr. html).

The sea bottom topography in the Famagusta (Gazimağusa) Region changes in concordance with the land topography. Although the inclination of the sea bottom is very low in the east of the region, it suddenly increases off the Poyraz Cape, in the east of the Boğaz town. While the sea depth of 500 meters around Famagusta (Gazimağusa) is reached 9 km off the coast, this depth is 3.5 km off Poyraz Cape. The inclination decreases again, off the Kurnyalı, east of the Poyraz Cape (Ayili). In this section, there are places reached a depth of 200 meters at a distance of 13 km.

A gently inclined bottom topography (2-2.5%) is observed between Famagusta (Gazimağusa) and the Strait up to a water depth of 50 meters. This inclination decreases further at shallower parts than 20 meters. There are wide beaches on the shores of these aforementioned shallow slopes (Figure 2a, b) (TR-341, 2007; TR-342, 2014; TR-343, 2017; TR-344, 2012; Eryılmaz and Yücesoy Eryılmaz, 2003; Report 1, 1987; Report 2, 1988; Report 3, 1990; Report 4, 1991; Report 5, 1992).

## 3.2. Physical and Chemical Properties of Sea Water

### *3.2.1. Temperature*

In the Güzelyurt Bay-Kyrenia (Girne) Region of Cyprus, seasonal water temperature varies according to the depth. In spring it is 17.50-18.55 °C at the surface, 17.51-17.56 °C at a depth of 50 meters, and in the summer 28.17-29.14 °C at the surface, 18.09-20.20 °C at a depth of 50 meters. In the autumn it is 21.12-22.06 °C at the surface and 19.41-21.90 °C at a depth of 50 meters, while in the winter it varies between 16.60-17.42 °C at the surface and 16.25-17.24 °C at a depth of 50 meters (Figure 3a) (Eryılmaz, 2004).

In the Cyprus-Famagusta (Gazimağusa) region, the seasonal temperature distributions of water (Figure 4a) were measured as 17.03-17.61 °C at the surface in the spring season, and 16.54-17.41 °C at a depth of 50 meters. In summer it varies between 27.98-29.13 °C at the surface, 18.33-19.12 °C at a depth of 50 meters, and in the autumn 21.19-21.57 °C at the surface, 20.86-21.42 °C at a depth of 50 meters. In the winter, it changes between 16.53-17.75 °C at the surface, and 16.56-17.51 °C at a depth of 50 meters (Figure 4a) (Eryılmaz, 2004).

### *3.2.2. Salinity*

In the measurements made in Güzelyurt Bay and Kyrenia (Girne) Region, salinity values at surface and 50-meter water depth were determined as follows. In the spring, it is 39.02-39.40‰ at the surface, 38.98-39.40‰ at 50 meter-depth, and in the summer, it is 39.01-39.26‰ at the surface, 38.82-39.07‰ at 50 meter-depth. In the autumn, it is between 39.05-39.22‰ at the surface and 38.89-39.23‰ at 50 meter-depth. In the winter, these values were determined as 38.62-39.02‰ at the surface and 38.82-38.97‰ at 50 meter-depth (Figure 3b) (Eryılmaz, 2004).

Salinity values determined in the Famagusta (Gazimağusa) Bay are as follows: in the spring, 38.97-39.32‰ at the surface, 38.97-39.34‰ at 50 meter-depth; in the summer, 38.95-39.21‰ at the surface, 38.82-39.10‰ at 50 meter-depth; in the autumn, 38.94-39.36‰ at the surface, 39.02-39.55‰ at 50 meter-depth; in the winter, 38.57-39.09‰ at the surface, 38.78-38.99‰ at 50 meter-depth (Figure 4b) (Eryılmaz, 2004).

Table 2- Distributions of benthic foraminifera by stations.

| FORAMINIFERA | STATIONS | | | | | | | | | | | | | | | | | |
|---|---|---|---|---|---|---|---|---|---|---|---|---|---|---|---|---|---|---|
| | 1 | 2 | 3 | 4 | 5 | 6 | 7 | 8 | 9 | 10 | 11 | 12 | 13 | 14 | 15 | 16 | 17 | 18 |
| *Spiroplectinella sagittula* | | | | * | | | | | | | | | | | | | | |
| *Bigenerina nodosaria* | | | | | | | | | | | | * | * | | | | | |
| *Textularia bocki* | | | * | * | * | * | * | * | | | | * | * | | * | * | | |
| *Textularia conica* | | | | * | * | | | | | | | * | * | | | | | |
| *Patellina corrugata* | | | | * | | | | | | | | | | | | | | |
| *Nubecularia lucifuga* | | | | * | | | | | | * | | * | | | | | | |
| *Adelosina cliarensis* | | | | * | | | * | | | * | | * | | * | | | | |
| *Adelosina duthiersi* | | | * | * | | | | | | | | | | | | | | |
| *Adelosina mediterranensis* | | | | * | | * | | | | * | | * | | | | * | | |
| *Adelosina partschi* | | | * | | | | | | * | | | | | | | | | |
| *Adelosina pulchella* | | | | | | * | | | | | | | | | | | | |
| *Spiroloculina angulata* | | | | | | | | | | | | | | * | | | | |
| *Spiroloculina angulosa* | | | | | | | | | | | | * | | | | | | |
| *Spiroloculina antillarum* | | | | * | | | * | | | | | * | | * | | | | |
| *Spiroloculina depressa* | | | | | * | | | | | | | | | | | | | |
| *Spiroloculina excavata* | | | | * | | | | | | | | * | | | | | | |
| *Spiroloculina tenuiseptata* | | | | * | | | | | | | | * | | | | | | |
| *Hauerina diversa* | | | | | | | * | | | | | * | | | | | | |
| *Cycloforina contorta* | | | | * | | | | | | | | | | | | | | |
| *Massilina secans* | | | | | | | | | | | | * | | | | | | |
| *Quinqueloculina bidentata* | | | | | | | | | | | | * | | | | | | |
| *Quinqueloculina disparilis* | | | | | | | | | | * | | | | | | | | |
| *Quinqueloculina jugosa* | | | | | | | | | | * | | | | | | | | |
| *Quinqueloculina lamarckiana* | | | | | | | | | | | | * | | | | | | |
| *Quinqueloculina seminula* | * | | | | | | * | | | | | * | | * | * | | * | |
| *Miliolinella subrotunda* | | | | | | | | | | * | | | | | | | | |
| *Pseudotriloculina laevigata* | | | | * | | | | | | * | | * | | | | | | |
| *Triloculina marioni* | | | | * | | * | | | | * | | * | | * | | | | |
| *Triloculina tricarinata* | | | | | | | | | | | | | | * | | | | |
| *Sigmoilinita costata* | | | | * | | * | | | | | | | | | | | | |
| *Sigmoilinita edwardsi* | | | | | | | | | | * | | | | | | | | |
| *Coscinospira hemprichii* | | * | | | | | * | | * | * | | * | | | | * | | |
| *Laevipeneroplis karreri* | | | * | | | | | | | | | | | | | | | |
| *Peneroplis pertusus* | | * | * | * | * | * | * | * | * | * | * | * | * | * | * | * | * | * |
| *Peneroplis planatus* | | * | * | | | * | * | | | | * | | | | | * | | |
| *Amphisorus hemprichii* | | | | | | | | | | * | | * | | | | | | |
| *Sorites orbiculus* | | * | * | | | | * | | | | | * | * | | | | | |
| *Amphicoryna scalaris* | | | | * | | | | | | | | | | | | | | |
| *Rosalina bradyi* | | | | * | | | | | | | | * | | * | | | | * |
| *Rosalina floridensis* | | | | | | | | | | | | * | | | | | | |
| *Lobatula lobatula* | | | | * | | | | * | | | | * | * | | | | | |
| *Cyclocibicides vermiculatus* | | | | | | | | | | | | * | | | | | | |
| *Planorbulina mediterranensis* | | | | * | | | | | | | | | | | | | | |
| *Miniacina miniacea* | | | | | | | | * | | | | | | | | | | |
| *Amphistegina lobifera* | * | * | * | * | * | * | * | * | * | * | | * | * | * | * | * | * | * |
| *Ammonia tepida* | | | | | | | | | | | | | | | | | | * |
| *Porosononion subgranosum* | | | | | | | * | | | | | | | | | | | |
| *Elphidium crispum* | | | | * | | | | | | * | | | * | | | | | |

Table 3- Distributions of ostracods by stations.

| OSTRACODA | STATIONS | | | | |
|---|---|---|---|---|---|
| | 2 | 4 | 5 | 10 | 12 |
| *Acantocythereis hystrix* | | * | | | |
| *Aurila convexa* | | * | * | | * |
| *Bosquetina carinella* | | * | | | |
| *Cytheretta judaea* | | | | | * |
| *Cytherois sp.* | | | | | * |
| *Ekpontocypris prifera* | | * | | | |
| *Jugosocythereis prava* | * | * | | | |
| *Loxoconcha bairdi* | | * | | | |
| *Loxoconcha gibberosa* | | * | | | |
| *Neonesidea corpulenta* | | * | | | * |
| *Neonesidea formosa* | * | * | | | * |
| *Cushmanidea elongata* | | | | | * |
| *Urocythereis crenulosa* | * | * | | * | * |
| *Xestoleberis communis* | | * | | | |
| *Xestoleberis depressa* | | * | | | |

### *3.2.3. Current Systems*

The current system seen in the study area develops in accordance with the circulation system of the Eastern Mediterranean (Figure 5). Based on the results of seasonal current measurements in the Güzelyurt Bay (Figure 6) and the Kyrenia (Girne) Region (Figure 7), the surface currents are generally from east to west. However, some variable currents occur in the shallower waters depending on local winds and coastal morphology (Eryılmaz, 1998, 2004; Eryılmaz and Yücesoy Eryılmaz, 2002; Millot and Taupier-Letage, 2005; Meriç et al., 2018*c*; Report 1, 1987; Report 2, 1988; Report 3, 1990; Report 4, 1991; Report 5, 1992).

According to the results of seasonal short-term flow measurements in Famagusta (Gazimağusa) Region (Figure 8), surface currents are generally from south to north as a result of the average flow velocity and directions, in concordance with the circulation system

Table 4- Distributions of molluscs by stations.

| MOLLUSCA | | STATIONS | | | | | | | |
|---|---|---|---|---|---|---|---|---|---|
| | | 3 | 6 | 13 | 12 | 10 | 7 | 4 | 8 |
| Gastropoda | *Jujubinus exasperatus* | | | | | | | * | |
| | *Homalopoma sanguineum* | | | | | | | * | |
| | *Tricolia pullus* | * | | | | | | | * |
| | *Cerithium scabridum* | * | | | | | | | |
| | *Bittium latreillii* | * | * | | | * | * | * | * |
| | *Bittium reticulatum* | * | * | | | * | * | | * |
| | *Cerithidium submammillatum* | * | | | | | | * | |
| | *Turritella communis* | | | | | | | * | |
| | *Epithonium sp.* | | | | | * | | | |
| | *Rissoa similis* | * | * | | | | | | |
| | *Pusillina lineolata* | * | | | | | * | | * |
| | *Setia sp.* | | | * | | | * | | |
| | *Alvania amati* | | | | | | | | * |
| | *Alvania cimex* | | * | | * | | * | | |
| | *Alvania lanciae* | * | | | | | | | |
| | *Truncatella subcylindrica* | | | * | | | | | |
| | *Strombus persicus* | * | | | | | | | |
| | *Mangelia cf. angelinae* | * | | | | | | | |
| | *Parthenina interstincta* | | | | | * | | | |
| | *Parthenina suturalis* | | | | | * | * | | |
| | *Turbonilla multilirata* | * | | | | | | | |
| | *Turbonilla pusilla* | | * | | | | | | |
| Bivalvia | *Ctena decussata* | | | | | | | | * |
| | *Glans trapezia* | | | | | | | * | |

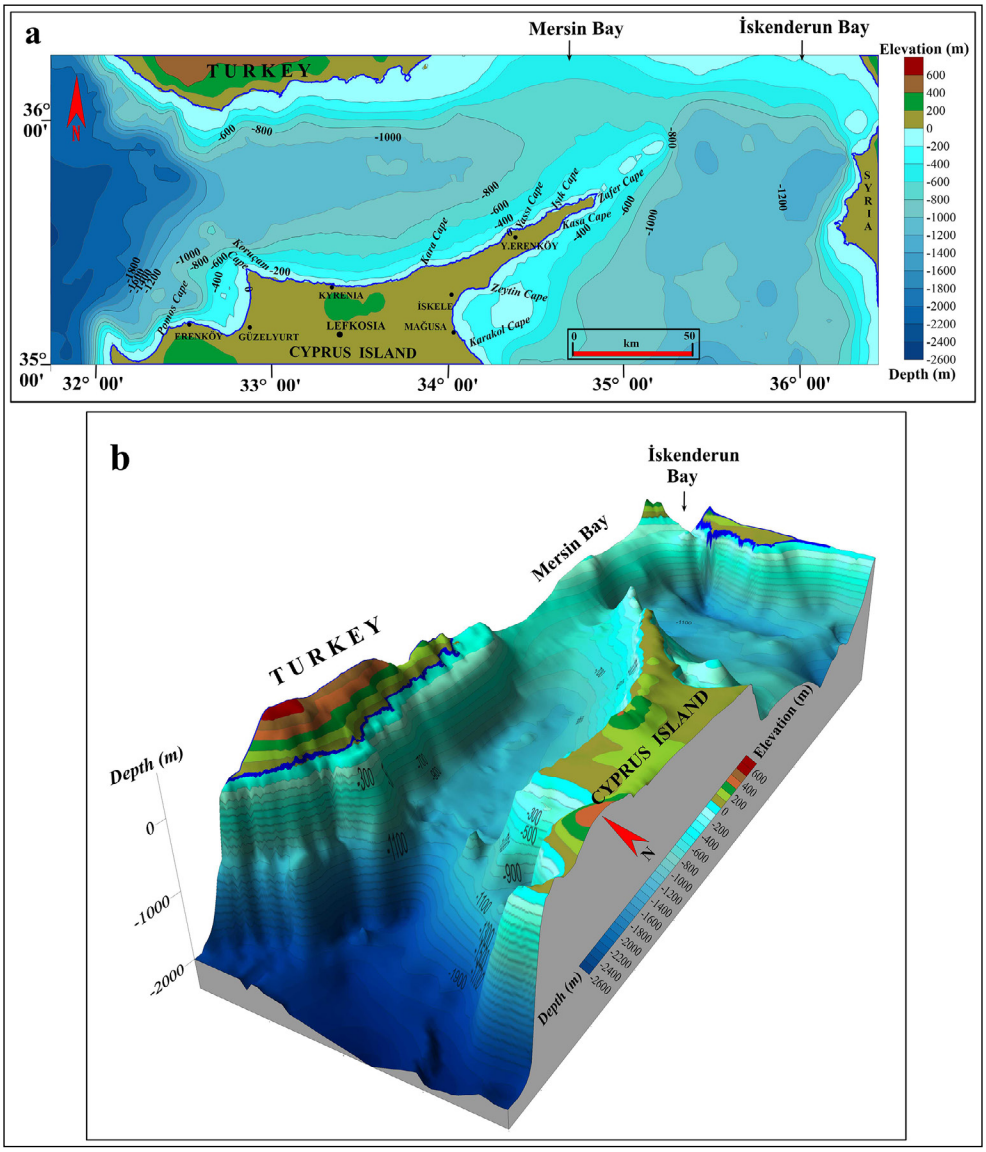


Figure 2- Bathymetry map and block diagram; a)Bathymetry map of the northern part of Cyprus and eastern Mediterranean, b) 3D bathymetry and morphological view of the northern part of Cyprus and the Eastern Mediterranean (depths in meters) (TR-341, 2007; TR-342, 2014; TR-343, 2017; TR-344, 2012; Eryılmaz, 2004).

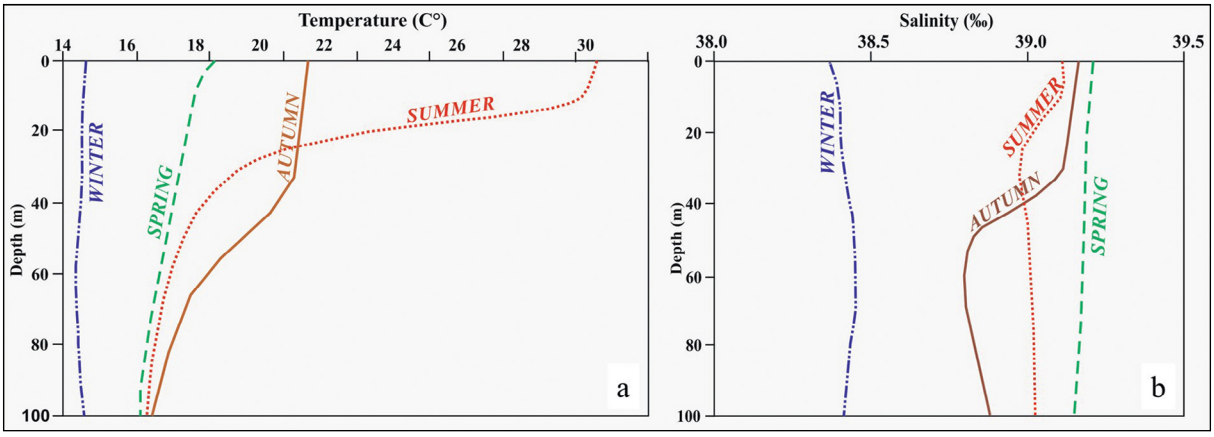


Figure 3- a) Seasonal average temperatures of Güzelyurt Bay-Kyrenia (Girne) Region, b) seasonal average salinity values (Eryılmaz, 2004).

of the Eastern Mediterranean (Figure 5). However, some variable currents occur in the shallower waters depending on local winds and coastal morphology (Eryılmaz, 1998, 2004; Eryılmaz and Yücesoy Eryılmaz, 2002; Millot and Taupier-Letage, 2005; Meriç et al., 2018*c*; Report 1, 1987; Report 2, 1988; Report 3, 1990; Report 4, 1991; Report 5, 1992).

### 3.3. Distribution of bottom sediments

Various coast types are observed in the Kyrenia (Girne) Region. The region to the east of Koruçam Cape is under the influence of northern winds. This region is of the high coastal type and inclination of the bottom topography is high. For this reason, wave erosion is effective on the coast, creating cliff-type coasts there. On the other hand, in areas with soft rock assemblages, an indented, protruding coastline occurred due to further erosion by the wave effect. Less eroded places extend towards the sea like a headland. Sandy pocket beaches were formed between the headlands. On the coasts in Koruçam and around, the dominant wave direction is west and northwest, and the land topography in this region consists of low coasts. Flat lands consisting of materials carried by streams were eroded by the sea and formed the low coasts. As the waves carried all the material it could carry to the offshores, only gravels larger than 5 cm left on the shore. As a result of the erosion of the mountainous land on the coasts to the west of the Güzelyurt Bay, seaside cliffs occurred. Small pocket beaches are observed between the high coasts. Gravels and blocks of various sizes are scattered in the sea in front of the eroded rocky shores (Figure 9) (Kırca and Eryılmaz, 1987, 1989, 1997; Eryılmaz and Kırca, 1998; Eryılmaz and Yücesoy Eryılmaz, 2002, 2003, 2019; Eryılmaz et al., 2002; Eryılmaz, 2004; Özhan, 1988; Report 1, 1987; Report 2, 1988; Report 3, 1990; Report 4, 1991; Report 5, 1992).

In the bottom sediments in the Kyrenia (Girne) Region, grain size decreases from the coast towards the offshore. There are sandy deposits in small-scale bays and pocket beaches in the coastal area between Koruçam Cape and Zafer Cape. Scree, as gravels and blocks, is commonly seen on the headlands and in the shallow-marine parts of the high coast. From 3-4 meter-depth of the sea towards the open sea, as a narrow strip parallel to the shore, first sand and then silty sand fields are seen. Sand and silty sand fields are spread over a wider area between Mutlu Cape and Koruçam Cape. After sandy silt, there is a narrow strip of sandy muddy field. After that, the bottom is completely muddy. The initial depth of muddy areas in the region is generally 200 meters. However, also in shallower areas in places, mud is observed (Figure 9) (Eryılmaz, 2004).

In the Güzelyurt Bay, coastal and near-coast areas are gravelly. As moving away from the coast, sand, silty sand, sandy silt and sandy mud sorting is seen. After that, there are muds covering large areas. The gravelly ground forming a 5-10 meter strip around the coastline of the Güzelyurt Bay could not be drawn on the map (Figure 9) (Eryılmaz, 2004). Coastal forms in Famagusta (Gazimağusa) Bay are in concordance with the inclination of the sea bottom topography at near-coast. High coasts as in form of the cliff are seen around Poyraz Cape and in the south of Karakol Cape which are exposed to wave movements. The coasts outside

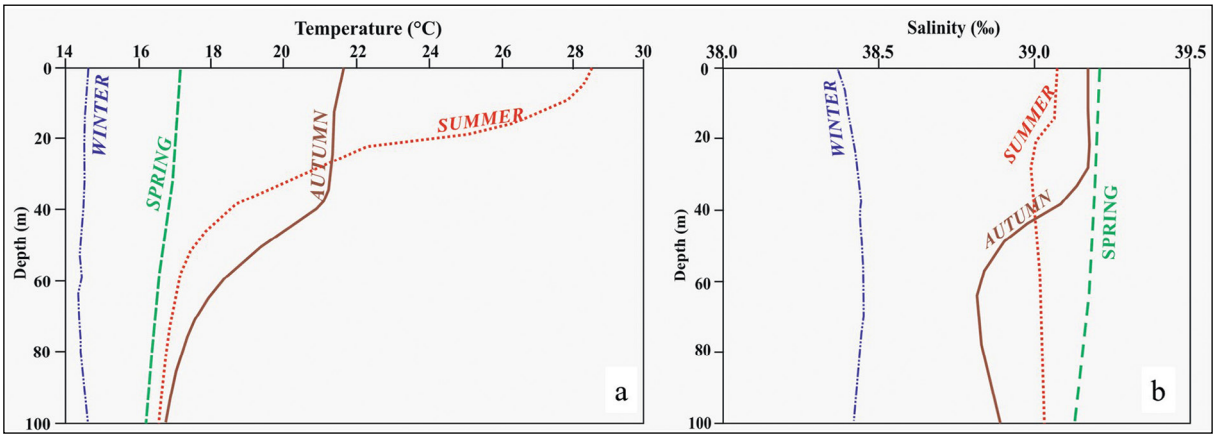


Figure 4- a) Seasonal average temperatures of Famagusta (Gazimağusa) Bay, b) seasonal average salinity values (Eryılmaz, 2004).

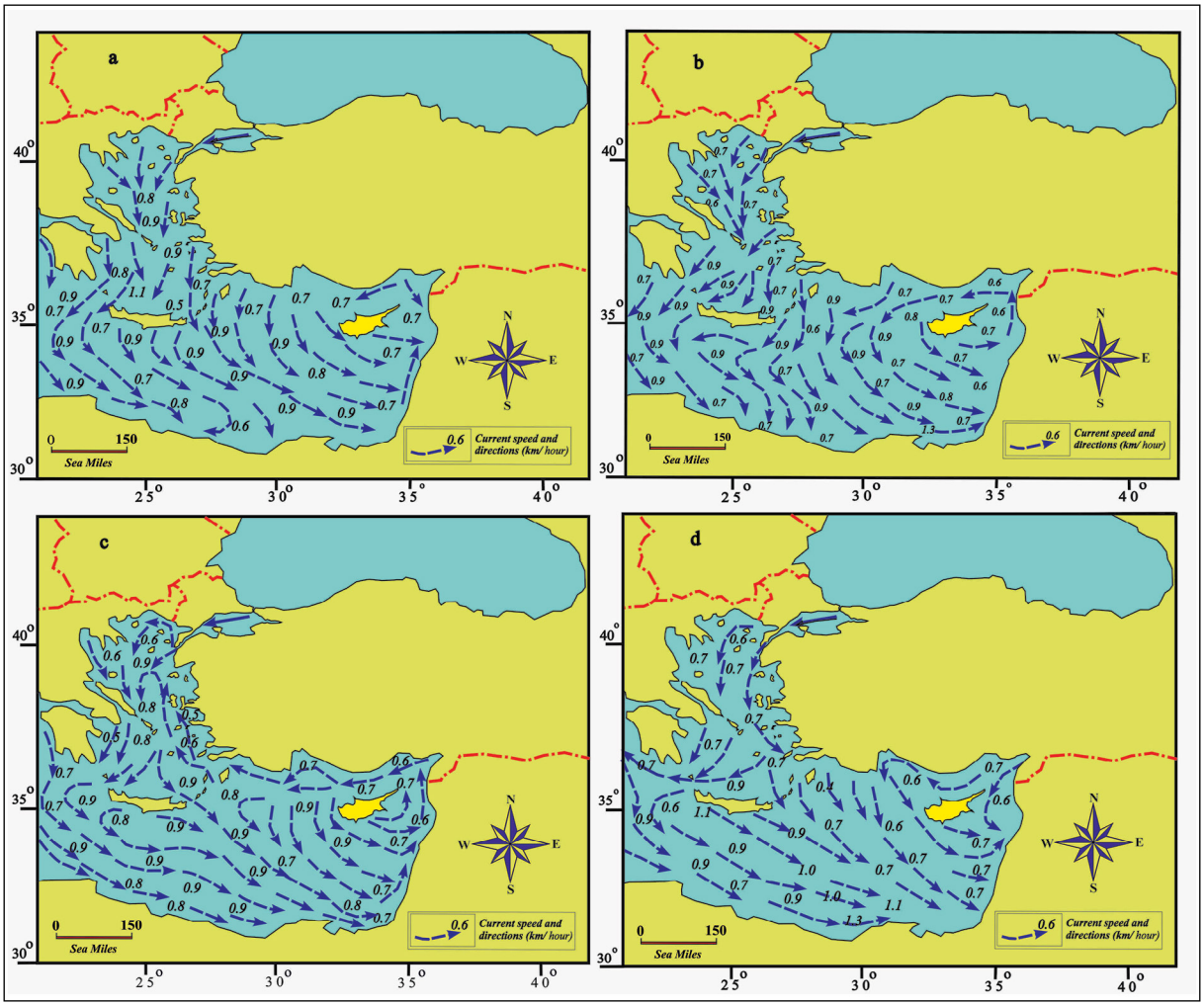


Figure 5- Eastern Mediterranean general current systems; a) spring, b) summer, c) autumn, d) winter (Eryılmaz, 1998, 2004; Eryılmaz and Yücesoy Eryılmaz, 2002; Millot and Taupier-Letage, 2005; Meriç et al., 2018*b*; Report 1, 1987; Report 2, 1988; Report 3, 1990; Report 4, 1991; Report 5, 1992).

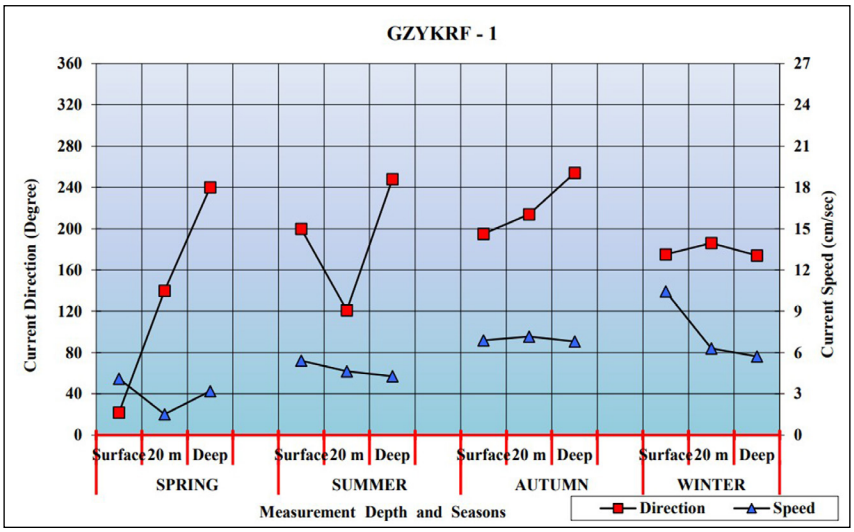


Figure 6- Recent, speeds and directions of the current in Güzelyurt Bay (Eryılmaz, 2004).

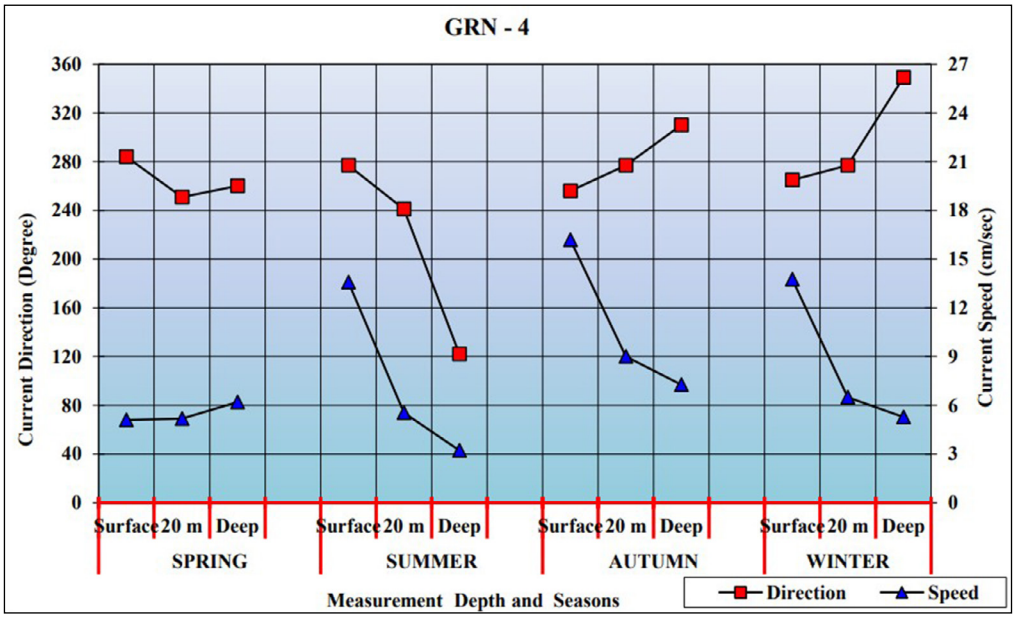


Figure 7- Recent, speeds and directions of the current in Kyrenia (Girne) Region (Eryılmaz, 2004).

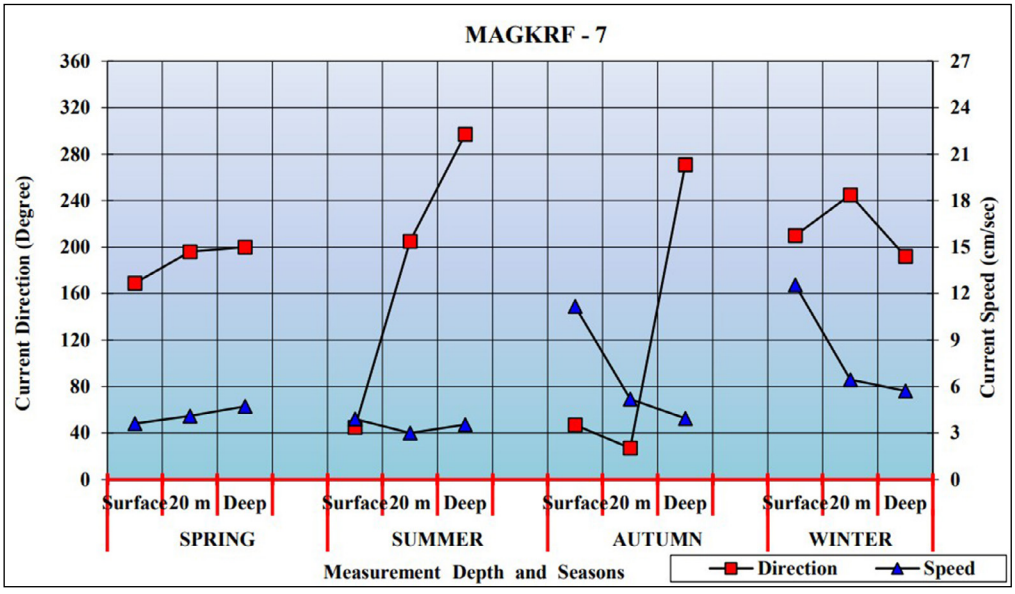


Figure 8- Recent, speeds and directions of the current in Famagusta (Gazimağusa) Bay (Eryılmaz, 2004).

these regions are low coasts that are completely sandy beaches. Small scale indentations are not common in the bay. In the Famagusta (Gazimağusa) Region, a distinct array of materials is observed, depending on the depth, from the coast towards the offshore. The bottom feature extending in the form of sandy beaches on the shore offers a spread up to a depth of 20 meters. Bottom sediment distribution is observed in silty sand and sandy silt feature up to a depth of 50 meters, and a sandy mud feature from 50 to 100 meters. Deeper marine sections contain mud. Streams, reaching the sea from the land, only transport a small amount of water during rainy times, due to their irregular regimes they are not featured to change the general sedimentation pattern of the bay. Terrestrial pebbles are found at the mouths of the creeks in places. In the Güzelyurt Gulf and the Kyrenia (Girne) Region, in Karpass Cape - Güzelyurt Bay, there are thin strips of clay and clayey materials after a depth of 200 m (Figure 9) (Kırca and Eryılmaz, 1987, 1989, 1997; Eryılmaz and Kırca,

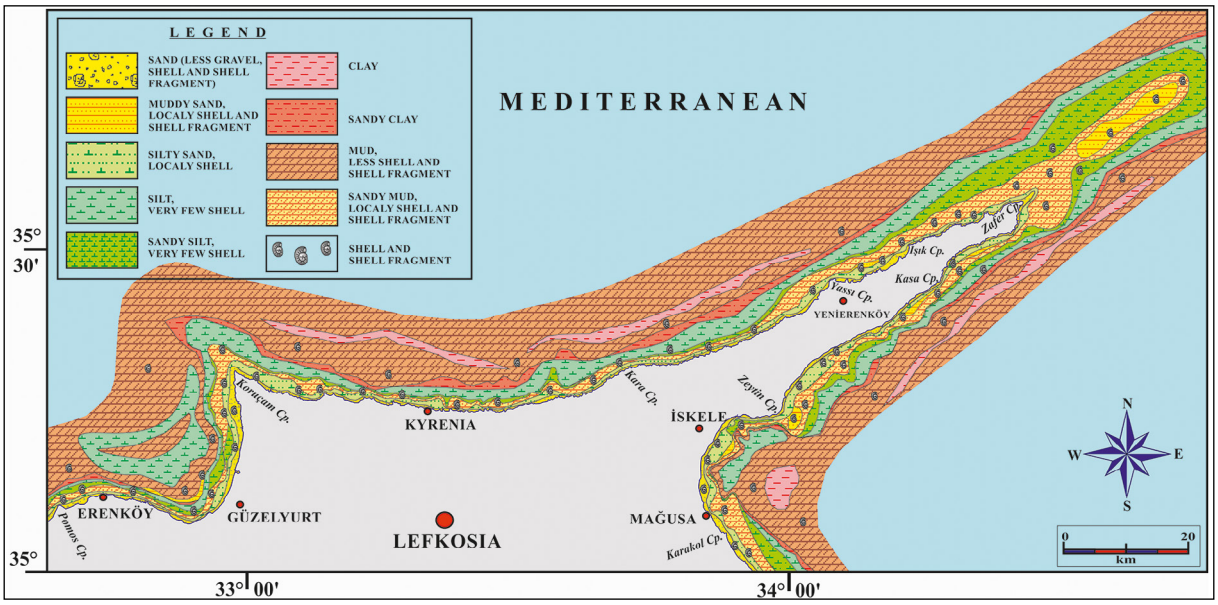


Figure 9- Recent sediment distribution in the northern part of Cyprus (Kırca and Eryılmaz, 1987, 1989, 1997; Eryılmaz and Kırca, 1998; Eryılmaz and Yücesoy Eryılmaz, 2002, 2003, 2019; Eryılmaz et al., 2002; Eryılmaz, 2004) (Cp.: Cape).

1998; Eryılmaz and Yücesoy Eryılmaz, 2002, 2003, 2019; Eryılmaz et al., 2002; Eryılmaz, 2004; Özhan, 1988; Report 1, 1987; Report 2, 1988; Report 3, 1990; Report 4, 1991; Report 5, 1992).

## 4. Findings

### 4.1. Benthic Foraminiferal Assemblage

Benthic foraminifers of 18 young sediments obtained from different points and depths were identified based on Meriç et al. (2008*a*, *b*) and Meriç et al. (2018*b*, *c*). 30 genera and 48 species of benthic foraminifers were determined. These are: *Spiroplectinella sagittula*, *Bigenerina nodosaria*, *Textularia bocki*, *T. conica*, *Patellina corrugata*, *Nubecularia lucifuga*, *Adelosina cliarensis*, *A. duthiersi*, *A. mediterranensis*, *A. partschi*, *A. pulchella*, *Spiroloculina angulata*, *S. angulosa*, *S. antillarum*, *S. depressa*, *S. excavata*, *S. tenuiseptata*, *Hauerina diversa*, *Cycloforina contorta*, *Massilina secans*, *Quinqueloculina bidentata*, *Q. disparilis*, *Q. jugosa*, *Q. lamarckiana*, *Q. seminula*, *Miliolinella subrotunda*, *Pseudotriloculina laevigata*, *Triloculina marioni* Schlumberger, *T. tricarinata* d'Orbigny, *Sigmoilinita costata*, *S. edwardsi*, *Coscinospira hemprichii*, *Laevipeneroplis karreri*, *Peneroplis pertusus*, *P. planatus*, *Amphisorus hemprichii, Sorites orbiculus*, *Amphicoryna scalaris*, *Rosalina bradyi*, *R. floridensis*, *Lobatula lobatula*, *Cyclocibicides vermiculatus*, *Planorbulina mediterranensis*, *Miniacina miniacea*, *Amphistegina lobifera*, *Ammonia tepida*, *Porosononion subgranosum, Elphidium crispum* (Table 2). These species have the characteristics of Aegean Sea and Mediterranean fauna.

Individuals with colorful test were found in the samples collected from the station no 7, 10 and 12, as observed in the specimens from the Mediterranean and the Aegean coasts of Turkey. Among them, the most dominant species is *Peneroplis pertusus*. In *Amphistegina lobifera*, coloration is almost absent, as observed in Turkish Mediterranean coasts.

### 4.2. Ostracod Assemblage

6 of the 18 samples (2, 4, 5, 10, 12, 13) collected from the region contain ostracods. In identification of ostracods, Van Morkhoven (1963), Hartmann and Puri (1974), Bonaduce et al. (1975), Breman (1975), Yassini (1979), Guillaume et al. (1985), Athersuch et al. (1989), Zangger and Malz (1989), Mostafawi and Matzke-Karasz (2006), Joachim and Langer (2008), and MarBEF Data System (http://www.marbef.org/data/) were used. 12 genera and 15 species were identifed as follows: *Acantocythereis hystrix*, *Aurila convexa*, *Bosquetina carinella*, *Cytheretta judaea*, *Cytherois* sp., *Ekpontocypris prifera*, *Jugosocythereis*

*prava*, *Loxoconcha bairdi*, *Loxoconcha gibberosa*, *Neonesidea corpulenta*, *Neonesidea formosa*, *Cushmanidea elongata*, *Urocythereis crenulosa*, *Xestoleberis communis* and *X. depressa*. It was observed that the stations 4 and 12 have high diversity in genera and species (Table 3).

The determined species are known as common species also in the Mediterranean, Aegean Coasts, Adriatic Sea, Marmara and Turkish coasts.

4.3. Mollusc Assemblage

Regarding the Mollusc community, no individual of macroscopic size was found in the samples. In samples 3, 4, 6, 7, 8, 10, 12 and 13, the obtained individuals with microscopic size were bivalves and gastropods, representing a Mediterranean assemblage with quite a large number of *Jujubinus exasperatus, Homalopoma sanguineum*, *Tricolia pullus*, *Cerithium scabridum*, *Bittium latreillii*, *B. reticulatum*, *Cerithidium submammillatum*, *Turritella communis*, *Epithonium* sp., *Rissoa similis*, *Pusillina lineolata*, *Setia* sp., *Alvania amati*, *A. cimex*, *A. lanciae*, *Truncatella subcylindrica*, *Strombus persicus*, *Mangelia* cf. *angelinae*, *Parthenina interstincta*, *P. suturalis*, *Turbonilla multilirata*, *T. pusilla*, *Ctena decussata*, *Glans trapezia* specimens (Table 4) (Cossignani et al., 2011; Scaperrotta et al., 2009-2015).

4.4. Grain Size Content Findings

Grain size classification gives important data on geo-statistical identification of sediment, strength of sediment supplier and investigation of sedimentation environment (Sarı et al., 2014 and 2016). In addition, it is known that as the grain size of the sediment decreases, the surface area increases and stores more heavy metals in the sediment (Hallı et al., 2014). For these reasons, grain size is one of the most important features of lithogenic sediment, and its classification is given in Table 5.

While gravel and sand content were determined in all of the 18 surface samples taken from the Northern Cyprus coastline, silt and clay content was determined in only two samples and given as percentage in Table 6. Since the mud (silt + clay) content in 16 samples was below 2.5%, the silt and clay separation could not be made in these samples. According to the findings, gravel, sand, mud (silt + clay), silt and clay contents range between 0 - 42.20%, 53.78 - 99.49%, 0.40 - 8.57%, 2.60 - 8.14% 0.43 - 1.43%, respectively (Table 6 and Figure 10).

In the study area, while the gravel content was more than 4% in samples 1, 4, 5, 6, 8 and 13; no gravel detected in the samples 9, 11, 12, 14 and 17. In samples 2, 3, 7, 10, 15, 16 and 18, the gravel content is less than 1% (Table 6). The average gravel content in the study area was calculated as 5.66%.

In the sediments which grain size analysis was performed on, the highest sand content was measured in sample 16 taken between the coasts of Kyrenia (Girne) and Lapta, and the lowest in sample 13 taken from the Kyrenia (Girne) coast. The average sand content in the study area was calculated as 92.85%. As the result of the sieve analysis this was concluded; samples 8 and 13 are very coarse sand-dominated; samples 3, 4, 7, 10, 16 are coarse sand-dominated; samples 1, 2, 5, 6, 11, 14, 15, 18 are medium sand-dominated and samples 9, 12 and 17 are fine sand-dominated (Table 6).

Due to the low mud content in the samples of the study area, silt and clay contents were separated in 2 samples. While the silt content in the sample no 4 is 8.14, it is 2.60 in the sample no 13. The clay contents in these samples are 0.43 and 1.43, respectively (Figure 10).

Table 5- Classification of lithogenic sediments based on grain size (Folk, 1980).

| Grain diameter Millimeter (mm) | Grain diameter Micrometer (µm) | Grain diameter Phi (Φ) | Wentworth Size Class |
|---|---|---|---|
| 64-2 | >2000 | < -1 | Gravel |
| 2.0-0.063 | 2000 - 63 | (-1) - 4.0 | Sand |
| 0.063-0.002 | 63-3.9 | 4.0 - 8.0 | Silt |
| <0.02 | <3.9 | > 8 | Clay |

Table 6- Statistical distribution of grain size parameters of Northern Cyprus coastal sediments.

| Sample | Gravel (%) | Sand (%) | | | | | | Mud (%) | Silt (%) | Clay (%) |
|---|---|---|---|---|---|---|---|---|---|---|
| | | Total sand (%) | Very coarse sand (%) | Coarse sand (%) | Medium sand (%) | Fine sand (%) | Very fine sand (%) | | | |
| 1 | 9.26 | 89.33 | 13.45 | 22.87 | 50.19 | 2.82 | 0.00 | 1.4 | | |
| 2 | 0.18 | 98.46 | 0.10 | 3.93 | 48.84 | 45.56 | 0.02 | 1.36 | | |
| 3 | 0.57 | 98.38 | 14.29 | 66.37 | 17.42 | 0.26 | 0.06 | 1.05 | | |
| 4 | 4.10 | 87.32 | 30.47 | 34.38 | 12.64 | 7.03 | 2.81 | 8.57 | 8.14 | 0.43 |
| 5 | 9.23 | 89.41 | 19.54 | 21.80 | 40.56 | 7.48 | 0.11 | 1.36 | | |
| 6 | 7.31 | 92.27 | 10.14 | 33.82 | 46.57 | 1.73 | 0.00 | 0.42 | | |
| 7 | 0.33 | 98.93 | 1.28 | 61.42 | 27.53 | 8.05 | 0.10 | 0.75 | | |
| 8 | 25.50 | 73.86 | 41.51 | 29.93 | 2.07 | 0.11 | 0.13 | 0.64 | | |
| 9 | 0.00 | 99.08 | 0.00 | 0.00 | 33.34 | 65.46 | 0.37 | 0.92 | | |
| 10 | 0.84 | 98.57 | 5.54 | 78.86 | 13.73 | 0.32 | 0.12 | 0.60 | | |
| 11 | 0.00 | 99.38 | 0.00 | 0.00 | 41.19 | 57.86 | 0.26 | 0.62 | | |
| 12 | 0.00 | 97.62 | 0.52 | 2.55 | 37.58 | 56.13 | 0.84 | 2.38 | | |
| 13 | 42.19 | 53.78 | 24.99 | 17.38 | 9.26 | 1.58 | 0.43 | 4.03 | 2.60 | 1.43 |
| 14 | 0.00 | 99.44 | 0.33 | 29.09 | 67.48 | 2.53 | 0.00 | 0.56 | | |
| 15 | 1.29 | 98.17 | 0.99 | 8.75 | 85.11 | 3.33 | 0.00 | 0.54 | | |
| 16 | 0.11 | 99.49 | 0.10 | 64.55 | 33.07 | 1.73 | 0.10 | 0.40 | | |
| 17 | 0.00 | 99.16 | 0.00 | 0.29 | 32.19 | 65.94 | 0.74 | 0.84 | | |
| 18 | 0.92 | 98.64 | 0.82 | 4.04 | 69.65 | 24.14 | 0.00 | 0.44 | | |
| Minimum | 0.00 | 53.78 | 0.00 | 0.00 | 2.07 | 0.11 | 0.00 | 0.40 | | |
| Maximum | 42.19 | 99.49 | 41.51 | 78.86 | 85.11 | 65.94 | 2.81 | 8.57 | | |
| Mean | 5.66 | 92.85 | 9.12 | 26.67 | 37.13 | 19.56 | 0.34 | 1.49 | | |

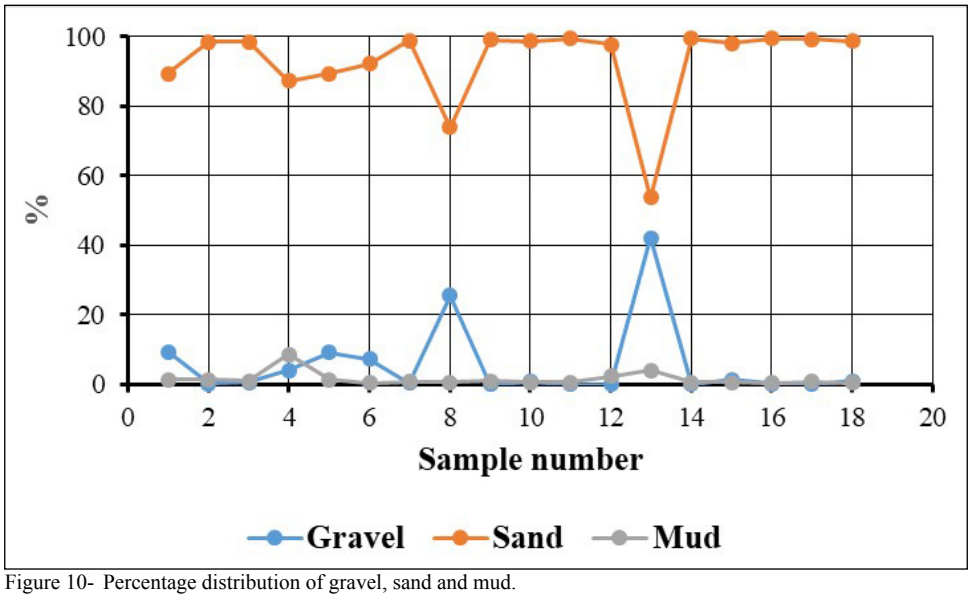


Figure 10- Percentage distribution of gravel, sand and mud.

4.5. Evaluation of Geochemical Analysis

In ICP-MS analyzes of sediments (Ce, Cs, Dy, Er, Eu, Gd, Ho, La, Lu, Nd, Pr, Rb, Sm, Tb, Tm, Y, Yb), the distribution of rare earth elements was measured lower than the earth's crust and the shale threshold values (Krauskopf, 1979) (Figures 11 and 12). While the distribution of elements versus sediments is parallel, only Y differs (Figure 13). Again in sediments, distribution of the elements among themselves is in the way that Rb> Ce> La> Y> Nd> Gd> Dy (Figure 13).

In the evaluation of the geochemical analysis of sediments, Ga and Tl elements were not detected. Cd, the toxic element, are lower than the threshold value (Krauskopf, 1979) in samples 5, 11, 12, 13, 14 and 17, while no data were obtained from the others. While in

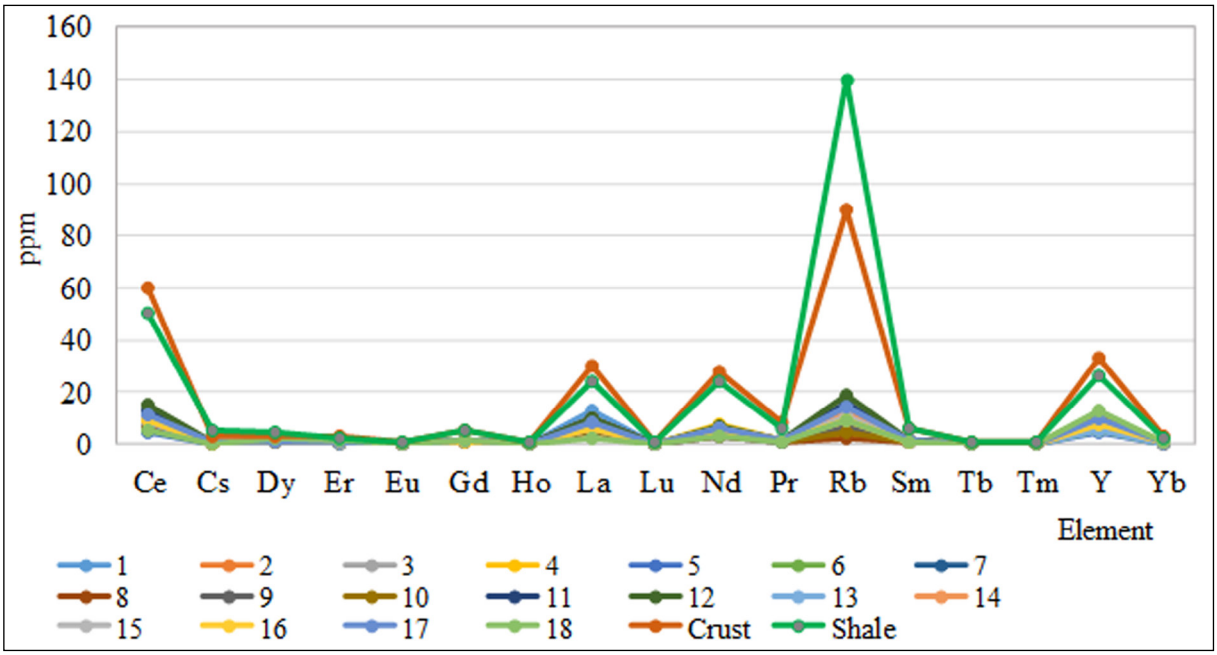


Figure 11- Comparison of the trace element distributions in the study area to those in the earth's crust and shale values (Krauskopf, 1979).

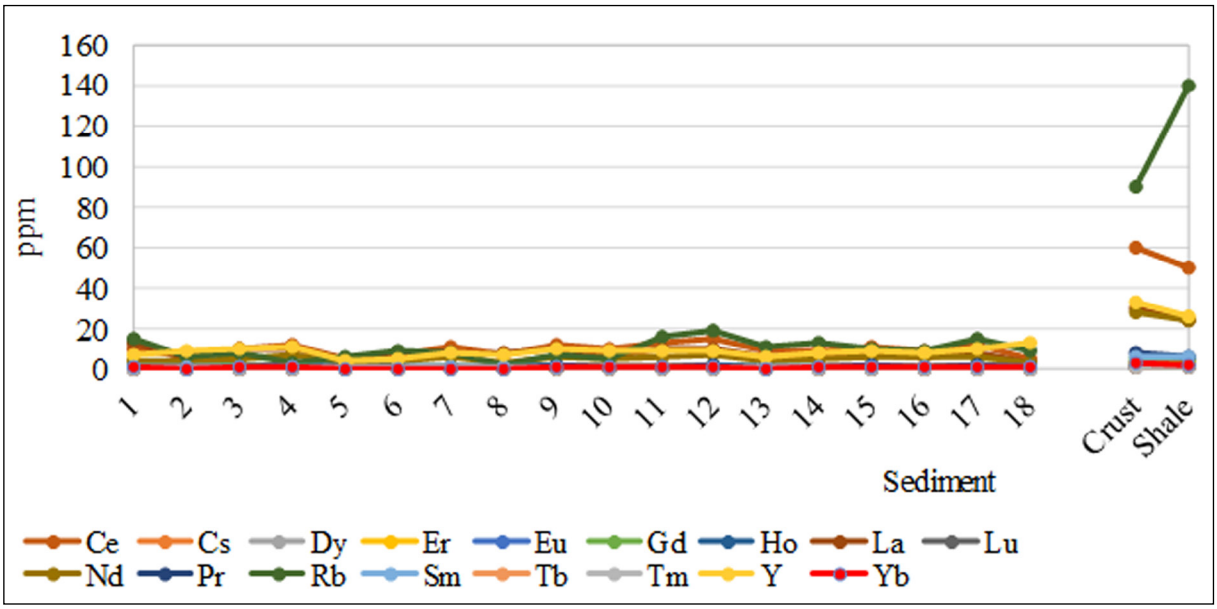


Figure 12- Comparison of the trace element distributions in sediments to those in the earth's crust and shale values (Krauskopf, 1979).

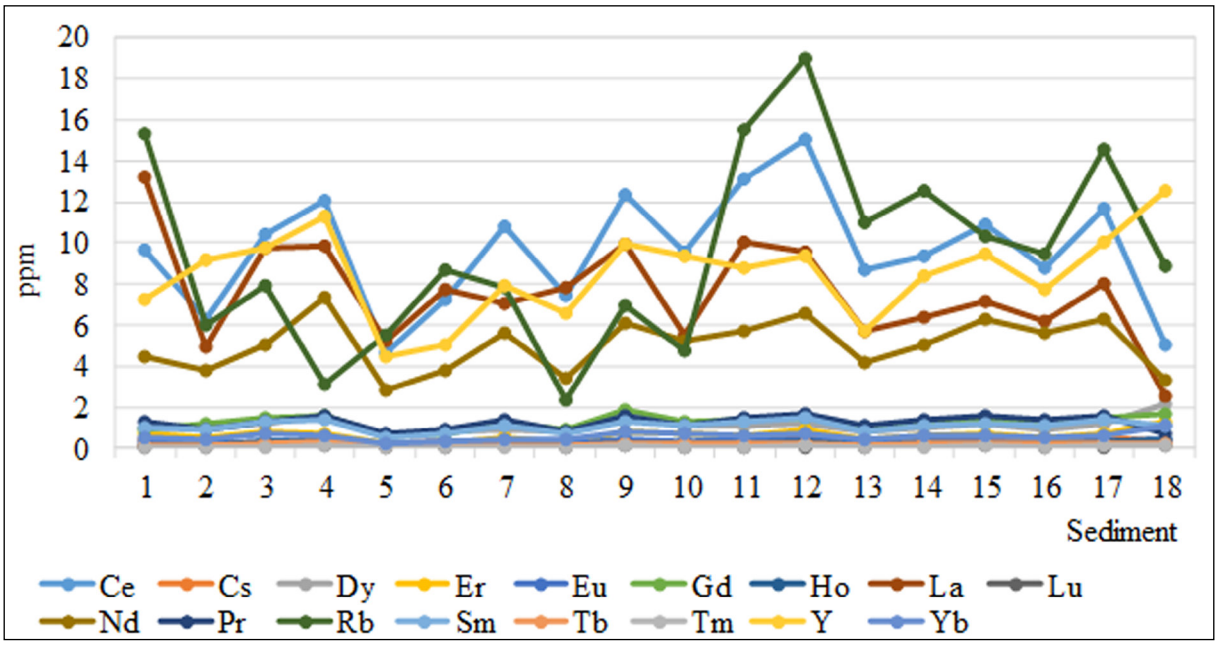


Figure 13- Distribution of the trace elements in sediments.

is lower than the threshold value in samples 4 and 9, data was not obtained in the others (Table 7). U, one of the radioactive elements, was found as higher than the earth's crust but lower than shale in samples no 4, 5, 6, and 13, and lower than the threshold values in other sediments (Figure 14).

Considering the trace elements in the samples which geochemical analysis conducted on, this can be seen that no trace element, except Sr, could exceed 0.1% in concentration. The relatively high Sr content suggests that the rocks might be carbonates deposited in the shelf environment. Negative anomaly of Ce and relatively high Ni values indicate a sedimentation that occurs in a shallow marine or shelf environment. The presence of elements that are expected to have higher concentrations in terrestrial units such as Pb, Zn, Ba at very low concentrations indicates that the terrestrial input is at minimum degree during sedimentation. The fact that the Mn element is below the detection limits of the analyzer also strengthens the argument that the samples do not belong to deep marine sediments.

## 5. Results

*Spiroloculina angulosa*, *S. antillarum*, *Hauerina diversa*, *Coscinospira hemprichii*, *Peneroplis pertusus*, *P. planatus*, *Amphisorus hemprichii, Sorites orbiculus* and *Amphistegina lobifera*, which constitute the foraminiferal assemblage identified in this study carried out on the Northern Cyprus coasts, are the alien foraminifera and are of Red Sea origin. *Amphistegina lobifera* was abnormally abundant compared to the other foraminifera. It has been determined that, this assemblage constitutes a poor alien foraminifera assemblage in comparison with those obtained in study (Meriç et al., 2008*a*; 2018*b*) conducted in the Mediterranean coasts in Turkey. Foraminiferal individuals with colored tests, of which *Peneroplis pertusus* is the dominant species, were found at stations 7, 10 and 12 from the samples studied.

It was determined that the obtained ostracod and mollusc genera and species were similar to the typical Mediterranean and Aegean Sea community and that there is no abnormality in their tests.

Sample no 4, in which individuals of foraminifera, ostracod, gastropod and bivalve are observed, is characterized by high ratio of very coarse sand, very fine sand, mud and silt. In sample no 8, which includes individuals of foraminifera, gastropod and bivalves, very coarse sand is in the highest ratio, medium and fine sand is the lowest. Foraminifera, ostracod and gastropod individuals were found in sample no 10, which has the highest coarse sand ratio, and low fine sand and mud ratio. In sample no 12, in which foraminifera has a high abundance, ostracod and

Table 7- Geochemical analysis results of sediments (ND: no data; *Krauskopf, 1979).

| | 1 | 2 | 3 | 4 | 5 | 6 | 7 | 8 | 9 | 10 | 11 | 12 | 13 | 14 | 15 | 16 | 17 | 18 | Earth's crust* | Shale* |
|---|---|---|---|---|---|---|---|---|---|---|---|---|---|---|---|---|---|---|---|---|
| **Cd** | ND | ND | ND | ND | 0.099 | ND | ND | ND | ND | ND | 0.039 | 0.036 | 0.075 | 0.147 | ND | ND | 0.127 | ND | 0.2 | 0.3 |
| **Ce** | 9.645 | 6.289 | 10.376 | 12.075 | 4.649 | 7.222 | 10.782 | 7.42 | 12.383 | 9.573 | 13.136 | 15.03 | 8.695 | 9.389 | 10.895 | 8.736 | 11.65 | 5.006 | 60 | 50 |
| **Cs** | 0.445 | 0.241 | 0.239 | 0.204 | 0.202 | 0.296 | 0.278 | 0.182 | 0.324 | 0.218 | 0.423 | 0.519 | 0.443 | 0.381 | 0.387 | 0.3 | 0.487 | 0.292 | 3 | 5 |
| **Dy** | 0.953 | 0.962 | 1.164 | 1.581 | 0.51 | 0.786 | 0.945 | 0.803 | 1.434 | 1.103 | 1.062 | 1.206 | 0.835 | 1.027 | 1.233 | 0.907 | 1.214 | 2.105 | 3.00 | 4.30 |
| **Er** | 0.671 | 0.5 | 0.769 | 0.693 | 0.206 | 0.259 | 0.553 | 0.272 | 0.847 | 0.734 | 0.61 | 0.873 | 0.462 | 0.634 | 0.673 | 0.509 | 0.67 | 1.253 | 2.80 | 2.70 |
| **Eu** | 0.329 | 0.237 | 0.298 | 0.328 | 0.197 | 0.295 | 0.287 | 0.262 | 0.401 | 0.337 | 0.439 | 0.394 | 0.287 | 0.296 | 0.317 | 0.279 | 0.327 | 0.429 | 1.20 | 1.10 |
| **Ga** | ND | ND | ND | ND | ND | ND | ND | ND | ND | ND | ND | ND | ND | ND | ND | ND | ND | ND | 15.00 | 19.00 |
| **Gd** | 0.909 | 1.148 | 1.5 | 1.565 | 0.594 | 0.72 | 1.192 | 0.901 | 1.868 | 1.264 | 1.428 | 1.492 | 0.96 | 1.211 | 1.343 | 1.187 | 1.52 | 1.65 | 5.40 | 5.20 |
| **Ho** | 0.178 | 0.14 | 0.302 | 0.341 | 0.089 | 0.15 | 0.223 | 0.164 | 0.259 | 0.265 | 0.275 | 0.3 | 0.148 | 0.201 | 0.232 | 0.188 | 0.287 | 0.381 | 1.20 | 1.20 |
| **In** | ND | ND | ND | 0.019 | ND | ND | ND | ND | 0.007 | ND | ND | ND | ND | ND | ND | ND | ND | ND | 0.10 | 0.10 |
| **La** | 13.157 | 4.929 | 9.709 | 9.848 | 5.266 | 7.687 | 7.066 | 7.784 | 9.95 | 5.518 | 10.04 | 9.595 | 5.729 | 6.343 | 7.126 | 6.151 | 8.039 | 2.494 | 30.00 | 24.00 |
| **Lu** | 0.047 | 0.077 | 0.104 | 0.095 | 0.021 | 0.061 | 0.088 | 0.037 | 0.137 | 0.084 | 0.075 | 0.073 | 0.062 | 0.087 | 0.111 | 0.062 | 0.074 | 0.167 | 0.50 | 0.60 |
| **Nd** | 4.484 | 3.749 | 4.99 | 7.369 | 2.854 | 3.784 | 5.594 | 3.411 | 6.136 | 5.249 | 5.698 | 6.533 | 4.123 | 5.05 | 6.319 | 5.622 | 6.264 | 3.337 | 28.00 | 24.00 |
| **Pr** | 1.315 | 0.885 | 1.336 | 1.585 | 0.67 | 0.883 | 1.381 | 0.832 | 1.605 | 1.12 | 1.484 | 1.665 | 1.084 | 1.371 | 1.587 | 1.368 | 1.596 | 0.701 | 8.20 | 6.10 |
| **Rb** | 15.277 | 6.004 | 7.958 | 3.13 | 5.519 | 8.73 | 7.787 | 2.346 | 6.961 | 4.725 | 15.541 | 18.93 | 11.02 | 12.544 | 10.335 | 9.437 | 14.535 | 8.843 | 90.00 | 140.00 |
| **Sm** | 0.959 | 0.912 | 1.265 | 1.343 | 0.564 | 0.681 | 1.08 | 0.666 | 1.27 | 1.103 | 1.245 | 1.452 | 0.77 | 1.088 | 1.216 | 1.129 | 1.339 | 1.097 | 6.00 | 5.80 |
| **Tb** | 0.141 | 0.139 | 0.205 | 0.287 | 0.106 | 0.131 | 0.168 | 0.128 | 0.228 | 0.221 | 0.186 | 0.246 | 0.093 | 0.215 | 0.246 | 0.2 | 0.224 | 0.276 | 0.90 | 0.90 |
| **Tl** | ND | ND | ND | ND | ND | ND | ND | ND | ND | ND | ND | ND | ND | ND | ND | ND | ND | ND | 0.50 | 1.00 |
| **Tm** | 0.027 | 0.053 | 0.078 | 0.111 | 0.039 | 0.075 | 0.081 | 0.021 | 0.1 | 0.078 | 0.085 | 0.09 | 0.059 | 0.047 | 0.129 | 0.077 | 0.09 | 0.141 | 0.50 | 0.50 |
| **Y** | 7.289 | 9.151 | 9.719 | 11.263 | 4.445 | 5.065 | 7.874 | 6.548 | 9.924 | 9.39 | 8.826 | 9.401 | 5.677 | 8.369 | 9.431 | 7.694 | 10.01 | 12.573 | 33.00 | 26.00 |
| **Yb** | 0.519 | 0.429 | 0.747 | 0.642 | 0.213 | 0.291 | 0.385 | 0.411 | 0.79 | 0.744 | 0.641 | 0.682 | 0.452 | 0.58 | 0.603 | 0.524 | 0.592 | 1.127 | 3.40 | 2.20 |
| **Th** | 1.015 | 0.48 | 0.954 | 0.529 | 0.473 | 0.58 | 0.876 | 0.414 | 0.855 | 0.669 | 1.121 | 1.31 | 1.016 | 0.693 | 0.812 | 0.75 | 1.086 | 0.311 | 7.20 | 12.00 |
| **U** | 0.891 | 1.367 | 0.912 | 1.849 | 2.789 | 2.52 | 0.841 | 1.1 | 1.091 | 1.064 | 0.997 | 1.017 | 1.916 | 1.183 | 1.097 | 1.292 | 1.139 | 0.357 | 1.80 | 3.70 |

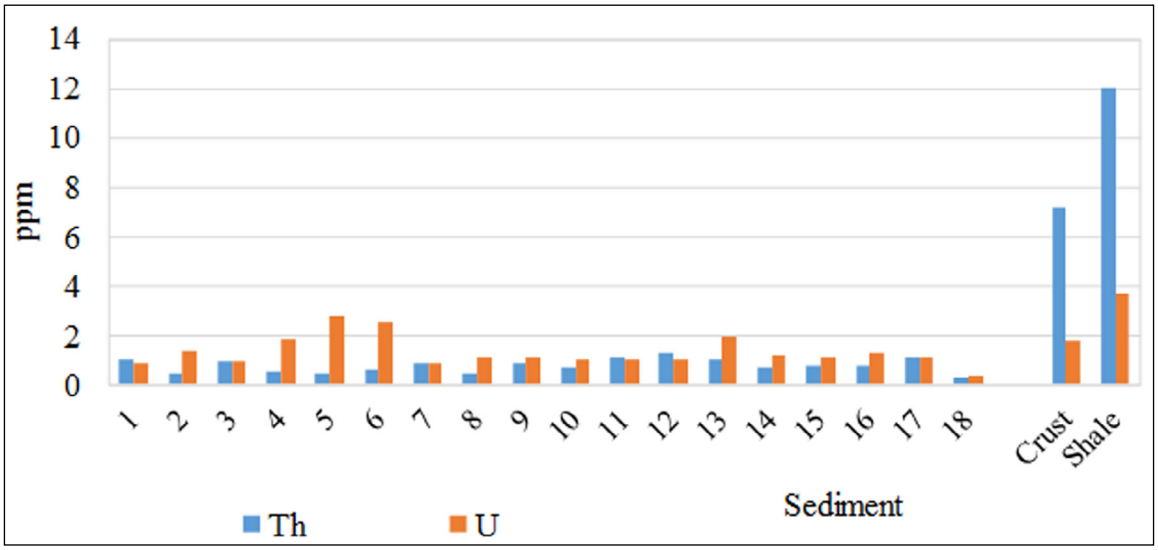


Figure 14- Comparison of the radioactive element distributions in the study area to those in the earth's crust and shale values (Krauskopf, 1979).

gastropod are also present, gravel is in the lowest ratio and fine sand is high. In sample 13, which includes foraminifera and gastropod individuals, medium sand is low and clay is in high ratio. Samples of 9, 11, 14, 15, 16, 17 and 18 containing only foraminifera individuals have low gravel and high sand ratio.

There are industrial raw materials and natural structures such as sand and gravels in the foothills of the Beşparmak Mountains in Nicosia, gypsum in the Güngör region and manganese in Beylerbeyi (close to the station number 1 and 11). While high quality marble found in Lapta (close to station number 7-12) of Kyrenia (Girne), high quality marble, manganese and brick raw materials are present in the İskele region (close to station number 10). There are minerals such as pyrite, zinc and copper in the foothills of the Troodos Mountains among the most important industrial raw materials and natural building materials of Southern Cyprus, natural building materials such as marble, sand and gravel are also known. In the north, compared to the south, there are mostly industrial raw materials such as manganese, copper and high-quality marble (Diner, 2012). It was stated that there is gypsum in Kaleburnu of Iskele in Famagusta (Gazimağusa) Bay (close to sediment area 10), manganese in Balalan Village, Ziyamet (between sediments no 2 and 5), high quality marbles in Yedikonuk and Büyükkonuk (close to the sediment no 5) (Diner, 2012). In Southern Cyprus, especially in the Troodos Mountains, Paphos and Limassol, zinc, pyrite, gravel, sand is found, while presence of copper, zinc and sand are known in the Katodris region (Diner, 2012).

The coasts between Lefke and Dipkarpaz where the sampling was carried out are Quaternary terrace and alluvium. Quantitative distribution of genera and species with regard to foraminifera, ostracod and mollusc (gastropod and bivalve) content of sediments is shown in Figure 15. While benthic foraminifera were observed in all sediments, ostracods in samples 2, 4, 5, 10, 12; gastropods in samples 3, 4, 6, 7, 8, 10, 12, 13, and bivalves (only one in each) were found in samples 4 and 8. While foraminifera were found in samples 1, 11, 14-18, all micro and macro fauna individuals were observed in only sample 4. While diversity of foraminifera in genera and species is high in samples 4, 7, 10 and 12; ostracod is high in sample 4 and gastropod in sample 3. No relationship between trace and radioactive elements and abundance of faunal individuals in sediments is seen (Figures 16 and 17).

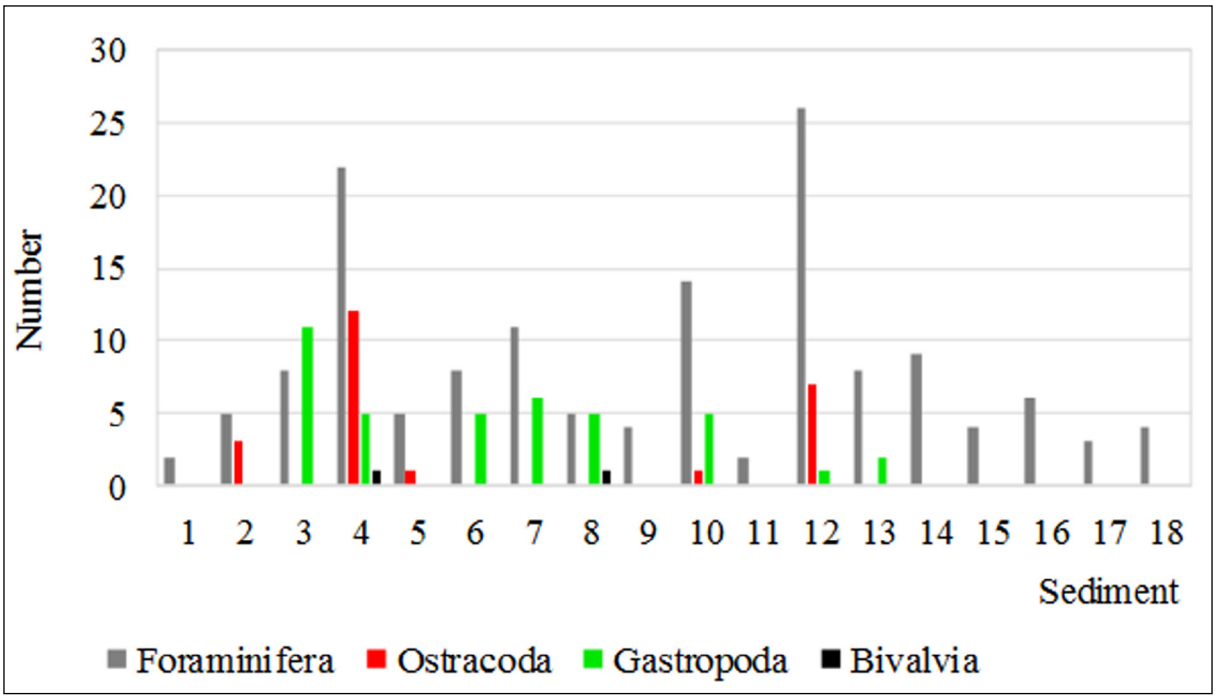


Figure 15- Quantitative distribution of fauna in sediments of the study area.

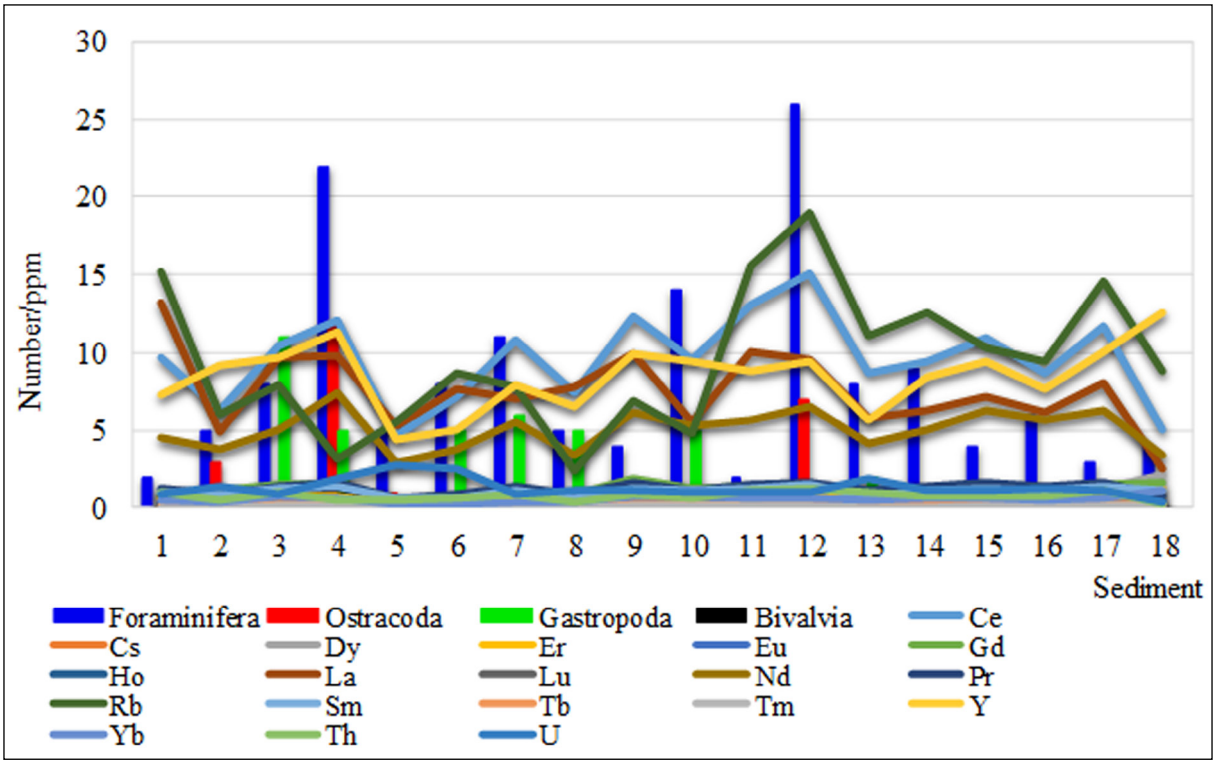


Figure 16- Quantitative distribution of trace elements and fauna in sediments of the study area.

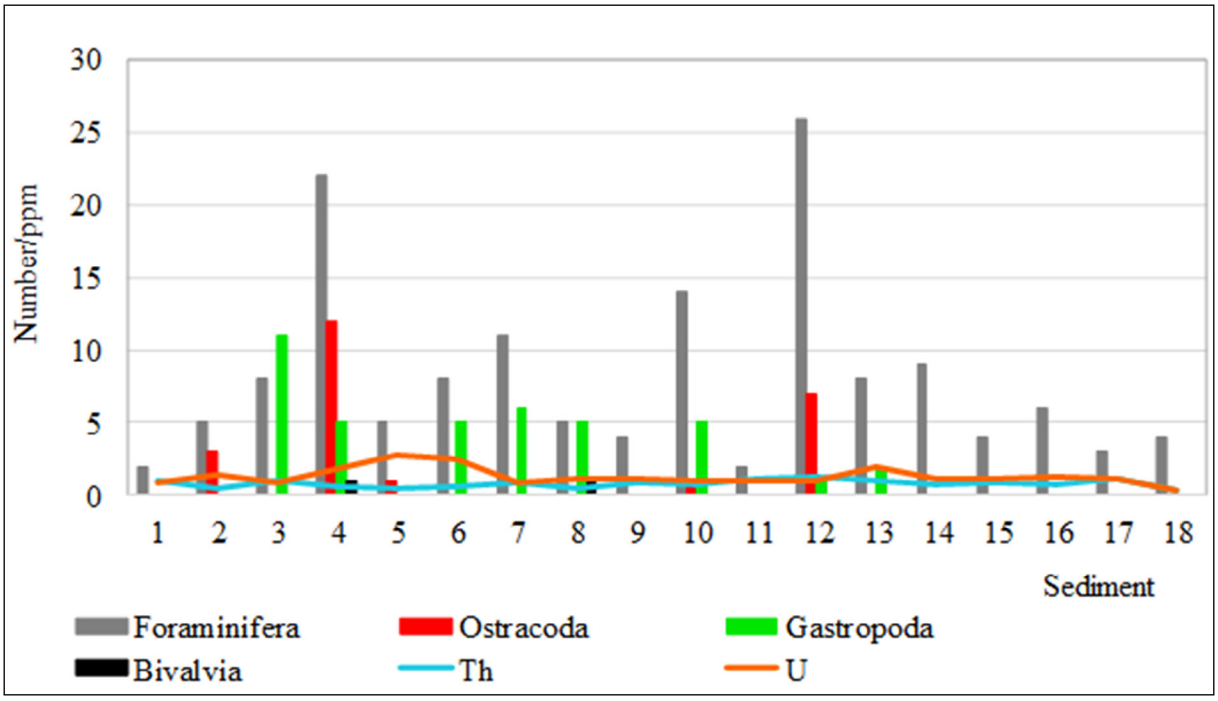


Figure 17- Quantitative distribution of radioactive elements and fauna in sediments of the study area.

## References


Athersuch, J., Horne, D. J., Whittaker, J. E. 1989. Marine and Brackish Water Ostracods (Superfamilies Cypridacea and Cytheracea): Keys and Notes for the Identification of the Species. Linnean Society of London and the Estuarine and Brackish-Water Sciences Association, 43, 1-343.

Babin, C. 1980. Elements of Palaeontology. John Wiley and Sons, 446. ISBN 0471 27577 8 (56 Bab).

Bignot, G. 1985. Elements of Micropaleontology**.** Graham and Trotman Ltd., 217.

Bonaduce, G., Ciampo, G., Masoli, M. 1975. Distribution of ostracoda in the Adriatic Sea. Pubblicazioni della Stazione Zoologica di Napoli 40, 1–304.

Breman, E. 1975. The Distribution of ostracodes in the bottom sediments of the Adriatic Sea. Vrije Universiteit te Amsterdam, Krips Repro, Meppel, 1-165.

Cossignani, T., Ardovani, R., Micali, P., Tiselli, M., Cossignani, V., Cecalupo, A. 2011. Malacologia Mediterranea: Atlante delle Conchiglie del Mediterraneo.

Diner, E. 2012. http://www.starkibris.net/index.asp?haberID=114714. 11 Mart 2012.

Eryılmaz, M. 1998. Doğu Akdeniz'in (Antalya Körfezi - Mersin Körfezi-İskenderun Körfezi - KKTC kıyıları) oşinografisi ve akıntı sistemleri raporu. Deniz Kuvvetleri Komutanlığı Seyir Hdrografi ve Oşinografi Dairesi, İstanbul (unpublished).

Eryılmaz, M. 2004. Güzelyurt-Gazi Gazimağusa (KKTC) bölgeleri arası güncel çökel dağılım haritası. Kıyı ve Deniz Jeolojisi Sempozyumu, 13-15 Eylül 2004, Yıldız Teknik Üniversitesi, İstanbul, 72-73.

Eryılmaz, M., Kırca, Z. 1998. 1/75000 ölçekli Kıbrıs, KKTC Kıyıları, Yüzey Sediment Dağılımları Haritası. Deniz Kuvvetleri Komutanlığı Seyir Hidrografi ve Oşinografi Dairesi, İstanbul.

Eryılmaz, M., Yücesoy - Eryılmaz, F. 2002. Antalya Körfezi'nin oşinografik yapısı ve güncel çökel dağılımı. 55. Türkiye Jeoloji Kurultayı Bildiri Özleri Kitabı, TMMOB Jeoloji Mühendisleri Odası, 11-15 Mart 2002, Ankara, 88-90.

Eryılmaz, M., Aydın, Ş., Türker, A. 2002. Ege Denizi'nin güncel çökel dağılım haritası. 55. Türkiye Jeoloji Kurultayı Bildiri Özleri Kitabı, 11-15 Mart 2002, Ankara, 91-92.

Eryılmaz, M., Yücesoy Eryılmaz, F. 2003. İskenderun Körfezi'nin güncel çökel dağılım haritası. 56. Türkiye Jeoloji Kurultayı Bildiri Özetleri Kitabı, 14-20 Nisan 2003, Ankara, 286-287.

Eryılmaz, M., Yücesoy Eryılmaz, F. 2019. Oceanography and sediment distribution of the Mersin Gulf (East Mediterranean - Turkey). Seventh International Symposium Monitoring of Mediterranean coastal

areas: problems and measurement techniques, Livorno (Italy), 19-20-21 June 2018, Livorno, Italy.

Folk, R. L. 1974. Petrology of Sedimentary Rocks. Hemphill Publishing Company, Austin, 170.

Folk, R. L. 1980. Petrology of Sedimentary Rocks. Hemphill Publishing Company, Austin, 184.

Galehouse, J. S. 1971. Sedimentation analysis, Carver, E. R. (Ed). Procedures in Sedimentary Petrology. Wiley, NewYork, 69-94.

Guillaume, M. C., Peypouquet, J. P, Tetart, J. 1985. Quaternaire et actuel. Atlas des Ostracodes de France. H. J. Oertli (Ed.). Bulletin Centres Rechearche Exploration Proceeding Elf-Aquitaine. Mémoire 9, 337-377.

Hallı, M., Sarı, E., Kurt, M. A. 2014. Assessment of arsenic and heavy metal pollution in surface sediments of the Ergene River, Turkey. Polish Journal of Environmental Studies 23, 1581-1590.

Hartmann, G., Puri, S. H. 1974. Summary of neontological and paleontotogical classification of ostracoda, Mitteilungen aus dem Zoologischen Staatsinstitut und Zoologischem Museum in Hamburg Band, 70, 7-73.

http://users.metu.edu.tr/kktctntm/KKTC_tarihi/adacogr.html. 2.09.2020

https://www.marbef.org/data/. 2.12.2019

Joachim, C., Langer, M. R. 2008. The 80 most common ostracods from the Bay of Fetovaia Elba Island (Mediterranean Sea). Universität Bonn, 29p.

Kırca, Z., Eryılmaz, M. 1987. 1/50000 ölçek Kıbrıs, Akdeniz, Girne Bölgesi Yüzey Sediment Dağılım Haritası (Tane Büyüklüğüne Göre). Deniz Kuvvetleri Komutanlığı Seyir Hidrografi ve Oşinografi Dairesi Başkanlığı, İstanbul.

Kırca, Z., Eryılmaz, M. 1989. 1/50000 ölçek Kıbrıs, Akdeniz, Gazimağusa Körfezi Yüzey Sediment Dağılım Haritası (Tane Büyüklüğüne Göre). Deniz Kuvvetleri Komutanlığı Seyir Hidrografi ve Oşinografi Dairesi Başkanlığı, İstanbul.

Kırca, Z., Eryılmaz, M. 1997. 1/50000 ölçek Kıbrıs, Akdeniz, Güzelyurt Körfezi Yüzey Sediment Dağılım Haritası (Tane Büyüklüğüne Göre). Deniz Kuvvetleri Komutanlığı Seyir Hidrografi ve Oşinografi Dairesi Başkanlığı, İstanbul.

Krauskopf, K. B. 1979. Introduction to Geochemistry (2. Basım). McGraw Hill Book Coy, 617.

McManus, J. 1991. Grain size determination and interpretation. Tucker, M. (Ed). In Techniques in Sedimentology. Blackwell, Oxford, 63-85.

Meriç, E., Avşar, N., Yokeş, M. B. 2008*a*. Some alien foraminifers along the Aegean and southwest coasts of Turkey. Micropaleontology 54(3-4), 307-349.

Meriç, E., Avşar, N., Nazik, A., Yokeş, M. B., Dinçer, F. 2008*b*. A review of benthic foraminifers and ostracodes of the Antalya coast. Micropaleontology 54(3-4), 199-240.

Meriç, E., Yokeş, M. B., Avşar, N., Dinçer, F. 2015*a*. New observations of alien foraminifera on the Turkish coasts of the Aegean Sea (2008-2011). International Journal of Environment and Geoinformatics 2(2),77-87.

Meriç, E., Yokeş, M. B., Avşar, N., Dinçer, F. 2015*b*. Main introduction way of Indo-Pacific and Red Sea originated benthic foraminifers to the Eastern Mediterranean. International Journal of Environment and Geoinformatics 2(3), 07-12.

Meriç, E., Yokeş, M. B., Avşar, N., Kıyak, N. G., Öner, E., Nazik, A., Demirtaşlı, E., Dinçer, F., Öztürk, M. Z. 2016. Did Amphistegina lobifera larsen migrated the Mediterranean via Suez Canal? Quaternary International 401, 91-98. http://dx.doi.org/10.1016/j.quaint.2015.08.088.

Meriç, E., Yokeş, M. B., Avşar, N., Dinçer, F. 2018*a*. Did Spiroloculina antillarum, Articulina carinata, Coscinospira hemphrichii, Peneroplis pertusus, P. planatus, Sorites orbiculus, Astacolus insolithus, Siphonina tubulosa, Amphistegina lessonii and A. lobifera reach the Mediterranean via the Suez Canal? International Journal of Environment and Geoinformatics 5(3), 378-385.

Meriç, E., Avşar, N., Yokeş, M. B., Dinçer, F. 2018*b*. İskenderun Körfezi ve Samandağ (Adana-Hatay) kıyılarında gözlenen yabancı bentik foraminiferler. Hacettepe Üniversitesi Yerbilimleri 39(3), 253-262.

Meriç, E., Barut, İ. F., Yokeş, B., Eryılmaz, M., Yücesoy-Eryılmaz, F., Dinçer, F. 2018*c*. Doğu Ege Denizi Türkiye kıyılarında varlığı bilinen veya düşünülen deniz içi termal çıktılar çevresinde gözlenen bentik foraminifer topluluklarında belirlenen değişimler ve etkenler. Hacettepe Üniversitesi Yerbilimleri 39(3), 207-220.

Millot, C., Taupier-Letage, I. 2005. Circulation in the Mediterranean the Mediterranean Sea. Handbook of Environmental Chemistry, 29-66, doi:10.1007/b107143. ISBN 978-3-540-25018-0.

Mostafawi, N., Matzke-Karasz, R. 2006. Pliocene Ostracoda of Cephalonia, Greece. The unrevised species of Uliczny (1969). Revista Española de Micropaleontología 38, 11-48.

Özhan, G. 1988. Sismik yansıma verileri ışığında Kuzeydoğu Akdeniz. Türkiye Jeoloji Bülteni 31, 51-62.

Report 1. 1987. Akdeniz, Mersin Körfezi, Mersin Körfezi, İskenderun Körfezi, Kıbrıs (Girne-Gazimağusa) Bölgesi oşinografi çalışmaları ve sonuç raporu (Nisan 1987). Deniz Kuvvetleri Komutanlığı Seyir Hidrografi ve Oşinografi Dairesi Başkanlığı, İstanbul.

Report 2. 1988. Akdeniz, Mersin Körfezi, Mersin Körfezi, İskenderun Körfezi, Kıbrıs (Girne-Gazimağusa) Bölgesi oşinografi çalışmaları ve sonuç raporu (Temmuz 1988). Deniz Kuvvetleri Komutanlığı Seyir Hidrografi ve Oşinografi Dairesi Başkanlığı, Report No: 218-219-220-221, İstanbul.

Report 3. 1990. Akdeniz, Mersin Körfezi, Mersin Körfezi, İskenderun Körfezi, Kıbrıs (Girne-Gazimağusa) Bölgesi oşinografi çalışmaları ve sonuç raporu (Nisan 1990). Deniz Kuvvetleri Komutanlığı Seyir Hidrografi ve Oşinografi Dairesi Başkanlığı, Report No: 255-256-257-258, İstanbul.

Report 4. 1991. Akdeniz, Mersin Körfezi, Mersin Körfezi, İskenderun Körfezi, Kıbrıs (Girne-Gazimağusa) Bölgesi oşinografi çalışmaları ve sonuç raporu (Şubat 1991). Deniz Kuvvetleri Komutanlığı Seyir Hidrografi ve Oşinografi Dairesi Başkanlığı, Report No: 278-279-280-281, İstanbul.

Report 5. 1992. Turmeos I and Turcyos I cable route survey: Anamur (Bozyazı)-Girne, Marmaris-İstanbul fiber optik kablo güzergahı çalışmaları. Deniz Kuvvetleri Komutanlığı Seyir Hidrografi ve Oşinografi Dairesi Başkanlığı, ALCATEL, İstanbul.

Sarı, E., Ünlü, S., Balcı, N., Koldemir, B. 2014. Distribution and contamination of heavy metals in the surface sediments of Ambarlı Port area (İstanbul, Turkey). Ekoloji 23(90), 1-9.

Sarı, E., Çukrov, N., Franciskoviç Bilinski, S., Kurt, M. A., Hallı, M. 2016. Contamination assessment of ecotoxic metals in recent sediments from the Ergene River, Turkey. Environmental Earth Sciences 75 (1051) 1-11.

Scaperrotta, M., Bartolini, S., Bogi, C. 2009-2015. Accrescimenti - Stadi di accrescimento dei Molluschi marini del Mediterraneo - Stages of growth of marine molluscs of the Mediterranean Sea, I-VI.

TR-341. 2007. Akdeniz, KKTC Gemitaşı Burnu-Limantaşı Burnu, Seyir Haritası (Ölçek: 1/100.000). Deniz Kuvvetleri Komutanlığı Seyir Hidrografi ve Oşinografi Dairesi, İstanbul.

TR-342. 2014. Akdeniz, Kıbrıs Adası Mersinli - Boğaz, Seyir Haritası (Ölçek: 1/100.000). Deniz Kuvvetleri Komutanlığı. Seyir Hidrografi ve Oşinografi Dairesi, İstanbul.

TR-343. 2017. Akdeniz Kıbrıs Adası Güneydoğu Sahili Kiti (Çiti) Burnu - Zeytin Burnu, Seyir Haritası (Ölçek: 1/100.000). Deniz Kuvvetleri Komutanlığı. Seyir Hidrografi ve Oşinografi Dairesi, İstanbul.

TR-344. 2012. Akdeniz Kıbrıs Adası Güney Sahili Aspro (Beyaz) Burnu - Pyla (Pila) Burnu Seyir Haritası (Ölçek: 1/100000). Deniz Kuvvetleri Komutanlığı Seyir Hidrografi ve Oşinografi Dairesi, İstanbul.

Van Morkhoven, F. P. C. M. 1963. Post-Palaeozoic Ostracoda. Their Morphology, Taxonomy, and Economic Use, II, Generic Descriptions, Amsterdam - London - New York, Elsevier Publishing Company, 1-478.

Wenthworth, C. K. 1922. A scale for grade and class terms for clastic sediments. The Journal of Geology 30 (5), 377-392.

Yassini, I. 1979. The littoral system ostracodes from the bay of Bou-İsmail, Algiers, Algeria, National Iranian Oil Company. Revista Espanola de Micropaleontologia XI, 353-416.

Yokeş, M. B., Meriç E., Avşar, N., Öncel, M. S., Eryilmaz, M., Barut, İ. 2014. The expanded population of Amphistegina lobifera at Üç Adalar and Beş Adalar (Antalya, Turkey), Marine Biodiversity Records 7(e2), doi:10.1017/S175526721400044X.

Zangger, E., Malz, H. 1989. Late Pleistocene, Holocene, and recent ostracods from the Gulf of Argos, Greece. Courier Forschungsinstitut Senckenberg 113, 159-175.

Bulletin of the Mineral Research and Exploration

http://bulletin.mta.gov.tr

# The distribution of elements in the alteration of feldspatic minerals

Kıymet DENİZ[a*], Yusuf Kağan KADIOĞLU[a,b], Tamer KORALAY[c] and Bahattin GÜLLÜ[d]

[a]*Ankara University, Faculty of Engineering, Department of Geological Engineering, Ankara, Turkey*
[b]*Ankara University, Earth Sciences Application and Research Centre (YEBIM), Ankara, Turkey*
[c]*Pamukkale University, Faculty of Engineering, Department of Geological Engineering, Denizli, Turkey*
[c]*Aksaray University, Faculty of Engineering, Department of Geological Engineering, Aksaray, Turkey*

*Research Article*

Keywords:
Foid Syenite, Alteration, Glass and Ceramic Raw Material, Özvatan, Central Anatolia.

**ABSTRACT**

Feldspar (alkali feldspar and plagioclases) and in recent years feldspathoid minerals are used as raw materials in the ceramic-glass industries. The igneous rocks such as granite, syenite and foid syenite which mainly contain these minerals have the potential to be raw materials. Some inclusions within the feldspatic minerals affect extremely negatively the desired values for raw material. In this study, the effective processes in the alteration of feldspatic minerals within the Özvatan foid syenites, the effects of alteration minerals in the raw material were evaluated and the effects of the elements released by alteration on the environment were revealed. The foid syenites consist of nepheline, orthoclase, plagioclase, cancrinite, sodalite, amphibole, biotite, pyroxene, melanite with a rare amount of sphene, zircon, apatite and fluorite. The contents of the sericite and kaolinite, which are formed as a result of an alteration of these rocks, increase in direct proportion to alteration degree. As a result of the alteration index values, foid syenites samples show the low degreed decomposed property. According to the calculated mobility index (MI) from chemical analyses, there is a quantitative decrease in the major oxides such as $SiO_2$, $Al_2O_3$, $Na_2O$, $K_2O$, CaO and $Fe_2O_3$ in the foid syenites. In accordance with the all data, Özvatan foid syenites have been exposed both weathering and hydrothermal alteration and the effect of hydrothermal alteration are observed more frequently in the altered rock. While the excess of diaclase structures within the rock provides ease of operation, on the other hand, it accelerated the weathering and alteration processes.

*Received Date: 19.11.2020*
*Accepted Date: 22.03.2021*

## 1. Introduction

Feldspathic (feldspar and feldspathoid) minerals are found at excess rates in felsic intrusive rocks. Due to representing the main mineral composition in rocks with alkali feldspar granite, alkali feldspar syenite, and foid syenite in composition, these rocks are important in terms of their potential to be industrial raw materials. Nearly all feldspar and feldspathoid minerals are used as raw materials for different purposes in many different fields (glass, ceramic, paint, plastic, rubber industry, etc.) in recent years. With the daily increasing requirements of feldspar and feldspathoid raw materials in different fields, there has been an intensification of geological and technological studies about this topic. For this reason, studies about the assessment of pegmatitic deposits in addition to intrusive rocks that contain abundant feldspathic minerals and may be a source of feldspar and especially altered portions of these rocks have gained importance. However, potential deposits are used in the marble industry due to the

Citation Info: Deniz, K., Kadıoğlu, Y. K., Koralay, T., Güllü, B. 2021. The distribution of elements in the alteration of feldspathic minerals. Bulletin of the Mineral Research and Exploration 166, 167-188. https://doi.org/10.19111/bulletinofmre.901035

**Corresponding author: Kıymet DENİZ, kdeniz@eng.ankara.edu.tr*

colour homogeneity of fresh intrusive rocks, lack of many fractures, and high block yield. For this reason, determining the usefulness of altered portions with high fracture rates, which cannot be used in the marble sector, for glass and ceramic industries especially and including this in the economy is highly important in terms of the best use of our natural resources. Mineralogy, mineral, and rock chemistry studies are very important to determine the quality and class of feldspar and feldspathoid minerals to be used in the glass and ceramic industry. Enrichment processes for altered intrusive rocks without economic value make it possible to operate them. It is necessary to determine the accompanying impurities in feldspathic minerals with mineralogical and spectroscopic methods and to use the most appropriate and economic separation techniques according to the composition of impurities. It is possible to remove these impurities with physical methods like magnetic separation and flotation.

Many studies were performed about the alteration of magmatic rocks and especially feldspar minerals and the element exchanges within the rocks with alteration (Gürsoy, 1999; Karakaya et al., 2001*a*, 2001*b*; Ng et al., 2001; Piché and Jébrak, 2004; Karakaya et al., 2012; Mathieu, 2016, 2018; Yazar, 2018; Akçe and Kadıoğlu, 2020; Ulusoy and Kadıoğlu, 2021). Feldspar minerals within granitic rocks may transform to kaolin under atmospheric conditions or hydrothermal effects (Gürsoy, 1999). Deniz and Kadıoğlu (2011) stated that smectites within the Buzlukdağ foid syenite (Kırşehir - Kaman) in the Central Anatolia region were derived from the alteration of biotite, amphibole and pyroxene minerals, kaolinite came from alteration of leucite, nepheline and partly from orthoclase and illite formations resulted from alteration of more alkali feldspar and partly feldspathoids (nepheline and leucite).

Enrichment processes are very important in terms of increasing the quality and yield of feldspathic minerals. Process related to purifying feldspathic raw materials includes hand-washing, breaking, grinding, classifying according to size, magnetic or electrostatic separation, and flotation (Gürsoy, 1999). Başıbüyük and Ekincioğlu (2019) performed investigations about the potential of pseudoleucite syenites located in İsahocalı (Kırşehir) as raw material and stated that minerals with potential as raw materials could be enriched using a dry magnetic separator as these rocks were not altered and that they were suitable for raw material. Studies about purifying raw materials by removing accessory minerals found as inclusions within feldspar (apatite, rutile, etc.) or secondary minerals forming as a result of alteration and/or weathering have been performed for many years (Bayraktar et al., 1997, 1999; Gürsoy, 1999; Negm et al., 2000; Erdinç, 2007; Marinov et al., 2010; Başıbüyük and Ekincioğlu, 2019; Ötekaya et al., 2020). A study by Kademli (2004) stated that mica minerals were the main source of iron among feldspar minerals that can be used as raw material in the glass and ceramic industry. They stated that mica can be separated using traditional methods such as flotation and magnetic separation in addition to the spiral enrichment method using the effect of gravity. This technique is much more effective for separation of mica with fine grain size and can be used to reduce flotation stages.

Impurities in feldspathic minerals generally result from the presence of inclusion minerals like hornblende, biotite, chlorite, apatite and sphene. Impurities in feldspathic minerals used in industry are generally determined by examining the content of element values such as Fe, Ti, Mn and Mg. Apart from these elements, when the chemical %K content increases, especially in weathered feldspathic minerals, impurities caused by muscovite and sericite minerals may lead to insidious and hidden contamination. The study area of the Kayseri Özvatan region was chosen due to rocks without silica saturation and foid syenite composition being rich in feldspathic components. The feldspathic minerals from the study area were investigated in mineralogical, textural and chemical senses for components causing impurities. Additionally, the type and ratio of the elements released by the decomposition of feldspathic minerals in the study area and which minerals they contribute to the formation of the environment were determined.

## 2. Material and Method

Thin sections of 150 samples collected from intrusive rocks that crop out in the vicinity of Özvatan town of Kayseri province have been made and mineralogical and petrographic investigations have been performed by Zeiss brand Axio model polarizing microscope to determine mineralogical compositions, textural features and alteration types of rocks. As a result of result of the petrographic investigations, samples that were not arenised and

weathered were prepared for geochemical analyses (major oxide and trace element). Sample preparation and polarised energy distribution X-Ray Fluorescence Spectrometry (PEDXRF) measurement details were completed according to Deniz and Kadıoğlu (2018, 2019). With the aim of determining the chemistry and types of feldspar and feldspathoid minerals found within the rock, electron probe micro analysis (EPMA) analyses performed on polished and carbon-coated thin sections. A JEOL brand JXA 8230 model device with 20 kV voltage and 20 nA current was used for EPMA analyses. Point measurements of feldspathoid minerals had a diameter of 20 µm for the area of the electron beam. Mineral standards used for each element in the measurements are diopside (Mg, Ca), albite (Na), orthoclase (Si, Al, K), fluorite (F), rhodonite (Mn), olivine (Fe), titanium oxide (Ti), and barite (Ba). Detection limits of the standards for each measured element were 150 ppm for Mg, 188 ppm for Na, 242 ppm for Si, 1087 ppm for F, 94 ppm for Mn, 85 ppm for Al, 104 ppm for Fe, 27 ppm for K, 69 ppm for Ti, 176 ppm for Ba and 39 ppm for Ca. The standard deviation of the standards for each measured element were 0.18% for Mg, 0.30% for Na, 0.08% for Si, 0.26% for F, 0.11% for Mn, 0.12% for Al, 0.21% for Fe, 0.08% for K and 0.07% for Ti, Ba and Ca. To determine alteration mineralogy, measurements were taken from samples with different degrees of alteration by using an Inel brand Equinox 1000 model X-Ray Diffractometer (XRD) device at 30 mA and 30 kV using a cobalt (Co) anode. All analytical studies were completed in the Earth Sciences Application and Research Centre (YEBIM) laboratories of Ankara University.

## 3. Geology of the Study Area

The study area is bounded to the north by the İzmir Ankara Erzincan Suture Zone (IAESZ), to the west by the Tuz Gölü Fault (TGF) and to the east by the Ecemiş Fault Zone (EFZ) and is located in the southeast section of the rough triangle between Ankara, Sivas and Niğde cities in the central Anatolian region. It is located in and around Özvatan (Hayriye - Çukurköy) town located nearly 55 km northeast of Kayseri (Figure 1a). Observed rocks in the study area can be separated into three groups as metamorphic units, magmatic units and cover units. The metamorphic units comprise Palaeozoic schist and Permian marbles belonging to the Central Anatolia Metamorphics (CAM) (Figure 1b). The magmatic units are represented by Upper Cretaceous intrusive (Özvatan foid syenite), sub-volcanic and Cenozoic extrusive rocks.

The magmatic rocks in the study area were called Atdere foid syenite by Özkan (1987) and Hayriye pluton by Kadıoğlu et al., (2006). In this study, it was appropriate to call the syenitic composition rocks outcropping near Özvatan town with different degrees of weathering the Özvatan foid syenite (Figure 1b and 2a, Deniz et al., 2018*a*). Previous studies (e.g., Kraeff and Pasquare, 1966) mentioned the presence of silica-saturated and silica-unsaturated rocks in the region, while previous studies by the authors and this study only observed the presence of syenite composition rocks that were not silica saturated (e.g., Deniz et al., 2018*a*, *b*). Syenites containing quartz in the region were determined to have secondary quartz forming with the effect of silicification due to hydrothermal alteration. Syenitic composition intrusive rocks have intruded into schist and marble composition rocks in the study area. Dykes with felsic and mafic composition cut the syenitic units with sharp contacts and hydrothermal veins containing calcite, fluorite and barite are present (Deniz et al., 2018*a*). Volcanic rocks with basalt composition were observed in the southern sections of the study area (Deniz et al., 2018*b*). The cover units, which are not included in the research topic, are represented by Eocene - Upper Miocene continental clastics. The youngest formation in the study area is Quaternary alluvium (Özaksoy and Göktan, 1996).

## 4. Mineralogy and Petrography

Özvatan foid syenites are light grey, grey, and pinkish-grey colour with phaneritic texture (Figure 2b - 2g). The unit with diaclase structure (Figure 2b) displays different rates of alteration (Figure 2c, d, and e). The degree of alteration is more pronounced along with diaclase structures, with the colour of the rock displaying variation from grey to pink linked to the severity of alteration (Figure 2g). In hand samples, nepheline, K-feldspar, garnet, biotite, amphibole and fluorite crystals are very visible (Figure 2f, g). The Özvatan foid syenites have holocrystalline hypidiomorphic texture, with main mineralogic composition of 20 - 50% nepheline, 70 - 90% orthoclase, 20 - 30% plagioclase, 1 - 5% cancrinite, 1 - 3% sodalite, 0 - 3% amphibole, 0 - 4% biotite, 1 - 3% pyroxene, 1 - 6% melanite and lower rates of 0 - 1%

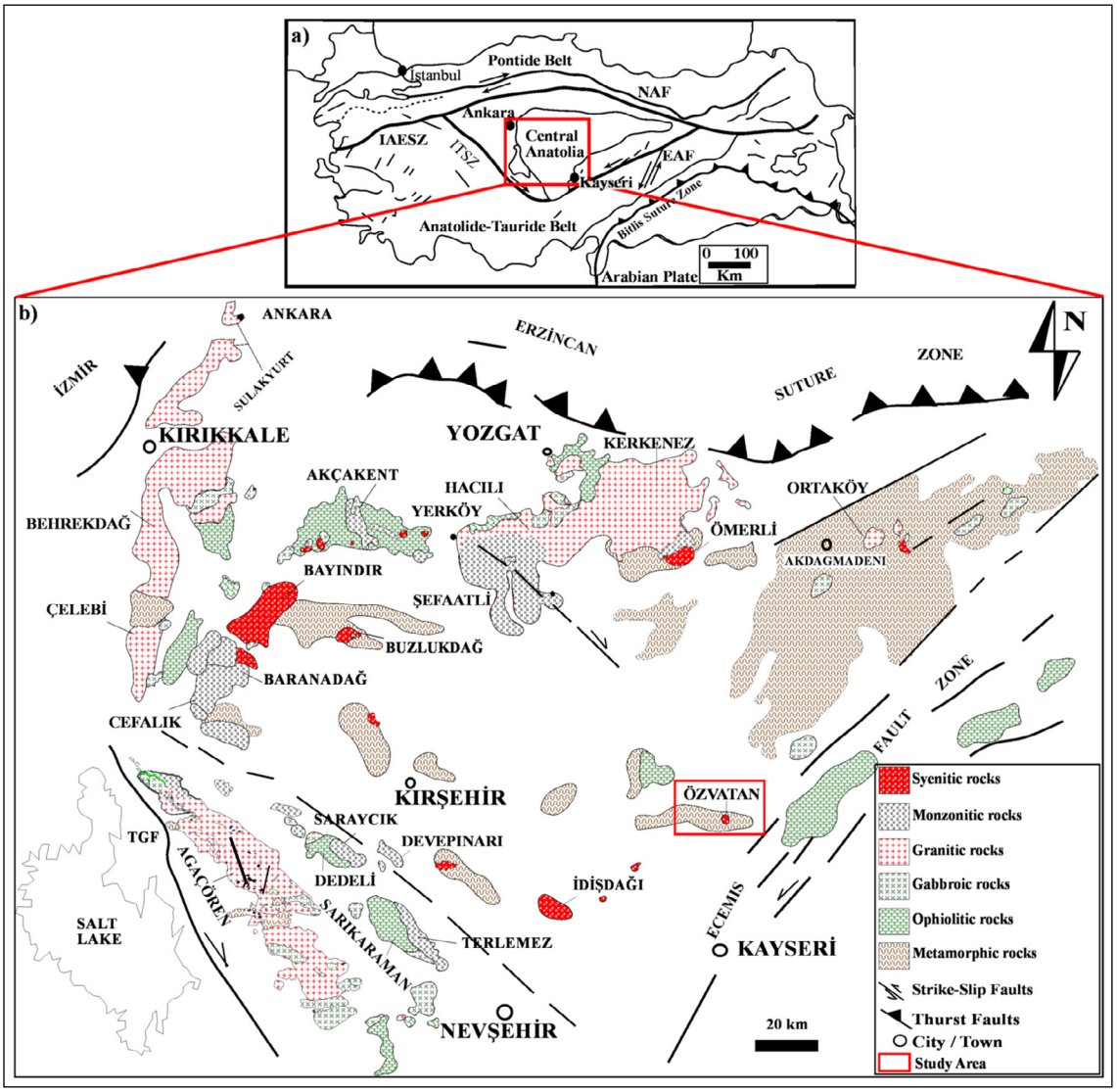


Figure 1- a) Map showing location of central Anatolia in Turkey (modified from Bozkurt and Mittwede, 2001), b) geological map showing location of the study area (modified from Kadıoğlu et al., 2006).

for other minerals (titanite, zircon, apatite and fluorite) (Figure 3a - d). Syenite rocks may be divided into sub-groups according to the abundance of minerals like cancrinite, sodalite, amphibole, biotite, pyroxene, and melanite in the rock. According to Confocal Raman Spectroscopy (CRS) performed to determine types in the group minerals, amphibole minerals are actinolite; pyroxene minerals are diopside; cancrinite minerals are vishnevite; mica minerals are biotite and phlogopite; feldspathoid minerals are nepheline and sodalite and garnet minerals have melanite composition.

Alteration types including argillisation, sericitization, carbonation, albitisation, uralitisation, opacification and iron hydroxidation are commonly observed in the altered samples (Figure 3e - i). As the degree of alteration increases, the secondary alteration products within the rock naturally increase (Figure 3e - i). Sericite and kaolinite minerals were detected from XRD analyses for identification of alteration products (Figure 4).

Within the Özvatan foid syenites, low proportions of mafic magmatic enclaves (MME) and magma segregation enclaves were observed. The composition of MMEs are foid gabbro and foid monzogabbro. Magma segregation enclaves formed as a result of clustering of biotite and amphibole minerals (Kadıoğlu and Güleç, 1996, 1999).

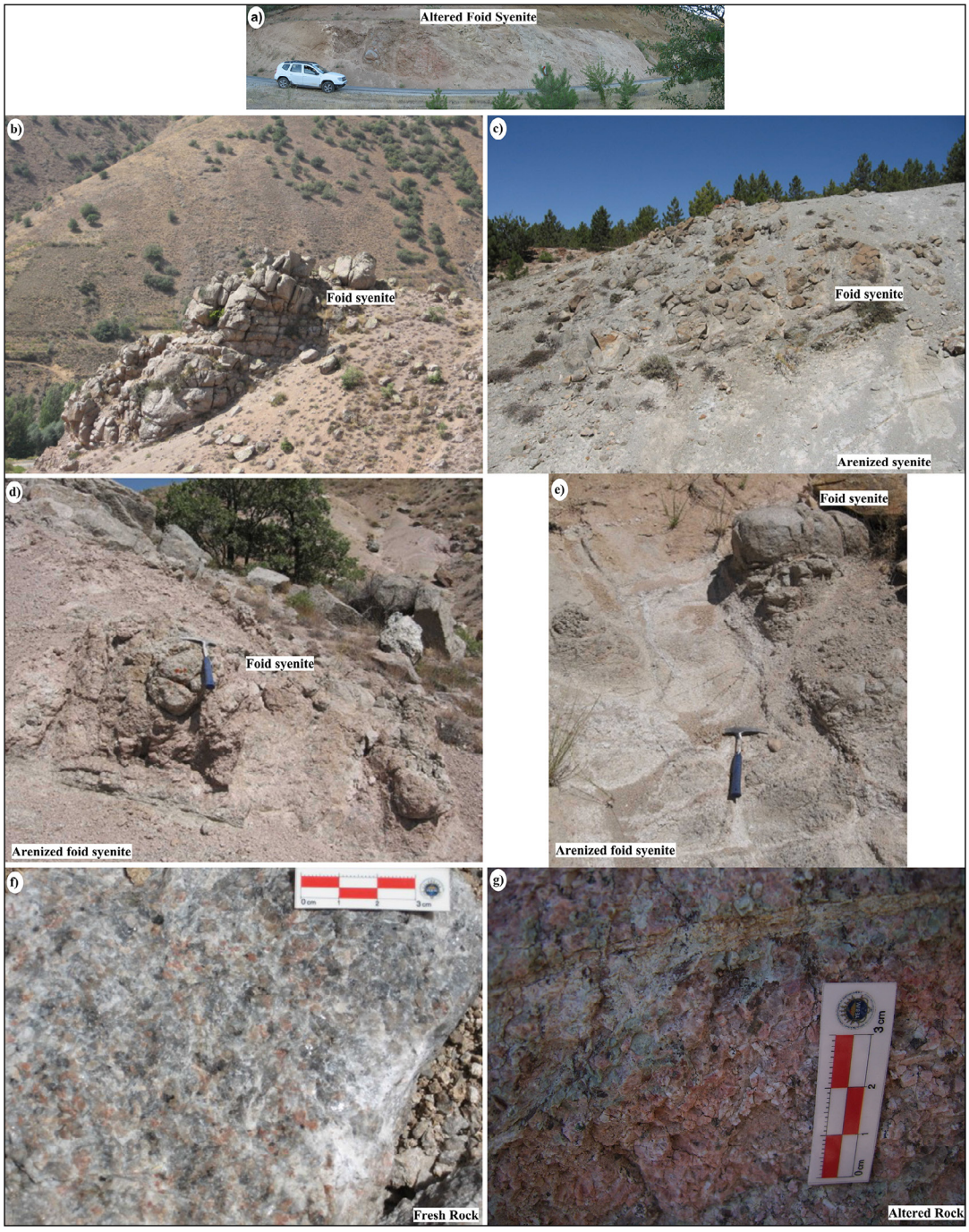


Figure 2- Field appearance of Özvatan foid syenites; a) general altered syenite outcrop, b) diaclase structures in altered syenites, c), d), e) appearance of arenitised syenite, f) macroscopic appearance of fresh syenite and g) macroscopic appearance of altered syenite.

XRD analyses were performed on fresh samples and differentially altered samples. On XRD diffractograms, nepheline and orthoclase minerals are dominant in the fresh rock (Figure 4). Sericite is mostly observed as an alteration mineral and when the degree of alteration in the rock increases, the proportion of this mineral in the rock increases (Figure 4). In addition to sericite, kaolin was also observed as the dominant alteration mineral in rocks with IV Group alteration degree (Figure 4). Sericite and kaolin minerals are more dominant in weathered rocks compared to fresh rock. (Figure 4).

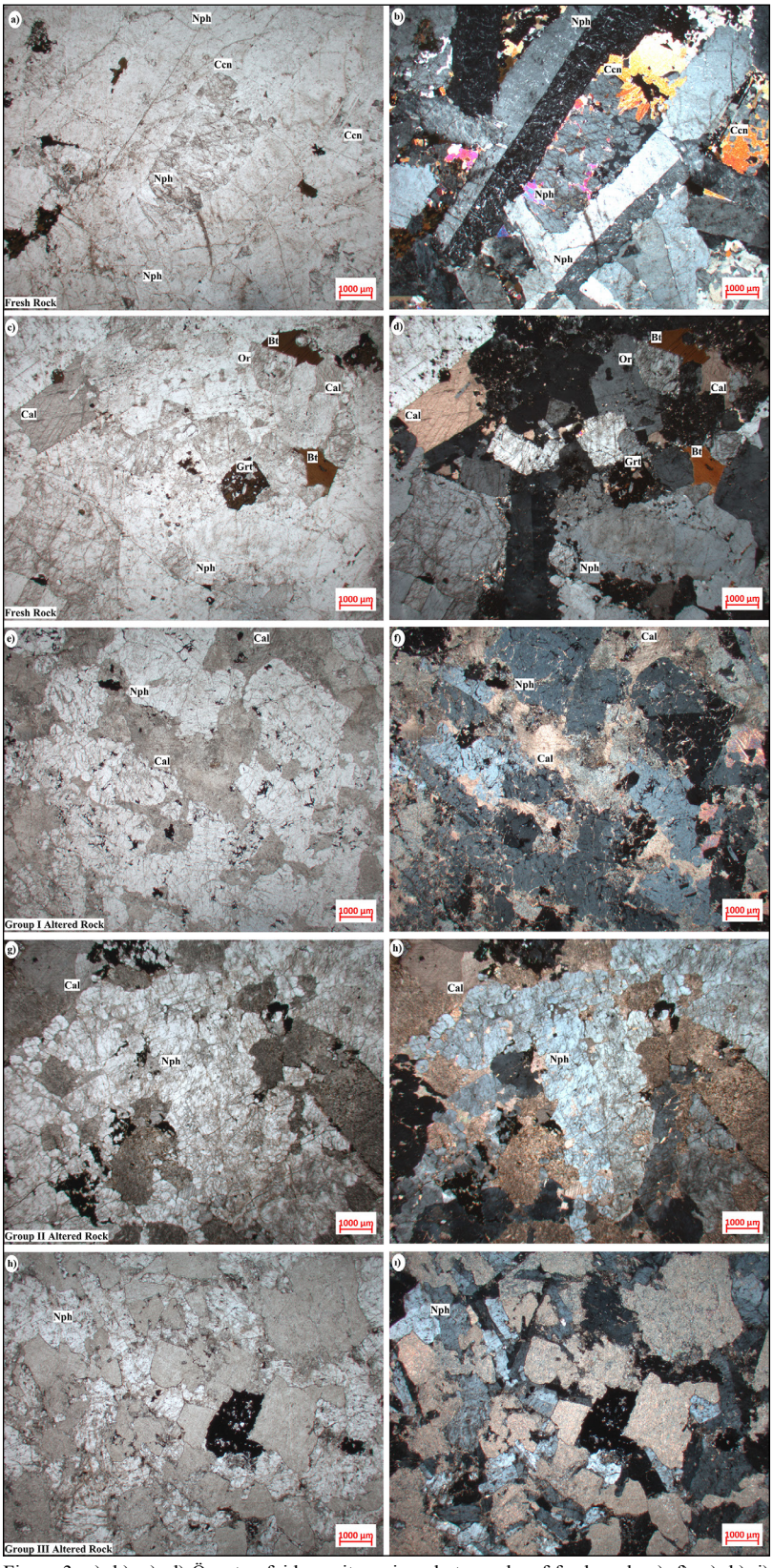


Figure 3- a), b), c), d) Özvatan foid syenites microphotographs of fresh rock, e), f), g), h), i) microphotographs of altered rock (a, c, e, g, h: parallel Nicol images, b, d, f, h, i: cross Nicol images and Bt: biotite, Cal: calcites, Ccn: cancrinite, Grt: garnet, Kln: kaolinite, Nph: nepheline, Or: orthoclase, Ser: sericite).

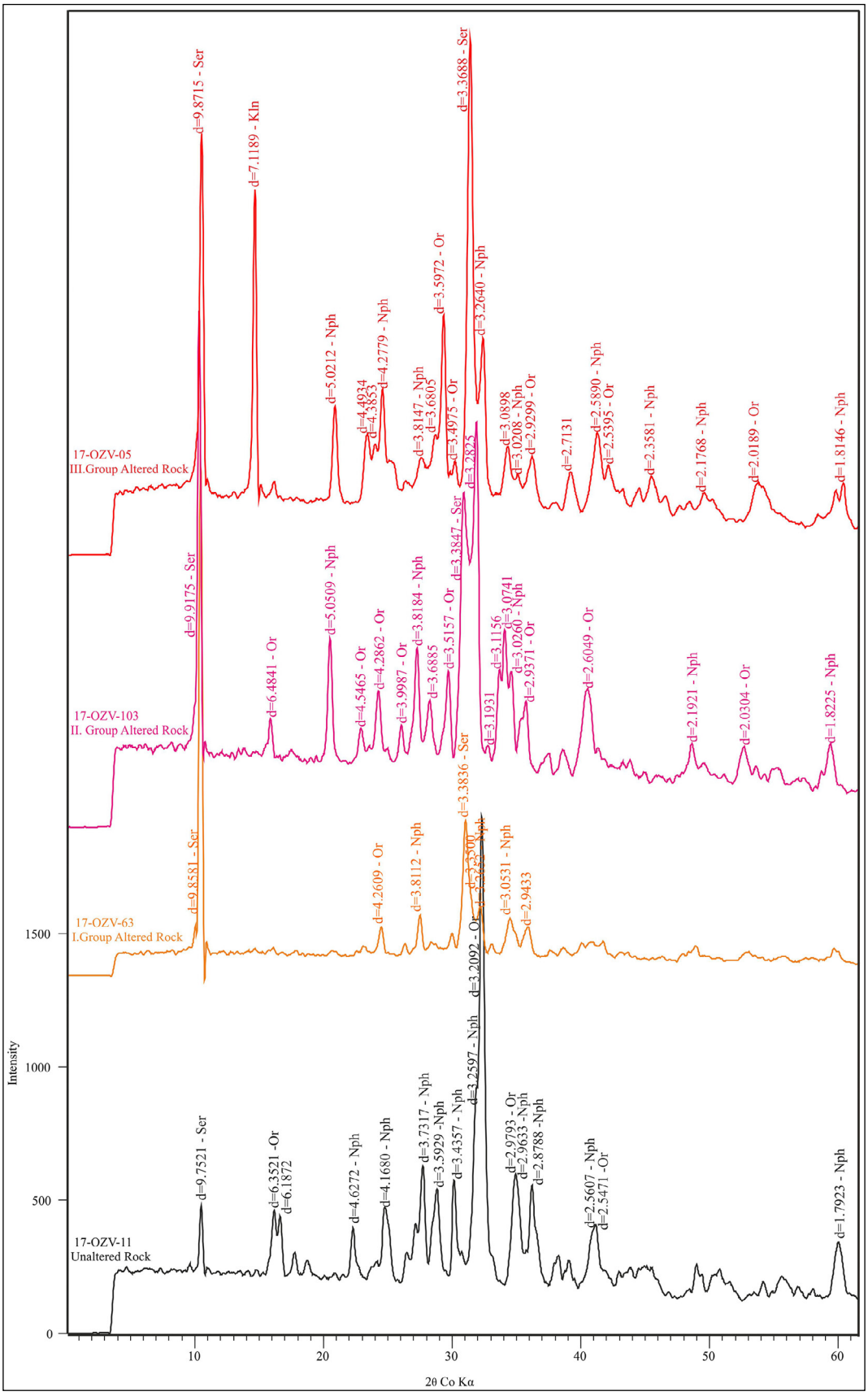


Figure 4- XRD diffractograms for fresh and altered Özvatan foid syenites.

## 5. Feldspar and Feldspathoid Chemistry

Mineral chemistry analysis results for minerals of the feldspar (alkali feldspar, plagioclase) and feldspathoid (nepheline, cancrinite, sodalite) groups are given in Tables 1 and 2. Accordingly, nephelines contain 41 - 45% $SiO_2$, 31 - 32% $Al_2O_3$, 14 - 16% $Na_2O$, 5 - 7% $K_2O$ and 0.3 - 0.5% FeO (Table 1). The composition of cancrinite group minerals within syenites was determined as vishnevite (Deniz et al., 2017).

The feldspar minerals contain 62 - 65% $SiO_2$, 18 - 22% $Al_2O_3$, 0.6 - 10.6% $Na_2O$, 0.1 - 16.1% $K_2O$, 0.01 - 3.13% CaO and 0.01 - 0.16% FeO (Table 2). Alkali feldspar minerals within syenite rocks were orthoclase and plagioclase minerals were oligoclase with bitownite composition in core sections determined in mineral chemistry studies (Table 2). This situation is a marker that a magma mixing process was effective during formation of the rocks.

## 6. Geochemistry of Whole Rock Alteration

Geochemical analysis results for Özvatan foid syenite samples are given in Table 3 and Table 4. When the whole-rock geochemistry of foid syenite samples with negligible degree of weathering as a result of petrographic investigation are examined, $SiO_2$ contents varied from 49 - 61%, $K_2O$ content from 4 - 11%, $Na_2O$ amounts were 3 - 8%, $Al_2O_3$ contents were 19 - 26% and $Fe_2O_3$ amounts were 1 - 7%. Total alkali ($Na_2O+K_2O$) amounts vary between 7 - 19%. Similarly, the content of $SiO_2$, $Al_2O_3$, $Na_2O$, $K_2O$, CaO, and $Fe_2O_3$ in the foid syenite samples with advanced degree of alteration change between 41 - 78% , 10 - 26%, 0.04 - 4.70%, 4.0 - 12.4%, 0.9 - 16.4% and 0.7 - 14.3%, respectively (Table 3).

The LOI values were calculated because of identifying whether rocks in the study area were altered and the number of volatile compounds (Table 3). For the LOI calculations, powdered samples were weighed to 2 g and placed in heat-resistant porcelain crucibles and were left in an ash oven at 1050 °C for 24 hours. The samples were taken out of the oven after they were weighed again and mass loss was calculated for LOI values as a percentage. Rocks with feldspathoid content contain minerals rich in terms of volatile compounds, so the LOI values were higher than magmatic rocks not containing feldspathoid minerals. Accordingly, it is seen that the LOI values of altered samples is more higher compared to fresh rock samples.

During weathering processes, significant changes may occur in rock and/or mineral chemistry. The degree of alteration of a rock may be determined according to alteration indexes proposed by a variety of researchers. The Özvatan foid syenite samples with

Table 1- Mineral chemistry results for representative nepheline minerals of Özvatan syenites (OZV: Özvatan, NPHL: nepheline).

| | **17-OZV-26-1-NPHL1** | | | | | |
|---|---|---|---|---|---|---|
| **No.** | **1** | **3** | **5** | **7** | **10** | **12** |
| **$SiO_2$** | 45.38 | 46.79 | 41.47 | 41.53 | 44.21 | 41.94 |
| **$Al_2O_3$** | 32.37 | 31.18 | 31.63 | 32.30 | 31.10 | 31.91 |
| **FeO** | 0.50 | 0.43 | 0.50 | 0.30 | 0.53 | 0.54 |
| **CaO** | 0.23 | 0.10 | 0.08 | 0.11 | 0.17 | 0.17 |
| **$Na_2O$** | 15.29 | 14.99 | 16.24 | 15.52 | 15.63 | 15.44 |
| **$K_2O$** | 5.29 | 6.31 | 7.32 | 7.36 | 7.01 | 7.41 |
| **Total** | 99.07 | 99.81 | 97.25 | 97.11 | 98.66 | 97.44 |
| **Cation values calculated according to oxygen 32** | | | | | | |
| **Si** | 8.70 | 8.93 | 8.31 | 8.29 | 8.64 | 8.35 |
| **Al** | 7.32 | 7.01 | 7.46 | 7.60 | 7.17 | 7.49 |
| **$Fe^{+2}$** | 0.08 | 0.07 | 0.08 | 0.05 | 0.09 | 0.09 |
| **Ca** | 0.05 | 0.02 | 0.02 | 0.02 | 0.04 | 0.04 |
| **Na** | 5.68 | 5.54 | 6.31 | 6.01 | 5.93 | 5.96 |
| **K** | 1.30 | 1.53 | 1.87 | 1.87 | 1.75 | 1.88 |

Table 2- Mineral chemistry results for representative feldspar minerals of Özvatan syenites (OZV: Özvatan, ORT: orthoclase, PLG: plagioclase).

| | 17-OZV-11-3-ORT1 | 17-OZV-29-1-ORT1 | | | | | | | | | | OZV-12-16-4-PLG1 |
|---|---|---|---|---|---|---|---|---|---|---|---|---|
| **No.** | **1** | **1** | **2** | **3** | **4** | **5** | **6** | **7** | **8** | **9** | **10** | **4** |
| **$SiO_2$** | 64.59 | 63.86 | 64.15 | 63.73 | 64.59 | 62.27 | 63.34 | 65.30 | 64.18 | 64.13 | 64.37 | 64.30 |
| **$Al_2O_3$** | 18.69 | 19.02 | 19.47 | 19.17 | 18.57 | 19.10 | 18.09 | 18.14 | 18.79 | 18.53 | 18.28 | 22.22 |
| **FeO** | 0.16 | 0.12 | 0.13 | 0.01 | 0.11 | 0.08 | 0.08 | 0.09 | 0.08 | 0.12 | 0.12 | 0.03 |
| **CaO** | 0.02 | 0.02 | 0.02 | 0.03 | 0.02 | 0.02 | 0.02 | 0.01 | 0.01 | 0.01 | 0.02 | 3.13 |
| **$Na_2O$** | 1.36 | 0.80 | 0.79 | 0.62 | 0.82 | 0.81 | 0.65 | 0.79 | 0.81 | 0.82 | 0.93 | 10.61 |
| **$K_2O$** | 15.09 | 15.70 | 15.92 | 16.01 | 15.83 | 15.94 | 16.04 | 15.92 | 15.59 | 16.08 | 15.87 | 0.07 |
| **BaO** | 0.02 | 0.61 | 0.51 | 0.66 | 0.85 | 0.65 | 0.76 | 0.65 | 1.11 | 0.62 | 0.64 | 0.01 |
| **Total** | 99.95 | 100.13 | 101.00 | 100.23 | 100.80 | 98.87 | 98.99 | 100.92 | 100.59 | 100.30 | 100.23 | 100.39 |
| **Cation values calculated according to oxygen 32** | | | | | | | | | | | | |
| **Si** | 10.36 | 10.06 | 10.11 | 10.08 | 10.18 | 9.94 | 10.26 | 10.17 | 10.20 | 10.21 | 10.28 | 11.40 |
| **Al** | 4.00 | 4.00 | 4.09 | 4.04 | 3.90 | 4.06 | 3.91 | 3.77 | 3.98 | 3.93 | 3.89 | 5.25 |
| **Fe** | 0.05 | 0.04 | 0.04 | 0.00 | 0.03 | 0.03 | 0.02 | 0.03 | 0.02 | 0.04 | 0.04 | 0.01 |
| **Ca** | 0.01 | 0.01 | 0.01 | 0.01 | 0.01 | 0.01 | 0.01 | 0.00 | 0.00 | 0.00 | 0.01 | 1.11 |
| **Na** | 0.73 | 1.39 | 0.83 | 0.97 | 0.97 | 1.41 | 0.25 | 1.61 | 0.55 | 0.62 | 0.57 | 0.31 |
| **K** | 9.68 | 9.90 | 10.04 | 10.13 | 9.98 | 10.17 | 10.40 | 9.92 | 9.92 | 10.24 | 10.14 | 0.05 |
| **Ba** | 0.01 | 0.19 | 0.16 | 0.21 | 0.27 | 0.21 | 0.24 | 0.20 | 0.35 | 0.20 | 0.20 | 0.00 |
| | | | | | | | | | | | | |
| **Orthoclase** | 92.92 | 87.66 | 92.29 | 91.19 | 91.10 | 87.78 | 97.56 | 86.04 | 94.68 | 94.24 | 94.63 | 3.51 |
| **Albite** | 7.00 | 12.29 | 7.66 | 8.72 | 8.84 | 12.18 | 2.37 | 13.92 | 5.28 | 5.72 | 5.31 | 21.31 |
| **Anorthite** | 0.07 | 0.06 | 0.06 | 0.09 | 0.07 | 0.04 | 0.07 | 0.03 | 0.04 | 0.04 | 0.06 | 75.18 |

chemical analyses performed had the Ruxton ratio (R), Chemical Index of Alteration (CIA), Chemical Index of Weathering (CIW), Plagioclase Index of Alteration (PIA), Ishikawa Alteration Index (AI), Chlorite-Carbonate-Pyrite Index (CCPI), Advanced Argillic Alteration Index (AAAI), Sesquioxide Content Index (SOC), Leach Factor (LC), and Residue Factor (Rc) calculated (Table 5) and results are given in Table 6 (Ruxton, 1968; Parker, 1970; Roaldset, 1972; Nesbitt and Young, 1982; Harnois and Moore, 1988; Li et al., 1995; Fedo et al., 1995; İrfan, 1996; Souri et al., 2006; Fiantis et al., 2010).

The R ($SiO_2/Al_2O_3$) is a simple weathering index used for acidic and intermediate rocks (Ruxton, 1968; Fiantis et al., 2010). The R value for an altered rock is >10 and this value reduces when the degree of weathering increases. For the foid syenite samples, the R values vary from 2.0 to 6.6 and the samples were determined to be partially weathered (Tables 5 and 6). The relatively high values may be due to the abundant amounts of feldspar minerals within the rocks which are easily affected by weathering.

The CIA is used to measure the degree of transformation of feldspars to clay minerals (Nesbitt and Young, 1982; Fiantis et al., 2010). The CIA values increase in parallel to the increase in clay minerals within the rock. The CIA values for the Özvatan foid syenites vary from 44 to 78 and CIA values for magmatic rocks without weathering are below 50 (Tables 5 and 6).

The CIW proposed by Harnois (1988) is also defined as the A/CN ratio. There appear to be high rates of similarity and compatibility between CIW values and CIA values. The CIW calculations ignore the $K_2O$ value. The CIW values for syenites in the study area were 38 - 96 and feldspar minerals in the rocks were determined to partly transform to clay minerals based on weathering (Tables 5 and 6). The CIW values of magmatic rocks vary from ≤50 - 100 and the CIW values of foid syenite samples changes 38 to 96 (Tables 5 and 6).

The PIA is calculated as an alternative to CIW. Plagioclase minerals commonly found in silicate rocks

Table 3- Major element oxide chemical analysis results of Özvatan syenites (LOI: loss on ignition).

| Identification | Group | Element | $SiO_2$ | $TiO_2$ | $Al_2O_3$ | $Fe_2O_3$ | MgO | MnO | CaO | $Na_2O$ | $K_2O$ | $P_2O_5$ | $SO_3$ | $Cr_2O_3$ | $V_2O_5$ | Cl | LOI | Total |
|---|---|---|---|---|---|---|---|---|---|---|---|---|---|---|---|---|---|---|
| | | Unit | % | % | % | % | % | % | % | % | % | % | % | % | % | % | % | % |
| **Fresh Foid Syenite** | | 17-OZV-11 | 56.80 | 0.08 | 23.29 | 2.37 | 0.02 | 0.10 | 3.55 | 10.08 | 9.13 | 0.08 | 1.30 | 0.02 | 0.01 | 0.44 | 2.49 | 99.67 |
| **Altered Foid Syenite** | **I** | 17-OZV-04 | 53.77 | 0.12 | 26.58 | 4.49 | 0.45 | 0.09 | 1.45 | 0.04 | 7.36 | 0.04 | 0.11 | 0.00 | 0.00 | 0.01 | 5.32 | 99.83 |
| | | 17-OZV-05 | 55.84 | 0.12 | 25.76 | 4.26 | 0.35 | 0.07 | 0.93 | 0.04 | 6.19 | 0.01 | 0.09 | 0.00 | 0.01 | 0.01 | 6.36 | 99.99 |
| | | 17-OZV-93 | 53.81 | 0.07 | 25.56 | 2.03 | 0.22 | 0.08 | 2.95 | 0.50 | 10.01 | 0.03 | 0.06 | 0.01 | 0.00 | 0.00 | 5.02 | 99.85 |
| | **II** | 17-OZV-06 | 46.97 | 0.53 | 19.90 | 6.42 | 2.58 | 0.26 | 5.93 | 0.05 | 8.71 | 0.09 | 0.09 | 0.01 | 0.01 | 0.01 | 8.46 | 99.99 |
| | | 17-OZV-07 | 43.27 | 2.08 | 12.81 | 14.34 | 10.07 | 0.84 | 3.72 | 0.05 | 8.01 | 0.03 | 0.10 | 0.15 | 0.02 | 0.01 | 4.54 | 100.00 |
| | | 17-OZV-18 | 55.75 | 0.04 | 22.29 | 1.92 | 0.14 | 0.09 | 4.28 | 4.77 | 8.99 | 0.04 | 0.41 | 0.00 | 0.01 | 0.01 | 5.47 | 99.46 |
| | | 17-OZV-60 | 51.65 | 0.07 | 24.59 | 2.02 | 0.25 | 0.07 | 4.67 | 0.04 | 10.12 | 0.09 | 0.20 | 0.00 | 0.01 | 0.00 | 5.97 | 99.73 |
| | | 17-OZV-62 | 55.08 | 0.16 | 21.77 | 2.43 | 0.24 | 0.08 | 5.71 | 0.04 | 9.87 | 0.09 | 0.17 | 0.00 | 0.01 | 0.00 | 4.40 | 100.02 |
| | | 17-OZV-85 | 55.22 | 0.11 | 21.35 | 2.43 | 0.29 | 0.12 | 4.61 | 4.17 | 9.44 | 0.05 | 0.17 | 0.01 | 0.01 | 0.01 | 5.32 | 99.14 |
| | | 17-OZV-90 | 55.77 | 0.09 | 23.88 | 2.50 | 0.15 | 0.11 | 2.47 | 0.57 | 11.75 | 0.02 | 0.06 | 0.01 | 0.01 | 0.01 | 2.99 | 99.83 |
| | | 17-OZV-102 | 56.25 | 0.01 | 23.69 | 1.32 | 0.10 | 0.05 | 3.04 | 0.04 | 12.37 | 0.06 | 0.07 | 0.00 | 0.01 | 0.01 | 3.00 | 99.97 |
| | | 17-OZV-103 | 55.37 | 0.10 | 23.26 | 2.71 | 0.13 | 0.13 | 4.03 | 0.04 | 11.63 | 0.07 | 0.06 | 0.00 | 0.01 | 0.01 | 2.52 | 100.02 |
| | | 17-OZV-106 | 62.89 | 0.17 | 21.51 | 2.41 | 0.70 | 0.10 | 3.16 | 4.58 | 4.30 | 0.03 | 0.31 | 0.00 | 0.01 | 0.00 | 4.08 | 99.68 |
| | | 17-OZV-107 | 78.65 | 0.01 | 11.87 | 0.78 | 0.34 | 0.03 | 1.84 | 4.34 | 4.81 | 0.00 | 0.07 | 0.00 | 0.00 | 0.00 | 1.46 | 99.88 |
| | **III** | 17-OZV-57 | 42.29 | 0.07 | 20.21 | 2.74 | 0.10 | 0.12 | 14.39 | 0.05 | 8.03 | 0.14 | 0.13 | 0.00 | 0.01 | 0.00 | 10.98 | 99.22 |
| | | 17-OZV-81 | 47.88 | 0.04 | 20.56 | 1.68 | 0.10 | 0.09 | 10.60 | 0.04 | 10.02 | 0.11 | 0.14 | 0.00 | 0.01 | 0.00 | 8.46 | 99.70 |
| | | 17-OZV-84 | 41.86 | 0.09 | 20.10 | 1.80 | 0.19 | 0.13 | 15.61 | 0.04 | 7.88 | 0.14 | 0.10 | 0.02 | 0.01 | 0.01 | 11.45 | 99.39 |
| | | 17-OZV-100 | 46.06 | 0.18 | 20.86 | 3.56 | 0.16 | 0.19 | 10.79 | 0.05 | 10.85 | 0.09 | 0.06 | 0.00 | 0.01 | 0.01 | 7.16 | 99.98 |
| | | 17-OZV-13 | 46.61 | 0.96 | 14.45 | 8.01 | 5.44 | 0.17 | 8.20 | 0.70 | 6.13 | 0.70 | 0.09 | 0.03 | 0.02 | 0.02 | 8.61 | 99.43 |
| | | 17-OZV-16 | 42.20 | 1.26 | 11.48 | 7.73 | 6.74 | 0.18 | 13.92 | 0.79 | 5.11 | 1.20 | 0.14 | 0.08 | 0.03 | 0.01 | 9.43 | 99.51 |
| | | 17-OZV-20 | 54.57 | 0.27 | 10.18 | 2.46 | 0.07 | 0.25 | 16.44 | 0.05 | 8.21 | 0.11 | 0.08 | 0.02 | 0.01 | 0.02 | 7.34 | 100.04 |
| | | 17-OZV-54 | 41.00 | 0.03 | 18.74 | 2.82 | 0.41 | 0.15 | 16.32 | 0.04 | 7.15 | 0.17 | 0.12 | 0.01 | 0.01 | 0.02 | 13.01 | 99.95 |
| | | 17-OZV-56 | 41.91 | 0.01 | 19.48 | 1.77 | 0.11 | 0.13 | 16.10 | 0.05 | 7.79 | 0.14 | 0.06 | 0.00 | 0.01 | 0.00 | 11.68 | 99.21 |
| | | 17-OZV-58 | 51.19 | 0.07 | 19.31 | 3.25 | 0.56 | 0.14 | 7.69 | 0.05 | 9.87 | 0.12 | 0.29 | 0.02 | 0.02 | 0.02 | 7.08 | 99.62 |
| | | 17-OZV-63 | 47.17 | 0.67 | 15.70 | 8.98 | 4.39 | 0.15 | 5.87 | 0.05 | 10.06 | 0.08 | 0.08 | 0.03 | 0.05 | 0.00 | 6.75 | 99.99 |
| | | 17-OZV-101 | 53.80 | 0.13 | 17.51 | 4.83 | 0.12 | 0.16 | 9.29 | 0.04 | 9.72 | 0.07 | 0.05 | 0.00 | 0.01 | 0.00 | 4.33 | 100.02 |

Table 4- Trace element chemical analysis results of Özvatan syenites.

| Identification | Group | Element | Co | Ni | Cu | Zn | Ga | As | Rb | Sr | Y | Zr | Nb | Mo | Sn | Sb |
|---|---|---|---|---|---|---|---|---|---|---|---|---|---|---|---|---|
| | | Unit | ppm | ppm | ppm | ppm | ppm | ppm | ppm | ppm | ppm | ppm | ppm | ppm | ppm | ppm |
| **Fresh Foid Syenite** | | 17-OZV-11 | 18.30 | 7.70 | 3.30 | 97.00 | 20.80 | 6.40 | 179.50 | 2333.00 | 0.70 | 213.00 | 44.60 | 5.30 | 0.90 | 0.90 |
| **Altered Foid Syenite** | I | 17-OZV-04 | 12.60 | 4.40 | 0.90 | 187.50 | 69.50 | 20.30 | 297.90 | 712.90 | 0.80 | 1165.00 | 262.00 | 4.90 | 0.90 | 9.10 |
| | | 17-OZV-05 | 21.60 | 2.10 | 1.10 | 148.40 | 73.20 | 9.60 | 257.30 | 341.20 | 0.70 | 1907.00 | 243.10 | 5.70 | 2.30 | 11.40 |
| | | 17-OZV-93 | 26.20 | 1.80 | 0.90 | 93.50 | 29.20 | 4.20 | 219.10 | 1576.00 | 0.70 | 164.10 | 58.50 | 3.00 | 0.60 | 0.80 |
| | II | 17-OZV-06 | 16.50 | 42.80 | 1.10 | 292.70 | 28.80 | 2.00 | 276.80 | 2132.00 | 8.60 | 384.00 | 115.90 | 4.00 | 1.00 | 1.00 |
| | | 17-OZV-07 | 40.60 | 408.20 | 1.50 | 970.70 | 30.20 | 0.80 | 522.60 | 418.20 | 1.20 | 185.60 | 262.60 | 5.00 | 1.90 | 1.00 |
| | | 17-OZV-18 | 16.70 | 5.80 | 1.20 | 85.90 | 20.10 | 7.90 | 201.00 | 5211.00 | 0.90 | 514.00 | 69.80 | 4.40 | 1.00 | 1.00 |
| | | 17-OZV-60 | 14.60 | 6.10 | 4.90 | 77.30 | 19.40 | 5.40 | 284.00 | 2627.00 | 0.80 | 199.00 | 31.70 | 3.80 | 0.90 | 0.90 |
| | | 17-OZV-62 | 20.60 | 5.70 | 7.80 | 88.00 | 21.20 | 4.10 | 278.50 | 3014.00 | 0.90 | 167.00 | 52.30 | 3.80 | 0.90 | 0.90 |
| | | 17-OZV-85 | 27.60 | 8.20 | 2.40 | 74.80 | 24.70 | 5.60 | 229.90 | 3718.00 | 0.80 | 433.00 | 38.50 | 3.30 | 1.00 | 1.20 |
| | | 17-OZV-90 | 9.70 | 3.60 | 0.80 | 145.30 | 32.30 | 3.10 | 308.60 | 783.80 | 0.70 | 13.00 | 25.70 | 2.60 | 0.80 | 0.80 |
| | | 17-OZV-102 | 20.70 | 1.20 | 0.60 | 46.40 | 19.50 | 5.40 | 407.20 | 1711.00 | 0.90 | 153.40 | 29.60 | 3.60 | 0.90 | 1.00 |
| | | 17-OZV-103 | 13.60 | 3.00 | 2.20 | 80.10 | 19.70 | 1.80 | 453.90 | 2133.00 | 1.00 | 170.00 | 31.80 | 3.90 | 1.00 | 1.00 |
| | | 17-OZV-106 | 27.90 | 14.30 | 36.60 | 53.90 | 31.90 | 0.60 | 85.30 | 769.40 | 1.40 | 132.10 | 226.30 | 3.30 | 0.80 | 6.60 |
| | | 17-OZV-107 | 13.10 | 3.20 | 0.80 | 20.00 | 18.50 | 0.50 | 72.00 | 99.50 | 0.40 | 13.70 | 8.30 | 2.40 | 0.80 | 0.70 |
| | III | 17-OZV-57 | 13.00 | 5.40 | 1.20 | 112.70 | 17.60 | 5.20 | 189.30 | 4515.00 | 0.90 | 207.00 | 34.40 | 3.60 | 1.10 | 1.00 |
| | | 17-OZV-81 | 22.90 | 6.00 | 1.20 | 48.10 | 17.90 | 4.50 | 276.00 | 3455.00 | 0.90 | 394.00 | 37.70 | 6.50 | 0.50 | 1.10 |
| | | 17-OZV-84 | 10.80 | 5.30 | 1.00 | 58.60 | 16.40 | 4.10 | 342.70 | 2971.00 | 0.90 | 141.00 | 69.40 | 3.40 | 0.90 | 1.00 |
| | | 17-OZV-100 | 31.10 | 2.30 | 1.40 | 63.00 | 13.40 | 0.70 | 424.20 | 3019.00 | 5.20 | 309.00 | 41.30 | 4.50 | 1.10 | 1.20 |
| | | 17-OZV-13 | 43.90 | 56.00 | 7.20 | 145.80 | 17.20 | 6.20 | 278.90 | 566.20 | 19.50 | 277.20 | 21.50 | 3.80 | 1.80 | 1.00 |
| | | 17-OZV-16 | 34.90 | 86.20 | 37.60 | 104.40 | 20.80 | 2.90 | 173.80 | 1255.00 | 23.70 | 567.00 | 36.90 | 5.00 | 1.20 | 1.00 |
| | | 17-OZV-20 | 15.60 | 8.90 | 2.20 | 43.60 | 22.70 | 4.50 | 161.50 | 1792.00 | 47.70 | 639.00 | 169.50 | 4.90 | 1.10 | 1.00 |
| | | 17-OZV-54 | 23.30 | 4.80 | 1.00 | 37.00 | 16.10 | 5.60 | 373.30 | 3931.00 | 3.60 | 223.00 | 21.10 | 4.00 | 1.10 | 1.10 |
| | | 17-OZV-56 | 14.80 | 6.50 | 1.10 | 20.80 | 18.00 | 5.00 | 213.50 | 3763.00 | 0.90 | 260.00 | 29.30 | 4.00 | 1.10 | 1.10 |
| | | 17-OZV-58 | 17.70 | 10.20 | 4.70 | 87.80 | 15.50 | 5.30 | 272.50 | 3130.00 | 4.90 | 175.00 | 37.00 | 4.00 | 1.00 | 1.00 |
| | | 17-OZV-63 | 66.70 | 36.60 | 1.00 | 149.10 | 17.70 | 2.40 | 513.00 | 1205.00 | 5.80 | 79.30 | 66.10 | 3.70 | 0.90 | 0.90 |
| | | 17-OZV-101 | 12.00 | 4.00 | 0.90 | 89.90 | 15.50 | 4.30 | 371.20 | 1771.00 | 0.90 | 186.00 | 42.60 | 3.80 | 1.00 | 1.00 |

Table 4- Trace element chemical analysis results of Özvatan syenites (continued).

| Identification | Group | Element | Cs | Ba | La | Ce | Hf | Ta | W | Hg | Tl | Pb | Bi | Th | U |
|---|---|---|---|---|---|---|---|---|---|---|---|---|---|---|---|
| | | Unit | ppm | ppm | ppm | ppm | ppm | ppm | ppm | ppm | ppm | ppm | ppm | ppm | ppm |
| Fresh Foid Syenite | | 17-OZV-11 | 3.70 | 409.10 | 278.50 | 406.10 | 2.20 | 3.40 | 241.80 | 1.70 | 2.30 | 37.10 | 1.30 | 112.30 | 30.00 |
| Altered Foid Syenite | I | 17-OZV-04 | 3.50 | 125.20 | 78.80 | 100.80 | 15.30 | 11.70 | 68.90 | 1.10 | 3.70 | 117.60 | 1.60 | 42.90 | 50.50 |
| | | 17-OZV-05 | 6.40 | 69.40 | 93.20 | 115.10 | 20.40 | 13.00 | 35.20 | 0.90 | 3.20 | 71.80 | 0.80 | 101.20 | 41.80 |
| | | 17-OZV-93 | 3.10 | 106.90 | 305.90 | 405.70 | 3.20 | 6.00 | 89.20 | 0.90 | 3.70 | 33.80 | 0.50 | 85.90 | 17.70 |
| | II | 17-OZV-06 | 4.10 | 1659.00 | 75.00 | 134.70 | 6.90 | 2.70 | 86.10 | 1.40 | 1.40 | 52.40 | 1.40 | 50.40 | 52.10 |
| | | 17-OZV-07 | 12.40 | 838.20 | 177.60 | 333.90 | 3.90 | 4.50 | 21.60 | 1.20 | 1.70 | 31.70 | 0.90 | 50.80 | 33.60 |
| | | 17-OZV-18 | 6.10 | 2307.00 | 243.80 | 338.50 | 2.80 | 4.00 | 152.00 | 1.60 | 4.70 | 68.10 | 1.30 | 99.90 | 34.40 |
| | | 17-OZV-60 | 3.90 | 1527.00 | 126.30 | 214.60 | 5.10 | 4.40 | 99.80 | 1.20 | 2.50 | 25.60 | 1.40 | 115.90 | 58.60 |
| | | 17-OZV-62 | 4.10 | 2138.00 | 112.30 | 187.10 | 3.20 | 3.80 | 143.20 | 2.20 | 2.10 | 22.60 | 0.70 | 96.10 | 63.10 |
| | | 17-OZV-85 | 3.20 | 489.40 | 249.60 | 355.90 | 2.40 | 2.50 | 133.70 | 1.40 | 2.70 | 30.20 | 0.70 | 90.50 | 29.90 |
| | | 17-OZV-90 | 2.70 | 27.70 | 28.80 | 40.10 | 1.40 | 1.80 | 80.00 | 1.10 | 4.20 | 23.50 | 0.50 | 16.80 | 12.20 |
| | | 17-OZV-102 | 4.20 | 2382.00 | 80.70 | 123.70 | 2.20 | 4.20 | 157.40 | 1.40 | 3.70 | 50.60 | 0.70 | 14.00 | 8.20 |
| | | 17-OZV-103 | 5.50 | 3599.00 | 102.80 | 161.20 | 2.20 | 2.40 | 104.50 | 1.30 | 4.70 | 40.50 | 1.10 | 79.90 | 16.80 |
| | | 17-OZV-106 | 3.50 | 156.80 | 266.60 | 329.90 | 2.70 | 13.50 | 54.60 | 1.00 | 1.20 | 62.40 | 2.40 | 42.30 | 86.70 |
| | | 17-OZV-107 | 6.00 | 157.30 | 27.60 | 32.20 | 1.50 | 4.10 | 422.50 | 1.80 | 1.50 | 5.00 | 0.50 | 3.60 | 12.50 |
| | III | 17-OZV-57 | 4.30 | 2943.00 | 103.50 | 165.00 | 2.90 | 2.50 | 33.40 | 1.20 | 1.70 | 32.30 | 1.20 | 65.60 | 21.20 |
| | | 17-OZV-81 | 4.60 | 3310.00 | 107.70 | 191.40 | 6.50 | 4.10 | 60.10 | 1.50 | 3.50 | 28.30 | 0.40 | 95.80 | 21.00 |
| | | 17-OZV-84 | 4.30 | 2509.00 | 102.80 | 176.20 | 2.50 | 2.40 | 72.20 | 1.20 | 1.50 | 40.00 | 1.90 | 73.80 | 22.90 |
| | | 17-OZV-100 | 4.70 | 3262.00 | 346.40 | 465.90 | 2.70 | 5.50 | 105.50 | 1.50 | 3.50 | 39.00 | 0.90 | 82.20 | 9.70 |
| | | 17-OZV-13 | 31.40 | 1862.00 | 77.20 | 169.10 | 9.50 | 3.70 | 30.80 | 1.00 | 1.00 | 24.50 | 0.70 | 37.20 | 8.80 |
| | | 17-OZV-16 | 4.30 | 1787.00 | 99.60 | 222.70 | 9.60 | 4.20 | 24.60 | 1.10 | 0.50 | 22.90 | 0.70 | 29.80 | 58.90 |
| | | 17-OZV-20 | 4.40 | 1982.00 | 430.80 | 594.90 | 9.00 | 2.40 | 113.30 | 1.40 | 2.10 | 50.60 | 1.10 | 145.90 | 64.30 |
| | | 17-OZV-54 | 4.70 | 3860.00 | 342.20 | 568.50 | 2.80 | 2.40 | 29.40 | 1.10 | 2.20 | 28.20 | 0.90 | 142.70 | 15.40 |
| | | 17-OZV-56 | 4.40 | 4293.00 | 201.30 | 305.50 | 2.80 | 2.60 | 55.30 | 1.10 | 2.40 | 31.20 | 0.80 | 89.10 | 10.20 |
| | | 17-OZV-58 | 4.50 | 3454.00 | 273.30 | 432.00 | 2.60 | 2.80 | 148.00 | 1.60 | 2.60 | 26.20 | 1.30 | 139.30 | 44.00 |
| | | 17-OZV-63 | 20.10 | 470.10 | 35.20 | 71.40 | 3.00 | 2.70 | 95.60 | 1.50 | 3.60 | 26.70 | 0.80 | 7.40 | 49.70 |
| | | 17-OZV-101 | 4.40 | 2584.00 | 152.50 | 264.90 | 1.80 | 2.50 | 118.90 | 1.50 | 2.70 | 42.40 | 0.50 | 77.60 | 15.10 |

Table 5- Alteration indexes, calculate formulas and classification values used in this study.

| Weathering Index | Abbreviation | Formula | Fresh value | Weathered value | I degree altered rocks | I degree altered rocks | III degree altered rocks | IV degree altered rocks |
|---|---|---|---|---|---|---|---|---|
| | | | | | **This study** | | | |
| Chemical Index of Alteration | CIA | $100[(Al_2O_3/Al_2O_3+CaO+Na_2O+K_2O)]$ | ≤50 | 100 | 50-55 | 55-78 | 65-78 | >78 |
| Chemical Index of Weathering | CIW | $100[(Al_2O_3/Al_2O_3+CaO+Na_2O)]$ | ≤50 | 100 | 50-65 | 65-88 | 88-96 | >96 |
| Plagioclase Index of Alteration | PIA | $100[(Al_2O_3-K_2O/Al_2O_3+CaO+Na_2O-K_2O)]$ | ≤50 | 100 | 50-55 | 55-80 | 80-95 | >95 |
| Ishikawa Alteration Index | AI | $100[K_2O+MgO)/(K_2O+MgO+Na_2O+CaO)]$ | 20-65 | >60 | 60-65 | 65-75 | 75-87 | >87 |
| Chlorite-Carbonate-Pyrite Index | CCPI | $100[(MgO+FeO)/(MgO+FeO+Na_2O+K_2O)]$ | 15-85 | >65 | 60-65 | 65-75 | 75-85 | >85 |
| Advanced Argillic Alteration Index | AAAI | $100[(SiO_2)/(SiO_2+10*MgO+10*CaO+10*Na_2O)]$ | 20-60 | >60 | 60-65 | 65-70 | 70-80 | >80 |
| Sesquioxide Content Index | SOC | $Al_2O_3+Fe_2O_3$ | - | - | 20-25 | 25-30 | 30-40 | >40 |
| Leach factor | Lc | $SiO_2/(K_2O+Na_2O+CaO+MgO)$ | - | - | 1,5-2,5 | 2,5-5,0 | 5,0-7,5 | >7,5 |
| Residue factor | Rc | $(Al_2O_3+Fe_2O_3)/(K_2O+Na_2O+CaO+MgO)$ | - | - | 0,5-1,5 | 1,5-2,0 | 2,0-4,0 | >4,0 |
| Mobility Index | MI | $R_pR^i_w/R_wR^i_p$ | - | - | - | - | - | - |

rapidly alter compared to other minerals (Fiantis et al., 2010). For this reason, the PIA is used with the aim of finding an approach to weathering status of plagioclase minerals. The optimum weathering degree is 100 and considering fresh samples should have values lower than 50, the plagioclase minerals in syenites appear to be partly weathered (Tables 5 and 6).

The AI, CCPI and AAAI are associated with changes due to hydrothermal alteration (Ishikawa et al., 1976; Large et al., 2001; Williams and Davidson, 2004). The calculated AI values of the Özvatan foid syenites vary between 31 - 87 (Tables 5 and 6). This rate should be higher than 60 in the samples that underwent both mineralogical and chemical changes by undergoing hydrothermal alteration (Ishikawa et al., 1976). Accordingly, it was revealed that the Özvatan foid syenites were exposed to hydrothermal alteration and were heavily affected by these hydrothermal solutions. The CCPI values were 10 - 75 and AAAI values were 16-80 for the Özvatan foid syenites (Tables 5 - 6). Considering the CCPI values for altered rocks are >65 and AAAI values are >60, some samples appear to be above these limit values (Tables 5 and 6).

While calculating the SOC, major oxides such as $Al_2O_3$ and $Fe_2O_3$ with oxygen and metal ratio 3:2 are used. Due to the insoluble content of these major oxides, an increase in SOC value indicates excess leaching or intense oxidation resulting in enrichment of ferric iron due to oxidation of ferrous iron (Ng et al., 2001). The SOC values vary from 12 to 31 in weathered foid syenite samples (Tables 5 and 6). When compared with values for the fresh rock, some samples show high SOC values (Tables 5 and 6). A similar situation exists for Lc and Rc values (Tables 5 and 6). The Lc values were 1.6 - 7.4 and the Rc values were 0.5 - 4.0 on the weathered samples (Tables 5 and 6). In the light of all these assumptions, it was determined that rocks were significantly altered (Tables 5 and 6).

## 7. Discussion

Class I feldspars/feldspathoids for usage in ceramic production should have 9.00% $K_2O$ content, 3.00% $Na_2O$ amount, 10.00% total alkali ($Na_2O$ + $K_2O$) and 0.10% $Fe_2O_3$ amount (TSE 11325, 1994). When the mineral chemistry results for feldspars are examined, % $K_2O$ and total alkali content are much above the estimated limit values and iron content appears to

Table 6- Calculated alteration indexes of Özvatan syenites (abbreviations are given in Table 5).

| Identification | Group | Element | CIA | CIW | PIA | AI | CCPI | AAAI | SOC | Lc | Rc |
|---|---|---|---|---|---|---|---|---|---|---|---|
| **Fresh Foid Syenite** | | 17-OZV-11 | 50.58 | 63.08 | 50.95 | 40.16 | 11.07 | 29.38 | 25.66 | 2.49 | 1.13 |
| **Altered Foid Syenite** | **I** | 17-OZV-04 | 75.01 | 94.68 | 92.78 | 83.94 | 40.04 | 73.44 | 31.08 | 5.78 | 3.34 |
| | | 17-OZV-05 | 78.24 | 96.38 | 95.29 | 87.11 | 42.46 | 80.96 | 30.01 | 7.44 | 4.00 |
| | | 17-OZV-93 | 65.50 | 88.11 | 81.84 | 74.78 | 17.60 | 59.48 | 27.59 | 3.93 | 2.02 |
| | **II** | 17-OZV-06 | 57.54 | 76.90 | 65.18 | 65.38 | 50.68 | 35.43 | 26.32 | 2.72 | 1.52 |
| | | 17-OZV-07 | 52.10 | 77.27 | 56.01 | 82.75 | 75.18 | 23.82 | 27.15 | 1.98 | 1.24 |
| | | 17-OZV-18 | 55.26 | 71.12 | 59.50 | 50.22 | 13.02 | 37.76 | 24.22 | 3.07 | 1.33 |
| | | 17-OZV-60 | 62.37 | 83.91 | 75.43 | 68.74 | 18.26 | 51.00 | 26.62 | 3.42 | 1.76 |
| | | 17-OZV-62 | 58.21 | 79.09 | 67.39 | 63.73 | 21.20 | 47.87 | 24.19 | 3.47 | 1.52 |
| | | 17-OZV-85 | 53.96 | 70.87 | 57.58 | 52.58 | 16.69 | 37.83 | 23.79 | 2.98 | 1.28 |
| | | 17-OZV-90 | 61.74 | 88.70 | 79.95 | 79.66 | 17.69 | 63.60 | 26.38 | 3.73 | 1.76 |
| | | 17-OZV-102 | 60.52 | 88.49 | 78.60 | 80.19 | 10.23 | 63.92 | 25.01 | 3.62 | 1.61 |
| | | 17-OZV-103 | 59.71 | 85.11 | 74.08 | 74.28 | 19.62 | 56.84 | 25.98 | 3.50 | 1.64 |
| | | 17-OZV-106 | 64.12 | 73.54 | 68.98 | 39.25 | 26.00 | 42.68 | 23.92 | 4.94 | 1.88 |
| | | 17-OZV-107 | 51.91 | 65.74 | 53.30 | 45.46 | 10.95 | 54.65 | 12.65 | 6.94 | 1.12 |
| | **III** | 17-OZV-57 | 47.35 | 58.32 | 45.75 | 36.03 | 26.04 | 22.53 | 22.95 | 1.87 | 1.02 |
| | | 17-OZV-81 | 49.87 | 65.89 | 49.75 | 48.74 | 15.04 | 30.82 | 22.25 | 2.31 | 1.07 |
| | | 17-OZV-84 | 46.06 | 56.21 | 43.83 | 34.00 | 20.08 | 20.90 | 21.90 | 1.76 | 0.92 |
| | | 17-OZV-100 | 49.03 | 65.81 | 48.01 | 50.40 | 25.49 | 29.52 | 24.42 | 2.11 | 1.12 |
| | | 17-OZV-13 | 49.02 | 61.88 | 48.32 | 56.52 | 66.33 | 24.53 | 22.45 | 2.28 | 1.10 |
| | | 17-OZV-16 | 36.68 | 43.83 | 30.22 | 44.62 | 71.04 | 16.44 | 19.21 | 1.59 | 0.72 |
| | | 17-OZV-20 | 29.19 | 38.18 | 10.68 | 33.43 | 23.44 | 24.79 | 12.65 | 2.20 | 0.51 |
| | | 17-OZV-54 | 44.35 | 53.38 | 41.46 | 31.60 | 31.00 | 19.65 | 21.56 | 1.71 | 0.90 |
| | | 17-OZV-56 | 44.86 | 54.67 | 41.98 | 32.85 | 19.38 | 20.49 | 21.25 | 1.74 | 0.88 |
| | | 17-OZV-58 | 52.31 | 71.40 | 54.96 | 57.42 | 27.73 | 38.17 | 22.55 | 2.82 | 1.24 |
| | | 17-OZV-63 | 49.57 | 72.64 | 48.82 | 70.96 | 56.97 | 31.40 | 24.68 | 2.32 | 1.21 |
| | | 17-OZV-101 | 47.91 | 65.25 | 45.53 | 51.33 | 33.63 | 36.29 | 22.34 | 2.81 | 1.17 |

be far below the desired limit value (Table 3). When mineral chemistry is investigated, the feldspathic minerals in the region may have class I feldspar features and can be said to be very appropriate raw materials for the ceramic industry (Tables 1 and 2). The $K_2O$, $Na_2O$ and total alkali contents of nepheline minerals within the rock are much above the estimated values and appear to be higher quality raw materials compared to feldspar minerals (Tables 1 and 2). Alkali element contents determine and affect the usage area of feldspathic (feldspar and feldspathoid) raw materials in the glass and ceramic industries (Lewicka, 2010). For example, feldspathic raw materials to be used for glass and ceramic tile production need to have $Na_2O$ content higher than 7%, for use in the production of white ceramic goods, $K_2O$ amount should be larger than 10%, while colourizing oxides like $Fe_2O_3$ and $TiO_2$ should have low values such as 0.15% and 0.05%, respectively (Lewicka, 2010). Accordingly, it is understood from the analysis results that the nepheline minerals in the Özvatan foid syenites are appropriate for both glass and ceramic tile production and white ceramic goods production. However, it is necessary to investigate secondary formations like sericite, kaolinite, and illite within these rocks.

On the MFW diagram, M represents the mafic source, F is the felsic source and W is the altered/

weathered products (Ohta and Arai, 2007). When the plot of the Özvatan foid syenite samples on the MFW diagram is examined, it appears they plot outside the area for fresh magmatic rock (Figure 5a) (Ohta and Arai, 2007). The majority of samples plot in the Fe-saponite and nontronite (smectite) fields on the MFW diagram with some close to the montmorillonite field and some close to the illite field (Figure 5b). There may be a transformation of mafic minerals within the rock (amphibole, pyroxene and biotite) into Fe-

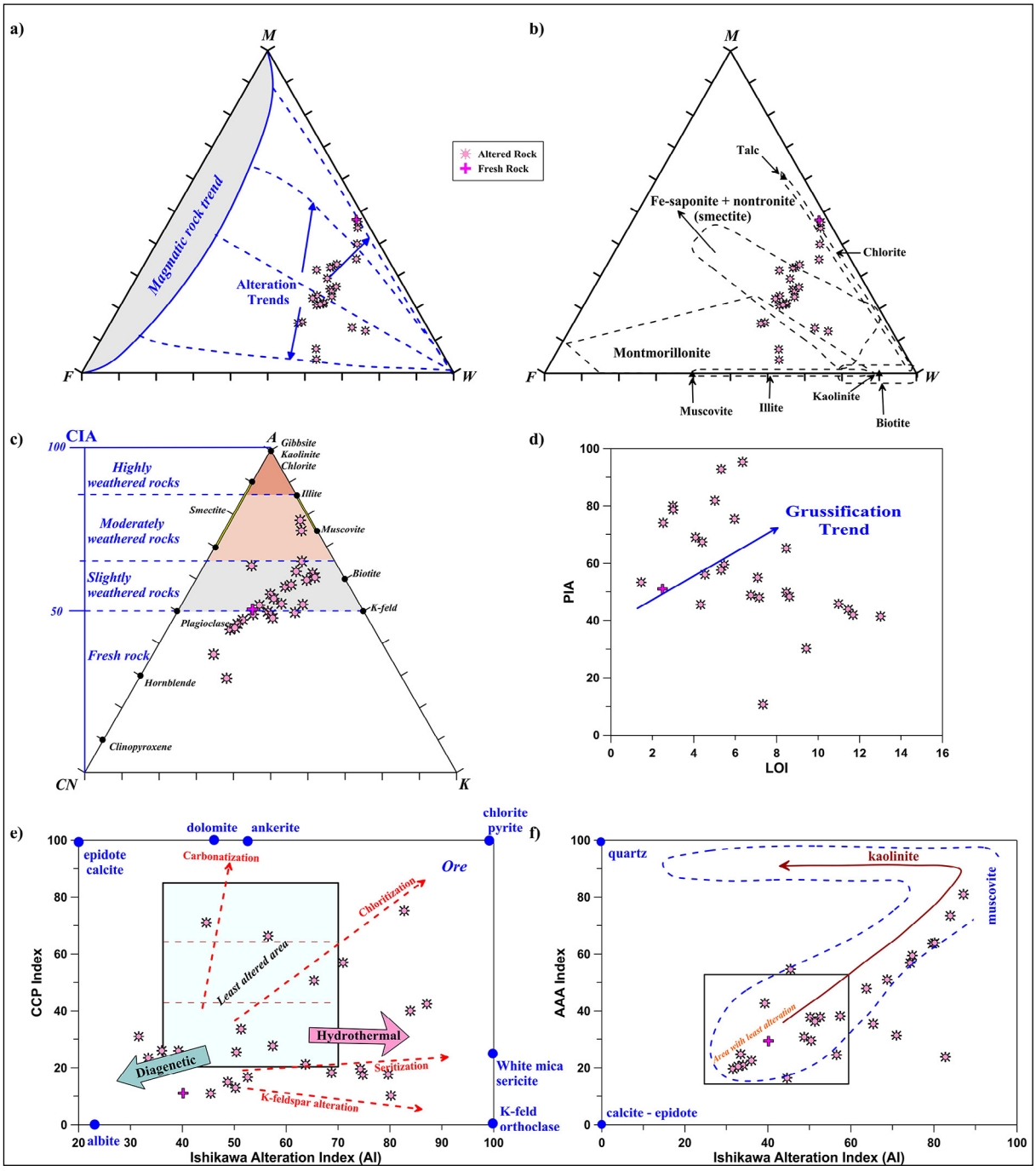


Figure 5- Özvatan foid syenites; a), b) plots on MFW pyramid diagram (Ohta and Arai, 2007), c) plot on ACNK diagram and classification according to CIA (Nesbitt and Young, 1982), d) variation diagram for PIA against LOI values (Fedo et al., 1995), e) plot on variation diagram for CCPI against AI (Large et al., 2001; Mathieu, 2018), f) plot on variation diagram of AAAI against AI (Williams and Davidson, 2004).

saponite and nontronite (smectite). Sericite and illite transformation of K-feldspar minerals may be present. Due to weathering of minerals within the rock, changes occur in the colour of the rock. While light dirty white and greyish colours in the rock are mostly due to clay minerals like kaolinite formed as a result of weathering in the feldspathic minerals, pinkish colours can be associated with iron hydroxide (limonite) minerals.

The $CaO + Na_2O - Al_2O_3 - K_2O$ (CNAK) triangle classification diagram was used with chemical components to determine the degree of weathering and alteration of foid syenite samples in the study area (Figure 5c). On the CNAK diagram, the Özvatan foid syenites plot in three different areas of unweathered (fresh rock), slightly weathered (partly altered rock) and moderately weathered (moderately altered rock) (Figure 5c). The correlation between the increase in LOI values and PIA for the rocks displays regular variation (Figure 5d).

In order to reveal whether the alteration is due to the effect of surface conditions or the effect of deep solutions, the AI versus the CCPI was drawn (Large et al., 2001). It was observed that the Özvatan foid syenites were altered mostly by the effect of hydrothermal solutions (Figure 5e). The samples degraded with the effect of hydrothermal alteration show trends toward orthoclase and sericite points on the diagram indicating sericitization of K-feldspars (Figure 5e). Against AI, it can be stated in the AAAI variation diagram that the degree of alteration of the rocks is variable and has a trend toward muscovite formations to argillisation (Figure 5f) (Williams and Davidson 2004).

According to the CNAK diagram, syenites can be divided into three groups and the degrees of alteration for these groups were determined and interpretations were made. Accordingly, the stages/degrees I, II and III were used for unweathered (fresh rock), slightly weathered (rock with a mild degree of alteration) and moderately weathered (rocks with a moderate degree of alteration), respectively (for definitions of weathering stages/degrees see GCO 1988). Moving from the degree I to III, alteration and weathering increase. The CIA, CIW, PIA, AI, AAAI, SOC, Lc and Rc values increase with the alteration from the degree I to III, while the LOI values reduce and the CCPI values display a similar relationship (Figure 6). With

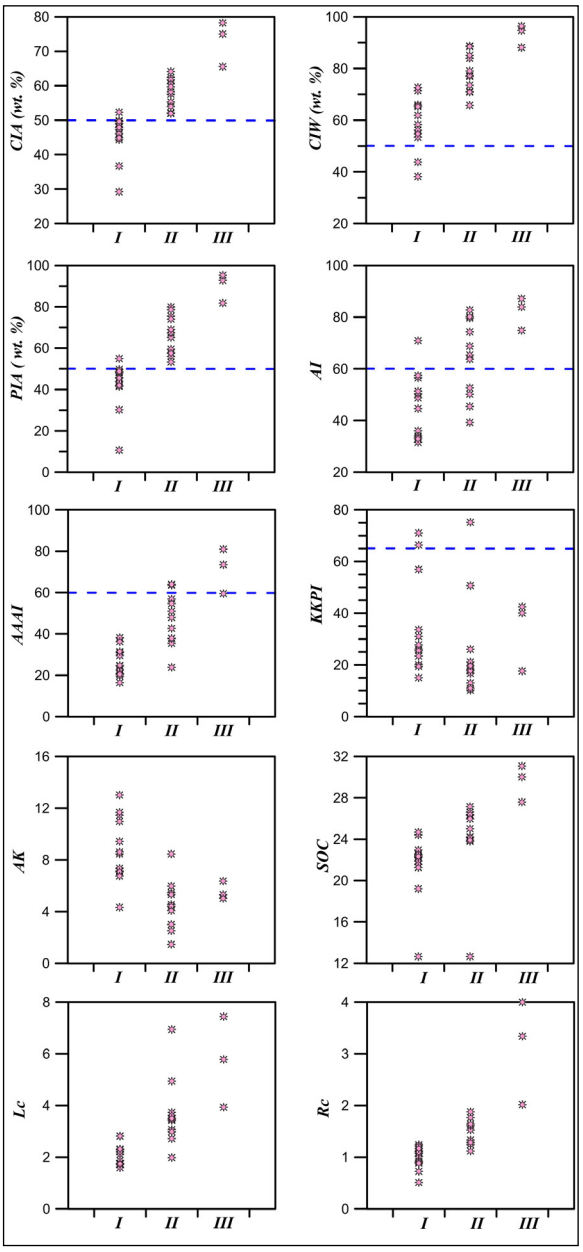


Figure 6- Variation diagrams for degree of alteration of altered Özvatan foid syenites against some alteration indexes (CIA: chemical index of alteration, CIW: chemical index of weathering, PIA: plagioclase index of alteration, AI: Ishikawa alteration index, AAAI: advanced argillic alteration index, CCPI: chlorite-carbonate-pyrite index, LOI: loss on ignition, SOC: sesquioxide content index, $L_C$: leach factor, $R_C$: residue factor).

weathering, the proportions of sericite, kaolinite and illite are determined with XRD increase which allows these alteration degrees to be determined.

In order to better understand weathering processes and to find an approach to element mobility, the MI was calculated (Ng et al., 2000, 2001).

$R_pR^i_w/R_wR^i_p$ (1)

In the equation, $R_p$ is the percentage of stable components in major (fresh) rock, $R^i_p$ is the percentage of unstable components (i) in the major (fresh) rock, Rw is the percentage of stable components in the altered rock and $R^i_w$ is the percentage of unstable components in the altered rock (Ng et al., 2000, 2001).

In the calculations, MgO is taken as a stable component, and the mobility of $Na_2O$, $K_2O$, $Al_2O_3$, $SiO_2$, CaO, $Fe_2O_3$ and LOI values are investigated. For each alteration degree, the mean values for MI, major oxides and LOI were taken and the diagram of MI against alteration degree was drawn (Figure 7). As the amount of the component increases, the gain or loss proportions ($X_{gp}$) are positive and MI>1; contrary to this as the amount of component reduces the $X_{gp}$ value is negative and MI<1 (Ng et al., 2001). According to the diagram of MI against alteration (weathering) degree, $Na_2O$, $K_2O$, $Al_2O_3$, $SiO_2$, CaO, $Fe_2O_3$ and LOI had MI values lower than 1 (Figure 7). For the Özvatan foid syenites, the $K_2O$, $Al_2O_3$, $SiO_2$ and $Fe_2O_3$ amounts show a similar relationship during weathering processes, with a severe reduction from fresh rock to degree I alteration and then a slight reduction moving toward degree III alteration (Figure 7). This situation can be associated with the formation of kaolin. The increase in $Fe_2O_3$ amounts moving from degree II to degree III is related to the oxidation of FeO and transformation to $Fe_2O_3$ during alteration. The CaO amount shows a clear reduction moving from degree I to degree III alteration (Figure 7).On the other hand, LOI values reduce as the degree of alteration increases. While the opposite situation is expected to be observed in felsic intrusive rocks, this situation in magmatic rocks including foid may be associated with the presence of volatile components like excess halogen elements within feldspathoid minerals. The amount of $Na_2O$ shows an irregular correlation from the fresh rock to the altered rock. The amount of $K_2O$, $Al_2O_3$, and $SiO_2$ reduces with the alteration of feldspar minerals. This reduction must have occured mainly by the separation of illite and $[K_{0.65}Al_{2.0}(Al_{0.65}Si_{3.35}O_{10})(OH)_2]$ and kaolinite $[Al_2(Si_2O_5)(OH)_4]$ from the feldspars.

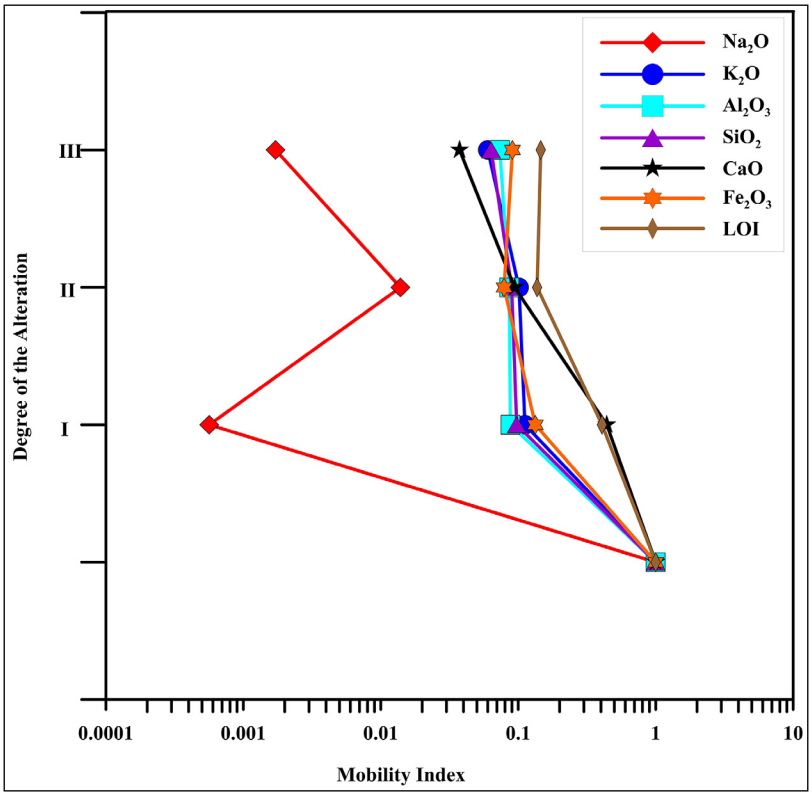


Figure 7- Diagram showing variation in mobility index (MI) values for major oxide elements and loss on ignition values for altered Özvatan foid syenites linked to degree of alteration (Ng et al., 2001).

Feldspathic minerals are chosen in the ceramic production due to high Na and K content. The raw material used in all ceramic operations is chosen by direct examination of chemical composition. For this reason, the quality of the raw material is determined by looking at the total Na and K content rather than mineralogy of the analysed material. Thus, all minerals containing K within the rock contribute to this calculation. Muscovite and sericite minerals which are formed as a result of the alteration, are poor in iron and rich in K so they contribute to this proportion and increase the K content ratio of the raw material. However, these minerals negatively affect the impurity of feldspathic minerals. For this reason, ceramic raw material processing stages should be planned by determining the mineralogical, alteration type and rates of the raw material in detail. Mathieu (2018), in his study for the determination of hydrothermal alteration, stated that Ca and Na reduced with sericitization whereas K increased or decreased (Equations 2 and 3). Due to the effect of this fluid with low temperature, sericite mineral formation is more common than muscovite. Sericite and muscovite are found in such igneous rocks as weathering products. Both muscovite and sericite contain K so they cause an increase in the K content in whole rock analyses as well as feldspathic minerals.

$$3KAlSi_3O_8 \text{ (Orthoclase)} + 2H^+ \text{ (Fluid)} <==> KAl_3Si_3O10(OH)_2 \text{ (Sericite)} + 2K^+ \text{ (Fluid)} + 6SiO_2 \text{ (Quartz)} \quad (2)$$

$$4(Na,K)AlSi_3O_8 \text{ (Alkali Feldspar)} + 2H^+ \text{ (Fluid)} <==> NaAlSi_3O8 \text{ (Albite)} + KAl_3Si_3O10(OH)_2 \text{ (Sericite)} + 6SiO_2 \text{ (Quartz)} + 2Na^+ \text{ (Fluid)} \quad (3)$$

As shown in the equations, K elements released from feldspathic minerals as a result of alteration cause sericite and additionally kaolinite formation according to XRD results. Some of the released Na becomes albite while some remains free and is removed and may form evaporate minerals (halite and globerite) in evaporitic environments. For this reason, the abundance of ions in free form occurring with alteration of feldspathic minerals and physicochemical conditions cause formation of appropriate evaporitic rocks. This situation provides an important contribution to form Tuzla lake located in the study area.

In the diagram drawn by using $K_2O$ and $Na_2O$ in order to approach the Özvatan foid syenites as raw materials, it is seen that the alkali oxide values are desired for the raw materials (Figure 8).

Feldspathic minerals are used as a melter in the ceramic industry and lower the melting point when compared to other ceramic raw materials (Gürsoy, 1999). Due to strong fluxing features, Na-rich feldspars or Na-rich feldspathoid minerals are more preferred in modern rapid-firing technologies and glazes (Gürsoy, 1999; Levin et al., 1969; Ehlers, 1972; Lewicka, 2010). Considering the results of geochemical analysis, the amount of $Na_2O$ severely reduces with alteration (Table 3). It has been determined that the lack of observation of fresh mineral or mineralization linked to Na values in the region indicates it may have leached and been removed from the environment. With the reduction of the Na content of the rock or minerals, it will increase the melting temperature of raw material during ceramic production, in this case, it will cause slow melting and reduce work efficiency and increase the amounts of fuel (Harben and Kuzvart, 1997; Abouzeid and Negm, 2014). Feldspars with high Na amount have lower viscosity and glazing temperature compared to feldspars with high potassium (K) and are more predisposed to shrinkage during firing (Ryan, 1978; Köprülü, 1997; Tayçu, 2009). Therefore, in the glazing phase, products with Na content are more preferred compared to minerals containing K.

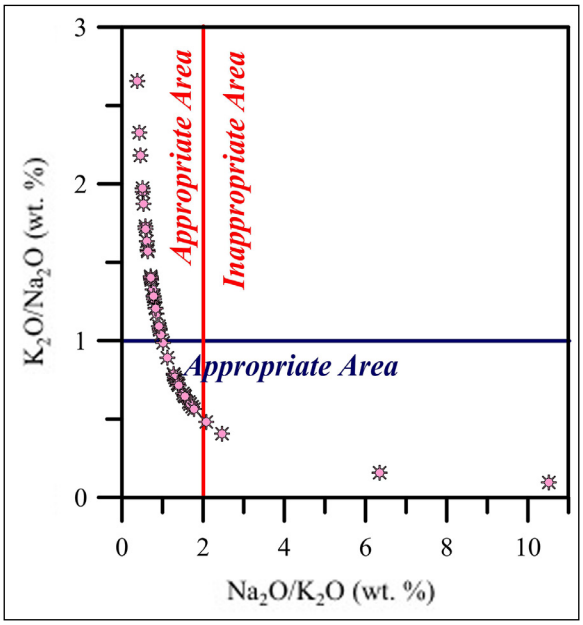


Figure 8- Variation diagram for $Na_2O/K_2O$ against $K_2O/Na_2O$ for altered Özvatan foid syenites (wt. : weight, Deniz and Kadıoğlu, 2018).

In this context, it has been revealed that the fresh samples of Özvatan syenites were determined to enter the more useful rock group for the glazing stage, while altered samples are more useful for the major ceramic paste. With the use of K-rich feldspars a melt with high viscosity will be formed and its resistance against deformations (cracking, etc.) that may occur during firing will increase. Since the plagioclase minerals found at very low rates in the rock have very close softening and melting degrees, and may cause deformation during firing, it will be more appropriate to use them in glaze production. Additionally, crushing and grinding stages in processing before they are offered for sale will facilitate the use of sections of the Özvatan foid syenite with excess arenisation as raw material. This is because the feldspar to be used in ceramic paste must be grinded very well to increase the melting ability and to ensure better mixing with other components (Gürsoy, 1999). For this reason, reducing the processing stages of the rock that has weathered in a certain grain size will save both time and money.

## 8. Results

Due to the distinctive diaclase structure and highly fractured in terms of structural elements in the region, it was determined that the Özvatan foid syenite were altered at different rates. According to the field and laboratory results obtained, as the degree of alteration of the Özvatan foid syenites increased, the transformation rates of feldspathic minerals to sericite and kaolin minerals increased. According to the whole-rock geochemistry and mineral chemistry results, the percentage of $Na_2O$ in the rock has reduced significantly as a result of weathering processes. This situation occurred in association with the loss of alkali components from feldspar and feldspathoid minerals especially as a result of weathering and alteration due to atmospheric effects (air), and surface waters and hydrothermal solution and their transformation into sericite and kaolinite minerals. Mineralogical and geochemical data shows that the alteration of the rock due to both the effect of weathering and hydrothermal conditions is clearly observed. The K and Na (alkali) elements emerging with weathering of the Özvatan syenites appear to provide an important contribution to new mineral formations (kaolinite and sericite) and evaporitic mineralisation by transported elements (Na).

The excess diaclase structures in the rock provide convenience for processing, while they affect the chemical composition of feldspar and feldspathoid minerals in the rock. The variation in element ratios in the rock and minerals with alteration will play an effective role in determining the area of use for feldspar and feldspathoid minerals. Minerals such as sericite and muscovite may cause impurities by forming small inclusions in feldspathic minerals which are insidious contaminants in raw materials. It is necessary to remove these minerals from the product with the flotation method. The excess presence of iron or oxide minerals in the form of inclusions may provide an advantage for the flotation (metal oxide flotation) and magnetic separator stages. Due to the release of very small size color-giving impurities contained, the Özvatan altered foid syenite does not represent high-quality ceramic raw material in terms of both yield and concentration quality.

## Acknowledgements

This study was partly supported within the scope of Ankara University Scientific Research Projects (BAP) number 17B0443003 and Ministry of Development project 2012K120440. We offer our thanks to the esteemed anonymous reviewers who contributed to the manuscript with their valued opinions and recommendations.

## References

Abouzeid, A. Z. M., Negm, A. T. A. 2014. Characterization and beneficiation of an Egyptian nepheline syenite ore. International Journal of Mineralogy 2014, 1-9.

Akçe, M., Kadıoğlu, Y. K. 2020. S - tipi granitlerin seramik sanayisinde kullanılması: Sarıhacılı, Yozgat. 5. International Conference on Material Science and Technology (IMSTEC 2020), 16 - 18 October 2020, Nevşehir, Turkey, 214-220.

Başıbüyük, Z., Ekincioğlu, G. 2019. Investigation of the usability of pseudoleucites in Central Anatolia alkali syenites as ındustrial raw materials. Mineralogy - Significance and Applications, http://dx.doi.org/10.5772/intechopen.89588.

Bayraktar, İ., Ersayın, E., Gülsoy, Ö. Y. 1997. Upgrading titanium bearing Na-feldspar by flotation using sulphonates, succinamate and soaps of vegetable oils. Minerals Engineering I(12), 1363-1374.

Bayraktar, İ., Ersayın, E., Gülsoy, Ö. Y., Ekmekçi, Z., Can, M. 1999. Temel seramik ve cam hammaddelerimizdeki (feldispat, kuvars ve kaolin) kalite sorunlan ve çözüm önerileri. 3. Endüstriyel Hammaddeler Sempozyumu, 14-15 Ekim 1999, İzmir, Türkiye, 22-33.

Bozkurt, E., Mittwede, S. K. 2001. Introduction to the geology of Turkey - a synthesis. International Geology Review 43, 578-594.

Deniz, K., Kadıoğlu, Y. K. 2011. Alkalin magmatik kayaçların ayrışmasıyla oluşan kil mineralleri: Buzlukdağı siyenitoyidi, Orta Anadolu, Türkiye. Prof. Dr. Nuri MUNSUZ Ulusal Toprak ve Su Sempozyumu, 25 - 27 Mayıs 2011, Ankara, Türkiye, 13-17.

Deniz, K., Kadıoğlu, Y. K. 2018. Nefelin siyenitlerin seramik sanayiinde kullanılma potansiyeli: Buzlukdağ örneği. Pamukkale Üniversitesi, Mühendislik Bilimleri Dergisi 24(6), 1209-1219.

Deniz, K., Kadıoğlu, Y. K. 2019. Investigation of feldspar raw material potential of alkali feldspar granites and alkali feldspar syenites within central Anatolia. Bulletin of the Mineral Research and Exploration 158, 265-289.

Deniz, K., Kadıoğlu, Y. K., Koralay, T., Güllü, B. 2017. Type and formation of cancrinite within the alkaline ıntrusive rocks: Özvatan (Kayseri) - Turkey. Goldschmidt Symposium 2017, 13 - 18 Ağustos 2017, Paris, France.

Deniz, K., Kadıoğlu, Y. K., Koralay, T., Gullu, B. 2018*a*. Petrology of the Özvatan foid bearing syenites, Kayseri, central Anatolia, Turkey. The 36th National and the 3rd International Geosciences Congress, 25 - 27 February 2018, Tehran, Iran.

Deniz, K., Kadıoğlu, Y. K., Gullu, B. 2018*b*. Amarat bazaltlarının petrolojisi (Kayseri - Türkiye). Uluslararası Katılımlı 8. Jeokimya Sempozyumu, 2 - 6 Mayıs 2018, Antalya, Türkiye, 51-52.

Ehlers, E. G. 1972. The Interpretation of Geological Phase Diagrams. W.H. Freeman and Co, San Francisco, 280.

Erdinç, A. Z. 2007. K-feldispat / kuvars ayrımında optimum flotasyon koşullarının belirlenmesi. Yüksek Lisans Tezi, Dokuz Eylül Üniversitesi, Maden Mühendisliği Bölümü, 119, İzmir (unpublished).

Fedo, C. M., Nesbitt, H. W., Young, G. M. 1995. Unraveling the effects of potassium metasomatism in sedimentary rocks and paleosols, with implications for paleoweathering conditions and provenance. Geology 23, 921-924.

Fiantis, D., Nelson, M., Shamshuddin, J., Goh, T. B., Van Ranst , E. 2010. Determination of the geochemical weathering indices and trace elements content of new volcanic ash deposits from Mt. Talang (West Sumat ra) Indonesia. Eurasian Soil Science 43(13), 1477-1485.

Geotechnical Control Office. 1988. Guide to rock and soil descriptions (GEOGUIDE 3). Geotechnical Control Office, Civil Engineering Services Department, Hong Kong.

Gürsoy, Y. H. 1999. Sarıkaya yöresi altere granitlerinden feldspatın kazanımı. Yüksek Lisans Tezi, Osmangazi Üniversitesi, 112, Eskişehir (unpublished).

Harben, P. W., Kuzvart, M. 1997. Industrial Minerals A Global Geology. Londyn, Industrial Minerals Information Ltd., 462.

Harnois, L., Moore, J. M. 1988. Geochemistry and origin of the ore chimney formation: a transported paleoregolith in the Grenville Province of Southeastern Ontario, Canada. Chemical Geology 69(3-4), 267-289.

İrfan, T. Y. 1996. Mineralogy, fabric properties and classification of weathered granites in Hong Kong. Quarterly Journal of Engineering Geology 29, 5-35.

Ishikawa, Y., Sawaguchi, T., Iwaya, S., Hariuchi, M. 1976. Delineat ion of prospect ing targets for Kuroko deposits based on modes of volcanism underlying dacite and alteration halos. Mining Geology 26, 105-117.

Kademli, M. 2004. Feldispat cevherinden spiral zenginleştirici ile mikanın uzaklaştırılması. Yüksek Lisans Tezi, Hacettepe Üniversitesi, Fen Bilimleri Enstitüsü, Maden Mühendisliği Anabilim Dalı, 100, Ankara (unpublished).

Kadıoğlu, Y. K., Güleç, N. 1996. Mafic microgranular enclaves and ınteraction between felsic and mafic magmas in the Ağaçören İntrusive suite: evidence from petrographic features and mineral chemistry. International Geology Review 38, 854-867.

Kadıoğlu, Y. K., Güleç, N. 1999. Types and genesis of the enclaves in central Anatolian granitoids. Geological Journal 34, 243-256.

Kadıoğlu, Y. K., Dilek, Y., Foland, K. A. 2006. Slab break-off and syncollisional origin of the Late Cretaceous magmatism in the Central Anatolian crystalline complex. Geological Society of America 409, 381-415.

Karakaya, M. Ç., Karakaya, N. 2001*a*. Kaolin occurrences in the Erenler Mountain Volcanics, Southwest Konya Province, Turkey. International Geology Review 43, 711-721.

Karakaya, M. Ç., Karakaya, N. 2001*b*. Hydrothermal alteration of the Saplica volcanic rocks, Şebinkarahisar, Turkey. International Geology Review 43, 953-962.

Karakaya, M. Ç., Karakaya, N., Küpeli, Ş., Yavuz, F. 2012. Mineralogy and geochemical behavior of trace elements of hydrothermal alteration types in the volcanogenic massive sulfide deposits, NE Turkey. Ore Geology Reviews 48, 197-224.

Köprülü Tunç, F. 1997. Sintering kinetics of feldspar by the rising temperature technique. Doktora Tezi, Ege Üniversitesi, 46, İzmir (unpublished).

Kraeff, A., Pasquare, G. 1966. Kayseri ilinin kuzey kesiminde Çukurköy'de nefelin ihtiva eden indifai kayaçlar. Bulletin of the Mineral Research and Exploration, 121-125.

Large, R. R., Gemmell, J. B., Paulick, H., Huston, D. L. 2001. The alteration box plot: a simple approach to understanding the relationship between alterat ion mineralogy and lithogeochemist ry associated with volcanic - hosted massive sulfide deposits. Economic Geology 96(5), 957-971.

Lewicka, E. 2010. Conditions of the feldspathic raw materials supply from domestic and foreign sources in Poland. Gospodarka Surowcami Mineralnymi 26(4), 5-18.

Levin, E. M., Robbins, C. R., McMurdie, H. F. 1969. Phase Diagrams for Ceramists. The American Ceramic Society, Columbus, Ohio, USA, 601.

Li, W. D.,Wang, W. B., Cheng, Z. F., Zhou, H. M. 1995. Geochemistry of Lateritization Process and the Possibility of Forming Lateritic Type Gold Deposits in Southern China. Geological Press (In Chinese with English abstract).

Marinov, M., Valchev, A., Nishkov, M., Grigorova, I. 2010. Feldspar concentrates from albite granites. 2nd International Symposium on the Processing of Industrial Minerals, İstanbul, Turkey.

Mathieu, L. 2016. Quantifying hydrothermal alteration with normative minerals and other chemical tools at the Beattie syenite, Abitibi greenstone belt, Canada. Geochemistry Exploration Environment. Analysis 16, 233-244.

Mathieu, L. 2018. Quantifying hydrothermal alteration: a review of methods. Geosciences 8(245), doi:10.3390/geosciences8070245.

Negm, A. T., Abouzeid, A. Z., Boulos, T., Ahmed, H. 2000. Nepheline syenite processing for glass and ceramic ındustries. Physicochemical Problems of Mineral Processing 34, 5-16.

Nesbitt, H. W., Young, G. M. 1982. Early Proterozoic climates and plate motions inferred from major element chemistry of Lutites. Nature 299.

Ng, C. W. W., Guan, P., Tang, W. H. 2000. Weathering mechanisms and indices of volcanic rocks in Hong Kong. GeoEng 2000 International Congress, Melbourne, Australia, 2, 524.

Ng, C. W. W., Guan, P., Shang, Y. J. 2001. Weathering mechanisms and indices of the igneous rocks of Hong Kong, Quarterly. Journal of Engineering Geology and Hydrogeology 34, 133-151.

Ohta, Y., Arai, H. 2007. Statistical empirical index of chemical weathering in igneous rocks: a new tool for evaluating the degree of weathering. Chemical Geology 240, 280-297.

Ötekaya, B., Bilir, K., Gürsoy, H., Uçbaş, Y., Bozkurt, R., Çiftçi, M. 2020. Recovery of feldspar from altered granites. 8th International Mineral Processing Symposium, Antalya, Turkey.

Özaksoy, V., Gökten, E. 1996. Özvatan - Felahiye (Kayseri) dolayının stratigrafisi ve tektoniği. Türkiye Jeoloji Bülteni 39(1), 31-42.

Özkan, M. H. 1987. Hayriye (Kayseri) Nefelin-siyenit intrüzyonlarının petrografik ve jeokimyasal incelemesi. Yüksek Lisans Tezi, Ankara Üniversitesi, Fen Bilimleri Enstitüsü, 118, Ankara (unpublished).

Parker, A. 1970. An index of weathering for silicate rocks. Geological Magazine 107(6), 501-504.

Piché, M., Jébrak, M. 2004. Normative minerals and alteration indices developed for mineral exploration. Journal of Geochemical Exploration 82, 59-77.

Roaldset, E. 1972. Mineralogy and geochemistry of Quaternary clays in the Numedal Area, Southern Norway. Norsk Geologisk Tidsskrift 52, 335-369.

Ruxton, B. P. 1968. Measures of the degree of chemical weathering of rocks. Journal of Geology 76, 518-527.

Ryan, W. 1978. Properties of Ceramic Raw Materials. 2nd Edition, Pergamon Press, London, 123.

Souri, T., Watanabe, M., Sakagami, K. 2006. Contribution of Parker and product indexes to evaluate weathering condition of yellow brown forest soils in Japan. Geoderma 130, 346-355.

Tayçu, A. 2009. Seramik sağlık gereçleri pişirim koşullarının incelenmesi. Yüksek Lisans Tezi, Anadolu Üniversitesi, 194, Eskişehir (unpublished).

TS11325. 1994. Feldispat seramik sanayinde kullanılan Türk standartları, Türk Standartları Enstitüsü, Ankara.

Ulusoy, E., Kadıoğlu, Y. K. 2021. Petrography and geochemical decomposition parameters of crystalline rocks; Demirköy intrusive body (DIB), NW Turkey. Bulletin of the Mineral Research and Exploration 165, 253-365.

Williams, N. C., Davidson, G. J. 2004. Possible submarine advanced argillic alterat ion at the Basin Lake prospect, Western Tasmania, Australia. Economic Geology 99(5), 987-1002.

Yazar, E. 2018. Alteration mineralogy, mineral chemistry and stable isotope geochemistry of the Eocene pillow lavas from the Trabzon area, NE Turkey. Journal of African Earth Sciences 138, 149-166.

Bulletin of the Mineral Research and Exploration

http://bulletin.mta.gov.tr

# Imaging the tectonic components under the Eastern Mediterranean and Black Sea with gravity (satellite) data

Ceyhan Ertan TOKER[a]* and Emin U. ULUGERGERLİ[b]

[a]*General Directorate of Mineral Research and Exploration, Department of Marine Research, Ankara, Turkey*
[b]*Çanakkale Onsekiz Mart University, Faculty of Engineering, Terzioğlu Campus, Çanakkale, Turkey*

*Short Note*

Keywords:
Gravity, East Mediterranean, Cyprus Arc, Antalya Arc.

*Received Date: 03.03.2021*
*Accepted Date: 28.07.2021*

**ABSTRACT**

Tectonic structures in the Black Sea and the Levantine Sea were mapped using satellite gravity data. The relationship between Antalya and Cyprus arcs is revealed by the deformation traces of the arc formation. The Cyprus arc which over the slice that disappears from the South of the Anaximander seamounts to the Northeast, can traceable at the western end of the Antalya Bay. The distinction of western and eastern basins in the Black Sea is also mapped. Due to the low spatial resolution, additional studies with higher resolution are required.

## 1. Introduction

Data processing methods applied to satellite gravity data are similar to those applied to data collected on land. The large area coverage of the satellite data and the resolution obtained due to the measurement ranges offer the opportunity to examine large-scale tectonic structures. Unlike satellite data, undesirable information that appears as surface effect in data collected on land and added to the measured values needs to be filtered out. Satellite gravity data are less noisy and more stable compared to data collected on land. Therefore, we choose satellite gravity data for this study because it is more suitable for imaging long-wavelength structures with the Upward Continuation (UC) process, in which the signature of the deep structures is increased. In addition to the vertical derivative operator and the UC process, the boundaries of large wavelength structures become clear with the help of the depth transform and it is seen that the boundary relations become suitable for interpretation. (e.g., Pınar et al., 1994).

In this study, unlike previous studies, it was shown that the tectonic elements can be mapped at regional scale with the help of continuation-filter operators. The findings were interpreted in terms of economic value.

## 2. Data and Method

The gravity data used in this stud are the gridded data obtained from the satellite data with a point spacing of approximately 7 km (Figure 1). With the UC method, a 2-dimensional (2D) UC map was created in accordance with a height of $0.215^0$. This value is equivalent to height at approximately 0.350 km. At this interval, large structural elements with high detectability can be observed. As an example, fractured and interlaced structures located between Aegean and Cyprus arcs can be observed as regional structural elements (Figure 2). However, in the north of the Central Mediterranean ridge, south of the Anaksimander sea mountains, at the western end of

Citation Info: Toker, C. E., Ulugelgerli, E. 2021. Imaging the tectonic components under the Eastern Mediterranean and Black Sea with gravity (satellite) data. Bulletin of the Mineral Research and Exploration 166, 189-194. https://doi.org/10.19111/bulletinofmre.975929

**Corresponding author: Ceyhan Ertan TOKER, toker.ertan@gmail.com*

the Cyprus arc; there is a strike at the deeper part of the Antalya bay.

With the crustal depth transform relation approximate Moho depth (Wollard and Strange, 1962)

$$\text{Depth} = 40.5 - [32.5 * \text{atan}(G + \frac{75}{275})] \quad (1)$$

where G is gravity value.

In the study, the first vertical derivative of the gravity data was calculated, then UC was applied. Then, depth transformation was performed using Wollard and Strange (1962)'s depth transformation. 3D visualization of tectonic and structural elements at a depth range of approximately 14-42 km given in Figure 3.

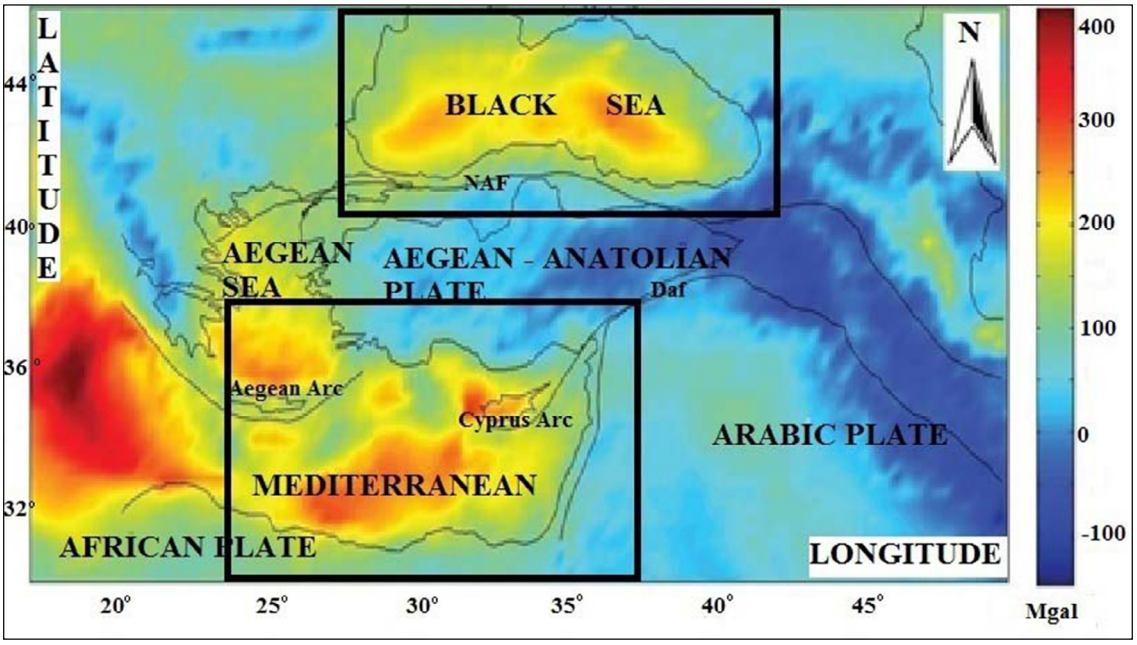


Figure 1- Bouguer gravity data and study areas. (http://bgi.obs-mip.fr/)

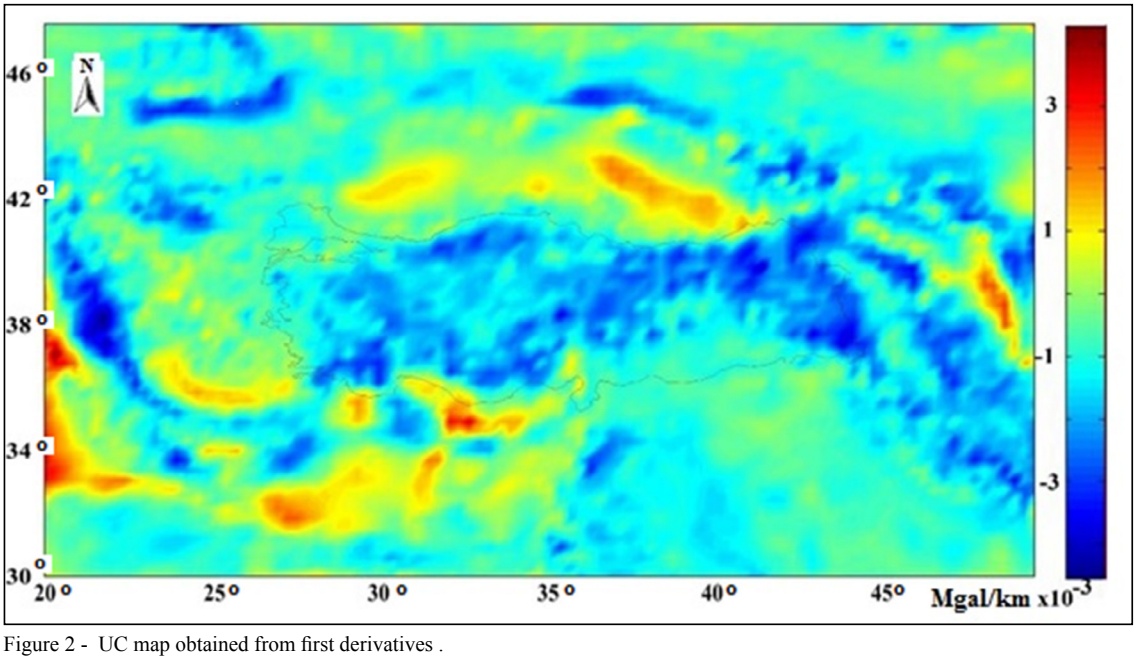


Figure 2 - UC map obtained from first derivatives .

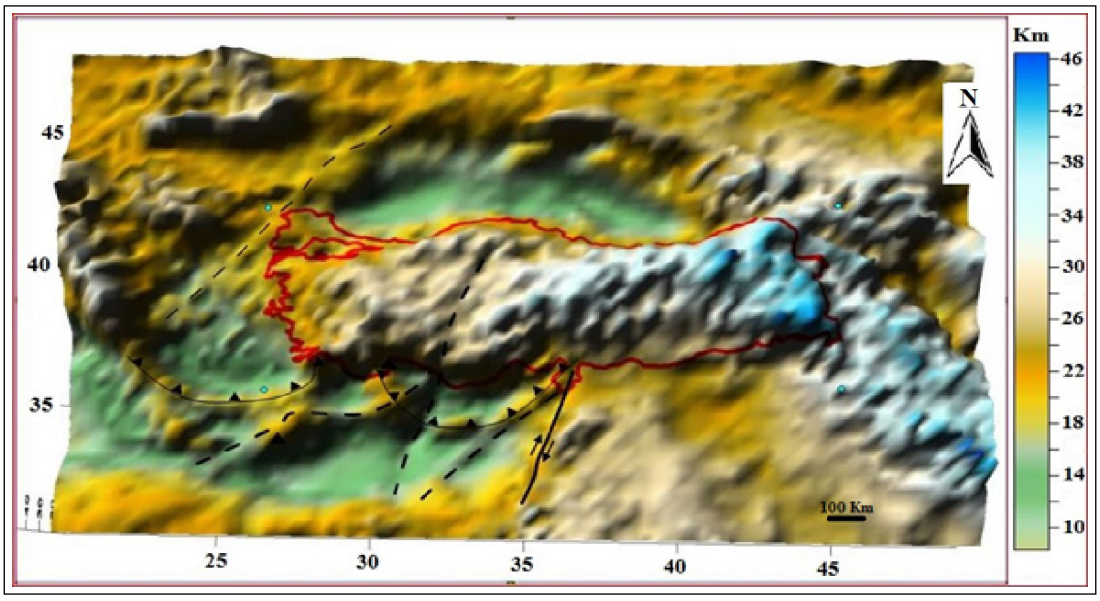


Figure 3- Regional crustal structure with Moho trend.

## 3. Results

Ergün et al. (2005) stated in their study that the boundary between the African plate and the Aegean/ Anatolian microplates is in the process of transition from subduction to collision along the Cyprus arc (Figure 4). The continuation of the movement is also the cause of current tectonic structures.

In the light of the tectonic elements described in Figure 4a, the findings in this study can be given in the following way.

In the Bouguer gravity map (Figure 1) high amplitudes, reaching 300-400 mgal intensities, define the marine area data (Herodotus Basin), and the light blue sections in the 0-75 mgal range define the terrestrial crust.

In dark blue structures, the resolution in gravity, which develops due to the elevation of the asthenosphere, decreases to the range of 50 – 100 mgal. This structure starts from Southern Anatolia, which is divided by the Aksu thrust, and extends to Iran. The deposition area of the Aegean graben system in front of the Aegean arc is separated from its surroundings with a value range of 200-300 mgal.

Both basins of the Black Sea are prominent (200-300 mgal) and host thick sedimentary sequences. With the proposed process steps, discontinuities in the density distribution in the Antalya Bay and Cyprus arc were also revealed. The projection of the dashed lines indicates the lost plate slice.

Figure 2 shows the UC map. Structural elements and tectonic traces become more evident when compared to the first map. The distinction observed in the Eastern Black Sea basins also emerges among other structural elements. When the Eastern Mediterranean is examined in terms of structural elements; Aegean arc, Cyprus arc and Anaximander uplift causing discontinuity between them are evident. In the Levantine Sea, the tectonic border has emerged between the Iskenderun Bay and the Nile delta in the northeast direction, where the Cyprus arc is tangent. The Dead Sea Transform Fault can be traced. The tectonic line extending at a steeper angle from the gulf to the 300$^{o}$ longitude of the Antalya slice, which is also highlighted by the earthquake foci, and the uplift between the Pliny and Strabo trenches were defined (Figures 4a and 4b). In the literature, Le pichon et al., (2019) stated that the Eastern Mediterranean is the continental lithosphere south of the Cyprus arc (Lebanon coast), Bouguer gravity data support this suggestion.

## 4. Discussion

The line connecting the Peloponnese Peninsula and Turkish Thrace border extends in the northeast

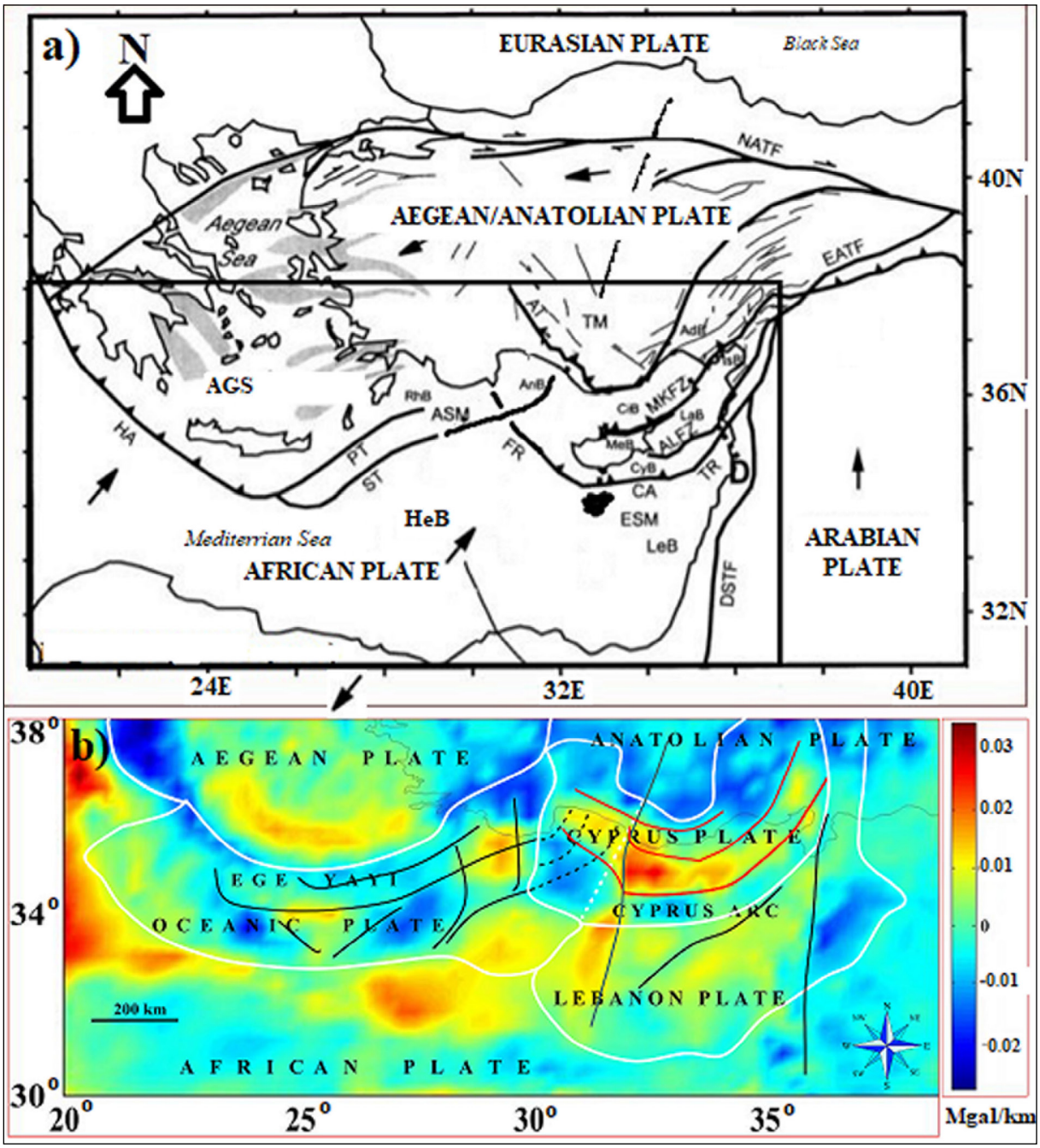


Figure 4- a) Main geological elements (structures) of the Eastern Mediterranean (modified from Ergün et al., 2005). Main geological elements of the Eastern Mediterranean (Figure 4) modified from Ergün et al., (2005); dark arrows show directions of plate movements. Shaded gray represent Aegean graben systems. Dark black area Eratosthenes seamounts. The main deformation axis is indicated by a sawtooth line. The nomenclatures are as follows. AdB, Adana Basin; AGS, Aegean Graben System; ALFZ, Amanos - Larnaca Fault Zone; AnB, Antalya Basin; ASM, Anaximander Seamount; AT, Aksu Thrust; CA, Cyprus spring; CiB; the Cilician Basin; CyB, Cyprus Basin; DSTF, Dead Sea Transform Fault. EATF, East Anatolian Fault; ESM, Eratosthenes Seamount; FR, Florence ascent; HA, Hellenic Arc, b) structural discontinuities.

direction and this may be a large-scale tectonic contact (Figure 3).

The Lebanese plate is divided into three parts by two NE directional tectonic lines starting from the West Nile Delta in the south of the Cyprus Arc (Figure 3).

Despite the intersecting appearance of the Cyprus Arc and the Antalya slice on the map, it can be predicted that they may be at different depths and that the Antalya slice will probably be deeper and cannot be observed on the surface in seismic tomography studies (Figure 4). Looking at the crustal structure of the Black Sea associated with Moho; It is thought that there may be a subduction from the Aegean Sea to the Black Sea in Western Thrace and this subduction is effective in the geological and tectonic evolution of Thrace (Figures 3, 4, 6). In the Central Black Sea, there are traces of plate-sized movements due to the effect of the Anatolian block under the compression effect regime.

Examination of the obtained results in terms of natural resources reveals the following results. The delta of the Danube covers a very deep mid-sea basin. In terms of geological history, even before the Danube river formed after the Pleistocene in the Western Black Sea region, there was sufficient depth for sedimentation and the formation of hydrocarbon reserves in this region (Figure 5).

The result of the boundary analysis performed with the standard deviation moving window filter (Toker, 2019) on the gravity data of the Black Sea region presented that the compression forms regional tectonic boundaries, including the edges of the western and eastern basins (Figure 6).

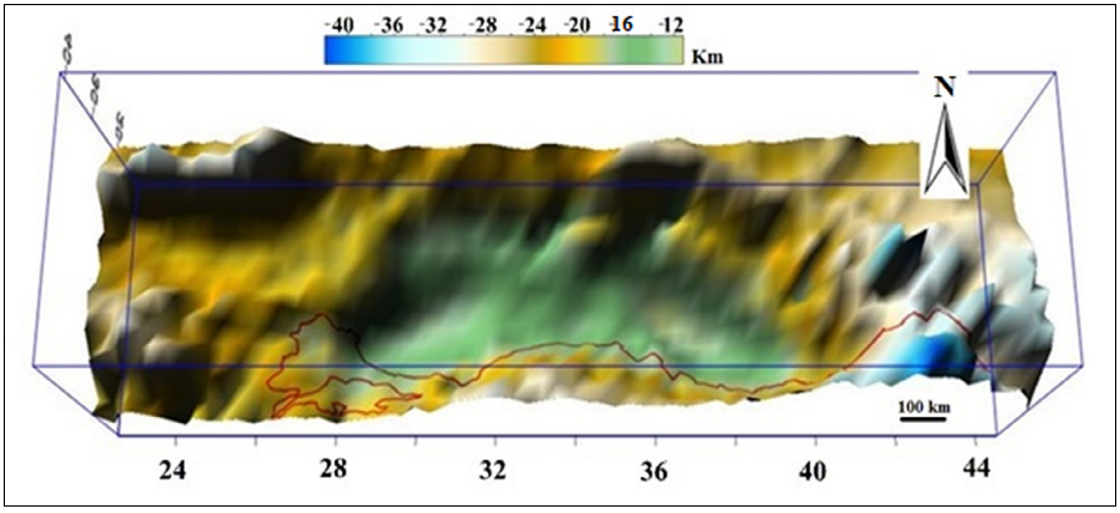


Figure 5 - Crustal structure of the Black Sea with Moho trend.

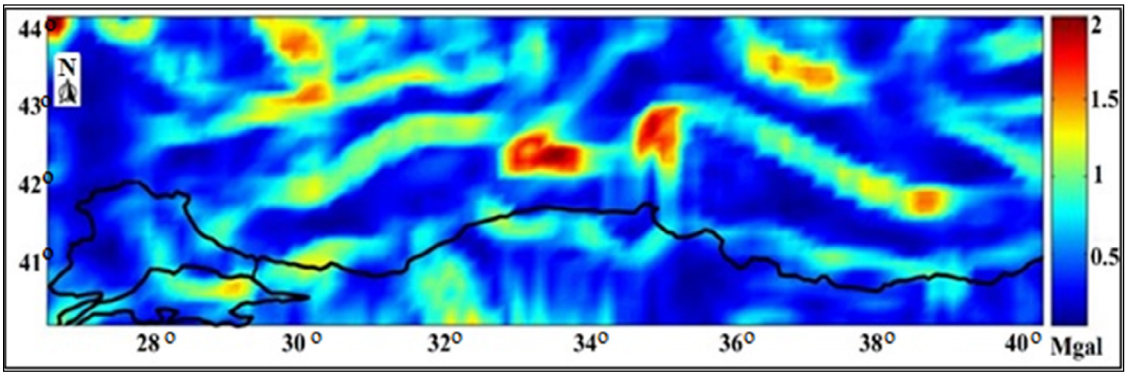


Figure 6 – The result of 2D standard deviation moving window filter.

Considering that the aforementioned reserve area is observed on a deeply integrated tectonic boundary, and considering that passive continental boundaries adjacent to the main ocean basins constitute one-third of the hydrocarbon basins in the world, the importance of imaging long-wavelength structure boundaries becomes clear (e.g. Mann et al., 2003).

Due to the compression of Central-North Anatolia, the perpendicular borders (valleys perpendicular to the sea) were formed at the base of the crust, and there are transition zones in the basins in front of these borders. We believe that these areas should also be investigated in terms of economic resources (Figure 5 and 6).

## 5. Results

In the study, regional structures were examined in the light of gravity data and boundary relations of large-scale structures were investigated. Considering the results of the hydrocarbon exploration studies carried out in the Western Black Sea Region, the regions within the exclusive economic zone where similar depths and associated average seismic velocities are expected should be investigated in detail.

This approach would also be appropriate for the Mediterranean. The locations of the basins that will provide sufficient depth can be mapped. However, thrusts within the stacks are an obstacle to carry out detailed studies.

## Acknowledgements

We thank Doç. Dr. Y. ERDOĞAN, General Manager of Mineral Research and Exploration, and the employees of the institution for providing the working conditions. We developed a computer program to calculate the depth at each gravity point using the depth transform. It can be obtained from the authors.

## References

BGI. Bureau Gravimetrique International. doi:10.18168/BGI.

Capponi, M., Sampietro, D. 2018. East Mediterranean Sea crustal structure from GOCE-based global gravity data. http://www3.ogs.trieste.it/gngts/files/2018/S31/Riassunti/Capponi..pdf (01.07.2021).

Ergün, M., Okay, S., Sarı, C., Oral, E. Z., Ash, M., Hall, J., Miller H. 2005. Gravity anomalies of the Cyprus Arc and their tectonic implications. Marine Geology 221, 349-358.

Gahagan, L., Gordon, M. B. 2003. In Halbouty, M. T. (Ed.). Giant oil and gas fields of the decade 1990-1999. American Association of Petroleum Geologistis Memoir 78, 15-105.

Pınar, R., Akçığ, Z., Özeren, H. A. 1994. Yukarı analitik uzanım yöntemi ile alçak geçişli süzgeçlerin eşlemesi. Jeofizik 8, 45-61.

Le Pichon, X., Şengör, A. C., İmren, C. 2019. A new approach to the opening of the eastern Mediterranean Sea and the origin of the Hellenic subduction zone. Part 2: The Hellenic subduction zone. Canadian Journal of Eart Sciences. Special Issue 1144,1162.

Toker, C. E. 2019. A brief note on the effects of floating standard deviation (non-derivative) and horizontal gradient (derivative) filters. Bulletin of Mineral Research and Exploration 159, 235-237.

Wollard, G. P., Strange, W. E. 1962. Gravity anomalies and crust of the earth 323 in the Pacific basin. In: The Crust of the Pacific Basin. Geophysical Monograph 324(6), 60-80.

## ACKNOWLEDGEMENT

We would like to thank to the honored reviewers whose names are written below by contributing to the Bulletin of the Mineral Research and Exploration during the article review process between 6th of December 2020 and 30th of November 2021 in the name of the Executive Publication Editorial.

Peyman AFZAL (IRANIAN)
Mutluhan AKIN (Nevşehir-TURKEY)
Jason Richard ALI (CHINA)
Murat ALKAN (İzmir-TURKEY)
Hamdi ALKAN (Van-TURKEY)
Fetullah ARIK (Konya-TURKEY)
Nicholas ARNDT (FRANCE)
Fırat ATALAY (Ankara-TURKEY)
Abdullah ATEŞ (Ankara-TURKEY)
Ahmet Deniz Baş (Muğla-TURKEY)
Özcan BEKTAŞ (Sivas-TURKEY)
Ansuya BHANDARI (INDIA)
Andrea Regina BIEDERMANN (SWITZERLAND)
Viviana BOLANOS BENITEZ (IRELAND)
Sonay BOYRAZ ASLAN (Ankara-TURKEY)
Gülcan BOZKAYA (Denizli-TURKEY)
Aydın BÜYÜKSARAÇ (Çanakkale-TURKEY)
Mustafa Can CANOĞLU (Sinop-TURKEY)
Ferdi CIHANGIR (Trabzon-TURKEY)
Atila Gürhan ÇELİK (Giresun-TURKEY)
Hasan ÇETİN (Adana-TURKEY)
Emin ÇİFÇİ (İstanbul-TURKEY)
Yahya ÇİFTÇİ (Ankara-TURKEY)
Okay ÇİMEN (Tunceli-TURKEY)
Attila ÇİNER (İstanbul-TURKEY)
Prentiss DE JESUS (USA)
Cengiz DEMİR (Trabzon-TURKEY)
Yılmaz DEMİR (Rize-TURKEY)
Mehmet Kürşat DİLMAÇ (Erzurum-TURKEY)
Nuri DOLMAZ (İzmir-TURKEY)
Derman DONDURUR (İzmir-TURKEY)
Cahit DÖNMEZ (Ankara-TURKEY)
Zafir EKMEKÇİ (Ankara-TURKEY)
Yaşar EREN (Konya-TURKEY)
İlker ERTEM (Ankara-TURKEY)
KORHAN ESAT (Ankara-TURKEY)
Ehsan FARAHBAKHSH (IRANIAN)
Neven GEORGIEV (BULGARIA)
Dave GILES (ENGLAND)
Cem GÖK (Denizli-TURKEY)
Tolga GÖNENÇ (İzmir-TURKEY)
Muhittin GÖRMÜŞ (Ankara-TURKEY)
Kary GREEN (USA)
Bahattin GÜLLÜ (Aksaray-TURKEY)
Bahattin GÜLLÜ (Aksaray-TURKEY)
Hakan GÜNEYLİ (Adana-TURKEY)
Alper GÜRBÜZ (Niğde-TURKEY)
Ömer Feyzi GÜRER (Kocaeli-TURKEY)
Zülfü GÜROCAK (Elazığ-TURKEY)
Alastair H. F. ROBERTSON (ENGLAND)
Nurullah HANİLÇİ (İstanbul-TURKEY)
Cahit HELVACI (İzmir-TURKEY)
Wentao HUANG (CHINA)
Yusuf Kağan KADIOĞLU (Ankara-TURKEY)
Hakan KARSLI (Trabzon-TURKEY)
Tanju KAYA (İzmir-TURKEY)
Erol KAYA (İzmir-TURKEY)
Caner KAYA ÖZER (Yozgat-TURKEY)
Nuretdin KAYMAKÇI (Ankara-TURKEY)
Nizamettin KAZANCI (Ankara-TURKEY)
Serdar KESKİN (Trabzon-TURKEY)
Sinan KOŞAROĞLU (Sivas-TURKEY)
Hülya KURŞUN (Sivas-TURKEY)
Tom LAMONT (İNGİLTERE)
Marco MAFFIONE (İNGİLTERE)
Michele MARRONI (ITALY)
Robert MARSCHIK (GERMANY)
Atike NAZİK (Adana-TURKEY)
Roland OBERHäNSLI (GERMANY)
Abdullah OBUT (Ankara-TURKEY)
Kemal Mert ÖNAL (Sivas-TURKEY)
Vehbi ÖZACAR (İzmir-TURKEY)
Reha ÖZEL (Ankara-TURKEY)
Çağlar ÖZKAYMAK (Afyon-TURKEY)
Serkan ÖZTÜRK (Gümüşhane-TURKEY)
Ali ÖZVAN (Van-TURKEY)
Oya PAMUKÇU (İzmir-TURKEY)
Luan PHAM (VIETNAMESE)
Ali POLAT (Sivas-TURKEY)
Tamer RIZAOĞLU (Kahramanmaraş-TURKEY)
Azad SAĞLAM SELÇUK (Van-TURKEY)
Salah SALEH (EGYPT)
Taylan SANÇAR (Tunceli-TURKEY)
Levent SELÇUK (Van-TURKEY)
Şeref SÖNMEZ (İstanbul-TURKEY)
Harun SÖNMEZ (Ankara-TURKEY)
Kemal TASLI (Mersin-TURKEY)
Senem TEKİN (Adıyaman-TURKEY)
Gültekin TOPUZ (İstanbul-TURKEY)
Ayşenur TUNCUK (Isparta-TURKEY)
Ahmet TURAN (İstanbul-TURKEY)
Ekrem TUŞAT (Konya-TURKEY)
Koray ULAMIŞ (Ankara-TURKEY)
Emin ULUGERGERLİ (Çanakkale-TURKEY)
Uğur ULUSOY (Sivas-TURKEY)
Mehmet UTKU (İzmir-TURKEY)
Bora UZEL (İzmir-TURKEY)
Anne VAN DE WEERD (HOLLAND)
Wilma WESSELS (HOLLAND)
Mark WILLIS (USA)
Azemeraw WUBALEM (ETHIOPIA)
Nail YILDIRIM (Elazığ-TURKEY)
Ayça YURDAKUL ÇIRMIK (İzmir-TURKEY)

## Publication Rules for the "Bulletin of the Mineral Research and Exploration"

### 1. Purposes

• To contribute to the establishment of scientific communication issues in earth sciences both in Turkey and internationally.

• To contribute to economic (mining, oil and gas, geothermal etc.), environmental and social (geoheritage etc.) studies in Turkey and in the World.

• To make the earth science scientific research and applications made by the MTA on publicly known,

• To use the bulletin as an effective tool in the international publication exchange by keeping it at a high level in terms of quality, scope and format,

• To contribute to the efforts of developing Turkish as a language of science and removing foreign words.

### 2. Scope-Attribute

In order for manuscripts to be published in the Bulletin of the Mineral Research and Exploration, they must have at least one of the following qualifications:

#### 2.1. Research Articles and Reviews

*2.1.1. Original Scientific Researches*

• Such articles cover original scientific research and its results that contribute to the fundamental issues of earth sciences, research and evaluation of underground resources, and examine the environmental problems in terms of earth sciences,

• It covers research that apply new approaches and methods in solving problems related to earth sciences.

*2.1.2. Review Articles*

• They cover studies that compile previous research on subjects of earth sciences with a critical approach and put forward a new opinion on that subject.

#### 2.2. Criticism and Response Articles

• Articles that criticize all or part of an article of the bulletin in the latest issue are published in the following first issue, if submitted within six months at the latest from the date of publication digitally.

• Before the publication, review articles are sent to the responsible author of the criticized article to make a response.

• If the criticism is not responded within foreseen time, the criticism letter is published alone, subsequent replies are not published. Replies are not allowed to be re-criticized.

• In criticizing and replying, scientific discussion and ethical rules should be followed. Criticism and response manuscripts should not exceed four pages, including figures, if available.

#### 2.3. Brief Notes

• In "Brief Notes" section of the Bulletin of the Mineral Research and Exploration, the brief, objective and concise articles reflecting the data obtained from scientific researches and applications carried out in the area of earth sciences or new findings related to previously unknown geosciences in Turkey are given place.

• The articles arranged in the "Brief Notes" section are published without waiting in the first or in the second issue the latest, after the date they are sent to the Chair of the Editorial Board in order to ensure rapid communication.

• Articles requested to be published in the "Brief Notes" section should not exceed four pages, including all figures and tables.

### 3. Submission and Acceptance for Manuscripts

• The manuscripts submitted to be published in the Bulletin of the Mineral Research and Exploration should be prepared in TURKISH and / or ENGLISH in accordance with the Publishing Rules of the Bulletin of the Mineral Research and Exploration, and submitted via electronic application at http://dergi.mta.gov.tr/index.php.

• The manuscript must not have been previously published partially or completely elsewhere (except in abstract form).

• Manuscripts submitted with the request for publication in the Bulletin of the Mineral Research and Exploration should not exceed 30 pages, including all illustrations. The articles exceeding 30 pages can be published if deemed appropriate by referees and editors.

• In the submitted manuscript, the number of figures and tables should be given in proportion to the main text in a ratio of 1/3.

• Corresponding author is asked to suggest at least three referees for the evaluation of the manuscript. (The proposed referees and the authors should not have any joint work within the last two years).

• Manuscripts that do not comply with the Publishing Rules for the Bulletin of the Mineral Research and Exploration in terms of quality and form are directly returned without being examined in terms of content.

• Manuscripts deemed appropriate in terms of format are sent to at least two expert referees for review by the Editorial Board of the Bulletin of the Mineral Research and Exploration.

• Authors should make the referee corrections and suggestions sent to them within 20 days and upload to the system.

• Comments from referees are evaluated by the Editors and associated editors. Manuscripts deemed necessary to be corrected are sent back to the authors with a request for correction. Whether the suggested corrections have been made or not is checked by the Editorial Board.

• In the revision proposals given by the editors and referees, if there are suggestions that are not accepted by the author and have not been corrected, a report explaining the reason for rejecting these suggestions by the author should be sent to the Editorial Board together with the corrected copies.

• After the last control at the printing stage, the pre-print of the manuscript is sent to the authors in pdf format and the printing control is requested.

• Articles, not accepted for publication are not returned to the authors, for the unpublished articles, a letter is written to the responsible author indicating the reason for rejection.

**4. Language and Period of Publication**

• The Bulletin of the Mineral Research and Exploration is published three times a year, each issue as being in Turkish and the other in English languages.

• The spelling rules of the Turkish Language Association are valid for the spelling rules for the Turkish issue. However, in spelling of the words related to earth sciences, the spelling forms of technical terms are used in accordance with the decision of the Editorial Board (For example; underground, ground, earth's crust, etc.).

**5. Spelling Draft**

• The text of the manuscripts to be sent for the first review with the request to be published in the Bulletin of the Mineral Research and Exploration should be written in A4 (29.7 x 21 cm) size, word format, Times New Roman 10 pt., normal with 2.0 line spacing.

• At the bottom, top, left and right of the page 2.5 cm indent must be left. Formulas that require the use of special letters and symbols should be presented in computer media.

• In all subtitles, the initials of all words must be capital. First degree headings to be used in the article should be written in Times New Roman, 10 pt., bold and left aligned by giving numbers. Secondary headings should be written in Times New Roman, 10 pt., normal font and left aligned by giving numbers. Third-degree headings should be written in Times New Roman, 10 pt., italic font and left-aligned by giving numbers. Fourth-order headings should be written in Times New Roman, 10 pt., italic, aligned to the left, without giving numbers, and the text should continue after the title without a colon and a paragraph (see example article: www.dergi.mta.gov.tr).

• One blank line should be left after paragraphs in the text.

• Paragraph headings should be written 0.5 mm indentation.

• One article should respectively contain;

-Title

-Author's Name and Surname and * sign

- Abstract

- Key words

- Introduction

- Main Text

- Discussion

- Results

- Acknowledgements

- Reference sections.

• Line and page numbers must be added to the article text.

### 5.1. Title of the Article

• The title should reflect the subject of the article as briefly, clearly and adequately as possible. Subjects that are not sufficiently covered in the article should not be included in the title. The first letter of the title should be capitalized and the other words should be in lowercase letters (except for proper names) in Times New Roman, 10 pt. and bolded.

### 5.2. Author Name, Address and E-Mail Address

• The first name of the authors should be in lowercase (except the first letter), and the surname should be in capital letter and without any title.

• Only the name of the organization should be specified in the occupational address after the name and surname of the authors (position should not be specified).

• ORCID number should be taken from www.orcid.org and placed under the address.

• In articles written by more than one author, numbers should be placed on surnames of the authors, the address information should be included in the bottom line with a single line spacing. In this section, the corresponding author of the article should be indicated by using an asterisk (*) and the corresponding author's e-mail, telephone and other contact information must be provided.

• Abbreviations should not be used in writing the author's name and address. Addresses should be given in Turkish in Turkish publication and in English in English publication.

### 5.3. Abstract

• Abstract should be written at a level that can be understood without referring to the other parts of the article.

• The abstract should be organized as a brief presentation of the sections in the article, reflect the purpose of the article, be informative, and should be written in a way to emphasize new data and results on the subject.

• Short and simple sentences should be used in writing the abstract.

• In the abstract, there should not be any reference to other parts and illustrations of the article or to other articles.

• Information not mentioned in the main text should not be included in the abstract.

• The abstract should not exceed approximately 200 words and should be written as a single paragraph.

• Abstract should be written in Times New Roman, 10 pt., normal text with single line spacing.

• "ABSTRACT" should not be placed for the articles to be included in "Brief Notes" section.

• The English abstract should be given under the heading "ABSTRACT".

### 5.4. Key words

In order to facilitate searches, five keywords that will indicate the general content of the article should be selected and specified in this section. Words used in the title should not be repeated.

### 5.5. Introduction

• In this section, the necessary information for preparatory and facilitative to understand the article such as the purpose of the study, its location, methods of study and previous reviews on the subject should be given.

• If an unusual way is followed in naming, classification and abbreviations within the text of the manuscript, its reason should be stated in this section.

• Each of the topics to be included in this section can create a separate paragraph or a subtitle can be given for each of them when necessary (e.g. method, material, terminology and etc.).

• This section can again be used when reminder information is needed to facilitate the understanding of the article (e.g. statistical information, formulas, experimental or application methods and etc.).

### 5.6. Main Body of Article

• Constitutes the main body of the article.

• In this section, the data, findings and opinions that are intended to be transferred to the reader on the subject are mentioned.

• The data used in other parts of the article such as "Abstract", "Discussions", "Results" originate from this part.

• Care should be taken not to deviate from the purpose

stressed in the "Introduction" section of the article when dealing the topics. Information that does not contribute to the achievement of the purpose of the article or that is not used to reach the conclusion should not be included.

• All data used in this section and all opinions put forward should be proven by the findings obtained from the studies or based on a source by reference.

• The way and method to be followed in handling the topics vary according to the characteristics of the topics covered.

• Subject headings in necessary numbers with different stages should be used in this section.

**5.7. Discussions**

• The data and findings objectively conveyed in the "Main Text" section of the article should be discussed by the author in this section. Discussions should be separate from the "Results" section.

**5.8. Results**

• New data and findings obtained from the review that constitutes the subject of the article should be stated concisely and concretely in this section.

• Subjects that are not adequately addressed and / or covered in the main text should not be included in this section.

• The results can be given as items in order to emphasize the research results and make the expression understandable.

**5.9. Acknowledgements**

• In this section, important contributions in the realization of the study, which is the subject of the article, are indicated. An attitude that will distract this section from its main purpose should not be taken in the Acknowledgements.

Contribution should be stated as short and concise as possible to the persons and/or organizations that provided assistance (reading, writing, language assistance, etc.) during the research, and should not take an attitude that would distract this section from its main purpose.

**5.10. References**

• In this section, only the documents mentioned in the article should be included in complete.

• Abbreviations should be avoided in naming the publications and journals.

• The mentioned documents should be written in Times New Roman and 9 pt.

• The first line of the references should be written as justified to the left margin of the page, and the other lines should be written by giving a hanging indent value of 1.25.

• The references should be listed in alphabetical order, taking into account the surnames of the authors.

• If one author has more than one work in the same year, lowercase alphabet letters should be used right after the year of publication and the letters should be italic (e.g. Saklar, 2011*a, b*).

• If more than one document of the same author is cited, first his / her single-name publications in chronological order, then double-names according to the second author's surname in chronological order, and then multi-names according to the alphabetical order of the authors' surnames and publication year should be given.

***For example:***

Corradini, C. 2007. The conodont genus Pseudooneotodus Drygant from the Silurian and Lower Devonian of Sardinia and the Carnic Alps (Italy). Bollettino-Societa Paleontologica Italiana 46 (2/3), 139-148.

Corradini, C., Corriga, M. G. 2010. Silurian and lowermost Devonian conodonts from the Passo Volaia area (Carnic Alps, Italy). Bollettino della Società Paleontologica Italiana 49 (3), 237-253.

Corradini, C., Corriga, M. G. A. 2012. Pridoli – Lochkovian conodont zonation in Sardinia and the Carnic Alps: implications for a global zonation scheme. Bulletin of Geosciences 87 (4), 635-650.

Corradini, C., Serpagli E. 1999. A Silurian conodont biozonation from late Llandovery to end Pridoli in Sardinia (Italy), In Serpagli (Ed.), Studies on conodonts: Proceedings of the 7th European Conodont Symposium. Bollettino della Società Paleontologica Italiana 37 (2-3) (1998), 255-273.

Corradini, C., Corriga, M. G., Männik, P., Schönlaub, H. P. 2015. Revised conodont stratigraphy of the Cellon section (Silurian, Carnic Alps). Lethaia 48 (1), 56-71.

Corradini, C., Leone, F., Loi, A., Serpagli, E. 2001.Conodont Stratigraphy of A Highly Tectonised Silurian-Devonian Section in The San Basilio Area (Se Sardinia, Italy). Bollettino Della Societa Paleontologica Italiana 40 (3), 315-323, 1 Pl.

Corradini, C., Pondrelli, M., Serventi, P., Simonetto, L. 2003. The Silurian cephalopod limestone in the Monte Cocco area (Carnic Alps, Italy): conodont biostratigraphy. Revista Española de Micropaleontologia 35 (3), 285-294.

• If documents of different authors with the same surname are mentioned, they should be written in alphabetical order, considering their first names.

• If the document is in a periodical publication (if it is an article), information about the document is given in the following order: Authors ' surname, first letters of the authors' first names. Year of publication. The name of the article. The name of the publication in which the article was published, volume number and / or issue number with the first letters in capital, the numbers of the first and last page of the document. Punctuation marks like comma and etc. after journal names should not be used.

• In the examples below, the information about the mentioned documents is organized according to different document types, taking into account the punctuation marks.

***For example:***

Gürsoy, M. 2017. Munzur Dağları Alt Miyosen çökelleri mollusk topluluğu ve paleoekolojisi (Doğu Anadolu, Türkiye). Maden Tetkik ve Arama Dergisi 155, 75-99.

Pamir, H. N. 1953. Türkiye'de kurulacak bir Hidrojeoloji Enstitüsü hakkında rapor. Türkiye Jeoloji Bülteni 4, 1, 63-68.

Robertson, A. H. F. 2002. Overview of the genesis and emplacement of Mesozoic ophiolites in the Eastern Mediterranean Tethyan region. Lithos 65, 1-67.

• If the document is a book: authors' surnames, authors' first names. Year of publication. Title of the book with capital letters. The name of the publishing organization or the name of the publication in which the document was published, the volume and / or issue number, and the total number of pages of the book should be specified, respectively.

***For example:***

Einsele, G. 1992. Sedimentary Basins. Springer Verlag, 628.

Ketin, İ., Canıtez, N. 1956. Yapısal Jeoloji. İTÜ, 308.

Meriç, E. 1983. Foraminiferler. Maden Tetkik ve Arama Genel Müdürlüğü Eğitim Serisi, 26, 280.

• If the document is published in a book containing the articles of various authors, the usual order for the document included in a periodical publication is followed until the end of the document title. Then the editors' surnames and initials and the abbreviation of the editor word "Ed." is written in parentheses. Then, the title of the book in which the document is located is written with the first letters in capital letters. Name of publishing organization. The place of publication, the volume number of the publication in which the document was published, and the numbers of the first and last pages of the document should be written.

***For example:***

Anderson, L. 1967. Latest information from seismic observations. Gaskell, T. F. (Ed.). The Earth's Mantle. Academic Press. London, 335-420.

Göncüoğlu, M. C., Turhan, N., Şentürk, K., Özcan, A., Uysal, S., Yalınız, K. 2000. A geotraverse across northwestern Turkey. Bozkurt, E., Winchester, J. A., Piper, J. D. A. (Ed.). Tectonics and Magmatism in Turkey and the Surrounding Area. Geological Society of London. Special Publication, 173, 139-162.

• If it is desired to specify the name of a book in which the writings of various authors are collected as a document; following the surnames and names of the book's editors, in parentheses the "Ed." statement is written. Year of publication. Title of the book with capital letters. The name of the publishing organization or the name of the publication in which the document was published, the volume and / or issue number and the total number of pages of the book should be specified.

***For example:***

Gaskel, T. F. (Ed.). 1967. The Earth's Mantle. Academic Press, 520.

• If the document is "published abstract", information about the document is given in the following order: Authors' surnames, authors' first names. Year of publication. Name of the document (paper). The name, date and place of the meeting where the paper is published, and the first and last page numbers in the book containing the abstract should be written.

***For example:***

Öztunalı, Ö., Yeniyol, M. 1980. Yunak (Konya) yöresi kayaçlarının petrojenezi. Türkiye Jeoloji Kurumu 34. Bilim Teknik Kurultayı, Ankara, 36.

Yılmaz, Y. 2001. Some striking features of the Anatolian geology. 4. International Turkish Geology Symposium, 24-28 Eylül 2001, Adana, 13-14.

• If the mentioned document has not been published like report, lecture notes and etc., the word "unpublished" should be written at the end of the information about the document in parentheses after the information about the document is given in the usual order for the document in a periodical publication.

***For example:***

Akyol, E. 1978. Palinoloji ders notları. EÜ Fen Fakültesi Yerbilimleri Bölümü, 45, İzmir (unpublished).

Özdemir, C., Biçen, C. 1971. Erzincan ili, İliç ilçesi ve civarı demir etütleri raporu. Maden Tetkik Arama Genel Müdürlüğü, Rapor No: 4461, 21, Ankara (unpublished).

• For unpublished courses, seminars and similar notes, the course organizer after document name. The place of the meeting. Title of the book and relevant page numbers should be given.

***For example:***

Walker, G.R., Mutti, E. 1973. Turbidity facies and facies associations. Society for Sedimentary Geology Pacific Section Short Course. Annaheim. Turbitides and Deep Water Sedimentation, 119-157.

• If the document is a thesis; author's surname, initial of the author's first name. Year of publication. Name of the thesis. The type of the thesis, the university where it was given, the total number of pages, its province and the word "unpublished" are written in parentheses.

***For example:***

Akıllı, H. 2019. Polatlı-Haymana (Ankara) civarı sıcak sularının izotop jeokimyası (δ18O, δD, 3H, δ13C, δ34S, 87Sr/86Sr) ve ana iz element bileşimleri ile incelenmesi. PhD Thesis, Ankara University, 255, Ankara (unpublished).

Argun Aktan, Ö. 2019. Marmara Denizi Batı Kıta Sahanlığı Yüzeysel Çökellerinde Jeojenik ve Antropojenik Ağır Metal Zenginleşmesine Yönelik Araştırmalar (Şarköy Kanyonu, KB Türkiye). MSc Thesis, Ankara University, 179, Ankara.

• Anonymous works should be arranged according to the publishing institution.

***For example:***

MTA. 1964. 1/500.000 ölçekli Türkiye Jeoloji Haritası, İstanbul Paftası. Maden Tetkik ve Arama Genel Müdürlüğü, Ankara.

• For the documents that are in print, no date is put after the name of the author, the name of the article and the source to be published should be specified and the word "in print" and / or "in review" should be written at the end (in parentheses).

***For example:***

Ishihara, S. The granitoid and mineralization. Economic Geology 75$^{th}$ Anniversary (in press).

• Information downloaded from the Internet should be given in the form of the name of the institution, its web address, and the date on which the web address was accessed. Turkish references should be given directly in Turkish and should be written in Turkish characters.

***For example:***

ERD (Earthquake Research Department of Turkey). http://www.afad.gov.tr. 3 March 2013.

• While citing the source, the original language should be adhered to, and the title of the article should not be translated.

**6. Illustrations**

• All of the drawings, photographs, plates and tables used in the article are referred to as "illustrating".

• Illustrations should be used when their use is unavoidable or when they make the subject easier to understand.

• In the selection and arrangement of the format and size of the illustrations, an attitude should be made to prevent loss of space as much as possible considering the page length and layout of the bulletin.

• The number of illustrations used should be proportional to the size of the text.

• All illustrations should be submitted in separate files regardless of the text.

• Abbreviations should not be used in illustration explanations in the text and should be numbered in the order of mention within the text.

• Photographs and plates must be submitted as a computer file in which all details can be seen for the examination of the article, with EPS, TIFF or JPEG extension and at least 300 dpi resolution.

### 6.1. Figures

• Drawings and photographs other than the plate to be included in the article are evaluated together as "Figure" and numbered in the order of mention in the text.

• The figures should be prepared in computer considering the dimensions of a single column width as 7.4 cm or double column width as 15.8 cm. The figure area with its caption should not exceed 15.8x21 cm.

• While preparing the figures, unnecessary details should not be included and care should be taken not to use more space than necessary for the transfer of information.

• In figure descriptions, a space should be left after the word "Figure" is written, and the number is given in the usual sequence number, followed by a hyphen (-) and a space again, and a description of the relevant figure should be written. If the figure legend exceeds the bottom lines, the following lines should to be written after the "Figure 1-" statement alignment. Figure descriptions should be created as follows, without exceeding the edges of the figure and justified on both sides.

***For example:***

Figure 1- The district of Sandıklı (Afyon); a) geological map of the southwest, b) the general vertical section of the study area (Seymen, 1981), c) Turkey's most important neotectonic structures (modified from Koçyiğit, 1994).

• Drawings should be drawn in computer properly, clean and with care.

• The use of thin lines that may disappear when minimized in figures should be avoided.

• Symbols or letters used in all drawings should not be less than 2 mm (7 pt.) in Times New Roman.

• All standardized symbols used in the drawings should preferably be explained in the drawing, if they are too long then they should be explained in the figure below.

• Bar scale should be used in all drawings and the north direction should be indicated on all maps.

• The name of the author, description of the figure, figure number should not be included in the drawing.

• Photographs should reflect the aims of the subject and should be in adequate numbers.

• Figures should be framed.

### 6.2. Plates

• Plates should be used in cases where multiple photographs are required to be printed together on a special paper.

• Plate dimensions must be equal to the size of the bulletin's usable area of the page.

• Figure numbers should be written under each of the figures on the plate and bar scale should be used.

• Original plates must be attached to the final copy to be submitted in the case of acceptance of the manuscript.

• Figures and plates should be numbered among themselves and independently. Figures should be numbered with Latin numerals and plates with Roman numerals (eg Figure 1, Plate I).

• There should be no explanation text on the figures inside the plate.

### 6.3. Tables

• All tables should be arranged in word format and should be prepared in Times New Roman.

• Tables should not exceed the size of 15x8 cm together with the table caption.

• Table explanations should be created without exceeding the edges of the figure and justified as in the example below.

***For example:***

Table 1- Hydrogeochemical analysis results of geothermal waters in the study area.

**7. Nomenclature and Abbreviation**

• Abbreviations must be in the accepted international or national form. Unusual nomenclature and abbreviations that are not standardized in the article should be avoided. In cases where it is deemed necessary to use such nomenclature and abbreviations, the way and method followed should be explained.

• There should not be a dot between the words initials used in standard abbreviations (such as MTA, DSİ).

• Abbreviations of geography aspects should be made in English (N, S, E, W, NE and etc.).

The word group to be abbreviated should be written clearly where it is mentioned first time and the abbreviation should be given in parentheses, then only the abbreviated form should be written throughout the article.

• Systems with international validity (m, inch, etc.) should be used as the unit of measure. Decimals should be separated with commas in Turkish articles and with a period in English articles.

• The names of figures, plates and tables in the article should not be abbreviated. For example, "As seen in the generalized stratigraphic section of the region (Figure 1) …….".

**7.1. Stratigraphic Nomenclature**

• Stratigraphic nomenclature should be done in accordance with the Stratigraphical Classification and Nomenclature Rules prepared by Turkey Stratigraphy Committee (TSC).

(https://www.mta.gov.tr/v3.0/sayfalar/birimler/belgeler/Stratigrafi_adlama_kurallari.pdf )

• Attention should be paid to the use of formation names accepted (formalized) by the TSC. If the formation name used is official, the letter "F" should be capitalized, and if it is informal and plural, the letter "f" should be written in lowercase. For example; Bostancı Formation (formal), Kaynarca formation (unofficial), Baltalimanı, Trakya and Tarlaağızı formations (plural).

**7.2. Chronostatigraphic and Geochronologic Nomenclature**

• "International Chronostratigraphic Chart" (https://stratigraphy.org/chart), which is updated annually by the International Stratigraphic Committee, should be taken into consideration in chronostratigraphic and geochronological nomenclature.

• Position within a chronostratigraphic unit can be expressed in adjectives indicating the position, for example: lower, middle, upper and etc. When using these adjectives, it should be decided whether the lower, middle and upper distinction is formal / informal in the International Chronostratigraphic Chart.

***For example:***

lower Miocene, Upper Holocene and etc.

• When stating the time where a geochronological unit is, temporal adjectives such as; early, middle, late and etc. are used. When using these adjectives, the International Chronostratigraphic Chart should be taken into consideration to decide whether the adjectives begin with capital or lowercase letters.

***For example:***

early Miocene, Late Holocene etc.

**7.3. Paleontological Nomenclature and Spelling of Fossil Names**

• Original names of fossils should be used.

***For example:***

*Nummulites* with limestone

• Fossil genus and species names are written in italics, cf., aff. and gr. etc. expressions are written as normal (perpendicular). When writing fossil names for the first time, the surnames of the people who identify them and the year in which they were first defined should be written. In later uses, the surnames and the year in which they are defined may not be written. The surnames and dates of identifiers coming at the end of the fossil names are not references, they should not be included in the mentioned documents.

***For example:***

*Alveolina aragonensis* Hottinger, 1960 not a reference.

*Alveolina* cf. *aragonensis* Hottinger, 1960 not a reference.

*Alveolina* aff. *aragonensis* Hottinger, 1960 not a reference.

*Alveolina* gr. *aragonensis* Hottinger, 1960 not a reference.

• After the first use of the same genus in the text is written clearly, it can be abbreviated as in the example so that it will not be confused with another genus in later use.

***For example:***

*Alveolina aragonensis, A. polathensis, A. ellipsoidalis* etc.

• If the date is in parentheses after the person describing it after the name of the fossil in the text, this is a reference and should be included in the mentioned documents.

***For example:***

*Alveolina aragonensis* Hottinger (1960) is a reference.

• The following rules should be taken into account when writing the systematic paleontologic section.

a. First of all, genus, species and subspecies to be identified should be written in hierarchical order like the order, upper family, family type species and so on. Later, the species to be described should be written together with the surnames and date of the people who defined the subspecies name. If there is a photograph of the described fossil, the plate or figure with the photograph should be added under the fossil name. The names of the authors listed here are not references, so they are not included in the reference.

***For example:***

Order: Foraminiferida Eichwald, 1830

Superfamily: Alveolinacea Ehrenberg, 1839

Family: Alveolinidae Ehrenberg, 1839

Type Genus: *Borelis* de Montfort, 1808

Type Species: *Borelis melenoides* de Montfort, 1808
= *Nautilus melo* Fichtel and Moll, 1798

*Borelis vonderschmitti* (Schweighauser, 1951)

(Plate II, Figure 3-5 or Figure 3A-H).

b. Similar or synonyms (synonym) list should be left-aligned in chronological order. The page and figure number of the synonymous fossil in the relevant study should be included in the synonymous list. Authors in the synonymous list are references and must be included in the references.

***For example:***

**1951** *Neoalveolina vonderschmitti* **Schweighauser**, page 468, figures 1-4.

**1974** *Borelis vonderschmitti* (Schweighauser), **Hottinger**, page 67, plate 98, figures 1-7.

c. After the synonymous list is given, the definition, explanations (similarities and differences), dimensions, material, stratigraphic distribution (according to the characteristics of the fossil) should be written.

d. If the fossil is defined for the first time (new species) in the systematic paleontology section, the origin of the name, holotype, type locality, material, description, explanation (similarity and differences), age and geographical distribution, dimensions (according to the features that define the fossil) should be written. Photographs of the fossil identified for the first time by the authors must necessarily be placed in plates or figures.

e. Bar scale indicating the size of fossils must be used definitely in plates / figures.

## 8. References

• In the references to be made in the Main Text, only the surnames of the authors and the publication year of the mentioned article should be specified. Referencing should be arranged according to one of the following examples:

• Referring to a publication with a single author (in chronological order):

-Altınlı (1972, 1976) defined the Bilecik sandstone in detail.

It is known that the fold axes of the Devonian and Carboniferous units around İstanbul are N-S trending (Ketin, 1953, 1956; Altınlı, 1999).

• Referring to a publication with two authors:

- The upper parts of the unit include Ilerdian fossils (Sirel and Gündüz, 1976; Keskin and Turhan, 1987, 1989).

• Referring to a publication with more than two authors:

- According to Caner et al. (1975), the Alıcı formation reflects the conditions of fluvial environment.

- Unit disappears by wedging towards E (Tokay et al., 1984).

• Referring to a reference in another publication:

It is known that Lebling mentioned about the existence of Liassic around Çakraz (Lebling, 1932; Charles, 1933).

• When referring to the works of the authors with the same surname in the same year, referring the authors' first names by writing their initials:

- Many studies have been done in the field of structural geology in the study area (Gutnic et al., 1979; Yılmaz A., 1983; Yılmaz, İ., 1983; Poisson et al., 1984 etc.).

**9. Prints Sent to Authors**

Two copies of the relevant issue published in the Bulletin of the Mineral Research and Exploration are sent to the authors.

**10. Terms of Publication and Copyrights**

• Some or all of the articles to be published in the Bulletin of the Mineral Research and Exploration should not have been published before.

• Authors who submit a publication to the Bulletin of the Mineral Research and Exploration are deemed to have accepted the bulletin's publication rules in advance.

• The copyright of the manuscripts accepted for publication and converted into publications belongs to the General Directorate of Mineral Research and Exploration (MTA).

The authors of the study sign the relevant forms within the scope of the provisions specified in the Regulation of the Editorial Board regarding the transfer of copyright and submit them to the Editorial Board. After the publication of the article, MTA may pay royalty fees to the authors of the article for their declarations within the scope of the "Regulation on the Editorial and Processing Fees to be paid by the Public Organizations and Institutions".

NOTE: Information and forms about Bulletin of the Mineral Research and Exploration can be accessed from the website: http://dergi.mta.gov.tr/index.php.